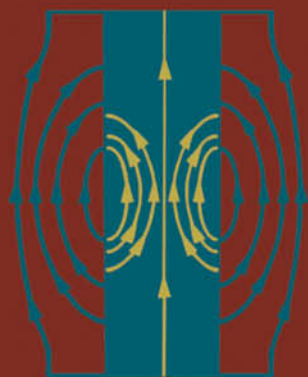


Handbook of Microwave Technology

VOLUME I

Components and Devices



Edited by
T. Koryu Ishii



**Handbook of
Microwave Technology**

VOLUME I

This Page Intentionally Left Blank

Handbook of Microwave Technology

VOLUME I

Components and Devices

Edited by

T. Koryu Ishii

*Department of Electrical and Computer Engineering
Marquette University
Milwaukee, Wisconsin*



ACADEMIC PRESS

San Diego New York Boston London Sydney Tokyo Toronto

This book is printed on acid-free paper. ☺

Copyright © 1995 by ACADEMIC PRESS, INC.

All Rights Reserved.

No part of this publication may be reproduced or transmitted in any form or by any means, electronic or mechanical, including photocopy, recording, or any information storage and retrieval system, without permission in writing from the publisher.

Academic Press, Inc.

A Division of Harcourt Brace & Company
525 B Street, Suite 1900, San Diego, California 92101-4495

United Kingdom Edition published by
Academic Press Limited
24-28 Oval Road, London NW1 7DX

Library of Congress Cataloging-in-Publication Data

Handbook of microwave technology / edited by T. Koryu Ishii.

p. cm.

Includes index.

Contents: v. 1. Components and devices -- v. 2 Applications.

ISBN 0-12-374696-5 (v. 1). -- ISBN 0-12-374697-3 (v. 2)

1. Microwave devices--Handbooks, manuals, etc. I. Ishii, T.

Koryu (thomas Koryu), date.

TK7876.H345 1995

621.381'3--dc20

94-48777

CIP

PRINTED IN THE UNITED STATES OF AMERICA

95 96 97 98 99 00 MM 9 8 7 6 5 4 3 2 1

Contents of Volume I

Contributors xxxix

Preface xl

CHAPTER I

Microwave Transmission Lines

P. Pramanick and P. Bhartia

1. Introduction to Transmission Lines	1
Transmission Line Equations	1
2. Two-Wire Line	2
3. Coaxial Lines	5
Q-Factor of Coaxial Lines	7
Modes in a Coaxial Line	9
Other Forms of a Coaxial Line	11
A General Equation for Attenuation in Two-Wire and Coaxial Lines	12
4. Waveguides	13
Rectangular Waveguide	14
Circular Waveguide	22

5. Finlines	28
Propagation Constant	29
Characteristic Impedance	33
Losses	34
6. Dielectric Waveguides	34
Propagation Constant	35
Losses in Dielectric Waveguides	38
Characteristic Impedance of Imageguides	42
Other Forms of Dielectric Waveguide: Trapped Image Guides	43
References	45

CHAPTER 2

Microstrip Lines

J. K. Kwon

1. Microstrip Lines	47
Materials	47
Static TEM Parameters	48
Analysis Formulas [1 – 3]	49
Synthesis Formulas [2, 3, 5]	50
Effects of Conductor Thickness [6]	50
Dispersion [7, 8]	50
Losses in a Microstrip Line [9]	51
Effect of Enclosure [10]	52
2. Microstrip Discontinuities	53
Open-End	53
Gap in a Microstrip [11]	54
Transverse Split [12]	55
Steps in Width [13]	55
Right-Angled Bend [14]	56
T-Junction [11]	57
Cross Junction [15]	58
References	59

CHAPTER 3
Microwave Resonators

Robert A. Strangeway

1. Resonator Basics	61
One-Port Reflection Resonator	61
Two-Port Transmission Resonator	63
Skin Depth, δ	65
2. Two-Wire Line Resonators	65
3. Basic Coaxial Resonators	66
Foreshortened Coaxial Line Resonators (Reentrant Coaxial Cavity Resonators)	67
4. Rectangular Waveguide Cavities	68
5. Circular Cylindrical Waveguide Cavities	73
6. Spherical Cavities	80
7. Dielectric Resonators	80
8. Loop – Gap Resonators	83
One Loop – n Gap Resonator	83
Two Loop – One Gap Resonator	84
9. Microstrip Resonators	85
Microstrip Rectangular Resonators	85
Microstrip Circular Resonators	86
Microstrip Ring Resonators	87
10. Fabry – Perot Resonators	88
11. YIG Resonators	89
12. Traveling-Wave Resonators	90
References	91

CHAPTER 4
Microstrip Line Components

R. K. Hoffmann

1. Introduction	95
2. Straight Planar Ribbon Inductor	96
Straight Metal Strip in Free Space	96

Metal Strip on a Substrate without Ground Metallization	98
Metal Strip on a Substrate with Ground Metallization	98
3. Round Wire Inductor	99
Single Round Wire in Free Space	99
Round Wire above a Conducting Plane	100
4. Planar Ring Inductors	101
Rectangular Ring	101
Circular Ring	103
5. Planar Circular Spiral Inductor	103
General Construction of Spiral Inductors	104
Spiral on a Substrate without Ground Metallization	105
Spiral on a Substrate with Ground Metallization	107
6. Planar Rectangular and Square Spiral Inductors	107
General Construction of the Spiral	108
Spiral on a Substrate without Ground Metallization	109
Spiral on a Substrate with Ground Metallization	111
7. Planar Dielectric – Film Overlay Capacitors	111
Construction	112
Technology	112
General Electrical Properties for Arbitrary Loss and Arbitrary Frequency	112
Electrical Properties for Low Frequency, Low Dielectric Loss, and Arbitrary Conductor Loss	114
8. Microstrip Disk Capacitors	115
Circular Disk Capacitor	115
Rectangular Disk Capacitor	116
9. Microstrip Series Gap Capacitor	118
Type of Series Gap Capacitors	119
Symmetrical Gap	119
Asymmetrical Gap	120
10. Open-Ended Microstrip	121
11. Microstrip Short Circuits	122
Round Shorting Metal Post	124
Equivalent Circuits	124
Electrical Properties of a Round Metal Post	124
Alternative Short Circuit Shapes	126

12. Step Changes in a Strip Conductor Width of Microstrip Lines (Impedance Steps)	127
13. Right-Angled Bends of Microstrip Lines	128
Nonchamfered Symmetric Bend	129
Chamfered Symmetrical Bend	130
14. Absorbing Microstrip Terminations	131
Overview	131
Direct Grounded Lumped Terminations	132
Virtual Grounded Lumped Terminations	134
Distributed Terminations	135
15. Coaxial-to-Microstrip Transitions	136
Basic Construction	136
Electrical Model	136
Alternative Types	138
References	138

CHAPTER 5

Microstrip Line Components: Suspended-Substrate Technique

U. Bochtler and F. M. Landstorfer

1. Basics	143
2. Parameters for Single Lines	145
3. Parameters for Coupled Lines	145
References	153
Additional Sources	153

CHAPTER 6

Microwave Filters

Randall W. Rhea

1. Historical Perspective	155
2. The Low-Pass Prototype	155
Butterworth Approximation	156
Scaling Prototype Values	157

Low-Pass Filter Example	159
Chebyshev Approximation	159
Controlled Phase Prototypes	160
Elliptic Approximations	162
3. L – C Filter Transformations	163
High-Pass Transformation	163
All-Pole Bandpass Transformation	164
Bandstop Filter Transform	165
Narrow-Band Bandpass Transforms	166
Elliptic Bandpass Transforms	170
4. Bandpass Transform Distortion	171
Arithmetic Symmetry	171
Blinchikoff Flat Delay Bandpass	172
5. Distributed Filters	172
Lumped – Distributed Equivalents	172
Reentrance	174
Discontinuities	174
Stepped Impedance Low-Pass Filter	175
Elliptic Low-Pass Filter	177
Hybrid High-Pass Filter	177
Top-C-Coupled Distributed Resonators	178
End-Coupled Half-Wave Resonators	178
Parallel-Coupled Half-Wave Resonator Bandpass	179
Hairpin Bandpass	180
Comline Bandpass	181
Interdigital Bandpass	181
6. Computer Simulation	182
Synthesis	182
Circuit Simulation	182
Field Simulation	183
7. Dissipation Loss	184
Unloaded Q Definitions	184
Loaded Q Definitions	185
Low-Pass Loss	185
Bandpass Loss	186

8. Component Technology	186
Capacitor	186
Inductor	188
TEM and Quasi-TEM Modes	191
Waveguide	192
Other Technologies	193
References	197

CHAPTER 7

Directional Couplers

Stephen Jon Blank and Charles Buntschuh

1. Definition and Basic Properties	199
2. Waveguide Aperture Couplers	201
Bethe-Hole Coupler	202
Multihole Waveguide Couplers	205
Riblet Short-Slot Coupler	211
Schwinger Reversed-Phase Coupler	211
Moreno Crossed-Guide Coupler	212
3. Coupled-Line Couplers	213
4. Branch-Line, Branch-Guide, and Rat-Race Couplers	225
Branch-Line Couplers	226
Branch-Guide Couplers	228
Rat-Race Couplers	230
5. Developments	232
References	232

CHAPTER 8

Microwave Ferrite Devices

Jerzy Krupka and Wojciech Glogier

I. Ferrite Materials for Microwave Applications	235
Microwave Properties of Ferrite Materials Magnetized to Saturation	235
Properties of Ferrite Materials for the Partially Magnetized State	236
Microwave Properties of Ferrite Materials for High-Power Levels	237

2. Electromagnetic Waves in a Ferrite Medium	237
Plane Waves in an Infinite Ferrite Medium	237
Waves in Ferrite-Loaded Waveguides	239
3. Ferrite Phase Shifters	241
Rectangular Waveguide Phase Shifters with Transversely Magnetized Ferrite Elements	241
Circular or Squared Waveguide Reciprocal Dual-Mode Phase Shifters	244
Rectangular Waveguide Reciprocal Phase Shifters with Longitudinally Magnetized Ferrite Elements (Reggia – Spencer Phase Shifters)	246
Stripline and Microstrip Phase Shifters	247
4. Ferrite Circulators and Isolators	249
Basic Geometries and Parameters of Ferrite Element Circulators	249
Y-Junction Circulators	251
Isolators	254
5. YIG Devices	256
YIG Filters	256
YIG Power Limiters	257
6. Ferrite Switches	257
References	258

CHAPTER 9

Microwave Solid-State Devices

Cam Nguyen

1. Microwave Mixer and Detector Diodes	261
Introduction	261
Structure and Characteristics	261
Fabrication	266
Operation	266
Models	266
2. Microwave Varactor Diodes	268
Introduction	268
Structure and Characteristics	269
Fabrication	271

Operation	271
Models	271
3. Microwave PIN Diodes	272
Introduction	272
Structure and Characteristics	272
Fabrication	272
Operation	272
Models	275
4. Microwave GUNN Diodes	276
Introduction	276
Structure and Characteristics	277
Fabrication	278
Operation	278
Models	279
5. Microwave IMPATT Diodes	280
Introduction	280
Structure and Characteristics	281
Fabrication	282
Operation	282
Models	283
6. Microwave Bipolar Junction Transistors	284
Introduction	284
Structure and Characteristics	288
Fabrication	291
Operation	292
Models	292
7. Microwave Field Effect Transistors	293
Introduction	293
Structure and Characteristics	297
Fabrication	300
Operation	300
Models	302
References	302

CHAPTER 10
Transferred Electron Devices

S. J. Jerome Teng

1. Introduction	307
Historical Background	308
2. Device Physics	309
Negative Differential Mobility (NDM)	309
Velocity-Field Characteristics	310
Electron Dynamics of NDM	312
3. Device Design and Fabrication	313
Material Growth	313
Device Design	316
Device Fabrication	321
4. Gunn Oscillator and Circuits	325
Mechanically Tuned Gunn Oscillators	325
Rectangular Cavity	328
Electronically Tuned Gunn Oscillator	335
Cavity-Stabilized Gunn Oscillators (CSGO)	342
5. Gunn Amplifiers	346
6. Noise Characteristics	350
Gunn Oscillator Noise	350
Phase-Locked Gunn Oscillator	353
7. Power Combining Techniques	354
Resonator Cavity Combiners	354
Series-Operation Combiners	355
References	356

CHAPTER 11
Microwave IMPATT Diode Amplifiers and Oscillators

David P. Klemer

1. IMPATT Diode Principles	363
2. IMPATT Diode Fabrication	368
3. Commercial IMPATT Diode Specification	373

4. IMPATT Diode Amplifier Design	377
5. IMPATT Diode Oscillator Design	382
6. Noise Characteristics of IMPATT Diode Oscillators and Amplifiers	384
References	386

CHAPTER 12**Microwave Transistor Oscillators and Amplifiers**

Aksel Kiiss

Part A: AMPLIFIERS

1. Introduction — Amplifier Classification	391
2. Low-Noise Amplifiers	392
Moderate Bandwidth Amplifiers	392
Octave Band Designs	392
Multi octave Designs	394
Ultra-Wide-Band Designs	394
3. Amplifier Design	394
Transistor Biasing	396
Characterizing the Transistor by Its S-Parameters	398
Amplifier Characterization	405
Bipolar Amplifiers	405
GaAs FET Amplifiers	405
Low-Noise Amplifier Design	407
Single-Stage Amplifier Design	407
Low-Noise Amplifiers Using Low-Loss Isolators	408
Balanced Amplifier Design	410
Lossless Feedback	411
The Fundamentals of Distributed Amplifier Design	412
Multistage Amplifier Design	415
Temperature Dependence of the Amplifier Gain and Noise Figure	418
Temperature Compensation	419
Cryogenically Cooled Low-Noise Amplifiers	419
Computer-Aided Amplifier Design	421

4. Power Amplifiers	423
Moderate Bandwidth Amplifiers	426
Octave Band Power Amplifiers	426
Multi octave and Ultra-Wide-Band Power Amplifiers	428

Part B: OSCILLATORS

1. Introduction	428
2. Free-Running Oscillators	429
Electronically Tuned Oscillators	429
Mechanically Tuned Oscillators	433
3. Internally or Externally Controlled Oscillators	438
Phase-Locked Frequency Sources	438
Sources of Noise in Phase-Locked Oscillators	439
Phase-Locked Oscillator Design Approaches	439
Phase-Locked Oscillator Classification	441
Fixed Frequency Phase-Locked Oscillators	442
4. Frequency Synthesizers	448
Direct Frequency Synthesis	449
Indirect Frequency Synthesis	452
Indirect Frequency Synthesizers	453
5. Frequency Multipliers	458
Frequency Doublers	458
Higher Order Frequency Multipliers	459
Reference	460

CHAPTER 13

Microwave Detectors, Mixers, Converters, and Harmonic Generators

T. Koryu Ishii

I. Microwave Amplitude Modulation Detectors	461
Basic Circuit	461
Two-Wire Line AM Detector Circuit	463
Coaxial Line AM Detector Circuit	464

Waveguide AM Detector Circuit	465
Microstrip-Line AM Detector Circuit	467
2. Microwave Frequency Modulation Detectors	470
Basic Principles	470
VHF or HF PLL or Long-Wave IC	472
Microwave FM Detector Circuits	473
3. Microwave Phase Modulation Detectors	477
4. Microwave Mixers	478
Coaxial Line Microwave Mixers	479
Waveguide Mixers	480
Microstrip-Line Mixers	482
Lumped Parameter Microwave Mixers	484
5. Microwave Up-Converters	485
Waveguide Up-Converters	486
Microstrip-Line Up-Converters	487
Lumped Parameter Up-Converters	487
6. Microwave Down-Converters	487
7. Microwave Parametric Amplifiers	487
8. Amplitude Modulation Noise in Detectors, Mixers, Converters	487
The Thermal Noise	487
The Shot Noise	487
The ($1/f$) Noise (Surface Static and Trap Noise)(Flicker Noise)	488
The Total Amplitude Modulation (AM) Noise [4]	488
The Tangential Signal Sensitivity (TSS)	488
9. Phase Modulation Noise in Detectors, Mixers, and Converters	489
10. Microwave Harmonic Generators	489
11. Packaging Configurations of Microwave Detectors, Mixers, Converters, and Harmonic Generators	490
Microwave Detector Packaging	490
Microwave Mixer Packaging	492
Microwave Converter Packaging	494
Microwave Harmonic Generator Packaging	494
References	495

CHAPTER 14**Electron Beam Formation, Focusing, and Collection
in Microwave Tubes**

Richard True

1. Introduction	497
2. Description of Electron Guns	498
Pierce Gun Basics	498
Gridded Pierce Guns	502
Other Solid Beam Guns	505
Hollow Beam Guns	507
3. Electron Emission	511
Electron Emission Basics	511
Cathode Loading Determination	513
Dispenser Cathodes	514
Oxide Cathodes	515
Cathode Heaters	516
4. Computer Codes Used in Beam Optical Design	518
Design Methodology	518
Beam Optics Codes	521
Other Codes	526
5. Optical Design of Electron Guns	530
Basic Design	530
External Electrodes	532
Tunnel Emittance and Gridded Guns	536
Voltage Standoff	538
6. Beam Focusing	539
Magnetic Focusing Basics	539
Periodic Permanent Magnet Focusing	540
Solution Splicing and Emittance Growth	544
Uniform Field Focusing	548
Other Types	551
7. Electron Beam Collection	552
Single-Stage Collectors	552
Spent Beam Models	553

Multistage Depressed Collectors	556
Secondary Emission and Mechanical Design	559
8. Gun and Beam Measurement	560
9. Summary and Reliability Issues	561
References	562

CHAPTER 15**Microwave Solid-State Switches, Phase Shifters,
and Attenuators**

T. Koryu Ishii

1. Microwave Solid-State Switches	569
Basics	569
Switching Configurations of SPST Switches	573
Switching Configurations of SPDT Switches	575
Switching Configurations of SPMT Switches	577
Switching Configurations of Transfer Switches	577
Sample Applications	579
Some Practical Microwave Solid-State Switches	582
2. Microwave Solid-State Phase Shifters	582
Basics	582
DC Biasing Configuration	585
Some Practical Varactor Diodes	585
3. Microwave Solid-State Attenuators	586
Basics	586
DC Biasing Configuration	586
Some Practical PIN Diodes	587
References	588

CHAPTER 16**Microwave Thermionic Density Modulated Devices
and Applications**

T. Koryu Ishii

1. Principles of Microwave Thermionic Triodes	589
2. Examples of Microwave Thermionic Triodes	592

3. Principles of Microwave Thermionic Tetrodes	604
4. Examples of Microwave Thermionic Tetrodes	606
5. Conclusions	616
References	616

CHAPTER 17

Microwave Impedance Matching Techniques

S. N. Prasad

1. Introduction	617
2. Narrow-Band Matching	618
Distributed Element Techniques	619
Lumped Element Techniques	629
Distributed and Lumped Element Techniques	636
3. Wide-Band Matching	640
Multisection Quarter-Wave Transformers	640
Tapered Transmission Line Transformers	652
Lumped and Distributed Matching Networks	656
Image Impedance Termination	658
4. Balanced to Unbalanced Transformations	660
Passive Baluns	660
Active Baluns	663
References	667
Further Reading	668
Index	671

Contents of Volume 2

Contributors xxi

Preface xxiii

CHAPTER I

Klystrons

Brian Roach

1. Klystron Characteristics	1
Introduction	1
RF Circuit	1
Electron Beam System	5
2. Klystron Applications	8
Linear Accelerator Applications	8
Communication Applications	9
Industrial Heating Applications	11
Radar Applications	12
3. Klystron Specification	12
Electronic Performance Parameters	14
Operating Parameters	17

Environmental Parameters	19
Life and Reliability	20
Physical Parameters	21
Miscellaneous Items	21
4. Design and Fabrication of Klystrons	22
Typical Design Methodology	22
Construction	24
5. Noise and Stability Characteristics	25
Noise	25
Stability	27
6. Klystron Protection	28
References	30

CHAPTER 2

Magnetrons

Wayne Love

1. Introduction	33
2. Microwaves	35
3. Components of the Magnetron	36
Cathode	37
Anode	41
Output	43
4. Space Charge	43
5. Magnetic Field	46
6. Power Adjustment	46
Pulsing	46
Reduction of Anode Current	47
Adjustment of Magnetic Field	48
Attenuation of Microwave Energy	50
7. Rieke Diagram	50
8. Power Supplies	51

9. Magnetron – System Interface	53
General	53
Common Problems and Causes	55
Additional Reading	55

CHAPTER 3

Traveling-Wave Thermionic Devices

Jeffrey D. Wilson

1. Introduction	57
2. Cathodes	57
Thermionic Emission	57
Secondary Emission	60
3. Electron Guns	60
Perveance	60
Convergence Ratio	60
Electron Gun Types	61
Grids	62
4. Electron Beam Focusing	62
Brillouin Flow	62
Confined Flow	63
Periodic Permanent Magnet Focusing	63
Thermal Beams	64
5. Linear-Beam Traveling-Wave Tubes	64
Applications	64
General Operation	65
Helical Circuit	65
Coupled-Cavity Circuit	67
High-Frequency Circuits	70
Attenuators and Severs	71
Transitions and Windows	72
Electron Beam Collectors	72
Simulation	74
6. Linear-Beam Backward-Wave Devices	77
Backward-Wave Amplifiers	77
Backward-Wave Oscillators	78

7. Magnetrons	79
Applications	79
General Operation	80
Anode Slow-Wave Circuit	80
Strapping	82
Coaxial Magnetrons	83
Simulation	84
8. Crossed-Field Amplifiers	84
Applications	84
General Operation	85
Power and Efficiency	85
High-Frequency CFA	86
Low-Noise High-Gain CFA	87
Amplitron	87
9. Crossed-Field Backward-Wave Oscillators	87
Applications	87
General Operation	88
Frequency Tuning	89
References	90

CHAPTER 4

Gyrotrons, Magnicons, and Ubitrons

Paul Tallerico

1. Introduction	97
2. Gyrotron Principles of Operation	98
3. Gyrotron Design	103
4. Gyrotron Structure	104
5. Gyrotron Fabrication	108
6. Gyrotron Performance	110
7. Prebunched Gyrotrons and the Magnicon	111
8. Gyrotron Applications	112
9. Gyrotron Mode Purity	114
10. Ubitron Principles	114

11. Ubitron Structure	115
12. Ubitron Performance	116
References	116

CHAPTER 5

The Peniotron

David Gallagher and Günter Döhler

1. Introduction	121
2. The Traditional Peniotron	123
Principle of Operation	123
Small-Signal Calculations	124
Large-Signal Calculations	126
Performance of Traditional Peniotrons	126
Traditional Peniotron Design	127
3. Nontraditional Peniotrons	130
Square and Rectangular Waveguides	130
The "True" Gyropeniotron	130
Circular Waveguides	131
The Magnetron-Type Peniotron	132
Other Peniotron and Peniotron-like Devices	133
References	133

CHAPTER 6

Thermodynamics of Microwave Devices

K. Fricke, V. Krozer, and H. L. Hartnagel

Nomenclature	137
1. Introduction	138
2. Conductive Heat Transfer	139
Steady-State Heat Conduction	139
Unsteady-State Heat Conduction	142
Electrical Equivalent of Thermal Conduction	145

3. Convective Heat Transfer	145
Single-Phase Convective Heat Transfer	145
Boiling Heat Transfer	149
4. Heat Transfer by Radiation	151
5. Measurement of the Thermal Resistance	155
IR Measurement	155
Liquid-Crystal Measurement	155
Electrical Measurement	156
6. Thermal Enhancement Techniques	156
7. Thermal Properties of Electronic Materials	163
References	164

CHAPTER 7

Microwave Antennas

John Hill and Mary Lynn Smith

1. Antenna Defined	168
Antenna Requirements and Specifications	168
2. Microwave Integrated Circuit (MIC) and Monolithic Microwave Integrated Circuit (MMIC) Antennas	187
3. Radiation Pattern Synthesis	193
Antenna Patterns with Nulls in Particular Directions	194
Antenna Patterns with Specific Distributions	194
Antenna Patterns with Low Sidelobes and Narrow Beams	194
4. Antennas for Missiles	195
UHF Antennas	196
S-Band Antennas	197
C-Band Beacon Antennas	198
5. Measuring RF Leakage of Test Couplers	199
6. Materials	201
Conductors	201
Dielectrics	203
References	204

CHAPTER 8**Propagation at Microwave Frequencies**

Ernest K. Smith

1. Introduction	207
General Relations	207
Atmospheric Refractive Index	212
Propagation in Free Space	213
Carrier-to-Noise Ratio (C/N)	214
2. Attenuation Mechanisms	215
Attenuation Due to the Gaseous Atmosphere	215
Attenuation Due to Rain	220
Attenuation Due to Fog and Cloud	227
Attenuation Due to Snow and Ice Crystals	227
Attenuation Due to Sand and Dust	228
3. Terrestrial Line-of-Sight Propagation	228
Diffraction Fading Due to Partial Obstruction of the Path	229
Fading Due to a Multipath and Scintillation	230
Fading Due to Variation in the Angle-of-Arrival	230
4. Propagation beyond the Horizon	230
Diffraction	231
Tropospheric Scatter	231
Atmospheric Ducting	232
5. Earth – Space Propagation	232
Geometry for the Geostationary Orbit	233
Ionospheric Effects	234
Tropospheric Effect	237
Mobile Satellite Propagation Effects	239
6. Mobile Propagation Effects	240
7. Short-Path Propagation	240
8. Noise	241
References	242

CHAPTER 9**Consumer Applications of Microwaves:
Microwave Ovens and Accessories**

Koji Iwabuchi, Ichiro Fukai, and Tatsuya Kashiwa

1. Microwave Oven Design Fundamentals [1]	249
Moding Region	249
Arcing Region	251
Overheating Region	251
Low-Efficiency Region	251
Recommended Region	252
2. Microwave Field Visualization	252
Background	252
Formulation	253
Example [11]	254
3. Microwave Leakage Minimization Design	256
Door Structures	256
Radial Line Filters [20, 21]	260
Perforated Plates and Wire Gauzes	260
4. Operation and Maintenance [24]	271
Operation Procedure	271
Maintenance	271
5. Microwave Oven Accessories and Containers	271
Accessories and Their Use	272
Containers and Their Use	272
References	274

CHAPTER 10**Industrial Applications of Microwaves**

T. Koryu Ishii

1. Microwave Heating	277
Temperature Rise	277
Approximate Equations for Temperature Rise	280
2. Microwave Curing	281
Rubber Curing	281
Tire and Asphalt Curing	284

3. Microwave Material Processing	284
Microwave Thawing	284
Microwave Drying	285
Microwave Heating	289
4. Microwave Applications in Agricultural Industries	293
5. Microwave Applications on Forest Products	296
6. Microwave Application on Sensing	297
7. Microwave Object Identification	300
Microwave Radiometer Technique	300
Microwave Monostatic or Bistatic Radar Technique	300
Microwave Reflection or Radiation Pattern Recognition Technique	300
8. Microwave Data Communications	300
General Configurations	300
Data	301
Modulator	301
Microwave Transmitter	301
Microwave Launcher	302
Microwave Transmission System	302
Microwave Catcher	303
Microwave Receiver	303
Data Display	303
References	303

CHAPTER 11

Biomedical Applications of Microwave Engineering

Joseph H. Battocletti

1. Electrical Properties of Biological Materials	309
2. Heat Deposition in Biological Material, Particularly Man	315
3. Exposure Guides and Standards	323
4. Microwave Hyperthermia for Cancer Treatment	327
The Bioheat Equation	328
Applicators	330
5. Microwave Monitoring, Imaging, and Sensing	332
One-Antenna, Active Sensing, Remote Life Detection	332

One-Antenna, Passive Scanning, Thermography or Radiometry	333
Two-Antenna, Microwave Imaging	337
References	340

CHAPTER 12

Chemical Applications of Microwaves

Thomas C. Ehlert

1. Microwave Absorption Spectroscopy	347
Introduction	347
Classifications of Molecules	347
Conditions	347
Rotational Energies	348
Resonant Frequencies	349
Probability of Absorption — Attenuation of Microwaves	350
Transition Cross Section	350
Population of the Lower Quantum State	351
Nuclear Statistical Weight	352
Limitations	352
Widths and Shapes of Spectral Lines	352
2. Nuclear Magnetic Resonance Spectroscopy	353
Introduction	353
Nuclear Magnetic Dipole Moment	353
Magnetic Dipole Moment Components	354
Magnetic Dipole Energy States	355
Allowed Transitions between Energy States	355
Details of Spectra	355
Relaxation Processes	357
Power Saturation	357
High-Field NMR	357
NMR Spectra of Solids	358
Fourier Transform NMR	358
3. Electron Spin Resonance Spectroscopy	359
Introduction	359
Electron's Magnetic Dipole Moment	359
Magnetic Dipole Moment Components	359

Magnetic Dipole Energy States	359
Allowed Transitions between Energy States	359
Spectra	360
Relaxation Processes	360
4. Chemical Synthesis and Analysis Using Microwave-Produced Plasmas	360
Apparatus	360
Theory	361
Synthesis	361
Analysis	362
5. Thermal Effects	362
Introduction	362
Heating	362
Reaction Rate Enhancement	363
References	363

CHAPTER 13

Electron Paramagnetic Resonance

James S. Hyde

1. Introduction	365
2. Continuous Wave Bridges: 0.5 – 35 GHz	368
One-Arm Bridges	369
Reference-Arm Bridges	375
Detection of Dispersion	378
Reference-Arm Bridge with a Low-Noise Microwave Amplifier	381
Notes on Advanced Microwave Bridges	383
3. Resonators for EPR Spectroscopy	384
Multipurpose TE102 Cavity	384
EPR Cavity Problems	386
Multipurpose Cavity Accessories	387
Conversion to Other Rectangular TE Modes	391
Other EPR Microwave Cavity Designs	395
Other Types of EPR Sample-Containing Structures	398
References	399

CHAPTER 14**Microwave Navigational Aides**

G. Stephen Hatcher and Goson Gu

Part A: THE GLOBAL POSITIONING SYSTEM

1. General Description	404
Space Segment	404
Control Segment	405
User Segment	405
2. Position Fixing	405
Concept of Position Fixing	405
Satellite-Position Acquisition and Radio Ranging	407
Clocks	407
Pseudoranges and Navigation Equations	408
3. Time Measurement	408
4. Velocity Measurement	409
5. Signal Structure	410
6. Navigation Message	410
7. Navigation Solution and Dilution of Precision	411
The Navigation Solution	411
Dilution of Precision (DOP)	413
8. Error Sources	414
Space Segment	414
User Segment	414
Propagation Link	415
9. Differential GPS	415
Concept of Differential GPS	415
Implementation of Differential GPS	415
10. Summary	416

Part B: DOPPLER NAVIGATION SYSTEM

1. General Description	417
2. Fundamental Principles of Doppler Radar	418

3. Functional Description of Doppler Radar	421
Antenna	421
Transmitter and Receiver	422
Frequency Tracker	422
4. Doppler-Radar Performance and Errors	423
Doppler-Radar Performance	423
Doppler-Radar Errors	424
5. The Navigation Computer	425
Additional Reading	425

CHAPTER 15

Microwave Applications for Law Enforcement

John Tomerlin and John Fuhrman

1. Introduction	429
2. Historical	431
3. Moving Radar	432
4. Mechanical Errors	433
5. Mechanical Interference	434
6. Photo Radar	435
7. Testing for Accuracy	436
Tuning Fork Calibration	437
Tuning Fork Tests	438
Microwave Transmission	438
Low-Voltage Supply	439
Doppler Audio	439
Electromagnetic Interference	439
Speed Accuracy	440
8. Does Radar Increase Safety?	448
Additional Reading	449

CHAPTER 16**Microwave Radio Communication**

George Kizer

1. Introduction	449
2. Equipment-Dependent Radio Performance	451
Analog Systems	451
Digital Systems	454
Estimating End-to-End Digital Radio Performance	457
3. Transmission-Path-Dependent Radio Performance	465
Transmission Path Loss	466
Received Signal Variation ("Fading")	472
Atmospheric (Nonrain) Absorption	473
Rain Loss	474
Reflection ("Fresnel Zone") Fading	477
Obstruction ("Diffraction") Fading	478
Power Fading	485
Duct Fading	486
Atmospheric Multipath Fading	487
4. Path Availability Calculations	492
5. Conclusion	501
References	502

CHAPTER 17**Microwave Instrumentation and Measurements**

Aksel Kiiss

1. Scattering Parameters	505
S-Parameter Measurements	505
Uncertainties Caused by Adaptor VSWR	512
Uncertainties Caused by the Harmonic Content of the Test Signal	512
Inaccuracies in Transmission Measurements (S_{21} and S_{12})	512
2. Transmission Measurements	514
Transmission Measurement Magnitude	514
Transmission Measurement Phase	516

3. Reflection Measurements	520
4. Electrical Delay	525
5. Group Delay	525
6. Noise Figure/Noise Temperature Measurements	527
Definitions of the Noise Figure/Noise Temperature	527
Noise Figure	528
Absolute Accuracy of Noise Figure Measurements	534
7. Microwave Power Measurements	538
Thermal-Based Power Detectors	538
Diode-Based Power Detectors	540
Diode-Based Power Meters	540
Frequency Calibration Factor	541
Peak Power Meters	542
Accuracy: How to Calculate Your Measurement Uncertainty	542
RSS and Worst-Case Calculations	544
Measurement Techniques for Improved Measurement Accuracy	544
8. Microwave Frequency Measurements (CW and Pulsed)	545
Single-Shot, Precision VCO Characterization	545
HP 5372A Specification Summary	546
Specifications	550
9. Measurement of Phase Noise Power Spectral Density	558
Short-Term Frequency Stability	560
Long-Term Frequency Stability (Figure 21)	568

CHAPTER 18

Microwave Mathematics

James Richie

1. Preliminary Definitions	569
Phasor Notation and Fourier Transform	569
2. Mathematical Functions for Microwave Engineering	571
Complex Functions	571
Generalized Functions	573
3. Vectors and Matrices	576
Definition	576

Properties	577
Hermitian Adjoint	578
Commutator and Anticommutator	578
Tensors and Dyadics	578
Group Theory	579
4. Vector Spaces	579
Definition	579
Linear Independence	580
Inner Product	580
Orthonormality	580
Gram-Schmitt Process	581
Inequalities	581
5. Linear Operator Theory	581
Definition	581
Properties	582
Inverse	582
Similarity Transformation	582
Projection Operators	583
Adjoint Operators	584
Unitary Operators	584
Eigenvalue Problem	584
6. Function Spaces	585
7. Vector Fields	586
Operations	587
Theorems	589
Vector Identities	589
8. Differential Equations and Their Solutions	589
Analytic Techniques	590
Numerical Solutions	595
9. Integral Equations and Their Solution	599
Tabulated Solutions	599
Asymptotic Methods	599
Numerical Solutions	600
References	602

CHAPTER 19
Microwave Materials

Hamid H. S. Javadi

1. Introduction	605
2. Dielectric Properties of Compounds	608
3. Properties of Manufactured Special-Purpose Compounds	620
4. Thin Films	636
5. Electromagnetic Properties of Metals	636
6. Physical and Electromagnetic Properties of Bulk and Thin-Film Superconductors	638
References	642
Index	645

This Page Intentionally Left Blank

Contributors

Numbers in parentheses indicate the pages on which the authors' contributions begin.

Prakash Bhartia (1) Defence Research Establishment Atlantic, Halifax, Nova Scotia, Canada.

Stephen Jon Blank (199) Department of Electrical Engineering, New York Institute of Technology, Old Westbury, New York 11568.

Ulrich Bochtler (143) Technologiezentrum, 70569 Stuttgart, Germany.

Charles Buntschuh (199) Microwave Engineering Services, Huntington, New York 11743.

Wojciech Glogier (235) Zaktad materialów magnetycznych, "POLFER," 01-029 Warszawa, Dzielnabo, Poland.

Reinmut K. Hoffmann (95) Universitat der Bundeswehr München, Fachbereich ET/FH, D-85577 Neubiberg, Germany.

T. Koryu Ishii (461, 569, 589) Department of Electrical and Computer Engineering, Marquette University, Milwaukee, Wisconsin 53233.

Aksel Kiiss (391) MITEQ, Inc., Hauppauge, New York, 11788.

David P. Klemer (363) Department of Electrical Engineering, The University of Texas at Arlington, Arlington, Texas 76019.

Jerzy Krupka (235) Instytut Mikroelektroniki i Optoelektroniki, Politechniki Warszawskiej, 00-662 Warszawa, Kuszykowa 75, Poland.

Andrew J. K. Kwon (47) Department of Electrical Engineering, Milwaukee School of Engineering, Milwaukee, Wisconsin 53202.

F. M. Landstorfer (143) Institut für Hochfrequenztechnik, Universitat Stuttgart, 7000 Stuttgart 80, Germany.

- Cam Nguyen** (261) Department of Electrical Engineering, Texas A & M University, College Station, Texas 77843
- Protap Pramanick** (1) Department of Electrical Engineering, University of Saskatchewan, Saskatoon, Saskatchewan, Canada S7N OWO.
- S. N. Prasad** (617) Department of Electrical and Computer Engineering and Technology, Bradley University, Peoria, Illinois 61625.
- Randall W. Rhea** (155) Eagleware Corporation, Stone Mountain, Georgia 30087.
- Robert A. Strangeway** (61) Department of Electrical Engineering, Milwaukee School of Engineering, Milwaukee, Wisconsin, 53202.
- S. J. Jerome Teng** (307) Microelectronics, Hughes Aircraft Company, Torrance, California 90509.
- Richard True** (497) Litton Systems, Inc., San Carlos, California 94070.

Preface

The purpose of this book is to provide a compact, ready reference tool on practical microwave technology to practicing technicians, scientists, and engineers. Readers may be trained in the field of microwave technology or may be trained in their own field but not necessarily in the field of microwave technology. This book is written with care for the latter category of audience as well as for the former. Consequently, this book is also useful to people in business and industry as well as to science and engineering students who are involved in microwave technology. Not only is this book a ready reference tool at present but it is also a good investment for use in the future.

The emphasis of this book is to answer the question of "how to" rather than that of "why so." Chapters are full of useful formulas, charts, graphs, tables, examples, and diagrams for analysis and are designed for daily use. These reference resources are clearly explained and easily applicable to specific practical cases that the readers may encounter in their professional activities.

Naturally the field of microwave technology is so vast that, no matter how well covered, it is impossible to include everything in one volume of limited size. For this reason, the *Handbook of Microwave Technology* is split into two volumes. Volume 1 covers "Components and Devices" used in microwave circuits, and Volume 2 covers "Applications" of microwave technology. This enormously wide area of microwave technology, which spans both fundamentals and applications, is condensed into two, compact, conveniently portable volumes for easy reference. Since both volumes

are written independently of each other, the audience may choose one or both volumes depending on their needs.

For those who wish to acquire information beyond the materials presented in this book, complete lists of references are provided at the end of every chapter. The quest for "why so" and further information is realized by making full use of these references.

The editor thanks chapter contributors, suppliers of industrial resources, providers of permissions for copyrighted materials, and those who provided clerical assistance. He also acknowledges assistance from the publisher's staff. Without their assistance, perseverance, and patience, this book may never have been completed.

T. Koryu Ishii
Editor
Milwaukee, Wisconsin
1995

CHAPTER

I

Microwave Transmission Lines

P. Pramanick and P. Bhartia

I. Introduction to Transmission Lines

The purpose of uniform transmission lines is to transfer energy from a generator to a load. They can be of various types depending upon the application and the band of microwave or millimeter-wave frequency used. The length of a transmission line may vary from a fraction of a wavelength, in lumped element applications, to several wavelengths in distributed element circuitry. Open wire lines are used at frequencies far below the microwave band and are replaced by coaxial lines above 1 GHz. Above around 3 GHz, hollow metal tubes or waveguides and their various derivatives, such as finlines, etc., are used. Besides the metallic waveguides, surface waveguides and dielectric waveguides are also used at microwave and millimeter-wave frequencies.

Transmission Line Equations

Transmission lines used at microwave frequencies support modes which can be broadly divided into two types, the transverse electromagnetic (TEM) and the nontransverse electromagnetic (non-TEM) modes of prop-

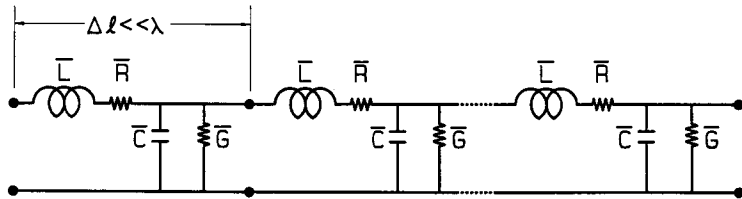


Figure 1. Lumped circuit representation of a distributed line.

agation. The four basic parameters that characterize the TEM mode are

1. the characteristic impedance, Z_0 ,
2. the phase velocity, v_p ,
3. the attenuation constant, α , and
4. the peak power handling capability, P_{\max} .

For the transmission line supporting a non-TEM mode, the above four parameters are dependent on the type of the supported mode, and the definition of Z_0 is nonunique. However, in all cases, the parameters are functions of the geometrical cross section and the material properties of the transmission line. Figure 1 shows the lumped element equivalent network of a transmission line supporting the TEM mode, where λ is the wavelength, L and R are the per unit lengths of the series inductance and series resistance, respectively, and C and G are the per unit lengths of the shunt capacitance and shunt conductance, respectively. Table 1 shows the functional relationships among the parameters of a TEM transmission line.

2. Two-Wire Line

Figure 2 illustrates the two-wire balanced transmission line. The constants for a two-wire line are given by [1]

$$Z_0 = \frac{120}{\sqrt{\epsilon_r}} \ln(2H/d) \Omega \quad (1)$$

$$\bar{L} = 0.4 \ln(2H/d) \text{ (mH/m)} \quad (2)$$

$$\bar{C} = 27.669 \epsilon_r / \ln(2H/d) \text{ (pf/m)} \quad (3)$$

$$\bar{R} = 16.6\sqrt{f}/d \mu\Omega, \text{ for copper,} \quad (4)$$

TABLE I
Summary of General Formulae for Transmission Lines

Quantity	General line expression	Ideal line expression	Approximate result for low-loss lines
Propagation constant, $\gamma = \alpha + j\beta$	$\sqrt{(\bar{R} + j\omega\bar{L})(\bar{G} + j\omega\bar{C})}$	$j\omega\sqrt{\bar{L}\bar{C}}$	See α and β below.
Phase constant, β	$\text{Im}(\gamma)$	$\omega\sqrt{\bar{L}\bar{C}} = \frac{\omega}{V_p} = \frac{2\pi}{\lambda}$	$\omega\sqrt{\bar{L}\bar{C}} \left[1 - \frac{\bar{R}\bar{G}}{4\omega^2\bar{L}\bar{C}} + \frac{\bar{G}^2}{8\omega^2\bar{C}^2} + \frac{\bar{R}^2}{8\omega^2\bar{L}^2} \right]$
Attenuation constant, α	$\text{Re}(\gamma)$	0	$\frac{\bar{R}}{2Z_0} + \frac{\bar{G}Z_0}{2}$
Characteristic impedance, Z_0	$\sqrt{\frac{\bar{R} + j\omega\bar{L}}{\bar{G} + j\omega\bar{C}}}$	$\sqrt{\frac{\bar{L}}{\bar{C}}}$	$\sqrt{\frac{\bar{L}}{\bar{C}}} \left[1 + j \left(\frac{\bar{G}}{2\omega\bar{C}} - \frac{\bar{R}}{2\omega\bar{L}} \right) \right]$
Input impedance, Z_i	$Z_0 \left[\frac{Z_L \cosh \gamma l + Z_0 \sinh \gamma l}{Z_0 \cosh \gamma l + Z_L \sinh \gamma l} \right]$	$Z_0 \left[\frac{Z_L \cos \beta l + jZ_0 \sin \beta l}{Z_0 \cos \beta l + jZ_L \sin \beta l} \right]$	
Impedance of shortened line ($Z_L = 0$)	$Z_0 \tanh \gamma l$	$jZ_0 \tan \beta l$	$Z_0 \left[\frac{\alpha l \cos \beta l + j \sin \beta l}{\cos \beta l + j \alpha l \sin \beta l} \right]$
Impedance of open line ($Z_L = \infty$)	$Z_0 \coth \gamma l$	$-jZ_0 \cot \beta l$	$Z_0 \left[\frac{\cos \beta l + j \alpha l \sin \beta l}{\alpha l \cos \beta l + j \sin \beta l} \right]$
Impedance of quarter-wave line	$Z_0 \left[\frac{Z_L \sinh \alpha l + Z_0 \cosh \alpha l}{Z_0 \sinh \alpha l + Z_L \cosh \alpha l} \right]$	$\frac{Z_0^2}{Z_L}$	$Z_0 \left[\frac{Z_0 + Z_L \alpha l}{Z_L + Z_0 \alpha l} \right]$
Impedance of half-wave line	$Z_0 \left[\frac{Z_L \cosh \alpha l + Z_0 \sinh \alpha l}{Z_0 \cosh \alpha l + Z_L \sinh \gamma \alpha l} \right]$	Z_L	$Z_0 \left[\frac{Z_L + Z_0 \alpha l}{Z_0 + \alpha L \alpha l} \right]$
Reflection coefficient, ρ (at the load location)	$\frac{Z_L - Z_0}{Z_L + Z_0}$	$\frac{Z_L - Z_0}{Z_L + Z_0}$	
Standing-wave ratio	$\frac{1 + \rho }{1 - \rho }$	$\frac{1 + \rho }{1 - \rho }$	

Note. λ , wavelength measured along a line; ω , angular frequency.

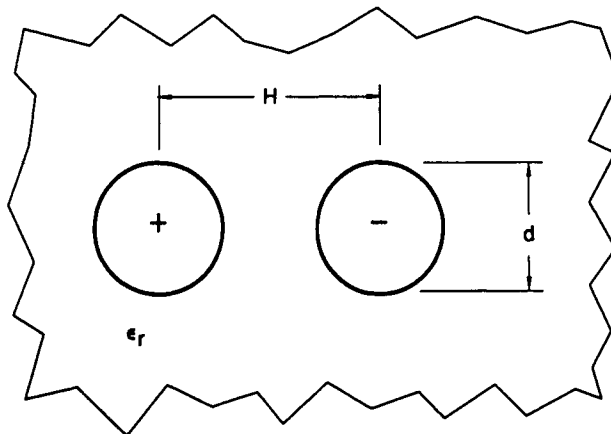


Figure 2. Two-wire transmission line.

where f is the operating frequency. A two-wire transmission is used up to a frequency at which the radiation loss is negligible and Z_0 , \bar{L} , and \bar{C} are illustrated in Figure 3 as a Function of H/d .

For reduced radiation loss and to obtain practically useful parameters, various other forms of two-wire transmission lines are also used. A few such configurations are shown in Table 2 along with the expressions for the characteristic impedances.

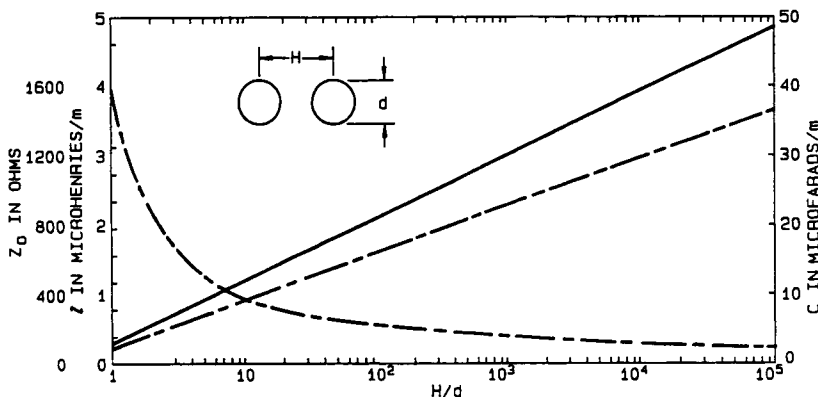
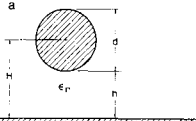
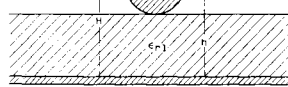
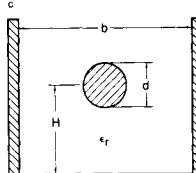
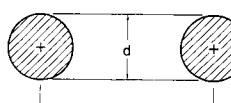
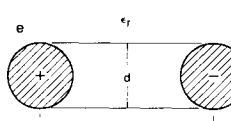


Figure 3. Characteristic impedance, inductance per unit length, and capacitance per unit length for a parallel wire transmission line as a function H/d . Reprinted with permission from *Electronic Designer's Handbook*, by L. J. Giacoletto, McGraw-Hill, New York, 1977.

TABLE 2
Characteristics of Open-Wire Lines

Structure	Formula for $z_0\sqrt{\epsilon_r}(\Omega)$
a	 $60 \ln \left\{ 1 + \frac{2h}{d} + 2 \left[\frac{h}{d} \left(1 - \frac{h}{d} \right) \right]^{1/2} \right\}$
b	 $60 [P(P+Q)]^{1/2}$ $P = \ln \left[1 + \frac{1}{2x} (1 + \sqrt{1 + 4x}) \right]$ $Q = \sum_{n=0}^{\infty} (-D)^{n+1} \ln \left(1 + \frac{2}{n+x} \right)$ $D = \frac{\epsilon_{r1} - \epsilon_r}{\epsilon_{r1} + \epsilon_r}, \quad x = d/4h$
c	 $60 \ln \left(\frac{4b}{\pi d} \tanh \frac{\pi H}{b} \right), \quad d \ll h, b$
d	 $120 \ln(x + \sqrt{x^2 - 1}), \quad x = H/d$
e	 $120 \ln(2H/d)$

3. Coaxial Lines

Coaxial lines find extensive use over the widest frequency spectrum, starting from ELF to the millimeter-wave band. Although coaxial lines can support non-TEM modes, the dominant mode is TEM. As a result, the characteristics of a coaxial line are obtained from static field analysis [3, 4].

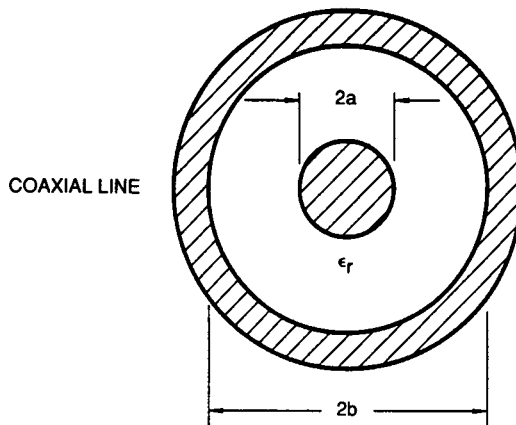


Figure 4. Coaxial line.

TABLE 3
Coaxial Line Characteristics

Parameter	Expression	Unit
Capacitance	$C = \frac{55.556\epsilon_r}{\ln(b/a)}$	pF/m
Inductance	$L = 200 \ln \frac{b}{a}$	nH/m
Characteristic impedance	$Z_0 = \frac{60}{\sqrt{\epsilon_r}} \ln \frac{b}{a}$	Ω
Phase velocity	$v_p = \frac{3 \times 10^8}{\sqrt{\epsilon_r}}$	m/s
Delay	$\tau_d = 3.33\sqrt{\epsilon_r}$	ns/m
Dielectric attenuation constant	$\alpha_d = 27.3\sqrt{\epsilon_r} \frac{\tan \delta}{\lambda_0}$	dB/unit length
Conductor attenuation constant (for copper at 20°C)	$\alpha_c = \frac{9.5 \times 10^{-5} \sqrt{f} (a+b) \sqrt{\epsilon_r}}{ab \ln(b/a)}$	dB/unit length
Cutoff wavelength for higher order modes	$\lambda_c = \pi\sqrt{\epsilon_r}(a+b)$	Unit of a or b
Maximum peak power	$P_{\max} = 44 E_{\max} ^2 a^2 \sqrt{\epsilon_r} \ln \frac{b}{a}$	kW

Note. λ_0 , free-space wavelength; $\tan \delta$, loss tangent of the dielectric; f , operating frequency in gigahertz; E_{\max} , breakdown electric field.

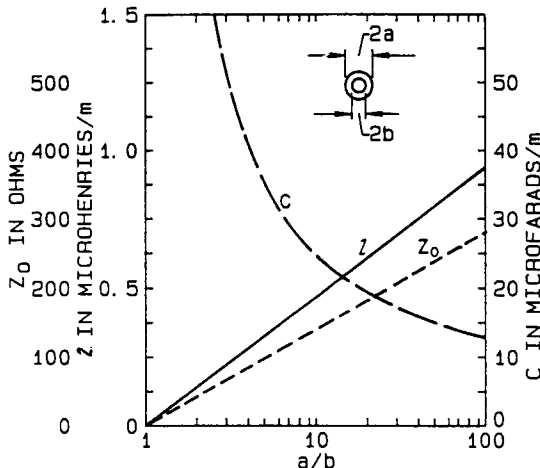


Figure 5. Characteristic impedance, inductance, and capacitance as a function of the ratio a/b for a coaxial line. Reprinted with permission from *Electronics Designer's Handbook*, by L. J. Giacoletto, McGraw-Hill, New York, 1977.

The parameters of a coaxial line, shown in Fig. 4 are listed in Table 3 as a functions of the geometrical dimensions. For values of the attenuation constant at temperatures other than 20°C, one should multiply the value of α in Table 3 by $[1 + 3.9 \times 10^{-3} (T - 20)]^{1/2}$, where T is in degrees centigrade. Figure 5 shows the variation of coaxial line parameters with the ratio a/b .

Q-Factor of Coaxial Lines

The Q -factor of a coaxial line is an important parameter in realizing microwave filters using coaxial line resonators. It is obtained from Equation (5) as

$$Q = (1/Q_c + 1/Q_d)^{-1}, \quad (5)$$

where the conductor quality factor, Q_c [5], is given by (see Figure 4)

$$Q_c = 379.1\sqrt{f_0} \ln(b/a)/(1/2a + 1/2b), \quad (6)$$

where a and b are in inches, f_0 is in gigahertz, and the dielectric quality

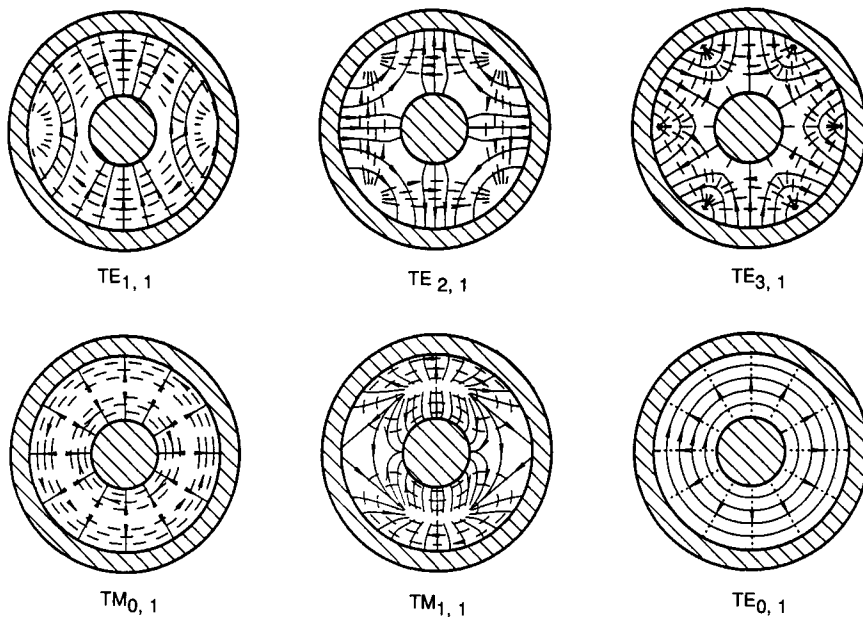


Figure 6. TE and TM coaxial modes. Reprinted with permission from *Electronics Designer's Handbook*, by L. J. Giacoletto, McGraw – Hill, New York, 1977.

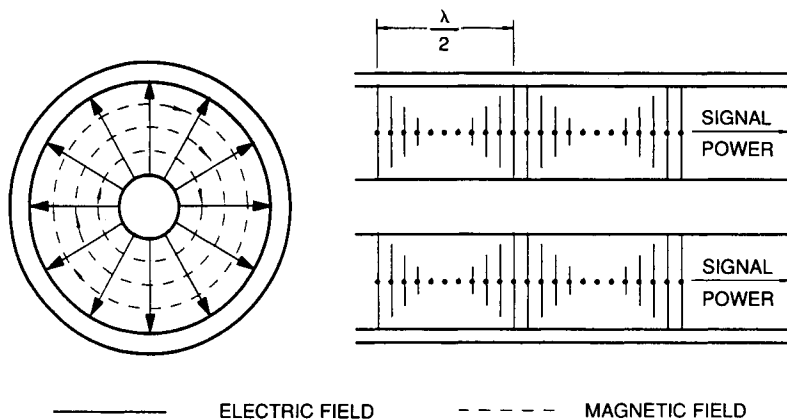


Figure 7. TEM coaxial line mode. Reprinted with permission from *Electronics Designer's Handbook*, by L. J. Giacoletto, McGraw – Hill, New York, 1977.

factor, Q_d , is given by

$$Q_d = 1 / \tan \delta, \quad (7)$$

where $\tan \delta$ is the loss tangent of the dielectric material filling the resonator.

Modes in a Coaxial Line

In the fundamental TEM mode of propagation in a coaxial line, which has no cutoff frequency, the electric and the magnetic fields lie in the transverse plane perpendicular to the direction of energy propagation. Besides the TEM mode, a coaxial line can support various non-TEM higher order modes, depending upon the frequency of operation. Such modes are

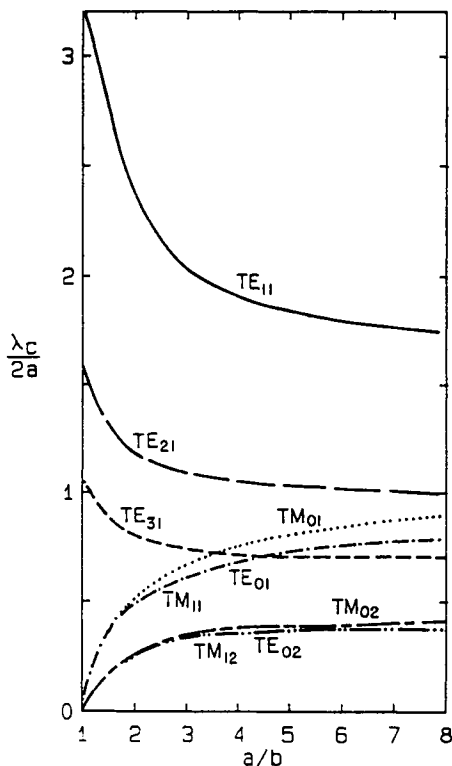


Figure 8. Relationship between cutoff wavelength and line dimensions for higher order coaxial modes. Reprinted with permission from *Microwave Transmission Design Data*, by Theodore Moreno, McGraw - Hill, New York, 1948.

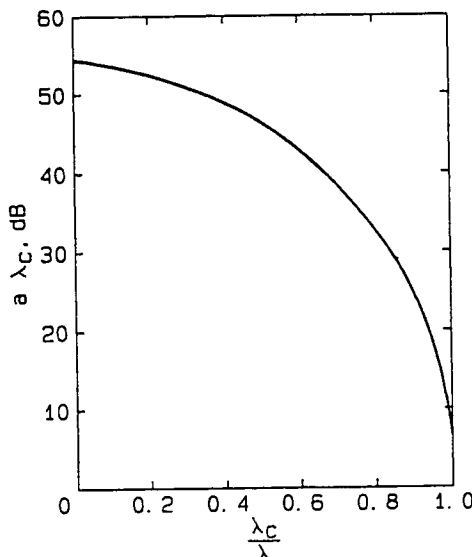


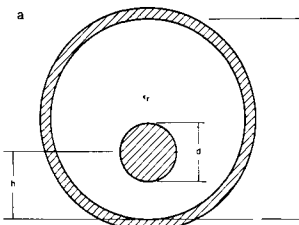
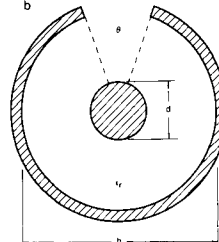
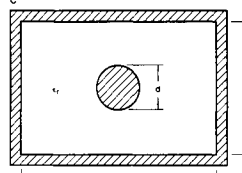
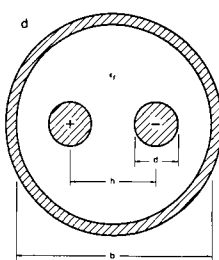
Figure 9. Relationship among attenuation, cutoff wavelength, and operating wavelength in the cutoff region. Reprinted with permission from *Microwave Transmission Design Data*, by Theodore Moreno, McGraw-Hill, New York, 1948.

referred to as TE_{mn} and TM_{mn} modes. For TE modes, there are no electric field components in the axial direction. In TM modes there are no magnetic fields in the axial direction. The subscript m denotes the number of full-period variations of the radial component of the field in the angular direction. The subscript n denotes the number of half-period variations of the angular component of the field in the radial direction. Figure 6 illustrates the field patterns of the first six higher order modes in a coaxial line. TE_{11} is the first higher order mode above the fundamental TEM mode. Figure 7 shows the field pattern of the TEM mode. Figure 8 illustrates the dependence of cutoff wavelengths of various higher order modes on the geometrical dimensions of a coaxial line.

Figure 9 shows the relationship among the operating wavelength, the cutoff wavelength, and the attenuation below the cutoff region. The attenuation is obtained from the following equation:

$$\alpha = \frac{6.274}{\lambda_c} \left[1 - \left(\frac{\lambda_c}{\lambda} \right)^2 \right]^{1/2} \quad (\text{nepers/unit length}). \quad (8)$$

TABLE 4
Formulae for $Z_0 \sqrt{\epsilon_r}(\Omega)$ of Various Derivatives of Coaxial Lines

Structure	Formula for $Z_0 \sqrt{\epsilon_r}(\Omega)$	Accuracy
a	$60 \ln \left[x + (x^2 - 1)^{1/2} \right]$ $X = \frac{d}{2b} + \frac{2h}{d} \left(1 - \frac{h}{b} \right)$ 	Exact
b	$60C_F \ln(b/d)$ $C_F = [1 + (0.046 - 0.005b/d)\theta^2]$ <p>where θ is in radians</p> 	0.5% for $\theta \leq 0.75\pi$ $2.3 \leq b/d \leq 3.5$
c	$60 \ln(1.078b/d) + A$ $A = [10 - 2.1(d/b)^2]B$ $B = \tanh[2.2(w/b - 1.0)]$ 	0.5% for $d/b \leq 0.65$
d	$120 \ln \left\{ 2P \left[(1 - Q^2)/(1 + Q^2) \right] \right\}$ <p>Not known</p> $P = h/d$ $Q = h/b$ $d \ll h, b$ 	

Other Forms of Coaxial Line

So far we have described coaxial lines with concentric conductors. Various other forms of coaxial lines are also used, as indicated in Table 4.

A General Equation for Attenuation in Two-Wire and Coaxial Lines

Consider a two-wire line with an arbitrary cross section, as shown in Figure 10. The attenuation in the line at frequency f in gigahertz is given by [6]

$$\alpha = \frac{\pi\sqrt{\epsilon_r}f}{0.2998} \left[1 - \frac{Z'_0}{Z_0} \right] \quad (\text{nepers/meter}), \quad (9)$$

where Z_0 is the characteristic impedance of the line and Z'_0 is that of the line when the dimensions are changed by the amount of skin depth, δ_s , as shown in Figure 10. δ_s is given by

$$\delta_s = 0.0822 \sqrt{\frac{\delta_r}{f}} \quad (\text{mils}), \quad (10)$$

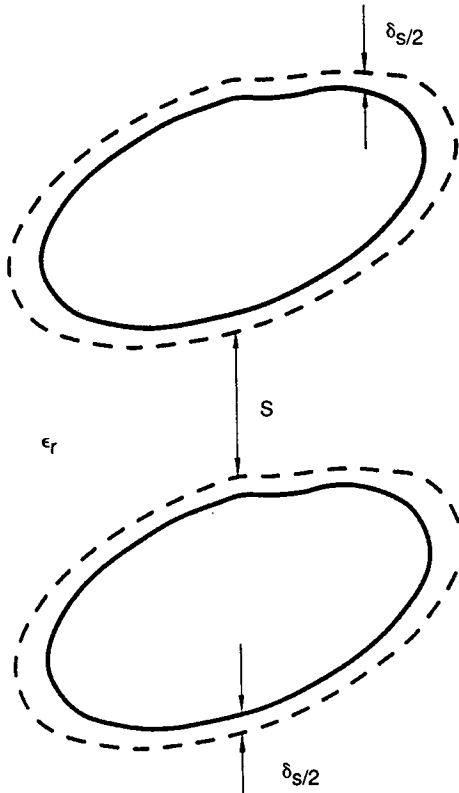


Figure 10. Loss calculation in a two-wire line.

where δ_r is the resistivity of the metal with respect to copper. Equation (9) is applicable to any of the transmission lines described so far.

4. Waveguides

Hollow metallic tubes, usually with rectangular or circular cross sections, are ideally suited for high-power and low-loss microwave applications. Such transmission lines are called waveguides. Due to the absence of any center conductor, waveguides support only TE and TM modes. Depending upon the cross section geometry of the waveguides, shown in Figure 11, simultaneous existence of two different modes with the same phase velocity is possible. Such modes are called degenerate modes. In multimoded waveguides more than one mode is allowed to propagate simultaneously.

Due to the non-TEM nature of the supported mode, the waveguide exhibits a high-pass filter-like behavior. Also due to the nonuniqueness of the voltage and the current, the characteristic impedance, Z_0 , cannot be uniquely defined. Z_0 may be defined in terms of the voltage-current ratio, the power-current ratio, or the power-voltage ratio, which gives

$$\left. \begin{aligned} Z_0(V, I) &= V/I \\ Z_0(P, I) &= 2P/II^* \\ Z_0(P, V) &= VV^*/2P \end{aligned} \right\} \quad (11)$$

or

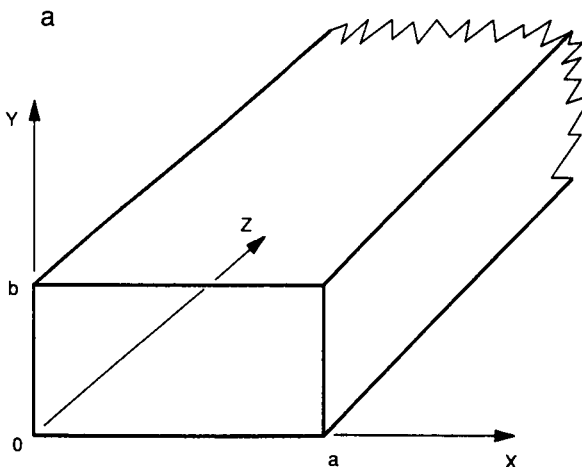


Figure 11a. Rectangular waveguide.

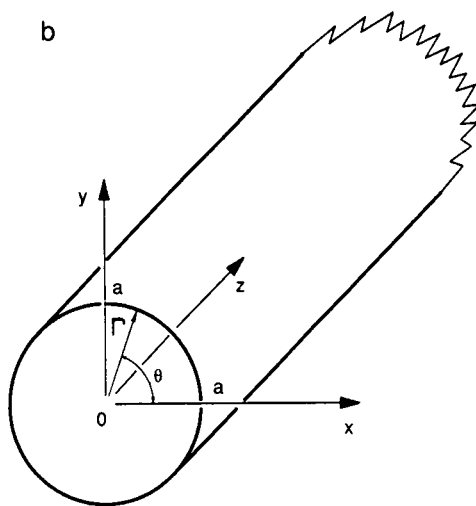


Figure 11b. Circular waveguide.

In the above equations the definitions of the voltage and the current are to some extent arbitrary, leading to different values of the characteristic impedance.

Rectangular Waveguide

Table 5 summarizes the general properties of TE_{mn} and TM_{mn} modes in a rectangular waveguide. Table 6 shows the electric and the magnetic field distributions of the first five modes in a rectangular waveguide. Figure 12 shows the sequence in which various modes come into existence as the operating frequency is raised, for the aspect ratios $b/a = 1$ and $\frac{1}{2}$. In most of the cases $b/a = \frac{1}{2}$ is used.

For TE_{mn} modes, the attenuation constant in a rectangular waveguide is given by

$$\alpha_{mn} = \frac{2R_s}{b\eta_0\sqrt{1 - \left(\frac{\lambda_0}{\lambda_c}\right)^2}} \left[\left\{ 1 + \frac{b}{a} \right\} \left(\frac{\lambda_0}{\lambda_c} \right)^2 + \frac{b}{a} \left\{ \frac{\epsilon_{0n}}{2} - \left(\frac{\lambda_0}{\lambda_c} \right)^2 \right\} \frac{m^2ab + n^2a^2}{m^2b^2 + n^2a^2} \right] \text{ (nepers/unit length), } (12)$$

TABLE 5
Properties of Waves in Empty Rectangular Waveguides

Property	TE _{mn} mode	TM _{mn} mode
Cutoff wave number, k_c	$\sqrt{\left(\frac{m\pi}{a}\right)^2 + \left(\frac{n\pi}{b}\right)^2}$	$\sqrt{\left(\frac{m\pi}{a}\right)^2 + \left(\frac{n\pi}{b}\right)^2}$
Propagation constant, γ_{mn}	$\sqrt{k_c^2 - k_0^2}$	$\sqrt{k_c^2 - k_0^2}$
Guide wavelength, λ_g	$\frac{\lambda_0}{\sqrt{1 - (k_c/k_0)^2}}$	$\frac{\lambda_0}{\sqrt{1 - (k_c/k_0)^2}}$
Group velocity, v_g	$c \frac{\lambda_0}{\lambda_g}$	$c \frac{\lambda_0}{\lambda_g}$
Phase velocity, v_p	$c \frac{\lambda_g}{\lambda_0}$	$c \frac{\lambda_g}{\lambda_0}$
Wave impedance, Z	$\frac{jk_0\eta_0}{\gamma_{mn}}$	$\frac{-j\gamma_{mn}\eta_0}{k_0}$
Longitudinal magnetic field, H_z	$k_c^2 \cos\left(\frac{m\pi x}{a}\right) \cos\left(\frac{n\pi y}{b}\right)$	0
Longitudinal electric field, E_z	0	$k_c^2 \sin\left(\frac{m\pi x}{a}\right) \sin\left(\frac{n\pi y}{b}\right)$
Transverse magnetic field		
H_x	$\frac{\gamma_{mn}m\pi}{a} \sin\left(\frac{m\pi x}{a}\right) \cos\left(\frac{n\pi y}{b}\right)$	$\frac{k_0n\pi}{b\eta_0} \sin\left(\frac{m\pi x}{a}\right) \cos\left(\frac{n\pi y}{b}\right)$
H_y	$\frac{\gamma_{mn}n\pi}{b} \cos\left(\frac{m\pi x}{a}\right) \sin\left(\frac{n\pi y}{b}\right)$	$-\frac{k_0m\pi}{a\eta_0} \cos\left(\frac{m\pi x}{a}\right) \sin\left(\frac{n\pi y}{b}\right)$
Transverse electric field		
E_x	$\frac{jk_0\eta_0n\pi}{b} \cos\left(\frac{m\pi x}{a}\right) \sin\left(\frac{n\pi y}{b}\right)$	$-\frac{\gamma_{mn}m\pi}{a} \cos\left(\frac{m\pi x}{a}\right) \sin\left(\frac{n\pi y}{b}\right)$
E_y	$-\frac{jk_0\eta_0m\pi}{a} \sin\left(\frac{m\pi x}{a}\right) \cos\left(\frac{n\pi y}{b}\right)$	$-\frac{\gamma_{mn}n\pi}{b} \sin\left(\frac{m\pi x}{a}\right) \cos\left(\frac{n\pi y}{b}\right)$

TABLE 6
Field Distribution of Modes in Rectangular Waveguides

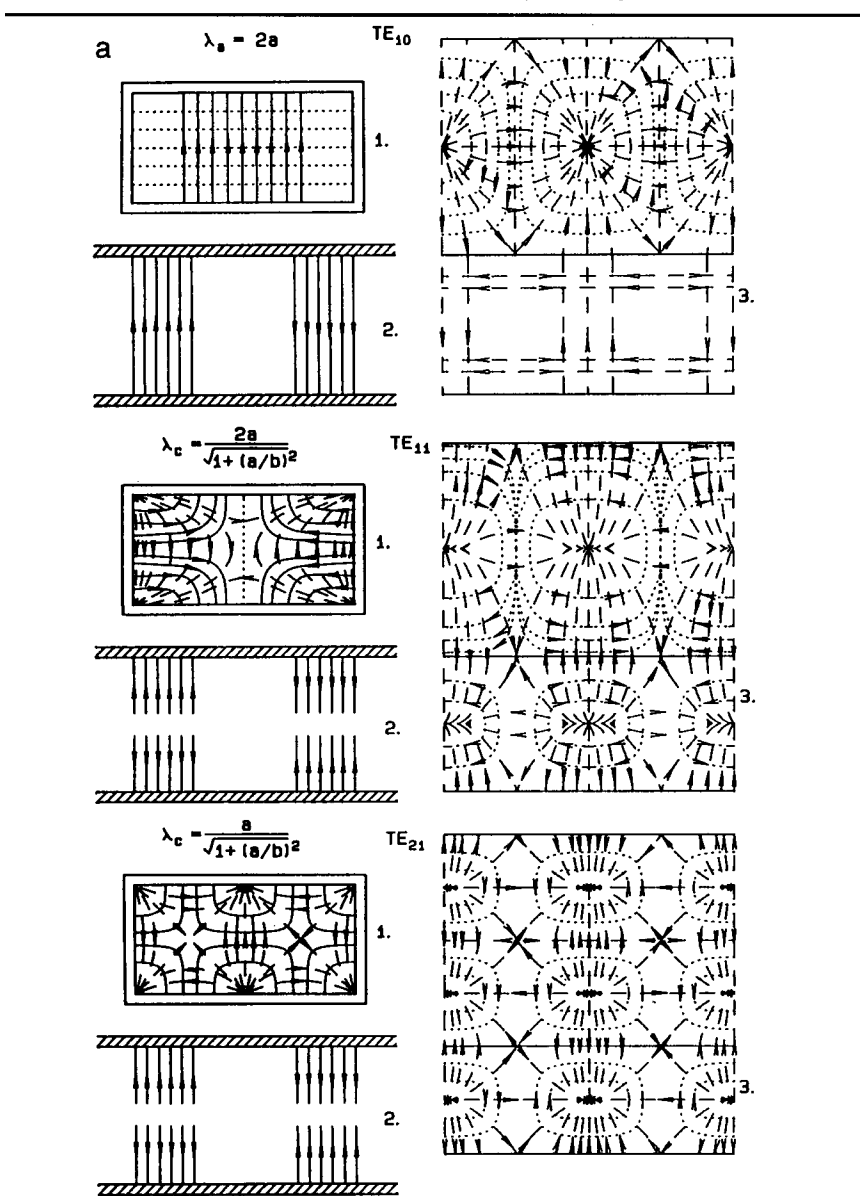
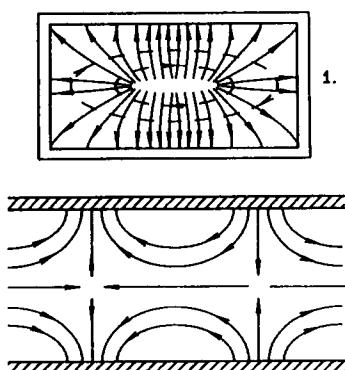
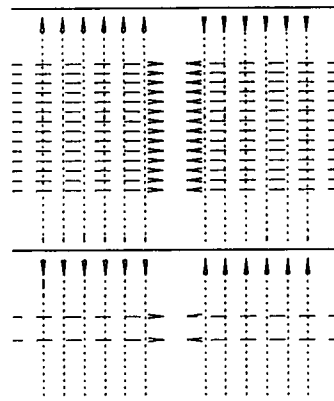


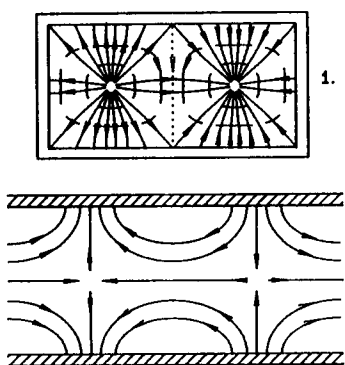
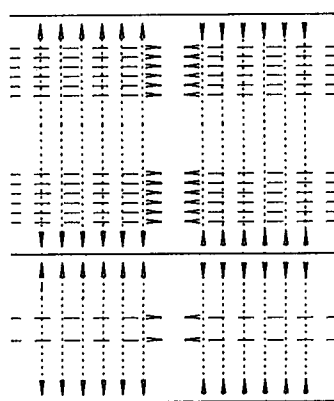
TABLE 6 (Continued)

b $\lambda_c = \frac{2a}{\sqrt{1+(a/b)^2}}$

TM₁₁

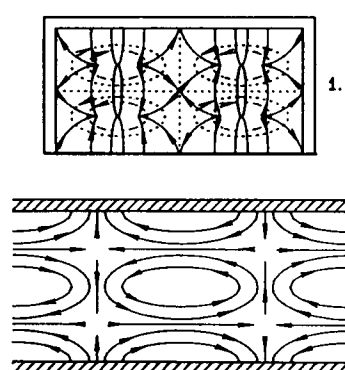
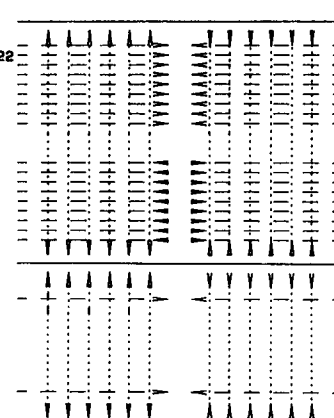
3.

$\lambda_c = \frac{a}{\sqrt{1+(a/b)^2}}$

TM₂₁

3.

c $\lambda_c = \frac{a}{\sqrt{1+(a/b)^2}}$

TM₂₂

3.

Note. 1, cross-sectional view; 2, longitudinal view; 3, surface view. (—) Current, (—) E-field, (···) H-field.

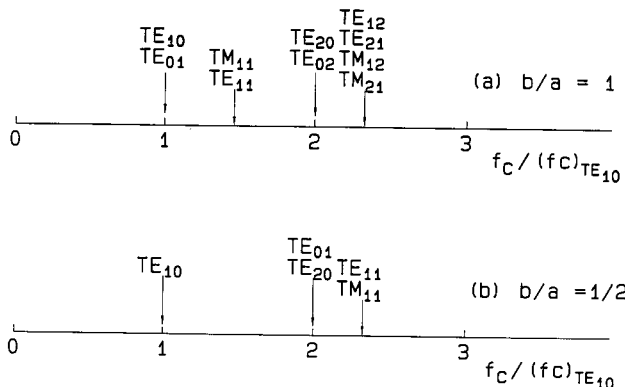


Figure 12. Relative cutoff frequencies of waves in rectangular waveguides. Reprinted with permission from *Fields and Waves in Communication Electronics*, by S. Ramo, J. R. Whinnery, and T. VanDuzar, Wiley, New York, 1965.

whereas, for the TM_{mn} modes, the attenuation constant is given by

$$\alpha_{mn} = \frac{2R_s}{b\eta_0\sqrt{1 - \left(\frac{\lambda_0}{\lambda_c}\right)^2}} \frac{m^2b^3 + n^2a^3}{m^2b^2a + n^2a^3} \quad (\text{nepers/unit length}), \quad (13)$$

where R_s is the surface resistance and $\eta_0 = 120\pi\Omega$ is the free space impedance. $\epsilon_{0n} = 1$ for $n = 0$ and 2 otherwise. Table 7 lists the properties of some commonly used waveguides [8].

Figure 13 shows the attenuation curves due to copper loss in rectangular waveguides with a fixed width. Such curves are based on the assumptions of the conductivity of pure copper and perfectly smooth walls. However, the surface roughness and the surface properties of the walls offer excess loss. Figure 14 shows the effects of surface roughness on waveguide attenuation, where δ is the skin depth [7].

The maximum power that can be handled by a rectangular waveguide is limited by dielectric breakdown and by heating due to conductor and dielectric losses. The peak power handling limit is decided by the electric breakdown, and the average power handling limit is decided by the conductor losses, dielectric losses, and the maximum allowable temperature rise. The limiting value of the peak power that can be handled by a rectangular waveguide, supporting the TE_{m0} or TE_{0n} mode, is given by

$$P_{\max}(\text{kW}) = 6.63 \times 10^{-7} abm^2 \sqrt{1 - \left(\frac{m\lambda_0}{2a}\right)^2} |E_{\max}|^2 \quad (14)$$

TABLE 7
Design Data of Rectangular Waveguides

EIA WG Designation WR()	Recommended operating range for TE ₁₀ mode (GHz)	Cutoff frequency for TE ₁₀ mode (GHz)	Theoretical CW power rating, lowest to highest frequency (MW)	Theoretical attenuation, lowest to highest frequency (db/100 ft)	Material alloy	Inside dimensions (in.)	JAN WG designation RG()/U
2300	0.32–0.49	0.256	1.53.0–212.0	0.051–0.031	Aluminum	23.000–11.500	
2100	0.35–0.53	0.281	120.0–173.0	0.054–0.034	Aluminum	21.000–10.500	
1800	0.41–0.625	0.328	93.4–131.9	0.056–0.038	Aluminum	18.000–9.00	201
1500	0.49–0.75	0.393	67.6–93.3	0.069–0.050	Aluminum	15.000–7.500	202
1150	0.64–0.96	0.513	35.0–53.8	0.128–0.075	Aluminum	11.500–5.750	203
975	0.75–1.12	0.605	27.0–38.5	0.137–0.095	Aluminum	9.750–4.875	204
770	0.96–1.45	0.766	17.2–24.1	0.201–0.136	Aluminum	7.700–3.850	205
650	1.12–1.70	0.908	11.9–17.2	0.317–0.212	Brass	6.500–3.250	69
				0.269–0.178	Aluminum		103
510	1.45–2.20	1.157	7.5–10.7			5.100–2.550	
430	1.70–2.60	1.372	5.2–7.5	0.588–0.385 0.501–0.330	Brass Aluminum	4.300–2.150	104 105
340	2.20–3.30	1.736	3.1–4.5	0.877–0.572 0.751–0.492	Brass Aluminum	3.400–1.700	112 113
284	2.60–3.95	2.078	2.2–3.2	1.102–0.752 0.940–0.641	Brass Aluminum	2.840–1.340	48 75
229	3.30–4.90	2.577	1.6–2.2			2.290–1.145	
187	3.95–5.85	3.152	1.4–2.0	2.08–1.44 1.77–1.12	Brass Aluminum	1.872–0.872	49 95
159	4.90–7.05	3.711	0.79–1.0			1.590–0.795	
137	5.85–8.20	4.301	0.56–0.71	2.87–2.30 2.45–1.94	Brass	1.372–0.622	50 106
112	7.05–10.00	5.259	0.35–0.46	4.12–3.21 3.50–2.74	Brass Aluminum	1.122–0.497	51 68
90	8.20–12.40	6.557	0.20–0.29	6.45–4.48 5.49–3.83	Brass Aluminum	0.900–0.400	52 67
75	10.00–15.00	7.868	0.17–0.23			0.750–0.375	
62	12.4–18.00	9.486	0.12–0.16	9.51–8.31 ---	Brass Aluminum	0.622–0.311	91
				6.14–5.36	Silver		107
51	15.00–22.00	11.574	0.080–0.107			0.510–0.255	
42	18.00–26.50	14.047	0.043–0.058	20.7–14.8 17.6–12.6 13.3–9.5	Brass Aluminum Silver	0.420–0.170	53 121 66
34	22.00–33.00	17.328	0.034–0.048			0.340–0.170	
28	26.50–40.00	21.081	0.022–0.031	— — 21.9–15.0	Brass Aluminum Silver	0.280–0.140	
				— 31.0–20.9	Brass Silver	0.224–0.112	96
22	33.00–50.00	26.342	0.014–0.020			0.188–0.094	
19	40.00–60.00	31.357	0.011–0.015	52.9–39.1	Brass	0.148–0.074	
15	50.00–75.00	39.863	0.0063–0.0090	—	Silver		97
12	60.00–90.00	48.350	0.0042–0.0060	— 93.3–52.2	Brasas Silver	0.122–0.061	
10	75.00–110.00	59.010	0.0030–0.0041			0.100–0.050	
8	90.00–140.00	73.840	0.0018–0.0026	152–99	Silver	0.080–0.040	
7	110.00–170.00	90.840	0.0012–0.0017	162–137	Silver	0.065–0.0325	
5	140.00–220.00	115.750	0.00071–0.00107	308–193	Silver	0.051–0.0255	
4	170.00–260.00	137.520	0.00052–0.00075	384–254	Silver	0.043–0.0215	
3	220.00–325.00	173.280	0.00035–0.00047	512–348	Silver	0.034–0.0170	

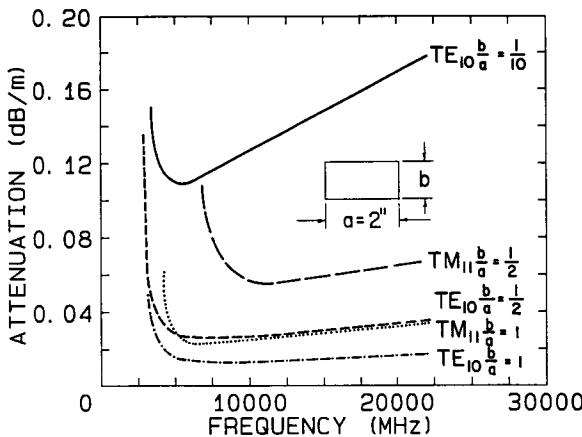


Figure 13. Attenuation due to copper losses in rectangular waveguides of fixed width. Reprinted with permission from *Fields and Waves in Communication Electronics*, by S. Ramo, J. R. Whinnery, and T. VanDuzar, Wiley, New York, 1965.

for the TE_{m0} mode, by

$$P_{\max}(\text{kW}) = 6.63 \times 10^{-7} abn^2 \sqrt{1 - \left(\frac{n\lambda_0}{2b}\right)^2} |E_{\max}|^2 \quad (15)$$

for the TE_{0n} mode, and by

$$P_{\max} = \frac{ab}{2} \frac{\beta_{mn} \left[\left(\frac{m}{a}\right)^2 + \left(\frac{m}{b}\right)^2 \right] \left[\left(\frac{b}{n}\right)^2 + \left(\frac{a}{m}\right)^2 \right]}{\eta_0 \epsilon_{0m} \epsilon_{0n}} |E_{\max}|^2 \quad (16)$$

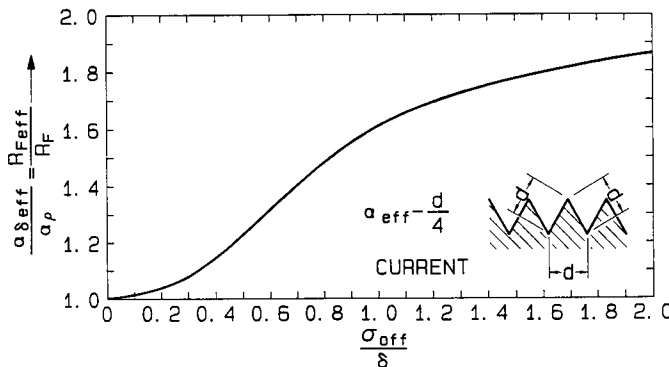


Figure 14. Effect of surface roughness on conductor loss. Reprinted with permission from *Handbook of Microwave Integrated Circuits*, by R. K. Hoffman, Artech House, Boston, 1988.

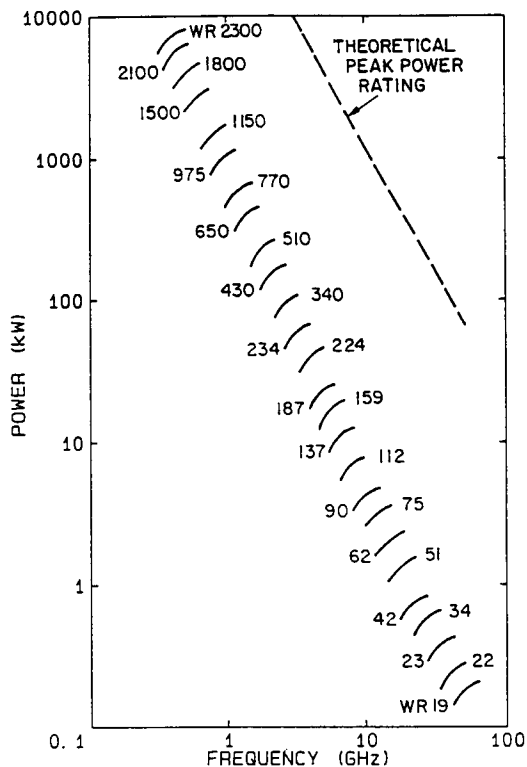


Figure 15. Peak-power-handling capability of standard rectangular waveguides for the TE_{10} mode.

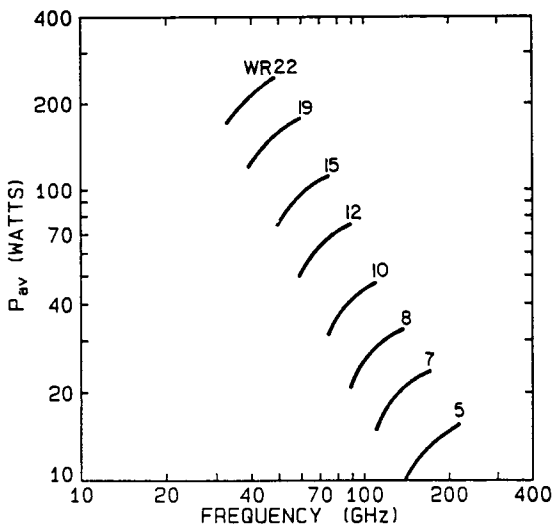


Figure 16. Average power rating for a rectangular waveguide.

TABLE 8
Values of ka for TE and TM Modes

n	m		
	1	2	3
Roots of $J'_n(k_h a) = 0$			
0	3.832	7.016	10.174
1	1.841 ^a	5.331	8.536
2	3.054	6.706	9.968
3	4.201	8.015	11.346
Roots of $J_n(k_e a) = 0$			
0	2.405	5.520	8.654
1	3.832	7.016	10.173
2	5.136	8.417	11.620
3	6.380	9.761	13.015

^aDominant mode of the circular waveguide.

for the TE_{mn} mode, where $\epsilon_{0m} = 1$ for $m = 1$ and 2 for $m > 1$. For dry air, at normal temperature and pressure, the dielectric breakdown occurs at a field strength of 2.9 mega volts/meter. Based on these data, P_{\max} is shown as a function of frequency in Figure 15 for the TE_{10} mode and various rectangular waveguides.

The average power handling capability of a waveguide is determined by the rise in temperature of the waveguide in an air environment. The temperature rise is calculated from the attenuation in the waveguide and the surface area of the waveguide. The maximum tolerable average power is limited by the maximum tolerable temperature rise and the ambient temperature. Figure 16 shows the theoretical curves of average power rating for a rectangular waveguide that come into play when the operating frequency is raised.

Circular Waveguide

Circular waveguides find applications in low-loss long-distance communication links. In particular, the TE_{01} mode of operation in a circular waveguide has the unique property of having a decreasing attenuation constant with an increasing operating frequency. This makes circular waveguides ideally suitable for many high-power, high- Q -filter applications. The values of normalized cutoff wavenumbers $k_h a$ and $k_e a$ for different modes are given in Table 8. The fundamental mode is TE_{11} .

TABLE 9
Properties of Waves in Empty Circular Waveguides

Property	TE _{nm} mode	TM _{nm} mode
Cutoff wavenumber k_c	k_h	k_e
Propagation constant, γ_{nm}	$\sqrt{k_h^2 - k_0^2}$	$\sqrt{k_e^2 - k_0^2}$
Guide wavelength, λ_g	$\lambda_0 / \sqrt{1 - \left(\frac{k_h}{k_0}\right)^2}$	$\lambda_0 / \sqrt{1 - \left(\frac{k_e}{k_0}\right)^2}$
Group velocity, v_g	$c \frac{\lambda_0}{\lambda_g}$	$c \frac{\lambda_0}{\lambda_g}$
Phase velocity, v_p	$c \frac{\lambda_g}{\lambda_0}$	$c \frac{\lambda_g}{\lambda_0}$
Wave impedance, Z	$\frac{j k_0 \eta_0}{\gamma_{nm}}$	$\frac{-j \gamma_{nm} \eta_0}{k_0}$
Longitudinal magnetic field, H_z	$k_h^2 J_h(k_h \rho) \cos n\phi$	0
Longitudinal electric field, E_z	0	$k_e^2 J_n(k_e \rho) \cos n\phi$
Transverse magnetic field		
H_ρ	$-\gamma_{nm} k_h J'_n(k_h \rho) \cos n\phi$	$-\frac{j k_0 n}{\rho \eta_0} J_n(k_e \rho) \sin n\phi$
H_ϕ	$\frac{\gamma_{nm} n}{\rho} J_n(k_h \rho) \sin n\phi$	$-\frac{j k_0 k_e}{\eta_0} J'_n(k_e \rho) \cos n\phi$
Transverse electric field		
E_ρ	$\frac{j k_{\eta_0 n}}{\rho} J_n(k_h \rho) \sin n\phi r$	$-\gamma_{nm} k_e J'_n(k_e \rho) \cos n\phi$
E_ϕ	$j k_0 \eta_0 k_h J'_n(k_h \rho) \cos n\phi$	$\frac{\gamma_{nm} n}{\rho} J_n(k_e \rho) \sin n\phi$

TABLE 10
Field Distribution in Circular Waveguides for TE and TM Modes

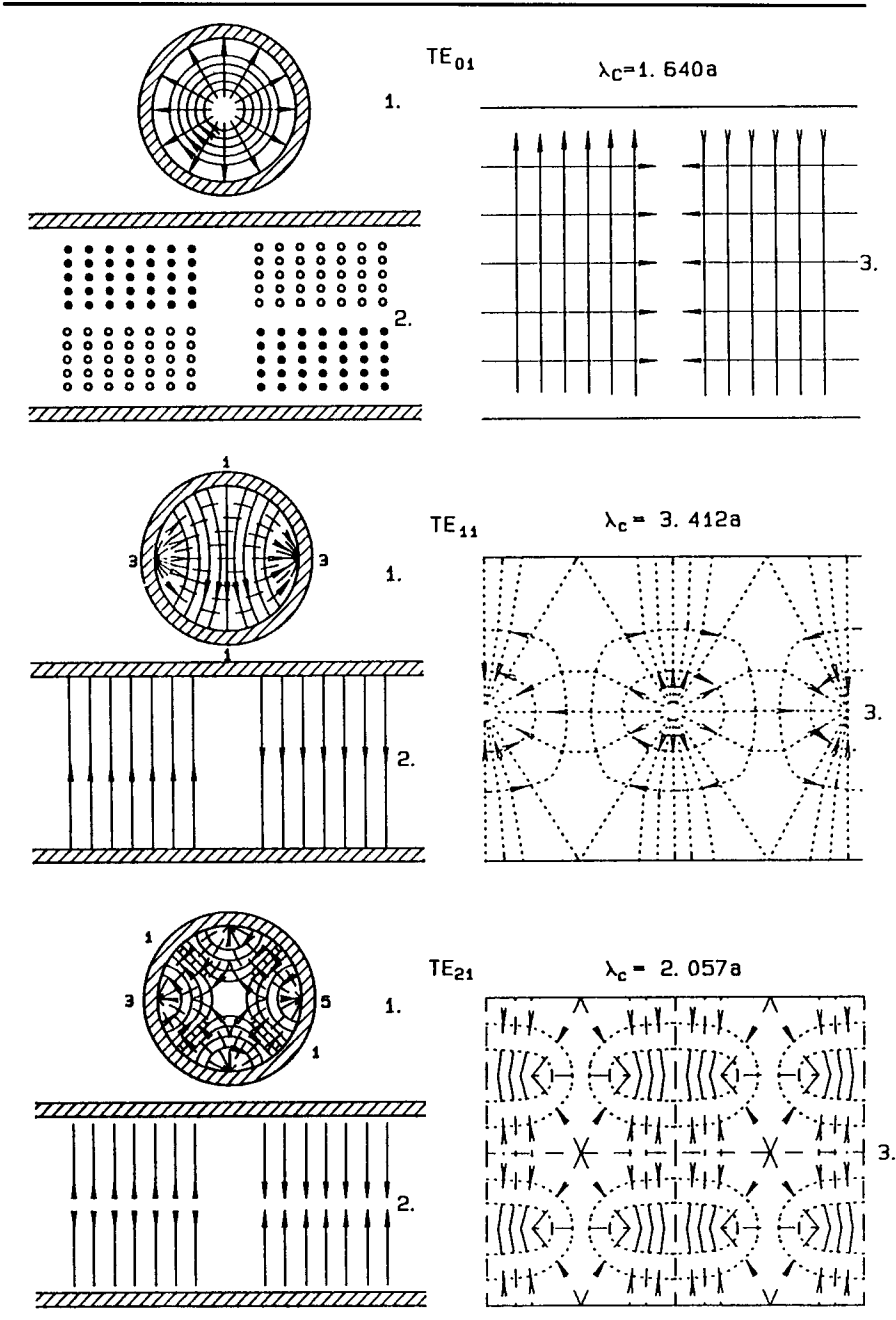
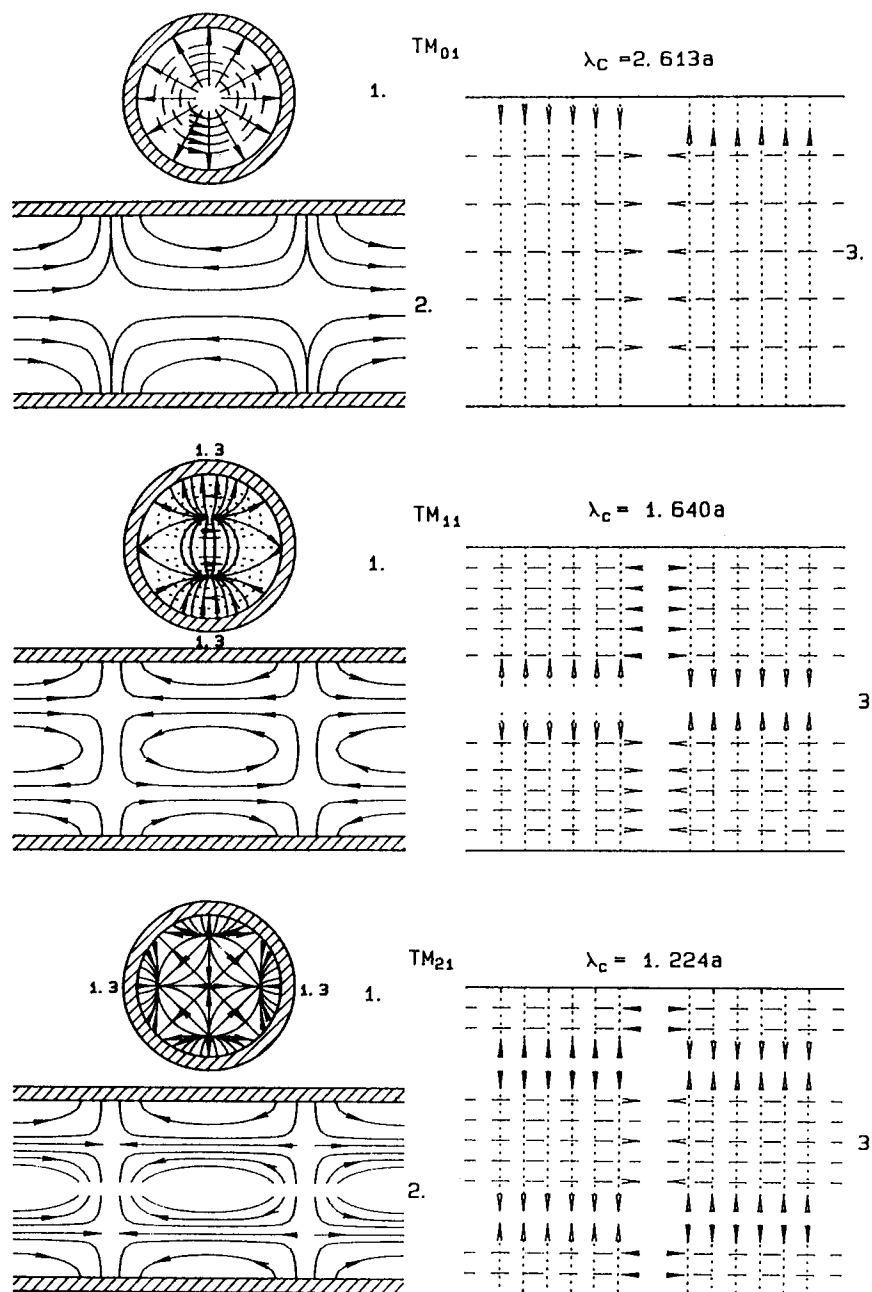


TABLE 10 (Continued)



Note. 1, cross-sectional view; 2, longitudinal view through plane l-l; 3, surface view from s-s. (—) Current, (—) E-field, (···) H-field.

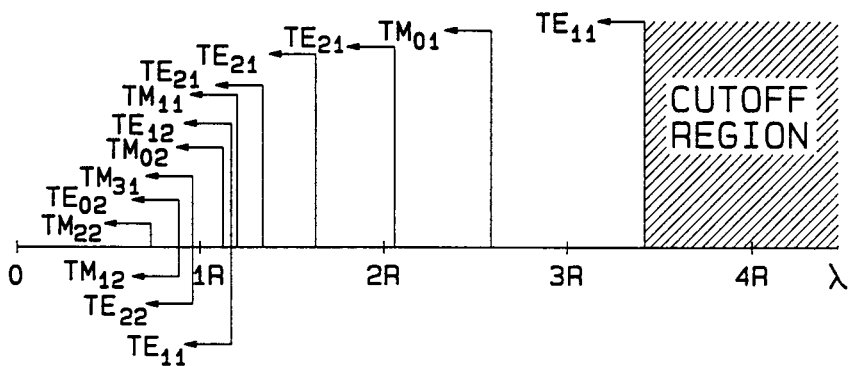


Figure 17. Cutoff wavelengths in a circular waveguide.

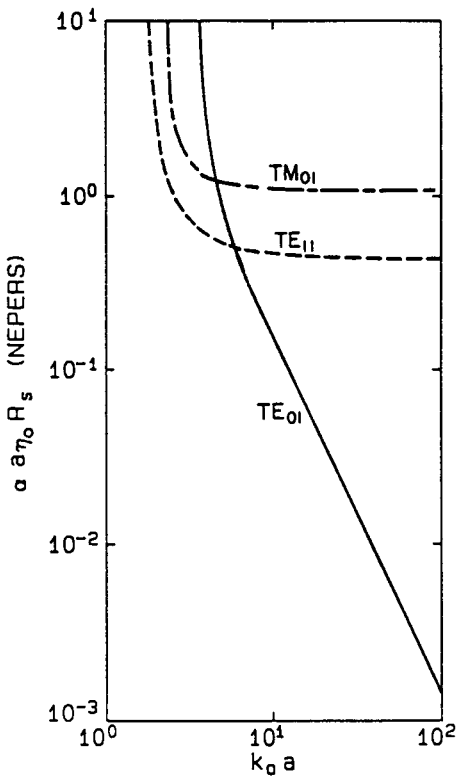


Figure 18. Attenuation vs $k_0 a$ in a circular waveguide.

Table 9 summarizes the general properties of TE_{mn} and TM_{mn} modes of a circular waveguide. Table 10 shows the magnetic and the electric field distributions of the first few modes of a circular waveguide. Figure 17 shows the order in which various modes propagate in a circular waveguide.

The attenuation constant in a circular waveguide is given by

$$\alpha_{mn} = \frac{R_s}{a\eta_0} \left(1 - \frac{k_h^2}{k_0^2}\right)^{-1/2} \left[\frac{k_h^2}{k_0^2} + \frac{h^2}{(k_h a)^2 - n^2} \right] \quad (\text{nepers/unit length}) \quad (17)$$

for TE_{mn} modes and by

$$\alpha_{mn} = \frac{R_s}{a\eta_0} \frac{k_0^2}{(k_0^2 - k_c^2)^{1/2}} \quad (\text{nepers/unit length}) \quad (18)$$

for TM_{mn} modes, where R_s is the surface resistivity. Figure 18 shows the attenuation versus $k_0 a$ curves in circular waveguides.

The peak and the average power handling capabilities of a circular waveguide are based on the same factors as those in a rectangular waveguide. Figure 19 shows the peak power versus $k_0 a$ curves in copper rectangular waveguides.

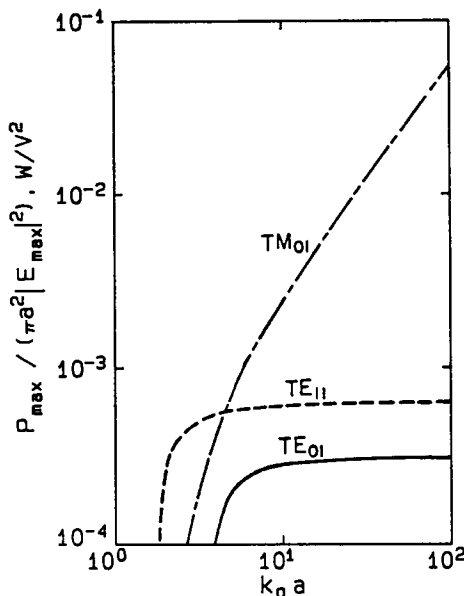


Figure 19. Peak power vs $k_0 a$ in a circular waveguide.

The maximum average power that can be handled by a circular waveguide is given by

$$P_{av} = \frac{4.343}{\alpha} Ah_c(T_w - T_a) \text{ (watts)}, \quad (19)$$

where α is the attenuation constants of the waveguide (dB/m), A is the surface area of a 1-m-long waveguide, h_c is the heat transfer coefficient [9,10], T_w is the maximum allowable temperature of the walls of the waveguide, and T_a is the ambient temperature.

5. Finlines

The finline can be considered a shielded slotline, with the finline being quasiplanar and suspended in the E -plane of a rectangular waveguide. Thus, in a given frequency band, the finline dimensions are identical to those of a commensurate waveguide. Figure 20 shows the cross sections of various finlines, and Figure 21 shows the three-dimensional views of three commonly used finlines. The structures may be regarded as dielectric, slab-loaded waveguides, with printed fins on the slab, or as a ridged waveguide with a zero-thickness ridge backed by a dielectric slab in the E -plane. the suspended fins concentrate the field energy in the fingap region, leading to a capacitive loading of the dominant HE mode of

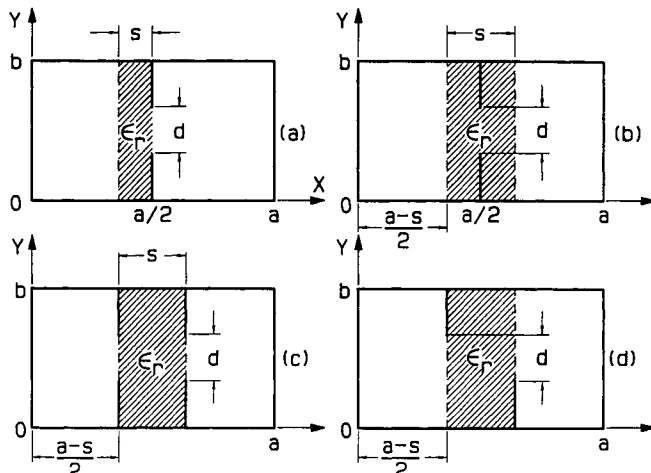


Figure 20. Cross sections of several finlines: (a) unilateral, (b) insulated, (c) bilateral, and (d) antipodal.

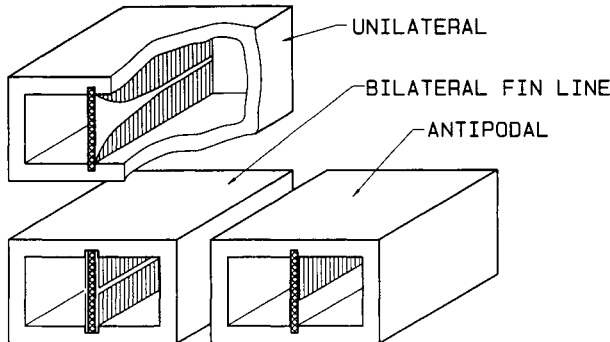


Figure 21. Three-dimensional views of three commonly used finlines.

propagation in the slab-loaded waveguide. This effectively lowers the cutoff frequency of the fundamental mode to a large extent and that of the next higher order mode to a small extent, thus leading to a larger fundamental mode bandwidth. Figures 22a, 22b, 22c, and 22d show the electric field distribution in unilateral, bilateral, antipodal, and bilateral coupled finlines, respectively. For an exhaustive account of finline characteristics and circuits, the reader is referred to Ref. [11]. Figures 23a and 23b show the propagation constant and the impedance characteristics of a *Ka*-band unilateral finline. The impedance is based on the power voltage definition. The computations were done using the conservation of complex power technique [12]. Such characteristics may also be obtained using various other techniques [13].

Propagation Constant

Finlines support hybrid modes. Hence, an exact determination of the propagation constant would require a full-wave solution to the associated boundary value problem. However, for all design purposes for which thin substrates of very low permittivity are used, the dominant HE and EH modes in a finline can be approximated by their TE and TM counterparts, respectively. Under such conditions, the propagation constant of a finline is given by

$$\beta = k_0 \sqrt{\epsilon_e(f)}, \quad (20)$$

where k_0 is the propagation constant in free space and $\epsilon_e(f)$ is the

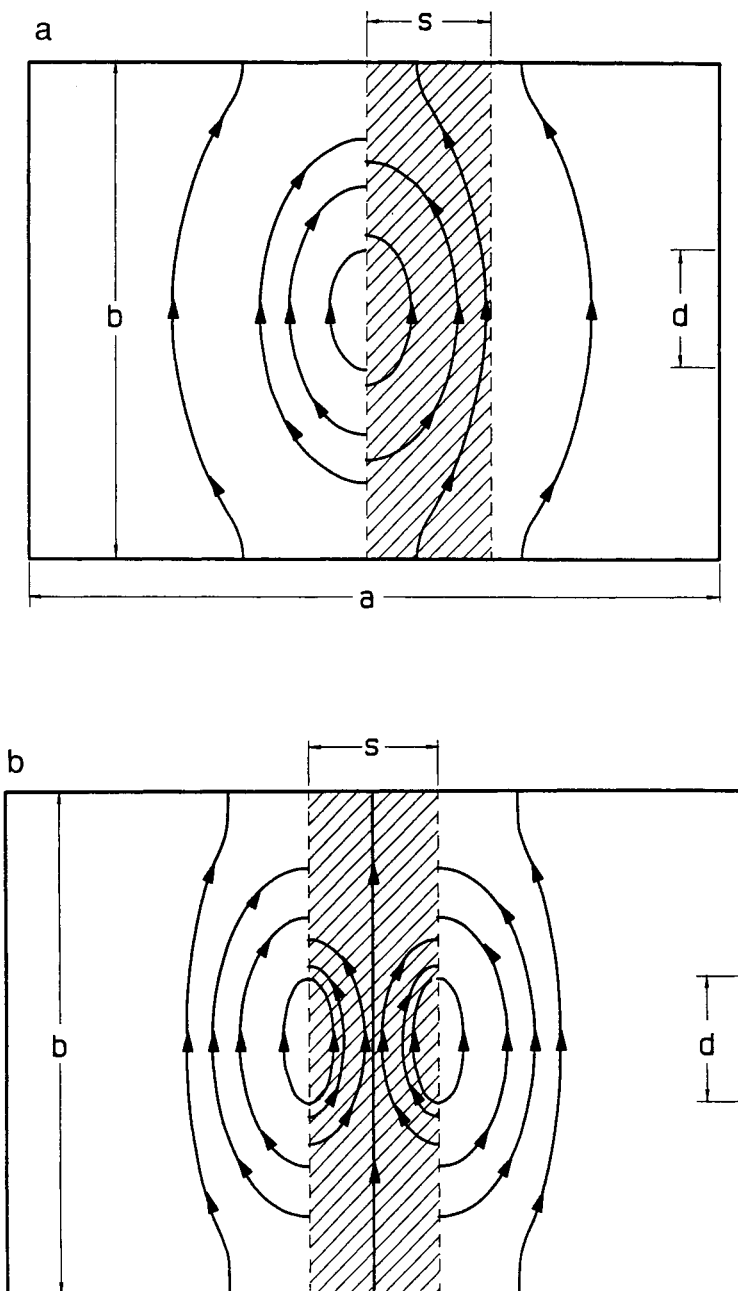


Figure 22. Distribution of transverse electric fields: (a) unilateral, (b) bilateral, (c) antipodal, and (d) coupled bilateral.

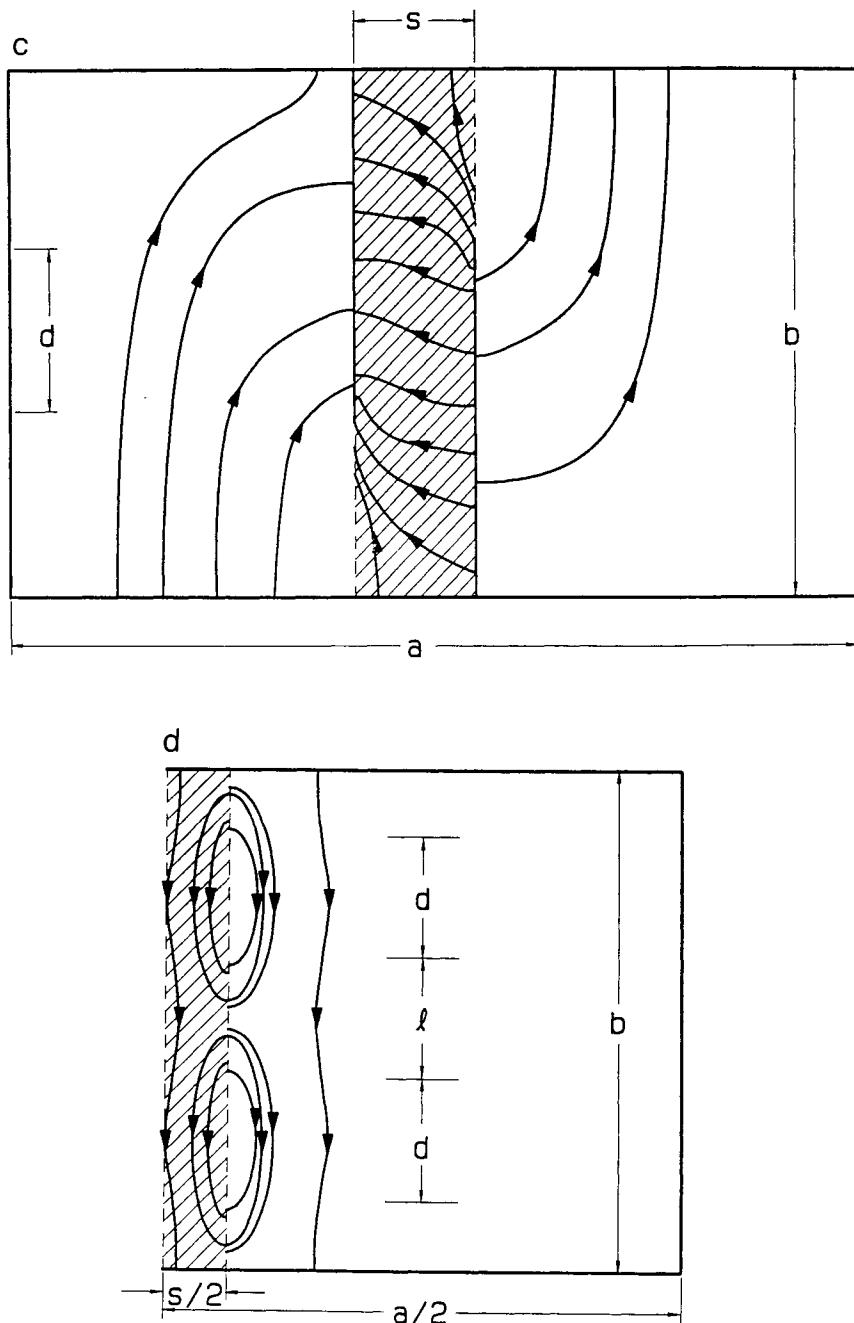


Figure 22. (Continued).

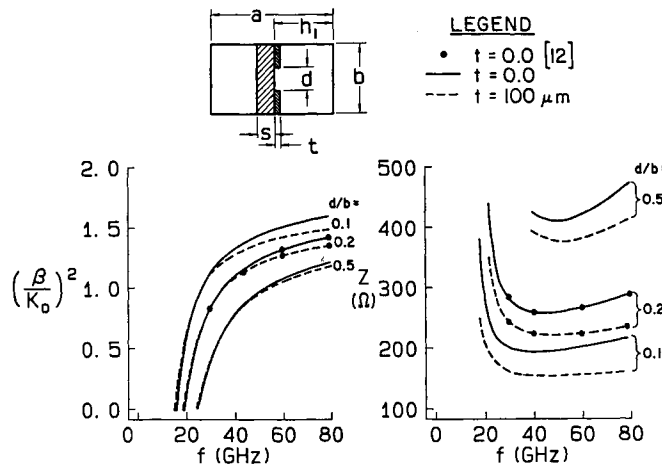


Figure 23. Effective dielectric constant and characteristic impedance versus frequency in unilateral finlines with different values of slit width. $a = 2b = 4.7752$ mm, $s = 0.127$ mm, $h_1 = 2.3876$ mm, and $\epsilon_r = 3.8$.

effective dielectric constant given by [14]

$$\epsilon_e(f) \cong k_c - \left(\frac{\lambda}{\lambda_{ca}} \right)^2, \quad (21)$$

where k_c , the equivalent dielectric constant, given by

$$k_c = \left(\frac{\lambda_{cf}}{\lambda_{ca}} \right)^2, \quad (22)$$

and λ_{cf} and λ_{ca} are the cutoff wavelengths of the finline with and without the dielectric substrate, respectively.

For unilateral finlines [15],

$$\lambda_{ca} = 2a \left\{ 1 + \frac{4}{\pi} \left(\frac{b}{a} \right) \left(1 + 0.2 \sqrt{\frac{b}{a}} \right) x \right\}^{1/2} \quad (23)$$

and

$$k_c = 1 + \frac{s}{a} \left[a_1 + b_1 \ln \csc \left(\frac{\pi}{2} \frac{d}{b} \right) \right] (\epsilon_r - 1), \quad (24)$$

where

$$a_1 = 0.4021 \left(\ln \frac{a}{s} \right)^2 - 0.7685 \ln \frac{a}{s} + 0.3932 \quad (25)$$

$$b_1 = 2.42 \sin \left(0.556 \ln \frac{a}{s} \right) \quad (26)$$

$$x = \text{Incsc} \left(\frac{\pi}{2} \frac{d}{b} \right). \quad (27)$$

For bilateral finlines [16],

$$\lambda_{cf} = 2(a - s) \left\{ 1 + \frac{4}{\pi} \left(\frac{b}{a - s} \right) \left(1 + 0.2 \sqrt{\frac{b}{a - s}} \right) x_b \right\}^{1/2} \quad (28)$$

$$x_b = x + \epsilon_r G_d \quad (29)$$

$$G_d = \eta_d \arctan \left(\frac{1}{\eta_d} \right) + \ln \left(1 + \eta_d^2 \right)^{1/2} \quad (30)$$

$$\eta_d = \left(\frac{s}{a} \right) \left(\frac{b}{a} \right) \left(\frac{d}{b} \right). \quad (31)$$

For λ_{ca} , use Equations (28) to (31) with $\epsilon_r = 1$. The above equations are correct to within $\pm 1\%$ for $s/a \leq \frac{1}{8}$, and $2.2 \leq \epsilon_r \leq 3.8$.

Characteristic Impedance

An unambiguous definition of the characteristic impedance is not possible for finlines because of the non-TEM nature of the supported mode. However, Meier [14], using a ridged waveguide model, has given an approximate definition. It is defined as [17]

$$Z_0 = Z_{0\infty} \sqrt{k_e(f) - \left(\frac{\lambda}{\lambda a} \right)^2} \quad (32)$$

$$k_e(f) \approx k_c. \quad (33)$$

For unilateral finlines,

$$Z_{0\infty} = \frac{240\pi(b/a)G}{1 + \left(\frac{4}{\pi} \right) \left(\frac{b}{a} \right) Gx}, \quad (34)$$

where

$$x = \ln \csc\left(\frac{\pi}{2} \frac{d}{b}\right)$$

$$G = 1 + (0.129\sqrt{x} + 0.000915)\sqrt{\frac{b}{a}}.$$

For bilateral finlines [16],

$$Z_{0\infty} = \frac{240\pi^2(p\bar{x} + g)b/(a - s)}{(0.385\bar{x} + 1.726)^2}, \quad (35)$$

where

$$\bar{x} = x_b - G_d(\epsilon_r - 1)$$

$$p = 0.097(b/\lambda)^2 + 0.01(b/\lambda) + 0.04095$$

$$q = 0.0031(b/\lambda_0) + 0.89.$$

Losses

Finline losses are comparable to those of a ridged waveguide of the same geometrical dimension, provided the substrate supporting the metallic fins occupies a negligible fraction of the finline cross section.

6. Dielectric Waveguides

Dielectric waveguides are used in integrated optics and millimeter wave circuits. In dielectric waveguides, the wave travels due to the total internal reflections at the boundary between two different dielectric materials. Figure 24 shows the generalized cross section of a dielectric waveguide.

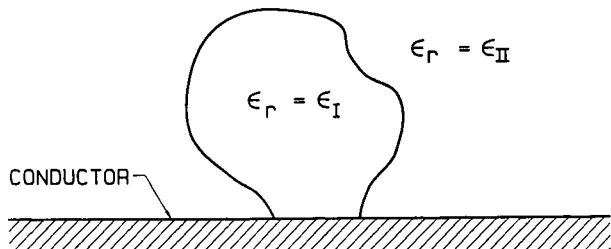


Figure 24. Dielectric waveguide.

The conductor loss in dielectric waveguides is extremely low. However, the loss due to the curvature, junction and discontinuities, etc. may be considerably large. Use of high permittivity and low loss dielectric materials alleviate this loss problem at the cost of very small size at millimeter waveband, and severe fabrication tolerance problems.

Propagation Constant

The complex propagation constant of dielectric waveguides can be determined using several numerical techniques [18–20]. Most accurate is the mode matching technique [20]. Among all the methods, the Effective Dielectric Constant technique [21] is the simplest for determining the phase constant of dielectric waveguides. Marcatelli's approximation [19] offers reasonable accuracy and closed form equations for the rectangular dielectric waveguide and its derivative, the image guide, shown in Figure 25. The propagation constants are given below [20].

Rectangular Dielectric Guide (Figure 25a)

$$k_z = (\epsilon_r k_0^2 - k_x^2 - k_y^2)^{1/2} \quad (36)$$

$$k_x = \frac{m\pi}{2a} \left[1 + \frac{1}{a\{(\epsilon_r - 1)k_0^2 - k_y^2\}} \right]^{-1} \quad (37)$$

$$k_y = \frac{n\pi}{2b} \left[1 + \frac{1}{\epsilon_r b \sqrt{(\epsilon_r - 1)k_0^2}} \right]^{-1} \quad (38)$$

$$k_{x0} = \{(\epsilon_r - 1)k_0^2 - k_x^2 - k_y^2\} \quad (39)$$

$$k_{y0} = \{(\epsilon_r - 1)k_0^2 - k_y^2\}, \quad (40)$$

where k_x and k_y , and k_{x0} and k_{y0} are the transverse propagation constants inside and outside the guide, respectively, as shown in Figure 25a, and k_0 is the free-space propagation constant. Figure 26 shows the normalized guide wavelengths for the first two modes as a function of frequency. The dominant mode is the E_{11}^y mode.

Imageguide

The propagation constant in an imageguide, shown in Figure 25b, is given by Equation (36), where k_x and k_y are the solutions of the following

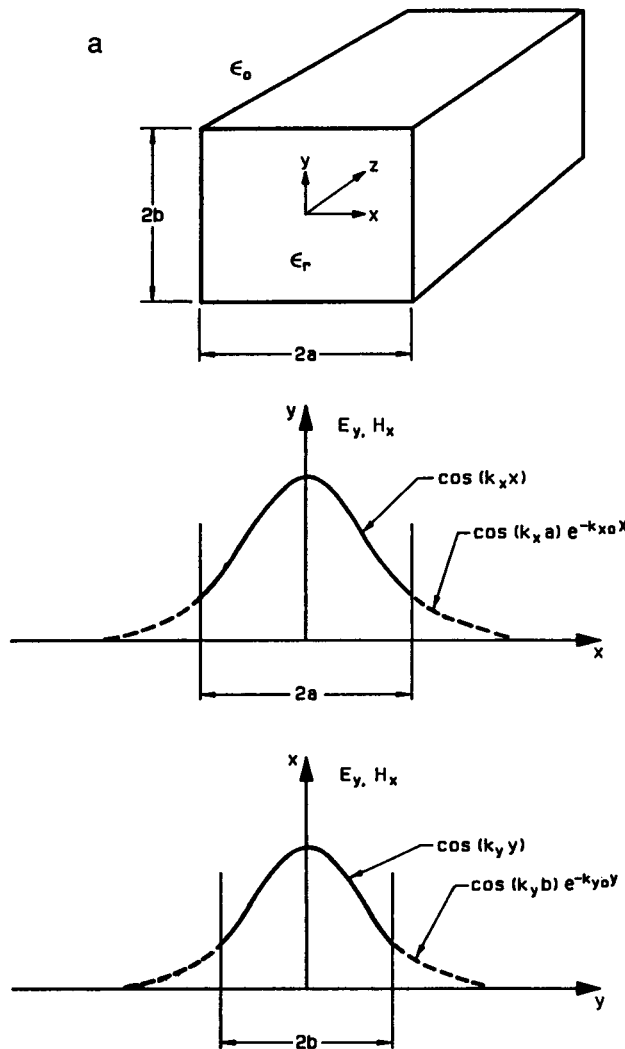


Figure 25a. Rectangular dielectric waveguide and the field distribution.

set of transcendental equations:

$$\tan(k_x a) = k_{x0}/k_x \quad (41)$$

$$k_x^2 = \epsilon_{re}(y) k_0^2 - k_z^2 \quad (42)$$

$$k_{x0}^2 = k_z^2 - k_0^2 = \{\epsilon_{re}(y) - 1\} k_0^2 - k_x^2 \quad (43)$$

$$\epsilon_{re}(y) = \epsilon_r - \left(\frac{k_y}{k_0}\right)^2 \quad (44)$$

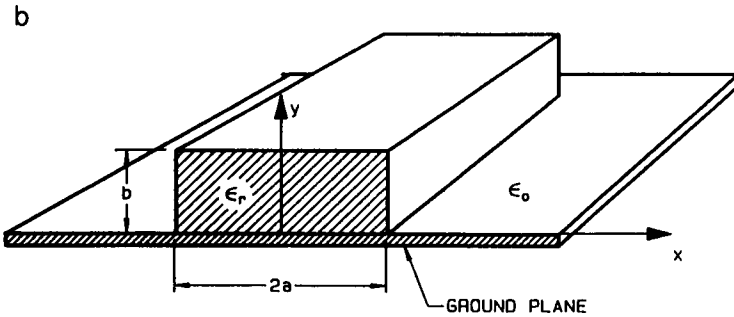


Figure 25b. Imageguide.

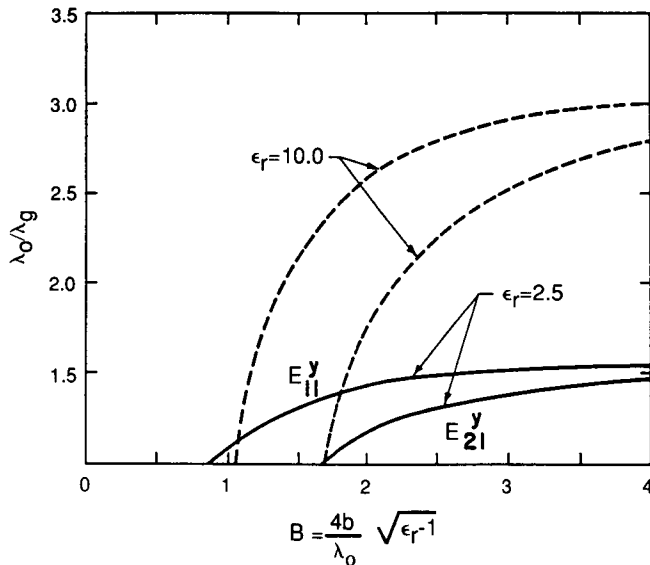
and

$$\tan(k_y b) = \epsilon_{re}(x) k_{y0} / k_y \quad (45)$$

$$k_y^2 = \epsilon_{re}(x) k_0^2 - k_z^2 \quad (46)$$

$$k_{y0}^2 = [\epsilon_{re}(x) - 1] k_0^2 - k_y^2 \quad (47)$$

$$\epsilon_{re}(x) = \epsilon_r - \left(\frac{k_x}{k_0} \right)^2 \quad (48)$$

Figure 26. λ_0 / λ_g for a dielectric guide with $a/b = 1$ versus normalized guide dimension B for different modes.

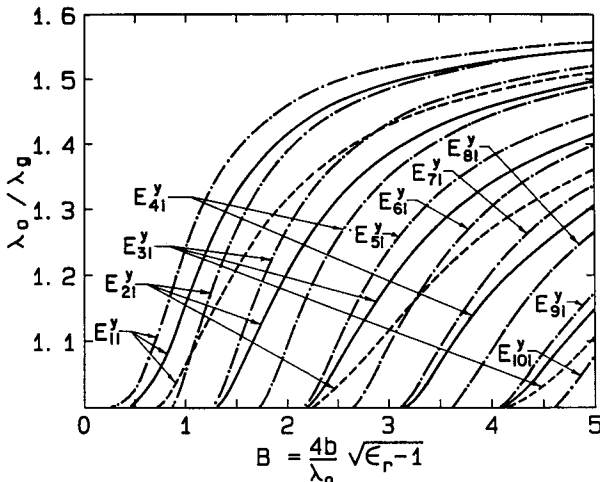


Figure 27. Dispersion curves for E_{mn}^y modes in an imageguide.

In solving Equations (41) and (45), the \tan^{-1} function should be considered in the first quadrant. Figure 27 shows the dispersion curves for E_{mn} modes in an imageline.

Losses in Dielectric Waveguides

Loss in Dielectric Rectangular Waveguides

Assuming a lossless external medium, the attenuation constant of a dielectric waveguide may be written as [22]

$$\alpha_d = R \frac{\pi}{\lambda_0} \epsilon_r \tan \delta, \quad (49)$$

where $\tan \delta$ is the loss factor of the material, and the scaling factor R , representing the relative amount of energy being propagated outside the dielectric guide, is given by

$$R = \frac{\frac{A}{\eta_0}}{\frac{A}{\eta_1} + \frac{B}{\eta_2} + \frac{C}{\eta_2}}, \quad (50)$$

where

$$A = \left\{ 1 + \frac{\sin(2k_x a)}{2k_x a} \right\} \left\{ 1 + \frac{\sin(2k_y b)}{2k_y b} \right\} \quad (51)$$

$$B = \frac{\cos^2(k_x a)}{k_x a} \left\{ 1 + \frac{\sin(2k_x b)}{2k_x b} \right\} \quad (52)$$

$$C = \frac{\cos^2(k_y b)}{(k_{y0} b)} \left\{ 1 + \frac{\sin(2k_x a)}{2k_x a} \right\} \quad (53)$$

$$\eta_1 = \frac{k_x^2 + k_y^2}{\omega \epsilon_0 \epsilon_r k_z} \quad (54)$$

$$\eta_2 = \frac{k_{x0}^2 + k_z^2}{\omega \epsilon_0 k_z} \quad (55)$$

and $\eta_0 = 120\pi\Omega$ (free-space impedance) $\epsilon_0 = 8.854 \times 10^{-12}$ farads/meter (free-space permittivity).

Losses in Imageguides

The attenuation constant in an imageguide is given by

$$\alpha = \alpha_c + \alpha_d, \quad (56)$$

where α_c is the attenuation constant due to the conductor loss, and α_d is the attenuation constant due to the dielectric loss. For the dominant E_{11}^y mode,

$$\alpha_c = \frac{R_s}{b} \frac{X + Y}{\frac{A}{\eta_1} + \frac{B}{\eta_2} + \frac{C}{\eta_2}}, \quad (57)$$

where

$$X = \frac{1}{\eta_1^2} \left\{ 1 + \frac{\sin(2k_x a)}{2k_x a} \right\} + \frac{1}{\eta_3^2} \left\{ 1 - \frac{\sin(2k_x a)}{2k_x a} \right\} \quad (58)$$

$$Y = \frac{1}{k_{x0} a} \left\{ \frac{\cos^2(k_x a)}{\eta_2^2} + \frac{\sin^2(k_x a)}{\eta_4^2} \right\}, \quad (59)$$

where, A , B , C , η_1 , and η_2 are given by Equations (51), (52), (53), (54),

and (55) respectively, and

$$\eta_3 = \left(\frac{k_z}{k_x} \right) \eta_1 \quad (60)$$

$$\eta_4 = \left(\frac{k_z}{k_{x0}} \right) \eta_2. \quad (61)$$

Figure 28 shows the conductor attenuation characteristics of the dominant E_{11}^y mode in an imageguide for $a = b$.

The attenuation constant due to the dielectric loss in an imageguide is given by Equation (49). The scaling factor, R_s , is obtained from Figure 29 for the most commonly used dielectric materials in imageguides.

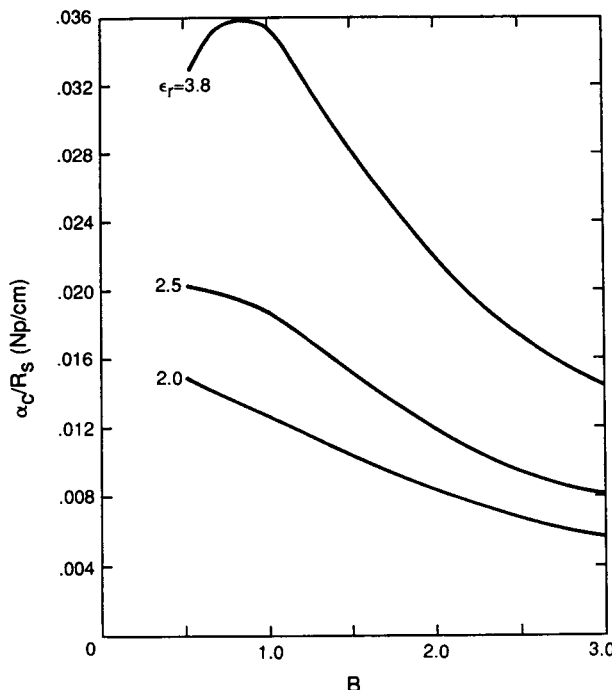


Figure 28. Conductor loss versus normalized thickness B for the E_{11}^y mode in an imageguide. ($a/b = 1$).

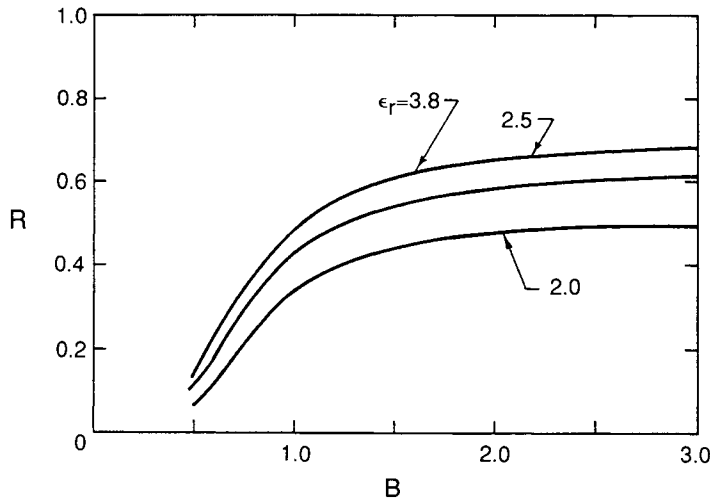


Figure 29. Scaling factor R versus normalized thickness B for the $\epsilon_{||}^\gamma$ mode in an imageguide ($a = b$).

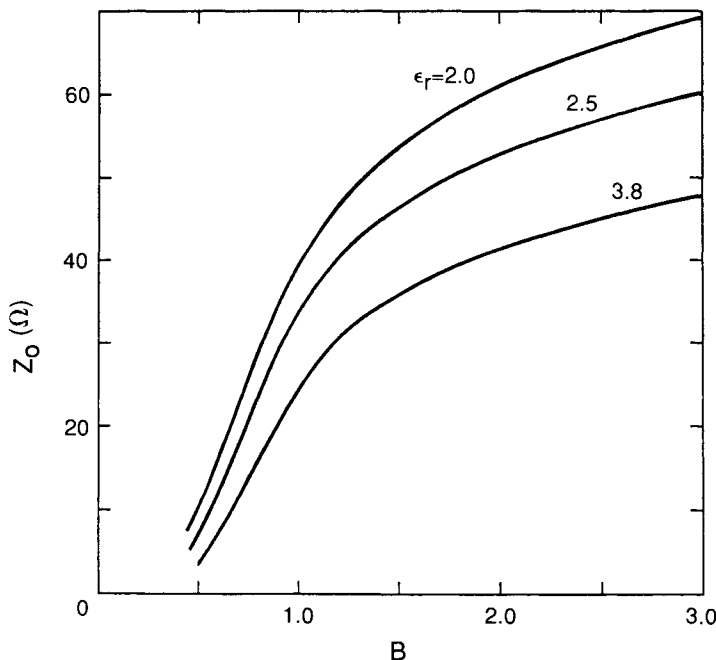


Figure 30. Imageguide characteristic impedance versus the normalized thickness B for the dominant $\epsilon_{||}^\gamma$ mode ($a = b$).

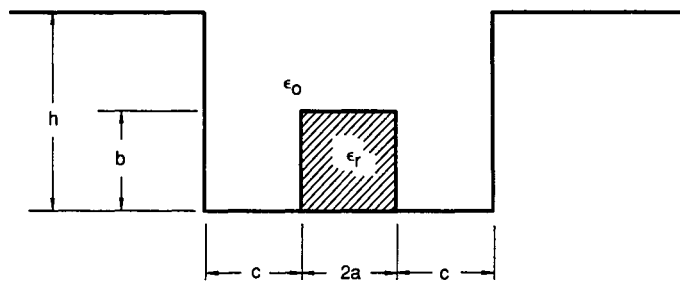


Figure 31. Trapped imageguide.

Characteristic Impedance of Imageguides

Since dielectric waveguides support non-TEM modes, the characteristic impedance cannot be uniquely defined. Following a power/current definition, the characteristic impedance of an imageguide is given by

$$Z_0 = \frac{b}{8a} \frac{\frac{A}{\eta_1} + \frac{B}{\eta_2} + \frac{C}{\eta_2}}{\left\{ \frac{\sin(k_x a)}{\eta_1 k_x a} + \frac{\cos(k_x a)}{k_x a} \right\}^2}. \quad (62)$$

Figure 30 shows the characteristic impedance variation in an imageguide as a function of the normalized thickness $B = 4b\sqrt{\epsilon_r - 1}/\lambda_0$.

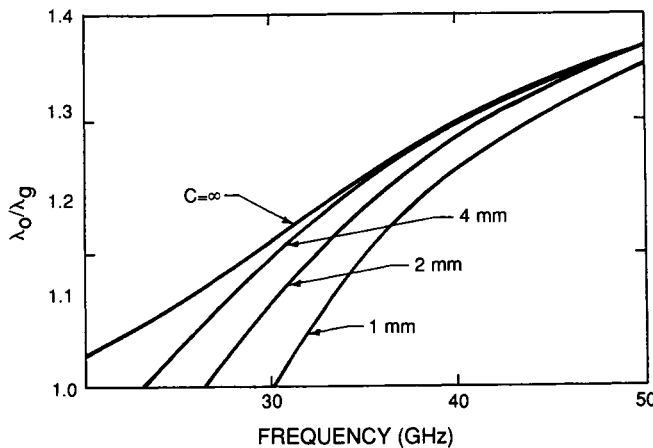


Figure 32. Typical dispersion curves for a trapped imageguide, $a = b = 2$ mm, $\epsilon_r = 2.56$. Reprinted with permission from IEEE Trans. MTT, Vol. 28, December 1980, by T. Itoh and B. Adelseek.

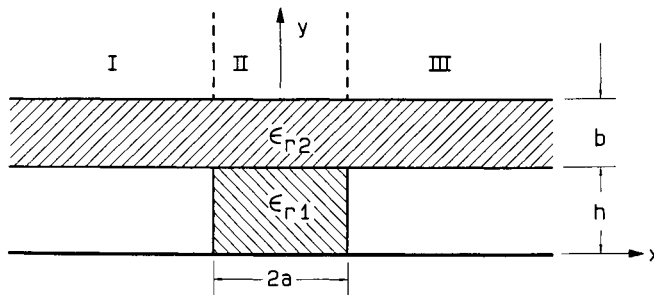


Figure 33. Inverted stripguide.

Other Forms of Dielectric Waveguide: Trapped Image Guides

Figure 31 shows the cross section of a trapped imageguide. The metallic side walls effectively bounce back any radiated field originating from bends and discontinuities in the dielectric line. For single mode operation, the reflected energy once again is coupled with the guided mode. Figure 32 shows the propagation characteristics of a trapped imageguide.

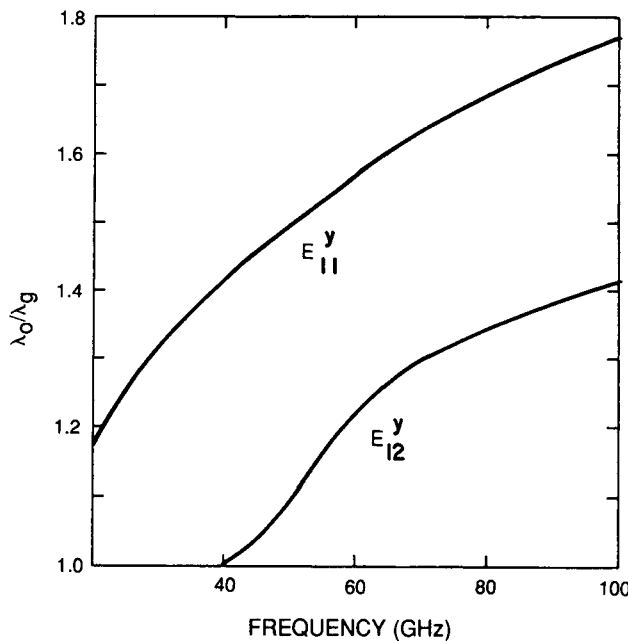


Figure 34. Dispersion characteristics for an inverted stripguide ($\epsilon_{r1} = 2.1$, $\epsilon_{r2} = 3.8$, $2a = 4$ mm, $b = h = 1.5875$ mm).

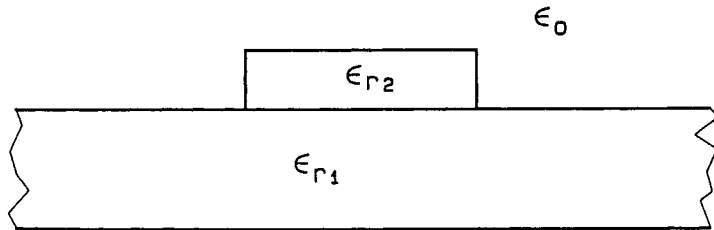


Figure 35. Insular guide ($\epsilon_{r2} > \epsilon_{r1}$).

Inverted Stripguide

The inverted stripguide, shown in Figure 33, offers a lower attenuation than any other dielectric waveguide containing a metal ground plane. Figure 34 shows the propagation characteristics for the dominant mode, E_{11}^y , and the next higher order mode, E_{12}^y , of a typical inverted stripguide.

Insular Guide

The insular guide, shown in Figure 35, is a modified imageguide with a dielectric slab interposed between the dielectric core and the ground plane. It is required that $\epsilon_{r2} > \epsilon_{r1}$, so that most of the propagating energy is confined in the core, resulting in low attenuation. An insular guide has twice the Q of an imageguide. Figure 36 shows the typical propagation characteristics of an insular guide.

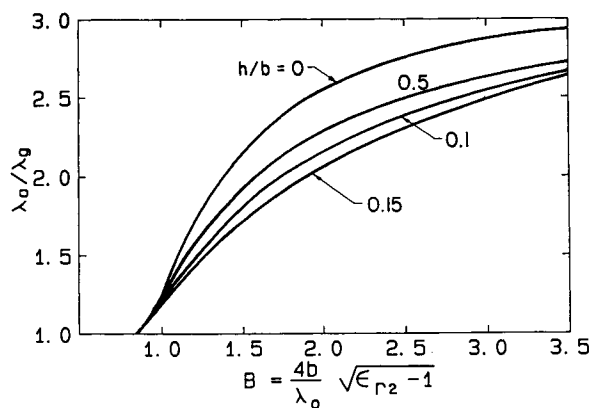


Figure 36. Dispersion curves for the ϵ_{11}^y mode in an insular guide ($a = b$, $\epsilon_{r1} = 2.25$, $\epsilon_{r2} = 9.8$).

References

- [1] L. J. Giacoletto, *Electronics Designers Handbook*. New York: McGraw-Hill, 1977.
- [2] K. Chang, eds., *Handbook of Microwave and Optical Components*, Vol. 1. New York: Wiley (Interscience), 1989.
- [3] C. G. Montgomery, R. H. Dicke, and E. M. Purcell, eds., *Principles of Microwave Circuits*. New York: McGraw-Hill, 1948.
- [4] S. Ramo, J. R. Whinnery, and T. Van Duzar, *Fields and Waves in Communication Electronics*, 2nd ed. New York: Wiley (Interscience), 1984.
- [5] Transtech, Inc., "A Designer's Guide to Microwave Dielectric Ceramics." Mar. 1988.
- [6] S. M. Perlow, Analysis of edge coupled shielded strip and slabline structures, *IEEE Trans. Microwave Theory Tech.*, Vol. MTT-35, pp. 522–529, May 1987.
- [7] S. P. Morgan, Effect of surface roughness on eddy current losses at microwave frequencies, *J. Appl. Phys.* Vol. 20, pp. 352–362, 1949.
- [8] M. I. Skolnik, *Radar Handbook*. New York: McGraw-Hill, 1970.
- [9] *Heating Ventilation Air-Conditioning Guide*, Chap. 5. New York: Am. Soc. Heat., Refrig. Air-Cond. Eng., 1960.
- [10] H. E. King, Rectangular waveguide theoretical CW average power rating, *IRE Trans. Microwave Theory Tech.*, Vol. MTT-11, pp. 349–357, July 1961.
- [11] P. Bhartia and P. Pramanick, Finline characteristics and circuits, in *Topics in Millimeter-Wave Technology* (K. J. Button, ed.), Vol. 1. San Diego: Academic Press, 1988.
- [12] R. Monsour and R. MacPhie, A unified hybrid mode analysis for planar transmission lines with multilayer isotropic/anisotropic substrates, *IEEE Trans. Microwave Theory Tech.*, Vol. MTT-35, pp. 1383–1391, Dec. 1987.
- [13] P. Bhartia and P. Pramanick, *E-Plane Integrated Circuits*. Norwood MA: Artech House, 1987.
- [14] P. J. Meier, Integrated finline millimeter components, *IEEE Trans. Microwave Theory Tech.*, Vol. MTT-22, pp. 1209–1216, Dec. 1974.
- [15] P. Pramanick and P. Bhartia, Accurate analysis equations and synthesis techniques for unilateral finlines, *IEEE Trans. Microwave Theory Tech.*, Vol. MTT-33, pp. 24–30, Jan. 1985.
- [16] P. Pramanick and P. Bhartia, CAD models for millimeter-wave finlines and suspended substrate microstriplines, *IEEE Trans. Microwave Theory Tech.*, Vol. MTT-33, pp. 1429–1435, Dec. 1985.
- [17] P. Pramanick and P. Bhartia, A new model for the apparent characteristic impedance of finned-waveguide and finlines, *IEEE Trans. Microwave Theory Tech.*, Vol. MTT-34, pp. 1437–1441, Dec. 1986.
- [18] K. Bierwirth, N. Schlz, and I. Arndt, Finite-difference analysis of rectangular dielectric waveguide structures, *IEEE Trans. Microwave Theory Tech.*, Vol. MTT-34, pp. 1104–1114, Nov. 1986.
- [19] E. A. J. Marcatelli, Dielectric rectangular waveguide and directional coupler for integrated optics, *Bell Syst. Tech. J.*, Vol. 48, pp. 2071–2102, Sept. 1969.
- [20] J. E. Goal, A circular harmonic computer analysis of rectangular dielectric wave-guides, *Bell. Syst. Tech. J.*, Vol. 48, pp. 2133–2160, Sept. 1969.
- [21] R. M. Knox and P. D. Toulios, Integrated circuits for the millimeter through optical frequency range, *Proc. Symp. Submillimeter Waves*, New York, pp. 497–516, Mar. 1970.
- [22] P. Bhartia and J. J. Bahl, *Millimeter-Wave Engineering and Applications*. New York: Wiley (Interscience), 1984.

This Page Intentionally Left Blank

Microstrip Lines

J. K. Kwon

I. Microstrip Lines

DEFINITION: A microstrip line is a type of open transmission line that consists of a strip conductor and a ground plane separated by a dielectric medium. The geometry of a microstrip line is shown in Figure 1.

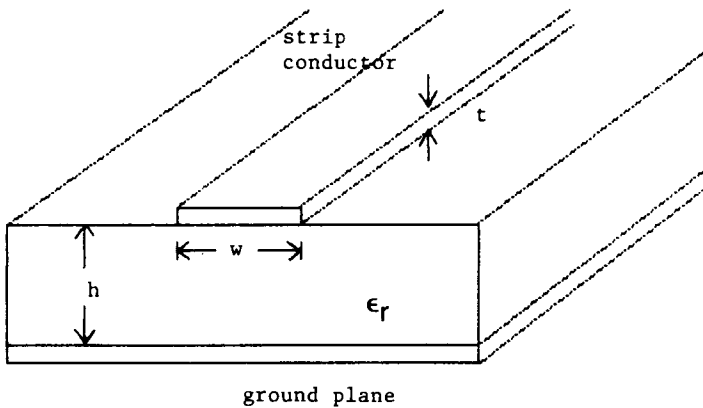


Figure 1. Geometry of a microstrip line

Materials

Typical dielectric substrate materials for microstrip [16] lines are shown in Table 1.

TABLE I
Dielectric Substrates

Material	ϵ_r	$10^4 \tan \delta$ (10 GHz)	Thermal conductivity (W/cm ² /°C)	Dielectric strength (KV/cm)
Alumina	9.7	2	0.3	4×10^3
Sapphire (Crystal)	9.4 and 11.6	1	0.4	4×10^3
Quartz (fused)	3.8	1	0.01	10×10^3
Glass (typical)	5	20	0.01	—
Polystyrene	2.53	4.7	0.001	280
Ferrite/garnet	13–16	2	0.03	4×10^3
GaAs (high resistivity)	12.3	16	0.3	350
Si (high resistivity)	11.7	50	0.9	300
Air (dry)	1	0	0.00024	30

Static TEM Parameters

Characteristic Impedance of a Line

$$Z_0 = 1/(v_p C),$$

where C is the line capacitance per unit length and v_p , the phase velocity, is given by

$$v_p = c / \sqrt{\epsilon_{\text{eff}}},$$

where $c = 3 \times 10^8$ m/s and ϵ_{eff} is the effective relative dielectric constant, or microstrip permittivity.

Effective Dielectric Constant

$$\epsilon_{\text{eff}} = 1 + q(\epsilon_r - 1),$$

where the filling factor, q , has the bounds

$$\frac{1}{2} \leq q \leq 1.$$

Wavelength, λ_g

$$\lambda_g = \lambda_0 / \sqrt{\epsilon_{\text{eff}}},$$

where λ_0 is the free-space wavelength.

Physical Length, L

$$L = \theta \lambda_g / (2\pi),$$

where θ is the electric length in radians.

Analysis Formulas [1–3]

To compute the characteristic impedance, Z_0 , and the effective dielectric constant, ϵ_{eff} , assuming that the strip conductor thickness is negligible ($t/h \leq 0.005$), perform the following calculations.

Z_0 and ϵ_{eff}

For $w/h \leq 1$,

$$Z_0 = \frac{60}{\sqrt{\epsilon_{\text{eff}}}} \ln[8(h/w) + 0.25(w/h)],$$

where

$$\epsilon_{\text{eff}} = \frac{(\epsilon_r + 1)}{2} + \frac{(\epsilon_r - 1)}{2} \left\{ [1 + 12(h/w)]^{-1/2} + 0.041[1 - (w/h)]^2 \right\}.$$

For $w/h \geq 1$,

$$Z_0 = \frac{120\pi/\sqrt{\epsilon_{\text{eff}}}}{(w/h) + 1.393 + 0.667 \ln[(w/h) + 1.4444]},$$

where

$$\epsilon_{\text{eff}} = (\epsilon_r + 1)/2 + [(\epsilon_r - 1)/2][1 + 12(h/w)]^{-1/2}.$$

Wavelength in the Microstrip Line [4]

For $w/h \geq 0.6$,

$$\lambda' = \frac{\lambda_0}{\sqrt{\epsilon_r}} \left[\frac{\epsilon_r}{1 + 0.63(\epsilon_r - 1)(w/h)^{0.1255}} \right]^{1/2}.$$

For $w/h \leq 0.6$,

$$\lambda' = \frac{\lambda_0}{\sqrt{\epsilon_r}} \left[\frac{\epsilon_r}{1 + 0.6(\epsilon_r - 1)(w/h)^{0.0297}} \right]^{1/2}.$$

Synthesis Formulas [2, 3, 5]

To compute w/h , assuming, that the strip conductor thickness is negligible ($t/h \leq 0.005$), perform the following calculations.

For $w/h \leq 2$,

$$w/h = 8 \exp(A) / [\exp(2A) - 2].$$

For $w/h \geq 2$,

$$\begin{aligned} w/h &= (2/\pi) \{ B - 1 - \ln(2B - 1) \\ &\quad + [(\epsilon_r - 1)/2\epsilon_r] [\ln(B - 1) + 0.39 - 0.61/\epsilon_r] \}, \end{aligned}$$

where

$$A = (Z_0/60)[(\epsilon_r + 1)/2]^{1/2} + [(\epsilon_r - 1)/(\epsilon_r + 1)](0.23 + 0.11/\epsilon_r)$$

and

$$B = 592.2 / (Z_0 \sqrt{\epsilon_r}).$$

Effects of Conductor Thickness [6]

The following relations are useful when $t < h$ and $t < w/2$.

Effect on the Strip Width

For $w/h \leq 1/2\pi$,

$$(w/h)' = w/h \pm 1.25(t/\pi h)[1 + \ln(4\pi w/t)].$$

For $w/h \geq 1/2\pi$,

$$(w/h)' = w/h \pm 1.25(t/\pi h)[1 + \ln(2h/t)].$$

Note that the + sign is for analysis and the - sign is for synthesis.

Effect on the Effective Dielectric Constant

$$\epsilon_{\text{eff}}(t) = \epsilon_{\text{eff}} - \delta\epsilon_{\text{eff}},$$

where

$$\delta\epsilon_{\text{eff}} = [(\epsilon_r - 1)t/h] / [4.6\sqrt{w/h}].$$

Dispersion [7, 8]

The frequency below which dispersion may be neglected is given by

$$f_0 = 0.3 [Z_0 / (h\sqrt{\epsilon_r} - 1)]^{1/2}.$$

where h is in centimeters.

Effective Dielectric Constant

$$\epsilon_{\text{eff}}(f) = \epsilon_r - \frac{\epsilon_r - \epsilon_{\text{eff}}}{1 + G(f/f_p)^2} \quad (f \text{ is in gigahertz}),$$

where

$$f_p = 15.66Z_0/h \quad (h \text{ is in mils}).$$

Note that, when $f_p \gg f$, $\epsilon_{\text{eff}}(f) \approx \epsilon_{\text{eff}}$.

Characteristic Impedance

$$Z_0(f) = Z_{0T} - \frac{Z_{0T} - Z_0}{1 - G(f/f_p)^2},$$

where

$$G = [(Z_0 - 5)/60]^{1/2} + 0.004Z_0.$$

In the above equations, Z_{0T} is twice the characteristic impedance of a microstrip line of width w and height $2h$.

Losses in a Microstrip Line [9]

Attenuation Factor

$$\alpha = \alpha_a + \alpha_c,$$

where α_a is the dielectric loss factor and α_c is the conductor loss factor.

Dielectric Loss Factor

$$\alpha_a = 27.3 \frac{\epsilon_r}{\epsilon_r - 1} \frac{\epsilon_{\text{eff}} - 1}{\sqrt{\epsilon_{\text{eff}}}} \frac{\tan \delta}{\lambda_0} \quad (\text{dB/m}),$$

where $\tan \delta$ is the loss tangent of the dielectric.

Conductor Loss Factor

For $w/h \leq 1$,

$$\alpha_c = 1.38A \frac{R_s}{hZ_0} \frac{32 - (w/h)^2}{32 + (w/h)^2} \quad (\text{dB/m}).$$

For $w/h \geq 1$,

$$\alpha_c = 6.1 \times 10^{-5} A \frac{R_s Z_0 \epsilon_{\text{eff}}}{h} \left[(w/h)' + \frac{0.667(w/h)'}{(w/h)' + 1.444} \right] \text{ (dB/m)},$$

where

$$\begin{aligned} R_s &= (\pi f \mu_0 / \sigma)^{1/2} \\ A &= 1 + \frac{1}{(w/h)'} \left[1 + \frac{\ln(2B/t)}{\pi} \right] \\ B &= \begin{cases} h & \text{for } w/h \geq 1/2\pi \\ 2\pi w & \text{for } w/h \leq 1/2\pi, \end{cases} \end{aligned}$$

where σ is the conductivity of the conductor.

Effect of Enclosure [10]

Characteristic Impedance

For $w/h \geq 1$,

$$Z_{0(\text{shielded})} = Z_{0(\text{unshielded})} - P.$$

For $w/h \ll 1$,

$$Z_{0(\text{shielded})} = Z_{0(\text{unshielded})} - P \left\{ 1 - \tanh \left[\frac{0.48(w/h - 1)^{0.5}}{(1 + h'/h)^2} \right] \right\},$$

where

$$P = \frac{270}{\sqrt{\epsilon_{\text{eff}}}} \left[1 - \tanh \left(0.28 + 1.2\sqrt{(h'/h)} \right) \right]$$

and h' is the spacing between the strip and the top cover.

Effective Dielectric Constant

$$\epsilon_{\text{eff(shielded)}} = \frac{\epsilon_r + 1}{2} + \left[\epsilon_{\text{eff(unshielded)}} - \frac{\epsilon_r + 1}{2} \right] Q,$$

where

$$Q = \tanh \left[0.18 + 0.235h'/h - \frac{0.415}{(h'/h)^2} \right].$$

2. Microstrip Discontinuities

Open-End

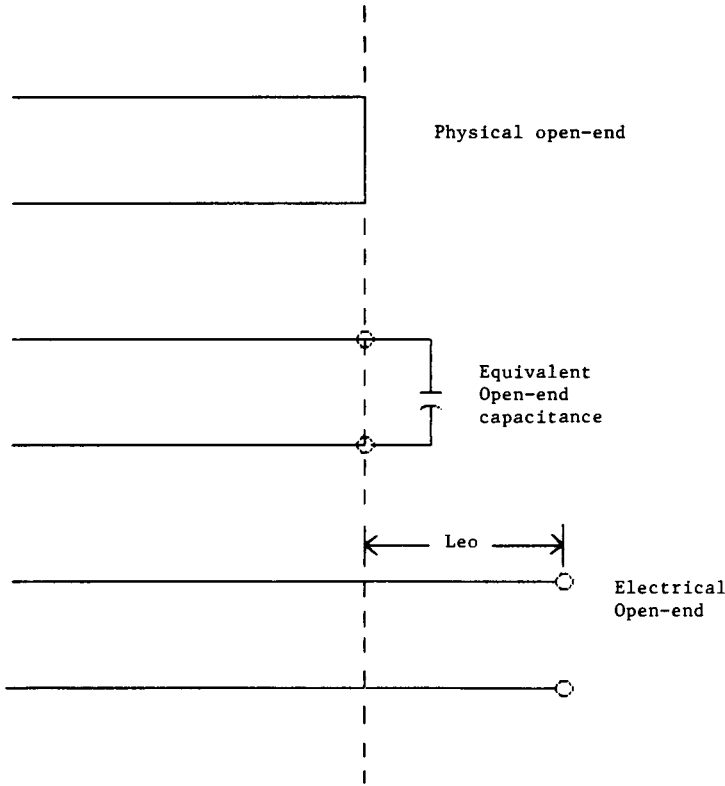


Figure 2. Microstrip open-end discontinuity and equivalent line length

End Effect Length [5]

$$L_{eo} = 0.412h \left(\frac{\epsilon_{\text{eff}} + 0.3}{\epsilon_{\text{eff}} - 0.258} \right) \left(\frac{w/h + 0.262}{w/h + 0.813} \right).$$

Open-End Capacitance

$$C_f = \epsilon_{\text{eff}}^{0.5} L_{eo} / (c Z_0),$$

where $c = 3 \times 10^8$ m/s.

Gap in a Microstrip [11]

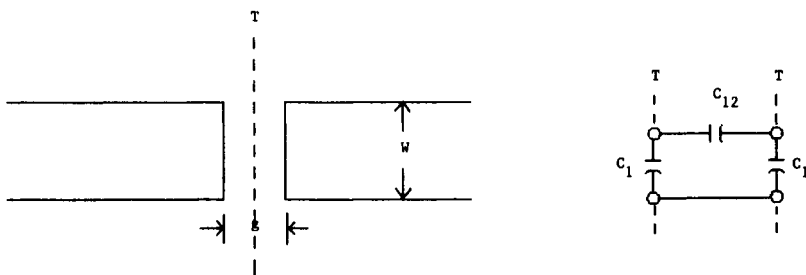


Figure 3. Gap in microstrip line and its equivalent circuit

The equivalent circuit capacitances C_1 and C_{12} are as follows:

$$C_1 = 0.5C_e$$

$$C_{12} = 0.5(C_0 - 0.5C_e).$$

For $\epsilon_r = 9.6$ and for $0.5 \leq w/h \leq 2$,

$$C_0/w = (g/w)^{mo} \exp(K_0) \quad (\text{pF/m})$$

$$C_e/w = (g/w)^{me} \exp(K_e) \quad (\text{pF/m}).$$

For $0.1 \leq g/w \leq 1.0$,

$$mo = \frac{w}{h} [0.627 \ln(w/h) - 0.3853]$$

$$K_0 = 4.26 - 0.631 \ln(w/h).$$

For $0.1 \leq g/w \leq 0.3$,

$$me = 0.8675$$

$$K_e = 2.043(w/h)^{0.12}.$$

For $0.3 \leq g/w \leq 1.0$,

$$me = \frac{1.565}{(w/h)^{0.16}} - 1$$

$$K_e = 1.97 - \frac{0.03}{w/h}.$$

The values of C_0 and C_e for other values of ϵ_r can be calculated using the

following expressions:

$$C_0(\epsilon_r) = C_0(9.6)(\epsilon_r/9.6)^{0.8}$$

$$C_e(\epsilon_r) = C_e(9.6)(\epsilon_r/9.6)^{0.9}.$$

Transverse Split [12]

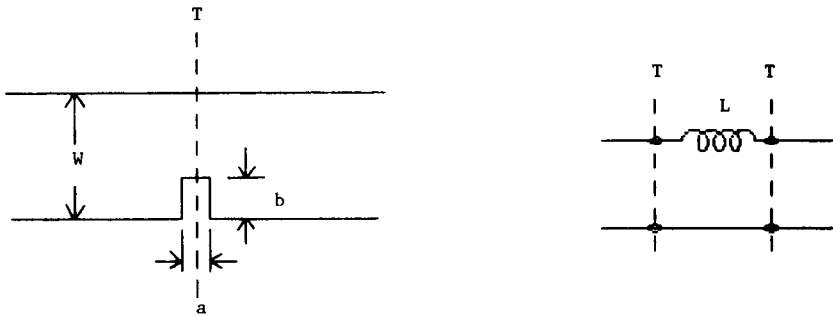


Figure 4. The transverse split and equivalent circuit

The equivalent series lumped inductance is as follows. For $0 \leq b/w \leq 0.9$ and for $a \leq h$,

$$L/h = \frac{\mu_0 \pi}{2} \left[1 - \left(Z_{0a}/Z'_{0a} \right) \right]^2,$$

where Z_{0a} and Z'_{0a} are the characteristic impedances of the air-filled microstrip lines with width w and $(w - b)$, respectively.

Steps in Width [13]

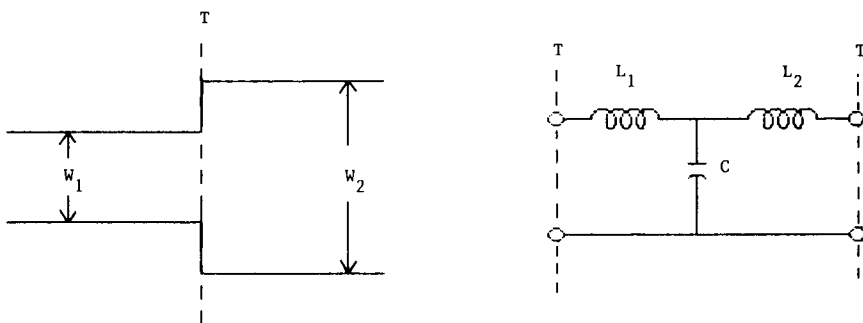


Figure 5. Microstrip step and the equivalent circuit

The equivalent junction inductances and capacitance are as follows:

$$L_1 = \frac{L_{w_1}}{L_{w_1} + L_{w_2}} L_s, \quad L_2 = \frac{L_{w_1}}{L_{w_1} + L_{w_2}} L_s,$$

and

$$L_s/h = 40.5(w_1/w_2 - 1) - 75(w_1/w_2) + 0.2(w_1/w_2 - 1)^2 \text{ (nH/m)},$$

where L_{w_1} and L_{w_2} are the inductances per unit length of the microstrips having widths w_1 and w_2 , respectively.

For $\epsilon_r \leq 10$ and for $1.5 \leq w_2/w_1 \leq 3.5$,

$$\frac{C}{\sqrt{w_1 w_2}} = (10.1 \log \epsilon_r + 2.33)(w_2/w_1) - 12.6 \log \epsilon_r - 3.17 \text{ (pF/m)}.$$

For $\epsilon_r = 9.6$, and for $3.5 \leq w_2/w_1 \leq 10$,

$$\frac{C}{\sqrt{w_1 w_2}} = 130 \log(w_2/w_1) - 44 \text{ (pF/m)}.$$

Right-Angled Bend [14]

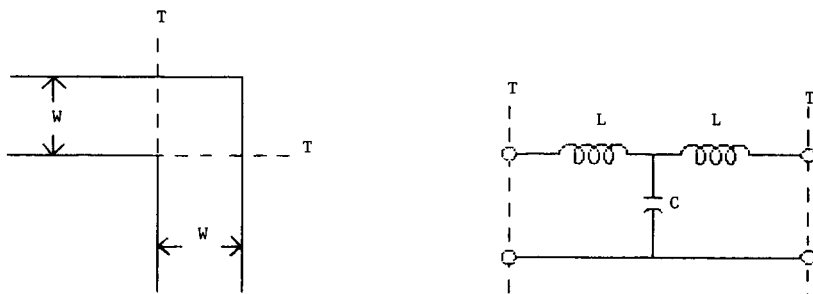


Figure 6. Right-angled microstrip bend and its equivalent circuit

Capacitance

For $w/h \leq 1$,

$$\frac{C}{w} = \frac{(14\epsilon_r + 12.5)w/h - (1.83\epsilon_r - 2.25)}{\sqrt{w/h}} + \frac{0.02\epsilon_r}{w/h} \text{ (pF/m)}.$$

For $w/h \geq 1$,

$$\frac{C}{w} = (9.5\epsilon_r + 1.25)w/h + 5.2\epsilon_r + 7.0 \quad (\text{pF/m}).$$

Inductance

$$\frac{L}{h} = 100(4\sqrt{(w/h)} - 4.21) \quad (\text{nH/m}).$$

T-Junction [11]

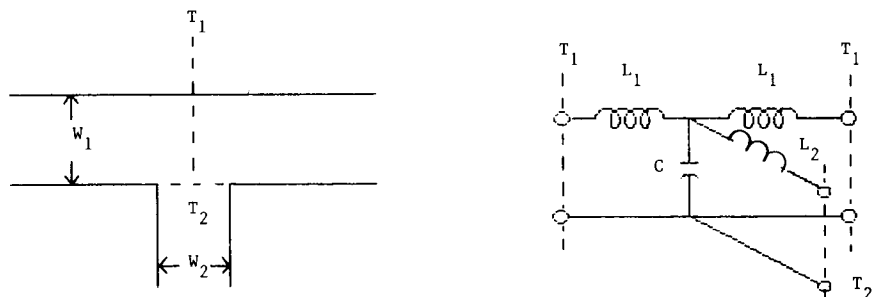


Figure 7. Microstrip T-junction and its equivalent circuit

The expressions for the equivalent circuit parameters for a T-junction with $\epsilon_r = 9.9$ and $Z_1 = 50 \text{ ohm}$ are given below. For $25 \leq Z_1 \leq 100$,

$$C/w_1 = \frac{100}{\tanh(0.0072Z_2)} + 0.64Z_2 - 261 \quad (\text{pF/m}).$$

For $0.5 \leq w_1/h$ and for $w_2/h \leq 2.0$,

$$L_1/h = -(w_2/h)[(w_2/h)(-0.016w_1/h + 0.064) + 0.016/(w_1/h)]L_{w_1} \quad (\text{nH/m}).$$

For $1 \leq w_1/h \leq 2.0$ and for $0.5 \leq w_2/h \leq 2.0$,

$$L_2/h = \{(0.12w_1/h - 0.47)w_2/h + 0.195w_1/h - 0.357 + 0.0283 \sin(\pi w_1/h - 0.75\pi)\}L_{w_2} \quad (\text{nH/m}),$$

where L_w is the inductance per unit length (nH/m) for a microstrip line of width w .

Cross Junction [15]

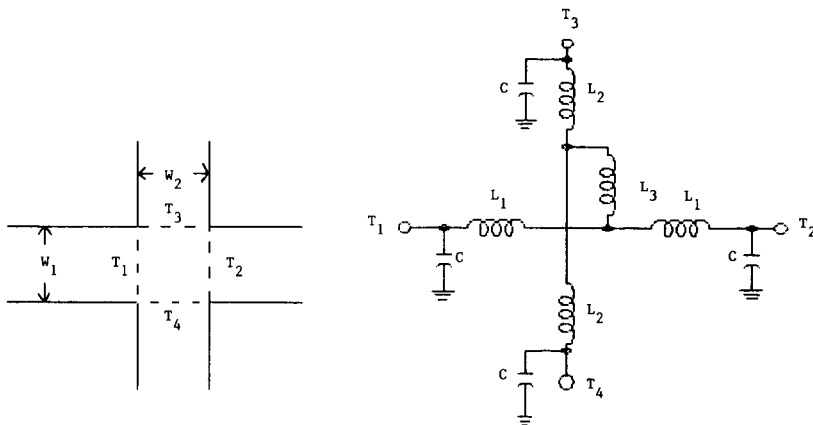


Figure 8. A microstrip cross-junction and its equivalent circuit

The expressions for C , L_1 , and L_3 are given as follows.

For $\epsilon_r = 9.9$, $0.3 \leq w_1/h \leq 3$, and $0.1 < w_2/h \leq 3$,

$$\begin{aligned} C/w_1 = 0.25 & \left[\left\{ 37.61w_2/h - 13.42(w_2/h)^{1/2} + 159.38 \right\} \right. \\ & \times \ln(w_1/h) + (w_2/h)^3 + 74w_2/h + 130 \left. \right] (w_1/h)^{-1/3} \\ & - 60 + 0.5/(w_2/h) - 0.375(w_1/h)(1-w_2/h) \quad (\text{pF/m}). \end{aligned}$$

For $0.5 \leq w_1/h$ and for $w_2/h \leq 2.0$,

$$\begin{aligned} L_1/h = & \left[\left\{ 165.6w_2/h + 31.2(w_2/h)^{1/2} - 11.8(w_2/h)^2 \right\} w_1/h \right. \\ & \left. - 32w_2/h + 3 \right] (w_1/h)^{-1.5} \quad (\text{nH/m}). \end{aligned}$$

The equation for L_2 is obtained by replacing w_1 with w_2 and vice versa.

For $0.5 \leq w_1/h$ and for $w_2/h \leq 2.0$,

$$\begin{aligned} -L_3/h = & 337.5 + [1 + 7/(w_1/h)]/(w_2/h) \\ & - 5w_2/h \cos[0.5\pi(1.5 - w_1/h)] \quad (\text{nH/m}). \end{aligned}$$

References

- [1] M. V. Schneider, Microstrip lines for microwave integrated circuits, *Bell Syst. Tech. J.*, Vol. 48, pp. 1421–1444, 1969.
- [2] H. A. Wheeler, Transmission-line properties of a strip on a dielectric sheet on a plane, *IEEE Trans. Microwave Theory Tech.*, Vol. M-25, pp. 631–647, Aug. 1977.
- [3] I. J. Bahl, and D. K. Trivedi, A designer's guide to microstrip, *Microwaves*, Vol. 16, pp. 174–182, May 1977.
- [4] H. Sobol, Extending IC technology to microwave equipments, *Electronics*, Mar. 1967.
- [5] E. O. Hammerstad, Equations for microstrip circuit design, *Proc. 5th Eur. Microwave Conf.*, pp. 268–272, 1975.
- [6] I. J. Bahl, and R. Garg, Simple and accurate formulas for microstrip with finite strip thickness, *Proc. IEEE*, Vol. 65, pp. 1611–1612, 1977.
- [7] G. Gonzalez, *Microwave Transistor Amplifiers*. Englewood Cliffs, NJ: Prentice-Hall, 1984.
- [8] B. Bianco *et al.*, Frequency dependence of microstrip parameters, *Alta Freq.*, Vol. 43, pp. 413–416, 1974.
- [9] R. A. Pucel, *et al.*, Losses in microstrip, *IEEE Trans. Microwave Theory Tech.*, Vol. MTT-16, pp. 342–350, 1968.
- [10] I. J. Bahl, Easy and exact methods for shielded microstrip design, *Microwaves*, Vol. 17, Dec. 1978.
- [11] R. Garg and I. J. Bahl, Microstrip discontinuities, *Int. J. Electron.*, Vol. 45, pp. 81–87, 1978.
- [12] W. J. R. Hoefer, Equivalent series inductivity of a narrow transverse slit in microstrip, *IEEE Trans. Microwave Theory Tech.*, Vol. MTT-25, pp. 822–824, Oct. 1977.
- [13] K. C. Gupta, R. Garg, and I. J. Bahl, *Microstrip Lines and Slotlines*, pp. 136–140. Dedham, MA: Artech House, 1979.
- [14] K. C. Gupta, R. Garg, and R. Chadha, *Computer-Aided Design of Microwave Circuits*. Dedham, MA: Artech House, 1981.
- [15] B. Easter, The equivalent circuit of some microstrip discontinuities in microstrip, *IEEE Trans. Microwave Theory Tech.*, Vol. MTT-23, pp. 655–660, Aug. 1975.
- [16] T. C. Edwards, *Foundation for Microstrip Circuit Design*. Chichester: John Wiley & Sons, 1987.

This Page Intentionally Left Blank

CHAPTER

3

Microwave Resonators

Robert A. Strangeway

I. Resonator Basics

One-Port Reflection Resonator

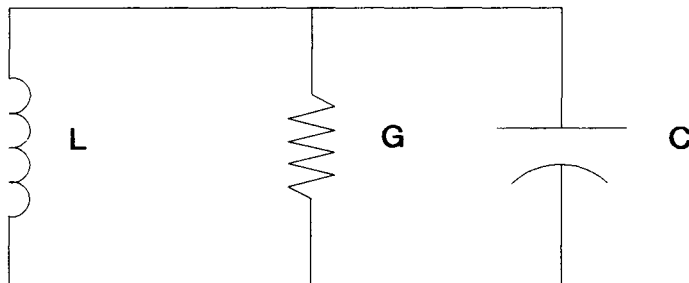


Figure 1. Parallel resonant circuit.

$$\omega_o = \frac{1}{\sqrt{LC}} = \text{resonant radian frequency}$$

$$Q_u = \frac{\omega_o C}{G} = \text{unloaded quality factor}$$

$$Y = G \left[1 + j Q_u \left(\frac{\omega}{\omega_0} - \frac{\omega_0}{\omega} \right) \right] = \text{circuit admittance.}$$

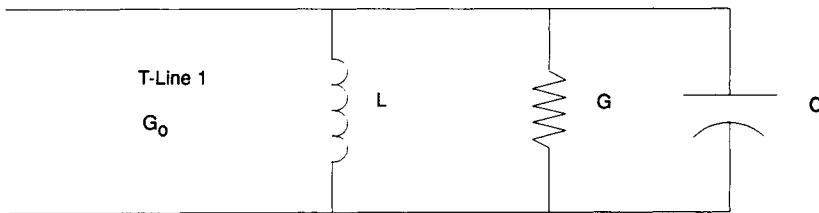


Figure 2. Lossless transmission line terminated in a resonant circuit.

If $\omega = \omega_o + \Delta\omega$, then in the vicinity of resonance, $\Delta\omega \ll \omega_o$, the approximate admittance expression is $Y = G(1 + jQ_u 2 \Delta\omega / \omega_o)$.

G_o = transmission line characteristic conductance

$$\beta = \frac{G_o}{G} = \text{coupling factor}$$

($\beta > 1$, overcoupled; $\beta = 1$, critically coupled; $\beta < 1$, undercoupled)

$$\Gamma = \frac{(\beta - 1) - jQ_u \frac{2\Delta\omega}{\omega_o}}{(\beta + 1) + jQ_u \frac{2\Delta\omega}{\omega_o}} = \text{reflection coefficient}$$

$$\text{unloaded } Q = Q_u = \frac{\omega_o C}{G}$$

$$\text{external } Q = Q_e = \frac{\omega_o C}{G_o}$$

$$\text{loaded } Q = Q_L = \frac{\omega_o C}{(G_o + G)}$$

$$\frac{1}{Q_L} = \frac{1}{Q_e} + \frac{1}{Q_u}$$

$$\frac{Q_u}{Q_L} = 1 + \beta$$

$$\frac{Q_u}{Q_e} = \beta$$

$|\Gamma_o|$ = reflection coefficient magnitude at ω_o

$$\beta = \frac{(1 - |\Gamma_o|)}{(1 + |\Gamma_o|)} \quad (\beta < 1)$$

or

$$\beta = \frac{(1 + |\Gamma_o|)}{(1 - |\Gamma_o|)} \quad (\beta > 1)$$

$|\Gamma_u|$ = reflection coefficient magnitude for Q_L measurement

$$|\Gamma_u| = \sqrt{\frac{(\beta - 1)^2 + 1}{(\beta + 1)^2 + 1}}$$

$|\Gamma_e|$ = reflection coefficient magnitude for Q_e measurement

$$|\Gamma_e| = \sqrt{\frac{(\beta - 1)^2 + \beta^2}{(\beta + 1)^2 + \beta^2}}$$

$|\Gamma_L|$ = reflection coefficient magnitude for Q_L measurement

$$|\Gamma_L| = \sqrt{\frac{(|\Gamma_o|^2 + 1)}{2}}.$$

Two-Port Transmission Resonator [23, pp. 240 – 241]

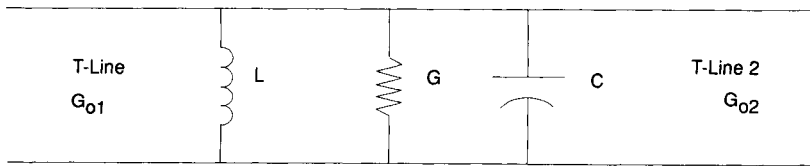


Figure 3. Two-port transmission resonator coupled to two transmission lines.

$$Q_u = \text{unloaded resonator } Q = \frac{\omega_o C}{G}$$

$$Q_{e_1} = \text{external } Q \text{ of input circuit} = \frac{\omega_o C}{G_{o_1}}$$

$$Q_{e_2} = \text{external } Q \text{ of output circuit} = \frac{\omega_o C}{G_{o_2}}$$

$$Q_{L_1} = \text{loaded } Q \text{ without port 2}$$

$$Q_{L_1} = \frac{\omega_o C}{G + G_{o_1}} = \frac{Q_u Q_{e_1}}{Q_u + Q_{e_1}}$$

Q_{L_1} = loaded Q without port 1

$$Q_{L_2} = \frac{\omega_o C}{G + G_{o_2}} = \frac{Q_u Q_{e_2}}{Q_u + Q_{e_2}}$$

$Q_{L_{1,2}}$ = loaded Q with both ports

$$Q_{L_{1,2}} = \frac{\omega_o C}{G + G_{o_1} + G_{o_2}}$$

$$\frac{1}{Q_{L_{1,2}}} = \frac{1}{Q_u} + \frac{1}{Q_{e_1}} + \frac{1}{Q_{e_2}}$$

$$\beta_1 = \text{port 1 coupling factor} = \frac{G_{o_1}}{G} = \frac{Q_u}{Q_{e_1}}$$

$$\beta_2 = \text{port 2 coupling factor} = \frac{G_{o_2}}{G} = \frac{Q_u}{Q_{e_2}}$$

$$\frac{Q_u}{Q_{L_{1,2}}} = 1 + \beta_1 + \beta_2$$

S_1 = standing-wave ratio of port 1 at resonance with port 2 matched

$$\gamma_1 = \frac{\beta_1}{1 + \beta_2}$$

$S_1 = \gamma_1$ if $\gamma_1 > 1$; otherwise $S_1 = 1/\gamma_1$

S_2 = standing-wave ratio of port 2 at resonance with port 1 matched

$$\gamma_2 = \frac{\beta_2}{1 + \beta_1}$$

$S_2 = \gamma_2$ if $\gamma_2 > 1$; otherwise $S_2 = 1/\gamma_2$

$|T_o|^2$ = power transmission coefficient at ω_o

$$|T_o|^2 = \frac{4\gamma_1}{(1 + \gamma_1)^2} \cdot \frac{\beta_1 - \gamma_1}{\beta_1} = \frac{4\beta_1\beta_2}{(1 + \beta_1 + \beta_2)^2}$$

[12, pp. 200–201].

Skin Depth, δ

$$\delta = \frac{1}{\sqrt{\pi f \mu \sigma}},$$

where μ is the permeability and σ is the conductivity (SI units for all variables).

2. Two-Wire Line Resonators

Resonance occurs when $L = \lambda_o/4$ (quarter wave) or $\lambda_o/2$ (half wave) and the line is properly terminated, usually with a short termination (an open termination tends to radiate). Radiation and termination reactances [21, pp. 286–288] will change f_o .

α = transmission line attenuation constant

β = transmission line phase constant.

The unloaded $Q = Q_u$ for a transmission line with low losses is $Q_u = (\beta/2\alpha)$ [7, pp. 77–79]. An approximate Q_u for a two-wire line resonator is $Q_u \approx (\mu d^2 \omega_o / 8 R_w a)$ [15, p. 150], where

$$R_w = \text{surface resistance} = \sqrt{\frac{\pi f \mu}{\sigma}}$$

σ = conductivity

μ = permeability

Loaded Q must incorporate termination losses [21, pp. 288–293]. Terman ([29, p. 1049] determined the Q for nonradiating two-wire copper lines as $Q = 0.0887\sqrt{fbJ}$, where $b = d$ in Figure 4 and J is read from the graph in Figure 5.

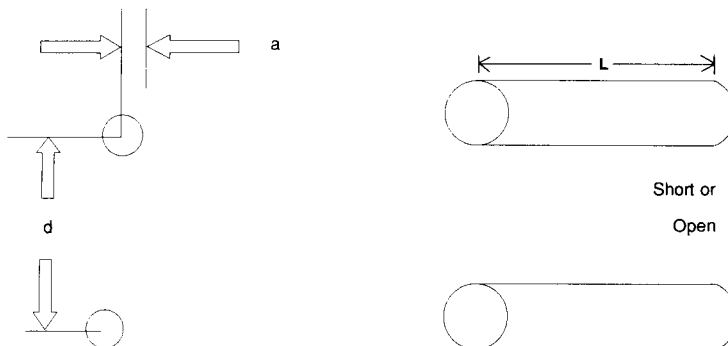


Figure 4. Basic two-wire line resonator.

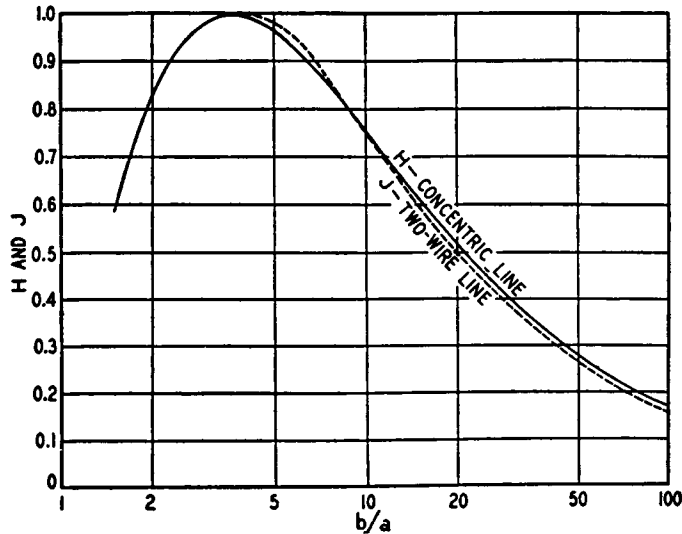


Figure 5. Terman's J factor (ignore other factors) [29, p. 1049] [© 1934 AIEE (now IEEE)].

3. Basic Coaxial Resonators [23, pp. 225 – 238]

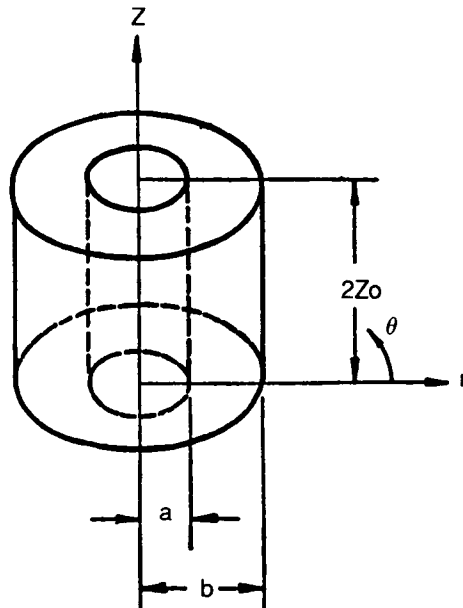


Figure 6. Coaxial resonator [23, p. 227]. Reproduced with permission of Artech House, Inc.

TEM mode resonant frequencies are as follows:

$$2Z_o = n\lambda_o/2,$$

where $n = 1, 2, 3, \dots$ and λ_o is the TEM wavelength. (Note. Here, Z_o is the half cavity length, not characteristic impedance.) Note that significant losses perturb f_o . Q is the unloaded quality factor; when $n = 1$,

$$\frac{Q\delta}{\lambda_o} = \frac{1}{4 + \frac{2Z_o}{b} \cdot \frac{1 + \frac{a}{b}}{\ln\left(\frac{b}{a}\right)}} \quad [23, \text{p. 226}],$$

where δ is the skin depth (see Section 1). Be warned that coaxial line resonators can support non-TEM modes. An approximate formula for the higher mode cutoff frequency, f_c , in coaxial transmission lines is [5, p. 259]

$$f_c = \frac{\frac{c}{\sqrt{\mu\epsilon}}}{\pi(a+b)},$$

where c is the free-space velocity of light, μ is the permeability of the medium, and ϵ is the permittivity of the medium.

Foreshortened Coaxial Line Resonators (Reentrant Coaxial Cavity Resonators)

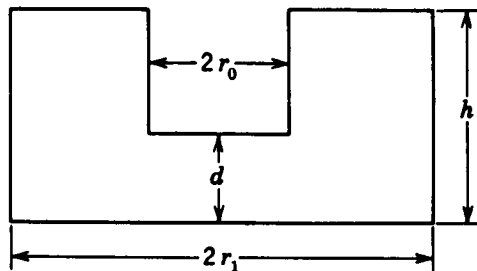


Figure 7. Foreshortened coaxial line resonator dimensions [15, p. 143]. [The figure was adapted from *Microwave Engineering*, 2nd ed., by T. Koryu Ishii, © 1989 by Harcourt Brace and Company reproduced with permission of the publisher.]

The resonant frequency is $f_o = (1/2\pi\sqrt{LC})$, where

$$L = \frac{\mu h}{2\pi} \ln \frac{r_1}{r_o}$$

$$C = \epsilon_o \left[\frac{\pi r_o^2}{d} - 4r_o \ln \left(\frac{2d}{e\sqrt{h^2 + (r_1 - r_o)^2}} \right) \right] \quad [10, \text{p. 349}]$$

and e is the base of natural logarithms. Resonant frequency design charts are also given in Moreno [23, pp. 230–238] and are accurate to within a few percent for gaps that are not too large. For these resonators, the approximate Q is

$$\frac{Q\delta}{\lambda_o} = \frac{2h}{\lambda_o} \cdot \frac{\ln \frac{r_1}{r_o}}{2 \ln \frac{r_1}{r_o} + h \left(\frac{1}{r_o} + \frac{1}{r_1} \right)} \quad [23, \text{p. 229}].$$

Xi *et al.* [53] analyze a coaxial reentrant cavity with a dielectric in the gap.

4. Rectangular Waveguide Cavities

$$\lambda_o = \sqrt{\left(\frac{l}{a}\right)^2 + \left(\frac{m}{b}\right)^2 + \left(\frac{n}{c}\right)^2}$$

MODE	$\frac{Q\delta}{\lambda_o}$
TE _{lmn}	$\frac{abc}{4} \cdot \frac{(p^2 + q^2)(p^2 + q^2 + r^2)^{3/2}}{ac[p^2r^2 + (p^2 + q^2)^2] + bc[q^2r^2 + (p^2 + q^2)^2] + abr^2(p^2 + q^2)}$
TE _{0mn}	$\frac{abc}{2} \cdot \frac{(q^2 + r^2)^{3/2}}{q^2c(b + 2a) + r^2b(c + 2a)}$
TE _{00n}	$\frac{abc}{2} \cdot \frac{(p^2 + r^2)^{3/2}}{p^2c(a + 2b) + r^2a(c + 2b)}$
TM _{lmn}	$\frac{abc}{4} \cdot \frac{(p^2 + q^2)(p^2 + q^2 + r^2)^{1/2}}{p^2b(a + c) + q^2a(b + c)}$
TM _{lmo}	$\frac{abc}{2} \cdot \frac{(p^2 + q^2)^{3/2}}{p^2b(a + 2c) + q^2a(b + 2c)}$
$p = \frac{l}{a} \quad q = \frac{m}{b} \quad r = \frac{n}{c}$	
$\lambda_o = \text{Resonant Free-Space Wavelength}$ $\delta = \text{Skin Depth}$	

Figure 8. Resonant wavelength and Q [28, Vol. I, p. 180]. Reproduced with permission of Artech House, Inc. Note that Bazzy [2] also provides many of the figures in this and the next chapter.

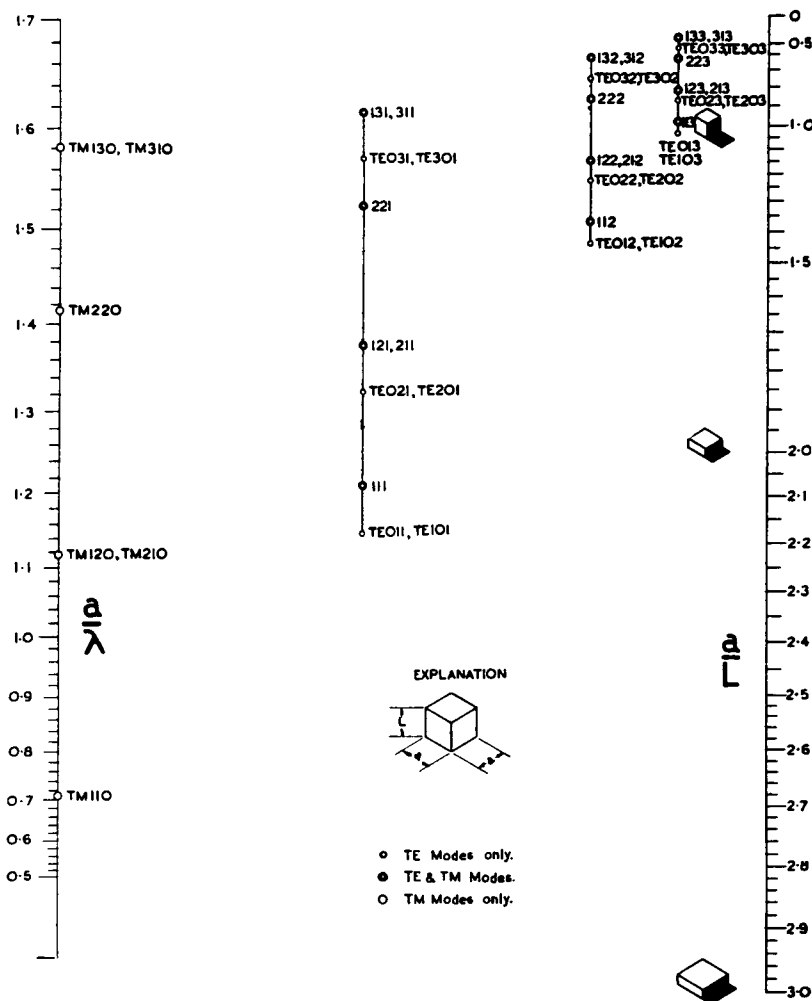


Figure 9. Mode lattice for square waveguide resonators [3, p. 834] [© 1947 IRE (now IEEE)].

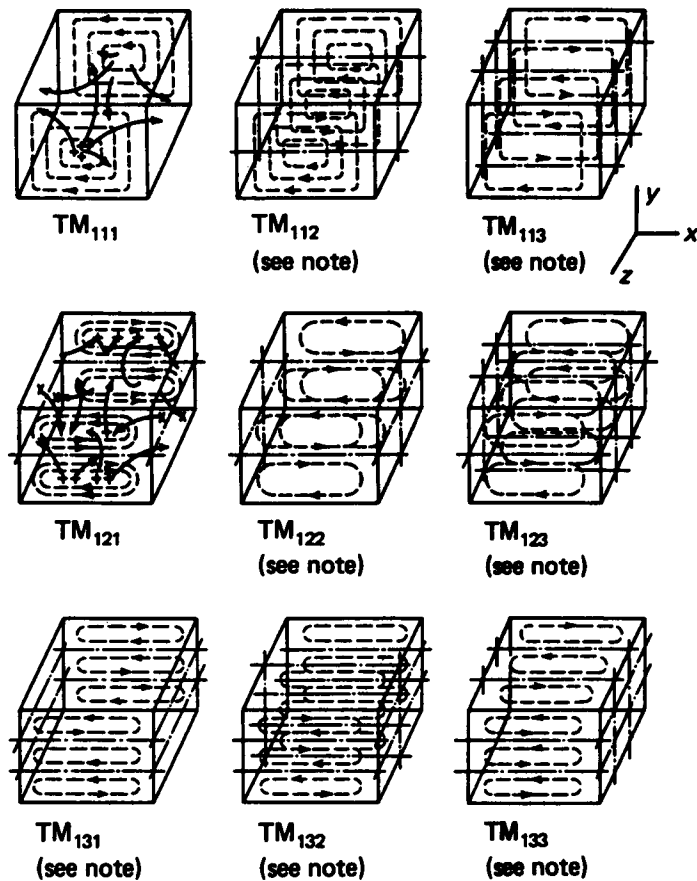


Figure 10. TM mode field pattern sketches. Solid lines, E ; dashed lines, H [15, p. 127]. [The figures are adapted from *Microwave Engineering*, 2nd ed., by T. Koryu Ishii, © 1989 by Harcourt Brace and Company reproduced with permission of the publisher.] Note: this mode is a repetition of the basic mode. Some field lines have been omitted for clarity.

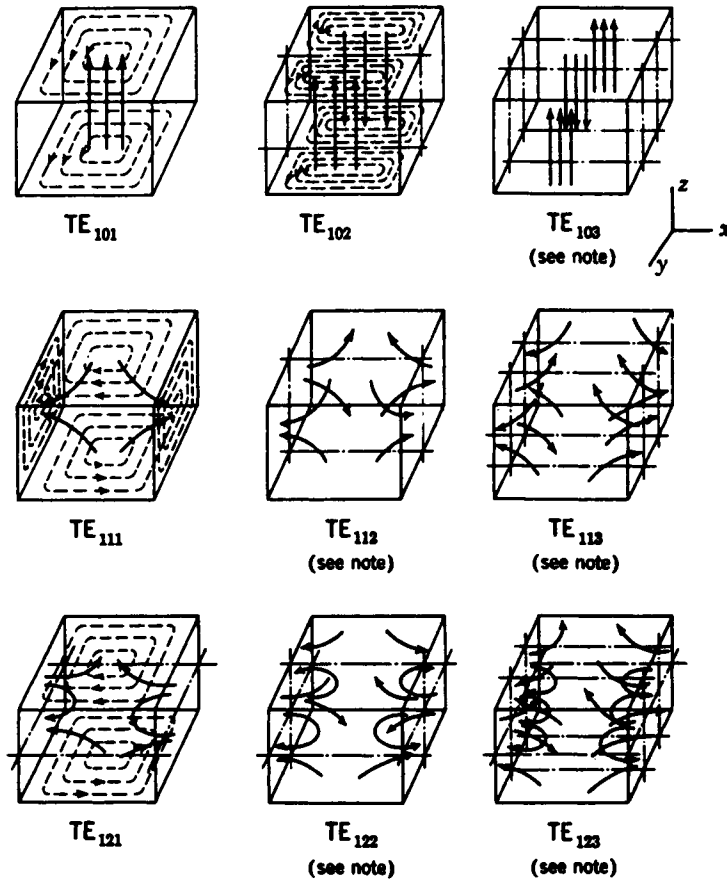


Figure 11. TE mode field pattern sketches. Solid lines, E; dashed lines, H [15, p. 125]. [The figures are adapted from *Microwave Engineering*, 2nd ed., by T. Koryu Ishii, © 1989 by Harcourt Brace and Company reproduced with permission of the publisher.] Note: this mode is a repetition of the basic mode. Some field lines have been omitted for clarity.

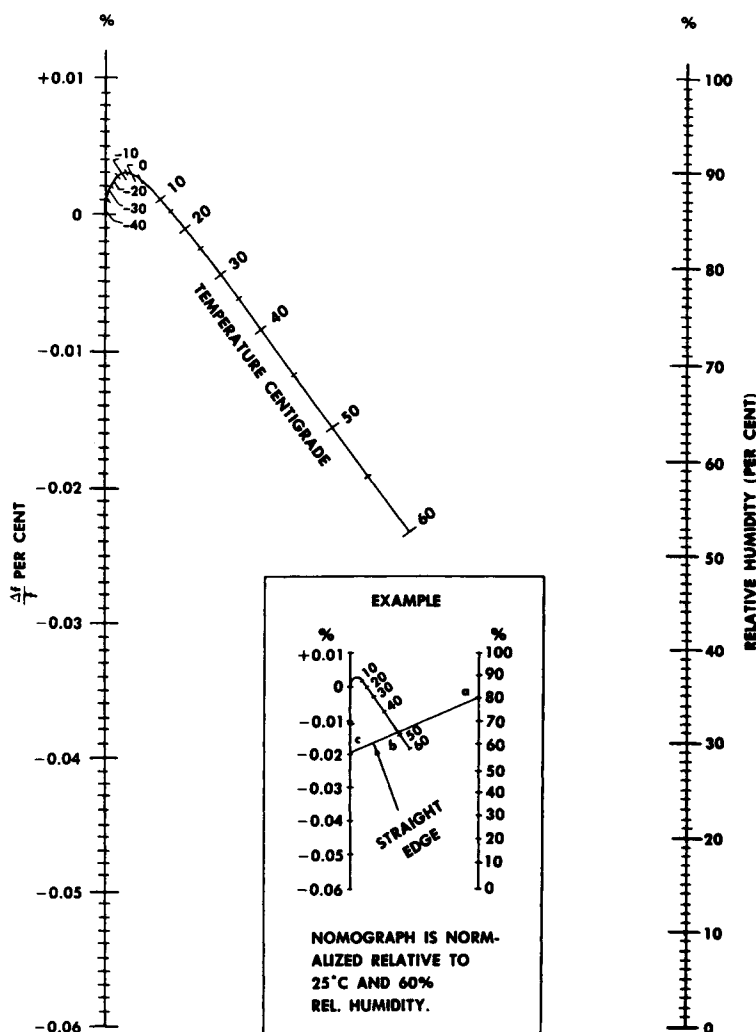
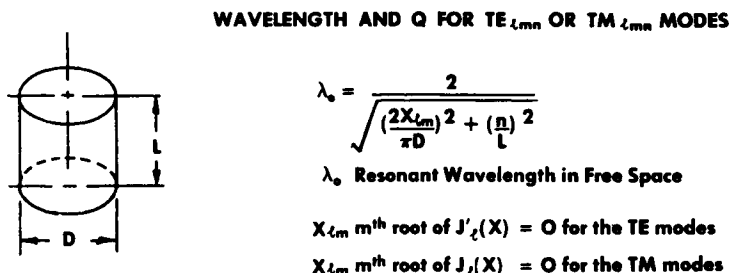


Figure 12. Humidity - cavity resonant frequency nomograph [28, Vol. I, p. 185]. Reproduced with permission of Artech House, Inc. [MIT Rad Lab Series, Technique of Microwave Measurement, Vol. II, 1944, McGraw-Hill; reproduced with permission of McGraw-Hill.]

5. Circular Cylindrical Waveguide Cavities



MODE	$Q \cdot \frac{\delta}{\lambda_0}$
TE _{l,mn}	$\frac{\left[1 - \left(\frac{l}{X_{lm}}\right)^2\right] [X_{lm}^2 + p^2 r^2]^{3/2}}{2\pi \left[X_{lm}^2 + p^2 r^2 + (1 - t) \left(\frac{prl}{X_{lm}}\right)^2\right]}$
TM _{l,mn}	$\sqrt{\frac{X_{lm}^2 + p^2 r^2}{2\pi (1 + t)}} \quad (n > 0)$
TM _{l,m0}	$\frac{X_{lm}}{\pi(2 + t)} \quad (n = 0)$

$$\delta = \text{Skin Depth} \quad r = \frac{D}{L} \quad p = \frac{n\pi}{2}$$

Figure 13. Resonant wavelength and Q [28, Vol. I, p. 180]. Reproduced with permission of Artech House, Inc. Note that the humidity – cavity resonant frequency nomograph appears in Figure 12.

THE FIRST TWENTY-FIVE ZEROS OF $J_m(x)$ AND $J_m'(x)$

No.	Value	Mode
1	1.841	TE_{11}
2	2.405	TM_{01}
3	3.054	TE_{21}
4	3.832	TM_{11}
5	3.832	TE_{01}
6	4.201	TE_{31}
7	5.136	TM_{21}
8	5.318	TE_{41}
9	5.332	TE_{12}
10	5.520	TM_{02}
11	6.380	TM_{31}
12	6.416	TE_{61}
13	6.706	TE_{22}
14	7.016	TM_{12}
15	7.016	TE_{02}
16	7.501	TE_{61}
17	7.588	TM_{41}
18	8.016	TE_{32}
19	8.417	TM_{22}
20	8.536	TE_{13}
21	8.578	TE_{71}
22	8.654	TM_{03}
23	8.771	TM_{51}
24	9.283	TE_{42}
25	9.647	TE_{81}

Figure 14. Bessel function zeros [23, p. 222]. Reproduced with permission of Artech House, Inc. Note that Saad [28, Vol. 2, pp. 192 – 195] has a more extensive listing.

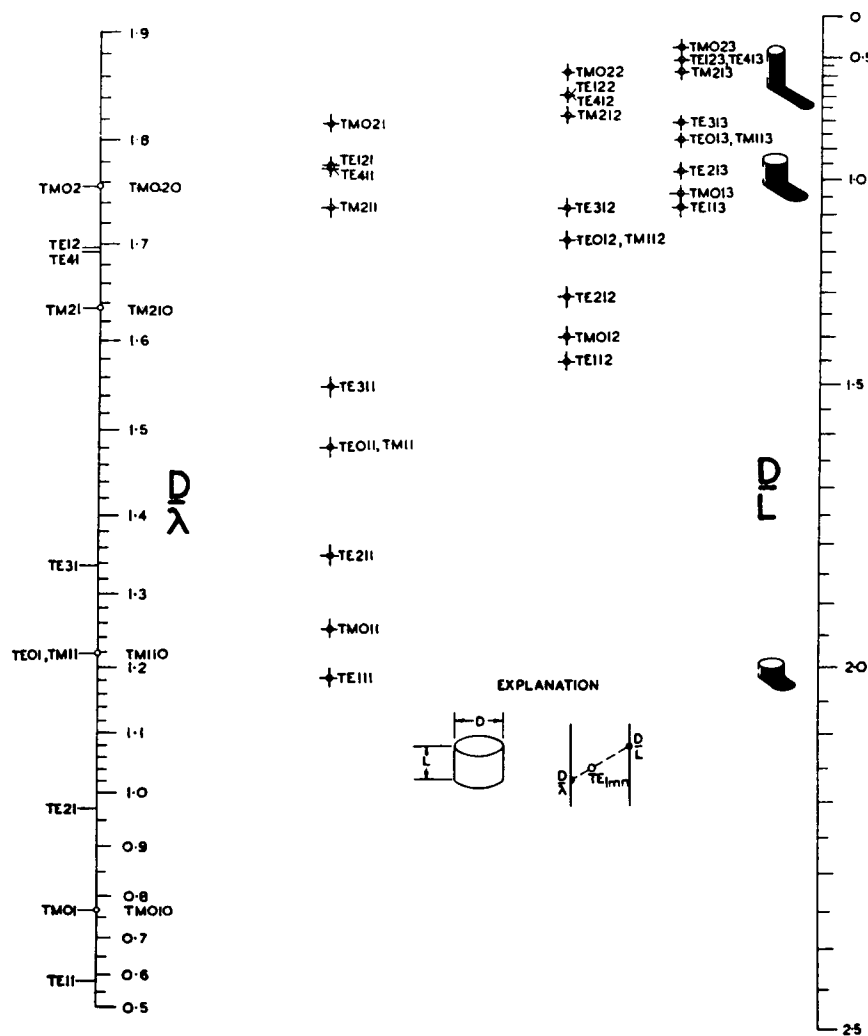


Figure 15. Mode lattice for cylindrical resonators [3, p. 832]. [© 1947 IRE (now IEEE)].

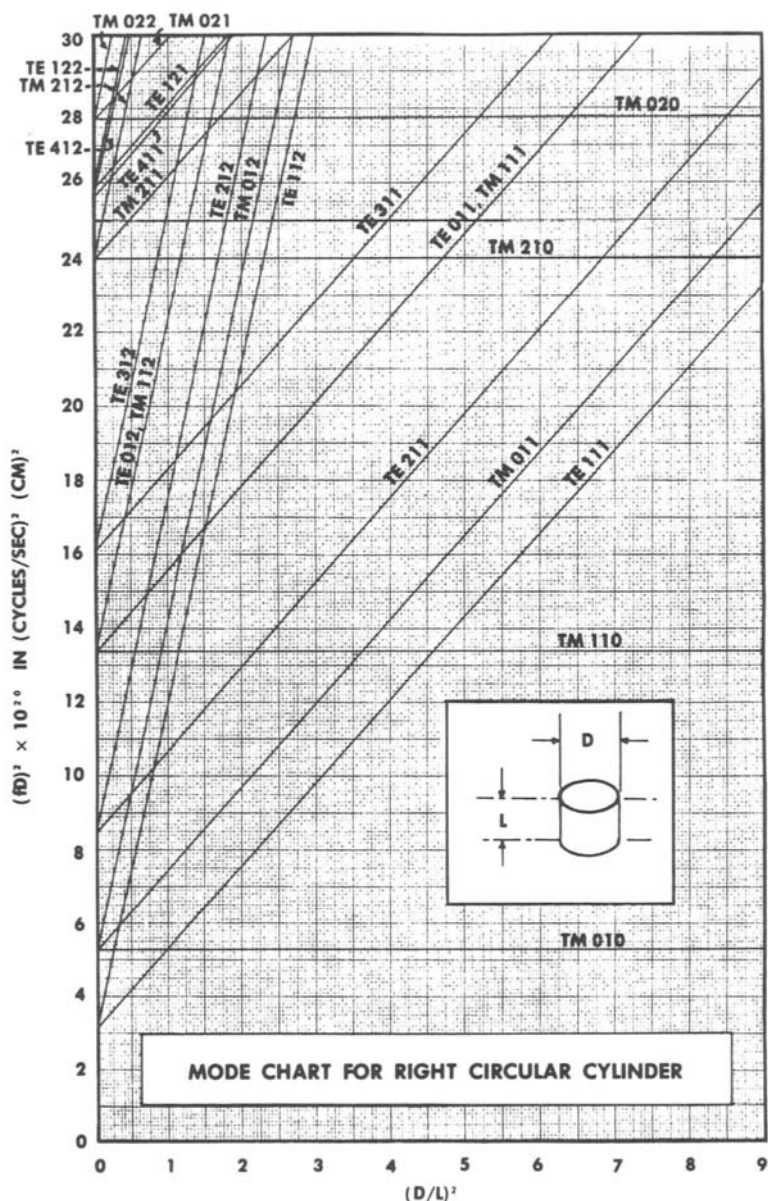


Figure 16. Mode chart for cylindrical resonators [28, Vol. I, p. 181]. Reproduced with permission of Artech House, Inc.

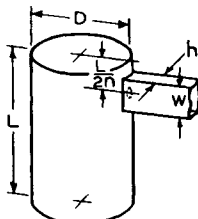
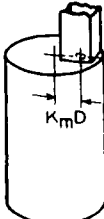
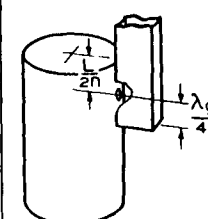
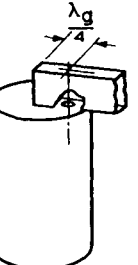
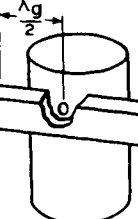
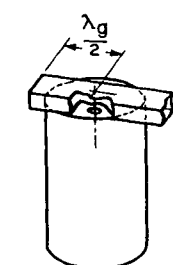
COUPLING METHOD	CASE					
	IA	IB	2A	2B	3A	3B
						
CIRCULAR ORIFICE	$\frac{\Delta f}{f} = -K_C \frac{\lambda^2 d^3}{D^4 L}$ $W_a = K_W \frac{\lambda^2 d^6}{\lambda g w h D^4 L}$	$\frac{\Delta f}{f} = -K_C \frac{n^2 \lambda^2 d^3}{D^2 L^3}$ $W_a = K_W \frac{n^2 \lambda^2 d^6}{\lambda g w h D^2 L^3}$	$\frac{\Delta f}{f}$ SAME AS IA $W_a = K_W \frac{\lambda g \lambda^2 d^6}{w^3 h D^4 L}$	$\frac{\Delta f}{f}$ SAME AS IB $W_a = K_W \frac{n^2 \lambda g \lambda^2 d^6}{w^3 h D^2 L^3}$	$\frac{\Delta f}{f}$ SAME AS IA W_a SAME AS IA	$\frac{\Delta f}{f}$ SAME AS IB W_a SAME AS IB
CONSTANTS	K_C TE 01n 0.316 TE 02n 1.058 TE 03n 2.225 K_W 0.1107 0.464 1.095 0.288 K_m 1.322 0.2403 0.1312 1.207	K_C TE 01n 0.316 TE 02n 1.058 TE 03n 2.225 K_W 0.464 0.836 0.0905 K_m 0.2403 0.1312 0.0905	K_W 0.331 1.108 2.330	K_W 0.1159 0.2089 0.302		
NOTATION: λ = FREE SPACE WAVELENGTH OF CAVITY RESONANCE λ_g = GUIDE WAVELENGTH			d = DIAMETER OF ORIFICE		NOTE: FOR FEED LIKE CASES 2 AND 3, BUT WITH WAVEGUIDE TERMINATED IN BOTH DIRECTIONS, DIVIDE W_a BY 2	
$W_a = \frac{1}{Q_a}$ = CAVITY LOADING						

Figure 17. Approximate orifice diameters for TE_{01n} mode cylindrical cavity coupling to TE_{10} rectangular waveguide [31, p. 420] [© 1946 AT & T. All rights reserved. Reprinted with permission]. Note that the calculated orifice diameters tend to be smaller than those determined experimentally [31, p. 419].

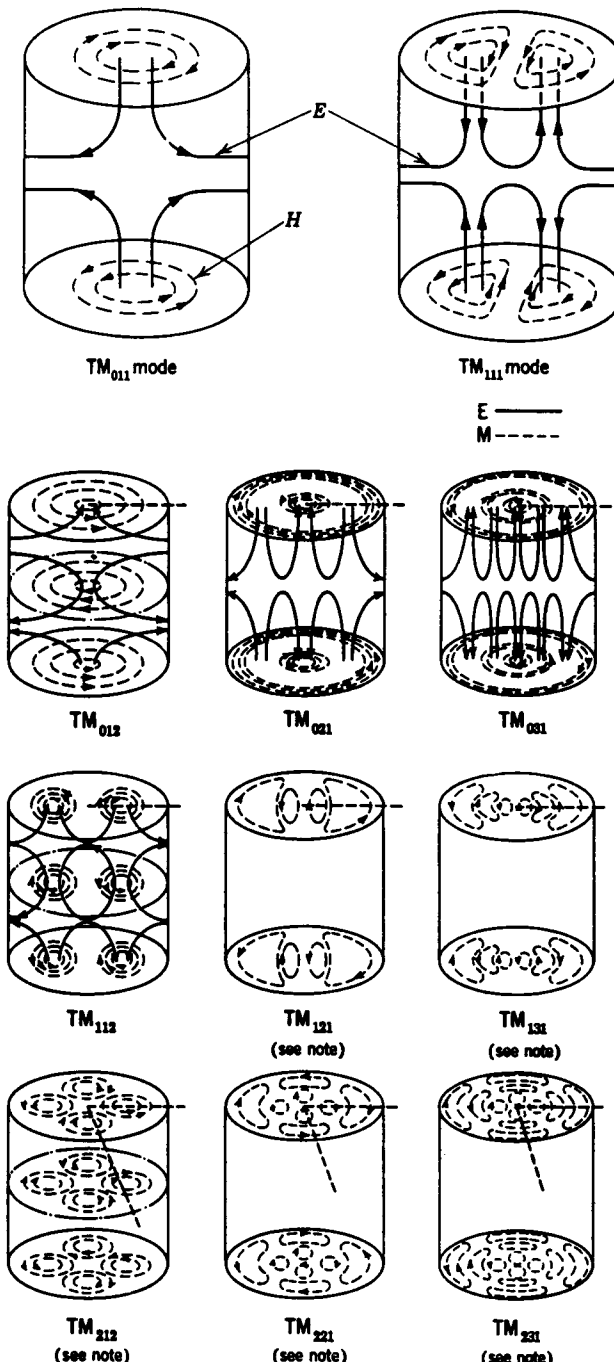


Figure 18. TM mode field pattern sketches [15, pp. 134–135]. [The figures are adapted from *Microwave Engineering*, 2nd ed., by T. Koryu Ishii, © 1989 by Harcourt Brace and Company reproduced with permission of the publisher.] Note: this mode is a repetition of the basic mode. Some field lines have been omitted for clarity.

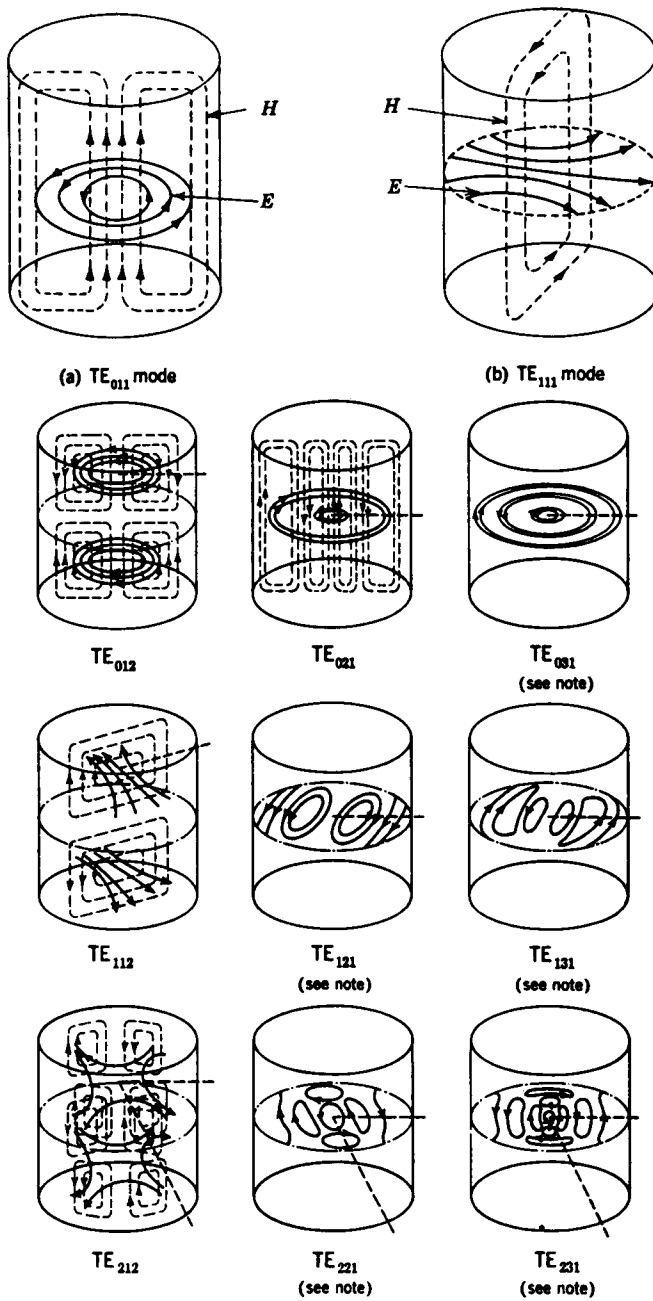


Figure 19. TE mode field pattern sketches [15, pp. 130–131]. [The figures are adapted from *Microwave Engineering*, 2nd ed., by T. Koryu Ishii, © 1989 by Harcourt Brace and Company reproduced with permission of the publisher.] Note: this mode is a repetition of the basic mode. Some field lines have been omitted for clarity.

6. Spherical Cavities [4, p. 380]

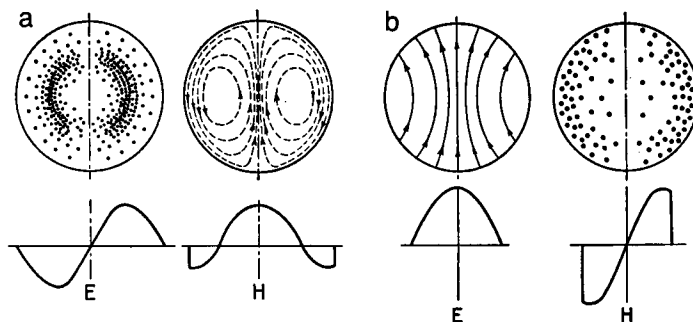


Figure 20. Field patterns for the lowest order modes in spherical cavities. (a) TE₁₁₀ mode. (b) TM₁₁₀ mode. [From A. B. Bromwell and R. E. Beam, *Theory and Applications of Microwaves*, © 1947 McGraw-Hill with permission of McGraw-Hill.]

$$\begin{aligned} a &= \text{spherical cavity radius} \\ \lambda_r &= \text{resonant wavelength} \\ \lambda_r &= 1.40a \text{ for TE}_{11m} \text{ modes} \\ \lambda_r &= 2.29a \text{ for TM}_{11m} \text{ modes.} \end{aligned}$$

7. Dielectric Resonators

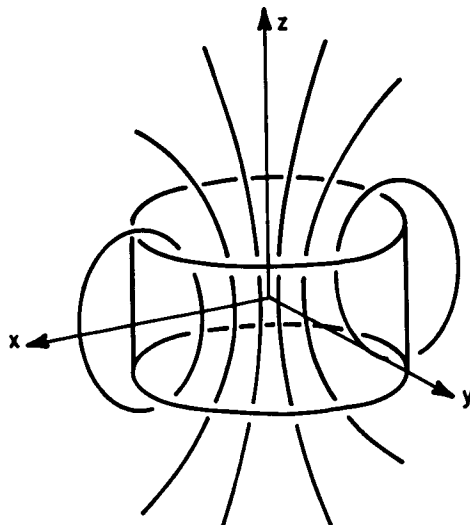


Figure 21. Dielectric resonator dimensions and magnetic field for the TE₀₁₈ mode [19, p. 2]. Reproduced with permission of Artech House, Inc.

The approximate resonant frequency, f_o , of a dielectric resonator (DR) in free space in the $\text{TE}_{01\delta}$ mode is

$$f_o = \frac{34}{a\sqrt{\epsilon_r}} \left[\frac{a}{L} + 3.45 \right] \text{ (GHz)} \quad [19, \text{ p. 3}],$$

where

a = radius of the DR in millimeters

L = length of the DR in millimeters

ϵ_r = relative permittivity of the DR.

This equation is accurate to approximately 2% under the conditions $0.5 < (a/L) < 2$ and $30 < \epsilon_r < 50$. More accurate and mathematically intensive calculation procedures which account for the environment around the resonator, such as a microstrip substrate and metal shields, exist (see, for example, [11, 17, 19, 26]). An example of a mode chart, from Pospieszalski [26, p. 235], is shown in Figure 22. Later literature improves the accuracy, ease of calculations, or both and includes references to several approximate and rigorous techniques [44, 45, 49].

The determination of the length of a DR for a given diameter and frequency can be calculated to within a few percent using Kajfez's procedure ([18]; also shown in [19, pp. 148–149]) for the Itoh and Rudokas

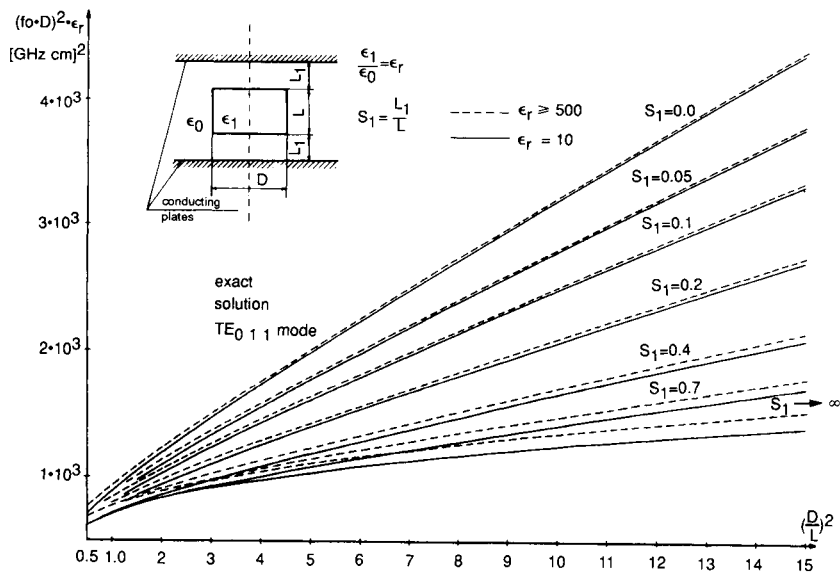


Figure 22. A DR mode chart [© 1979 IEEE].

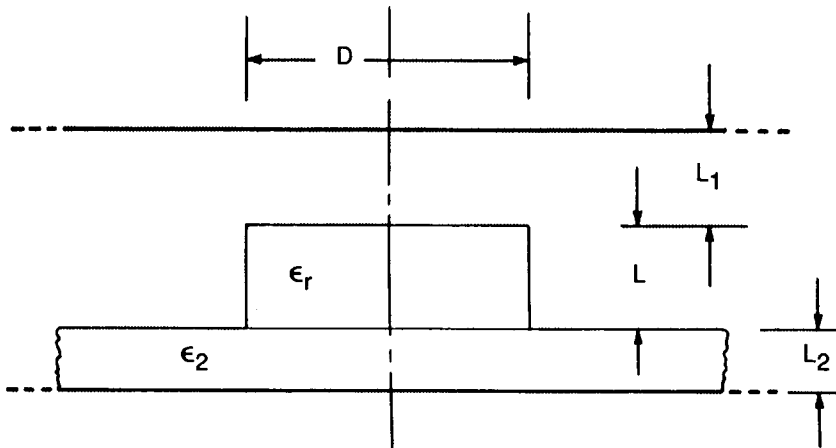


Figure 23. DR geometry and dimensions. ϵ_2 , is the substrate relative permittivity [18, p. 133] [© by Argus Business, reprinted with permission].

model [17]. Refer to Figure 23 for the geometry and variable definitions. Note the metallic cover at distance L_1 above the resonator. The straightforward calculations are listed below. Specify f_o . Select D :

$$\frac{5.4}{k_o \sqrt{\epsilon_r}} \leq D \leq \frac{5.4}{k_o \sqrt{\epsilon_2}},$$

where

$$k_o = \text{free-space propagation constant} = \omega \sqrt{\mu_0 \epsilon_0}$$

$$y_o = \sqrt{\left(k_o \frac{D}{2}\right)^2 (\epsilon_r - 1) - 2.405^2}$$

$$h = \frac{2}{D} \left[2.405 + \frac{y_o}{2.405 \left(1 + \frac{2.43}{y_o} + 0.291 y_o \right)} \right]$$

$$\beta = \sqrt{k_o^2 \epsilon_r - h^2}$$

$$\alpha_1 = \sqrt{h^2 - k_o^2}$$

$$\alpha_2 = \sqrt{h^2 - k_o^2 \epsilon_2}$$

$$L = \frac{1}{\beta} \left[\tan^{-1} \left(\frac{\alpha_1}{\beta} \coth \alpha_1 L_1 \right) + \tan^{-1} \left(\frac{\alpha_2}{\beta} \coth \alpha_2 L_2 \right) \right].$$

See [36, 39, 47] for dielectric ring resonators. See [37, 38, 40, 48, 51] for whispering gallery mode dielectric resonators.

8. Loop – Gap Resonators

One Loop – n Gap Resonator [8, pp. 515 – 517]

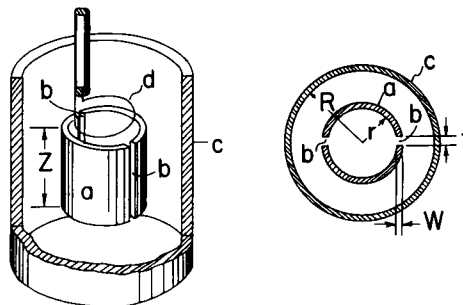


Figure 24. One loop – n gap resonator ($n = 2$ shown). Dimensions and features: a, loop; b, gaps; c, shield; d, inductive coupler; Z, resonator length; r, resonator radius; R, shield radius; t, gap separation; W, gap width [8, p. 516]. Reprinted with permission of Harcourt Brace and Company.

A coarse approximation for resonant frequency f_o is

$$C = \frac{\epsilon WZ}{tn} \quad L = \frac{\mu_o \pi r^2}{Z} \quad f_o = \frac{1}{2\pi\sqrt{LC}}.$$

To account for the shield and fringing fields in the gap effects on resonant frequency, use the following equation:

$$f_o = \frac{1}{2\pi} \sqrt{1 + \frac{r^2}{R^2 - (r + W)^2}} \sqrt{\frac{nt}{\pi W \epsilon \mu_0}} \frac{1}{r} \sqrt{\frac{1}{1 + 2.5 \left(\frac{t}{W}\right)}}.$$

This equation is generally within 10% of measured resonant frequencies between 1 and 10 GHz.

δ = skin depth

Q_o = unloaded Q

$$\frac{1}{Q_o} = \frac{1}{Q_1} + \frac{1}{Q_2},$$

where

$$Q_1 = \frac{\frac{r}{\delta} \left[1 + \frac{r^2}{R^2 - (r + W)^2} \right]}{\left[1 + \left(1 + \frac{W}{r} + \frac{R}{r} \right) \left(\frac{r^2}{R^2 - (r + W)^2} \right)^2 \right]}$$

$$Q_2 = \frac{1.7 \times 10^5 t}{f_0^{3/2} \epsilon W Z \left(1 + 2.5 \left(\frac{t}{W} \right) \right)}.$$

Mehdizadeh *et al.* [22] give corrections to f_o and Q_o for the finite length of the resonator.

Two Loop – One Gap Resonator, [9, pp. 1096 – 1097]

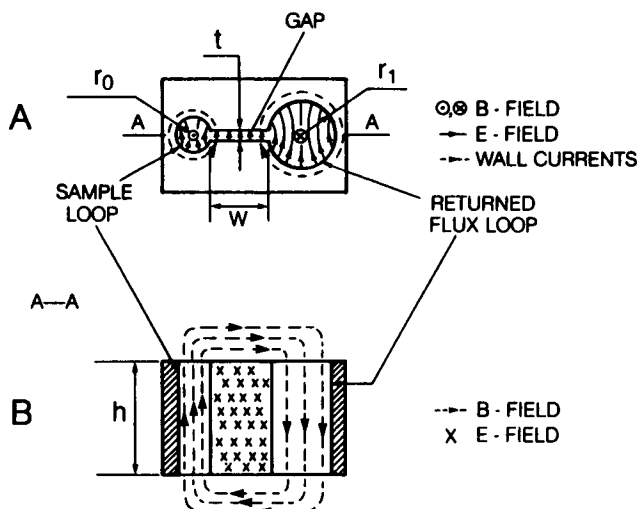


Figure 25. Two loop – one gap resonator. Reproduced with permission from Froncisz *et al.* Rev. Sci. Instrum., Vol. 57, pp. 1095 – 1099, 1986 and its publisher, American Institute of Physics.

A coarse approximation for resonant frequency f_o is (c = speed of light):

$$f_o = \frac{c}{2\pi r_o} \sqrt{\frac{t \left(1 + \frac{r_o^2}{r_1^2} \right)}{\pi \epsilon W}}$$

The corrections applied depend on the frequency of interest [9, p. 1096]. For a 35-GHz resonator, corrections of magnetic flux in the gap and fringing electric field were used:

$$f_o = \frac{c}{2\pi} \sqrt{\frac{t(1+a)^2}{\epsilon_r W \left(1 + \frac{2.5t}{W}\right) \left[\pi r_o^2 + \pi a^2 r_1^2 + (1-a+a^2) \frac{Wt}{3} \right]}},$$

where

$$a = \frac{\frac{\pi r_o^2}{2} + \frac{tW}{2}}{\frac{\pi r_1^2}{2} + \frac{tW}{2}}$$

$$Q_o = \frac{2}{\delta} \cdot \frac{\pi r_o^2 + \pi r_1^2 a^2 + \left(\frac{1}{3}\right) W t (1 - a + a^2)}{2\pi r_o - t + (2\pi r_1 - t) a^2 + \left(\frac{2}{3}\right) W (1 - a + a^2)}.$$

The reader is referred to Wood *et al.* [33] for the three loop–two gap resonator. Finally, it is noted that several other loop–gap resonator configurations exist; see, for example, Hyde and Froncisz [14].

9. Microstrip Resonators

Microstrip Rectangular Resonators

The approximate resonant frequency, f_o [15, p. 152] is

$$f_o = \frac{\sqrt{\left(\frac{1}{2w}\right)^2 + \left(\frac{1}{2l}\right)^2}}{2\sqrt{\epsilon\mu}},$$

where

ϵ = permittivity of the microstrip dielectric

μ = permeability of the microstrip dielectric

$$Q \approx \frac{\omega_o d\mu}{4R_w} \quad [15, \text{p. } 153],$$

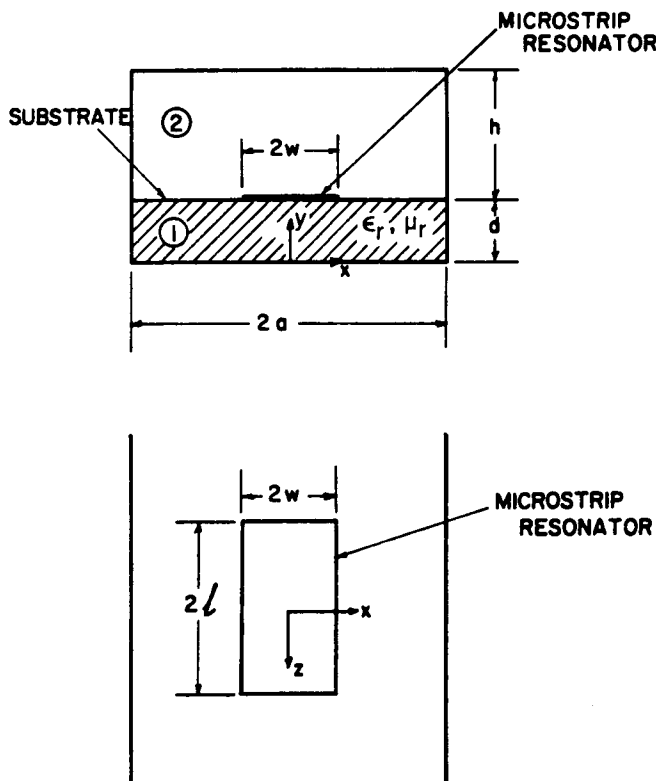


Figure 26. Microstrip rectangular resonator dimensions [16, p. 947] [© 1974 IEEE].

where

$$R_w = \text{surface resistance} = \sqrt{\frac{\pi f \mu}{\sigma}}$$

and σ = conductivity of the microstrip conductor. An accurate resonant frequency determination is given by Itoh [16], and an example of his results is reproduced in Figure 27. Wolff and Knoppik [32] give a method to calculate resonant frequency to within 1 to 2%. An improvement to 0.5% has been reported by Verma and Rostany [52]. Microstrip transmission line resonators are not covered here but should be treated as standard transmission line resonators, with appropriate end correction factors applied.

Microstrip Circular Resonators

a = circular resonator radius.

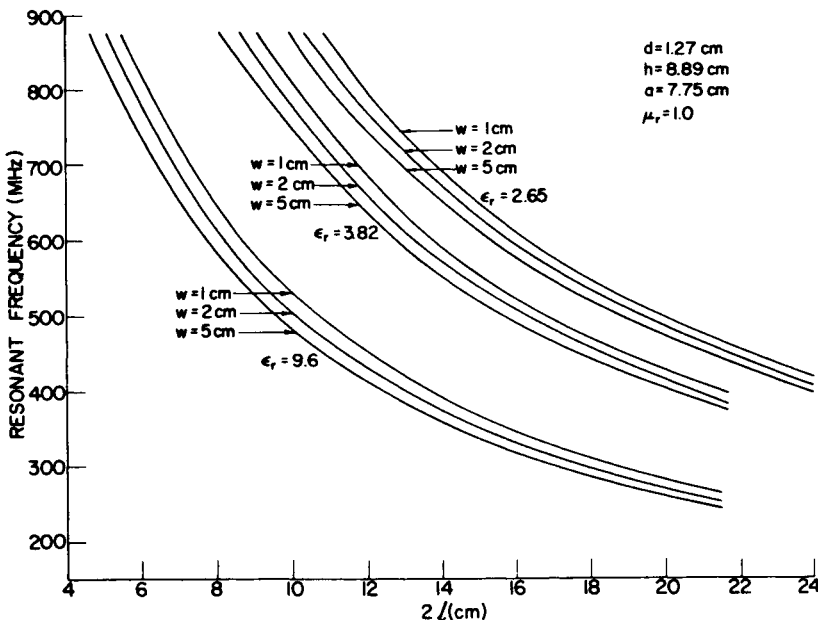


Figure 27. Rectangular resonator resonant frequencies [16, p. 950] [© 1974 IEEE].

Note that all other variables are as defined under Microstrip Rectangular Resonators. An approximate resonant frequency and Q are

$$f_o = \frac{3.832}{2\pi a\sqrt{\mu\epsilon}} \quad Q = \frac{\omega_o d \mu}{2R_w} \quad [15, \text{pp. 151--152}].$$

Wolff and Knoppik [32] give a method to calculate f_o to within approximately 1%. Bahl and Bhartia [1, pp. 79–82] review other calculation methods. Also see Ref. [50].

Microstrip Ring Resonators

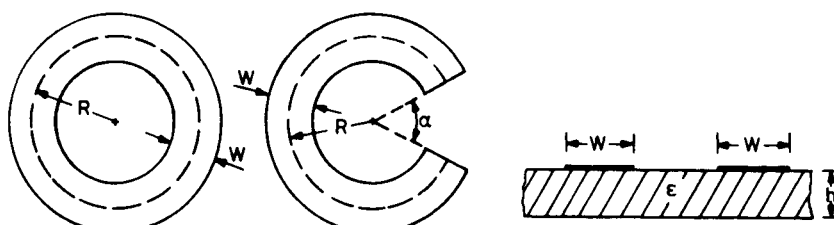


Figure 28. Closed and open ring resonators [30, p. 406] [© 1984 IEEE].

Wu and Rosenbaum [34] present a mode chart for the (closed) ring resonator. Khilla [20] presents a method to calculate f_o to within 1.5%. Tripathi and Wolff [30] present closed-form solutions for both the open and the closed ring resonators. Also see Ref. [50].

10. Fabry – Perot Resonators [6, pp. 337 – 344]

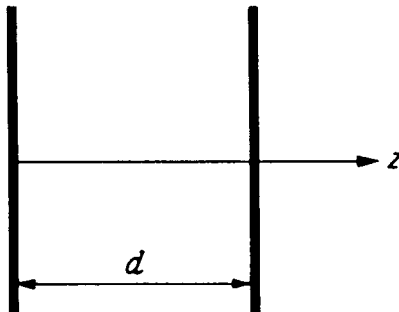


Figure 29. Ideal Fabry – Perot resonator [6, p. 338] [Robert Collin, *Foundations for Microwave Engineering*, © 1966 by McGraw – Hill, with permission of McGraw – Hill].

The ideal resonant frequency is $f_o = (cn/2d)$, where

$$n = 1, 2, 3, \dots \quad (\text{mode})$$

c = speed of light.

The ideal unloaded equation is $Q = (\pi n Z_o / 4 R_w)$, where

R_w = surface resistance of the reflectors

$$R_w = \sqrt{\frac{\pi f \mu}{\sigma}}$$

Z_o = intrinsic impedance of free space

$$Z_o = \sqrt{\frac{\mu_o}{\epsilon_o}}.$$

Practical Fabry–Perot resonators must be coupled. Collin [6, pp. 339–344] describes one way of accomplishing this with circular holes in the end-plates. The effects of the coupling holes on f_o and Q are derived.

Also, Fabry–Perot resonators often use spherical reflectors to ensure the confinement of the reflections [27, pp. 570–577]. See Refs. [35, 41, 42, 46] for equivalent circuits, coupling, and resonant frequency calculations of Fabry–Perot (open) resonators.

II. YIG Resonators

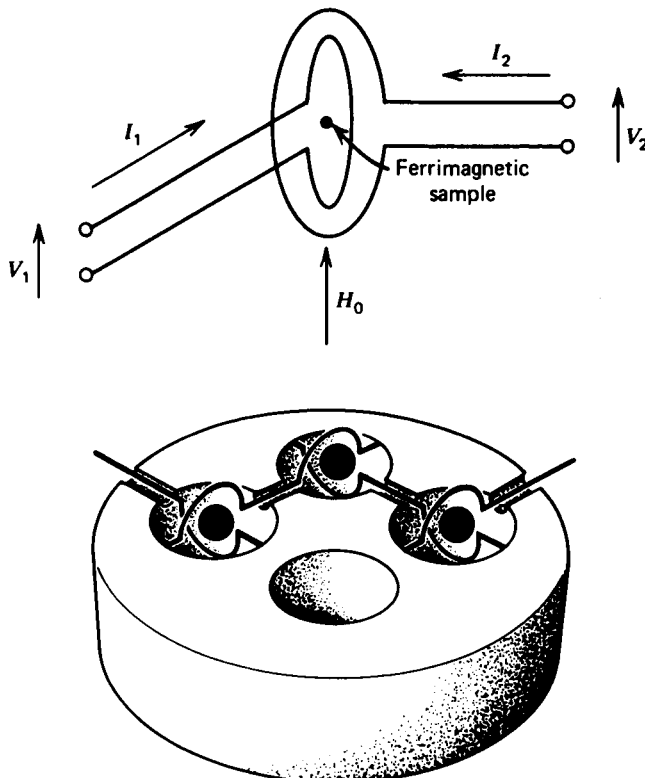


Figure 30. A three-stage YIG filter [From J. Helszajn, *Passive and Active Microwave Circuits*. Copyright © 1978 John Wiley & Sons, Inc. Reprinted by permission of John Wiley & Sons, Inc.]

YIG = yttrium iron garnet ($\text{Y}_3\text{Fe}_5\text{O}_{12}$) [25, p. 211]

f_o = resonant frequency

$$f_o = \frac{\Gamma}{2\pi} \cdot (H_o \pm H_a),$$

where

$$\Gamma = 0.221 \frac{\text{MHz}}{A/m} \quad [1, \text{p. 112}; 25, \text{p. 211}]$$

H_0 = external biasing magnetic field intensity

H_a = inner anisotropic field of the YIG crystal.

Note that the magnitude and sign depend on the orientation of the YIG crystal in the magnetic field. Osbrink [24] examines the Q of YIG spheres. YIG resonators are often used in filters and tuned oscillators. They are tuned linearly with respect to magnetic field bias. Mezak and Vendelin [43] review loop-coupled YIG resonator modeling.

12. Traveling-Wave Resonators

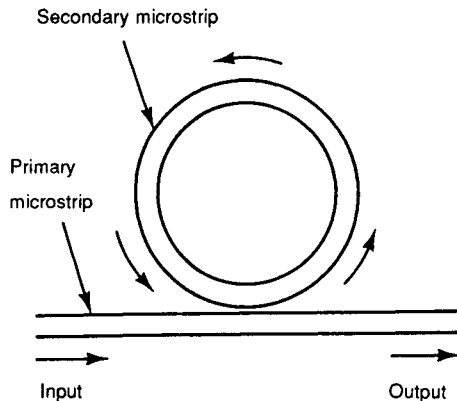


Figure 31. A traveling-wave resonator in a microstrip [15, p. 172]. [The figure was adapted from *Microwave Engineering*, 2nd ed., by T. Koryu Ishii, © 1989 by Harcourt Brace and Company, reproduced with permission of the publisher.]

If the length of the secondary line is a multiple of whole wavelengths, a resonance response (absorption) will occur [12, pp. 201–202; 15, pp. 172–173]. Harvey also discusses how the traveling wave may be used to increase the fields' amplitudes in the resonant ring.

References

- [1] I. Bahl and P. Bhartia, *Microwave Solid State Circuit Design*. New York: John Wiley & Sons, 1988.
- [2] W. Bazzi, publishers, *The Microwave Engineers' Handbook and Buyers' Guide*, 1963 ed. Brookline, MA: Horizon House, 1962.
- [3] R. N. Bracewell, Charts for resonant frequencies of cavities, *Proc. IRE*, Vol. 35, pp. 830–841, Aug. 1947.
- [4] A. B. Bronwell and R. E. Beam, *Theory and Applications of Microwaves*, pp. 377–383. New York: McGraw-Hill, 1947.
- [5] G. B. Brown, R. A. Sharpe, W. L. Hughes, and R. E. Post, *Lines, Waves, and Antennas: The Transmission of Electric Energy*, 2nd Ed. New York: John Wiley & Sons, 1973.
- [6] R. E. Collin, *Foundations for Microwave Engineering*. New York: McGraw-Hill, 1966.
- [7] C. W. Davidson, *Transmission Lines for Communications with CAD Programs*, 2nd Ed. New York: Wiley-Halsted Press, 1989.
- [8] W. Froncisz and J. S. Hyde, The loop-gap resonator: A new microwave lumped circuit ESR sample structure, *J. Magn. Reson.*, Vol. 47, pp. 515–521, 1982.
- [9] W. Froncisz, T. Oles and J. S. Hyde, Q-band loop-gap resonator, *Rev. Sci. Instrum.*, Vol. 57, pp. 1095–1099, 1986.
- [10] K. Fujisawa, General treatment of Klystron resonant cavities, *IRE Trans. Microwave Theory Tech.*, Vol. MTT-6, pp. 344–358, Oct. 1958.
- [11] W. Geyi and W. Hongshi, Solution of the resonant frequencies of a microwave dielectric resonator using boundary element method, *IEE Proc., Part H*, Vol. 135, pp. 333–338, Oct. 1988.
- [12] A. F. Harvey, *Microwave Engineering*. London: Academic Press, 1963.
- [13] J. Helszajn, *Passive and Active Microwave Circuits*. New York: John Wiley & Sons, 1978.
- [14] J. S. Hyde and W. Froncisz, Loop-gap resonators, in *Advanced EPR: Applications in Biology and Biochemistry* (A. J. Hoff, ed.), pp. 277–306. Amsterdam: Elsevier, 1989.
- [15] T. K. Ishii, *Microwave Engineering*, 2nd Ed. San Diego: Harcourt Brace Jovanovich, 1989.
- [16] T. Itoh, Analysis of microstrip resonators, *IEEE Trans. Microwave Theory Tech.*, Vol. MTT-22, pp. 946–952, Nov. 1974.
- [17] T. Itoh and R. S. Rudokas, New method for computing the resonant frequencies of dielectric resonators, *IEEE Trans. Microwave Theory Tech.*, Vol. MTT-25, pp. 52–54, Jan. 1977.
- [18] D. Kajfez, Elementary functions procedure simplifies dielectric resonator's design, *Microwave Syst. News*, Vol. 12, pp. 133–140, June 1982 (© Argus Business).
- [19] D. Kajfez and P. Guillon, eds., *Dielectric Resonators*. Norwood, MA: Artech House, 1986.
- [20] A. M. Khilla, Ring and disk resonator CAD model, *Microwave J.*, pp. 91–105, Nov. 1984.
- [21] R. W. P. King, H. R. Mimno, and A. H. Wing, *Transmission Lines, Antennas, and Wave Guides*. New York: Dover, 1965.
- [22] M. Mehdizadeh, T. K. Ishii, J. S. Hyde, and W. Froncisz, Loop-gap resonator: A lumped mode microwave resonant structure, *IEEE Trans. Microwave Theory Tech.*, Vol. MTT-31, pp. 1059–1064, 1983.
- [23] T. Moreno, *Microwave Transmission Design Data*. Norwood, MA: Artech House, 1989.
- [24] N. K. Osbrink, YIG-tuned oscillator fundamentals, *Microwave Syst. Designer's Handb.*, Vol. 13, pp. 207–225, Nov. 1983.
- [25] E. Pehl, *Microwave Technology*. Dedham, MA: Artech House, 1985.

- [26] M. W. Pospieszalski, Cylindrical dielectric resonators and their applications in TEM line microwave circuits, *IEEE Trans. Microwave Theory Tech.*, Vol. MTT-27, pp. 233–238, Mar. 1979.
- [27] S. Ramo, J. R. Whinnery, and T. Van Duzer, *Fields and Waves in Communication Electronics*. New York: John Wiley & Sons, 1965.
- [28] T. S. Saad, ed., *Microwave Engineers' Handbook*, Vols. 1 and 2. Dedham, MA: Artech House, 1971.
- [29] F. E. Terman, Resonant lines in radio circuits, *Electr. Eng. (Am. Inst. Electr. Eng.)*, Vol. 53, pp. 1046–1053, July 1934.
- [30] V. K. Tripathi and I. Wolff, Perturbation analysis and design equations for open- and closed-ring microstrip resonators, *IEEE Trans. Microwave Theory Tech.*, Vol. MTT-32, pp. 405–409, Apr. 1984.
- [31] I. G. Wilson, C. W. Schramm, and J. P. Kinzer, High Q resonant cavities for microwave testing, *Bell Syst. Tech. Vol.* 25, pp. 408–434, July 1946.
- [32] I. Wolff, and N. Knoppik, Rectangular and circular microstrip disk capacitors and resonators, *IEEE Trans. Microwave Theory Tech.*, Vol. MTT-22, pp. 857–864, Oct. 1974.
- [33] R. L. Wood, W. Froncisz, and J. S. Hyde, The loop-gap resonator. II. Controlled return flux three-loop, two-gap microwave resonators for ENDOR and ESR spectroscopy, *J. Magn. Reson.*, Vol. 58, pp. 243–253, 1984.
- [34] Y. S. Wu and F. J. Rosenbaum, Mode chart for microstrip ring resonators, *IEEE Trans. Microwave Theory Tech.*, Vol. MTT-21, pp. 487–489, July 1973.
- [35] H. Cam, S. Toutain, P. Gelin, and G. Landrac, Study of a Fabry–Perot cavity in the microwave frequency range by the boundary element method, *IEEE Trans. Microwave Theory Tech.*, Vol. MTT-40, pp. 298–304, Feb. 1992.
- [36] S.-W. Chen, and K. A. Zaki, Dielectric ring resonators loaded in waveguide and on substrate, *IEEE Trans. Microwave Theory Tech.*, Vol. MTT-39, pp. 2069–2076, Dec. 1991.
- [37] D. Cros and P. Guillon, Author's reply, *IEEE Trans. Microwave Theory Tech.*, Vol. MTT-40, pp. 1036–1038, May 1992.
- [38] D. Cros and P. Guillon, Whispering gallery dielectric resonator modes for W-band devices, *IEEE Trans. Microwave Theory Tech.*, Vol. MTT-38, pp. 1667–1674, Nov. 1990.
- [39] W. K. Hui, and I. Wolff, Dielectric ring-gap resonator for application in MMIC's, *IEEE Trans. Microwave Theory Tech.*, Vol. MTT-39, pp. 2061–2068, Nov. 1991.
- [40] E. N. Ivanov, D. G. Blair, and V. I. Kalinichev, Approximate approach to the design of shielded dielectric disk resonators with whispering-gallery modes, *IEEE Trans. Microwave Theory Tech.*, Vol. MTT-41, pp. 632–638, Apr. 1993.
- [41] T. Matsui, K. Araki, and M. Kiyokawa, Gaussian-beam open resonator with highly reflective circular coupling regions, *IEEE Trans. Microwave Theory Tech.*, Vol. MTT-41, pp. 1710–1714, Oct. 1993.
- [42] J. McCleary, M.-y. Li, and K. Chang, Slot-fed higher order mode Fabry–Perot filters, *IEEE Trans. Microwave Theory Tech.*, Vol. MTT-41, pp. 1703–1709, Oct. 1993.
- [43] J. A. Mezak, and G. D. Vendelin, CAD design of YIG tuned oscillators, *Microwave J.*, pp. 92–98, Dec. 1992.
- [44] R. K. Mongia, On the accuracy of approximate methods for analyzing cylindrical dielectric resonators, *Microwave J.*, pp. 146–150, Oct. 1991.
- [45] R. K. Mongia, Resonant frequency of cylindrical dielectric resonator placed in an MIC environment, *IEEE Trans. Microwave Theory Tech.*, Vol. MTT-38, pp. 802–804, June 1990.

- [46] R. K. Mongia and R. K. Arora, Equivalent circuit parameters of an aperture coupled open resonator cavity, *IEEE Trans. Microwave Theory Tech.*, Vol. MTT-41, pp. 1245–1250, Aug. 1993.
- [47] R. K. Mongia and P. Bhartia, Easy resonant frequency computations for ring resonators, *Microwave J.*, p. 105–108, Nov. 1992.
- [48] M. J. Niman, Comments on “Whispering gallery dielectric resonator modes for W-band devices,” *IEEE Trans. Microwave Theory Tech.*, Vol. MTT-40, pp. 1035–1036, May 1992.
- [49] J.-S. Sun and C.-C. Wei, Iterative method provides accurate resonator analysis, *Microwaves & RF*, Vol. 30, pp. 70–79, Dec. 1991.
- [50] F. Tefiku and E. Yamashita, An efficient method for the determination of resonant frequencies of shielded circular disk and ring resonators, *IEEE Trans. Microwave Theory Tech.*, Vol. MTT-41, pp. 343–346, Feb. 1993.
- [51] C. Vedrenne and J. Arnaud, Whispering-gallery modes of dielectric resonators, *IEE Proc., Part H*, Vol. 129, pp. 183–187, Aug. 1982.
- [52] A. K. Verma and Z. Rostamy, Resonant frequency of uncovered and covered rectangular microstrip patch using modified Wolff model, *IEEE Trans. Microwave Theory Tech.*, Vol. MTT-41, pp. 109–116, Jan. 1993.
- [53] W. Xi, W. R. Tinga, W. A. G. Voss, and B. Q. Tian, New results for coaxial re-entrant cavity with partially dielectric filled gap, *IEEE Trans. Microwave Theory Tech.*, Vol. MTT-40, pp. 747–753, Apr. 1992.

This Page Intentionally Left Blank

Microstrip Line Components

R. K. Hoffmann

I. Introduction

This chapter describes various components for hybrid and monolithic microwave integrated circuits (MICs and MMICs) with microstrip lines (Chapter 2) in thin-film technology (conductor thickness, 2–10 μm). Generally pure dielectric substrates with a relative dielectric constant, ϵ_r , and a low dielectric loss factor, $\tan \delta < 0.01$, are assumed. The most common substrate material for hybrid microwave integrated circuits [1–5] is 99.5% pure alumina (Al_2O_3) with $\epsilon_r = 9.8$, $\tan \delta = 0.0001$, and thicknesses of 0.635 mm (25 mil), 0.508 mm (20 mil), or 0.254 mm (10 mil). For special applications also fused quartz ($\epsilon_r = 3.78$) or sapphire (anisotropic, $\epsilon_r = 9.4$ and 11.6 in either principal axis) is used. Monolithic microwave integrated circuits [6–10] are produced on semiinsulating (high resistivity) GaAs substrates ($\epsilon_r = 12.9$, $\tan \delta = 0.002$ typically) with a thickness range of 0.1 to 0.2 mm.

The various components described in Sections 2 to 15 can be divided into five groups.

Group 1 (Sections 2 to 6): lumped inductive components

Group 2 (Sections 7 to 9): lumped capacitive components

Components of Groups 1 and 2 are used to build up lumped-element microwave integrated circuits in hybrid thin-film technology [11–15; 16,

Chap. 7] up to frequencies of approximately 20 GHz and in monolithic technology [6–10] up to frequencies of approximately 30 GHz. In lumped-element MICs lumped reactive elements are used instead of microstrip lines to build up passive circuits such as matching circuits, filters, and resonators.

Group 3 (Sections 10 to 13): microstrip discontinuities. They occur at any connection of lines, termination of lines, and change in line direction, i.e., at any deviation from the straight uniform line. These discontinuities have to be treated as individual components in the microwave circuit due to their immanent field distortions [1 and 2, Chap. 10; 3, Chap. I-A2; 4, Chap. 5; 5, Part VII; 16, Chaps. 5 and 6; 17, Chaps. 3 and 4; 18–23].

Group 4 (Section 14): absorbing microstrip terminations

Group 5 (Section 15): transitions from coaxial to microstrip lines

For other passive microstrip components refer to the following chapters: resonators, Chapter 3; filters, Chapter 6; directional couplers, Chapter 7; ferrite components, Chapter 8; matching circuits, Chapter 9; and antennas, Chapter 24.

2. Straight Planar Ribbon Inductor

Three kinds of straight planar ribbon inductors [13, 15, 16, Chap. 7, 24–29] shall be discussed, namely a thin straight metal strip in free space and a short length of strip conductor on a substrate with or without ground metallization, all three kinds being practical for inductances of approximately 0.1 to 5 nH.

Straight Metal Strip in Free Space

The equivalent circuit for a thin planar metal ribbon in free space (Figure 1a) of the length l , the width w , and the thickness t between the two reference planes T_1 and T_2 is a series combination of an inductor, L_1 , and a resistor, R_1 (Figure 1b), if the length l is very much smaller than the wavelength λ at the operating frequency. Gold or aluminum ribbons with typical dimensions $t = 5 \mu\text{m}$, $w = 0.02\text{--}0.5 \text{ mm}$, and $l = 0.3\text{--}2 \text{ mm}$ are used for connection of semiconductor devices to thin-film circuitry or interconnections within the circuitry with ultrasonic or thermocompression

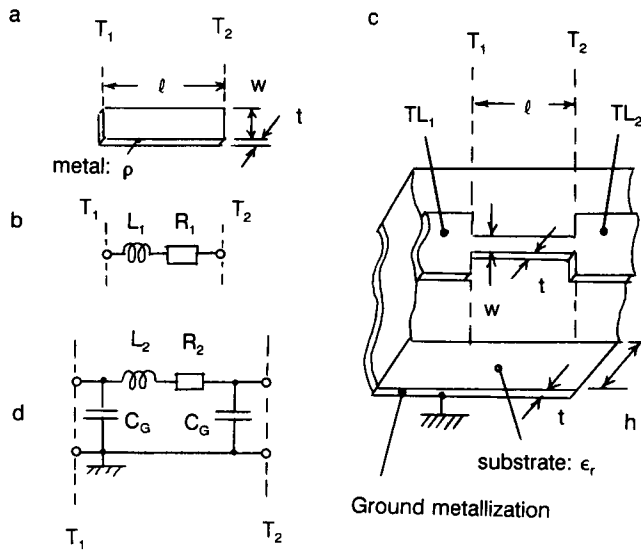


Figure 1. Straight planar ribbon inductor. Configuration (a) and equivalent circuit (b) of the ribbon in free space. (c) Strip conductor on a substrate with ground metallization between connecting transmission lines TL_1 and TL_2 . (d) Two-port equivalent circuit for the strip conductor on a substrate with ground metallization on the lower side.

bonding techniques. The *inductance* L_1 and the *resistance* R_1 are given by

$$L_1 = 0.2l \left(\ln \frac{2l}{w+t} + 0.5 + \frac{w+t}{3l} \right) \quad (1)$$

$$R_1 = \frac{R_S l}{2(w+t)} \cdot K = 4.13 \cdot 10^{-3} \frac{l}{w+t} \sqrt{\frac{\rho}{\rho_{Cu}}} f \cdot K \quad (2)$$

$$K = 1.06 + 0.5 \log \left(\frac{w}{t} \right) + 0.28 \left(\frac{t}{w} \right)^2, \quad (3)$$

where L_1 is in nonohenries, R_1 and R_S are in ohms, the frequency f is in gigahertz, the dimensions l , w , and t , are in millimeters, the resistivity ρ of the ribbon material is in $\Omega \cdot \text{cm}$, and the copper resistivity is $\rho_{Cu} = 1.72 \cdot 10^{-6} \Omega \cdot \text{cm}$. The nondimensional correction factor $K > 1$ takes into account the crowding of the current at the edges of the ribbon. Equation (3) is valid for aspect ratios in the range $1 \leq w/t \leq 100$. In Equation (1) the last term within the brackets may be neglected for long narrow ribbons according to $l > 50(w+t)$. Equation (2) gives the high-frequency resis-

tance R_1 , which applies if the skin effect dominates the current flow, i.e., if the thickness t is appreciably greater than twice the skin depth δ . The *skin depth* δ and the *surface resistivity* R_S are for conductor materials with a relative permeability of $\mu_r = 1$

$$\delta = 2.09 \sqrt{\frac{\rho}{\rho_{\text{Cu}}}} \frac{1}{f} \quad (4)$$

$$R_S = 8.24 \cdot 10^{-3} \sqrt{\frac{\rho}{\rho_{\text{Cu}}}} f, \quad (5)$$

where δ is in micrometers, R_S is in ohms, f is in gigahertz, and ρ and ρ_{Cu} (copper) are in $\Omega \cdot \text{cm}$. The *quality factor* Q of this inductor is thus $Q = 2\pi f L_1 / R_1$. The functional dependences of the equivalent circuit elements on the design parameters are $L_1/l = f(w/l, t/l)$ and $R_1 = \sqrt{\rho \cdot f} \cdot f(w/l, t/l)$.

Metal Strip on a Substrate without Ground Metallization

A strip conductor of a short length, $l \ll \lambda$, with the width w and the thickness t between the two planes T_1 and T_2 on a substrate without ground metallization on the lower side (upper side structure as in Figure 1c) is also modeled by the equivalent circuit of Figure 1b with L_1 and R_1 according to Equations (1) and (2), both being independent of the substrate ϵ_r .

Metal Strip on a Substrate with Ground Metallization

In microstrip circuits on substrates with ground metallization on the lower side, microstrip lines of short lengths $l \ll \lambda$ with small widths w compared with the adjacent lines TL_1 and TL_2 (Figure 1c) are used in semilumped low-pass filters and in matching networks. They have to be considered short transmission line lengths and are described by a full two-port equivalent circuit, shown in Figure 1d. Generally the conductor thickness $t = 0$ is assumed. Using the expression $L' = Z_{L0} \cdot \mu_0 / \eta_0$ for the inductance per unit length and an approximate expression for the free-space characteristic impedance, Z_{L0} , of the microstrip line, one obtains the *inductance* formula

$$L_2 = L'l = 0.2l \ln\left(\frac{8h}{w} + \frac{w}{4h}\right), \quad (6)$$

valid for $0 < w/h < 1$ and $t \ll w$, where L_2 is in nanohenries, L' is in nH/mm, l , w , and the substrate thickness h are in millimeters ($\eta_0 = 120\pi$ Ω = free-space impedance, $\mu_0 = 0.4\pi$ nH/mm = free-space permeability). Equation (6) is an approximation for small thickness $t \ll w$. Due to the influence of the ground conductor with reverse current, there is $L_2 \neq L_1$. The resistance R_2 in ohms is calculated from the resistance per unit length $R' = \alpha_0 \cdot Z_{L0}/4.34$ in Ω/mm of the microstrip line using $R_2 = R'l$, where l is in millimeters. Here Z_{L0} is the characteristic impedance in ohms and α_0 is the attenuation constant in dB/mm of the microstrip line of the dimensions w , h , and t in free space (i.e., on a substrate with $\epsilon_r = 1$). The *ground capacitances* C_G are calculated from the capacitance per unit length $C' = \sqrt{\epsilon_{r,\text{eff}}}/(Z_L \cdot c_0)$ of the microstrip line with the same dimensions as before, however, on the substrate with the real $\epsilon_r > 1$, using $C_G = C'l/2$. Here Z_L and $\epsilon_{r,\text{eff}}$ are the characteristic impedance and the effective dielectric constant of this line ($c_0 = 3 \cdot 10^{10}$ cm/s = velocity of light in free space). For small conductors $w/h \ll 1$ normally C_G is negligible. The effects of the discontinuities at the planes T_1 and T_2 are neglected in the above formulas. The basic functional dependences of the equivalent circuit elements on the design parameters are $L_2/l = f(w/h, t/h)$, $C_G/l = f(w/h, t/h, \epsilon_r)$, and $R_2 = \sqrt{\rho \cdot f} \cdot f(w/h, t/h)$ according to the static approximation.

3. Round Wire Inductor

Small round metal wires of aluminum or gold with diameters of $d = 10$ to $40 \mu\text{m}$ and lengths of $l = 0.3$ to 3 mm typically are used in hybrid MICs as bonding wires for the connection of semiconductor chips to the thin-film circuitry (chip-and-wire technique) and for the connection of the inner end of spiral inductors to the circuitry (see Sections 5 and 6). For short lengths $l \ll \lambda$ these wires behave as inductors [15, 16, Chap. 7; 25, 26, 29] with inductance values on the order of 0.2 to 5 nH.

Single Round Wire in Free Space

Bonding wires of short length l compared with the substrate thickness h in hybrid MICs on substrates with ground metallization as well as wires of any length $l \geq h$ and $l \leq h$ in MICs on substrates without ground metallization can be adequately represented as single wires in free space as shown in Figure 2a. For $l \ll \lambda$ the equivalent circuit is the same as for the ribbon inductor (Figure 2b), consisting of a lumped series combination of

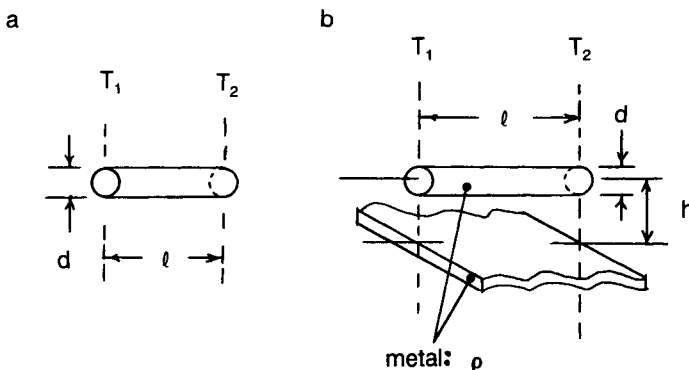


Figure 2. Straight round wire inductor. (a) In free space. (b) Over the conducting plane.

inductance L_1 and resistance R_1 , with values calculated according to

$$L_1 = 0.2l \left[\ln\left(\frac{4l}{d}\right) + \frac{d}{2l} - 0.75 \right] \quad (7)$$

$$R_1 = \frac{R_s \cdot l}{\pi d} = 2.63 \cdot 10^{-3} \frac{l}{d} \sqrt{\frac{\rho}{\rho_{Cu}}} f, \quad (8)$$

where L_1 is in nanohenries, R_1 and the skin-effect surface resistivity R_s according to Equation (5) are in ohms, the dimensions l and d are in millimeters, the metal resistivity ρ is in $\Omega \cdot \text{cm}$, $\rho_{Cu} = 1.72 \cdot 10^{-6} \Omega \cdot \text{cm}$ (copper), and the frequency f is in gigahertz. Equation (8) applies for high frequencies at which the skin effect dominates the current flow in the conductor; i.e., the skin depth calculated from Equation (4) is $\delta < 0.3d$. The *quality factor* of the wire inductor is $Q = 2\pi f L_1 / R_1$. The basic functional dependences of the equivalent circuit elements on the design parameters are $L_1/l = f(d/l)$ and $R_1 = \sqrt{\rho \cdot f} \cdot f(d/l)$.

Round Wire above a Conducting Plane

For long bonding wires with $l \geq h$ in microstrip circuits with ground metallization at the lower side of the substrate, the proximity effect of the ground metallization influences the inductance and has to be taken into account, thus leading to the model of a straight round wire above a conducting plane (Figure 2b), described by the two-port lumped equivalent

circuit of Figure 1d. Considering this structure a transmission line with the characteristic impedance Z_{L0} and the inductance per unit length $L' = Z_{L0} \cdot \mu_0 / \eta_0$, the *inductance* L_2 can be obtained for $l \leq \lambda/10$ by

$$L_2 = L'l = 0.2l \operatorname{arcosh}\left(\frac{2h}{d}\right), \quad (9)$$

where L_2 is in nanohenries, L' is in nH/mm, and the dimensions l , d , and h are in millimeters ($\mu_0 = 0.4\pi$ nH/mm and $\eta_0 = 120\pi\Omega$). If a dielectric substrate is placed between the wire and the ground plane, its dielectric constant ϵ_r does not influence L_2 according to the static approximation. Analogously the *parasitic resistance* R_2 can be calculated from the resistance per unit length of this line $R' = \alpha_0 \cdot Z_{L0} / 4.34$ using $R_2 = R'l$. α_0 is the attenuation coefficient in dB/length and Z_{L0} , the characteristic impedance for this transmission line without dielectric, i.e., for $\epsilon_r = 1$. The *ground capacitances* C_G are calculated from the capacitances per unit length $C' = \epsilon_0 \eta_0 \sqrt{\epsilon_{r,\text{eff}}} / Z_L$ of the real line on a substrate with the characteristic impedance Z_L and the effective relative dielectric constant $\epsilon_{r,\text{eff}}$ according to $C_G = 0.5C'l$. Here $\epsilon_0 = 1/(36\pi)$ pF/mm and $\eta_0 = 120\pi\Omega$. C_G is influenced by the ϵ_r of the substrate. In many cases for $d \ll h$ and $d \ll l$ the capacitance C_G can be neglected.

4. Planar Ring Inductors

Planar single turn loops in the forms of circular, rectangular, or square planar rings, fabricated as thin-film metal layers on substrates behave as inductors on circumferences much smaller than a wavelength [12, 14, 15, 25, 26, 28–30]. They are used to build up lumped resonators and matching circuits up to approximately 20 GHz. Practical inductance values are approximately 1 to 10 nH. For the following discussions the substrate is assumed to have no ground metallization.

Rectangular Ring

A rectangular ring of average side lengths l_1 and l_2 is built up by a thin strip conductor of width w and thickness $t \ll w$ (thin film, $t = 2$ to $10\ \mu\text{m}$), as can be seen in Figure 3a. Between the two reference planes T_1 and T_2 it is represented by the lumped equivalent circuit of the inductance L and the resistance R of Figure 3b for $l_1, l_2 \ll \lambda$. After Terman [25] the

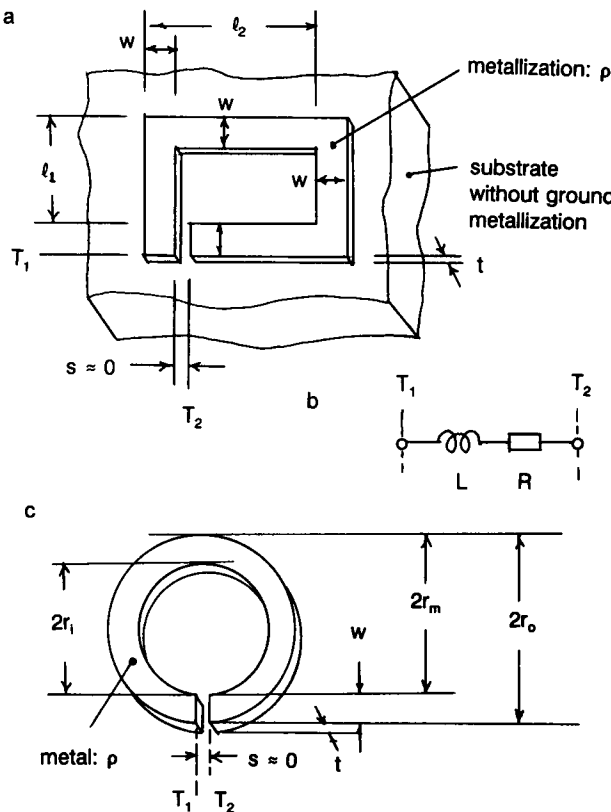


Figure 3. Single-turn planar loop inductors (rings). (a) Rectangular ring. (b) Equivalent circuit. (c) Circular ring.

inductance runs

$$L = 0.4l_1 \left[\ln \frac{2l_1 l_2}{(l_1 + d)(w + t)} + \frac{l_2}{l_1} \ln \frac{2l_1 l_2}{(l_2 + d)(w + t)} - \frac{l_1 + l_2}{2l_1} + \frac{2d}{l_1} + 0.447 \frac{w + t}{l_1} \right] \quad (10)$$

$$d = \sqrt{l_1^2 + l_2^2}, \quad (11)$$

where L is in nanohenries and all dimensions l_1 , l_2 , w , t , and d (diagonal) are in millimeters. The *resistance* R due to the finite resistivity ρ of the conductor material is given by $R = R_S(l_1 + l_2) \cdot K/(w + t)$ for high fre-

quencies at which the skin effect dominates the current flow; i.e., the skin depth δ according to Equation (4) is smaller than $t/3$. The surface resistivity R_S is given in Equation (5). The nondimensional correction factor K after Equation (3) accounts for the current crowding at the edges of the strip. The ϵ_r of the dielectric substrate has no influence on L and R . The functional dependences on the design parameters are $L/l_1 = f(w/l_1, l_2/l_1, t/l_1)$ and $R = \sqrt{\rho \cdot f} \cdot f(w/l_1, l_2/l_1, t/l_1)$, according to the static approximation.

Circular Ring

A circular ring of the inner, outer, and average radii r_i , r_o , and $r_m = (r_i + r_o)/2$, respectively, consisting of a single turn of a thin strip conductor of width w and thickness $t \ll w$, is shown in Figure 3c. The equivalent lumped element representation between the two planes T_1 and T_2 for circumferences $2r_m\pi \ll \lambda$ is also a series combination of L and R according to Figure 3b. The *inductance* L as given by Wheeler [30] for $t \ll w$ is approximately independent of t according to

$$L = \frac{12.5\pi r_m}{8 + 11\frac{w}{r_m}}, \quad (12)$$

where L is in nanohenries, and w and r_m are in millimeters. For high frequencies at which the skin depth is $\delta < t/3$ the *resistance* is $R = \pi R_S(2r_i + w)K/[2(w + t)]$. As before, the nondimensional correction factor K after Equation (3) accounts for the current crowding at the edges of the strip. The basic dependences of the equivalent circuit elements on the design parameters are $L/r_i = f(r_o/r_i, w/r_i)$ and $R = \sqrt{\rho \cdot f} \cdot f(r_o/r_i, w/r_i)$.

5. Planar Circular Spiral Inductor

Spiral inductors [6, 7, 9, 11–13, 15, 16, Chap. 7; 24–26, 28, 30, 31] are used together with lumped capacitors (film, interdigitated, and gap capacitors) to build up lumped element filters, resonators, matching networks, and transistor bias networks in hybrid and monolithic microwave integrated circuits up to approximately 20 GHz. Spirals are practical for inductance values between several nanohenries and several microhenries, varying the number of turns between 2 and 20.

General Construction of Spiral Inductors

Figure 4a exhibits the structure of a bare spiral without connecting elements to the circuit environment. These connecting elements are separately shown in Figures 4b to 4d. The outer end of the spiral is connected to the adjacent strip conductor S_1 by a short length of narrow strip. In

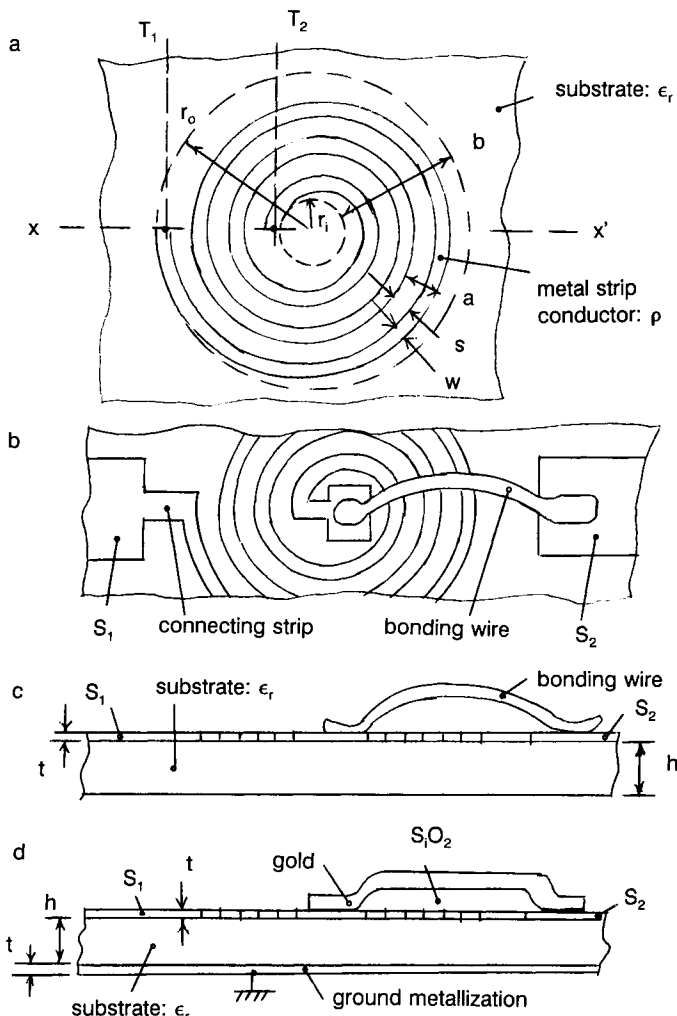


Figure 4. Planar circular spiral inductor. (a) Circular pattern without connecting elements. (b) Connection to adjacent strip conductors S_1 and S_2 by a narrow strip and bonding wire, respectively. (c) Cross section X-X' for a substrate without ground metallization and for a bonding-wire connection. (d) Cross section X-X' for a substrate with ground metallization and for a connection by dielectric crossover.

hybrid MICs the inner spiral end is connected to a second strip conductor S_2 of the circuitry by a bonding wire (gold of a typical diameter of $17 \mu\text{m}$), forming a loop from the inner metal bonding patch to S_2 (Figures 4b and 4c). In monolithic MICs dielectric crossovers with gold over SiO_2 dielectric (Figure 4d)—as known from field effect transistor technology—or alternately airbridges are used. Basically one distinguishes between two types of spirals that differ in their electric behavior: spirals on substrates without (Figure 4c) and with lower side ground metallization (Figure 4d), the former being used mainly for broadband lumped circuits up to approximately 2 GHz and the latter being used mainly for microstrip circuits up to the 20-GHz region. The geometrical parameters of the round spiral (Figure 4a) are the width w and thickness t of the strip conductor, the inner, outer, and average radii r_i , r_o , and r_m , the radial depth of winding $b = r_o - r_i$, the strip separation s , the pitch of winding $a = w + s$, and the number of turns n . Generally the layout is constructed for an Archimedes spiral with the radius r as a function of the angle φ as $r(\varphi) = r_i + \text{constant} \cdot \varphi$. However, in many cases the spiral layout is composed of semicircular arcs with the centers alternately shifted by $a/2$.

Spiral on a Substrate without Ground Metallization

The lumped element equivalent circuit for the spiral without connecting elements on a substrate without lower side ground metallization (Figure 4a) between the two references planes T_1 and T_2 is a parallel resonant circuit (Figure 5a). It consists of the inductance L_1 , the parasitic resistance

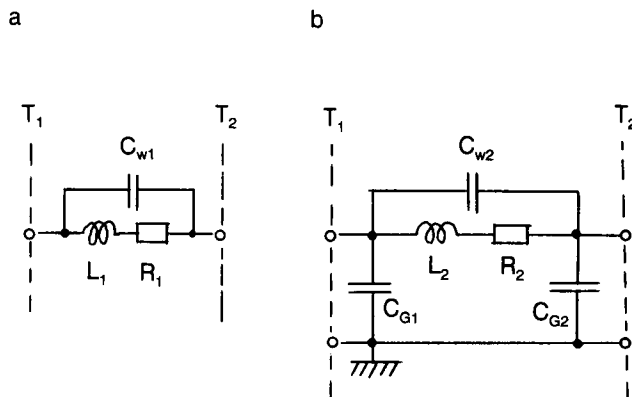


Figure 5. Lumped-element equivalent circuits for the spiral inductor. (a) Without and (b) with ground metallization of the substrate.

R_1 due to the conductor resistivity ρ , and the parasitic interturn capacitance C_{W1} due to the distributed capacitances between the adjacent turns. From Wheeler's approximation formula [30] the inductance L_1 runs for the case of thin conductors $t \ll w$

$$L_1 = \frac{12.5\pi n^2 r_m}{8 + 11 \frac{b}{r_m}} \quad (13)$$

$$b = r_o - r_i = an + w \quad (14)$$

$$r_o = r_i + b = r_i + an + w \quad (15)$$

$$r_m = \frac{r_o + r_i}{2} = r_i + \frac{an}{2} + \frac{w}{2}, \quad (16)$$

where L_1 is in nanohenries and all dimensions w , a , b , r_i , r_o , and r_m are in millimeters. Equation (13) has been derived for a current in an infinitesimal thin ribbon of the width b . Therefore r_i has to be chosen to be the starting radius of the inner strip conductor edge and r_o , as the end radius of the outer strip conductor edge. Furthermore w does not occur in Equation (13) since this equation has been originally derived for $w \approx a$ (spacing, $s \approx 0$).

An approximate expression for the winding capacitance C_{W1} can be derived using the distributed coupling capacitance per unit length C' between two adjacent strip conductors of the width w and the spacing s . Together with a formula for C' one obtains for $h \gg a$

$$C_{W1} = \frac{n-1}{n^2} (r_o + r_i) \pi C' = \frac{n-1}{n^2} (r_o + r_i) \pi \epsilon_0 (\epsilon_r + 1) \frac{K(k)}{K(k')} \quad (17)$$

$$k = \left[\tan \left(\frac{\pi}{4} \frac{w}{a} \right) \right]^2. \quad (18)$$

$K(k)$ and $K(k')$ are the complete elliptic integrals of the first kind of the modules k and the complementary modules $k' = \sqrt{1 - k^2}$, respectively. ϵ_r is the substrate relative dielectric constant, $\epsilon_0 = 1/(36\pi)$ pF/mm. From L_1 in Equation (13) and C_{W1} in Equation (17) the self-resonance frequency $f_R = 1/(2\pi\sqrt{L_1 C_{W1}})$ of the spiral can be calculated, limiting

the frequency range of practical use as an inductor below approximately $0.7f_R$.

An approximate expression for the parasitic resistance R_1 (Figure 5a) can be derived assuming uniform current flow in the strip conductor dominated by the skin effect, i.e., for high frequencies at which the skin depth after Equation (4) is $\delta < t/3$. Summing up the resistances per unit length over the entire strip conductor length of the spiral results in

$$R_1 = \frac{R_S n(r_i + r_o)\pi}{2w}, \quad (19)$$

where R_1 and the surface resistivity R_S calculated in Equation (5) are in ohms and the dimensions r_i , r_o , and w are in millimeters. The nondimensional correction factor $K = K(w/t)$ given in Equation (3) accounts for the current crowding at the edges of the strip. From L_1 in Equation (13) and R_1 in Equation (19) the quality factor of the spiral inductor $Q = 2\pi L_1/R_1$ can be calculated for $f \ll f_R$, neglecting the winding capacitance C_{W1} .

Spiral on a Substrate with Ground Metallization

If we consider a spiral on a substrate with ground metallization on the whole lower side between the two planes T_1 and T_2 (Figures 4a and 4d), we have to use the lumped two-port equivalent circuit of Figure 5b, containing additional parasitic shunt fringing capacitances C_{G1} and C_{G2} . For the same dimensions this spiral has a lower resonance frequency, f_R , and different values L_2 , R_2 , and C_{W2} compared with L_1 , R_1 , and C_{W1} of the spiral without ground metallization. A rigorous analysis of this spiral on a substrate with ground metallization has to take into account the distributed nature of inductive and capacitive coupling between the turns [31]. This leads to a network containing an array of n electromagnetically coupled microstrip lines. The S -parameters of the spiral modeled by this network have to be evaluated numerically on computers.

6. Planar Rectangular and Square Spiral Inductors

Circuit applications and practical inductance value ranges (several nanohenries to several microhenries for numbers of turns from 2 to 20) for rectangular spirals are the same as those for circular spirals (Section 5).

Applications and design for rectangular spirals are described in Refs. [6, 7, 9, 10, 15, 25, 26, 29, 32–35].

General Construction of the Spiral

Rectangular spirals are fabricated on substrates either without or with ground metallization (see Figures 4c and 4d), using bonding wire loop (Figures 4b and 4c) or dielectric crossover (Figure 4d) connecting techniques. The bare rectangular spiral without connecting elements between the two reference planes T_1 and T_2 , shown in Figure 6 is characterized by the geometrical parameters inner, outer, and average sidelengths d_{i1} , d_{o1} , and d_{m1} of one side and d_{i2} , d_{o2} , and d_{m2} of the other, the winding depth b , the width w and the thickness $t \ll w$ of the strip conductor, the conductor spacing s , the winding pitch $a = w + s$, and the number of turns n . The lumped equivalent circuit diagrams for rectangular spirals are the same as those for circular spirals (Figures 5a and 5b).

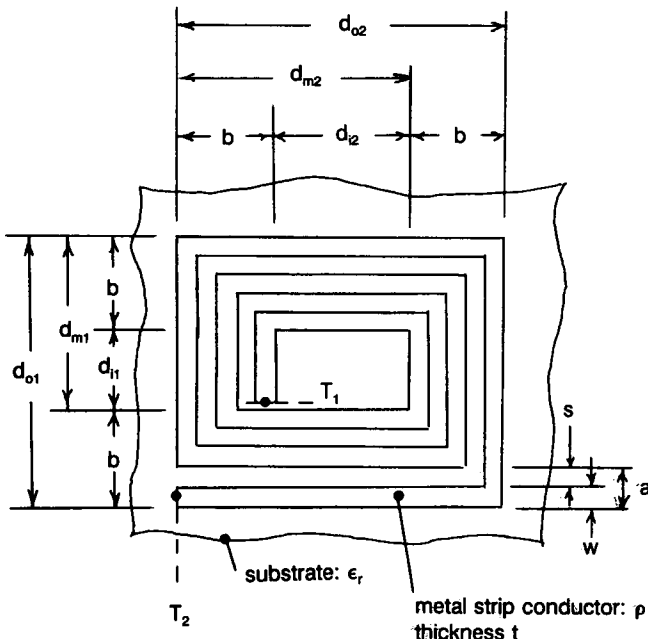


Figure 6. Planar rectangular spiral inductor without connecting elements.

Spiral on a Substrate without Ground Metallization

The *inductance* L_1 of a rectangular spiral between the two reference planes T_1 and T_2 on a substrate without ground metallization (equivalent circuit, Figure 5a) has been derived in Ref. [25]. It is given by

$$L_1 = 0.4n^2d_{m1} \left\{ \ln \left[\frac{2d_{m1}d_{m2}}{(d_{m1} + g)(b + t)} \right] + \frac{d_{m2}}{d_{m1}} \ln \left[\frac{2d_{m1}d_{m2}}{(d_{m2} + g)(b + t)} \right] - \frac{d_{m1} + d_{m2}}{2d_{m1}} + \frac{2g}{d_{m1}} + 0.447 \frac{b + t}{d_{m1}} \right\} \quad (20)$$

$$g = \sqrt{d_{m1}^2 + d_{m2}^2} \quad (21)$$

$$b = (n - 1)a + w \quad (22)$$

$$d_{o1} = d_{i1} + 2b = d_{m1} + b \quad (23)$$

$$d_{o2} = d_{i2} + 2b = d_{m2} + b \quad (24)$$

$$d_{m1} = \frac{d_{i1} + d_{o1}}{2} = d_{i1} + b \quad (25)$$

$$d_{m2} = \frac{d_{i2} + d_{o2}}{2} = d_{i2} + b, \quad (26)$$

where L_1 is in nanohenries and all dimensions d_{i1} , d_{m1} , d_{o1} , d_{i2} , d_{m2} , d_{o2} , b , a , w , t , and the diagonal g are in millimeters.

Considering now a *square spiral* with $d_{i1} = d_{i2} = d_i$, $d_{o1} = d_{o2} = d_o$ and $d_{m1} = d_{m2} = d_m$, one can simplify Equations (20) to (26) to

$$L_1 = 0.80n^2d_m \left[\ln \frac{d_m}{b + t} + 0.726 + 0.224 \frac{b + t}{d_m} \right] \quad (27)$$

using $b = (n - 1)a + w$, $d_o = d_i + 2b = d_m + b$ and $d_m = (d_i + d_o)/2 = d_i + b$, where L_1 is in nanohenries and the dimensions d_i , d_m , d_o , b , a , w , and t are in millimeters. A plot of the normalized inductance L_1/d_i versus the number of turns n for different values of the normalized winding pitch a/d_i for the square spiral according to expression Equation (27) is shown in Figure 7.

An approximate expression for the *winding capacitances* C_{W1} of the rectangular spiral (see the equivalent circuit, Figure 5a) can be derived

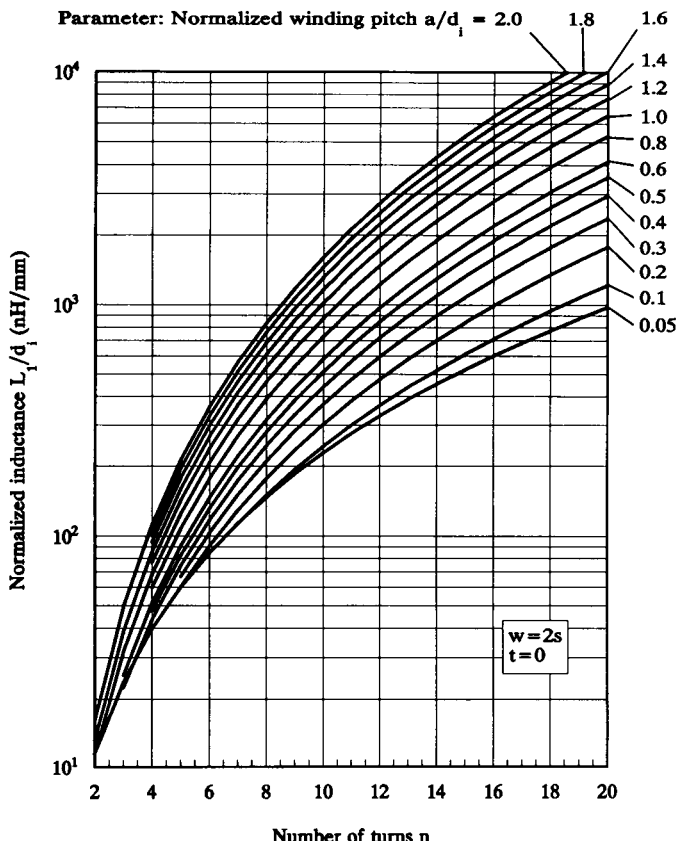


Figure 7. Normalized inductance L_1/d_i of the square planar spiral versus the number of turns n for different normalized pitches a/d_i ($w = 2s$, $t \approx 0$).

using the same method as that used for the circular spiral (Section 5): We start with the mutual capacitance per unit length C' between two adjacent strip conductors of the width w and the separation s (t is assumed to be zero) that can be extracted from Equation (17). Using the average length of the coupling gap between the adjacent conductors per one turn $l_m = 2(d_{m1} + d_{m2})$, we can compute $C_{W1} = (n - 1)C'l_m/n^2$. The *resonance frequency* of the spiral inductor is $f_R = 1/(2\pi\sqrt{L_1 C_{W1}})$, limiting the frequency range of practical use as an inductor up to approximately $0.7 f_R$.

An approximate expression for the *parasitic resistance* R_1 (see the equivalent circuit, Figure 5a) can be derived by summing up the resistances per unit length of the strip conductor over the entire length of the

spiral conductor, resulting in $R_1 = R_S K l_m n / [2(w + t)]$. This formula is valid for the high frequency range in which the skin depth δ after Equation (4) is $\delta < t/3$. R_S is the surface resistivity of the conductor material after Equation (5). The nondimensional correcting factor for the current crowding $K = K(w/t)$ is calculated from Equation (3). With L_1 of Equation (20) or (27) and with R_1 the *quality factor* of the spiral for $f \ll f_R$ becomes $Q = 2\pi f L_1 / R_1$.

Spiral on a Substrate with Ground Metallization

If we add a ground metallization at the bottom of the substrate (cross section, Figure 4d) carrying the spiral pattern (Figure 6), the two-port lumped-element equivalent circuit of Figure 5b, containing additional shunt fringing capacitances C_{G1} and C_{G2} , has to be used to model the spiral, provided that the linear spiral dimensions are small against the wavelength λ . In this case exact closed-form analytical expressions cannot be derived for the equivalent circuit elements L_2 , R_2 , C_{w2} , C_{G1} , and C_{G2} . For accurate prediction of the spiral behavior, a rigorous analysis has to be used, modeling the spiral by two orthogonally positioned electromagnetically coupled $4n$ -conductor microstrip line arrays [32, 33, 35]. Computer programs have to be used to perform this analysis in order to calculate the frequency-dependent spiral S-parameters.

7. Planar Dielectric – Film Overlay Capacitors

The planar dielectric film in-line conductor discussed in this section can be realized in thin-film technology as an MIM (metal insulator metal) capacitor and an MOM (metal oxide metal) capacitor, in semiconductor technology as an MOS (metal oxide semiconductor) capacitor, or in thick-film technology. Furthermore the basic planar dielectric film capacitor structure exhibits the same electrical behavior as hybrid single layer chip capacitors (“wafer capacitors”) and can therefore be used to model those wafer capacitor chips. Depending on the type of technology (i.e., type of system of deposited layers on the substrate) used, practical capacitance values are in the range between several picofarads and several nanofarads. Normally these capacitors are employed in hybrid and monolithic MICs as coupling and bypass capacitors for frequencies up to approximately 20 GHz. Since the dielectric layers in thin-film capacitors are usually very thin (typically $0.2 \mu\text{m}$ thick), the substrates have to exhibit very low surface roughness in order to avoid defects as, for example, pinholes in the dielectric layer. Thus fused silica or sapphire substrates are preferred to

Al_2O_3 substrates. Analyses of film capacitors are described in Refs. [6, 7, 9–13, 15, 16, Chap. 7; 24, 36–40].

Construction

The basic structure of a dielectric film capacitor between the two reference planes T_1 and T_2 on top of a substrate connected to the strip conductors S_1 and S_2 is shown in Figure 8a: The bottom electrode (metal layer of thickness t_1 and resistivity ρ_1) together with the dielectric film (thickness d , relative dielectric constant ϵ_r , and dissipation factor $\tan \delta$) and the top electrode (metal layer of thickness t_2 and resistivity ρ_2) forms a lossy parallel-plate capacitor with the area $b \cdot l$ (width b and length l). Thus the basic low-frequency capacitance formula $C = \epsilon_0 \epsilon_r lb / d$ applies. Conductor loss and dielectric loss are taken into account in the following discussion.

Technology

Dielectric and conductor materials as well as layer thicknesses d , t_1 , and t_2 and consequently the ranges of capacitance per unit area (capacitance density) differ depending on the type of fabrication technology used: For *SiO–Au thin-film hybrid technology* both electrodes consist of evaporated and electroplated gold ($t_1 = t_2 \approx 5 \mu\text{m}$, $\rho_1 = \rho_2 = 2.4 \cdot 10^{-6} \Omega \cdot \text{cm}$) and the dielectric film material is SiO ($d = 0.3$ to $3 \mu\text{m}$, $\epsilon_r \approx 6$, $\tan \delta \approx 0.001$). Thus the range of capacitance per unit area is approximately 20 to 200 pF/mm². Using *tantalum thin-film technology*, the bottom electrode consists of tantalum ($t_1 \approx 0.5 \mu\text{m}$) with a rather high resistivity of $\rho_1 = 15.6 \cdot 10^{-6} \Omega \cdot \text{cm}$. The dielectric film of Ta_2O_5 ($d = 0.05$ to $0.2 \mu\text{m}$, $\epsilon_r = 22$, $\tan \delta \approx 0.002$) is produced by anodizing the tantalum layer surface. The top electrode is made of evaporated and electroplated gold ($t_2 \approx 2 \mu\text{m}$). Therefore the range of capacitance density is approximately 1 to 4 nF/mm². These tantalum capacitors are normally used for frequencies below 1 GHz. For MMICs on GaAs substrates the bottom electrode consists of sputtered gold ($t_1 \approx 0.5 \mu\text{m}$, $\rho_1 = 2.3 \cdot 10^{-6} \Omega \cdot \text{cm}$), the dielectric layer with a thickness of 0.3 to 0.4 μm consists of either SiO_2 ($\epsilon_r = 5$ to 6) or Si_3N_4 ($\epsilon_r = 6$ to 7), and the top electrode consists of plated gold of several micrometers thickness.

General Electrical Properties for Arbitrary Loss and Arbitrary Frequency

The dielectric film capacitor between the two reference planes T_1 and T_2 (Figure 8a) is described for the general case of arbitrary length $l \geq \lambda$ and

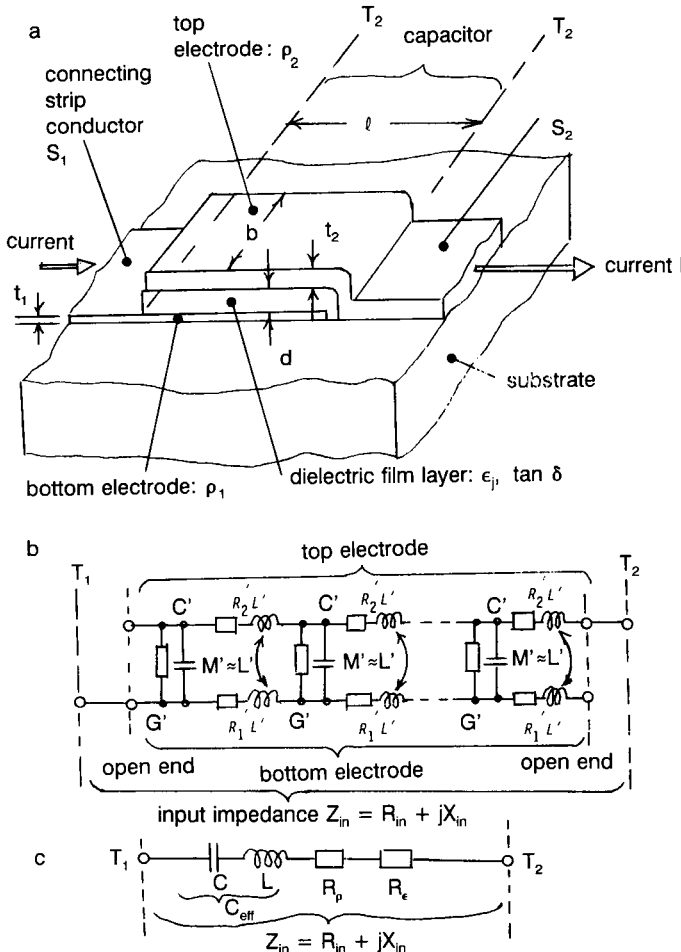


Figure 8. Planar dielectric film capacitor. (a) Structure. (b) High-frequency transmission line equivalent circuit. (c) Lumped-element equivalent circuit for low frequencies.

$l \leq \lambda$ (λ , wavelength), arbitrary dielectric loss $\tan \delta \geq 1$ and $\tan \delta \leq 1$, and arbitrary resistivities ρ_1 and ρ_2 by the model of a parallel-plate transmission line with distributed conductor and dielectric loss, which is open circuited at both ends, as shown in Figure 8b [40]. The only restrictions for the validity of this model are that the cross-sectional dimensions fulfill the conditions $d \ll \lambda$, $b \ll \lambda$, and $d \ll b$. The distributed parameters per unit length, i.e., the capacitance C' , the inductance L' and mutual inductance M' , the resistance R' , and the conductance G' , account for the capacitance between the plates, the current flow

within the electrodes, the electrodes losses ρ_1 and ρ_2 , and the dielectric loss $\tan \delta$. For $d \ll b$ there is $M' \approx L'$. Under the above mentioned conditions the *input impedance* of the one port between one electrode of the terminals T_1 and T_2 is given by

$$Z_{\text{in}} = R_{\text{in}} + jX_{\text{in}} = j\omega L + \frac{R_1 R_2}{R_1 + R_2} \left(1 - \frac{\tanh \frac{\gamma l}{2}}{\frac{\gamma l}{2}} \right) + (R_1 + R_2) \frac{\coth(\gamma l)}{\gamma l}, \quad (28)$$

$$\gamma l = \sqrt{\omega C(j + \tan \delta)(R_1 + R_2)}, \quad (29)$$

with $R_1 = R'_1 l$, $R_2 = R'_2 l$, the low-frequency capacitance $C = C'l$, $L = L'l$, and $G = G'l$. Using the capacitance density $C_A = \epsilon_0 \epsilon_r / d$ the capacitance per unit length is $C' = C_A b$. In the high-frequency range at which the skin effect dominates the current flow in both electrodes $i = 1$ and $i = 2$, the resistances per unit length are given by $R'_i = R_{Si}/b$, where R_{Si} is the surface resistivity calculated from Equation (5). This expression is valid only for small skin depth $\delta_i < t_i/3$, where δ_i is calculated after Equation (4). For low frequencies with a uniform current flow in the electrodes cross section, where $\delta_i \gg t_i$ is valid, another expression, $R'_i = \rho_i/(t_i b)$, has to be used. The *quality factor* of the capacitor can be calculated from $Q = |X_{\text{in}}| / R_{\text{in}}$.

Electrical Properties for Low Frequency, Low Dielectric Loss, and Arbitrary Conductor Loss

For low frequencies at which the length is $l \ll \lambda$ and for low dielectric loss $\tan \delta \ll 1$, still maintaining $d \ll \lambda$, $b \ll \lambda$, $d \ll b$, and the condition of arbitrary conductor losses ρ_1 and ρ_2 , however, the general expressions Equations (28) and (29) for the *input impedance* simplify, which leads to

$$Z_{\text{in}} = R_{\text{in}} + jX_{\text{in}} = R_\rho + R_\epsilon - j \left(\frac{1}{\omega C} - \omega L \right) = R_\rho + R_\epsilon - j \frac{1}{\omega C_{\text{eff}}}, \quad (30)$$

where $R_\rho = (R_1 + R_2)/3$ represents the conductor loss in both electrodes; $R_\epsilon = \tan \delta / (\omega C)$, the dielectric loss; and $C = C_A lb$, the low-

frequency capacitance calculated from the capacitance density $C_A = \epsilon_0 \epsilon_r / d$. The electrode inductance L reduces the capacitance C to a lower value, called the *effective capacitance* C_{eff} . At the *resonance frequency* $f_R = 1/(2\pi\sqrt{LC})$ there is $C_{\text{eff}} = 0$. The factor $\frac{1}{3}$ in the expression for R_p results from the linear decrease of longitudinal current over the length l of the electrodes from a maximum value at the beginning to zero at the end. Under the conditions of validity of Equation (30) the transmission line equivalent circuit of Figure 8b can be replaced by a lumped-element equivalent circuit, shown in Figure 8c. Under these conditions the *quality factor* Q of the capacitor

$$Q = \frac{Q_p Q_\epsilon}{Q_p + Q_\epsilon} \quad (31)$$

is a combination of the dielectric quality factor $Q_\epsilon = 1/\tan \delta$ and the conductor loss quality factor $Q_p = 3/[2\pi f C(R_1 + R_2)]$. For the last formula the inductance L has been neglected. For practical microstrip circuit design the inductance L is usually negligible both in Equation (30) and in the equivalent circuit (Figure 8c).

8. Microstrip Disk Capacitors

Microstrip disk capacitors [41–47] exhibit a capacitance in the range of approximately 0.1 pF to several picofarads between an arbitrarily shaped metallization patch (“disk”) on top of a substrate and the overall ground metallization on the lower side of the substrate. Usually circular or rectangular disks are used, for example, as parts of quasilumped low-pass filters, series resonant circuits, and matching networks up to typically 15 GHz. The disk structure behaves as a capacitor as long as all linear disk dimensions are small compared with the wavelength. At higher frequencies, at which this condition is not fulfilled, transverse resonances occur in this structure. This case will not be considered here.

Circular Disk Capacitor

The circular disk capacitor of Figure 9a is characterized by the diameter $d = 2r$ of the metal disk (copper or gold; thickness, $t = 5$ to $10 \mu\text{m}$

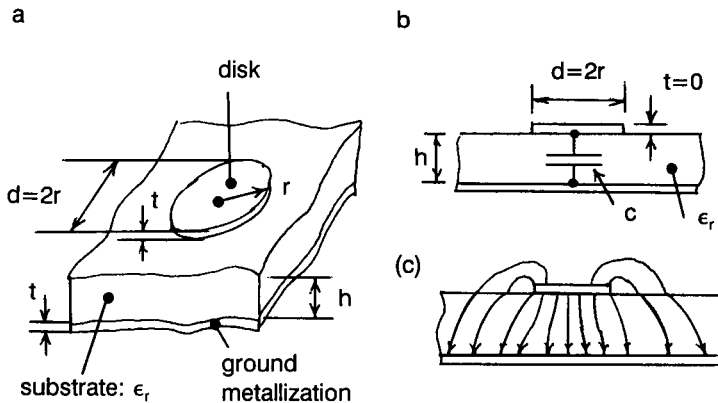


Figure 9. Circular disk capacitor. (a) Construction. (b) Equivalent capacitance C . (c) Electric field lines.

typically in thin-film technology) and the thickness h and relative dielectric constant ϵ_r of the substrate. The *capacitance* C (Figure 9b) is given by

$$C = C_p \left\{ 1 + \frac{2h}{\pi r \epsilon_r} \left[\ln \frac{r}{2h} + 1.41\epsilon_r + 1.77 + \frac{h}{r} (0.268\epsilon_r + 1.65) \right] \right\} \quad (32)$$

for $t = 0$. This approximation formula has been derived from numerical results calculated by the integral equation method [41]. The accuracy of Equation (32) compared with numerical results is better than 1% for $1 \leq \epsilon_r \leq 20$ and for $0 < h/d \leq 0.25$ and is better than 7% for $h/d < 0.5$. C is composed of the parallel-plate capacitance $C_p = \epsilon_0 \epsilon_r r^2 \pi / h$ and the fringing capacitance C_f according to $C = C_p + C_f$, as can be seen from the electric field lines of Figure 9c. The functional dependence is $C/h = f(r/h, \epsilon_r)$.

Rectangular Disk Capacitor

For the rectangular disk capacitor (Figure 10a) the disk on the upper side of the substrate is a rectangular metal patch with side lengths a and b . The metallization thickness t is assumed to be zero. The capacitance C parallel to the ground metallization can be calculated by an approximate method [42, 44] using the fringing capacitance of a microstrip transmission line. According to this method the total *capacitance* C is the sum of the

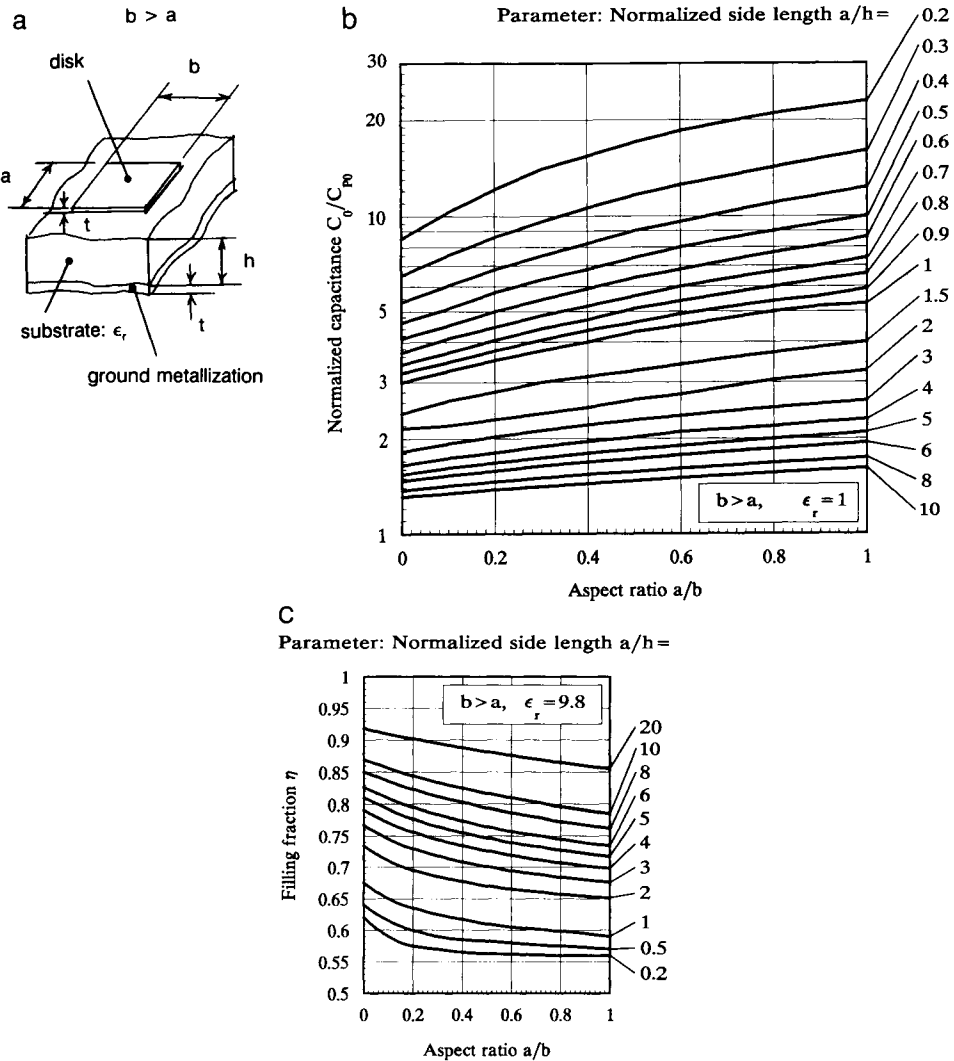


Figure 10. Rectangular disk capacitor. (a) Construction. (b) Capacitance C_0 for $\epsilon_r = 1$, normalized with the parallel-plate capacitance $C_{P0} = \epsilon_0 ab/h$. (c) Filling fraction $\eta = C/(C_0 \epsilon_r)$ for the disk capacitor on an Al_2O_3 substrate ($\epsilon_r = 9.8$).

parallel-plate capacitance $C_P = \epsilon_0 \epsilon_r ab/h$ and the fringing capacitances C_{f1} and C_{f2} of the edges with the lengths b and a , respectively:

$$C = C_P + 2C_{f1} + 2C_{f2}. \quad (33)$$

C_{f1} is approximately half the fringing capacitance of a microstrip line of linewidth a and length b on the same substrate as the disk capacitor. Hence $C_{f1} = 0.5(C'_1 - C'_{P1})b$. Here $C'_1 = \epsilon_0\eta_0/\sqrt{\epsilon_{r,\text{eff},1}}/Z_{L1}$ is the total capacitance of this microstrip line per unit length and Z_{L1} and $\epsilon_{r,\text{eff},1}$ are its characteristic impedance and effective dielectric constant ($\eta_0 = 120\pi\Omega$). $C'_{P1} = \epsilon_0\epsilon_r a/h$ is the parallel-plate capacitance per unit length of this line. Using the same method, the second fringing capacitance C_{f2} can be calculated from the parameters C'_2 , C'_{P2} , Z_{L2} , and $\epsilon_{r,\text{eff},2}$ of a microstrip line of width b on the same substrate having length a .

Using Equation (33) together with analytical expressions for Z_L of the microstrip line, one can calculate the total capacitance C_0 of a rectangular disk capacitor in free space (i.e., for $\epsilon_r = 1$), plotted in Figure 10b as a function of the dimensions. In this figure C_0 is normalized on the parallel-plate capacitance C_{P0} in free space. In order to calculate the total capacitance C of a disk capacitor on a substrate with $\epsilon_r > 1$ from C_0 , a filling fraction, η , is defined for capacitors on a substrate with $\epsilon_r > 1$ by

$$\eta = \frac{C}{C_0\epsilon_r}. \quad (34)$$

η relates the capacitance C of the (real) disk capacitor on substrate $\epsilon_r > 1$ to the capacitance $C_0\epsilon_r$ of a fictitious capacitor with the same dimensions in an environment completely (below and above the disk) filled with the dielectric material of ϵ_r . Values for η have been calculated for $\epsilon_r = 9.8$ (Al_2O_3 substrate) using Equations (33) and (34) and plotted versus a/b in Figure 10c. Thus the capacitance of the disk capacitor on the substrate is given by $C = \eta C_0\epsilon_r$ with C_0 and η from Figures 10b and 10c. The basic functional dependence of the capacitance on design parameters is $C/h = f(a/h, a/b, \epsilon_r)$.

9. Microstrip Series Gap Capacitor

Short series gap [1, Chap. 10.7; 2, Chap. 10.7; 17, Chap. 3; 48–52] in the strip conductor of a microstrip line exhibiting a series capacitive coupling between the open ends of the adjacent lines are used to build up end-coupled resonator bandpass filters in microwave integrated circuits. Practical series capacitance values are in the range of approximately 0.01 to 0.5 pF.

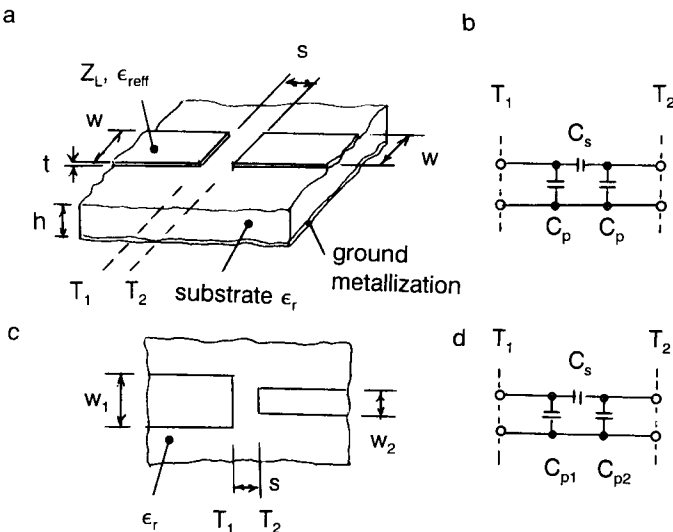


Figure 11. Microstrip series gap capacitor. (a) Symmetric gap. (b) Equivalent circuit for a. (c) Asymmetric gap. (d) Equivalent circuit for c.

Types of Series Gap Capacitors

Figure 11a shows a symmetrical coupling gap of the width s between two microstrip lines of the same line width w on a substrate of the thickness h and the relative dielectric constant ϵ_r with overall ground metallization on the lower side. The equivalent circuit (Figure 11b) between the two reference planes T_1 and T_2 at the strip conductor ends consists of a series coupling capacitance C_s and two parallel fringing capacitances C_p between the conductor open ends and the ground. The asymmetrical series gap of Figure 11c with different strip conductor widths w_1 and w_2 is described by the same type of equivalent circuit (Figure 11d); the parallel fringing capacitances C_{p1} and C_{p2} of both ends are different, however.

Symmetrical Gap

Figure 12 shows plots of the capacitances C_p and C_s of the equivalent circuit of Figure 11b for the symmetrical gap of Figure 11a for an Al_2O_3 substrate with $\epsilon_r = 9.6$ from results of Ref. [50] for conductor thickness $t = 0$.

Asymmetrical Gap

For the asymmetrical gap of Figure 11c Kirschning *et al.* [51] have derived analytical expressions for the *capacitances* C_S , C_{P1} , and C_{P2} of Fig. 11d by curve fitting methods using numerical results of a hybrid mode analysis. These expressions are given below:

$$C_S = 0.50hQ_1 \exp\left(-1.86\frac{s}{h}\right) \cdot \left\{1 + 4.19\left[1 - \exp\left(-0.785\sqrt{\frac{h}{w_2}} \cdot \frac{w_1}{w_2}\right)\right]\right\} \quad (35)$$

$$C_{P2} = C_{e2} \frac{Q_2 + Q_3}{1 + Q_2} \quad (36)$$

$$C_{P1} = C_{e1} \frac{Q_2 + Q_4}{1 + Q_2} \quad (37)$$

$$Q_1 = 0.04598 \left[0.03 + \left(\frac{w_2}{h}\right)^{Q_5}\right] \cdot (0.272 + 0.07\varepsilon_r) \quad (38)$$

$$Q_2 = 0.107 \left(\frac{w_2}{h} + 9\right) \cdot \left(\frac{s}{h}\right)^{3.23} + 2.09 \left(\frac{s}{h}\right)^{1.05} \cdot \frac{1.5 + 0.3\frac{w_2}{h}}{1 + 0.6\frac{w_2}{h}} \quad (39)$$

$$Q_3 = \exp\left[-0.5978\left(\frac{w_1}{w_2}\right)^{1.35}\right] - 0.55 \quad (40)$$

$$Q_4 = \exp\left[-0.5978\left(\frac{w_2}{w_1}\right)^{1.35}\right] - 0.55 \quad (41)$$

$$Q_5 = \frac{1.23}{1 + 0.12\left(\frac{w_1}{w_2} - 1\right)^{0.9}}, \quad (42)$$

where the capacitances C_S , C_{P1} , C_{P2} , C_{e1} , and C_{e2} are in picofarads and the dimensions h , w_1 , w_2 , and s are in millimeters. C_{e1} and C_{e2} are the open-end capacitances of single microstrip lines with the widths w_1 and w_2 , respectively, according to Section 10. These equations are valid for the

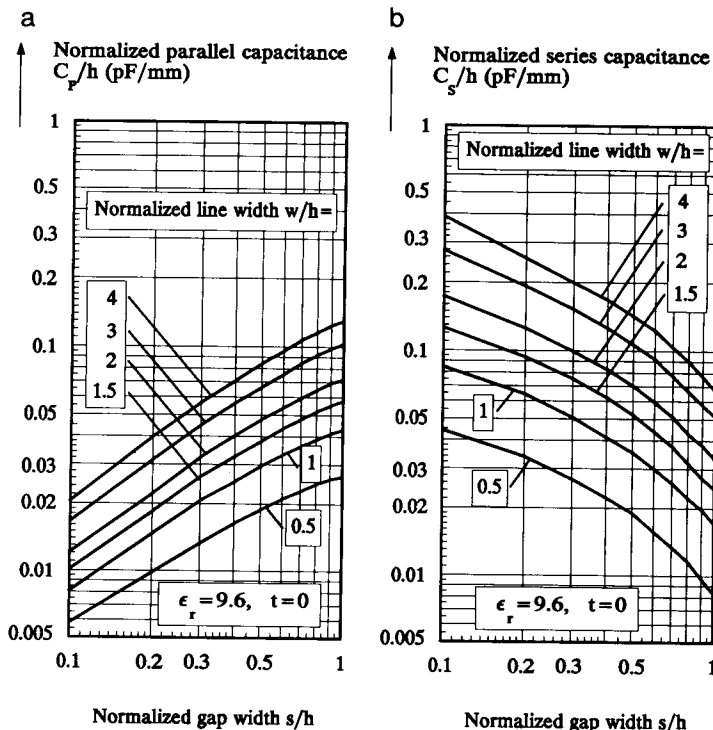


Figure 12. (a) Normalized parallel capacitance C_p/h and (b) normalized series capacitance C_s/h for the symmetrical gap of Figure 11a for $\epsilon_r = 9.6$ (Al_2O_3 substrate) and conductor thickness $t = 0$, after numerical calculations of Ref. [50].

ranges of the dimensions $0.1 \leq (w_1/h) \leq 3$, $0.1 \leq (w_2/h) \leq 3$, $1 \leq (w_1/w_2) \leq 3$, and $0.2 \leq (s/h) < \infty$, for ranges of the substrate dielectric constant $6 \leq \epsilon_r \leq 13$ and in the frequency range $0 \leq hf \leq 12$ GHz · mm ($w_1 > w_2$ assumed). The basic functional dependences for the normalized capacitances C_s/h , C_{p1}/h , and C_{p2}/h are of the form $f(w_1/h, w_2/h, s/h, \epsilon_r)$.

10. Open-Ended Microstrip

Microstrip open ends are part of resonators used in bandpass and band-stop filters and of open stubs used in matching networks. Quasistatic and hybrid model analyses are described in Refs. [1, Chap. 10.2; 2, Chap. 10.2; 4, Chap. 5; 16, Chap. 6; 17, Chap. 3; 48, 53–56].

The open-end structure considered here is an abruptly ending strip conductor of a microstrip line at any place on the upper side of the substrate, bearing an overall metallization on its lower side. The open end is characterized by the dimensions linewidth w , metallization thickness t , and substrate thickness h and by the relative dielectric constant ϵ_r of the substrate (Figure 13a). The discontinuity fringing field extending beyond the physical end of the metallic strip is modeled by a parallel capacitance C_e at the reference plane T (Figure 13b), defined at the strip conductor end. This *end capacitance* C_e can be modeled by an extra length, $\Delta l_e = C_e/C'$, of a uniform microstrip line with an ideal open circuit (without a fringing field) at its end, the so-called *equivalent end effect length* Δl_e (Figure 13c). In the previous equation $C' = \sqrt{\epsilon_{r,\text{eff}}}/(Z_L c_0)$ is the capacitance per unit length of the terminated microstrip line with the characteristic impedance Z_L and the effective relative dielectric constant $\epsilon_{r,\text{eff}}$ (c_0 = velocity of light in free space).

For low frequencies of approximately $hf \leq 20$ GHz/mm, Δl_e is independent of frequency. By curve fitting to the numerical static results of Ref. [53] Hammerstad [56] derived the approximate analytical expression for $t = 0$ given by

$$\frac{\Delta l_e}{h} = 0.412 \frac{(\epsilon_{r,\text{eff}} + 0.3) \cdot \left(\frac{w}{h} + 0.262\right)}{(\epsilon_{r,\text{eff}} - 0.258) \cdot \left(\frac{w}{h} + 0.813\right)}. \quad (43)$$

The accuracy is better than 5% for $0.3 \leq w/h \leq 2$ and $1 \leq \epsilon_r \leq 50$. A more complex set of formulas with better accuracy, $\leq 2.5\%$ for $0.01 \leq w/h \leq 100$ and $1 \leq \epsilon_r \leq 50$, is given in Ref. [55]. Figure 13d exhibits a plot of the *normalized equivalent length* $\Delta l_e/h$ calculated using the formula of Ref. [55] for the most important practical substrate materials. The basic functional dependences for both equivalent circuit parameters are $C_e/h = f(w/h, t/h, \epsilon_r)$ and $\Delta l_e/h = f(w/h, t/h, \epsilon_r)$ according to the static approximation. In many practical cases $t = 0$ is assumed, however.

III. Microstrip Short Circuits

Microstrip short circuits are used as terminations of microstrip resonators and stubs, for $\lambda/4$ -DC returns in bias circuits and for grounding of transistor leads in microwave integrated circuits. Analyses and design data of short circuits are given in Refs. [1, Chap. 10.6; 2, Chap. 10.6; 4, Chap. 5; 57–61].

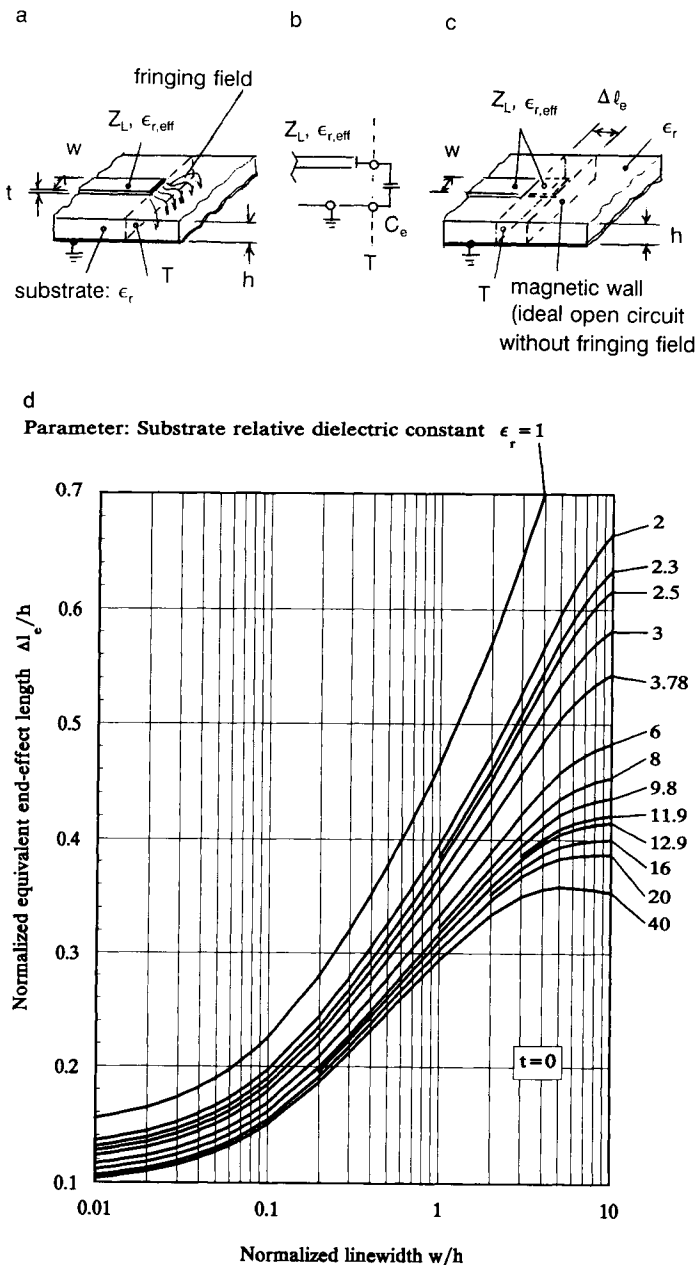


Figure 13. Microstrip open end. (a) Construction. (b) Equivalent and capacitance C_e . (c) Equivalent end effect length Δl_e . (d) Graph of $\Delta l_e/h$ versus normalized line width w/h for ϵ_r values of various substrate materials (polyolefin, $\epsilon_r = 2.3$; glass-fiber-reinforced PTFE, $\epsilon_r = 2.5$; fused quartz, $\epsilon_r = 3.78$; Al_2O_3 , $\epsilon_r = 9.8$; semi-insulating Si, $\epsilon_r = 11.9$; semi-insulating GaAs, $\epsilon_r = 12.9$; nonmagnetic ferrite, $\epsilon_r = 16$).

Round Shorting Metal Post

A frequently used technique of short-circuiting strip conductors to ground planes is to use the round shorting metal post of diameter d in the center of an abruptly ending strip conductor (Figure 14a). The post is pushed into a drilled hole in the substrate of thickness h and relative dielectric constant ϵ_r and then soldered to the strip conductor and the ground plane. In thin-film technology the holes are drilled in the uncoated substrate, and the inner surface of the hole is metallized in the sputtering and plating process at the same time as the generation of the structure at the substrate surface (via holes). The ranges of diameters are $d = 0.3$ to 0.6 mm for hybrid MICs and $d = 0.1$ to 0.2 mm for MMICs typically.

Equivalent Circuits

Two different equivalent circuits for the reactive properties of the non-ideal short circuit are shown in Figures 14b and 14c. The first form (Figure 14b) is a short-circuit inductance, L_S , at the reference plane T_1 at the center of the short-circuit post, modeling both the post inductance and the current distortion on the microstrip linear near the post. Generally, the normalized inductance L_S/h is a function of w/h , d/h , $h \cdot f$, and ϵ_r . The conductor thickness is usually assumed to be $t = 0$. For the static approximation, valid approximately up to $h \cdot f = 10$ GHz mm, L_S/h is a function of w/h and d/h only. Alternately the shorting metal post can be described by an ideally short-circuited uniform extension Δl_S of the microstrip line (Figure 14c), with the same parameters Z_L (characteristic impedance) and $\epsilon_{r,\text{eff}}$ (effective relative dielectric constant) as those of the connecting line. For small reactances $\omega L_S \ll Z_L$ the equivalent length is $\Delta l_S = L_S c_0 / (Z_L \cdot \sqrt{\epsilon_{r,\text{eff}}}) = L_S c_0 / Z_{L0}$, where Z_{L0} is the characteristic impedance of the microstrip line for $\epsilon_r = 1$ and c_0 is the velocity of light in free space. Again the functional dependence is $\Delta l_S/h = f(w/h, d/h)$ for the static approximation. For resonator design, for example, the total length has to be counted from the plane T_2 at the end of the extension Δl_S .

Electrical Properties of a Round Metal Post

Figure 14d exhibits a plot of the normalized static line extension $\Delta l_S/h$ of the short circuit post in Figure 14a. The values have been calculated by using a planar waveguide model for the short circuit post, introduced by Schulz [57]. This model has been analyzed for hybrid modes by using

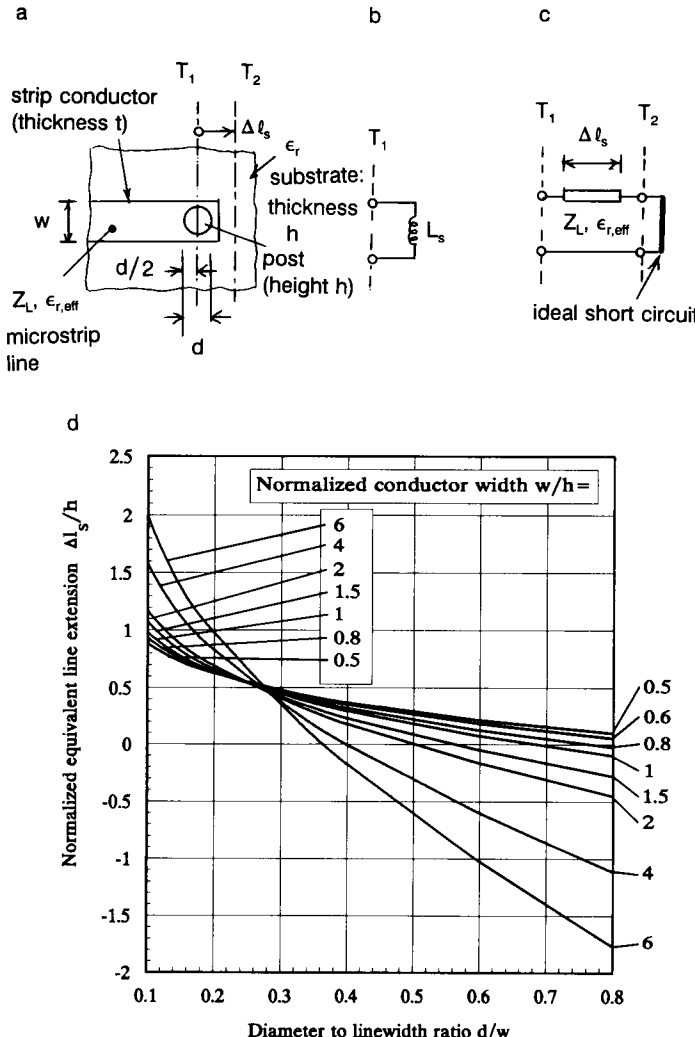


Figure 14. Short-circuiting metal post at the end of a microstrip line. (a) Construction. (b) Equivalent inductance L_s at the plane T_1 . (c) Equivalent line extension Δl_s ideally short-circuited at the plane T_2 . (d) Static values of the normalized equivalent line extension $\Delta l_s/h$ of the equivalent circuit (c) for the structure (a) for arbitrary substrate ϵ_r , calculated by use of the planar waveguide model [57].

the numerical method of lines [20, 21]. For the calculation of the values for Figures 5.14d, $h \cdot f = 0$ was assumed (static approximation). Thus the values are independent of ϵ_r . It can be seen from the plot that only for

small posts the position of T_2 is outside that of T_1 (positive sign of Δl_s). For large diameters d/w , T_2 is located a distance, $|\Delta l_s|$, inside the T_1 end of the conductor (negative sign of Δl_s). For small diameters $d/w \ll 1$ the value of Δl_s can be approximately calculated from the inductance of a round wire (Section 3), given by $L_s/h = 0.2[\ln(4h/d) - (d/(2h)) - 0.75]$.

Alternative Short Circuit Shapes

Figure 15 exhibits some alternative shapes of short circuits. The best approximation to an ideal short circuit is accomplished by the conducting wall perpendicular to the substrate surface at the end of the microstrip line, shown in Figure 15a. This form is therefore frequently used as microstrip reference-short for automated-network analyzer calibration in a microstrip environment. A further variant of a short circuit is a metal ribbon of length h and width b bonded to both the strip conductor and the substrate ground plane. This ribbon can be mounted either at the edge of the substrate (Figure 15b) as a wraparound strap or at any place on the substrate through a laser “drilled” rectangular hole (Figure 15c). The inductance is approximately calculated using the formula for the ribbon inductance in Section 2.

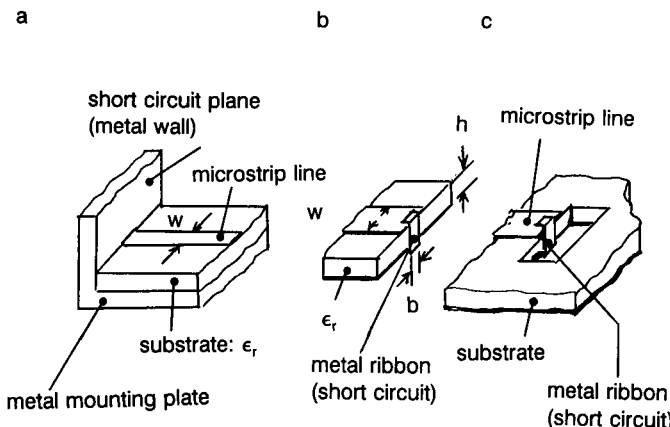


Figure 15. Alternative forms of microstrip short circuits. (a) Metal wall at the end of the microstrip line. Metal ribbon as a wraparound strap (b) at the edge of the substrate and (c) through a hole within the substrate.

12. Step Changes in the Strip Conductor Width of Microstrip Lines (Impedance Steps)

Junctions of two cascaded microstrip transmission lines of different characteristic impedance Z_{L1} and Z_{L2} are realized by steps in the strip conductor width from w_1 to w_2 , keeping the thickness h and relative dielectric constant ϵ_r of the substrate constant for either line. This type of discontinuity is encountered in low-pass filters, quarter-wavelength transformers, and matching networks in microwave integrated circuits. Analyses and design data for these steps are given in Refs. [1, Chap. 10.3; 2, Chap. 10.3; 4, Chap. 5; 16, Chap. 6; 17, Chap. 3; 18, 19, 62–64].

The step in the conductor width at the reference plane T is shown in Figure 16a. Field discontinuities are due to the increase in current density in the center region and due to the electric fringing field on the front edge

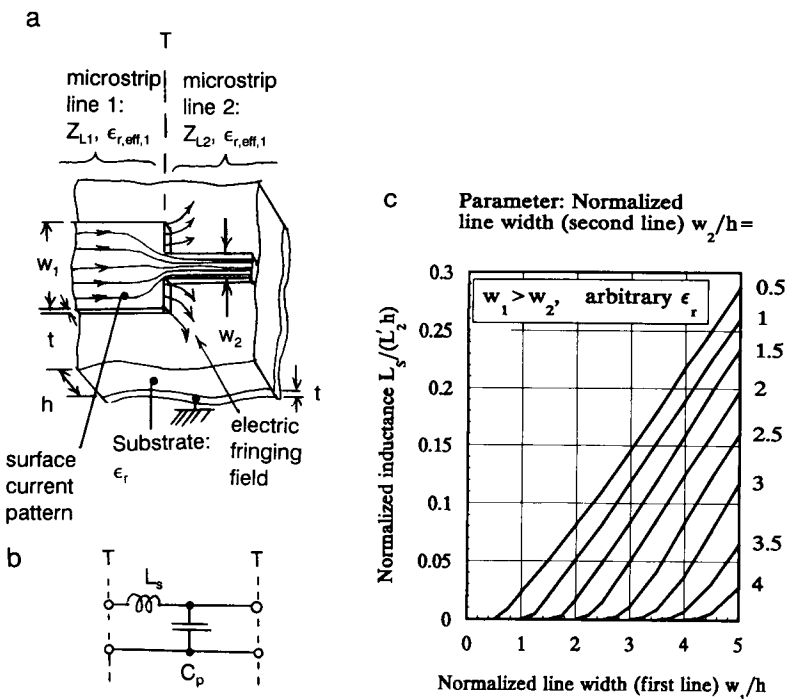


Figure 16. Step change in the conductor width (impedance step) of the microstrip line. (a) Configuration. (b) Static equivalent circuit. (c) Normalized static inductance $L_s/(L'_2 h)$ versus normalized line width w_1/h for conductor thickness $t = 0$ and arbitrary substrate ϵ_r (L'_2 = inductance per unit length of microstrip line 2).

of the wider conductor. The static lumped element equivalent circuit of Figure 16b comprises a series inductance, L_S , accounting for the current distortion, and a parallel capacitance, C_P , accounting for the electric fringing field. Using the static approximation one can determine the functional dependences of these elements as $L_S/h = f(w_1/h, w_2/h)$ and $C_P/h = f(w_1/h, w_2/h, \epsilon_r)$, assuming that the conductor thickness is $t = 0$.

Figure 16c shows a plot of the *static series inductance* L_S versus geometrical data, calculated using the numerical static Garlekin's method [62]. L_S is independent of ϵ_r . Using the planar waveguide model for the step [1, Chap. 10.3; 2, Chap. 10.3], one can derive an approximate equation for L_S by

$$\frac{L_S}{h} = \frac{\mu_0}{\pi} \ln \frac{1}{\sin \left(\frac{\pi}{2} \frac{Z_{L1}\sqrt{\epsilon_{r,\text{eff},1}}}{Z_{L2}\sqrt{\epsilon_{r,\text{eff},2}}} \right)} \quad (44)$$

where $\mu_0 = 0.4\pi$ nH/mm. In this equation $Z_{Li}\sqrt{\epsilon_{r,\text{eff},i}} = Z_{Loi} = Z_{Li}(\epsilon_r = 1)$ for $i = 1, 2$ is the characteristic impedance of either connecting microstrip line without a substrate, having the same dimensions, however. Values for C_P as function of dimensions and ϵ_r have been calculated [63] using a numerical Green's functions method. The *parallel capacitance* C_P can be approximated by the difference in open-ended capacitances $C_{e1}(w_1, h, \epsilon_r)$ of the wider line and $C_{e2}(w_2, h, \epsilon_r)$ of the smaller line, calculated in Section 10, according to $C_P(w_1, w_2, h, \epsilon_r) = C_{e1} - C_{e2}$.

13. Right-Angled Bends of Microstrip Lines

In many cases in which complex microstrip circuits are required on a single small substrate, changes in the direction of microstrip lines are needed to increase the packaging density of the circuit on the substrate and flexibility in the layout design. Normally an abrupt right-angled bend of the strip conductor, as can be seen in Figures 17a and 17b, is used for these purposes. When both connecting microstrip lines have the same characteristic impedance Z_L the bend is said to be symmetrical. Analyses and design data for microstrip bends are given by Refs. [1, Chap. 10.5; 2, Chap. 10.5; 4, Chap. 5; 16, Chap. 6; 17, Chap. 3; 18, 19, 23, 65–69].

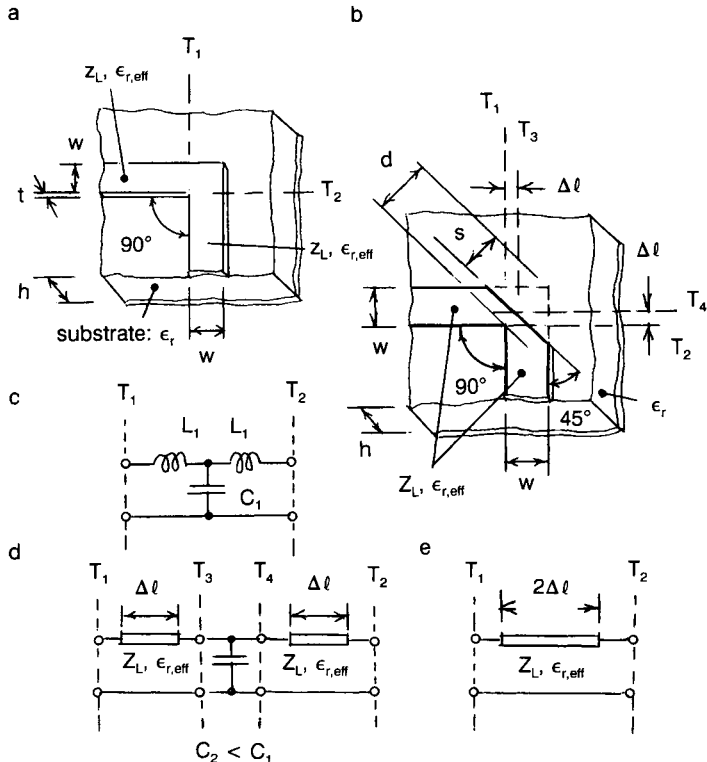


Figure 17. Right-angled symmetrical bend of the microstrip line. Configuration (a) of the basic, nonchamfered bend and (b) of the chamfered bend. (c) General static lumped-element equivalent circuit for the uncompensated bend for configurations a and b. (d) Transmission line equivalent circuit for the uncompensated bend for structures a and b. (e) Equivalent transmission line for the compensated bend, i.e., structure b with $s = s_{\text{opt}}$.

Nonchamfered Symmetric Bend

The nonchamfered bend of Figure 17a is described by the strip conductor width w , conductor thickness t (usually assumed to be $t = 0$), and the thickness h and relative dielectric constant ϵ_r of the substrate. The crowding of the current density at the inner corner and the distortion of the electric field at the inner and outer corners of the bend are modeled for low frequencies up to approximately $h \cdot f \leq 10 \text{ GHz} \cdot \text{mm}$ by a series inductance, L_1 , and a parallel capacitance, C_1 . These elements form the static lumped-element equivalent circuit (Figure 17c) between the two planes T_1 and T_2 located at the inner edges of the strip conductors. The

functional dependence of the elements is $L_1/h = f(w/h)$ and $C_1/h = f(w/h, \epsilon_r)$ for the static approximation and $t = 0$. Part of the lumped circuit of Figure 17c can be replaced by two sections of microstrip lines of the respective lengths Δl and the same parameters Z_L and $\epsilon_{r,\text{eff}}$ as those of the connecting lines, as shown in Figure 17d. This is done by choosing Δl such that $\Delta l \cdot L' = L_1$, where L' is the inductance per unit length of the connecting microstrip line. Then $2C' \cdot \Delta l$ has to be subtracted from C_1 . Thus an excess capacitance, $C_2 = C_1 - 2C' \cdot \Delta l$, remains in the circuit of Figure 17d, giving cause to parasitic signal reflections at the corner for the uncompensated bend of Figure 17a.

Chamfered Symmetrical Bend

To avoid reflections at the bend in practical circuits, the bend is chamfered as shown in Figure 17b. The relative chamfer is defined as $S = s/d \cdot 100\%$, where d is the total diagonal and s is that part of the diagonal which has been cut off. This reduces the capacitance C_1 in Figure 17c and therefore also C_2 in Figure 17d. The compensated bend is defined by $C_2 = 0$ and zero reflections. Experimental studies in Ref. [65] resulted in an *optimum chamfer* of $S_{\text{opt}} = 70\%$ for broadband compensation of microstrip lines of 50Ω characteristic impedance on an Al_2O_3 substrate ($\epsilon_r = 10.8$), valid for a frequency range of $0 < fh < 10 \text{ GHz} \cdot \text{mm}$. Furthermore the author of Ref. [65] experimentally derived the condition

$$S_{\text{opt}} = 52 + 65 \exp\left(-1.35 \frac{w}{h}\right)\% \quad (45)$$

for an optimum chamfer and compensation (reflection coefficient, $< 5\%$), being valid for different line widths, $w/h \geq 0.25$, and for $1 \leq \epsilon_r \leq 25$ and $fh \leq 10 \text{ GHz} \cdot \text{mm}$. S_{opt} is independent of ϵ_r to the first approximation. The compensated bend is modeled by an additional transmission line of the length $2 \cdot \Delta l$ between the two planes T_1 and T_2 , as shown in Figure 17e. This can be alternatively described by a shift in the reference plane from T_1 to T_3 by a distance of Δl and from T_2 to T_4 by the same distance in the chamfered structure of Figure 17b. By curve fitting the experimental results of Ref. [65] the equation

$$2 \frac{\Delta l}{h} = 0.5 \left(\frac{w}{h} \right)^{1.08} - \frac{0.45}{\sqrt{\epsilon_r}} - 0.12 \quad (46)$$

for the normalized total equivalent length of the compensated bend with an optimum chamfer can be derived. Equation (46) is valid for $0.1 \leq w/h \leq 10$ and $1 \leq \epsilon_r \leq 20$.

14. Absorbing Microstrip Terminations

Many microstrip devices in microwave integrated circuits need matched terminations or in other words matched loads at certain ports to operate properly. Among these devices are directional couplers, power dividers, and circulators. Matched microstrip loads are also needed as standards for calibration of automated network analyzers in a microstrip transmission line environment. In this section matched microstrip loads fabricated in thin-film technology are discussed [1, Chap. 1.7; 2, Chap. 1.7; 4, Chap. 8.1; 70–74]. Normally they are used to terminate microstrip lines of 50Ω characteristic impedance.

Overview

Generally a matched termination at the T_1 end of a microstrip line of characteristic impedance Z_L is defined by a reflection coefficient, $\Gamma = 0$, or a $VSWR = 1$ with reference to the microstrip impedance Z_L . Basically there exist two methods to realize a matched load. The first is a lumped resistor, $R = Z_L$, parallel to the end of the line at T_1 (*lumped termination*, Figure 18a). The second method is a *distributed termination* (Figure 18b) made of a high-loss nonuniform microstrip transmission line, which is several wavelengths long and has an increasing loss constant, $\alpha(z)$, over the line coordinate z starting at the plane T_1 . This line absorbs most of the

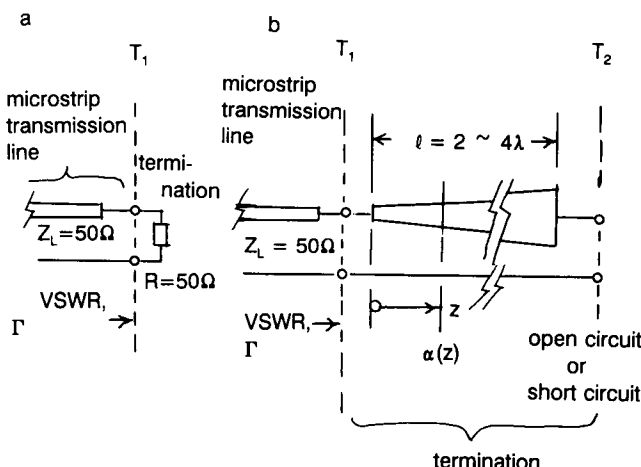


Figure 18. Basic methods for realizing matched transmission line terminations at the plane T_1 . (a) Lumped resistor $R = Z_L$. (b) Distributed termination (wave absorber).

energy of the incident wave at T_1 and of the reflected wave at the T_2 end, thus keeping the reflected voltage at T_1 on the order of 1% of the voltage of the incident wave. The basic design problems of loads are to avoid parasitic reactances and to achieve broadband performance.

Direct Grounded Lumped Terminations

A lumped termination at the plane T_1 according to Figure 18a is constructed by a planar rectangular thin-film resistor of side lengths $l \ll \lambda$ and $w \ll \lambda$ in line with the strip conductor on the surface of the substrate (Figure 19a). The far end (plane T_2) of this resistor has to be connected to the ground metallization on the bottom side of the substrate. Grounding can be achieved in two ways, by *direct grounding* (shown in Figure 19) and by *virtual grounding* (shown in Figure 20). Direct grounding is achieved by a short metal DC path between the T_2 far end of the planar resistor R and the ground metallization at the bottom of the substrate. Figure 19 shows several methods for direct grounding. The termination of Figure 19a uses a round hole in the substrate, metallized at the inner surface. The electrical properties of that metal post short circuit are described in Section 11. The termination of Figure 19b utilizes a wraparound metal strap at the edge of the substrate to achieve the short-circuit connection. Generally the planar rectangular resistor is deposited by thin-film techniques, using high-resistivity material such as chrome, nichrome, or tantalum, the layer thickness being $t_R \ll \delta$, where δ is the skin depth given in Equation (4). Typical values are $t_R = 0.01$ to $0.1 \mu\text{m}$. Thus skin effect has not to be taken into account and the surface resistivity (resistance of a square of metal film of thickness t_R) is $R_S = \rho/t_R$, where ρ is the resistivity of the resistor material. The total resistance of a rectangular resistor of length l and width w is therefore given by $R = R_S l/w$. Typical surface resistivity values are $R_S = 50$ to 100Ω . Frequently the adhesive layer for the thin-film process is used as resistive layer. In this case the conductive layer (e.g., 5- to $10-\mu\text{m}$ -thick copper or gold) is selectively etched away over the area of the resistor. All direct grounded lumped terminations exhibit increasing VSWR versus frequency f with $\text{VSWR} < 1.2$ for $0 < f < 6 \text{ GHz}$ and $\text{VSWR} < 1.4$ for $0 < f < 12 \text{ GHz}$ typically (50Ω microstrip line on $0.635\text{-mm-thick Al}_2\text{O}_3$ substrate). This is due to the capacitance C_P of the resistor patch against the ground and the short-circuit inductance L_S (equivalent circuit, Figure 19c). By special shaping of the planar resistor like a section of a circle and by a semicircular wraparound grounding (Figure 19d), proposed in Ref. [70], L_S can be reduced and the bandwidth of the termination at T_1 can be increased to $0 < f < 18 \text{ GHz}$ for $\text{VSWR} < 1.15$ for the termination of a 50Ω microstrip line on $0.635\text{-mm-thick Al}_2\text{O}_3$ substrate.

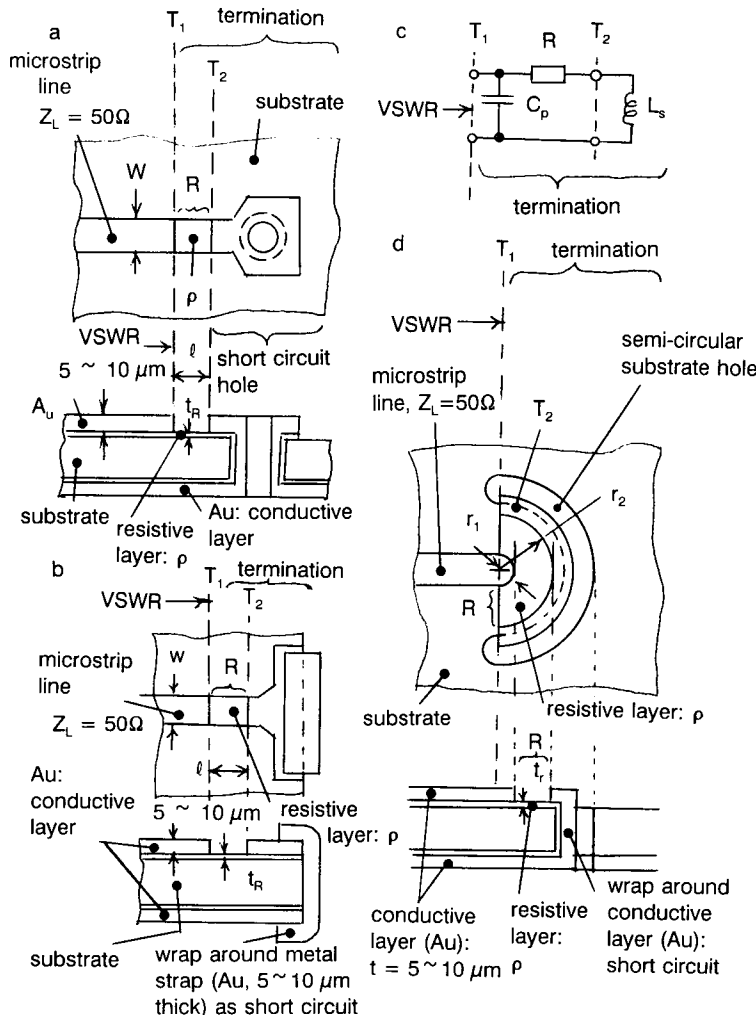


Figure 19. Direct grounded lumped terminations at plane T_1 . (a) Using a metallized round hole for grounding. (b) With a wrap-around metallization strap for grounding. (c) Lumped equivalent circuit at the plane T_1 . (d) Sector-shaped resistor with improved bandwidth according to Ref. [70].

thick Al_2O_3 substrate by a resistor with radii $r_1 = 0.6 \text{ mm}$ and $r_2 = 1.3 \text{ mm}$. The resistance of the circular structure is $R = \rho \cdot \ln(r_2/r_1)/(t_R \pi)$. A method for broadbanding rectangular film resistors of the type shown in Figure 19a is described in Ref. [71]: A simple microstrip matching circuit is connected in a series in front of the input plane T_1 of the resistor R , thus improving the bandwidth up to $0 < f < 18 \text{ GHz}$ for $\text{VSWR} < 1.5$.

Virtual Grounded Lumped Terminations

Virtual grounded lumped resistors used for matched terminations at the plane T_1 are depicted in Figure 20. This technique avoids the costly process of via holes or wraparound straps at the substrate edge. For virtual grounding commonly an open-circuited stub of the length $l = \lambda/4$ acts as short circuit at its T_2 input terminal (Figure 20a). Thus at the $\lambda/4$ -resonant frequency f_R of the stub the input impedance of the termination at the plane T_1 is R and the VSWR = 1.0. With frequency increasing or decreasing the VSWR at T_1 unfortunately increases, limiting the bandwidth to approximately 30% for $\text{VSWR} < 1.25$. For large bandwidths the characteristic impedance Z_{LS} of the stub should be as low as possible. A

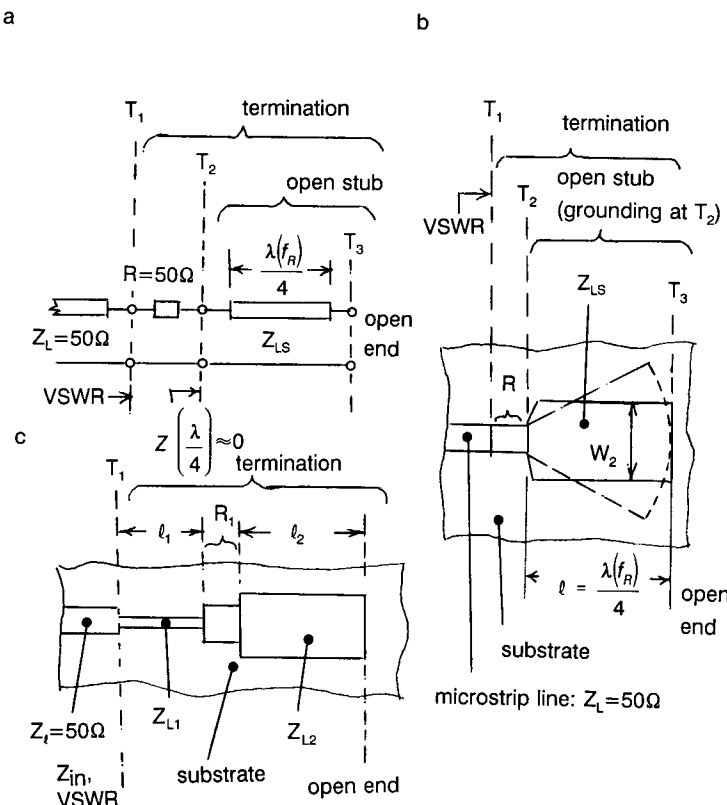


Figure 20. Virtual grounded lumped termination at plane T_1 . (a) Basic circuit using $\lambda/4$ open-circuited stub. (b) Realization using a uniform low-impedance stub (full lines) or a tapered line stub (dashed lines). (c) Broadband termination circuit designed using the filter theory approach after Ref. [73].

practical termination circuit using a uniform low impedance stub (solid lines) or a tapered stub (dashed lines) is shown in Figure 20b. A method for increasing bandwidth without direct grounding is presented in Ref. [73]: Resistors are parts of cascaded transmission line networks designed by filter theory for Tschebycheff or maximum flat bandpass filters. A second-order network of this type, in Figure 20c, for instance, exhibits a bandwidth of 79% around a center frequency of 4 GHz for $VSWR < 1.16$. Design data are $l_1 + l_2 \approx \lambda$, $R_1 = 80 \Omega$, and $Z_{L1} = 69.3 \Omega$, $Z_{L2} = 41.7 \Omega$ for an input impedance at T_1 of $Z_{in} = 50 \Omega$.

Distributed Terminations

Figure 21 shows a method to realize a distributed termination at the plane T_1 according to the basic circuit of Figure 18b. In order to achieve low input reflection coefficient Γ , the tapered termination line has to exhibit a low attenuation, α , and a characteristic impedance, $Z_{LT} = Z_L = 50 \Omega$, near its T_1 input terminal at $z \approx 0$. With increasing distance z from T_1 the $\alpha(z)$ has to increase. This can be obtained by a wedge of an insulator with high dielectric or magnetic loss $\tan \delta_e$ or $\tan \delta_\mu$ upon the strip conductor (e.g., lossy ferrite). Instead of the lossy wedge, a tapered transition from a low-resistance strip conductor (e.g., of gold) to a strip conductor made of a high-resistivity thin-film layer (e.g., nichrome), being several wavelengths long, can be used [1, Chap. 1.7; 2, Chap. 1.7].

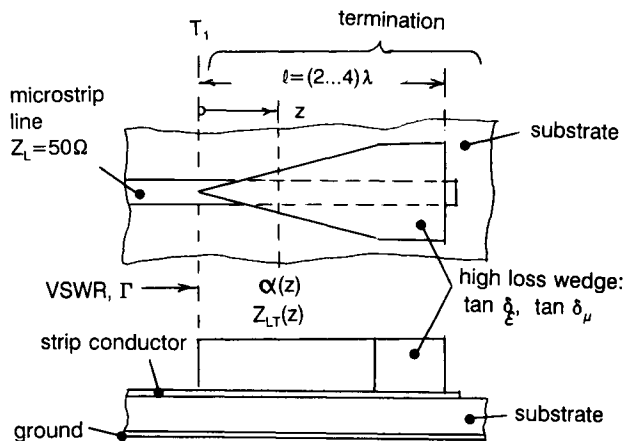


Figure 21. Distributed microstrip termination at the plane T_1 using a nonuniform high-loss line formed by a high-loss insulator wedge above the microstrip line.

15. Coaxial-to-Microstrip Transitions

When a microwave integrated circuit (e.g., an amplifier or a mixer) is to be combined with other RF units to build up a complete subsystem, it is usually mounted in a housing with coaxial connectors. Therefore a low-loss and low-reflection transition between the connecting microstrip line on the substrate of the microwave integrated circuit and the coaxial line of the connector is required, the characteristic impedance of both lines normally having a value of $Z_L = 50 \Omega$. The design of those microstrip transitions is treated in Refs. [1, Chap. 1.6; 2, Chap. 1.6; 4, Chaps. 7.2–7.4; 75–80].

Basic Construction

The basic construction of a coaxial-to-microstrip transition is shown in Figure 22a: A coaxial connector is mounted at the side of a housing consisting of a metal mounting plate for the substrate, of the side walls, and of a cover. The forward current flows from the inner conductor of the coaxial line to the strip conductor of the microstrip line via a spring fixed at the inner conductor end. When only temporary contact is required, a pressure contact of this spring is satisfactory. A permanent contact will be obtained by soldering or conductive-epoxy bonding the spring on the strip conductor. The return current path from the microstrip ground metallization on the bottom side of the substrate to the coaxial outer conductor is established via the metal mounting plate of the housing and the coaxial flange. Minimum current paths are required for both forward and reverse current. Therefore gaps have to be avoided at the connections from the flange to the mounting plate, between the substrate bottom side metallization and the mounting plate, and between the substrate edge and the connector flange.

Electrical Model

The purpose of the transition is to provide a transformation of the electromagnetic field configuration of the coaxial line to that of the microstrip line. An ideal transition has reflection coefficients $S_{11} = S_{22} = 0$ and an attenuation of $20\log|S_{21}| = 0$ dB between the two planes T_1 and T_2 on either transmission line for a broad frequency band. In the real transition, distortions of both the current flow and the electric field occur with respect to both the coaxial and the microstrip field configuration. These distortions are approximately modeled by the static lumped-element equivalent circuit of Figure 22b. The series inductance L_S results from the

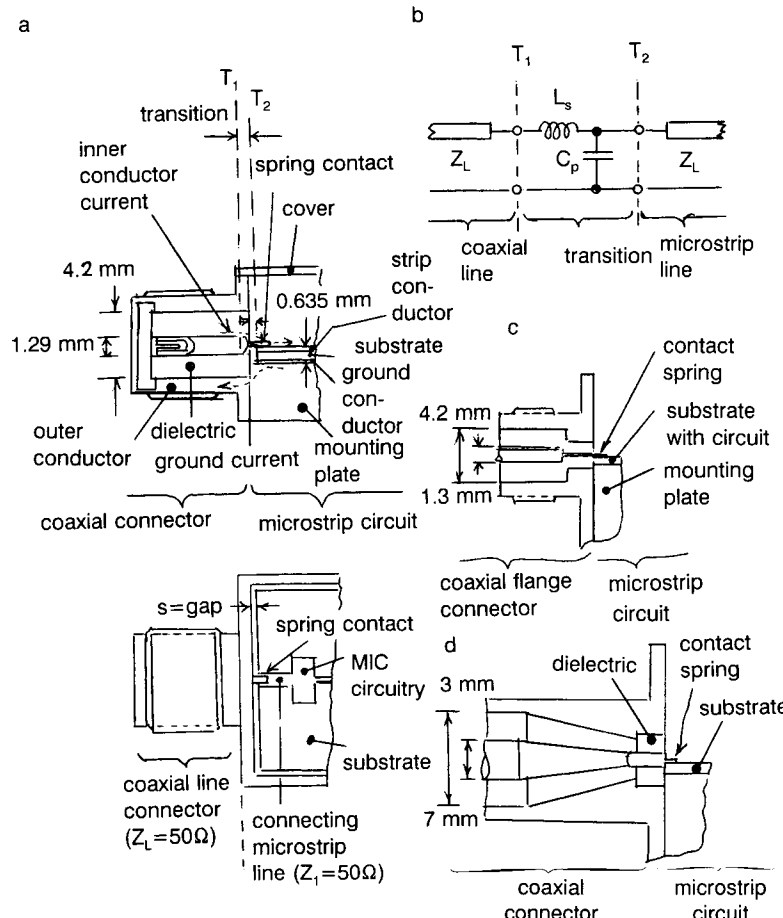


Figure 22. Various forms of coaxial-to-microstrip transitions. (a) Basic construction of a transition; coaxial line dimensions are for SMA-type connectors. (b) Static lumped-element equivalent circuit for abrupt transition of a. (c) Transition from an SMA-type coaxial connector with one-step cross-section reduction of the coaxial line to improve field matching. (d) Transition from an APC-7-type coaxial connector with continuously tapered cross-section reduction.

current distortion, mainly at the inner conductor spring, with cross-sectional dimensions much smaller than those of the coaxial line inner conductor. The parallel capacitance C_p is generated by the step at the connection between the coaxial outer connector and the housing mounting plate. L_s has to be dimensioned so that the broadband compensation of C_p is obtained. For this purpose the inner conductor is tapered near its end. A second purpose of this taper is to match the coaxial inner

conductor diameter to the linewidth of the microstrip line. Due to these parasitic effects the transition exhibits low-pass transfer characteristics with $VSWR < 1.1$ for SMA-type transitions and $VSWR < 1.05$ for APC-7-type transitions, connected to 50Ω microstrip lines on 0.635- or 1.27-mm-thick Al_2O_3 substrates over a frequency range of $0 < f < 12$ GHz typically.

Alternative Types

Other types of coaxial-to-microstrip transitions are shown in Figures 22c and 22d. These forms leave the concept of the abrupt transition of Figure 22a, and they try to approximate a “continuous” transition between the two cross sections that exhibits nearly ideal broadband performance. A first step into this direction is the transition of Figure 22c with a one-step cross-section reduction of the coaxial line. The closest approximation to a continuous transition is the transition of Figure 22d with a continuous taper of the inner and outer diameters of the coaxial line. Transitions from microstrip lines to other types of lines, for example, to waveguides are described in Refs. [1, Chap. 1.6; 2, Chap. 1.6; 4, Chap. 7.3; 81].

References

- [1] R. K. Hoffmann, *Integrierte Mikrowellenschaltungen*. Berlin: Springer-Verlag, 1983.
- [2] R. K. Hoffmann, *Handbook of Microwave Integrated Circuits*. Norwood, MA: Artech House, 1987. (Transl. of [1].)
- [3] J. Frey and K. Bhasin, *Microwave Integrated Circuits*. Norwood, MA: Artech House, 1985.
- [4] T. C. Edwards, *Foundations for Microstrip Circuit Design*. Chichester: John Wiley & Sons, 1981.
- [5] T. Itoh, *Planar Transmission Line Structures*. New York: IEEE Press, 1987.
- [6] R. A. Pucel, Design considerations for monolithic microwave circuits, *IEEE Trans. Microwave Theory Tech.*, Vol. MTT-29, pp. 513–534, June 1981.
- [7] R. S. Pengelly, Monolithic microwave integrated circuits—Part I, *IEEE MTT—S Newslett.*, pp. 39–48, Winter 1989.
- [8] R. S. Pengelly, Monolithic microwave integrated circuits—Part II, *IEEE MTT—S Newslett.*, pp. 24–33, Spring 1989.
- [9] R. A. Pucel, *Monolithic Microwave Integrated Circuits*. New York: IEEE Press, 1985.
- [10] R. S. Pengelly, *Microwave Field-Effect Transistors—Theory, Design and Applications*, 2nd Ed. Chichester: Research Studies Press, 1986.
- [11] D. A. Daly, S. P. Knight, M. Caulton, and R. Eckhold, Lumped elements in microwave integrated circuits, *IEEE Trans. Microwave Theory Tech.*, Vol. MTT-15, pp. 713–721, Dec. 1967.
- [12] R. S. Pengelly and D. Rickard, Design, measurement and application of lumped elements up to J-band, *Proc. 7th Eur. Microwave Conf.*, pp. 460–486, 1977.

- [13] M. Caulton, B. Hershenson, S. P. Knight, and R. E. deBrecht, Status of lumped elements in microwave integrated circuits—Present and future, *IEEE Trans. Microwave Theory Tech.*, Vol. MTT-19, pp. 588–599, July 1971.
- [14] C. S. Aitchison, R. Davies, I. D. Higgins, S. R. Longley, B. H. Newton, J. F. Wells, and J. C. Williams, Lumped circuit elements at microwave frequencies, *IEEE Trans. Microwave Theory Tech.*, Vol. MTT-19, pp. 928–937, Dec. 1971.
- [15] M. Caulton, Lumped elements in microwave integrated circuits, in *Advances in Microwaves* (L. Young and H. Sobol, eds.), Vol. 8, pp. 144–202. New York: Academic Press, 1974.
- [16] K. C. Gupta, R. Garg, and R. Chadha, *Computer-Aided Design of Microwave Circuits*. Norwood, MA: Artech House, 1981.
- [17] K. C. Gupta, R. Garg, and I. J. Bahl, *Microstrip Lines and Slotlines*. Dedham, MA: Artech House, 1979.
- [18] R. Jansen and N. Koster, A unified CAD basis for the frequency dependent characterization of strip, slot and coplanar MIC components, *Proc. 11th Eur. Microwave Conf.*, pp. 682–687, 1981.
- [19] W. Menzel and I. Wolff, A method for calculating the frequency dependent properties of microstrip discontinuities, *IEEE Trans. Microwave Theory Tech.*, Vol. MTT-25, pp. 107–112, Feb. 1977.
- [20] S. B. Worm and R. Pregla, Hybrid-mode analysis of arbitrarily shaped planar microwave structures by the method of lines, *IEEE Trans. Microwave Theory Tech.*, Vol. MTT-32, pp. 191–196, Feb. 1984.
- [21] R. Pregla and W. Pascher, The method of lines, in *Numerical Techniques for Microwave and Millimeter Wave Passive Structures* (T. Itoh, ed.), pp. 381–446. New York: John Wiley & Sons, 1989.
- [22] R. Kipp, C. H. Chan, A. T. Yang, and J. T. Yao, Simulation of high-frequency integrated circuits incorporating full-wave analysis of microstrip discontinuities, *IEEE Trans. Microwave Theory Tech.*, Vol. MTT-41, pp. 848–854, May 1993.
- [23] R. Kipp and C. H. Chan, Triangular-domain basis functions for full-wave analysis of microstrip discontinuities, *IEEE Trans. Microwave Theory Tech.*, Vol. MTT-41, pp. 1187–1194, June/July 1993.
- [24] M. Caulton and W. E. Poole, Designing lumped elements into microwave amplifiers, *Electronics*, pp. 100–110, Apr. 14, 1969.
- [25] F. E. Terman, *Radio Engineer's Handbook*. New York: McGraw-Hill, 1950.
- [26] F. W. Grover, *Inductance Calculations*. New York: Van Nostrand, 1946.
- [27] K. Wohak, Näherungsweise Berechnung der Induktivität von Dünnenschichtbahnen, *Frequenz*, Vol. 23, pp. 359–364, Dec. 1969.
- [28] C. Hentschel, Die Analyse von Schaltungen mit Dünnenschichtspulen, *Arch. Elektron. Uebertragungstechn.*, Vol. 26, pp. 319–328, July/Aug. 1972.
- [29] H. M. Greenhouse, Design of planar rectangular microelectronic inductors, *IEEE Trans. Parts, Hybrids Packag.*, Vol. PHP-10, pp. 101–109, 1974.
- [30] H. A. Wheeler, simple inductance formulas for radio coils, *Proc. IRE*, Vol. 16, pp. 1398–1400, Oct. 1928.
- [31] I. Wolff and H. Kapusta, Modeling of circular spiral inductors for MMIC's, *IEEE MTT—S Symp. Dig.*, pp. 123–126, 1987.
- [32] R. H. Jansen, L. Wiemer, H. J. Finley, J. R. Suffolk, B. D. Roberts, and R. S. Pengelly, Theoretical and experimental broadband characterization of multiturn spiral inductors in sandwich type GaAs MMIC's, *Proc. 15th Eur. Microwave Conf.*, pp. 946–951, 1985.
- [33] F. J. Schmückle and R. Pregla, the method of lines for the rigorous full wave analysis of rectangular bends of multiple-line-systems, *IEEE MTT—S Symp. Dig.*, 1992.

- [34] T. Becks and I. Wolff, Analysis of 3-D metallization structures by a full-wave spectral domain technique, *IEEE Trans. Microwave Theory Tech.*, Vol. MTT-40, pp. 2219–2227, Dec. 1992.
- [35] F. J. Schmückle, The method of lines for the analysis of rectangular spiral inductors, *IEEE Trans. Microwave Theory Tech.*, Vol. MTT-41, pp. 1183–1186, June/July 1993.
- [36] G. Mayer and K. H. Houska, SiO capacitors for high frequency thin film circuits, *Nachrichtentech. Z.*, Vol. 28, pp. 207–211, June 1975.
- [37] R. W. Berry, P. M. Hall, and M. T. Harris, *Thin Film Technology*. Princeton: Van Nostrand, 1968.
- [38] R. W. Wyndrum, P. D. Stark, F. P. Pelletier, and S. C. Lee, Analysis of bipolar interdigitated thin film capacitor, *Proc. Electron. Component Conf.*, pp. 350–358, 1969.
- [39] K. Wohak, Die Berechnung des komplexen Widerstands von Dünnschicht Kondensatoren, *Frequenz*, Vol. 24, pp. 66–70, Mar. 1970.
- [40] H. Katoh, Capacitors in microwave integrated circuits, *Electron. Commun. J.*, Vol. 54-B, pp. 39–46, No. 3, 1971.
- [41] W. C. Chew and J. A. Kong, Effects of fringing fields on the capacitance of circular microstrip disk, *IEEE Trans. Microwave Theory Tech.*, Vol. MTT-28, pp. 98–104, Feb. 1980.
- [42] I. Wolff, Statische Kapazitäten von rechteckigen und kreisförmigen Microstrip Scheibenkondensatoren, *Arch. Elektron. Uebertragungstech.*, Vol. 27, pp. 44–47, Jan. 1973.
- [43] P. Benedec and P. Silvester, Capacitance of parallel rectangular plates separated by a dielectric sheet, *IEEE Trans. Microwave Theory Tech.*, Vol. MTT-20, pp. 504–510, Aug. 1972.
- [44] I. Wolff and N. Knoppik, Rectangular and circular microstrip disk capacitors and resonators, *IEEE Trans. Microwave Theory Tech.*, Vol. MTT-22, pp. 857–864, Oct. 1974.
- [45] E. F. Kuester, Explicit approximations for the static capacitance of a microstrip patch of arbitrary shape, *J. Electromagn. Waves Appl.*, Vol. 2, No. 1, pp. 102–135, 1987.
- [46] F. Tefiku and E. Yamashita, Capacitance characterization method for thick-conductor multiple planar ring structures on multiple substrate layers, *IEEE Trans. Microwave Theory Tech.*, Vol. MTT-40, pp. 1894–1902, Oct. 1992.
- [47] A. K. Verma and Z. Rostamy, Resonant frequency of uncovered and covered rectangular microstrip patch using modified Wolff model, *IEEE Trans. Microwave Theory Tech.*, Vol. MTT-41, pp. 109–116, Jan. 1993.
- [48] M. Maeda, An analysis of gap in microstrip transmission lines, *IEEE Trans. Microwave Theory Tech.*, Vol. MTT-20, pp. 390–396, June 1972.
- [49] P. Benedek and P. Silvester, Equivalent capacitances for microstrip gaps and steps, *IEEE Trans. Microwave Theory Tech.*, Vol. MTT-20, pp. 729–733, Nov. 1972.
- [50] A. Gopinath and C. Gupta, Capacitance parameters of discontinuities in microstriplines, *IEEE Trans. Microwave Theory Tech.*, Vol. MTT-26, pp. 831–836, Oct. 1978.
- [51] M. Kirschning, R. H. Jansen, and N. H. L. Koster, Measurement and computer aided modeling of microstrip discontinuities by an improved resonator method, *IEEE GMTT Int. Microwave Symp. Dig.*, pp. 495–497, 1983.
- [52] P. Newham, Coupling across gap in thick microstrip line, *IEEE Proc., Part H*, Vol. 136, pp. 64–66, Feb. 1989.
- [53] P. Silvester and P. Benedek, Equivalent capacitances of microstrip open circuits, *IEEE Trans. Microwave Theory Tech.*, Vol. MTT-20, pp. 511–516, Aug. 1972.
- [54] R. H. Jansen and N. H. L. Koster, Accurate results on the end effect of single and coupled microstrip lines for use in microwave integrated circuits design, *Arch. Elektron. Uebertragungstech.*, Vol. 34, pp. 453–459, Nov. 1980.

- [55] M. Kirschning, R. H. Jansen, and N. H. L. Koster, Accurate model for open end effect of microstrip lines, *Electron. Lett.*, Vol. 17, No. 3, pp. 123–124, 1981.
- [56] W. O. Hammerstad, Equations for microstrip circuit design, *Proc. Eur. Microwave Conf.*, pp. 268–272, 1975.
- [57] U. Schulz, Bestimmung der Modellparameter von Stiften und Blenden in Wellenleitern mit Hilfe der Methode der Geraden, *Arch. Elektron. Uebertragungstech.*, Vol. 39, pp. 203–207, Mar. 1985.
- [58] W. J. R. Hoefer and A. Chatopadhyay, Evaluation of the equivalent circuit parameters of microstrip discontinuities through perturbation of a resonant ring, *IEEE Trans. Microwave Theory Tech.*, Vol. MTT-23, pp. 1067–1071, Dec. 1975.
- [59] D. G. Swanson, Grounding microstrip lines with via holes, *IEEE Trans. Microwave Theory Tech.*, Vol. MTT-40, pp. 1719–1721, Aug. 1992.
- [60] R. Sorrentino, F. Alessandri, M. Mongiardo, G. Avitabile, and L. Roselli, Full-wave modeling of via hole grounds in microstrip by three-dimensional mode matching technique, *IEEE Trans. Microwave Theory Tech.*, Vol. MTT-40, pp. 2228–2234, Dec. 1992.
- [61] P. H. Harms, J. F. Lee, and R. Mittra, Characterizing the cylindrical via discontinuity, *IEEE Trans. Microwave Theory Tech.*, Vol. MTT-41, pp. 153–156, Jan. 1993.
- [62] A. Gopinath, A. F. Thomson, and I. M. Stephenson, Equivalent circuit parameters of microstrip step change in width and cross junctions, *IEEE Trans. Microwave Theory Tech.*, Vol. MTT-24, pp. 142–144, Mar. 1976.
- [63] B. Easter, A. Gopinath, and I. M. Stephenson, Theoretical and experimental methods for evaluating discontinuities in microstrip, *Radio Electron. Eng.*, Vol. 48, Nos. 1/2, pp. 73–84, 1978.
- [64] C. N. Capsalis, N. K. Uzunoglu, C. P. Chronopoulos, and Y. D. Sigourou, A rigorous analysis of shielded microstrip asymmetric step discontinuity, *IEEE Trans. Microwave Theory Tech.*, Vol. MTT-41, pp. 520–523, Mar. 1993.
- [65] R. J. P. Douville and D. S. James, Experimental study of symmetric microstrip bends and their compensation, *IEEE Trans. Microwave Theory Tech.*, Vol. MTT-26, pp. 175–181, Mar. 1978.
- [66] P. Anders and F. Arndt, Microstrip discontinuity of capacitances and inductances for double steps, mitered bends with arbitrary angle, and asymmetric right angle bends, *IEEE Trans. Microwave Theory Tech.*, Vol. MTT-28, pp. 1213–1217, Nov. 1980.
- [67] A. Gopinath and B. Easter, Moment method of calculating discontinuity inductance of microstrip right-angled bends, *IEEE Trans. Microwave Theory Tech.*, Vol. MTT-22, pp. 880–883, Oct. 1974.
- [68] W. Menzel, Frequency-dependent transmission properties of truncated microstrip right-angle bends, *Electron. Lett.*, Vol. 12, No. 24, p. 641, 1976.
- [69] P. H. Harms and R. Mittra, Equivalent circuits for multiconductor microstrip bend discontinuities, *IEEE Trans. Microwave Theory Tech.*, Vol. MTT-41, pp. 62–69, Jan. 1993.
- [70] W. Fischer and W. Wiesbeck, Wideband microstrip termination, *Nachrichtentech. Z.*, Vol. 26, pp. 83–85, Feb. 1973.
- [71] D. Lacombe, A multi octave microstrip $50\text{-}\Omega$ termination, *IEEE Trans. Microwave Theory Tech.*, Vol. MTT-20, pp. 290–291, Apr. 1972.
- [72] C. Buoli, Microstrip attenuators and terminations realized with periodic electromagnetic structures, *Proc. 18th Eur. Microwave Conf.*, pp. 593–598, 1988.
- [73] L. J. P. Linner and H. B. Lunden, Theory and design of broadband nongrounded matched loads for planar circuits, *IEEE Trans. Microwave Theory Tech.*, Vol. MTT-34, pp. 892–896, Aug. 1986.

- [74] G. H. B. Thompson, An easy method of matching microstrip loads and attenuators, *IRE Trans. Microwave Theory Tech.*, Vol. MTT-9, p. 263, May 1961.
- [75] J. S. Izadian and S. M. Izadian, *Microwave Transition Design*. Norwood, MA: Artech House, 1988.
- [76] E. Smith, Transitions to microwave integrated circuits, *Commun. Int.*, pp. 22–26, July 1979.
- [77] R. L. Eisenhart, A better microstrip connector, *IEEE MTT—S Int. Microwave Symp. Dig.*, pp. 318–320, 1979.
- [78] S. O. Ajose and N. A. Mathews, Equivalent circuit of coaxial-to-microstrip connector over the 8–12 GHz range, *Electron. Lett.*, Vol. 13, No. 16, pp. 465–466, 1977.
- [79] B. Bianco, M. Parodi, S. Ridella, and F. Selvaggi, Launcher and microstrip characterization, *IEEE Trans. Instrum. Meas.*, Vol. IM-25, pp. 320–323, 1976.
- [80] B. Golja, H. B. Sequeira, S. Duncan, G. Mendenilla, and N. E. Byer, A. coplanar-to-microstrip transition for W-band circuit fabrication with 100- μ m-thick GaAs wafers, *IEEE Microwave Guided Wave Lett.*, Vol. 3, pp. 29–31, Feb. 1993.
- [81] J. H. C. van Heuven, A new integrated waveguide–microstrip transition, *IEEE Trans. Microwave Theory Tech.*, Vol. MTT-24, pp. 144–147, Mar. 1976.

Microstrip Line Components

Suspended-Substrate Technique

U. Bochtler and F. M. Landstorfer

I. Basics

Although microstrip technology is adequate for the majority of transmission line applications in the microwave range, suspended substrate technology offers some advantages when it comes to losses and dispersion characteristics.

Figure 1 shows the cross section of a single transmission line using the suspended substrate technique. In contrast to conventional microstrip lines, suspended substrate lines can essentially be regarded as a coaxial arrangement with the substrate supporting the inner strip conductor and the outer conductor being formed by the supporting case.

Only a small part of the electrical and magnetic field extends into the dielectric, whereas the dominating part is encountered in the air region. Hence, dielectric losses are small and the propagation is essentially TEM, which means low dispersion. In addition, inhomogeneities in the dielectric constant of the substrate material have comparatively little influence on the line characteristics.

To give a comparison, Figure 2 shows attenuation constants for two typical microwave lines using different technologies (substrate, $\text{DK} = 10.8$; $\tan \delta = 0.002$ at 10 GHz). Both lines have a characteristic impedance of 50Ω , and the dimensions of their cross sections are of the same order.

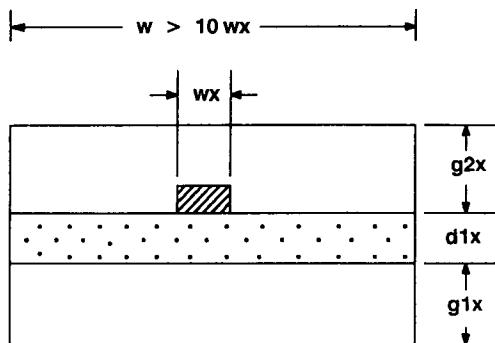


Figure 1. Suspended substrate single line.

The losses taken into consideration are

- losses in the metallization and
- losses caused by the dielectric

These values are obtained by a computation based on a quasielectrostatic approach using the method of moments [1] with pulses as base functions and point matching for testing. Losses with lines using suspended substrate technology are obviously considerably lower than those obtained with the conventional microstrip.

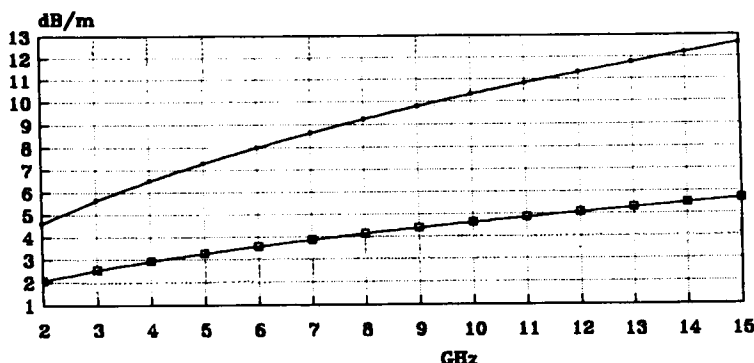


Figure 2. Attenuation constants of microstrip (●) and suspended substrate (□) lines (characteristic impedance, 50Ω).

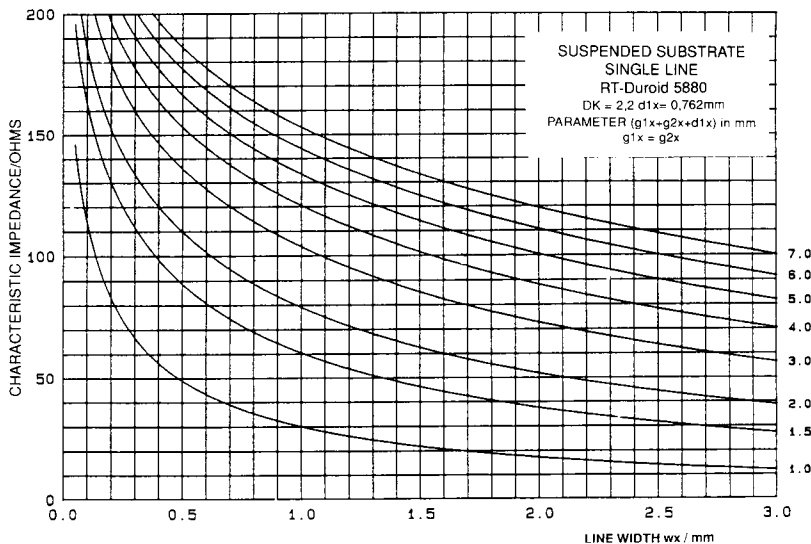


Figure 3. Characteristic impedance of a suspended substrate single line (substrate, RT 5880).

2. Parameters for Single Lines

A single-line configuration is characterized by its characteristic impedance and its effective dielectric constant or permittivity ϵ_{eff} (or phase velocity). The following values were computated using Smith's theory [2], which is based on a variational method. Figures 3–6 show the characteristic impedance, and Figures 7–10 report the effective permittivity for substrates often used. To avoid a field distortion by the sidewalls the width, w , of the housing is assumed to be greater than $10 wx$ (Figure 1).

3. Parameters for Coupled Lines

Coupled lines are commonly used to realize components such as directional couplers and interdigital filters. The following data are given for the case of two identical coupled lines using the suspended substrate technique as depicted in Figure 11. They were obtained by evaluating equations from Smith [2].

It is customary to describe the properties of such lines by their characteristics in even- and odd-mode propagation. Figure 12 shows the

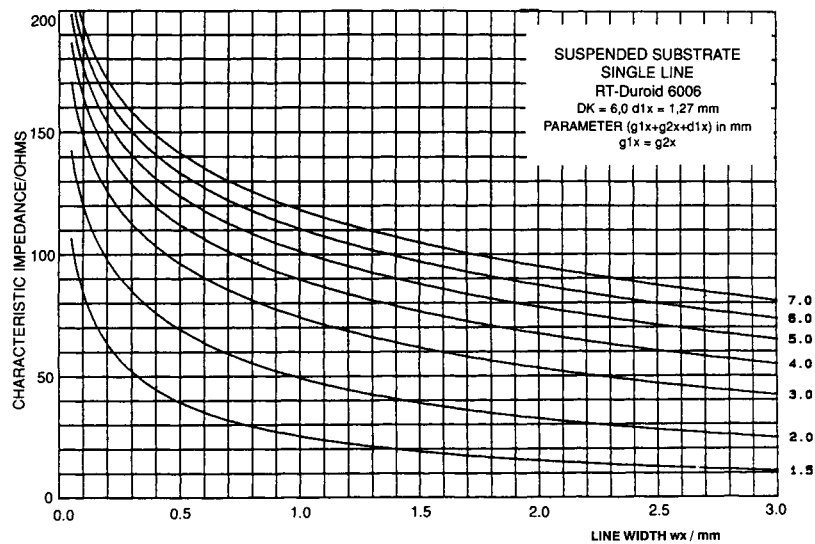


Figure 4. Characteristic impedance of a suspended substrate single line (substrate, RT 6006).

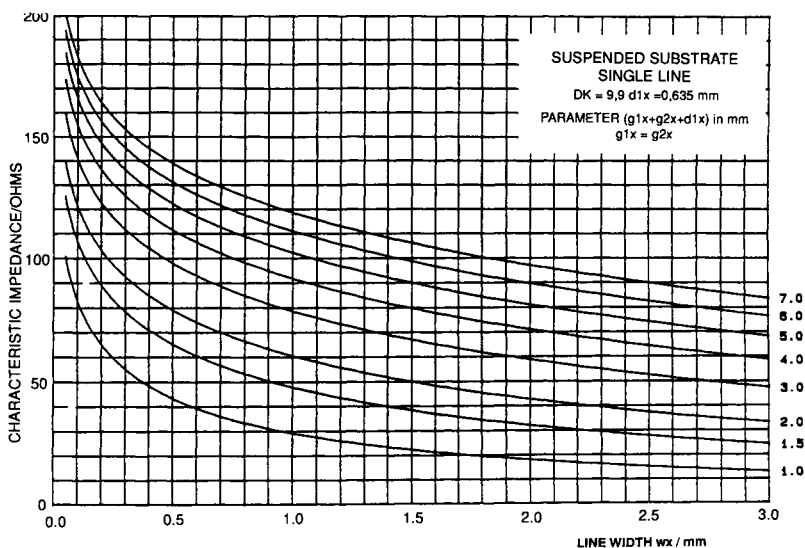


Figure 5. Characteristic impedance of a suspended substrate single line (substrate, AL203).

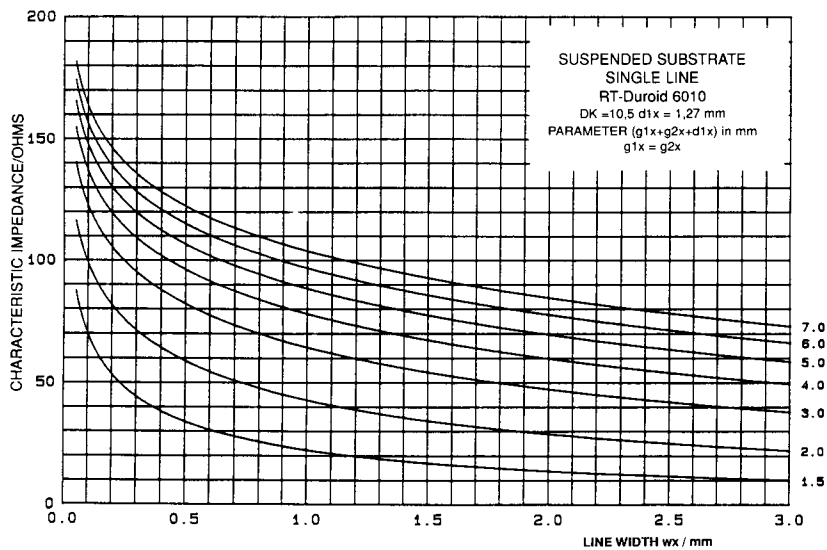


Figure 6. Characteristic impedance of a suspended substrate single line (substrate, RT 6010).

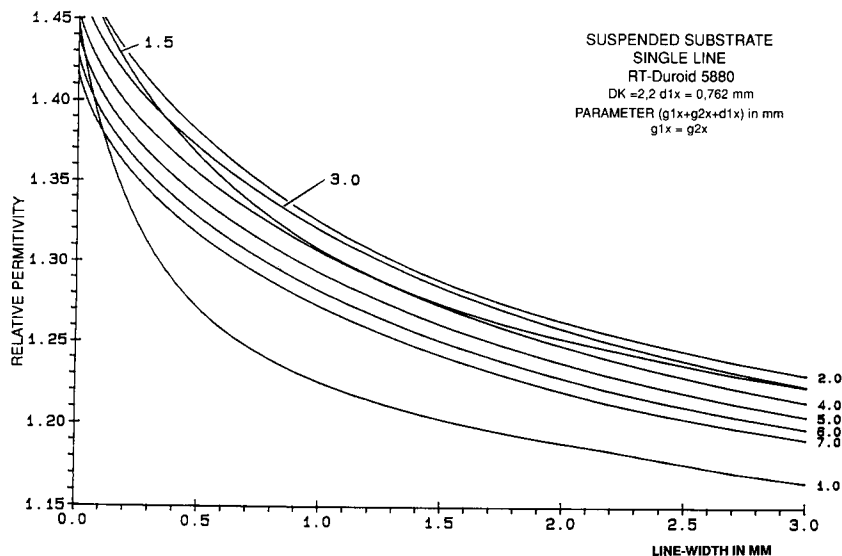


Figure 7. Relative permittivity of a suspended substrate single line (substrate, RT 5880).

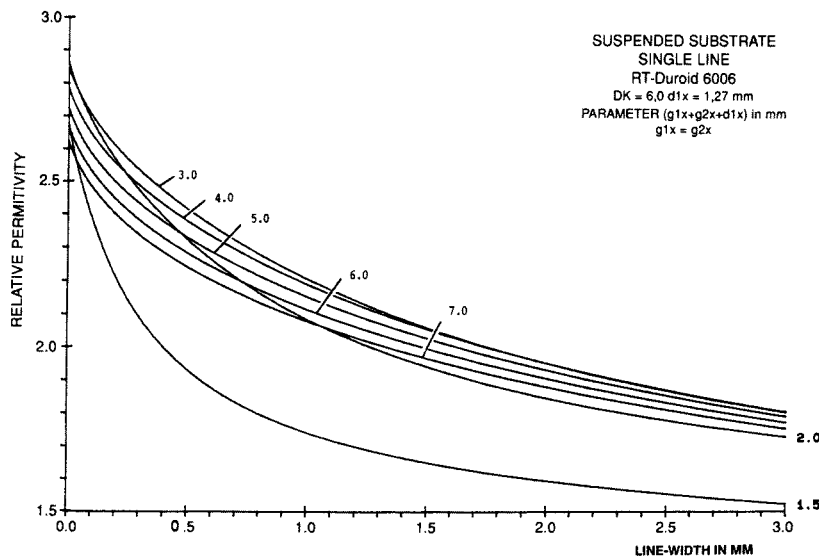


Figure 8. Relative Permittivity of a suspended substrate single line (substrate, RT 6006).

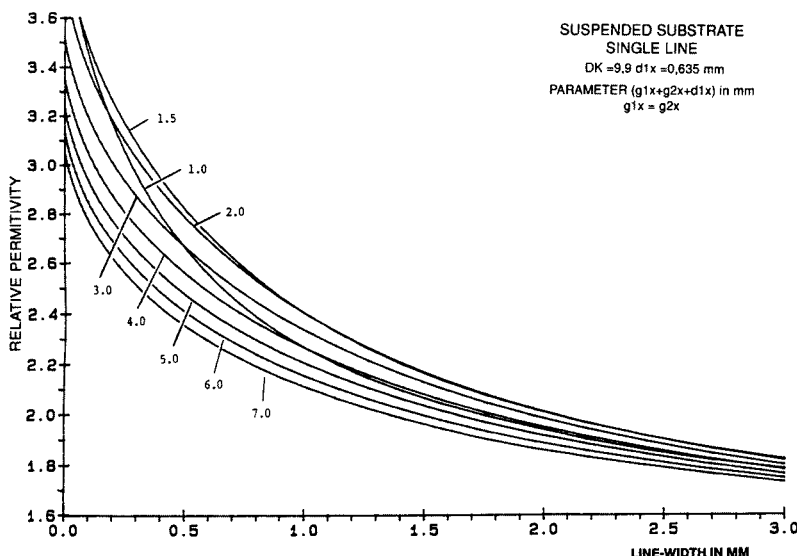


Figure 9. Relative Permittivity of suspended substrate single line (substrate, AL203).

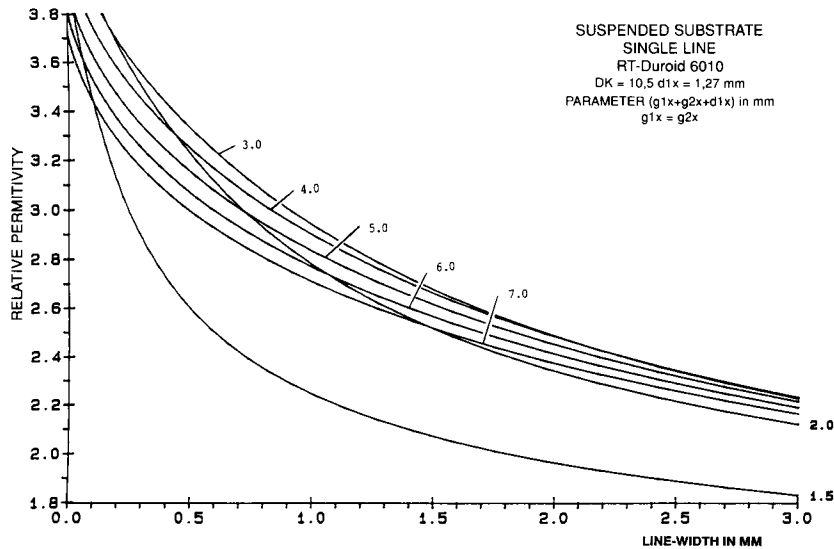


Figure 10. Relative Permittivity of a suspended substrate single line (substrate, RT 6010).

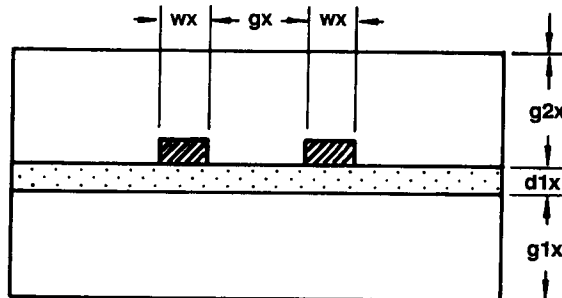


Figure 11. Suspended substrate coupled lines.

electric field lines for even and odd-mode excitation. The even- and odd-mode impedances of suspended substrate coupled lines are presented in Figures 13–15. It follows from Figure 12 that a greater part of the field occurs within the dielectric in the odd mode than in the even mode. Hence, we expect higher values of relative permittivity for the former, which is also validated by Figures 16–18. However, the effect is less pronounced than and contrary to that found with coupled conventional

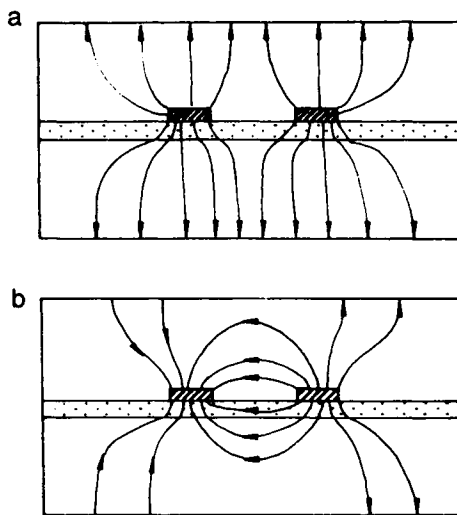


Figure 12. Coupled lines. E-field distribution in even (a) and odd (b) Modes.

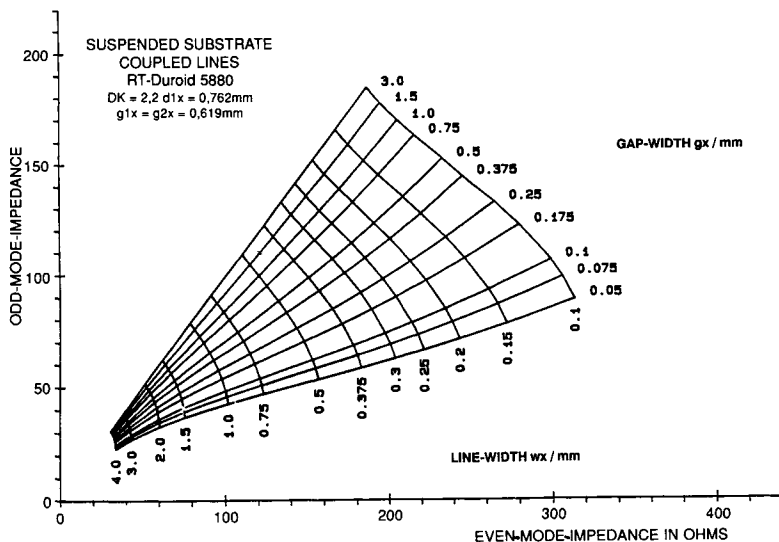


Figure 13. Even- and odd-mode impedances of suspended substrate coupled lines (substrate, RT 5880).

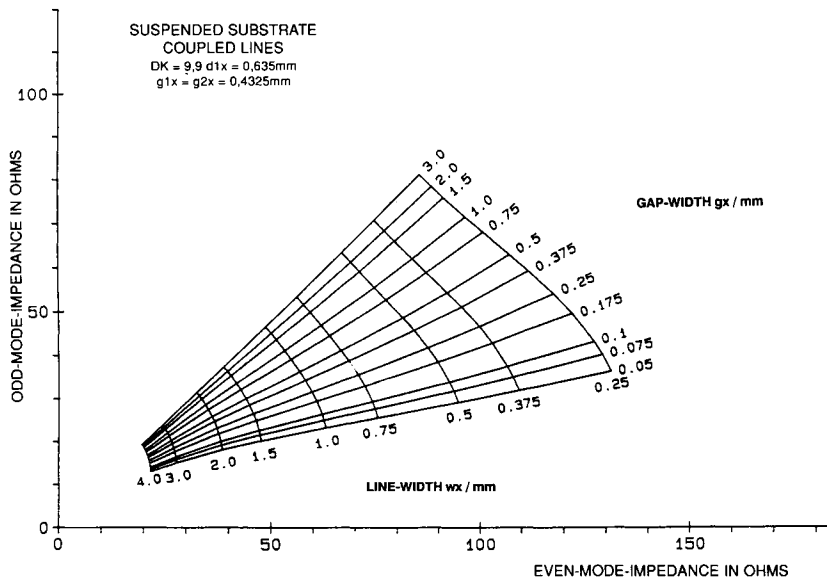


Figure 14. Even- and odd-mode, impedances of suspended substrate coupled lines (substrate, AL203).

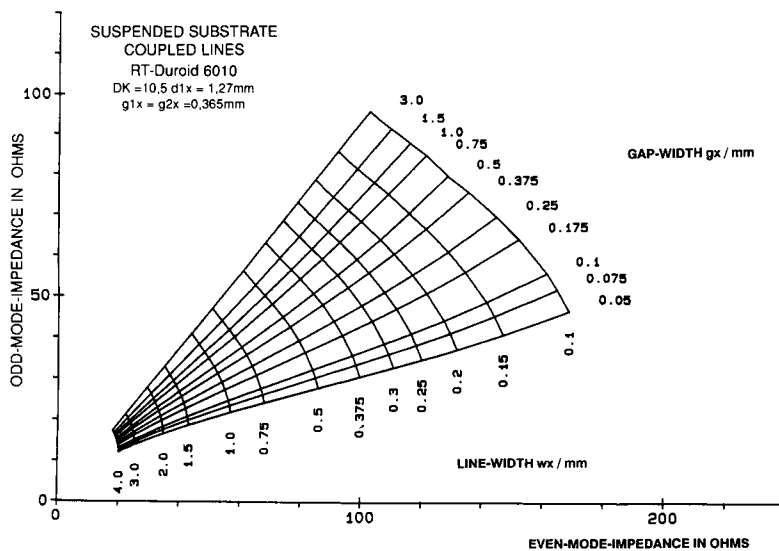


Figure 15. Even- and odd-mode impedances of suspended substrate coupled lines (substrate, RT 6010).

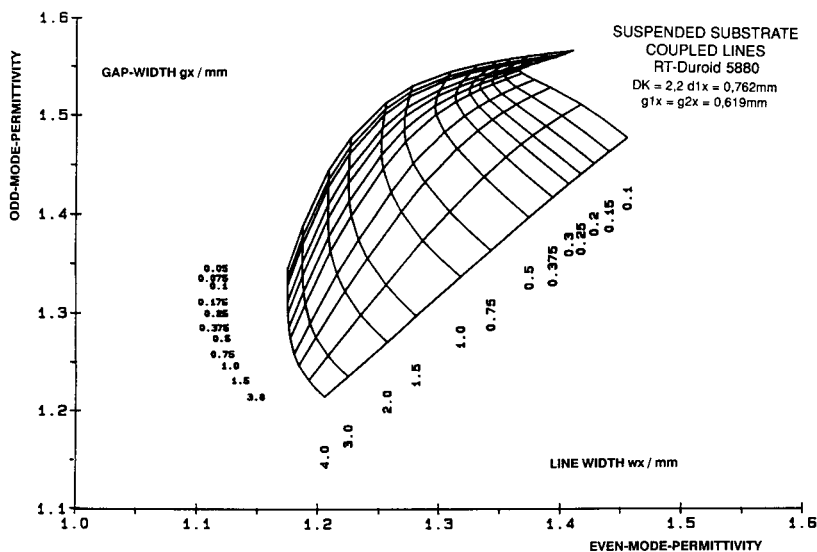


Figure 16. Even- and odd-mode permittivities of suspended substrate coupled lines (substrate, RT 5880).

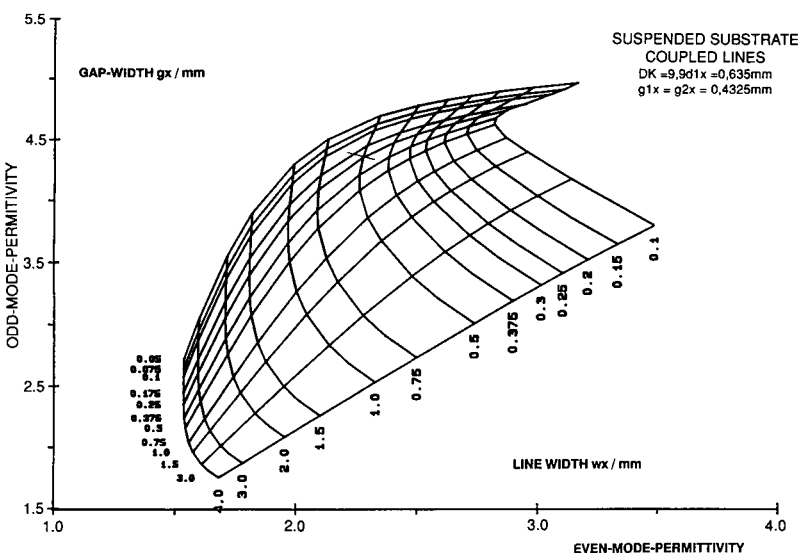


Figure 17. Even- and odd-mode permittivities of suspended substrate coupled lines (substrate, AL 203).

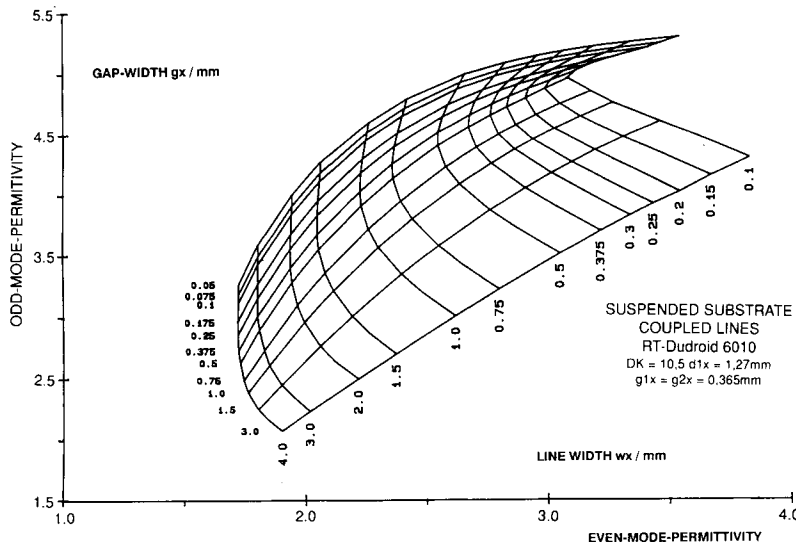


Figure 18. Even- and odd-mode permittivities of suspended substrate coupled lines (substrate, RT 6010).

microstrip lines. Nevertheless, the resulting difference in phase velocities should be taken into account [3] when designing components such as directional couplers.

References

- [1] A. Djordjevic, R. F. Harrington, T. Sarkar, and M. Bazdar, *Matrix Parameters for Multiconductor Transmission Lines*. Norwood, MA: Artech House, 1989.
- [2] J. Smith, The even- and odd-mode capacitance parameters for coupled lines in suspended substrate, *IEEE Trans. Microwave Theory Tech.*, Vol. MTT-19, pp. 424–431, 1971.
- [3] D. Kajfez, Effect of difference in odd- and even-mode wavelengths on a parallel-coupled bandpass filter, *Electron. Lett.*, Vol. 11, pp. 117–118, 1975.

Additional Sources

- Bochtler, U., and F. Endress, CAD program designs stripline couplers, *Microwaves RF*, Vol. 23, pp. 91–95, 1986.
- Brenner, H., Use a computer to design suspended-substrate ICs, *Microwaves*, Vol. 7, pp. 38–45, Sept. 1968.
- Bryant, T., Parameters of microstrip transmission lines and coupled pairs of microstrip lines, *IEEE Trans. Microwave Theory Tech.*, Vol. MTT-36, pp. 1021–1027, 1988.

- Denlinger, E. J., Losses of microstriplines, *IEEE Trans. Microwave Theory Tech.*, Vol. MTT-28, pp. 513–522, 1980.
- Easter, B., Parallel-coupled-line filters for inverted-microstrip and suspended-substrate MIC's, *Proc. 11th Eur. Microwave Conf., Kent*, pp. 164–170, 1981.
- Getsinger, W., Coupled rectangular bars between parallel plates, *IEEE Trans. Microwave Theory Tech.*, Vol. MTT-10, pp. 65–73, 1962.
- Ghione, G., and C. Naldi, Analytical formulas for coplanar lines in hybrid and monolithic MICs, *Electron. Lett.*, Vol. 20, pp. 179–181, 1984.
- Ghione, G., and C. Naldi, Parameters of coplanar waveguides with lower ground plane, *Electron. Lett.*, Vol. 19, pp. 734–735, 1983.
- Ghione, G., and C. Naldi, Coplanar waveguides for MMIC applications: Effect of upper shielding, conductor backing, finite-extent ground planes, and line-to-line coupling, *IEEE Trans. Microwave Theory Tech.*, Vol. MTT-35, pp. 260–267, 1987.
- Haffa, S., D. Holliman, and W. Wiesbeck, The finite difference method for S-parameter calculation of arbitrary three-dimensional structures, *IEEE Trans. Microwave Theory Tech.*, Vol. MTT-40, pp. 1602–1610, Aug. 1992.
- Hoffman, R., *Integrierte Mikrowellenschaltungen*. Berlin: Springer-Verlag, 1983.
- Howe, H., Jr., *Stripline Circuit Design*. Dedham, MA: Artech House, 1974.
- Howe, H., Jr., Synthesis of a class of strip-line filters, *IRE Trans. Circuit Theory*, Vol. CT-6, pp. 104–109, June 1958.
- Itoh, T., Overview of quasi-planar transmission lines, *IEEE Trans. Microwave Theory Tech.*, Vol. MTT-37, pp. 275–280, 1989.
- Jones, E., Coupled-strip-transmission-line filters and directional couplers, *IEEE Trans. Microwave Theory Tech.*, Vol. MTT-4, pp. 75–81, 1956.
- Kammler, D. W., Calculation of characteristic admittances and coupling coefficients for strip transmission lines, *IEEE Trans. Microwave Theory Tech.*, Vol. MTT-16, pp. 925–937, 1968.
- Kessler, A., A. Vlcek, A. and O. Zinke, Methoden zur Bestimmung von Kapazitäten unter besonderer Berücksichtigung der Teilflächenmethode, *Arch. Elektr. Übertragungstechn.*, Vol. 16, pp. 365–380, 1962.
- Kobayashi, M., and N. Sawada, Analysis and synthesis of tapered microstrip transmission lines, *IEEE Trans. Microwave Theory Tech.*, Vol. MTT-40, pp. 1642–1646, Aug. 1992.
- Ozaki, H., and J. Ishii, Synthesis of a class of strip-line filters, *IRE Trans. Circuit Theory*, Vol. CT-6, pp. 104–109, June 1958.
- Pregla, R., and S. G. Pintzos, Determination of the propagation constants in coupled microslots by a variational method, *Conf. Proc. 20th Eur. Microwave Conf. Budapest*, Vol. 2, p. 935, 1990.
- Tripathi, V. K., Asymmetric coupled transmission lines in an inhomogenous medium, *IEEE Trans. Microwave Theory Tech.*, Vol. MTT-23, pp. 734–739, 1975.
- Weeks, W. T., Calculation of coefficients of capacitance of multiconductor transmission lines in the presence of a dielectric interface, *IEEE Trans. Microwave Theory Tech.*, Vol. MTT-18, pp. 35–43, Jan. 1970.
- Wong, K. L., Y. T. Cheng, and J. S. Row, Resonances in a substrate-loaded cylindrical-rectangular microstrip-structure, *IEEE Trans. Microwave Theory Tech.*, Vol. MTT-41, pp. 814–819, May 1993.
- Yamashita, E., and R. Mittra, Variational method for the analysis of microstrip lines, *IEEE Trans. Microwave Theory Tech.*, Vol. MTT-16, pp. 251–256, 1968.
- Zhu, L., and E Yamashita, Full wave boundary integral equation method for suspended planar transmission lines, *IEEE Trans. Microwave Theory Tech.*, Vol. MTT-41, pp. 478–483, Mar. 1993.

Microwave Filters

Randall W. Rhea

I. Historical Perspective

Modern filters can be traced back to 1915, when Wagner in Germany and Campbell in the United States working independently proposed the filter. Previously selectivity was provided by a single series or shunt resonator. In 1923, Zobel at Bell Laboratories published a method for filter design using simple mathematics. His approximate "image parameter" technique was the only practical filter design method used for decades.

Around 1940, Darlington and Cauer published theories on the exact synthesis of networks to prescribed transfer functions. Due to heavy computational requirements, these methods remained primarily academic until digital computers were used to synthesize low-pass "prototypes." Although in practical use since the 1950s, this method is referred to as modern filter theory since it is the most recent of the triad of techniques. Over the last several decades, modern filter theory has been significantly embellished by many contributors.

The filter designer's library should include at least these three general references. *Handbook of Filter Synthesis* [30] which is extensive, *Electronic Filter Design Handbook* [28], which is easily read and current, and *Microwave Filters, Matching Networks and Coupling Structure* [15], which has excellent microwave coverage.

2. The Low-Pass Prototype

The ideal filter passes all desired passband frequencies with no attenuation and no phase shift, or at least linear phase, and totally rejects all

stop-band frequencies. The transition between pass and stop bands is sudden. This zonal filter is nonexistent. Modern filter theory begins with a finite-order polynomial transfer function to approximate the ideal response. Approximations are named after mathematicians credited with the development of the polynomial, such as Butterworth, Chebyshev, Bessel, etc. Increasing polynomial order results in a more zonal (selective) response.

A low-pass prototype is created when a low-pass filter is synthesized from a transfer function polynomial [28, pp. 1–3]. This prototype filter, normalized to 1Ω and 1 radian cutoff, has series inductors in henries and shunt capacitors in farads. Designing a specific low-pass filter is accomplished by simply scaling these prototype values (g -values) by the desired resistance and cutoff frequency. Designing high-pass, band-pass, distributed, helical, distributed, and other filters involves a transformation in addition to the scaling.

Butterworth Approximation

A fifth-order Butterworth low-pass prototype is shown in Figure 1. The amplitude response for a fifth-order Butterworth low-pass prototype is given as curve B in Figure 2. The attenuation monotonically increases in both the pass and the stop bands. The Butterworth attenuation is

$$L_a = 10 \log \left[1 + \left(\frac{f}{f_c} \right)^{2N} \right], \quad (1)$$

where n is the order, f is the frequency of interest, and f_c is the 3.01-dB

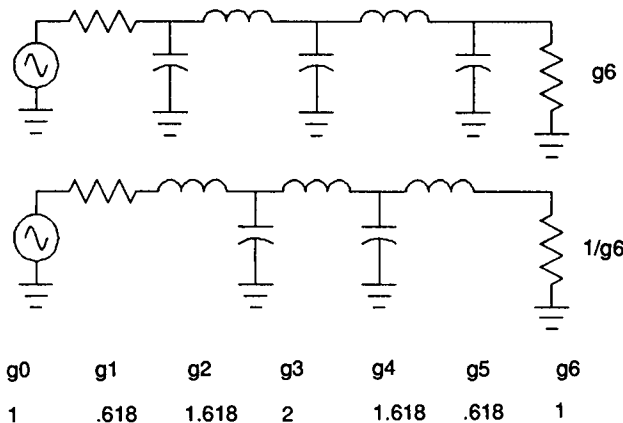


Figure 1. Low-pass prototype example of the fifth order with g -values for a Butterworth function.

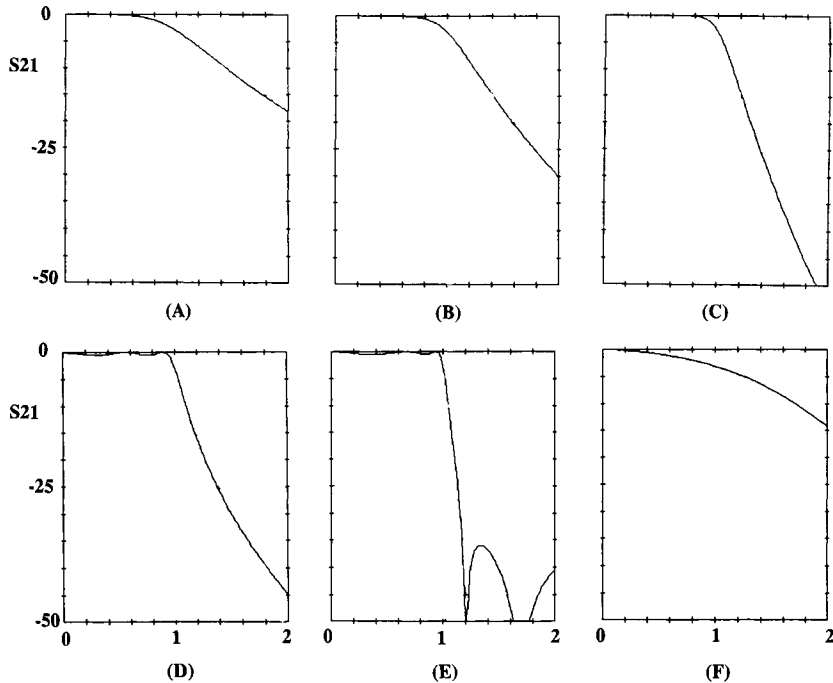


Figure 2. Amplitude responses of various low-pass filters with a cutoff frequency of 1 MHz. Curves A, B, and C are Butterworth prototypes of the third, fifth, and seventh orders, respectively. Curve D is a 0.5-dB ripple Chebyshev prototype of the fifth order. Curve E is a 0.5-dB ripple, 36-dB A_{\min} Cauer – Chebyshev prototype of the fifth order and curve F is a fifth-order Bessel prototype

cutoff frequency. In the lower portion of the pass band, the attenuation is nil and therefore the return loss is excellent.

Curves A and C in Figure 2 are Butterworth responses of the 3rd and 9th orders, respectively. Given in Table 1 are Butterworth prototype values to the 15th order. There are $N + 2$ g -values in the prototype. N -reactive values; g_0 , the normalized input termination resistance; and g_{N+1} , the normalized output termination resistance.

Scaling Prototype Values

The prototype g -values are scaled (denormalized) to the desired filter termination resistance and cutoff frequency as follows:

$$L = \frac{gR}{\omega} \quad (2)$$

$$C = \frac{g}{\omega R}, \quad (3)$$

TABLE I
Butterworth Low-Pass Prototype g -Values

N	g_0	g_1	g_2	g_3	g_4	g_5	g_6	g_7	g_8	g_9	g_{10}	g_{11}	g_{12}	g_{13}	g_{14}	g_{15}	g_{16}
1	1	2.000	1														
2	1	1.414	1.414	1													
3	1	1.000	2.000	1.000	1												
4	1	0.765	1.848	1.848	0.765	1											
5	1	0.618	1.618	2.000	1.618	0.618	1										
6	1	0.518	1.414	1.932	1.932	1.414	0.518	1									
7	1	0.445	1.247	1.802	2.000	1.802	1.247	0.445	1								
8	1	0.390	1.111	1.663	1.962	1.962	1.663	1.111	0.390	1							
9	1	0.347	1.000	1.532	1.879	2.000	1.879	1.532	1.000	0.347	1						
10	1	0.313	0.908	1.414	1.782	1.975	1.975	1.782	1.414	0.908	0.313	1					
11	1	0.285	0.831	1.310	1.683	1.919	2.000	1.919	1.683	1.310	0.831	0.285	1				
12	1	0.261	0.765	1.218	1.587	1.848	1.983	1.983	1.848	1.587	1.218	0.765	0.261	1			
13	1	0.241	0.709	1.136	1.497	1.771	1.942	2.000	1.942	1.771	1.497	1.136	0.709	0.241	1		
14	1	0.224	0.661	1.064	1.414	1.693	1.888	1.987	1.987	1.888	1.693	1.414	1.064	0.661	0.224	1	
15	1	0.209	0.618	1.000	1.338	1.618	1.827	1.956	2.000	1.956	1.827	1.618	1.338	1.000	0.618	0.209	1

where $\omega = 2\pi f$. After scaling, the filter input termination resistance is R ohms, and the output termination impedance is R times g_{N+1} . Since g_0 equals g_{N+1} in the Butterworth prototype table, the input and output termination resistances are equal.

Low-Pass Filter Example

Nearly all of the computational effort of low-pass filter design is stored in the low-pass prototype. All that remains to design a specific low-pass filter is scaling. Consider a fifth-order, 2300-MHz-cutoff Butterworth low-pass filter with the first element a series inductor. Using Equation (2),

$$L_1 = \frac{g_1 50}{2\pi 2.3 \times 10^9} = 2.14 \text{ nH}. \quad (4)$$

Likewise, L_3 is 6.92 nH and L_5 is 2.14 nH. Using Equation (3), C_2 is 2.24 pF and C_4 is 2.24 pF. Notice that Butterworth filter values are symmetric.

Chebyshev Approximation

The amplitude response for a fifth-order Chebyshev approximation is given as curve D in Figure 2. The pass band of the Chebyshev approximation has amplitude response ripple, in this case 0.5 dB. This also results in pass-band return loss ripple. The attenuation ripple, R_{dB} , and the return loss, RL_{dB} , are related as

$$RL_{\text{dB}} = -10 \log(10^{R_{\text{dB}}/10} - 1). \quad (5)$$

Greater ripple results in better selectivity, so the Chebyshev approximation offers a compromise between pass-band ripple and selectivity. The Butterworth prototype and 0-dB ripple Chebyshev approximation are identical.

The number of occurrences of zero slope in the Chebyshev pass-band response is equal to the order and number of reactive elements in the Chebyshev prototype, as is evidenced in Figure 2. This dictates that an even-order Chebyshev response has dc attenuation equal to the pass-band ripple. At dc the inductors and capacitors in a low-pass filter effectively vanish; so how does dc attenuation occur? The answer is by mismatch attenuation. The resistances terminating an even-order true Chebyshev response cannot be equal! The terminating resistance ratio increases with increasing ripple.

The Chebyshev cutoff corner is defined by Williams and Taylor [28] and Zverev [30] as 3.01-dB attenuation and by Matthaei *et al.* [15] as ripple attenuation. The former is consistent with the Butterworth definition, whereas the latter is consistent with a system performance viewpoint for which return loss is an important specification.

With the cutoff attenuation defined as the ripple value, the low-pass prototype g -values are [15, p. 99]

$$g_0 = 1 \quad (6)$$

$$g_1 = \frac{2a_1}{\gamma} \quad (7)$$

$$g_n = \frac{4a_{n-1}a_n}{b_{n-1}g_{n-1}}, \quad (8)$$

where

$$\beta = \ln\left(\coth \frac{R_{\text{dB}}}{17.37}\right) \quad (9)$$

$$\gamma = \sinh\left(\frac{\beta}{2N}\right) \quad (10)$$

$$a_n = \sin\left[\frac{(2n-1)\pi}{2N}\right] \quad (11)$$

$$b_n = \gamma^2 + \sin^2\left(\frac{n\pi}{N}\right). \quad (12)$$

For N odd,

$$g_{N+1} = 1. \quad (13)$$

For N even,

$$g_{N+1} = \coth^2\left(\frac{\beta}{4}\right). \quad (14)$$

Tables of Chebyshev prototype values are given in many filter references. Because there are an infinite number of Chebyshev prototypes and computation is now economic, formulas lessen the usefulness of Chebyshev tables.

Controlled Phase Prototypes

The Butterworth and Chebyshev transmission phase shift is not linear with frequency, but increases as the corner is approached. The nonlinear phase

causes objectionable distortion in certain system applications. Group delay is defined as

$$t_d = \frac{\partial\varphi}{\partial\omega}. \quad (15)$$

The linear phase results in flat group delay. The group delay of fifth-order Butterworth and that of 0.5-dB ripple Chebyshev low-pass responses are given in curves A and B, respectively, of Figure 3. Notice that group delay is asymptotically flat at DC but peaks near the cutoff. Much as a maximally flat amplitude response is approximated by the Butterworth response, a maximally flat group-delay response is approximated by the Bessel prototype. Bessel prototype values are given in Table 2. The group delay of a fifth-order Bessel prototype is given in curve C of Figure 3, and the amplitude response is curve F of Figure 2. As can be seen, the selectivity is extremely poor for the Bessel prototype, and the return loss is poor in much of the bass band. Also, selectivity improves little with increasing order.

As with the Chebyshev amplitude approximation, allowing linear-phase-error ripple improves selectivity. Equilinear phase-error prototypes are tabulated in Williams and Taylor [28, pp. 11–52]. Even with phase-error ripple, selectivity is far worse than Butterworth.

The amplitude and delay responses of minimum-phase networks are inseparably related. All passive ladder networks are minimum phase, and flat group delay is achieved only by sacrificing selectivity. This fundamental limitation may be circumvented by cascading nonladder all-pass networks

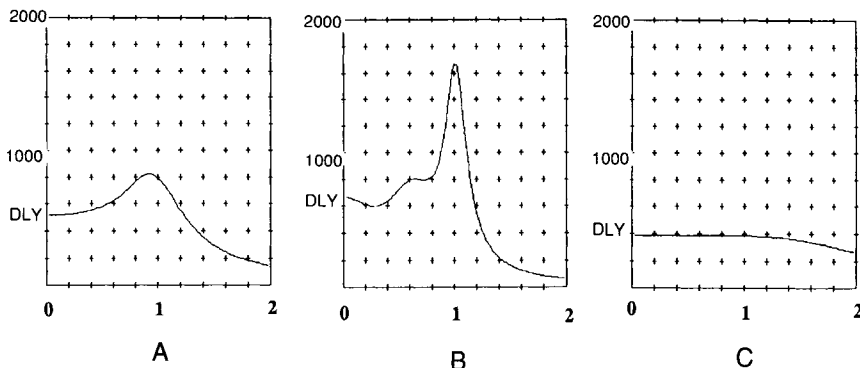


Figure 3. Group delay of various fifth-order low-pass filters with a cutoff frequency of 1 MHz. Curve A is a Butterworth prototype, curve B is a 0.5-dB ripple Chebyshev prototype, and curve C is a Bessel prototype.

TABLE 2
Bessel Low-Pass Prototype g -Values

N	g_0	g_1	g_2	g_3	g_4	g_5	g_6	g_7	g_8	g_9	g_{10}	g_{11}
2	1	0.576	2.148	1								
3	1	0.337	0.971	2.203	1							
4	1	0.233	0.673	1.082	2.240	1						
5	1	0.174	0.507	0.804	1.111	2.258	1					
6	1	0.136	0.400	0.639	0.854	1.113	2.265	1				
7	1	0.111	0.326	0.525	0.702	0.869	1.105	2.266	1			
8	1	0.919	0.272	0.441	0.594	0.730	0.870	1.096	2.266	1		
9	1	0.0780	0.231	0.377	0.511	0.631	0.741	0.864	1.086	2.265	1	
10	1	0.0672	0.200	0.327	0.445	0.553	0.649	0.742	0.856	1.078	2.264	1

with the filter [28, pp. 7–11], but circuit simplicity is severely compromised. Each all-pass section requires several components whose values are interdependent, making tuning difficult. A class of filters which are delay equalized to maximum flatness using a single all-pass section were developed by Rhea [18]. Selectivity for this filter class is near that of the Butterworth filter class.

Elliptic Approximations

The low-pass transfer approximations previously discussed are all pole; zeros of transmission occur only at infinite frequency. Series branches are inductive and shunt branches are capacitive. By incorporating a capacitor in parallel with series inductors or a series inductor with shunt capacitors, resonances which cause zeros of transmission at finite frequencies are formed. Responses with transmission zeros at finite frequencies are referred to as elliptic. They provide increased transition region steepness at the expense of attenuation well into the stop band.

The specific class of elliptic filters which have equal pass-band ripple and equal minimum attenuation peaks in the stop band is Cauer–Chebyshev. There are $(N - 1)/2$ finite-frequency transmission zeros and additional reactive elements in odd-order Cauer–Chebyshev prototypes and $(N - 2)/2$ finite-frequency transmission zeros in even-order prototypes. An elliptic low-pass prototype with 0.5 dB of pass-band ripple and 36-dB minimum attenuation in the stopband (A_{\min}) is given in Figure 4; the response is curve E in Figure 2. Extensive tables of Cauer–Chebyshev prototype values are given in Zverev [30, p. 168]. Equations (2) and (3) also scale elliptic prototype values.

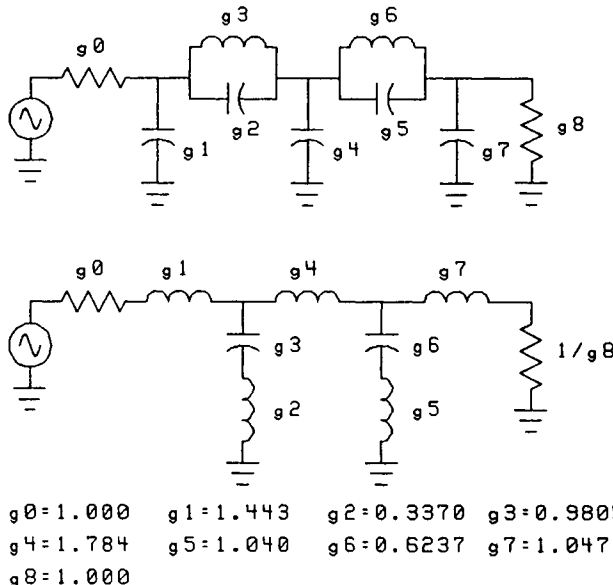


Figure 4. Low-pass prototype example of a fifth-order Cauer–Chebyshev function with g -values for 0.5-dB ripple and 36-dB A_{\min} .

3. L–C Filter Transformation

The design of high-pass filters requires a transformation in addition to scaling. This transformation is necessary to convert the low-pass prototype to a high-pass structure. Likewise, bandpass and bandstop filters require a structure transformation.

High-Pass Transformation

When $1/s$ is substituted for s in the low-pass transfer function, a high-pass response results. However, instead of synthesizing a high-pass prototype, it is only necessary to convert low-pass prototype inductors to capacitors by inverting the prototype values:

$$C_{hp} = \frac{1}{L_{lp}} \quad (16)$$

$$L_{hp} = \frac{1}{C_{lp}} \quad (17)$$

The high-pass filter consists of series capacitors and shunt inductors. This normalized high-pass filter is then scaled to the desired resistance and cutoff frequency using Equations (2) and (3).

All-Pole Bandpass Transformation

Bandpass filters are also designed by transformation of and scaling the low-pass prototype. Each low-pass prototype inductor is transformed into a series inductor and a series capacitor. Each prototype capacitor is transformed into a shunt inductor and a shunt capacitor. Therefore the bandpass has twice the number of reactive elements as the low-pass prototype. The bandpass transfer function has twice the order of the parent low-pass prototype. Shunning rigor, we will refer to the order of the bandpass as the order of the parent prototype.

For the bandpass, the lower cutoff frequency, f_{cl} , and the upper cutoff frequency, f_{cu} , are specified. We then define the center frequency, f_0 , the bandwidth, BW, and the fractional bandwidth, bw, as

$$f_0 = \sqrt{f_{cl} f_{cu}} \quad (18)$$

$$\text{BW} = f_{cu} - f_{cl} \quad (19)$$

$$\text{bw} = \frac{\text{BW}}{f_0}. \quad (20)$$

The percentage bandwidth is the fractional bandwidth multiplied by 100%. The transformed shunt element values are

$$C_{\text{bp shunt}} = \frac{C_{lp}}{\text{bw}} \quad (21)$$

$$L_{\text{bp shunt}} = \frac{1}{C_{\text{bp shunt}}}, \quad (22)$$

and the transformed series element values are

$$L_{\text{bp series}} = \frac{L_{lp}}{\text{bw}} \quad (23)$$

$$C_{\text{bp series}} = \frac{1}{L_{\text{bp series}}}, \quad (24)$$

where C_{lp} is a low-pass prototype capacitor g-value and L_{lp} is a low-pass prototype inductor g-value.

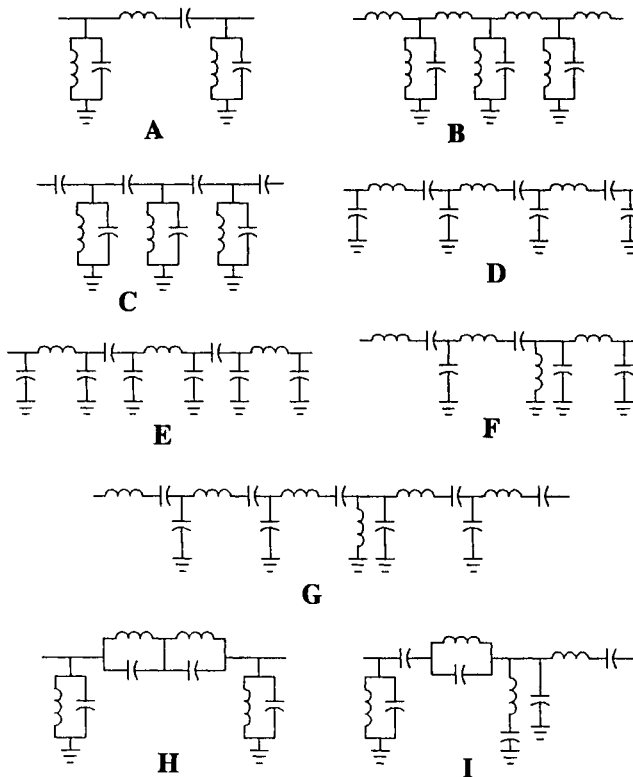


Figure 5. Conventional (A), approximate narrow-band (B–E), Blinchikoff (F), symmetric transform (G), and elliptic (H and I) bandpass filter structures.

The normalized bandpass values are scaled to the desired resistance and frequency using the denormalizing equations in Section 2, with f_0 as the frequency variable. The bandpass filter structure which results from the transformation of a third-order low-pass prototype is given in Figure 5a.

Bandstop Filter Transform

The bandstop filter has a series inductor and capacitor in shunt to ground for each shunt capacitor in the low-pass prototype and a parallel inductor–capacitor in series for each series inductor in the prototype. The

transformed shunt element values are

$$L_{\text{bs shunt}} = \frac{1}{C_{\text{lp bw}}} \quad (25)$$

$$C_{\text{bs shunt}} = \frac{1}{L_{\text{bp shunt}}}, \quad (26)$$

and the transformed series element values are

$$C_{\text{bs series}} = \frac{1}{L_{\text{lp bw}}} \quad (27)$$

$$L_{\text{bs series}} = \frac{1}{C_{\text{bp series}}}. \quad (28)$$

The normalized bandstop values are scaled to the desired resistance and frequency using the denormalizing equations in Section 2, with f_0 as the frequency variable.

Narrow-Band Bandpass Transforms

The bandpass transform involves simple mathematics, results in “exact” component values, and possesses an easily calculated amplitude response. Despite these desirable attributes, examination of Equations (21)–(24) reveals that, as the fractional bandwidth is decreased, the ratio of inductor values and the ratio of capacitor values in the bandpass become extreme. This results in realization difficulty, and, below about 10% bandwidth, the conventional bandpass transform becomes impractical.

To overcome this and other problems which will be discussed, a number of other bandpass transformations have been developed. These transformations typically yield only approximate component values. However, they have desirable performance or realization attributes.

Top-C-Coupled, Parallel Resonators

One such structure is given in Figure 5c. All resonators are parallel L–C in shunt. These resonators are coupled to each other and externally using series capacitors. All inductors are of equal value. Furthermore, the external coupling reactors control the internal filter impedance level, and a specific inductor value may be chosen. This degree of freedom and a single resonator form significantly enhance realizability.

At frequencies well above the passband, the shunt inductors effectively vanish and the coupling and resonator capacitors form cascaded voltage dividers. As the bandwidth is increased, the coupling capacitors become larger, the voltage dividers provide little attenuation, and selectivity and ultimate rejection above the passband are poor. Conversely, the series coupling capacitors and shunt inductors result in excellent selectivity and ultimate rejection below the passband.

Design equations are given in Matthaei *et al* [15, p. 482]. Matthaei's expressions were manipulated to be consistent with our previous normalized bandpass terminology. Design begins with the selection of the normalized inductance of the inductors. For example, for a filter terminating in 50Ω , choosing $100\text{-}\Omega$ reactance inductors yields $L = 2$. Then the total node capacitance at each resonator, C_t , is

$$C_t = \frac{1}{L}. \quad (29)$$

The coupling capacitors are then

$$C_{n,n+1} = \text{bw} \frac{C_t}{\sqrt{g_n g_{n+1}}}, \quad (30)$$

where n indexes the shunt resonators sequentially and ranges from 1 to N . The input coupling capacitor is

$$C_{01} = \frac{J_{01}}{\sqrt{1 - (R_a J_{01})^2}}, \quad (31)$$

where

$$J_{01} = \sqrt{\frac{C_t \text{bw}}{g_0 g_1}}. \quad (32)$$

$C_{N,N+1}$ is found using the same expressions with the appropriate indexes. R_a and R_b are the normalized input and output terminating resistance, respectively, typically 1.

The actual capacitance placed in parallel with each inductor is the total node capacitance, C_t , minus the coupling capacitors connected to that node. Internal coupling capacitors are used directly, whereas external coupling capacitors and their terminating resistances are first converted to parallel $R\text{-}C$ models to determine the node loading capacitances. There-

fore, the parallel capacitors are

$$C_1 = C_t - \frac{C_{01}}{(C_{01}^2 + 1)} - C_{12} \quad (33)$$

$$C_N = C_t - \frac{C_{N,N+1}}{(C_{N,N+1}^2 + 1)} - C_{N-1,N} \quad (34)$$

$$C_n = C_t - C_{n-1,n} - C_{n,n+1}. \quad (35)$$

The normalized resistance and reactive values are then scaled to the desired resistance and frequency as before.

The design expressions are approximate and errors increase with increasing bandwidth. For this reason, and because of the response asymmetry, this transform becomes unsuitable above about 20% bandwidth. Therefore, this and other similar structures are referred to as approximate narrow-band filters. Above about 5% bandwidth, correction factors due to Cohn [3, p. 187] and reviewed by Matthaei *et al.* [15, p. 481] are recommended.

The response of a fifth-order, 0.5-dB Chebyshev, 20% bandwidth filter of this type is given as curve A in Figure 6. Greater selectivity and group delay occur below the passband as previously discussed.

Top-L-Coupled, Parallel Resonators

When greater attenuation is required above the passband, the structure given in Figure 5b may be used. It is similar to the previous structure except that coupling inductors are used instead of coupling capacitors. The response is given as curve B in Figure 6. Design methods are similar to and may be deduced from top-C-coupled design methods [Equations (29)–(35)].

The top-C- and top-L-coupled structures are excellent narrow-band filters and provide alternatives when increased attenuation on either the low side or the high side of the passband is desired.

A disadvantage of these approximate narrow-band structures is poor economy. Notice that there are three elements for each reactive element in the low-pass prototype, plus an additional element. The two end coupling elements vanish with an appropriate parallel inductor value, but this may not be a desirable value from a realization viewpoint. One advantage of the top-C-coupled structure is that the number of inductors is minimized.

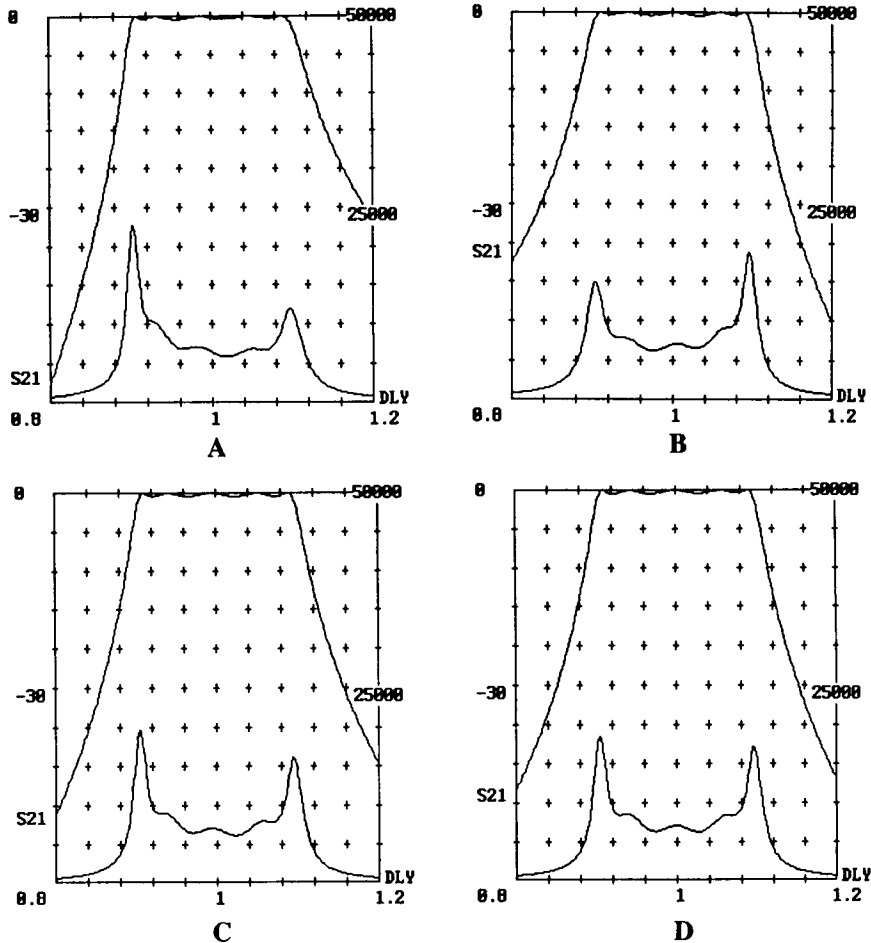


Figure 6. Amplitude and delay responses of top-C-coupled (A), top-L-coupled (B), conventional (C), and symmetric transform (D) bandpass filters with 20% bandwidth.

Shunt-C-Coupled, Series Resonators

An approximate narrow-band structure which provides increased attenuation above the passband while minimizing the number of inductors is given in Figure 5d. Design equations are again similar to those for the top-C-coupled filter. The response is essentially identical to the response of the top-L-coupled filter. The series resonators may be less desirable from a construction viewpoint because both ends of the inductor are above

the ground potential. Also, parasitic capacitance to the ground at the node between the series inductor and the capacitor can be problematic.

Tubular Structure

Floating nodes are eliminated in the series resonator structure by splitting the series capacitors into two series capacitors, one on each side of the series inductors. Then the T-networks of capacitors which are formed are converted to π -networks using the well-known T– π network equivalency. Design begins with the shunt-C-coupled series resonator equations. The resulting structure is given in Figure 5e and is the basis of commercially popular tubular bandpass filters. Placed within a tubular housing are large diameter slugs with their capacitance to the ground and each other and axially oriented series inductors on a dielectric support rod. The resulting structure is compact and relatively parasitic free with excellent stop-band characteristics.

Elliptic Bandpass Transforms

The previous bandpass transforms were applied to all-pole transfer function approximations. In the elliptic bandpass transformation, each finite transmission zero in the low-pass prototype results in two finite transmission zeros geometrically centered below and above the bandpass pass band.

Conventional Elliptic Bandpass

The physical structure resulting from the conventional elliptic bandpass transformation has a parallel $L-C$ in shunt for each low-pass prototype shunt capacitor and two parallel $L-C$ networks cascaded in series for each parallel $L-C$ in series low-pass prototype branches. The structure is given in Figure 5g. There is one inductor for each low-pass prototype branch plus an additional inductor for each low-pass prototype finite transmission zero.

Much like the conventional all-pole bandpass transformation, this structure has extreme ratios of element values with decreasing bandwidth. Also, the response is threatened by a parasitic capacitance to the ground at the floating node between the $L-C$ pairs in the series branch. Design equations for the elliptic bandpass transformation are given by Williams and Taylor [28, pp. 5–27].

Zig-Zag Transformation

Saal and Ulbrich [20] presented design equations for an improved elliptic bandpass transform which saves an inductor for each low-pass

prototype finite transmission zero. The transform is available only for even-order low-pass prototypes.

No bandpass structure provides more selectivity per inductor than the zig-zag. Removing an inductor from series branches also reduces the parasitic capacitance problem. Tuning is easier than that of the conventional elliptic transform because, when constructed with precision capacitors, tuning is accomplished by adjusting the internal inductors for the correct zero frequencies and finally adjusting the two end inductors.

A reason that the zig-zag is not more prevalent is that finding component values by manual calculation is not worthwhile. Williams and Taylor [28, pp. 8–16] give equations suitable for the fourth order, but at a higher order a computer is required. With economic computing today, this structure should become more popular.

4. Bandpass Transform Distortion

Arithmetic symmetry is often desired and results in group delay symmetry. Unfortunately, the conventional bandpass transform results in geometric amplitude symmetry and asymmetric group delay. None of the popular bandpass transforms result in arithmetic symmetry. Asymmetry worsens with increasing bandwidth.

All published bandpass transforms also distort the phase and group delay attributes of the low-pass transfer function. For example, a bandpass designed by transforming a Bessel low-pass function does not possess flat delay in the passband.

Arithmetic Symmetry

We have considered symmetry in the conventional, top-*C*-coupled and top-*L*-coupled bandpass transforms. The top-*C*-coupled filter gives greater attenuation below the passband and the top-*L*-filter gives greater attenuation above the passband. What structure would result in arithmetic symmetry? Carassa [2] proved that arithmetic symmetry in a bandpass structure is possible if the number of transmission zeros at infinite frequency is three times the number at DC (multiplicity ratio is 3 : 1).

The conventional bandpass, the conventional elliptic bandpass, and the zig-zag bandpass have an equal number of zeros at infinite frequency and DC. Therefore, the selectivity and group delay are greater below the passband. The multiplicity ratio for the top-*C*-coupled filter is 1:(2*N* + 1) which is far less than 3 : 1 and the structure has very poor symmetry. The multiplicity ratio is (2*N* + 1):1 for the top-*L*-coupled filter. This structure

has a multiplicity ratio of 3 : 1 for the trivial case of $N = 1$, but the ratio increases with increasing order and therefore has greater selectivity and group delay above the passband.

Rhea [17] proposed a structure which has a multiplicity ratio of 3 : 1 for even order and asymptotically approaches 3 : 1 with increasing odd order. A bandpass resulting from a sixth-order low-pass prototype using this transformation is given in Figure 5f. The amplitude and delay response of a fifth-order symmetric transform bandpass is given in Figure 6d. The symmetry of this transform is excellent to bandwidths as wide as 70%. The symmetry of conventional and approximate narrow-band filters at 70% bandwidth is much worse than the responses given in Figure 6 for 20% bandwidth.

Blinchikoff Flat Delay Bandpass

All published low-pass to bandpass transforms, including the symmetric transform just discussed, destroy the phase attributes of the low-pass function. As with symmetry, the destruction worsens with increasing bandwidth.

Recognizing the transform as the culprit, Blinchikoff and Savetman [1] synthesized a transfer function with nearly flat delay directly as a bandpass structure. The normalized values were published for second- and fourth-order filters with 30 to 70% bandwidth. The fourth-order structure is given in Figure 5g. Notice that the multiplicity ratio is 3 : 1. Although Blinchikoff published only second- and fourth-order values, a similar result for general order is obtained by beginning with the symmetric transformed Bessel low-pass function and optimizing the bandpass component values for flat delay.

5. Distributed Filters

Previously lumped element filters were considered. Next, transmission line (distributed) filter structures are considered. Practical distributed structures are designed by beginning with L - C structures and utilizing distributed equivalents of the lumped reactances. Other distributed filters are designed by beginning with the low-pass prototype and utilizing transforms specifically developed for distributed structures.

Lumped–Distributed Equivalents

The input impedance of a lossless transmission line shorted at the opposite end is reactive, and the magnitude is equal to the line characteristic

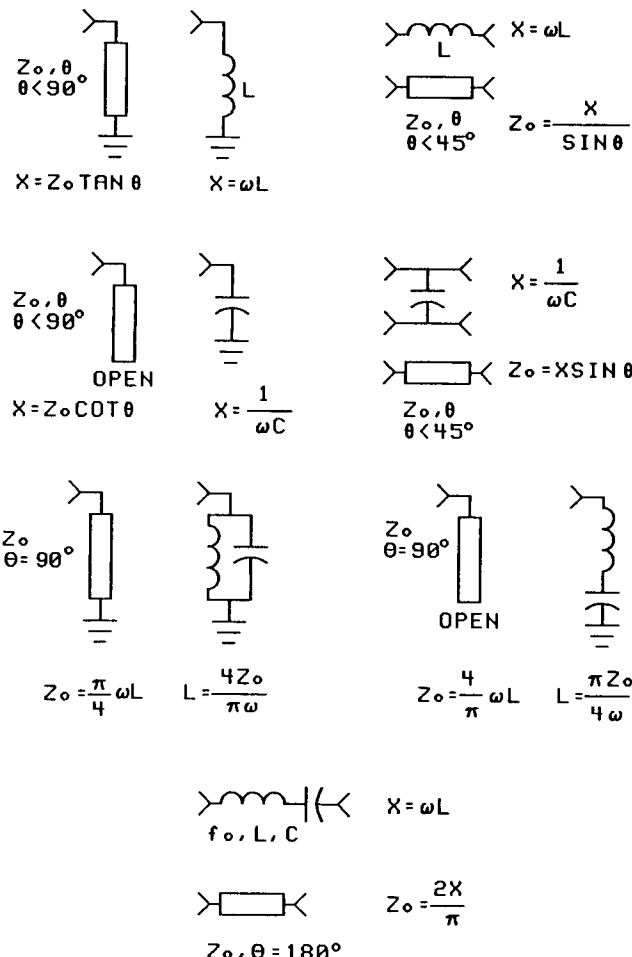


Figure 7. Lumped and distributed equivalent element relationships.

impedance times the tangent of the electrical length of the line. If the line length is less than 90° , the reactance is positive. If the electrical length is less than approximately 22° at the highest frequency of interest, the tangent function is nearly linear and the reactance increases linearly with frequency much like an inductor. This relation is depicted in Figure 7a.

A transmission line open at the opposite end looks much like a capacitor if the electrical length at the highest frequency is short. A series inductor is approximated by a short, high-characteristic-impedance, series transmission line, and a shunt capacitor is approximated by a short,

low-impedance, series transmission line. These relations are depicted in Figures 7b through 7d.

The above relations describe distributed and lumped single-element equivalents. A transmission line 90° long, shorted at the opposite end, possesses a high-impedance resonance much like a parallel $L-C$ resonator. At resonance, the behaviors of the lumped and distributed resonators are similar when the inductor reactance is $4/\pi$ times the characteristic impedance of the line. This is depicted in Figure 7e. Series resonators also have transmission-line equivalents to the ground and in series to the transmission path as shown in Figures 7f and 7g.

Distributed filter structures can be developed by replacing inductors, capacitors, resonators, or all three with distributed equivalents. If all lumped reactors are replaced, a purely distributed filter results. If only a portion of the reactors is replaced, a hybrid filter is created with both lumped and distributed elements. The radian frequency, ω , used for equivalent calculations in Figure 7, is the cutoff frequency for low-pass and high-pass filters and the center frequency for bandpass and bandstop filters.

Reentrance

Because transmission line behavior is trigonometric, it is harmonic. A shorted transmission line behaves like an inductor at low frequencies. At an electrical length of 90° , the shorted line resonates and possesses a high-input impedance, and, for longer lengths, the impedance is periodic and may be high, low, inductive, or capacitive. The passband of distributed filters may reoccur at frequencies as low as two or three times the initial passband frequency, severely compromising stopband attenuation.

Discontinuities

The realization of filters using distributed elements necessarily involves the interconnection of physical structures. At higher frequencies, discontinuities such as line ends, steps in line widths, bends, and T and cross junctions affect the behavior of these structures. Filter behavior is predicted by including lumped element discontinuity models in the overall structure.

Sufficiently accurate discontinuity models for practical filter development are known for popular processes such as microstrip, stripline, and coax; however, model accuracy is ultimately compromised with increasing operating frequency or physical size. Improved accuracy at higher frequencies and unusual geometries are simulated by electromagnetic modeling.

Electromagnetic simulation is orders of magnitude less computationally efficient than circuit simulation so both methods are important.

Stepped Impedance Low-Pass Filter

Shown in Figure 8a is a stepped impedance low-pass filter. It is realized in planar media by cascading narrow and wide transmission-line elements. In

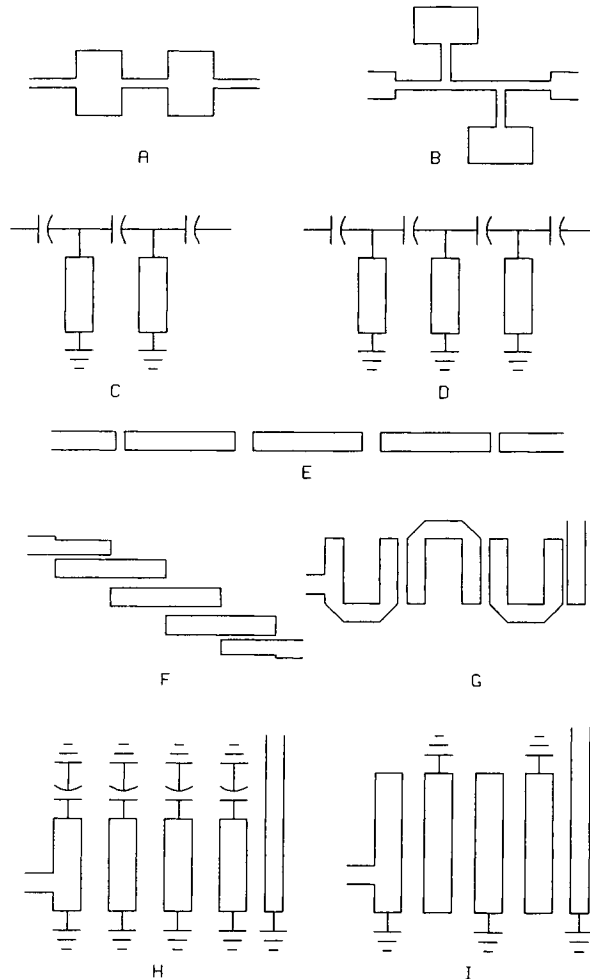


Figure 8. Planar distributed low-pass (A and B), hybrid high-pass (C), hybrid bandpass (D), and coupled bandpass (E – I) filter structures.

coaxial form, it is typically constructed with a constant outer diameter and a stepped center conductor. The large inner diameter sections may include dielectric loading to further reduce the impedance. Stepped-Z low-pass filters can be designed by converting a lumped design using the lumped-distributed equivalents given in Figure 7 for which inductors are replaced with high-impedance lines and capacitors are replaced with low-impedance lines.

The conversion is compromised by the fact that the lumped-distributed equivalences of Figure 7 are not exact. It is evident from Figure 7b that a series inductor has an infinite number of distributed equivalents. Short electrical length dictates high line impedance. For shunt capacitors, short electrical length dictates low line impedance. Given in Figure 9a are the insertion loss and return loss of a stepped impedance, distributed, 2250-MHz-cutoff, low-pass filter with ideal lines designed from a fifth-order 0.0432-dB ripple Chebyshev prototype. The solid traces are computed with electrical line lengths of 1° at the cutoff frequency, whereas the dashed traces are computed with line lengths of 30° . The response with 1° lines is nearly identical to that of an ideal $L-C$ low-pass filter. The 30° line filter has passband ripple and return loss error, a cutoff below the desired frequency, and poor attenuation well into the stop band.

Unfortunately it is not practical to design distributed filters with short lines because the required line impedances become extreme. The 1° filter cited above requires impedances as low as 0.64Ω and as high as 5160Ω which are impossible to realize. The 30° filter requires impedances ranging from 18.2 to 180Ω .

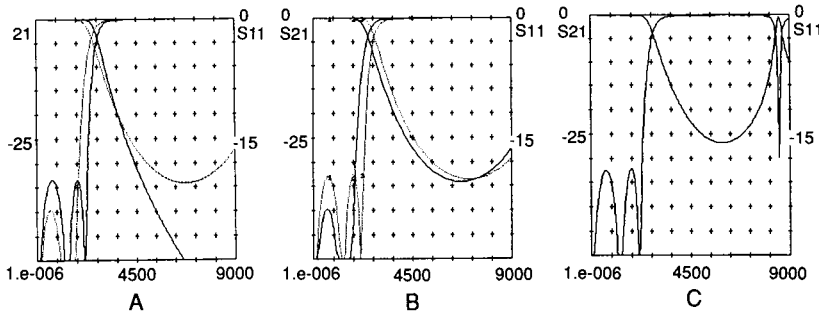


Figure 9. Curve A is stepped-impedance low-pass filter with 1° line length (solid) and 30° line length (dotted). Curve B is the same 30° line-length design (B) before (solid) and after (dotted) optimization to recover the response. Curve C includes step discontinuities in the computation and optimization to recover from step effects.

Given in Figure 9b are the responses of the 30° filter before (solid traces) and after (dashed traces) optimization of line lengths to attempt to recover the passband response and cutoff frequency. Passband recovery was successful, but the stop-band attenuation remains poor. After optimization, the line lengths range from 25.6° to 32.8°.

The impedance steps are significant discontinuities. The response of the previous low-pass filter, modeled with physical line descriptions and discontinuities, is given in Figure 9c for 25-mil-thick Teflon glass microfiber substrate material. The responses are given before (solid traces) and after (dashed traces) optimization to attempt to compensate for the deleterious effects of the step discontinuities. Notice further degradation of the stop-band performance by the discontinuities.

Thinner substrates reduce discontinuity effects because line widths and therefore the physical size of discontinuities are reduced proportionally to the substrate thickness. However, thicker substrates have higher unloaded Q which is critical in certain filter applications. Discontinuity modeling in stepped impedance low-pass filters is critical because of the extreme ratio of line widths. Discontinuities in other distributed filter structures may be less significant at a given frequency.

Elliptic Low-Pass Filter

Given in Figure 8b is a planar distributed filter structure for a fifth-order elliptic prototype. Inductors are again realized as high impedance lines and capacitors to the ground, as low impedance lines.

Matthaei *et al.* [15, p. 374] gives a design procedure which makes use of three-element lumped models of distributed elements. This yields a more precise theoretical design than that obtained using the models in Figure 7. However, the large step discontinuities in this elliptic low-pass structure have a profound effect on the response, and the most effective design procedure is optimization using a high-speed circuit simulator, beginning with either the simple equivalents of Figure 7 or the procedures of Matthaei *et al.*

Hybrid High-Pass Filter

Absent from Figure 7 is a distributed equivalent of the series capacitor. Series capacitive reactance may be realized by coupled lines, a conductor gap in a series line, or meshed conductor fingers. However, large series capacitive values are difficult to achieve in distributed form. Leadless surface mount capacitors are small, are economic, and have acceptable Q

up to microwave frequencies. This affords the opportunity to realize filters in hybrid format with distributed inductive or resonator elements and lumped series or shunt capacitors.

An example is the hybrid high-pass structure in Figure 8c. The required shunt inductor values for high-pass filters are such that the lines are relatively short for practical line impedances. Well into the high-pass passband the shorted lines approach 180° in length and the passband is destroyed. However, since the lines may be relatively short, the destruction occurs at several times the cutoff frequency.

This filter structure is effectively designed by converting the shunt inductors of an $L-C$ high-pass filter to shorted lines using the equivalence in Figure 7a. Using lines with as high a characteristic impedance as practical results in shorter lines and greater passband bandwidth.

Top-C-Coupled Distributed Resonators

Shown in Figure 8d is a hybrid bandpass filter structure with distributed resonators and lumped coupling capacitors. It is similar to the hybrid high-pass except that the lines are near 90° long instead of being short. It is designed by beginning with the narrow-band top-C-coupled $L-C$ bandpass in Figure 6-5c and converting the parallel resonators to distributed resonators using the equivalence of Figure 7e. The coupling capacitors load the resonators, and the resonators are somewhat less than 90° long at the center frequency.

This filter has the same limitations as the $L-C$ version: at bandwidths above about 15%, the response is asymmetric and the design equations are less accurate. The distributed resonator version suffers the additional problem that, at resonator reentrance, the series coupling reactances are low and stop-band attenuation is almost nil.

End-Coupled Half-Wave Resonators

Up to this point we have considered distributed filter structures designed from the viewpoint of the $L-C$ filter and distributed equivalents. This unifies lumped and distributed theories and allows the distributed designer to take advantage of the rich experience in $L-C$ filter design. However, the equivalents are only approximate. Next we will consider distributed filter structures designed using theories based more directly on the properties of distributed resonators. Fortunately, these theories also begin with the low-pass prototype so we may take advantage of the many available low-pass prototype formulas and tables.

Given in Figure 8e is the end-coupled half-wave resonator, or capacitive-gap, bandpass filter. The resonators are nearly 180° long, but are shortened by capacitive loading from the coupling reactors. The coupling capacitors are formed by gaps in the conductor. Design procedures are given by Matthaei *et al.* [15, p. 411]. This filter has been realized in planar media such as microstrip and stripline, as well as in coaxial-rod and resonator bar forms. For wider bandwidths, the coupling reactances become low and are difficult to realize in planar form. The input and output capacitors are especially susceptible to this problem and can be replaced with lumped capacitors.

Reentrance occurs at approximately twice the initial passband frequency. The ultimate stop-band attenuation is achieved midway between the passband frequencies, and, with wide bandwidth, the ultimate attenuation is severely compromised.

Parallel-Coupled Half-Wave Resonator Bandpass

Shown in Figure 8f is the parallel-coupled half-wave resonator bandpass filter. Each resonator is positioned to couple to adjacent resonators along one half its length. This affords higher coupling than placing resonators end to end and therefore works well to wider bandwidths, about 15%. The stagger positioning also results in shorter physical length. It is best suited for planar implementation.

If certain simplifying assumptions are made, the design expressions below are due to Matthaei *et al.* [15, p. 472]. The structure is defined by the even- and odd-mode impedances of each coupled-line pair.

$$\frac{J_{01}}{Y_0} = \left(\frac{\pi bw}{2g_0 g_1} \right)^{1/2} \quad (36)$$

$$\frac{J_{N,N+1}}{Y_0} = \left(\frac{\pi bw}{2g_N g_{N+1}} \right)^{1/2} \quad (37)$$

$$\left. \frac{J_{j,j+1}}{Y_0} \right|_{j=1 \text{ to } N-1} = \frac{\pi bw}{2} \frac{1}{\sqrt{g_j g_{j+1}}} \quad (38)$$

$$Z_{oej,j+1} \Big|_{j=0 \text{ to } N} = Z_0 \left[1 + \frac{J_{j,j+1}}{Y_0} + \left(\frac{J_{j,j+1}}{Y_0} \right)^2 \right] \quad (39)$$

$$Z_{ooj,j+1} \Big|_{j=0 \text{ to } N} = Z_0 \left[1 - \frac{J_{j,j+1}}{Y_0} + \left(\frac{J_{j,j+1}}{Y_0} \right)^2 \right], \quad (40)$$

where $Z_o = 1/Y_o$ is the filter-terminating characteristic impedance.

Stray capacitance to the ground at each end of the resonators requires that the resonators be constructed shorter than half-wave. In microstrip, the propagation velocities of the even and odd modes are dissimilar. The average velocity is used for design.

These secondary effects are easily simulated and corrected using tuning or optimization by digital computer. In general, the line widths and spacings of each coupled pair are different. This results in small steps in width at resonator midpoints. This minor inconvenience usually can be eliminated by choosing one average width and optimizing the spacings using computer simulation.

For bandwidths above about 5%, the spacing of the end resonators to the external lines becomes small and the etching tolerance may be significant. This is sometimes mitigated by using a quarter-wave impedance transformer or tapping into the end resonators to raise the internal impedance level of the filter [29].

In pure TEM-mode media such as stripline, the first reentrance occurs at three times the passband frequency. In microstrip or with slight mistuning, a spurious mode occurs near twice the passband frequency.

Hairpin Bandpass

At lower frequencies, the parallel-coupled half-wave resonator filter is long. The length may be reduced by folding the resonators into hairpin structures, as shown in Figure 8g. The properties of the hairpin are similar to those of the parallel-coupled bandpass. For a given substrate thickness, at higher frequencies the length-to-width ratio becomes low and folding the resonators becomes impractical. Therefore, the hairpin is indicated at UHF and lower microwave frequencies or on thin substrates.

Ideally the design expressions for the parallel-coupled filters could be used. However, hairpin design is complicated by two factors. The line between the resonator bends decreases the length of the coupling sections so that the coupled sections are less than a quarter-wavelength. This can be mathematically dealt with [8]. However, the bend discontinuities are more problematic.

Practical hairpin filters are readily designed by beginning with an ideal parallel-coupled bandpass and then using digital computer optimization to compensate for end capacitance, dissimilar propagation velocities, shortened coupling elements, and bends [19]. By adding discontinuities and folding the structure one resonator at a time, the number of optimization variables is reduced and progress is rapid.

Figure 8g illustrates two methods of external coupling to the hairpin. Typically one method is applied to both ends. Tapped line external

coupling, depicted on the left of Figure 8g, also can be applied to the straight parallel-coupled filter.

Comline Bandpass

The comline bandpass filter structure is shown in Figure 8h. All resonators are grounded on adjacent ends, and capacitive loading is applied to the opposite ends. When the lines are a quarter-wavelength long, the electric and magnetic fields exactly cancel and the coupling is zero for all spacings. Therefore the lines must be less than 90° long and capacitive loading is applied to achieve resonance. The required capacitors represent added realization complexity; however, they provide a method of tuning and relieve construction tolerance which becomes especially critical for narrow bandwidth. Shorter resonators also naturally result in extended reentrant frequencies and broadened stop-bandwidth.

The comline has been realized in both planar and mechanical forms. In both forms it is unusually compact. This and the stop-band performance contribute to its suitability for a wide range of applications. Design processes for mechanical rod and bar [15, p. 497] are typically based on mutual and self-capacitance, whereas even- and odd-mode-impedance-based procedures [26] are more appropriate for planar structures because even- and odd-mode data are more readily available for these media.

Unfortunately, the comline structure is not directly simulated by popular digital computer circuit simulation programs because each internal line is coupled to a line on either side, and the coupled line models in popular simulators deal only with coupled pairs. The comline is effectively modeled [10] by the top- L -coupled $L-C$ bandpass in Figure 5b except that reentrance is ignored. Digital computer field simulation of the comline is feasible at the expense of significantly greater execution time.

Interdigital Bandpass

The interdigital bandpass filter structure is shown in Figure 8i. Resonators are grounded on opposite ends, the lines are a quarter-wavelength long, and therefore reentrance occurs at three times the passband frequency. The interdigital also is realized in both planar and mechanical forms. It is not quite as compact as the comline but has somewhat higher unloaded Q and is therefore an excellent choice for narrow bandwidth filters.

Much like the comline, design procedures for mechanical rod and bar [15, p. 614] are typically based on mutual and self-capacitance, whereas even- and odd-mode-impedance-based procedures are appropriate for

planar structures. The interdigital filter also is not directly simulated by popular digital computer circuit simulation programs.

6. Computer Simulation

Only a few decades ago, the numeric processor used by practicing engineers was the slide rule. Mathematics was applied to the synthesis problem and the resulting simplified design expressions were evaluated using a slide rule, pencil, and paper. A prototype was constructed, perturbations caused by necessary simplifications were observed, and a modified design was retested with additional prototypes. System performance was consistent with the engineering methods available at the time.

An engineer with a slide rule can perform less than one floating-point multiply or divide per second with three significant digits of precision. Batch and time-share digital computing greatly impacted engineering, and today an economic digital computer is capable of over a million floating-point operations per second with significant precision. More than speeding design, this sheer power provides additional design methods.

Synthesis

In a more conventional sense, the digital computer is used to quickly evaluate the simplified synthesis expression previously solved by slide rule. These processes barely exercise the capability of modern digital computers but simplify design. Software effectively organizes solutions and expertise in a convenient design environment [7] and can evaluate more complex synthesis expressions which are less practical with simpler computational techniques.

It was the digital computer which made practical the synthesis of filter transfer approximations such as Chebyshev approximations, as discussed in Section 1. The digital computer also can be used to synthesize more general and user-defined transfer functions [21].

Circuit Simulation

A more revolutionary application of the digital computer is to simulate the performance of the design prior to prototype construction. Simulation in the microwave industry was popularized with the time-share of the Compact program beginning in 1973 and rapidly advanced to deal with a wide range of components and models, parasitics, and distributed element

discontinuities [23, 25]. These complexities overwhelm the synthesis process but are readily handled by modern simulators.

Digital computer simulation is so rapid that repeated circuit evaluations are practical and circuit tuning and optimization become effective. A circuit simulator based on chain matrix network reduction techniques [23] achieves execution times below 2 ms per frequency for moderate-complexity circuits on machines operating at one million floating-point operations per second (1 MFLOPS). Although not as mathematically elegant as synthesis, from a reasonable starting position, numeric optimization realizes designs which consider practical realities and engineering constraints, and the number of prototype cycles is often reduced.

Examples of the types of problems which can be addressed by these techniques include $L-C$ filter component Q and parasitics, step discontinuities in the stepped-impedance low-pass filter, Ts and steps in the planar elliptic low-pass filter, end discontinuities and dissimilar propagation velocities in the parallel-coupled bandpass, folding the parallel-coupled bandpass into the hairpin bandpass, and losses in all of these filters.

Field Simulation

Popular microwave circuit programs simulate the effects of discontinuities using lumped element models. These models are developed by attempting to find model component values which are a function of discontinuity geometry and which match as closely as possible measured data. This works well to an upper frequency limit if the number of geometric and electrical parameters is limited. Millimeter-wave and other processes less conventional than standard microstrip, such as inverted or suspended substrates, multiedielectric structures, and high-dielectric-constant substrates, are not handled well by modeling.

LINMIC + [14] extends capabilities by using once full-wave field simulation to create process-specific data stored in tables. This improves accuracy at higher frequencies and provides for a wider range of parameters at speeds equivalent to those of analytical model simulation. With sufficiently high frequencies and certain geometries, modeling fails and field simulation is indicated.

Planar Field Simulation

In planar microwave circuitry, via holes and finite-conductor thicknesses exist, but conductor currents are primarily constrained to a plane. However, the electromagnetic fields which are produced are three dimensional. Field simulators based on these conditions are often referred to as

2.5D simulators. Available digital computer programs include em, EMSim, and SFPMIC+ [5, 6, 22]. Analytical modeling is avoided, and more general cases and improved accuracy are provided. These programs can deal with multiple dielectric layers and to a more limited extent, with multiple conductor layers. Execution times vary depending on the specific algorithms and circuit complexity, but typically are minutes per frequency on digital computers performing 1 MFLOPS. Although orders of magnitude slower than circuit simulation, when circuit simulation is impractical, 2.5D simulation is an important tool for design verification.

3D Simulation

When the circuit to be simulated is truly three dimensional and currents are not primarily constrained to a plane, full 3D finite-element field simulation is indicated. The Hewlett-Packard High-Frequency Structure Simulator [9] calculates *S*-parameters for multiport structures with unrestricted dielectric and conductor geometry. The computational effort required for this flexibility is extreme, and execution times on powerful workstations are more than an order of magnitude slower than those of 2.5D simulation and thousands of times slower than those of fast circuit simulators.

7. Dissipation Loss

Practical lumped and distributed elements have dissipative loss. Electric-field dissipation occurs in lossy dielectrics and with current flow in lossy conductors. Various component technologies have significantly different loss mechanisms and magnitudes, and certain circuit configurations are more susceptible to perturbation by practical component losses. There is an important distinction between component- and network-induced loss effects.

Unloaded *Q* Definitions

Component *Q* is defined as the ratio of stored to dissipated energy. It is referred to as unloaded *Q*. For lumped elements, if the loss resistance is modeled in series with the reactance, the unloaded *Q* is

$$Q_u = \frac{\omega L}{R_s} = \frac{1}{\omega C R_s} \quad (41)$$

and, if the resistance is in parallel with the reactance,

$$Q_u = \frac{R_p}{\omega L} = \omega C R_p. \quad (42)$$

For distributed elements a multiple of a quarter-wavelength in length,

$$Q_u = \frac{\pi \lambda_{g0}}{\alpha_t \lambda_0^2}, \quad (43)$$

where λ_{g0} is the wavelength in the line at f_0 , λ_0 is the wavelength in air, and α_t is the line attenuation in nepers per unit length.

Unloaded Q is a measure of component quality. The maximum available unloaded Q varies among component technologies. Finite unloaded Q results in passband insertion loss, heating in power applications, response shape perturbation, return loss perturbation, and limited attenuation at frequencies of transmission zeros.

Loaded Q Definitions

Loaded Q is a design parameter of bandpass and bandstop structures.

$$Q_L = \frac{f_0}{BW} = \frac{1}{bw}, \quad (44)$$

where f_0 is the geometric center frequency, BW is the absolute bandwidth, and bw is the fractional bandwidth. The percentage bandwidth is 100% bw.

Low-Pass Loss

Finite unloaded Q results in low-pass passband attenuation which increases as the corner frequency is approached. This results in response roll-off at the corners and has the effect of rounding the amplitude response. At dc and low frequencies, the insertion loss in decibels due to finite unloaded Q for low-pass filters is

$$IL_{dc} = \frac{4.34 \Sigma g}{Q_{u \text{ ave}}} \quad (45)$$

where Σg is the sum of all reactive g -values in the prototype and $Q_{u \text{ ave}}$ is the average inductor and capacitor unloaded Q . Interestingly, the shape of the insertion loss as a function of frequency is exactly proportional to the shape of the group delay response if component Q is modeled as a

constant series resistance for inductors and a constant parallel resistance for capacitors.

Bandpass Loss

For a single resonator, the insertion loss at resonance due to finite unloaded Q is

$$\text{IL}_0 = 20 \log\left(\frac{Q_u}{Q_u - Q_1}\right). \quad (46)$$

For multisection bandpass filters, the band center insertion loss in decibels due to finite unloaded Q is

$$\text{IL}_0 = 4.34 \Sigma g \frac{Q_1}{Q_u} \quad (47)$$

Again, the shape of the insertion loss as a function of frequency is proportional to the bandpass group delay response.

Notice an important distinction. For the low-pass filter, once a prototype is selected, only unloaded Q affects the loss and, if Q_u is large, the loss is small. However, with the bandpass, loss is a function of bandwidth. Even if Q_u is high, narrow bandwidth filters have significant insertion loss. For example, Σg for a fifth-order Butterworth prototype is 6.472. IL_0 with an unloaded-to-loaded Q ratio of 300 is 0.094 dB, with a ratio of 100, is 0.28 dB, and with a ratio of 30, is 0.94 dB. For a 10% bandwidth filter IL_0 less than 0.1 dB requires component Q s near 3000.

8. Component Technology

A number of technologies are available for the reactive elements in the filter structure. Early technologies included lumped inductors and capacitors. Bulk quartz crystal piezoelectric resonators and coaxial and waveguide elements matured during and after World War II. Later, planar structures such as stripline and microstrip became popular. More recent advancements include high-dielectric-constant materials and MMIC structures. Each have application-specific advantages.

Capacitor

The basic capacitor consists of two conducting plates separated by a dielectric material. The capacitance is given by

$$C = \frac{8.85 \times 10^{-12} \epsilon_r A}{S}, \quad (48)$$

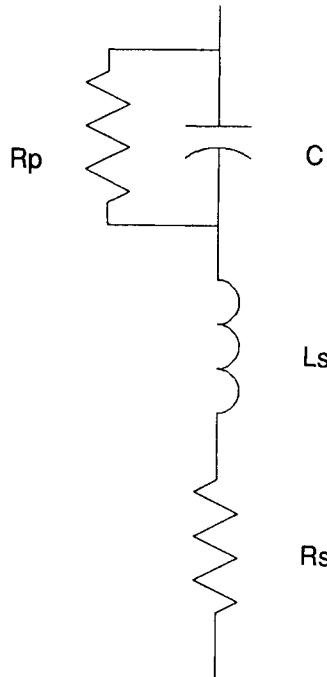


Figure 10. Capacitor model, including losses and lead inductance.

where ϵ_r is the relative dielectric constant, A is the plate area in square meters, and S is the plate spacing in meters. The relative dielectric constant of air is 1.

A simple but practical capacitor model is given in Figure 10. At high frequencies, R_p is generally insignificant. Capacitor leads are inductive. Even chip capacitors have series inductance. At higher frequencies, the inductive reactance reduces the total reactance and causes the effective capacitor value to increase. At resonance, the impedance is resistive, and above resonance the reactance is inductive and increases with frequency.

A rough estimate of the series inductance is 20 nH per inch of conduction and displacement current path length. For example the inductance of a chip capacitor 0.05 in. long is approximately 1 nH, whereas the inductance of a monolithic capacitor with 0.2 in. of lead spacing and approximately 0.4 in. of effective path length is 8 nH. A 20-pF chip capacitor with 1 nH of lead inductance has an effective capacitance of 21.5 pF by 300 MHz and resonates at 1.13 GHz.

At VHF frequencies and lower, the unloaded Q of high-frequency capacitors can be several thousand. Inductor unloaded Q is typically lower

so capacitor unloaded Q is often ignored. At UHF and microwave frequencies, more careful capacitor selection is advised. Lower value capacitors typically yield higher unloaded Q , and a higher internal filter impedance is used to reduce capacitor values.

Inductor

The basic inductor consists of a coil of wire wound in the form of a solenoid. Wheeler's 1928 formula for the inductance in microhenries [27], accurate to about 1%, for a single-layer solenoid with an air core and a length-to-radius ratio of > 0.17 is

$$L = \frac{n^2 r^2}{9r + 10l}, \quad (49)$$

where n is the number of turns, r is the solenoid radius to the wire center, and l is the solenoid length.

A practical inductor model is given in Figure 11. The inductance L is given by Equation (49). The series resistor, R_s , models the finite unloaded

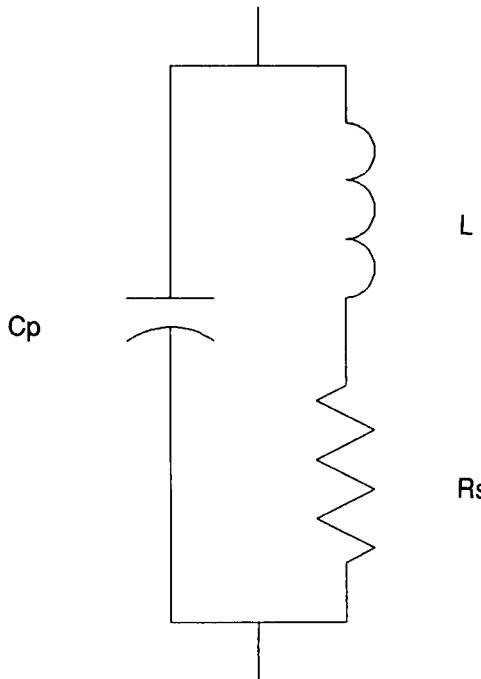


Figure 11. Inductor model, including losses and self-capacitance.

Q as given in Equation (41). C_p is the effective parasitic winding capacitance. C_p for unshielded solenoids with one end grounded is about 2.5 pF per inch of solenoid radius for l/r ratios from 0.8 to 5.0 [16].

$$C_p \approx 2.5r, \quad (50)$$

where r is the solenoid radius in inches.

The effective inductance increases and unloaded Q decreases as the parasitic capacitive reactance becomes significant. The parasitic parallel resonant frequency is

$$f_0 = \frac{1}{2\pi\sqrt{LC_p}}. \quad (51)$$

Above resonance the coil reactance becomes capacitive and begins decreasing. The parasitic capacitance also reduces the unloaded Q . The effective unloaded Q as reduced by the parasitic capacitance is

$$Q_u \approx Q_{uo} \left[1 - \left(\frac{f}{f_0} \right)^2 \right], \quad (52)$$

where Q_{uo} is the unloaded Q without parasitic capacitance and f is the operating frequency. Q_u approaches zero as parasitic resonance is approached.

Solenoid Q_{uo} is a function of wire conductivity, the frequency, and inductor size. For single-layer solenoids of copper wire with the wire diameter equal to 40 to 80% of the wire center-to-center spacing [11, pp. 4–6]

$$Q_{uo} = 2rA\sqrt{f}, \quad (53)$$

where r is the solenoid radius in inches, f is the operating frequency in megahertz, and A is a factor dependent on the solenoid l/r ratio. A is 30 at $l/r = 0.2$, 100 at $l/r = 2$, and asymptotically approaches 130 at $l/r = 20$. Equation (53) suggests that an inductor with arbitrarily large unloaded Q exists for a suitably large radius. However, increasing the radius increases the parasitic capacitance and there is a maximum size and Q_u .

Plotted in Figure 12 are Q_u versus frequency for four copper-wire solenoid inductors of decreasing size and turns, including the effect of parasitic capacitance. Each solenoid has an l/r ratio of 4.

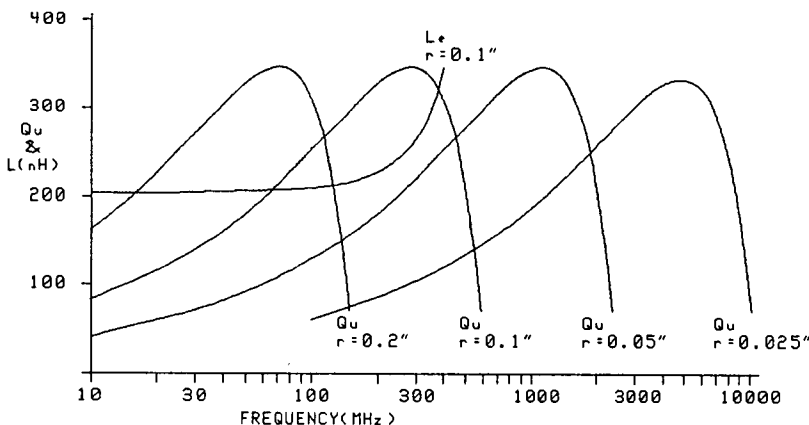


Figure 12. Inductor unloaded Q versus frequency for solenoids with a radius of 0.2 to 0.025 in. Also given is the effective inductance versus frequency for the solenoid with a radius of 0.1 in. Solenoid parameters are presented in the following table.

r (in.)	Length (in.)	Turns	C_e (pF)
0.2	0.8	20	0.54
0.1	0.4	10	0.27
0.05	0.2	5	0.14
0.025	0.1	2.5	0.07

Resonance for each inductor occurs at the frequency at which the Q_u curves would intersect the $Q_u = 0$ axis. Maximum Q_u occurs at approximately 50% of the resonant frequency. However, notice from the plotted inductance of the 0.1-in. radius inductor that the inductance is substantially increased by the parasitic capacitance and it is advisable to operate well below 50% of the resonant frequency.

Although solenoids with other l/r ratios and turns would yield a different set of plots, Figure 12 illustrates a number of important factors concerning solenoid inductor design. There exists an upper limit on available solenoid inductor Q_u . Unloaded Q s above 300 are difficult to attain. At a given frequency, increased size yields increased Q_u , provided operation is well below the resonant frequency. And, finally, higher frequency operation forces smaller solenoid size. At microwave frequencies microminiature or process construction techniques are indicated.

Curves A and B in Figure 13 are the approximate volumes in cubic inches for solenoids with $l/r = 6$ and Q_u equal to 100 and 200, respectively. These volumes include clearance sizes for component separation or

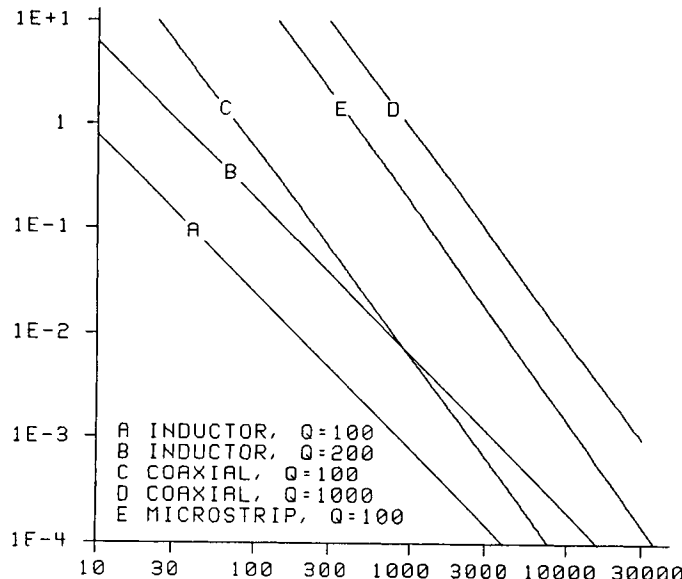


Figure 13. Volume versus frequency with constant unloaded Q for various reactor technologies. Inductor and microstrip volumes include separation allocations.

shielding. The occupied space assumes an occupied radius 3.5 times the solenoid radius and an occupied length 11 times the solenoid radius.

TEM and Quasi-TEM Modes

Homogeneous dielectric constant distributed media such as coax and stripline are normally operated in a TEM mode below TE and TM mode cutoff frequencies. Propagation in microstrip is quasi-TEM and can be assumed to be TEM for many practical applications. For a given operation frequency, the physical size of distributed elements, limited by TE and TM cutoff, can be larger than that of lumped inductors. Therefore, the unloaded Q of distributed elements can be higher than that of lumped elements provided the distributed elements are larger.

The unloaded Q of distributed resonators equal to a multiple of a quarter-wavelength is

$$Q_u = \frac{1}{\frac{1}{Q_c} + \frac{1}{Q_d}}, \quad (54)$$

where Q_c is the unloaded Q impacted by conductor loss and Q_d is the

unloaded Q impacted by dielectric loss. For copper coaxial resonators

$$Q_c = 1.215 \times 10^4 \sqrt{f} \frac{B \ln(b/d)}{1 + b/d} \quad (55)$$

$$Q_d = \frac{1}{\tan \delta}, \quad (56)$$

where b and d are the outer and inner conductor diameter in inches, f is the frequency in gigahertz, and $\tan \delta$ is the dielectric material loss tangent.

Coaxial resonator volume versus frequency with copper metallization and Teflon dielectric loading for $Q_u = 100$ and $Q_u = 1000$ is plotted in Figure 13 as curves C and D, respectively. No separation spacings are required because coax is self-shielding. Notice that, at 1 GHz, a distributed resonator is approximately 10× larger than an inductor with the same Q_u . However, distributed resonators are capable of providing higher Q_u . By increasing distributed resonator volume another 100×, a Q_u of 1000 is achieved. Particularly at lower frequencies, much of the volume of distributed resonators is due to length. The TE mode cutoff frequency in gigahertz, which limits the diameter of coaxial resonators, is

$$f_c = \frac{7.51}{\sqrt{\epsilon_r}} \frac{1}{b + d}. \quad (57)$$

Expressions for stripline and microstrip conductor and dielectric losses are more complex. Digital computer programs are used to predict microstrip and stripline loss. The volume of a microstrip resonator vs frequency for $Q_u = 100$ is given as curve E in Figure 13 for copper metallization and Teflon-loaded glass microfiber PWB material [24]. The substrate thickness was varied to achieve the specified Q . With a constant substrate thickness, such as 0.062 in., Q_u degrades below about 200 MHz and increases above 200 MHz. Because microstrip is not self-shielding, spacings of 5× the substrate thickness on each side of the microstrip and a cover height of 10× the substrate thickness were assumed. Microstrip filter structures can be quite large below 1 GHz, even with only moderate Q_u .

Waveguide

At higher microwave frequencies, TE- or TM-mode waveguides are practical resonators. Filter structures and design procedures are given in Matthaei *et al.* [15].

The unloaded Q of an air-filled copper waveguide is

$$Q_u = \frac{A}{a\sqrt{f}}, \quad (58)$$

where A is a constant, a is the broad dimension of a rectangular guide or the diameter of a circular guide in inches, and f is the operating frequency in gigahertz. For TE_{mo} modes in a rectangular guide with a b/a ratio of 0.45, $A = 3500$ at an operating frequency of 1.3 times the waveguide cutoff frequency and $A = 4500$ at 2 times the cutoff frequency. For a rectangular guide with a b/a ratio of 0.5, $A = 3800$ at 1.3 times the cutoff frequency and 4800 at 2 times the cutoff frequency. For the TE_{11} mode in a circular guide, $A = 6000$ at 1.3 times the cutoff frequency and 9000 at 2 times the cutoff frequency.

Other Technologies

To this point, we have considered inductors with air cores and distributed elements with low-dielectric-constant materials such as Teflon. Materials with a high dielectric constant, with a relative permeability greater than 1, or which are piezoelectric offer additional component options.

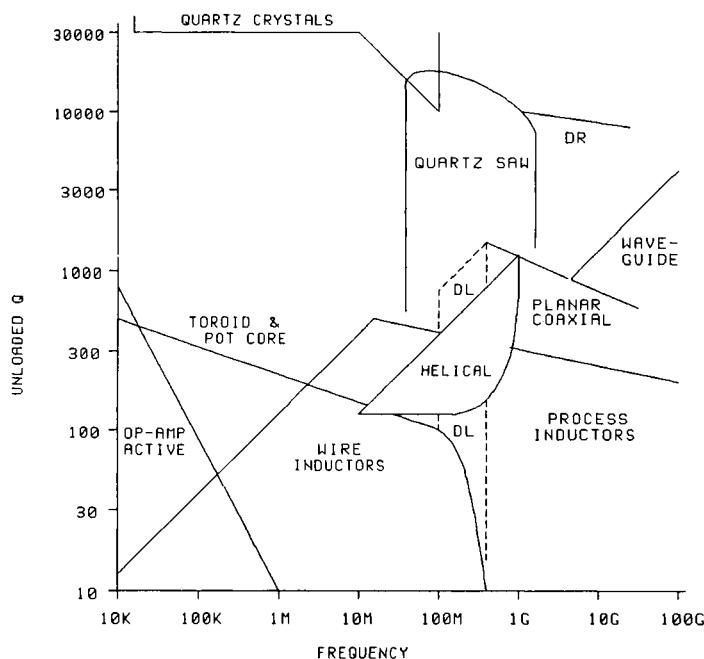


Figure 14. Component technology unloaded Qs. Inductors range from the lower left to the lower right. TEM-mode planar and coaxial components also lie under the process inductors. The dielectric loaded (DL) section extends the practical lower frequency limit of the TEM components. The dielectric resonator (DR) region also lies under the quartz SAW.

TABLE 3
Properties of High-Dielectric-Constant Temperature-Stable Ceramic Materials

Material	ϵ_r	T_c (ppm /°C)	Q_d vs frequency (GHz)				
			0.5	2	6	12	18
Trans-Tech 8600	80	9/6/3/0/-3/-6	10,000	5,500	1,500		
Trans-Tech 8800	38.3–36.6	4/2/0		18,000	8,000		
Trans-Tech 8500	36.4–35.7	9/6/3/0/3		20,000	9,000	5,000	
Trans-Tech 8700	30.6–27.6	4/2/0/-2/-4			17,000	8,000	5,500
Siemens $\epsilon_r = 88$	91.8–89.8	12/9/6/3/0/-3	5,000	2,500	1,000		
Siemens $\epsilon_r = 38$	38.8–37.4	12/9/6/3/0/-3		12,000	7,000	3,000	
Siemens $\epsilon_r = 29$	29.3–28.4	6/3/0			16,000	7,500	4,500
Murata U series	38.9–36.6	10/8/6/4/2/0/-2/-4	15,000	6,500	3,500		
Murata R series	31.3–29.2	6/4/2/0		20,000	10,000	6,500	
Murata E series	24.9–24.2	6/4/2/0		33,000	16,000	5,500	

Figure 14 diagrams unloaded Q versus frequency for a number of component technologies. These data should be considered only a guideline; precise values are a function of many parameters and tradeoffs. In general, the upper left limits of component regions are defined by physical size. These limits are extended by larger than usual size. With lumped inductors, the lower right region represents small physical size. In the extreme, wire-wound inductors are abandoned and process inductors are used. The upper right limits are defined by parasitics or moding and are more difficult to extend.

Ceramic materials containing titanates, zirconates, glass, and alumina, providing relative dielectric constants up to 80 or more and with excellent temperature stability, are now available. They are used as substrates for planar circuits, as dielectric loading for coaxial resonators, or as bulk resonators. A table of material properties is given in Table 3.

Permeability Loaded Inductors

Materials which have a permeability greater than 1 and which do not introduce excessive loss are used to concentrate magnetic fields and increase inductance for a given inductor size. Metallic powders with a ceramic binder provide temperature-stable materials with relative permeabilities to over 500 for use through HF frequencies. Ceramic mixtures of metal oxides and carbonates called ferrites with relative permeabilities to nearly 10,000 are used to 100 KHz and those with lower permeabilities are used to VHF frequencies. At higher frequencies, core losses become excessive.

Cylindrical cores slightly longer than the solenoid winding are used to increase inductance for a given physical size. Cylindrical cores shorter than the solenoid winding and moved along the winding axis are used for inductance tuning, with the greatest inductance with the core centered.

The effective permeability of a core is the factor by which the inductance is increased over the value with an air core. For a cylindrical core, the effective permeability is as much a function of the l/r ratio of the core as it is the relative permeability of the core. For example, the effective permeability of a core of relative permeability 125 and with an l/r ratio of 8 is 16.4 with an l/r ratio of 16 is 36.3 [4].

Toroid-shaped cores realize much of the relative permeability of the core material. They also confine magnetic fields well and minimize shielding requirements. The effective permeability is somewhat below the material permeability, and inductance is tuned slightly by compressing or spreading the winding evenly about the core. Compressed windings yield higher inductance.

The inductance of the toroid form windings in microhenries is approximately

$$L = 0.0117\mu_0 n^2 t \log(\text{OD}/\text{ID}), \quad (59)$$

where μ_0 is the permeability relative to air and t is the core thickness in inches. The greatest field concentration occurs with pot core inductors. At submegahertz frequencies, compact size and unloaded Q s near 1000 are realized [28, pp. 9–16].

Dielectric Loaded TEM Mode

Finished dielectric loaded coaxial resonators with terminals are commercially available from a number of sources. Unloaded Q considerations are identical to more conventional coaxial resonators except that the resonator length and therefore the volume are reduced by the square root of the relative dielectric constant. Their greatest utility is therefore below microwave frequencies, at which conventional lines are lengthy. Coaxial resonator unloaded Q is found from Table 3 data using Equations (54) to (56).

Dielectric Resonators

Microwave resonators may be formed using bulk ceramic material, typically in cylindrical form. The resonant frequency of a bulk resonator well isolated from an enclosing housing is given to within about 2% by Kajfez and Guillon [12, p. 3].

$$f_r = \frac{34}{a\sqrt{\epsilon_r}} \left(\frac{a}{H} + 3.45 \right) \quad (60)$$

for

$$0.5 < \frac{a}{H} < 2 \quad (61)$$

and

$$30 < \epsilon_r < 50, \quad (62)$$

where a and H are the cylindrical radius and height in millimeters, respectively. Algorithms for the resonant frequency is proximity to a housing and for more general parameters are discussed by Kajfez and Guillon [12].

Surface Acoustic Wave Devices

Surface acoustic wave (SAW) devices utilize photolithographic generated interdigital electrodes to launch and receive acoustic waves on the

surface of a piezoelectric substrate such as quartz [13]. The practical frequency range of SAWs is 50 to 1200 MHz, although below about 250 MHz the substrate tends to be large and relatively expensive.

SAW devices benefit from the excellent temperature stability and unloaded Q of quartz and can be manufactured at low cost in volume. A typical unloaded Q is 12,000 at 350 MHz to 6000 at 1000 MHz. SAW filter selectivity is excellent, and the significant differential group delay of conventional reactive filters is absent, but is replaced with a smaller, rapidly changing, "fine-grain" delay. SAW filters provide excellent selectivity and narrow bandwidths in a small package at UHF frequencies. SAW filter disadvantages include a high insertion loss for some configurations, tooling requirements, and fixed frequency operation. SAW resonator pulling is very difficult and tuneable filters are not possible. SAWs are capable of only moderate power handling capability, typically +30 dBm at 250 MHz and +18 dBm at 1000 MHz.

References

- [1] H. R. Blinchikoff and M. Savetman, Least-squares approximation to wide-band constant delay, *IEEE Trans. Circuit Theory*, Vol. CT-19, July 1972.
- [2] F. Carassa, Band-pass filters having quasi-symmetrical attenuation and group-delay characteristics, *Alta Freq.*, Vol. 30, No. 7, 1961.
- [3] S. Cohn, Direct-coupled-resonator filters, *Proc. IRE*, Vol. 45, Feb. 1957.
- [4] EEPal Computer Program, Eagleware Corp., Stone Mountain, GA.
- [5] em Computer Program, Sonnet Software, Liverpool, NY.
- [6] EMSim Computer Program, EEsof, Inc., Westlake Village, CA.
- [7] =FILTER= Computer Program, Eagleware Corp., Stone Mountain, GA.
- [8] U. H. Gysel, New theory and design for hairpin-line filters, *IEEE Trans. Microwave Theory Tech.*, Vol. MTT-22, May 1974.
- [9] HFSS Computer Program, Hewlett-Packard Co., Santa Clara, CA.
- [10] I. C. Hunter and J. D. Rhodes, Electronically tunable microwave bandpass filters, *IEEE Trans. Microwave Theory Tech.*, Vol. MTT-30, Dec. 1982.
- [11] E. C. Jordan, ed., *Reference Data for Engineers: Radio, Electronics, Computer, and Communications*. Indianapolis: McMillan, 1985.
- [12] D. Kajfez and P. Guillon, eds., *Dielectric Resonators*. Oxford, MS: Vector Fields, 1990.
- [13] R. J. Kansy, Understanding SAW resonators, *Microwaves RF*, Vol. 22, Nov. 1983.
- [14] LINMIC + Computer Program, Jansen Microwave, Ratingen, Germany.
- [15] G. Matthaei, L. Young, and E. M. T. Jones, *Microwave Filters, Impedance-Matching Networks, and Coupling Structures*. Dedham, MA: Artech House, 1980.
- [16] R. G. Medhurst, H. F. Resistance and self-capacitance of single-layer solenoids, *Wireless Eng.*, Feb. / Mar. 1947.
- [17] R. W. Rhea, Symmetrical filter design, *RF Expo East Proc.*, Cardiff, Englewood, CO, 1989.
- [18] R. W. Rhea, Singly-equalized filters, *RF Des. Mag.*, Oct. 1990.
- [19] R. W. Rhea, Distributed hairpin bandpass, *RF Compute!* (Eagleware Corp.), Vol. 3, No. 1, 1991.

- [20] R. Saal and E. Ulbrich, On the design of filters by synthesis, *IRE Trans. Circuit Theory*, Vol. CT-5, Dec. 1958.
- [21] S / FILSYN Computer Program, DGS Associates, Santa Clara, CA.
- [22] SFPMIC+ Computer Program, Jansen Microwave, Ratingen, Germany.
- [23] =SuperStar= Computer Program, Eagleware Corp., Stone Mountain, GA.
- [24] =TLINE= Computer Program, Eagleware Corp., Stone Mountain, GA.
- [25] Touchstone Computer Program, EEsof, Inc., Westlake Village, CA.
- [26] A. D. Vincze, Practical design approach to microstrip combline-type filters, *IEEE Trans. Microwave Theory Tech.*, Vol. MTT-22, Dec. 1974.
- [27] H. A. Wheeler, Simple inductance formulas for radio coils, *Proc. IRE*, Vol. 16, Oct. 1928; Vol. 17, Mar. 1929.
- [28] A. B. Williams and F. J. Taylor, *Electronic Filter Design Handbook: LC, Active, and Digital Filters*. New York: McGraw-Hill, 1988.
- [29] J. S. Wong, Microstrip tapped-line filter design, *Trans. Microwave Theory Tech.*, Vol. MTT-27, Jan. 1979.
- [30] A. I. Zverev, *Handbook of Filter Synthesis*. New York: John Wiley & Sons, 1967.

Directional Couplers

Stephen Jon Blank and Charles Buntschuh

I. Definitions and Basic Properties

A directional coupler as treated here is a passive, reciprocal four-port coupler in which power incident on one port, the input, is split between two other ports, the coupled and through-ports, and little or no power emerges from the fourth, isolated, port. With the ports numbered as in Figure 1, with the scattering matrix [1, 2] configured as

$$S = \begin{bmatrix} S_{11} & S_{21} & S_{31} & S_{41} \\ S_{21} & S_{22} & S_{32} & S_{42} \\ S_{31} & S_{32} & S_{33} & S_{43} \\ S_{41} & S_{42} & S_{43} & S_{44} \end{bmatrix}, \quad (1)$$

and with P_1 as the input power and P_i as the power out of the i th port, the coupling is defined by

$$C = -10 \log \frac{P_3}{P_1} = -20 \log |S_{31}| \quad (\text{dB}), \quad (2)$$

the isolation by

$$I = -10 \log \frac{P_4}{P_1} = -20 \log |S_{41}| \quad (\text{dB}), \quad (3)$$

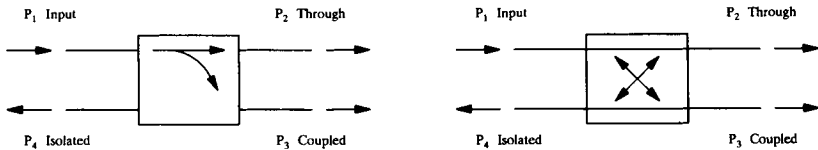


Figure 1. Two common symbols for directional couplers and power flow conventions. Reprinted with permission from David M. Pozar, *Microwave Engineering*, © 1990 Addison-Wesley Publishing.

and the direct transmission by

$$T = -10 \log \frac{P_2}{P_1} = -20 \log |S_{21}| \quad (\text{dB}). \quad (4)$$

The directivity is the power out the isolated port relative to the coupled power and is defined by

$$D = I - C = -10 \log \frac{P_4}{P_3} = -20 \log \frac{|S_{41}|}{|S_{31}|} \quad (\text{dB}). \quad (5)$$

In an ideal directional coupler, no power is delivered to port 4 and $D = I = \infty$.

This port numbering is commonly used for waveguide couplers. Other numbering systems are also used. Frequently, on coupled-line couplers, the coupled, isolated, and through-arms are numbered 2, 3, and 4, respectively.

By proper choice of the phase references, we have $S_{21} = S_{43} = \alpha$, $S_{31} = \beta e^{j\theta}$, and $S_{42} = \beta e^{j\phi}$, where α and β are real and θ and ϕ are phase constants. An ideal lossless directional coupler is perfectly matched and has infinite directivity: $S_{ii} = 0$, $i = 1, 2, 3, 4$, $S_{41} = S_{32} = 0$, and $\alpha^2 + \beta^2 = 1$. Two common choices for θ and ϕ are (1) symmetric coupler, $\theta = \phi = \pi/2$, and (2) antisymmetric coupler, $\theta = 0$, $\phi = \pi$.

The scattering matrix of an ideal, symmetric 3-dB coupler, called a quadrature hybrid, is, at its center frequency,

$$S = \frac{1}{\sqrt{2}} \begin{bmatrix} 0 & -j & -1 & 0 \\ -j & 0 & 0 & -1 \\ -1 & 0 & 0 & -j \\ 0 & -1 & -j & 0 \end{bmatrix}, \quad (6)$$

whereas that of an ideal antisymmetric 3-dB coupler, called a magic-T or

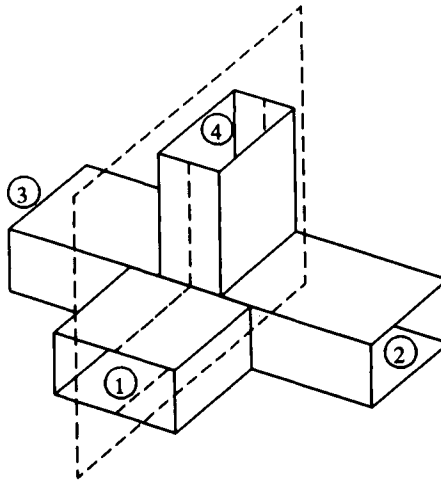


Figure 2. Waveguide magic T. Adapted with permission from Peter A. Rizzi, *Microwave Engineering: Passive Circuits*, © 1987 Prentice-Hall, Inc.

rat-race hybrid, is

$$S = \frac{1}{\sqrt{2}} \begin{bmatrix} 0 & -j & -j & 0 \\ -j & 0 & 0 & j \\ -j & 0 & 0 & -j \\ 0 & j & -j & 0 \end{bmatrix}. \quad (7)$$

A waveguide magic T is a classic example of an antisymmetric 3-dB directional coupler. From Figure 2, it is seen to be a combination of *E*- and *H*-plane Ts. If a TE₁₀-mode wave is incident at port 1, there are waves of equal magnitude and waves phase coupled to ports 2 and 3, and no power is coupled to port 4; incident at port 4, the waves are coupled to ports 2 and 3 with equal magnitude but of opposite phase, and no power is coupled to port 1. Magic Ts are available with an isolation of 30 dB or greater and a coupling balance of 0.1 dB or less over the waveguide bandwidth. In this chapter we divide directional couplers into three categories: (1) waveguide aperture, (2) coupled-line, and (3) branch-line couplers.

2. Waveguide Aperture Couplers

This class of couplers depends on the electromagnetic properties of one or more apertures cut into the common wall between two waveguides.

Among this class are the Bethe-hole [3, 4], the multihole [5–7], the Riblet short-slot [8, 9], the Schwinger reversed-phase [10], and the Moreno cross-guide [10] couplers.

Bethe-Hole Coupler

A single small hole in the common broadwall between two rectangular waveguides, a Bethe-hole, can provide directional coupling [3]. The two guides of a Bethe-hole may be either parallel or skewed (Figure 3).

For the parallel-guide TE_{10} -mode case, with a circular hole of radius r_0 and an offset s of the hole from the guide sidewall, the scattering amplitudes $|S_{31}|$ and $|S_{41}|$ are given by

$$|S_{31}| = F(f)r_0^3 \quad (8a)$$

$$|S_{41}| = B(f)r_0^3, \quad (8b)$$

where $F(f)$ and $B(f)$, the forward and backward wave intrinsic amplitudes, are functions of frequency, but are assumed to be independent of the hole radius, and are given by

$$F(f) = \frac{2\pi f Z_{10}}{ab} \left[\frac{2\epsilon_0}{3} \sin^2 \frac{\pi s}{a} - \frac{4\mu_0}{3Z_{10}^2} \left(\sin^2 \frac{\pi s}{a} + \frac{\pi^2}{\beta^2 a^2} \cos^2 \frac{\pi s}{a} \right) \right] \quad (9a)$$

$$B(f) = \frac{2\pi f Z_{10}}{ab} \left[\frac{2\epsilon_0}{3} \sin^2 \frac{\pi s}{a} + \frac{4\mu_0}{3Z_{10}^2} \left(\sin^2 \frac{\pi s}{a} - \frac{\pi^2}{\beta^2 a^2} \cos^2 \frac{\pi s}{a} \right) \right], \quad (9b)$$

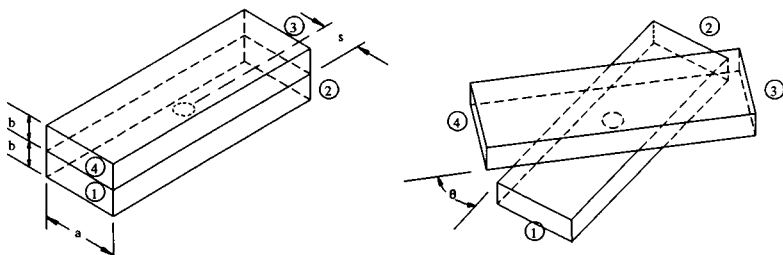


Figure 3. Bethe-hole directional coupler. (a) Parallel guides. (b) Skewed guides. Reprinted with permission from David M. Pozar, *Microwave Engineering*, © 1990 Addison-Wesley Publishing.

where

$$f_c = \frac{c}{2a}, \quad Z_{10} = \frac{\sqrt{\frac{\mu_0}{\epsilon_0}}}{\sqrt{1 - \left(\frac{f_c}{f}\right)^2}}, \quad \text{and} \quad \beta = \frac{2\pi f}{c} \sqrt{1 - \left(\frac{f_c}{f}\right)^2}.$$

Solving Equation (9a) for s , for $F(f) = 0$, yields the hole offset for backward coupling to port 4 and isolation to port 3:

$$s = \frac{a}{\pi} \sin^{-1} \left(\frac{1}{\sqrt{2 - \frac{1}{2} \left(\frac{f}{f_c} \right)^2}} \right). \quad (10)$$

It should be noted that real values of s can be obtained only for a restricted range of frequencies, $f/f_c = 1$ to $\sqrt{2}$, as shown in Figure 4.

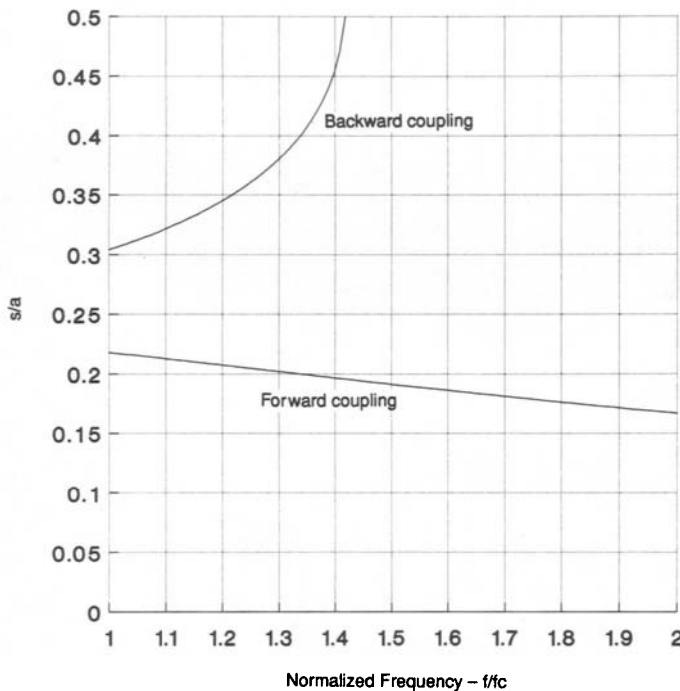


Figure 4. Hole offset s/a vs normalized frequency f/f_c for ideally directive Bethe-hole couplers.

The offset s determines the isolation to port 3. The hole radius r_0 determines the coupling to port 4 and can be found for a given frequency, offset, and coupling from

$$r_0 = \left[\frac{10^{-(C/20)}}{|B(f)|} \right]^{1/3}. \quad (11)$$

For example, Figure 5 shows r_0 as a function of C for values from 10 to 30 dB for WR-90 waveguide, with $a = 2.286$ cm, $b = 1.016$ cm, $f = 8.75$ GHz, and $s = 0.909$ cm. The coupling and directivity as a function of frequency of a Bethe-hole coupler in the same guide with $r_0 = 0.431$ cm are shown in Figure 6.

It is possible to find values for s to give forward coupling to port 3 by solving Equation (9b) for $|B(f)| = 0$. Values of s/a as a function of the

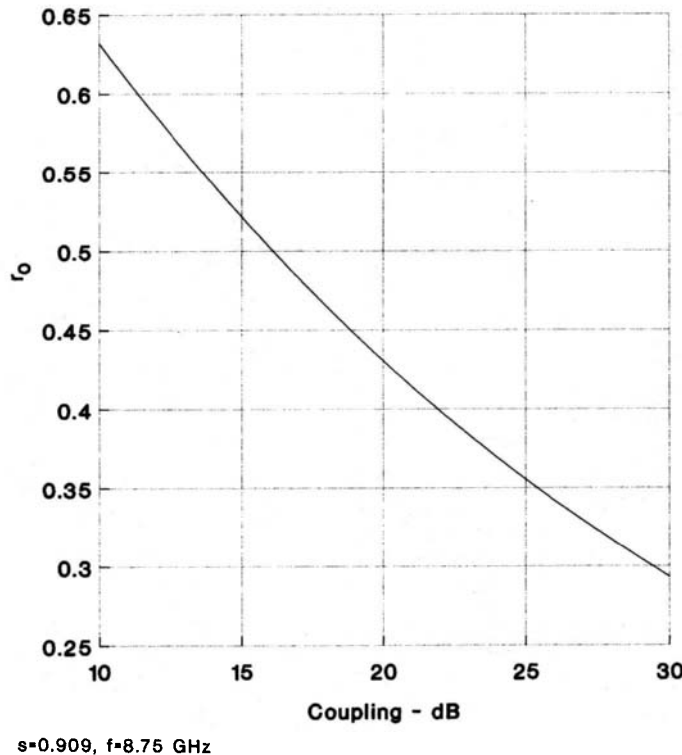


Figure 5. Hole radius vs coupling for Bethe-hole couplers with backward wave coupling.

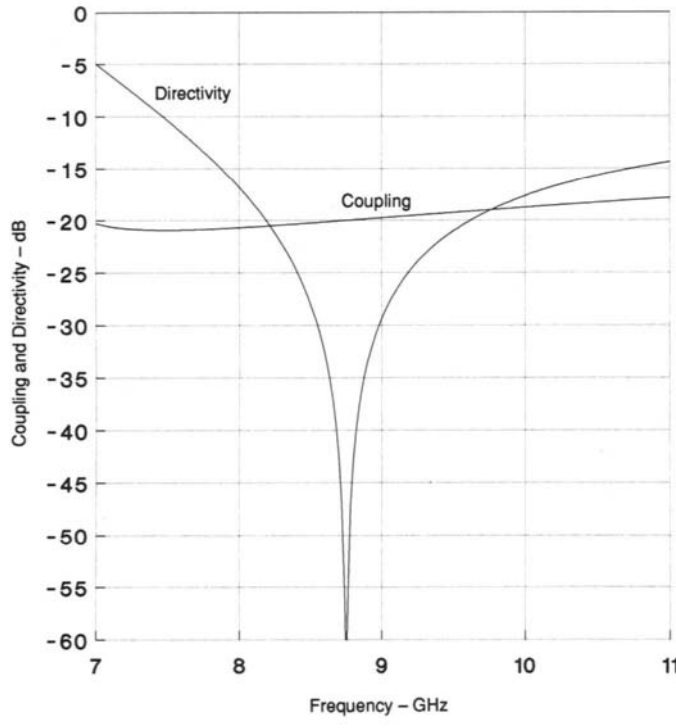


Figure 6. Coupling and directivity vs frequency for a single-hole Bethe-hole coupler.

normalized frequency for forward coupling are shown in Figure 4. This case is generally of less practical interest as it requires coupling holes relatively close to the guide sidewall.

The hole may be on the centerline of the skewed Bethe-hole coupler, $s = a/2$, and the angle θ may be adjusted for isolation at port 3. The skewed geometry, however, is often a fabrication and packaging disadvantage [3].

Multihole Waveguide Couplers

The narrow-band directivity performance of the single-hole coupler is evident from Figure 6. High directivity over a much greater bandwidth can be obtained using an array of coupling holes offset s from the centerline and spaced one-quarter wavelength apart at the center frequency f_0

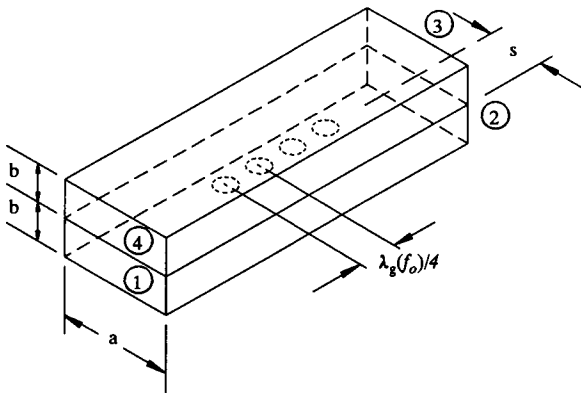


Figure 7. Multi-hole broadwall waveguide coupler.

(Figure 7). With this arrangement, the forward-coupled-wave contributions from each hole are added in phase at port 3, whereas the backward wave contributions cancel at port 4. The cancellations occur essentially pairwise from the holes, so it shall be assumed that the total number of holes, $N + 1$, is even and that the distribution of hole radii is symmetric, i.e., $r_n = r_{N-n}$. The coupling and directivity responses are given by

$$C(f) = -20 \log \left| F(f) \sum_{n=0}^N r_n^3 \right| \quad (12)$$

$$D(f) = -20 \log \left| B(f) \sum_{n=0}^N r_n^3 e^{-jn\pi d(f)} \right| - C(f), \quad (13)$$

where $F(f)$ and $B(f)$ are given by Equation (9), r_n is the hole diameters, and $d(f)$ is the ratio of guide wavelengths at f_0 and f :

$$d(f) = \sqrt{\frac{f^2 - f_c^2}{f_0^2 - f_c^2}}. \quad (14)$$

The design problem is to find the values of r_n which achieve a specified minimum directivity, D_m , over a specified bandwidth (f_1, f_2) . It is usual to synthesize the directivity response with either a binomial or a Chebychev design.

Binomial Design

For a specified coupling, minimum directivity, and bandwidth, N is obtained from

$$N = - \frac{D_m}{20 \log |\cos \theta_1|}, \quad (15)$$

where

$$\theta_1 = \frac{\pi}{2} d(f_1) = \frac{\pi}{2} \sqrt{\frac{f_1^2 - f_c^2}{f_0^2 - f_c^2}}$$

$$\theta_2 = \pi - \theta_1 = \frac{\pi}{2} d(f_2).$$

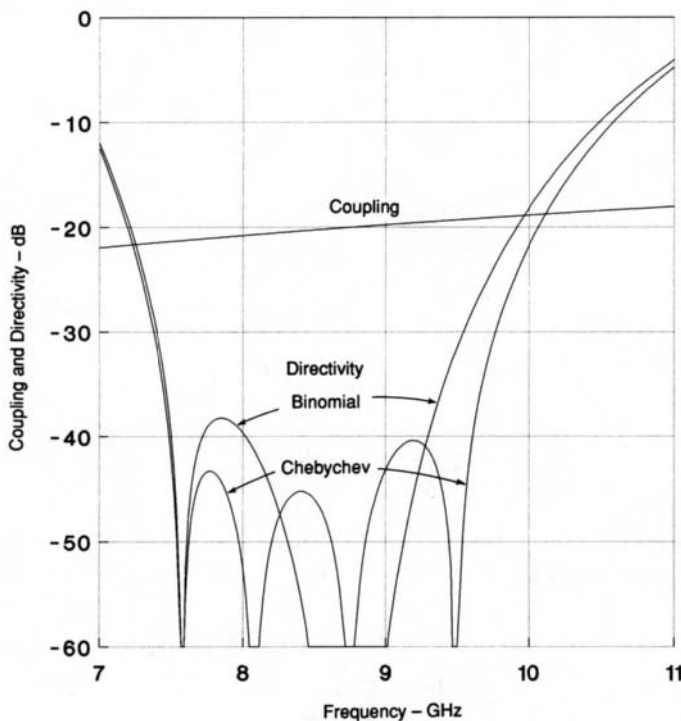
Alternatively, given N , Equation (15) can be used to find f_1 and f_2 . The values of the hole radii r_n , $n = 0, 1 \dots (N - 1)/2$, are given by

$$r_n = \left[\frac{10^{-C/20} C_n^N}{|F(f_0)| \sum_0^N C_n^N} \right]^{1/3}, \quad (16)$$

where

$$C_n^N = \frac{N!}{(N - n)!n!}.$$

For example, with $C = 20$ dB, $D_m = 40$ dB, $f_0 = 8.75$ GHz, $f_1 = 8.24$ GHz, and $f_2 = 9.3$ GHz in a WR-90 waveguide with $s = a/4$, we obtain $N = 3$, $r_0 = 3.16$ mm, and $r_1 = 4.55$ mm. Inserting these binomial values for r_n into Equations (12) and (13), the coupling, $C_b(f)$, and directivity, $D_b(f)$, responses are obtained, as shown in Figure 8. The directivity, $D_b(f)$, deviates from an ideal, maximally flat binomial response due to the effects of the $F(f)$ and $B(f)$ terms. Examination of the $D_b(f)$ response shows that the lower frequency for $D_m = 40$ dB is 8.0 GHz, not 8.24 GHz as calculated for an ideal binomial response. Furthermore, if D_m is reduced to 38.5 dB, a bandwidth from $f_1 = 7.5$ GHz to $f_2 = 9.35$ GHz is obtained. The corresponding ideal binomial response, with $F(f)$, $B(f) = 1$, is shown in Figure 9.



WR-90 Guide, $f_0=8.75$ GHz

Figure 8. Performance of four-hole binomial and Chebychev couplers.

Chebychev Design

A Chebychev response can be obtained by calculating N and r_n , $n = 0, 1 \dots (N - 1)/2$, from

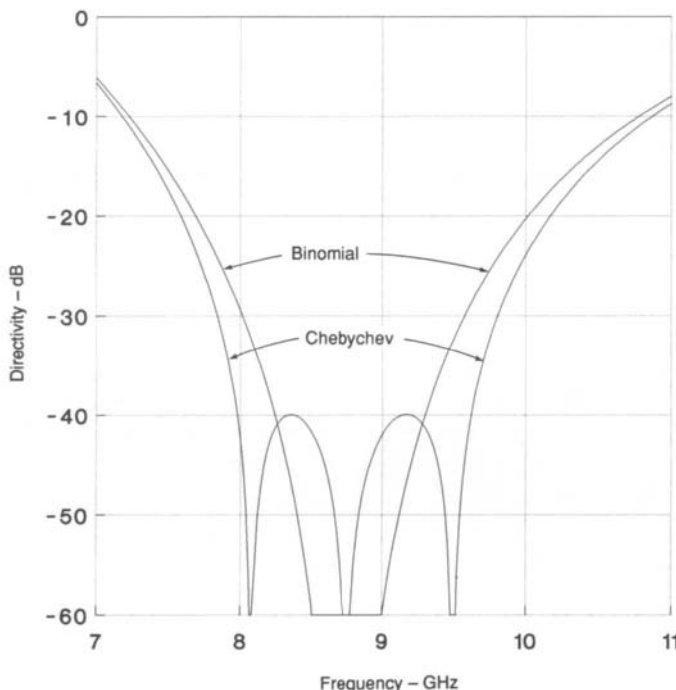
$$N = \cosh^{-1} \left[\frac{10^{D_n/20}}{\cosh^{-1}(\sec \theta_1)} \right] \quad (17)$$

and

$$r_n = \left\{ \frac{k}{2\pi} \int_0^{2\pi} \cos[(N - 2n)\beta] T_N(\sec \theta_1 \cos \theta) d\theta \right\}^{1/3}, \quad (18)$$

where $\theta_1 = \pi d(f_1)/2$, $\theta_2 = \pi - \theta_1$,

$$k = \frac{10^{-(C+D_n)/20}}{|F(f_0)|},$$



WR-90 Guide, $f_0=8.75$ GHz

Figure 9. Ideal directivity vs frequency for ideal four-hole binomial and Chebychev couplers.

and

$$\begin{aligned} T_N &= \cos(N \cos^{-1}(\sec \theta_1 \cos \theta)) \\ &= N\text{th order Chebychev polynomial of argument } \sec \theta_1 \cos \theta. \end{aligned}$$

An ideal Chebychev response gives the optimum compromise between directivity and bandwidth. That is, for a specified directivity, it gives the maximum bandwidth; alternatively, for a specified bandwidth, it gives the maximum directivity. However, due to the $F(f)$, $B(f)$ terms, the actual response is only approximately Chebychev. For example, with $C = 20$ dB, $D_m = 40$ dB, and $f_0 = 8.75$ GHz in a WR-90 guide with $s = a/4$ and $N = 3$, values of $r_0 = 3.25$ mm and $r_1 = 4.51$ mm are obtained from Equation 18. For an ideal Chebychev response, bandwidth values of $f_1 = 8.0$ GHz and $f_2 = 9.6$ GHz are obtained.

Inserting these Chebychev values for r_n into Equations (12) and (13), the coupling $C_t(f)$ and directivity $D_t(f)$ responses, including the $F(f)$

and $B(f)$ terms, are obtained as shown in Figure 8. The calculated directivity response, $D_t(f)$, provides a somewhat greater bandwidth than the corresponding Chebychev response shown in Figure 9. For this example the lower frequency of a 40-dB bandwidth, calculated from $D_t(f)$, is 7.5 GHz, versus 8.0 GHz with an ideal Chebychev response. The coupling response of the binomial and Chebychev designs are nearly identical and are close to the ideal responses shown.

Optimum Design

The Bethe theory, upon which the above analysis and design techniques are based, is only approximate in that it assumes that the forward and backward wave responses, $F(f)$ and $B(f)$, are independent of hole size. It also assumes an infinitely thin common wall. Cohn [4] extended this theory to include the important effects of finite hole size and finite wall thickness. Levy [5–7] further refined and modified the theory to a point at which there is now available a rigorously accurate method of analysis. Levy's theory deals with the practically significant case of a double row of coupling apertures offset from the centerline and accounts for the effects of mutual coupling between the apertures in such a configuration.

These highly sophisticated analysis methods notwithstanding, there still remains the question of optimizing the design of a multihole coupler, i.e., of finding the design that optimizes the performance of a coupler according to some defined criteria. This question has been approached via numerical search methods. In this approach, the design variables, which are the hole radii, are represented by a vector $p = (r_0, r_1, \dots, r_n)$. The desired directivity response is specified by the function $D_{\text{des}}(f)$, and the actual directivity response by $D(f, p)$. The response $D(f, p)$ can be made to account rigorously for the very complicated effects of mutual coupling, intrinsic coupling, hole size, wall thickness, finite conductivity, and dielectric loss.

An error function, $e(p)$, is defined as the normed difference between the actual and the desired responses, i.e.,

$$e(p) = \|D(f, p) - D_{\text{des}}(f)\|.$$

The norm symbol ($\| \cdot \|$) represents some numerical measure of a varying function. A typical choice of norm is the maximum norm, giving

$$e(p) = \max_{f_1 < f < f_2} |D(f, p) - D_{\text{des}}(f)|. \quad (20)$$

An optimum design, p^* , is achieved when $e(p^*)$ is less than some specified value. The mathematics literature [11] contains many ingenious methods that can be used to search in the space of vectors p to find the

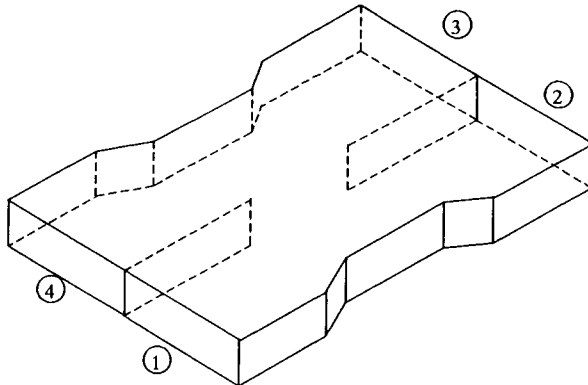


Figure 10. Riblet short-slot coupler. Reproduced with permission from David M. Pozar, *Microwave Engineering*, © 1990 Addison-Wesley Publishing.

optimum, p^* . The mathematical statement of the problem is

$$\min_p e(p) \rightarrow p^*.$$

This approach has been applied to the optimum design of multihole couplers and other microwave circuits and components and has achieved significant improvements to designs based on closed form, analytic methods [11, 12].

Riblet Short-Slot Coupler

The Riblet short-slot coupler [8] (Figure 10) consists of two waveguides with a common sidewall. Continuous coupling takes place in the region in which part of the common sidewall has been removed. A comprehensive theory for such continuous coupling has been developed by Miller [9]. For the case of the configuration in Figure 10, both the even TE_{10} and the odd TE_{20} modes are excited and can be utilized to cause cancellation at the isolated port and addition at the coupled port. The overall width of the interaction region is made less than $2a$ to prevent propagation of the undesired TE_{30} mode. The Riblet short-slot coupler is commonly designed to provide 3-dB coupling.

Schwinger Reversed-Phase Coupler

The Swinger reversed-phase coupler [10], as depicted in Figure 11, consists of two thin slots spaced $\lambda/4$ apart at the center frequency. This

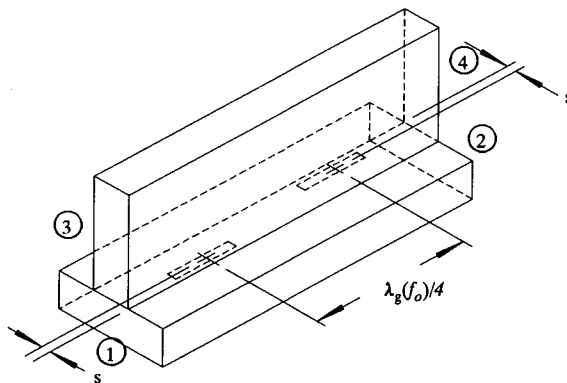


Figure 11. Swinger reversed-phase coupler. Reproduced with permission from David M. Pozar, *Microwave Engineering*, © 1990 Addison-Wesley Publishing.

results in coupling in the backward wave direction and isolation in the forward direction. Directivity is practically independent of frequency, whereas coupling is very frequency sensitive, the opposite of the multihole coupler discussed under multihole waveguide couplers.

Moreno Crossed-Guide Coupler

The Moreno crossed-guide coupler [10] consists of two waveguides at right angles, with coupling provided by two apertures in the common broad wall of the guides (Figure 12). The two apertures are on opposite sides of the waveguide centerline, placed so that they are at diagonally opposite corners of a square of side l , with $l = \lambda/4$ at the design center frequency. This results in coupling to the port to the left of the input port and isolation of the port to the right. Both the coupling and the directivity are

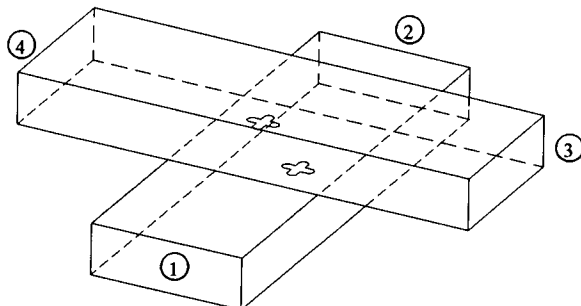


Figure 12. Moreno cross-guide coupler. Reproduced with permission from David M. Pozar, *Microwave Engineering*, © 1990 Addison-Wesley Publishing.

frequency dependent. The apertures are usually crossed slots in order to provide tight coupling.

3. Coupled-Line Couplers

Two parallel transmission lines in close proximity, sharing a common ground plane, have directional coupling properties. The simplest, basic coupler consists of two identical straight lines of common length, uniform cross-section, and homogeneous dielectric, with each of the four ports terminating in a resistance, Z_0 , as illustrated in Figure 13. (Note the change in port numbering from that used for waveguides, above.) Two orthogonal TEM modes may propagate: the even mode, excited by equal voltage drives on the two lines, $E_A = E_B$, and the odd mode, excited by opposite voltage drives, $E_A = -E_B$. The coupling properties, with drive at a single port, are obtained by superposition of the even and odd modes.

The coupler is completely described by three parameters:

$$Z_{0e} = \left. \frac{V_a}{I_A} \right|_{E_A = E_B} = \text{even-mode characteristic impedance}$$

$$Z_{0o} = \left. \frac{V_A}{I_A} \right|_{E_A = -E_B} = \text{odd-mode characteristic impedance}$$

$$\theta = 2\pi f \frac{l}{v_p} = \text{electrical length of coupler,}$$

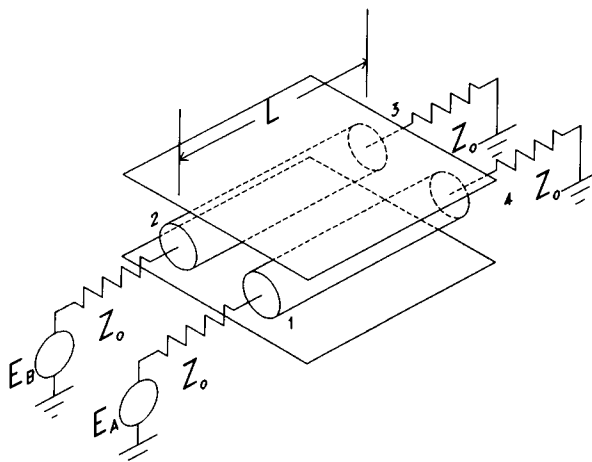


Figure 13. Coupled-line coupler.

where f is the frequency, $\nu_p = c/\sqrt{\epsilon_r}$ is the wave phase velocity, and ϵ_r is the medium relative dielectric constant. The impedance level of the coupler is

$$Z_k = \sqrt{Z_{0e} Z_{0o}}. \quad (21)$$

When $Z_k = Z_0$ the coupler is perfectly matched and has infinite directivity. The scattering matrix of the ideal matched, lossless coupler is, using the port numbering of Figure 13,

$$S = \begin{bmatrix} 0 & S_{21} & 0 & S_{41} \\ S_{21} & 0 & S_{41} & 0 \\ 0 & S_{41} & 0 & S_{21} \\ S_{41} & 0 & S_{21} & 0 \end{bmatrix}, \quad (22)$$

where

$$S_{21} = \frac{jk \sin \theta}{\sqrt{1 - k^2 \cos \theta + j \sin \theta}} = \text{coupled wave voltage} \quad (23)$$

$$S_{41} = \frac{\sqrt{1 - k^2}}{\sqrt{1 - k^2 \cos \theta + j \sin \theta}} = \text{direct wave voltage}, \quad (24)$$

and

$$k = \frac{Z_{0e} - Z_{0o}}{Z_{0e} + Z_{0o}} = \text{voltage coupling coefficient at midband}, \quad \theta = \pi/2. \quad (25)$$

Note that $S_{21}/S_{41} = jk \sin \theta / \sqrt{1 - k^2}$ is pure imaginary, meaning that the direct and coupled waves are in phase quadrature at all frequencies and couplings.

Figure 14 shows the coupling response in decibels for several values of k , normalized to the midband coupling and to a unit center frequency. This pattern repeats, *ad infinitum*, as frequency increases.

The bandwidth over which the coupling remains within a specified tolerance can be increased by cascading two or more couplers end to end to form a multisection coupler. For example, Figure 15 shows the coupling responses and phase differences for symmetrical and asymmetrical three-section 10-dB couplers, specified to have 0.5-dB coupling ripple. Note that symmetrical couplers, in which the coupling decreases symmetrically from the center to the ends, have $(N + 1)/2$ ripples and retain the 90° quadrature property of the single section couplers, whereas asymmetrical cou-

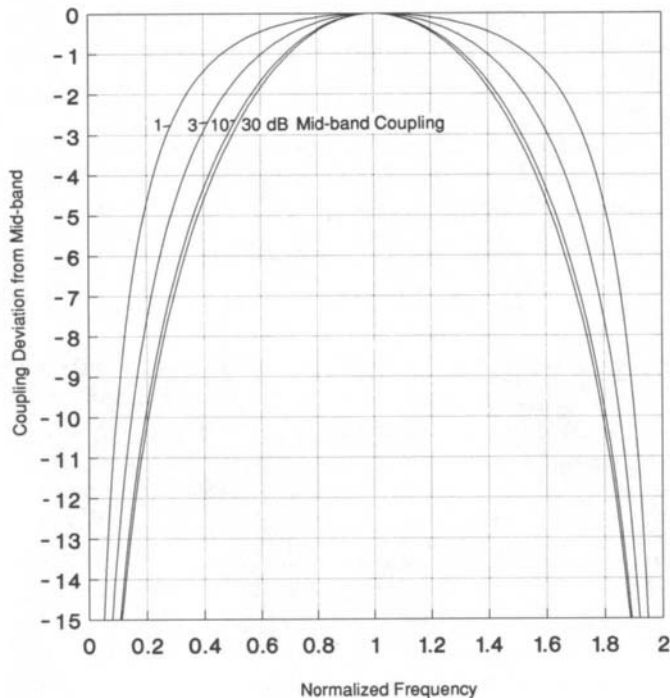


Figure 14. Coupling responses of idealized coupled-line couplers.

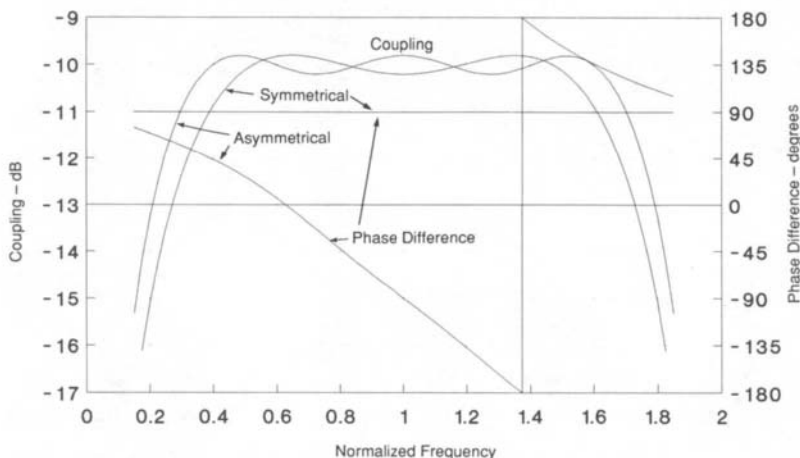


Figure 15. Responses of symmetrical and asymmetrical three-section, 0.2-dB-ripple, coupled-line couplers.

plers, in which the coupling decreases from one end to the other, have N ripples and are not quadrature couplers, but have a greater equal-ripple bandwidth.

Continuously tapered couplers have a high-pass coupling response; i.e., the coupling is theoretically flat to infinite frequency, and the low-frequency cutoff is determined by the total coupler length. The following references provide prescriptions for coupling variation along the length for various multisection and tapered couplers, which may be applied to any of the coupler types described in this section: stepped asymmetrical [13], stepped asymmetrical [14–16], tapered asymmetrical [17], and tapered symmetrical [18–20].

If the dielectric medium is not homogeneous, as in microstrip and many other multilayer planar structures, the propagation is no longer pure TEM, with the consequence that the line is dispersive, and the pattern of Figure 14 does not repeat with increasing frequency. Nevertheless, in most practical cases, at low enough frequencies, the deviation from TEM is slight—called quasi-TEM—and dispersion is ignored. The even and odd modes are still orthogonal, i.e., not coupled, but they will have different phase velocities and effective dielectric constants, with the result that when superposed they do not cancel to provide a perfect match and directivity. Also, because of this, multisection and tapered non-TEM couplers generally do not perform very well over large bandwidths, and each proposed case must be studied individually.

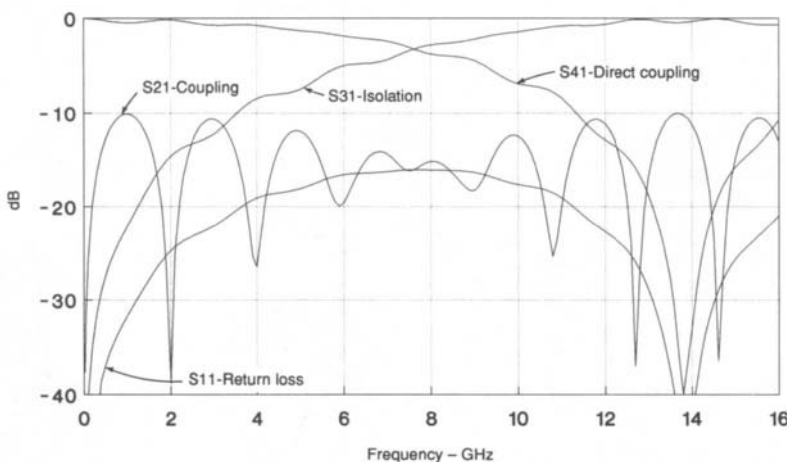


Figure 16. Wideband responses of a 10-dB microstrip coupler on 0.020-in. alumina, centered at 1 GHz.

The scattering parameters of the inhomogeneous dielectric coupler are

$$S_{11} = \frac{j(z_e^2 - 1)\sin\theta_e}{4z_e \cos\theta_e + 2j(z_e^2 + 1)\sin\theta_e} - \frac{j(z_o^2 - 1)\sin\theta_o}{4z_o \cos\theta_o + 2j(z_o^2 + 1)\sin\theta_o} \quad (26)$$

$$S_{21} = \frac{j(z_e^2 - 1)\sin\theta_e}{4z_e \cos\theta_e + 2j(z_e^2 + 1)\sin\theta_e} + \frac{j(z_o^2 - 1)\sin\theta_o}{4z_o \cos\theta_o + 2j(z_o^2 + 1)\sin\theta_o} \quad (27)$$

$$S_{31} = \frac{2z_e}{4z_e \cos\theta_e + 2j(z_e^2 + 1)\sin\theta_e} - \frac{2z_o}{4z_o \cos\theta_o + 2j(z_o^2 + 1)\sin\theta_o} \quad (28)$$

$$S_{41} = \frac{2z_e}{4z_e \cos\theta_e + 2j(z_e^2 + 1)\sin\theta_e} + \frac{2z_o}{4z_o \cos\theta_o + 2j(z_o^2 + 1)\sin\theta_o}, \quad (29)$$

where $z_e = Z_{0e}/Z_0$, $z_o = Z_{0o}/Z_0$ are normalized impedances and where $\theta_e = \omega l/v_{pe}$ and $\theta_o = \omega l/v_{po}$ are the electrical lengths of each mode. We still have $Z_k = \sqrt{Z_{0e}Z_{0o}}$ and $k = (Z_{0e} - Z_{0o})/(Z_{0e} + z_{0o})$, but the coupler is not matched for any Z_k , and the maximum coupling, which occurs

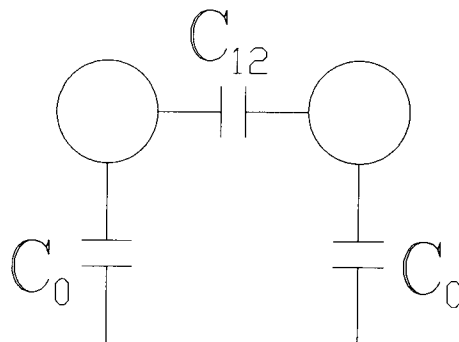


Figure 17. Coupled-line interelectrode capacitances.

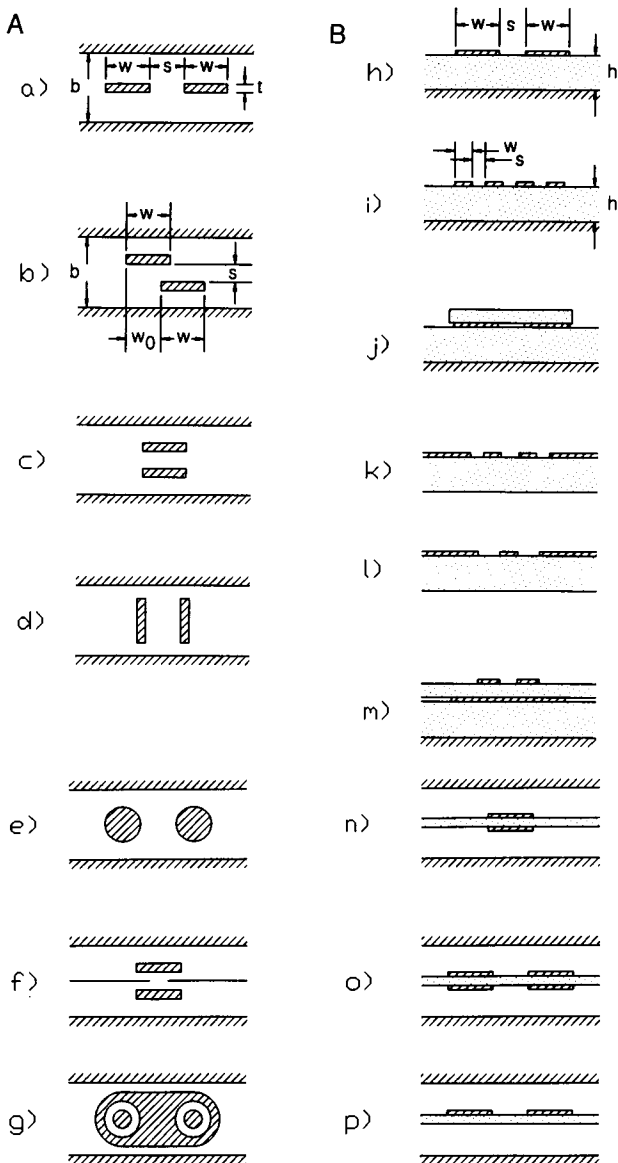
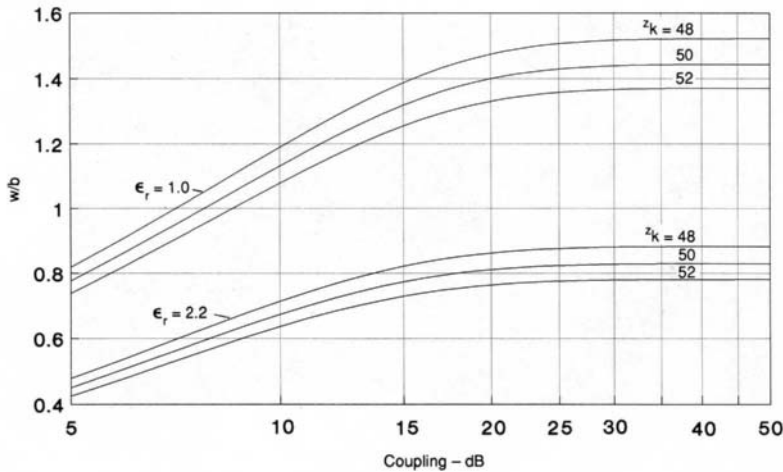


Figure 18. Common coupled-line coupler cross-sections. (A) Homogeneous dielectrics of the relative dielectric constant ϵ_r . (a) Edge-coupled stripline, $t = 0$ [11], and coupled rectangular bars, $t > 0$, [21]. (b) Offset-coupled striplines [22]. (c) Broadside-coupled stripline [23]. (d) Vertical broadside-coupled stripline [24]. (e) Coupled round rods [25]. (f) Slot-coupled stripline [26]. (g) Reentrant coupled lines [27]. (B) Inhomogeneous dielectrics. (h) Microstrip coupled lines [11]. (i) Interdigitated (Lange) coupler [28]. (j) Microstrip with dielectric overlay [29]. (k) Coplanar waveguide coupler [30]. (l) Coupled slotlines [30]. (m) Microstrip reentrant coupler [31]. (n) Broadside-coupled suspended substrate lines [32]. (o) Double-registered edge-coupled suspended substrate lines [33]. (p) Edge-coupled suspended substrate coupler [34].

a w/b vs coupling for $Z_k = 48, 50, 52$ ohms,
 $\epsilon_r = 1.0, 2.2$



b s/b vs coupling for $Z_k = 48, 50, 52$ ohms,
 $\epsilon_r = 1.0, 2.2$

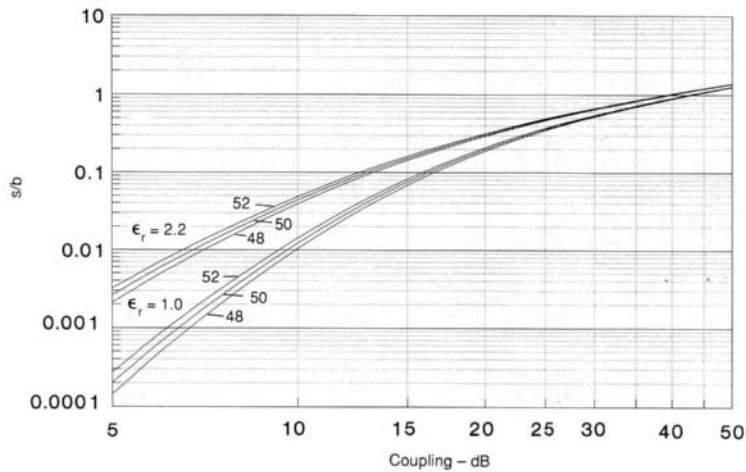


Figure 19. Edge-coupled stripline parameters for $Z_k = 48, 50$, and 52Ω and for $\epsilon_r = 1.0$, and 2.2.
(a) w/b vs coupling. (b) s/b vs coupling.

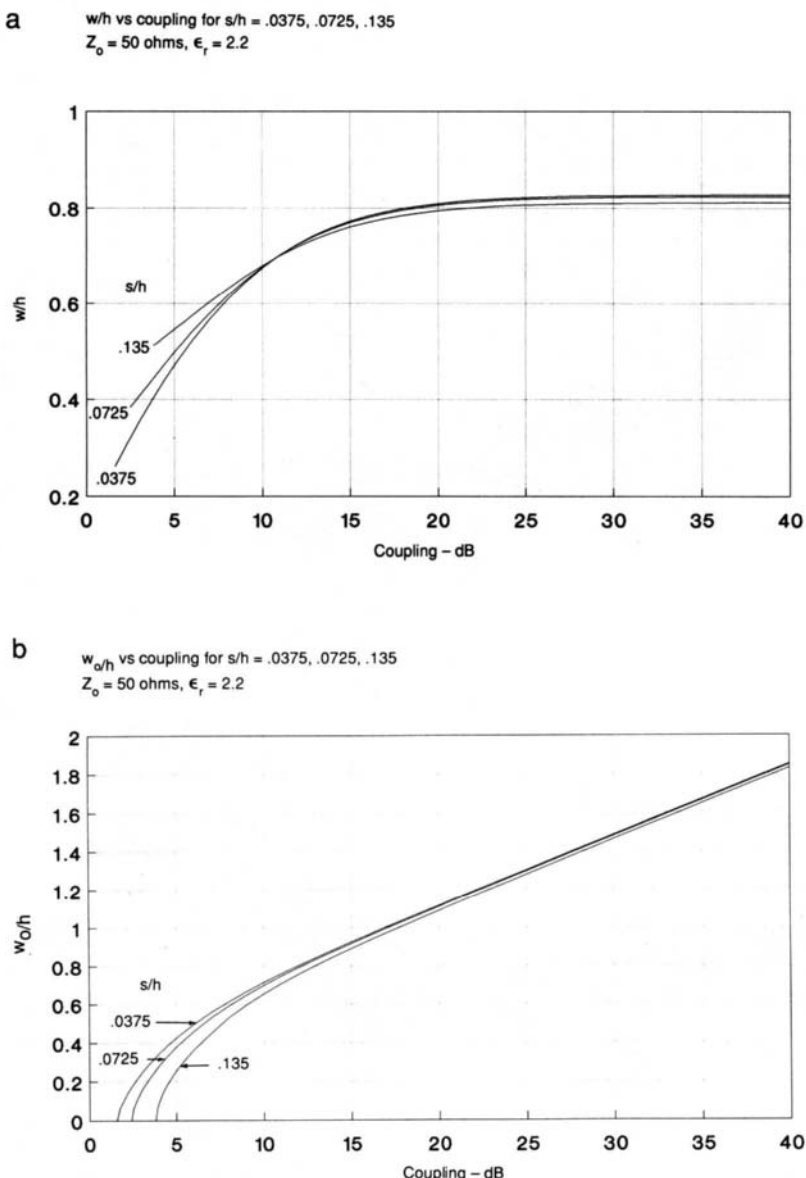
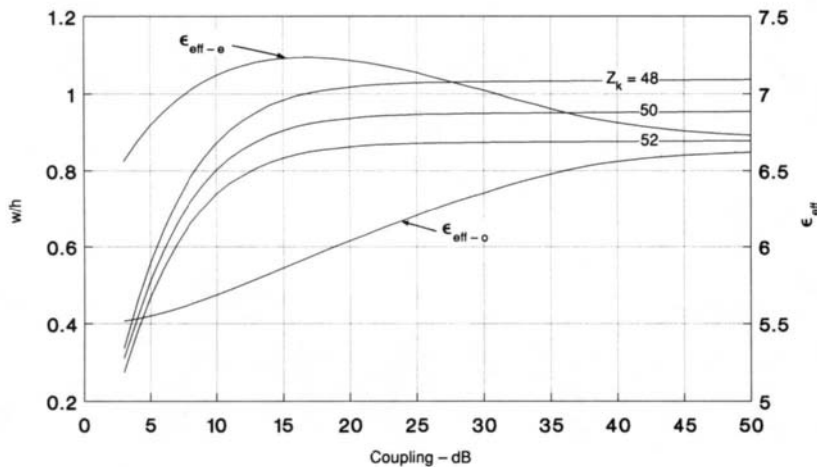


Figure 20. Offset-coupled stripline parameters for $s/h = 0.0375, 0.0725$, and 0.135 , for $Z_0 = 50 \Omega$, and for $\epsilon_r = 2.2$. (a) w/h vs coupling. (b) w_0/h vs coupling.

a w/h vs coupling for $Z_k = 48, 50, 52 \Omega$,
 $\epsilon_r = 10.0$; ϵ_{eff} for 50-ohms



b s/h vs coupling for $Z_k = 48, 50, 52 \Omega$,
 $\epsilon_r = 10.0$

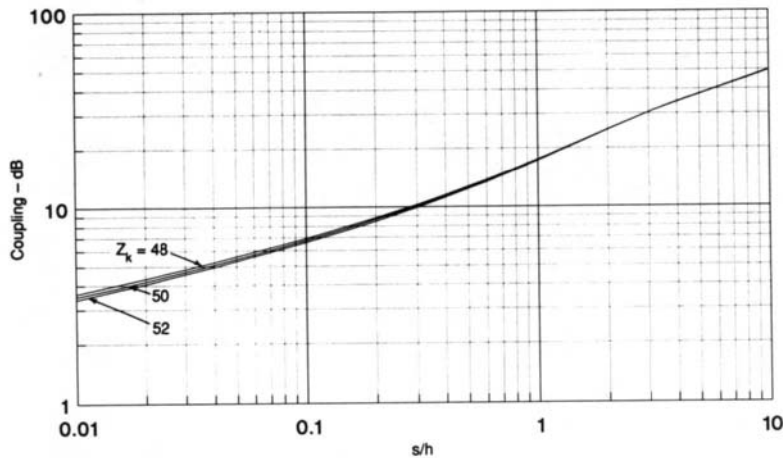
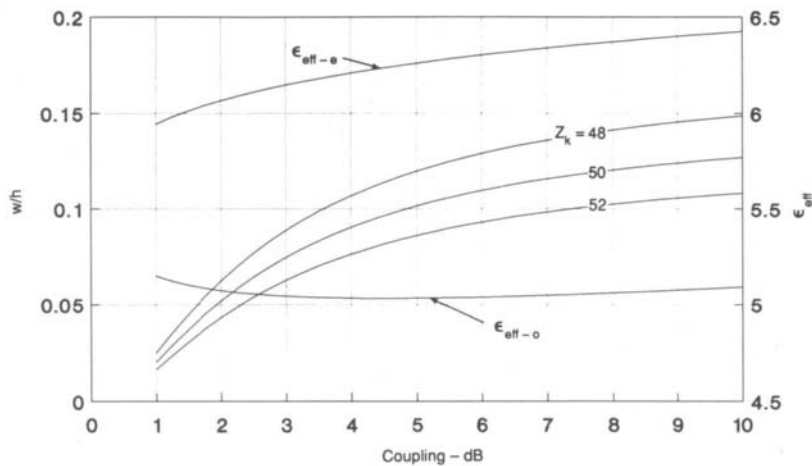


Figure 21. Microstrip coupled line parameters for $Z_k = 48, 50$, and 52Ω and for $\epsilon_r = 10$. (a) w/h and ϵ_{eff} for 50Ω vs coupling (b) s/h vs coupling.



b s/b vs coupling for $Z_k = 48, 50, 52$ ohms,
 $\epsilon_r = 10.0$

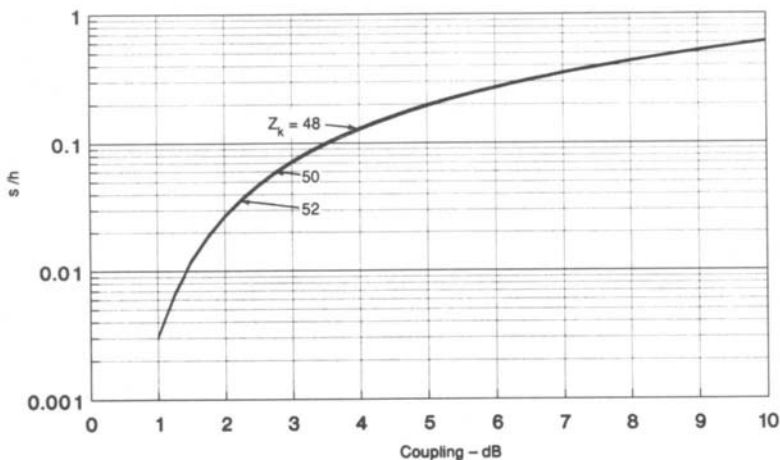


Figure 22. Interdigitated coupled line parameters for $Z_k = 48, 50$, and 52 Ω and for $\epsilon_r = 10$. (a) w/h and ϵ_{eff} for 50 Ω vs coupling. (b) s/h vs coupling.

when $(\theta_e + \theta_0)/2 = \pi/2$, is slightly less than k , due to the reflection and directivity losses. Figure 16 shows the computed coupling response of a typical 10-dB coupler on alumina, including the effects of unequal mode velocities and dispersion.

The design problem is to determine the physical dimensions of a desired coupler type for a given Z_k and k (or Z_{0e} and Z_{0o}) and dielectric constant ϵ_r . This is a formidable mathematical problem, even for the simplest geometries. Typically, for TEM and quasi-TEM formulations, the capacitances per unit length between the two lines and from each to the ground, (Figure 17) are calculated from electrostatics, and the even-

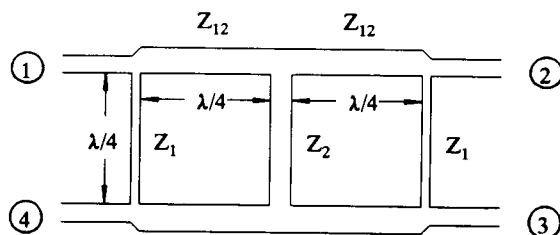


Figure 23. Planar branch-line coupler topology.

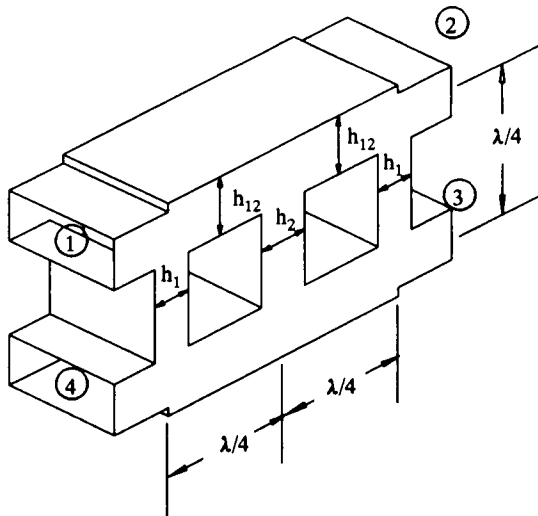


Figure 24. Waveguide branch-guide coupler.

and odd-mode impedances determined from the relations

$$Z_{0e} = \frac{1}{\nu_p C_0} \quad Z_{0o} = \frac{1}{\nu_p (C_0 + 2C_{12})}. \quad (30)$$

There are numerous computer programs commercially available which compute the impedances and effective dielectric constants for virtually any arbitrary cross-sectional geometry. Also, the popular microwave CAD/CAE packages have routines for both synthesis (dimensions from impedances) and analysis (impedances from dimensions) for stripline and microstrip lines. Coupled-line geometries which have been treated in the literature and for which some design data or formulas have been published are shown in Figure 18. Space precludes reproducing design data for all of them. Data for the four most common and important configurations are given in Figures 19 through 22, for specific values of the dielectric constant. All curves are for the zero-thickness approximation. Those for edge-coupled stripline and the microstrip lines are plotted for

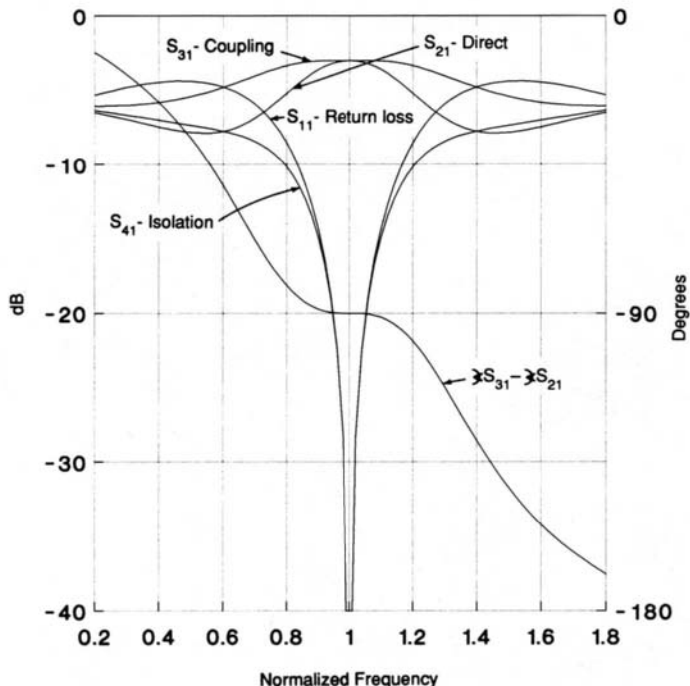


Figure 25. Coupler performance for a two-branch, 50-Ω, 3-dB branch-line hybrid.

$Z_k = 48, 50$, and 52Ω , to provide a rough indication of the sensitivity of 50Ω couplers to variations in the parameters. The data for offset-coupled 50Ω stripline couplers are given for three useful ratios of spacer thickness to ground plane spacing.

4. Branch-Line, Branch-Guide, and Rat-Race Couplers

Branch-line and branch-guide couplers are formed by coupling two main transmission lines together with two or more quarter-wavelength-long transmission lines, spaced by quarter-wavelengths along the coupled lines. For branch-line couplers, i.e., coax and planar configurations, the coupling lines are shunt connected, as illustrated for a three-branch coupler in Figure 23. The branches of a waveguide branch-guide coupler are normally series connected to the main line with E -plane Ts, as sketched in Figure 24, also for a three-branch coupler.

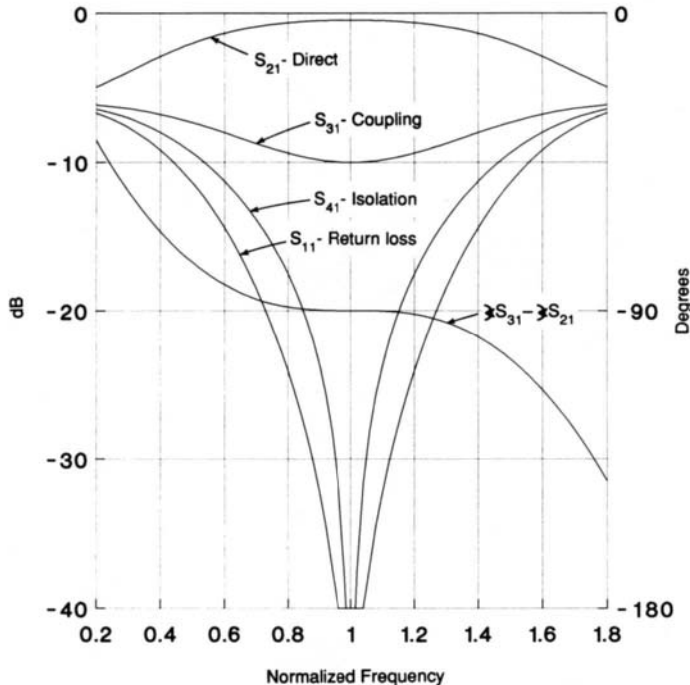
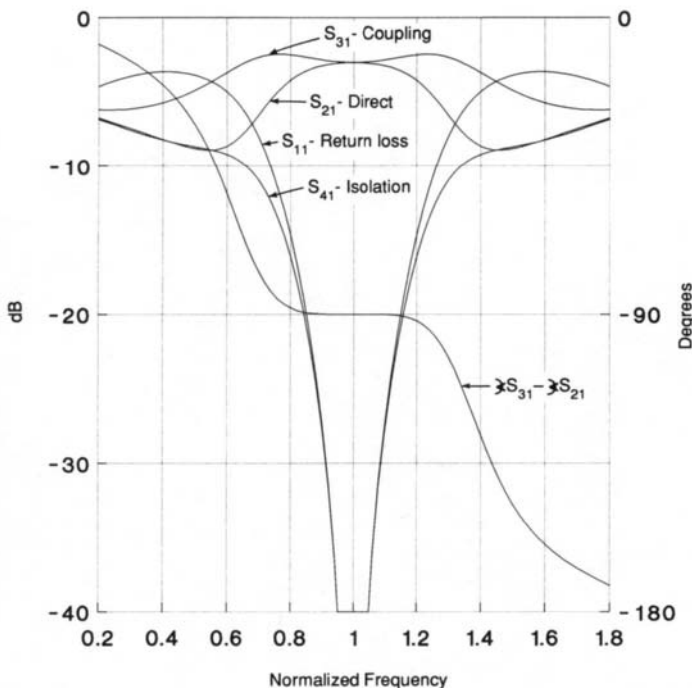


Figure 26. Coupler performance for a two-branch, 50Ω , 10-dB branch-line coupler.

The coupling value and the matching conditions uniquely determine the impedances of the branches and interconnects of two-branch couplers. For three or more branches, the additional degrees of freedom are used to increase the coupling bandwidth. Branch-line and -guide couplers have a much narrower band than coupled-line or waveguide couplers of the same number of sections or holes. Moreover, the impedance ranges involved are rather large, such that branch-line couplers of more than three sections or either branch-line or branch-guide couplers looser than 10 dB become impractical. Consequently, branch-line and -guide couplers find their widest use in tight-coupling applications, especially as 3-dB hybrids, in which coupled lines and multihole waveguide couplers become difficult to fabricate because of the narrow gaps or large holes required.

Branch-Line Couplers

Figures 25 through 28 show the computed responses for two-branch 3- and 10-dB couplers and three-branch Butterworth and Chebychev 3-dB hy-

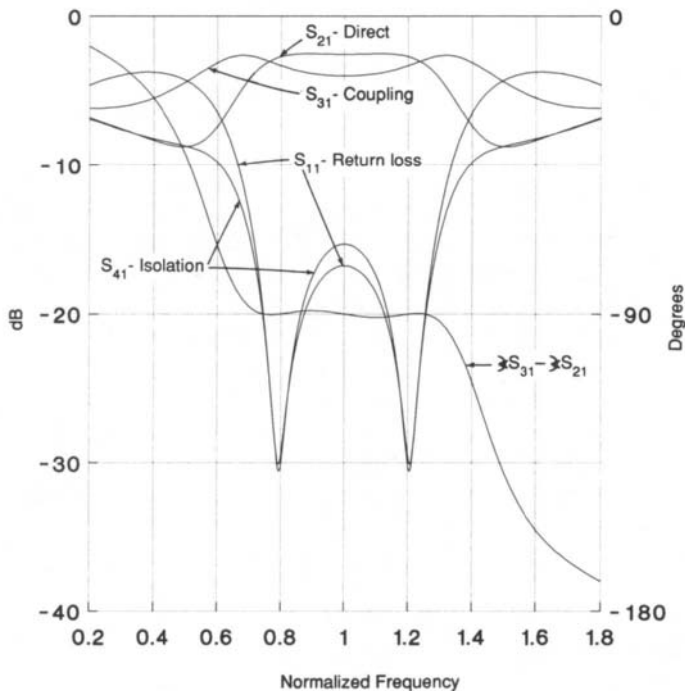


Butterworth Response

Figure 27. Coupler performance for a three-branch $50\text{-}\Omega$, 3-dB Butterworth branch-line hybrid.

brids. Note that the couplers are bandwidth limited in coupling, match, and directivity by about the same amount. Although branch-line couplers are not quadrature at all frequencies, the phase difference between the coupled and the direct arms is within 2° over the useful bandwidth, which is close enough for most applications. The two-branch 3-dB hybrids have a useful bandwidth of about 10%; three-branch Butterworth couplers have about 30% and Chebychev designs have over 50%, although the coupling imbalance is as great as 1.4 dB at midband.

Young [35] has given a formulation to design couplers with two to eight branches, in which the impedances for three or more branches are determined by an optimization procedure. Levy and Lind [36] have given tables of immitances for couplers of three to nine branches, derived by exact synthesis for maximally flat responses and almost exact for Chebychev, characteristics. The branch and main line impedances are plotted in Figure 29 as a function of the coupling for two- and three-branch couplers, from References [35] and [36], and for 50- Ω shunt-branch couplers for impedances up to 200 Ω .



Chebychev Response

Figure 28. Coupler performance for a three-branch, 50- Ω , 3-dB Chebychev branch-line hybrid.

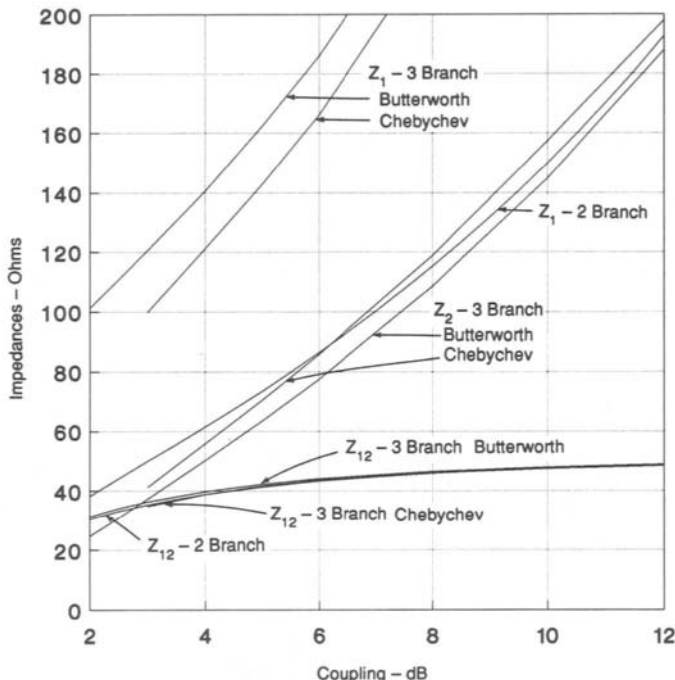


Figure 29. Impedances for two- and three-branch, 50- Ω , branchline couplers vs coupling.

Branch-Guide Couplers

In a waveguide, the impedance values required for each branch are determined by the guide heights, h_i . It is often convenient to maintain the main line impedance, Z_0 , in the main and coupled lines. This requires three or more coupling branches. Both coupling and directivity are frequency sensitive. To obtain tight coupling and high directivity over a wide frequency band, more than three branches may be required, and 10 or more branch designs are not uncommon. The design problem is to choose the branch line impedances, as determined by the h_i , in order to achieve the required coupling and directivity over a specified frequency band. Designs based on binomial and Chebychev distributions are given by Lormer and Crompton [37], Patterson [38], and Levy [39]. T-junction effects are accounted for in these references. Improvements in bandwidth performance can be achieved by using the main and coupled line impedances as design variables. Young has considered this case in Reference [39], and further improvements in performance are presented in References [36] and [40].

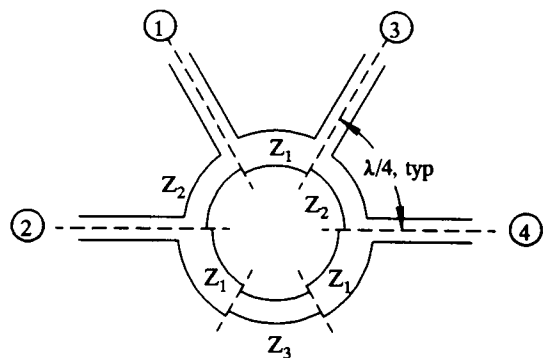


Figure 30. Planar rat-race coupler topology. Adapted with permission from Peter A. Rizzi, *Microwave Engineering: Passive Circuits*, © 1987 Prentice-Hall, Inc.

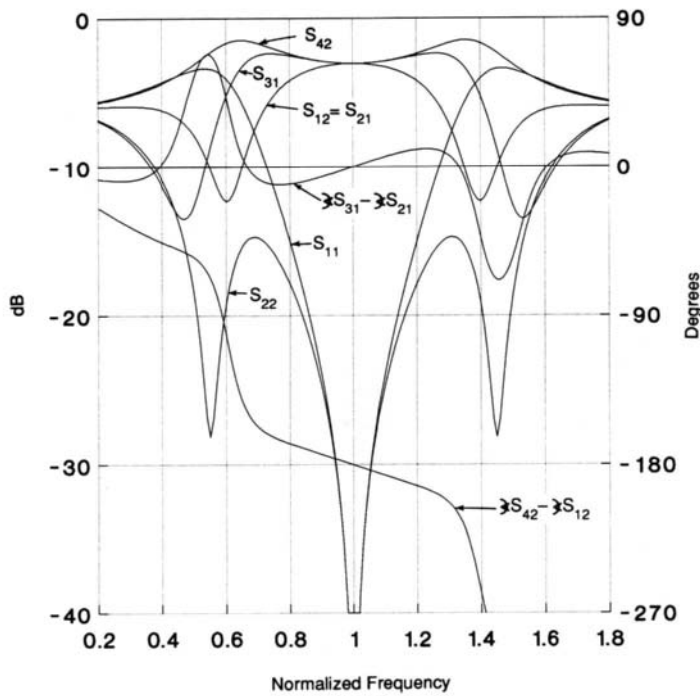


Figure 31. Coupler performance for a 3-dB, 50- Ω conventional rat-race hybrid.

Rat-Race Couplers

A rat-race coupler, or hybrid ring, consists of a $1\frac{1}{2}$ wavelength ring-shaped transmission line with four feed lines entering radially at points spaced as shown in Figure 30, in which the ports are numbered such that the scattering matrix of a 3-dB hybrid, at midband, is given by Equation (7). The feed lines are shunt connected in planar transmission media and normally series connected in a waveguide, although waveguide and coax rings are rarely implemented.

Figure 31 shows the principal responses of a conventional 50- Ω , 3-dB rat-race coupler in which $Z_1 = Z_2 = Z_3 = 70.7 \Omega$. For input into port 1, the power splits between port 2 and port 3, with port 4 isolated. The outputs are in phase at midband, and the phase difference deviates by several degrees at the edges of the useful bandwidth. For input at port 2, the power splits between port 1 and port 4, with port 3 isolated. At midband the phase difference between outputs is 180° , again with several degrees of variation over the useful bandwidth. The isolations, S_{41} and

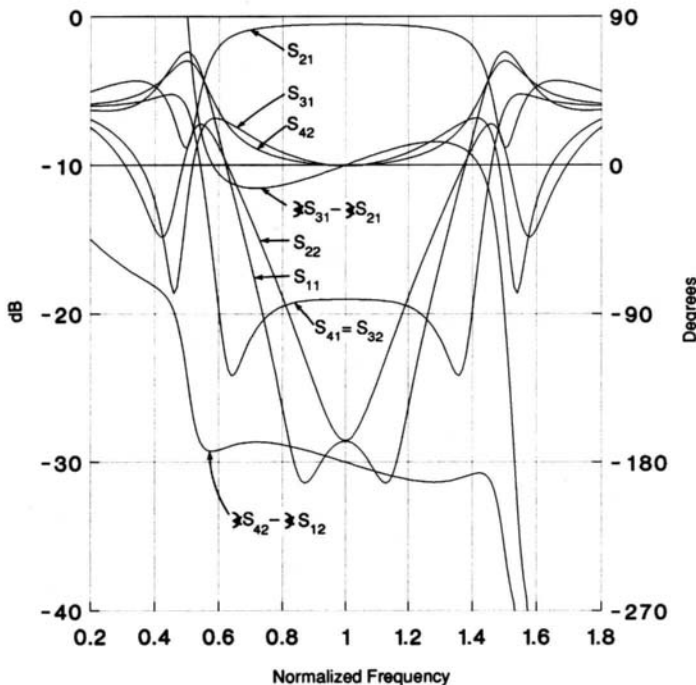


Figure 32. Coupler performance for a 3-dB, 50- Ω modified rat-race hybrid.

S_{32} , are not shown in the figure; they are both similar to the port 1 return loss, S_{11} . The useful bandwidth, over which the isolation and return loss are better than 20 dB and the coupling imbalance better than 1 dB, is about 30%.

The coupling, defined here by $S_{21} = S_{12}$, may be varied by appropriately altering the ring segment impedances Z_1 and Z_2 . As the coupling is made looser, the bandwidth with regard to return loss, isolation, and coupling deviation increases slightly, but the directivity bandwidth decreases substantially. For instance, for a conventional rat-race coupler in which the $\frac{3}{4}\lambda$ segment has a uniform impedance, $Z_3 = Z_1$ [41], a 10-dB coupler has a bandwidth of about 34% for a 1-dB coupling deviation and > 20 dB of isolation, whereas the bandwidth for 20 dB of directivity is only 14%. Agrawal and Mikucki [42] have analyzed a modified design, with $Z_3 = Z_2$, in which the coupling and isolation bandwidths are significantly broadened at the expense of relatively low directivity across the band. Figure 32 shows the characteristics of such a modified 10-dB rat-race coupler. Figure 33 provides the impedances for the ring segments vs the coupling for 50- Ω rat-race couplers of both types.

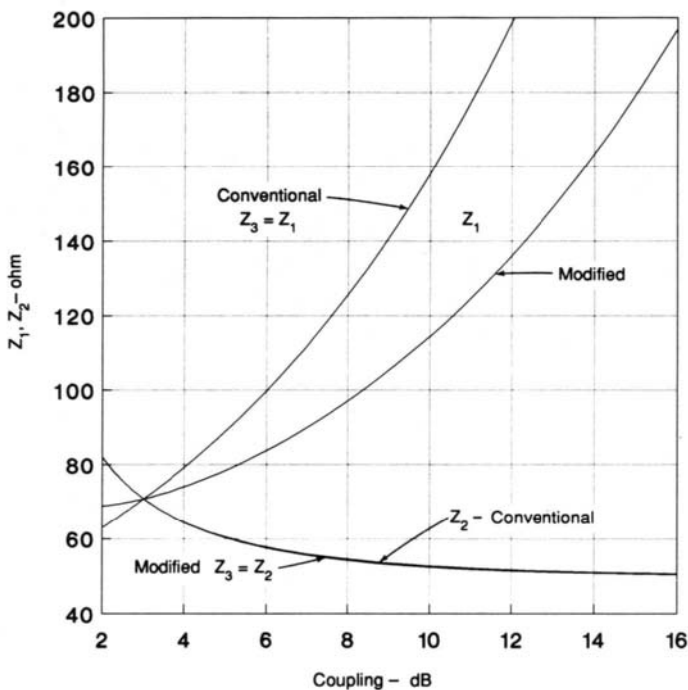


Figure 33. Impedances for conventional and modified 50- Ω rat-race couplers.

The broadbanding technique of March [43] replaces the $\frac{3}{4}\lambda$ segment with a 3-dB, $\lambda/4$ -coupled line coupler of impedance Z_1 , with normally coupled and direct ports shorted to the ground. This scheme provides a 3-dB hybrid with a 1-dB imbalance bandwidth of almost 3.5:1, 20 dB of return loss over 40%, and isolation always greater than 24 dB. Although this coupler has excellent performance, it is rarely used due to its difficult construction. Ashoka [44] has described a deft technique for extending the practically achievable ranges of coupling and bandwidth of both branch-line and rat-race couplers by using impedance and admittance inverters in place of extremely high- and low-transmission line impedances.

5. Developments

The design of basic microwave directional couplers is a mature field, such that most work has concentrated on refined mathematical analyses or reports of new couplers of novel structure or materials, which fall outside the scope of this chapter. One area, however, does deserve mention. With the steady growth in monolithic microwave integrated circuit technology, there has been concomitant interest in achieving the tight coupling and reduced size of microstrip-type couplers. Tight coupling is being achieved via multilayer couplers, i.e., couplers as in Figure 18h, but with one strip on top of the other, separated by another dielectric layer. Prouty and Schwarz [45], Tran and Nguyen [46], and Tsai and Gupta [47] provide much useful design information as well as a rich list of references. At the lower microwave frequencies, substantial size reduction can be achieved by employing lumped elements to some extent. Vogel [48] is an excellent starting point for applying this technique.

References

- [1] R. E. Collin, *Foundations of Microwave Engineering*. New York: McGraw-Hill, 1966.
- [2] D. M. Pozar, *Microwave Engineering*. Reading, MA: Addison Wesley, 1990.
- [3] H. A. Bethe, Theory of diffraction by small holes, *Phys. Rev.*, Vol. 66, pp. 163–182, 1944.
- [4] S. B. Cohn, Microwave coupling by large apertures, *Proc. IRE.*, Vol. 40, pp. 697–699, 1952.
- [5] R. Levy, Directional couplers, in *Advances in Microwaves* (L. Young, ed.), Vol. 1. New York: Academic Press, 1966.
- [6] R. Levy, Analysis and synthesis of waveguide multiaperture directional couplers, *IEEE Trans. Microwave Theory Tech.*, Vol. MTT-16, pp. 995–1006, Dec. 1968.
- [7] R. Levy, Improved single and multiaperture waveguide coupling theory, including explanation of mutual interaction, *IEEE Trans. Microwave Theory Tech.*, Vol. MTT-28, pp. 331–338, Apr. 1980.

- [8] H. J. Riblet, The short-slot hybrid junction, *Proc. IRE.*, Vol. 40, pp. 180–184, Feb. 1952.
- [9] S. E. Miller, Coupled wave theory and waveguide applications, *Bell Syst. Tech. J.*, Vol. 33, pp. 661–719, May 1954.
- [10] T. N. Anderson, Directional coupler design nomograms, *Microwave J.*, Vol. 2, pp. 34–38, May 1959.
- [11] K. C. Gupta, R. Garg, and R. Chadha, *Computer-Aided Design of Microwave Circuits*. Norwood, MA: Artech House, 1981.
- [12] S. J. Blank, An algorithm for the empirical optimization of antenna arrays, *IEEE Trans. Antennas Propag.*, Vol. AP-31, pp. 685–689, July 1983.
- [13] R. Levy, Tables for asymmetric multi-element coupled-transmission-line directional couplers, *IEEE Trans. Microwave Theory Tech.*, Vol. MTT-12, pp. 275–279, May 1964.
- [14] E. G. Cristal and L. Young, Theory and tables of optimum symmetrical TEM-mode coupled-transmission-line directional couplers, *IEEE Trans. Microwave Theory Tech.*, Vol. MTT-13, pp. 544–558, Sept. 1965.
- [15] P. P. Toulios and A. C. Todd, Synthesis of TEM-mode directional couplers, *IEEE Trans. Microwave Theory Tech.*, Vol. MTT-13, pp. 536–544, Sept. 1965.
- [16] J. P. Shelton and J. A. Mosko, Synthesis and design of wide-band, equal-ripple TEM directional couplers and fixed phase shifters, *IEEE Trans. Microwave Theory Tech.*, Vol. MTT-14, pp. 462–473, Oct. 1966.
- [17] F. Arndt, Tables for asymmetric Chebyshev high-pass TEM-mode directional couplers, *IEEE Trans. Microwave Theory Tech.*, Vol. MTT-18, pp. 633–638, Sept. 1970.
- [18] C. P. Tresselt, The design and construction of broadband, high-directivity, 90-degree couplers using nonuniform line techniques, *IEEE Trans. Microwave Theory Tech.*, Vol. MTT-14, pp. 647–656, Dec. 1966.
- [19] D. W. Kammler, The design of discrete N -section and continuously tapered symmetrical microwave TEM directional couplers, *IEEE Trans. Microwave Theory Tech.*, Vol. MTT-17, pp. 577–590, Aug. 1969.
- [20] G. Saulich, A new approach in the computation of ultrahigh degree equal-ripple polynomials for 90°-coupler synthesis, *IEEE Trans. Microwave Theory Tech.*, Vol. MTT-29, pp. 132–135, Feb. 1981.
- [21] W. Getsinger, Coupled rectangular bars between parallel plates, *IRE Trans. Microwave Theory Tech.*, Vol. MTT-10, pp. 65–72, Jan. 1962.
- [22] J. P. Shelton, Jr., Impedances of offset parallel-coupled strip transmission lines, *IEEE Trans. Microwave Theory Tech.*, Vol. MTT-14, pp. 7–14, Jan. 1966.
- [23] S. B. Cohn, Characteristic impedances of broadside-coupled strip transmission lines, *IRE Trans. Microwave Theory Tech.*, Vol. MTT-8, pp. 633–637, Nov. 1960.
- [24] S. Yamamoto, T. Azakami, and K. Itakura, Slit-coupled strip transmission lines, *IEEE Trans. Microwave Theory Tech.*, Vol. 14, pp. 524–553, Nov. 1966.
- [25] S. Roslonice, An improved algorithm for the computer-aided design of coupled slab lines, *IEEE Trans. Microwave Theory Tech.*, Vol. MTT-37, pp. 258–261, Jan. 1989.
- [26] J. H. Cloete, Rectangular bars coupled through a finite-thickness slot, *IEEE Trans. Microwave Theory Tech.*, Vol. MTT-32, pp. 39–45, Jan. 1984.
- [27] S. B. Cohn, Re-entrant cross-section and wideband 3-dB hybrid coupler, *IRE Trans. Microwave Theory Tech.*, Vol. MTT-11, pp. 254–258, July 1963.
- [28] R. M. Osmani, Synthesis of Lange couplers, *IEEE Trans. Microwave Theory Tech.*, Vol. MTT-29, pp. 168–170, Feb. 1981.
- [29] L. Su, T. Itoh, and J. Rivera, Design of an overlay directional coupler by a full-wave analysis, *IEEE Trans. Microwave Theory Tech.*, Vol. MTT-31, pp. 1017–1022, Dec. 1983.

- [30] K. Gupta, R. Garg, and I. Bahl, *Microstrip Lines and Slotlines*, Sect. 8.6. Dedham, MA: Artech House, 1986.
- [31] A. Pavio and S. Sutton, A microstrip re-entrant mode quadrature coupler for hybrid and monolithic circuit applications, *Proc. IEEE Int. Microwave Symp.* pp. 573–576, 1990.
- [32] I. Bahl and P. Bhartia, Characteristics of inhomogeneous broadside-coupled striplines, *IEEE Trans. Microwave Theory Tech.*, Vol. MTT-28, pp. 529–535, June 1980.
- [33] S. Koul and B. Bhat, Broadside, edge-coupled symmetric strip transmission lines, *IEEE Trans. Microwave Theory Tech.*, Vol. MTT-30, pp. 1874–1880, Nov. 1982.
- [34] M. Horne and F. Medina, Multilayer planar structures for high directivity directional coupler design, *IEEE Trans. Microwave Theory Tech.*, Vol. MTT-34, pp. 1442–1448, Dec. 1986.
- [35] L. Young, Branch guide directional couplers, *Proc. Natl. Electr. Conf.*, Vol. 12, pp. 723–732, 1956; L. Young, Synchronous branch guide couplers for low and high power applications, *IRE Trans. Microwave Theory Tech.*, Vol. MTT-10, pp. 459–475, Nov. 1962.
- [36] R. Levy and L. Lind, Synthesis of symmetrical branch-guide directional couplers, *IEEE Trans. Microwave Theory Tech.*, Vol. MTT-16, pp. 80–89, Feb. 1968.
- [37] P. D. Lormer and J. W. Crompton, A new form of hybrid junction for microwave frequencies, *IEE Proc.*, Vol. B104, pp. 261–264, May 1957.
- [38] K. G. Patterson, A method for accurate design of broadband multibranch waveguide couplers, *IRE Trans. Microwave Theory Tech.*, Vol. MTT-7, pp. 466–473, Oct. 1959.
- [39] R. Levy, A guide to the practical application of Chebyshev functions to the design of microwave components, *IEE Proc.*, Vol. C106, pp. 193–199, June 1959.
- [40] R. Levy, Zolotarev branch-guide couplers, *IEEE Trans. Microwave Theory Tech.*, Vol. MTT-21, pp. 95–99, Feb. 1973.
- [41] C. Pon, Hybrid-ring directional coupler for arbitrary power divisions, *IRE Trans. Microwave Theory Tech.*, Vol. MTT-9, pp. 529–535, Nov. 1961.
- [42] A. Agrawal and G. Mikucki, A printed-circuit hybrid-ring directional coupler for arbitrary power divisions, *IEEE Trans. Microwave Theory Tech.*, Vol. MTT-34, pp. 1401–1407, Dec. 1986.
- [43] S. March, A wideband stripline hybrid ring, *IEEE Trans. Microwave Theory Tech.*, Vol. MTT-16, p. 361, June 1968.
- [44] H. Ashoka, Practical realization of difficult microstrip line hybrid couplers and power dividers, *IEEE Int. Microwave Symp.*, pp. 273–276, 1992.
- [45] M. D. Prouty and S. E. Schwarz, Hybrid couplers in bilevel microstrip, *IEEE Trans. Microwave Theory Tech.*, Vol. MTT-41, pp. 1939–1944, Nov. 1993.
- [46] M. Tran and C. Nguyen, Modified broadside-coupled microstrip lines suitable for MIC and MMIC applications and a new class of broadside-coupled band-pass filters, *IEEE Trans. Microwave Theory Tech.*, Vol. MTT-41, pp. 1336–1342, Aug. 1993.
- [47] C.-M. Tsai and K. C. Gupta, A generalized model for coupled lines and its application to two-layer planar circuits, *IEEE Trans. Microwave Theory Tech.*, Vol. MTT-41, pp. 2190–2199, Dec. 1992.
- [48] R. W. Vogel, Analysis and design of lumped- and lumped-distributed-element directional couplers for MIC and MMIC applications, *IEEE Trans. Microwave Theory Tech.*, Vol. MTT-40, pp. 253–262, Feb. 1992.

Microwave Ferrite Devices

Jerzy Krupka and Wojciech Glogier

I. Ferrite Materials for Microwave Applications

In this chapter relationships among magnetic flux density B , internal intensity of magnetization M , and applied magnetic field H are taken to be, after Baden Fuller [5], as follows:

$$B = \mu_0 H + M \quad B = \mu H \quad M = \chi H.$$

Microwave Properties of Ferrite Materials Magnetized to Saturation

In a rectangular or cylindrical coordinate system with its z -axis parallel to an applied static magnetic field whose strength is sufficient to saturate ferrite material, permeability tensor has the following form [5, pp. 22–28],

$$[\mu] = \begin{bmatrix} \mu & j\kappa & 0 \\ -j\kappa & \mu & 0 \\ 0 & 0 & \mu_z \end{bmatrix}, \quad (1)$$

with

$$\mu_z = \mu_0$$

$$\mu = \mu_0 + \frac{\gamma M_s(\gamma H_0 + j\omega\alpha)}{(\gamma H_0 + j\omega\alpha)^2 - \omega^2} \quad (2)$$

$$\kappa = \frac{-\omega\gamma M_s}{(\gamma H_0 + j\omega\alpha)^2 - \omega^2}, \quad (3)$$

where M_s is the saturation magnetization, H_0 is the internal magnetic field strength in a ferrite medium, α is the damping factor related to the resonance linewidth ΔH by $\alpha = \Delta H / 2H_0$, $\gamma = 2.21 \times 10^5 g_{\text{eff}} / 2$ (rad/s/(A/m)) or $2.8 g_{\text{eff}} / 2$ (MHz/Oe), and g_{eff} is the effective gyro-magnetic ratio (for most ferrite materials $g_{\text{eff}} \approx 2$).

Imaginary parts of permeability tensor components calculated from these formulas are in good agreement with experiments only within the so-called spin-wave manifold (for a narrow range of H_0 or ω near ferromagnetic resonance). Outside this region another parameter, called the effective linewidth ΔH_{eff} [52], allows us to assess losses more accurately (ΔH_{eff} should be substituted instead of ΔH in the formulas for particular tensor components). It should be pointed out that ΔH_{eff} for particular materials may be several times smaller than ΔH . Imaginary parts of permeability tensor components and the effective linewidth ΔH_{eff} are usually not specified by manufacturers above ferromagnetic resonance.

Properties of Ferrite Materials for the Partially Magnetized State

For the completely demagnetized state, assuming additionally that $\omega > \omega_m$, the permeability tensor becomes a scalar whose real part was approximately given by a formula derived by Schrömann [47],

$$\mu_d = \mu_0 \left\{ \frac{1}{3} + \frac{2}{3} \left[1 - (\omega_m/\omega)^2 \right]^{1/2} \right\}, \quad (4)$$

where $\omega_m = \gamma M_s / \mu_0$. For the partially magnetized state, real parts of permeability tensor components can be approximated by the following semiempirical expressions, given by Green and Sandy [20],

$$\mu = \mu_d + (1 - \mu_d) (M/M_s)^{3/2} \quad (5)$$

$$\kappa = (M/M_s) (\omega_m/\omega) \quad (6)$$

$$\mu_z = \mu_d^{[1-(M/M_s)^{5/2}]}, \quad (7)$$

where M is the intensity of the average static internal magnetization.

Imaginary parts of the scalar permeability μ_d and permeability tensor components for the partially magnetized state are rarely specified by manufacturers. They can be approximated, for the components μ and κ , from the effective linewidth ΔH_{eff} if it is specified, but only for a limited range of external magnetic fields magnetizing ferrite.

Microwave Properties of Ferrite Materials for High-Power Levels

For high microwave power levels, ferrite materials exhibit anomalous absorption above a threshold critical field, H_c . The critical microwave magnetic field varies with the static magnetic field, and its minimum value is given in Reference [40, pp. 243–296],

$$H_c = \frac{2\Delta H_k(\omega/\omega_m)[1 - (\omega_0/\omega)]}{1 - (\omega_m/2\omega) + [1 + (\omega_m/2\omega)^2]^{1/2}}, \quad (8)$$

where $\omega_0 = \gamma H_0$ and ΔH_k is the spin-wave resonance linewidth.

2. Electromagnetic Waves in a Ferrite Medium

Plane Waves in an Infinite Ferrite Medium

Longitudinal Magnetization

A linearly polarized electromagnetic wave propagating along the direction of the static magnetic field in an infinite ferrite medium can be decomposed into two opposite rotating circularly polarized waves having different propagation constants. The propagation constant for a positive circularly polarized wave can be expressed in terms of scalar permeability $\mu + \kappa$ according to Equation (9).

$$\beta^+ = \omega [\epsilon(\mu + \kappa)]^{1/2}, \quad (9)$$

where ϵ is the permittivity of the ferrite medium.

For a negative circularly polarized wave, the propagation constant is a function of scalar permeability $\mu - \kappa$ [Equation (10)].

$$\beta^- = \omega [\epsilon(\mu - \kappa)]^{1/2}. \quad (10)$$

As the result of different propagation constants, the direction of polarization for a linearly polarized wave subject to rotation (known as Faraday rotation) in the plane perpendicular to the direction of propagation. The angle of Faraday rotation per unit length of the linearly polarized wave can be expressed in terms of propagation constants for circularly polarized waves as follows:

$$\psi = (\beta^+ - \beta^-)/2. \quad (11)$$

Transverse Magnetization

For transverse magnetization, there are two different propagation constants, one for the ordinary wave (microwave magnetic field parallel to

the direction of the DC field),

$$\beta = \omega [\epsilon \mu_z]^{1/2}, \quad (12)$$

and the other for the extraordinary wave (microwave magnetic field perpendicular to the direction of the DC field),

$$\beta = \omega [\epsilon \mu_{\perp}]^{1/2}, \quad (13)$$

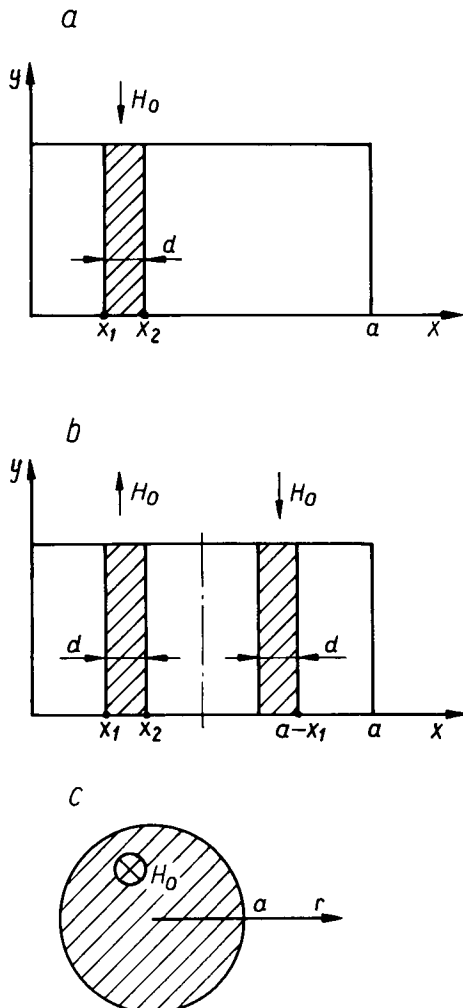


Figure 1. Examples of waveguides containing magnetized ferrites whose electromagnetic fields can be exactly found.

with

$$\mu_{\perp} = (\mu^2 - \kappa^2)/\mu. \quad (14)$$

Waves in Ferrite-Loaded Waveguides

Exact expressions for the electromagnetic fields in ferrite-loaded waveguides are available only for a few simple geometries of rectangular and circular cylindrical waveguides. Some of them are shown in Figure 1. For such cases exact electromagnetic field expressions and characteristic equations can be found, enabling design of ferite devices using such waveguides. Characteristic equations for these waveguides are presented below.

Characteristic Equation for a Transversely Magnetized Ferrite Slab (Figure 1a) [5, pp. 118–126]

$$\begin{aligned} & \frac{kk_f}{\mu_0\mu_{\perp}} \{ \tan(kx_1) + \tan[k(a - x_2)] \} \cot[k_f(x_2 - x_1)] \\ & - \frac{k\beta\kappa}{\mu_0\mu_{\perp}\mu} \{ \tan(kx_1) - \tan[k(a - x_2)] \} \\ & - \left[\left(\frac{k_f}{\mu_{\perp}} \right)^2 + \left(\frac{\kappa\beta}{\mu_{\perp}\mu} \right)^2 \right] \tan(kx_1) \tan[k(a - x_2)] + \left(\frac{k}{\mu_0} \right)^2 = 0, \end{aligned} \quad (15)$$

where $k_f^2 = \omega^2\epsilon\mu_{\perp} - \beta^2$ and $k^2 = \omega^2\epsilon_0\mu_0 - \beta^2$.

Characteristic Equation for Two Symmetrical Ferrite Slabs Transversely Magnetized in Opposite Directions (Figure 1b) [5, pp. 126–127]

$$\begin{aligned} & \frac{kk_f}{\mu_0\mu_{\perp}} \left\{ \tan(kx_1) \tan \left[k \left(\frac{1}{2}a - x_2 \right) \right] - 1 \right\} \cot[k_f(x_2 - x_1)] \\ & + \frac{k\beta\kappa}{\mu_0\mu_{\perp}\mu} \{ 1 + \tan(kx_1) \tan[k(\frac{1}{2}a - x_2)] \} \\ & + \left[\left(\frac{k_f}{\mu_{\perp}} \right)^2 + \left(\frac{\kappa\beta}{\mu_{\perp}\mu} \right)^2 \right] \tan(kx_1) + \left(\frac{k}{\mu_0} \right)^2 \tan \left[k \left(\frac{1}{2}a - x_2 \right) \right] = 0. \end{aligned} \quad (16)$$

Characteristic Equation for a Longitudinally Magnetized Completely Ferrite-Filled Circular Waveguide (Figure 1c) [21, Chap. 8]

$$(k_f^2/\gamma_1 - \gamma_1) J'_m(\gamma_1 a) - (k_f^2/\gamma_2 - \gamma_2) J'_m(\gamma_2 a) \\ - \frac{m\kappa\beta^2}{\mu a} (\gamma_1^{-2} - \gamma_2^{-2}) J_m(\gamma_1 a) J_m(\gamma_2 a) = 0, \quad (17)$$

where

$$k_f^2 = \omega^2 \epsilon \mu_{\perp} - \beta^2$$

$$\gamma_{1,2}^2 = \frac{1}{2} [\omega^2 \epsilon (\mu_{\perp} + \mu_z) - \beta^2 (1 + \mu_z / \mu)]$$

$$\pm \left\{ \frac{1}{4} [\omega^2 \epsilon (\mu_{\perp} - \mu_z) - \beta^2 (1 - \mu_z / \mu)]^2 + \omega^2 \epsilon \mu_z \kappa^2 / \mu^2 \right\}^{1/2}.$$

Examples of numerical solutions to Equations (15) through (17) for the dominant modes are presented in Figures 2–4. Characteristic equations and the results of computations for more complicated ferrite-dielectric filled waveguides can be found in many papers and textbooks. For rectangular waveguide structures, see, for example, Reference [14] or [33] and, for cylindrical ones, see Reference [5, Chap. 3].

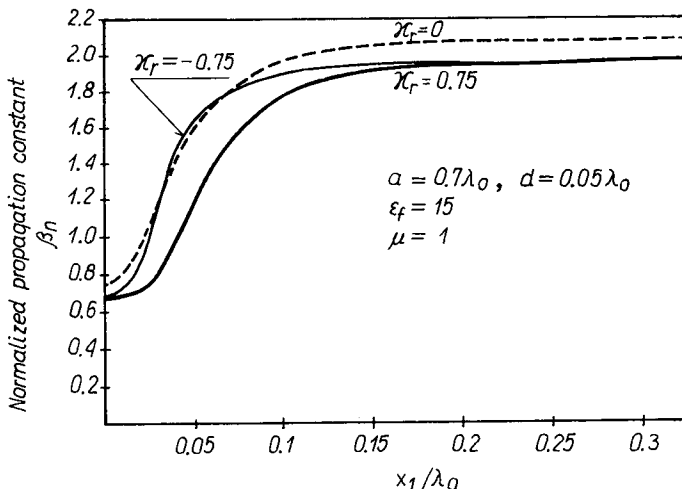


Figure 2. Normalized propagation constant, $\beta_n = \beta / (\omega / c)$, versus slab position for a rectangular waveguide containing one ferrite slab (Figure 1a).

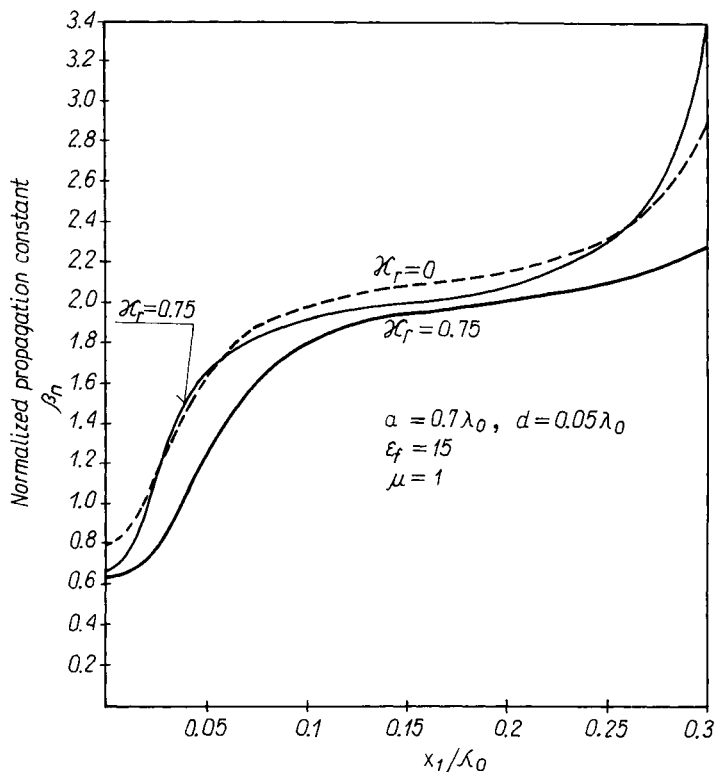


Figure 3. Normalized propagation constant, $\beta_n = \beta/(\omega/c)$, versus slab position for a rectangular waveguide containing two ferrite slabs (Figure 1b).

3. Ferrite Phase Shifters

The following characteristics are usually specified by manufacturers for ferrite phase shifters: differential phase shift (or number of bits for latching devices), peak power, average power, bandwidth, VSWR, insertion loss, switching speed, and switching energy. The ferrite phase shifters are usually made as waveguide devices, but sometimes other configurations are met.

Rectangular Waveguide Phase Shifters with Transversely Magnetized Ferrite Elements

The basic rectangular waveguide phase shifter configurations are shown in Figure 5. The most common are constructions with toroidal ferrite

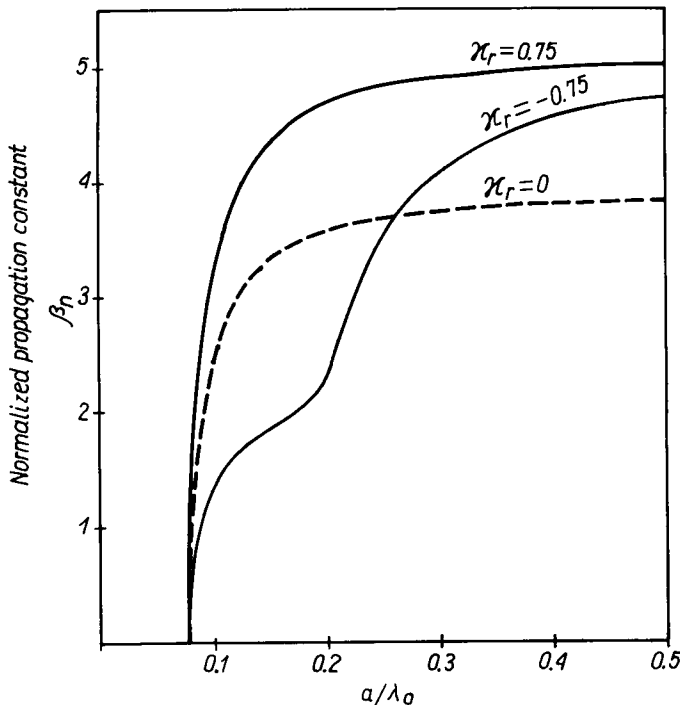


Figure 4. Normalized propagation constant, $\beta_n = \beta / (\omega/c)$, versus normalized ferrite radius for a circular waveguide made of metalized longitudinally magnetized ferrite (Figure 1c).

(Figure 5a), used to eliminate external magnets and reduce switching power and described in many papers (e.g., Reference [49]) and books (e.g., References [56] and [5]). Such phase shifters are most frequently made as latching devices, consisting of several sections of different length (Figure 6) to obtain the required phase shift in a digital fashion. The phase shift obtained in each section is proportional to its length. The first and the last sections of such a phase shifter are usually terminated by matching dielectric transformers which can be rigorously designed by the method described by Uher *et al.* [51]. The composite phase shifter shown in Figure 5b operates in a manner similar to that of the toroidal one, and it is useful for situations in which temperature stability is important [48]. The phase shift value for rectangular waveguide phase shifters can be computed exactly for multilayered ferrite-dielectric devices by obtaining the solution to the appropriate characteristic equation. For one or twin ferrite slab

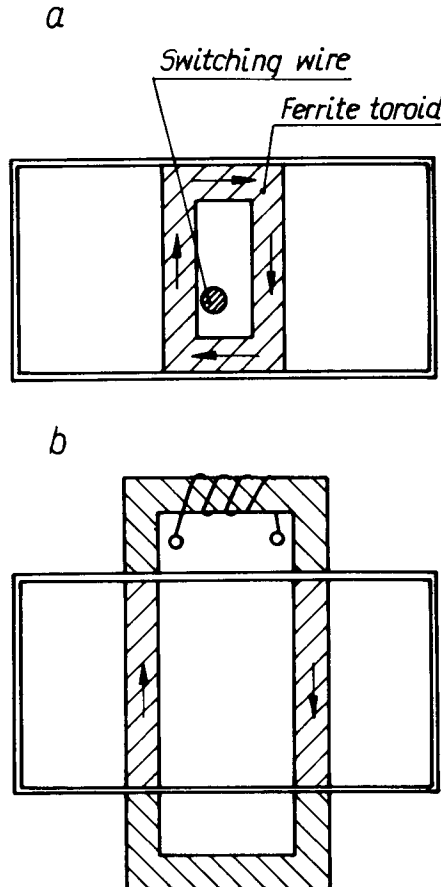


Figure 5. Typical nonreciprocal, rectangular waveguide phase shifter configurations: (a) latching remanent phase shifter with a ferrite toroid and (b) twin-slab phase shifter with external yokes.

phase shifters, this can be done by solving Equations (15) and (16). The differential phase shift for a twin slab nonreciprocal phase shifter can be deduced from the results presented in Figure 3. It is seen from this figure that for a fixed slab thickness the maximum value of the differential phase shift is obtained when two slabs contact each other; however, in practice a small air gap must exist. For phase shifters with a ferrite toroid, rigorous values for a differential phase shift also can be obtained [58], but more sophisticated methods of analysis must be used. Toroidal (or twin slab) phase shifters are nonreciprocal devices.

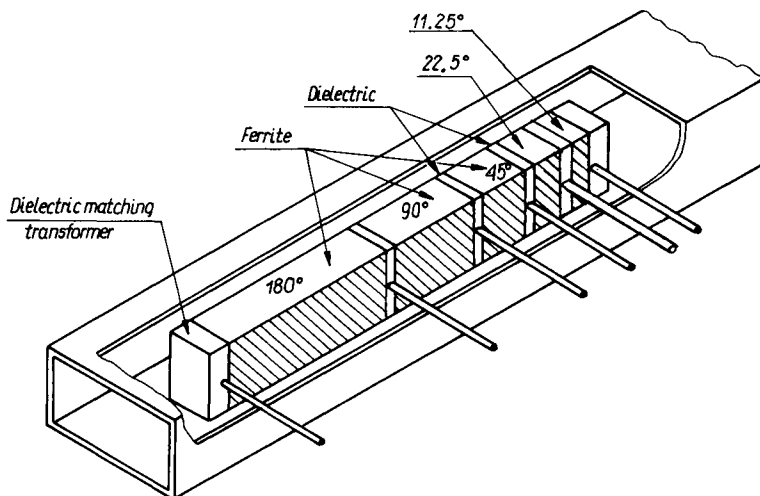


Figure 6. Five-bit latching remanent phase shifter with a ferrite toroid. Reproduced with permission from Ref. [5], © 1987 Peter Peregrinus Ltd., London.

Circular or Squared Waveguide Reciprocal Dual-Mode Phase Shifters

The typical geometry of a reciprocal dual-mode phase shifter is presented in Figure 7. It has been described in many papers (e.g., Reference [31]) and books (e.g., Reference [56]). A dual-mode phase shifter usually has two identical input/output sections, consisting of matching transformer

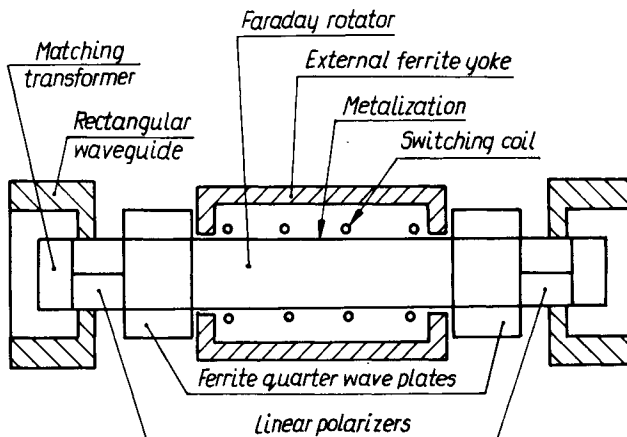


Figure 7. Typical geometry of a dual-mode phase shifter.

and polarizer sections and one variable phase shift section. Polarizer sections usually consist of linear polarizers and linear/circular polarizers. The linear/circular polarizer section can be constructed as 45° connection Faraday rotator and a quarter-wave plate or as a quarter-wave plane alone. These polarizers produce a circularly polarized wave for the variable phase shift section. Quarter-wave plates can be made using either isotropic material (ferrite or dielectric) or magnetized ferrite. Different constructions of quarter-wave plates are presented in Figure 8. The maximum differential phase shift per unit length in the Faraday rotator can be computed exactly with the aid of Equation (17). It corresponds to the two values of propagation constants computed for κ_{\max} and $-\kappa_{\max}$. As seen in Figure 4, the radius of the ferrite rod should be chosen in the range $0.12 < a/\lambda < 0.18$ to meet this requirement.

For the completely filled square waveguide, only approximate expressions for β^\pm are available, enabling evaluation of the length of the

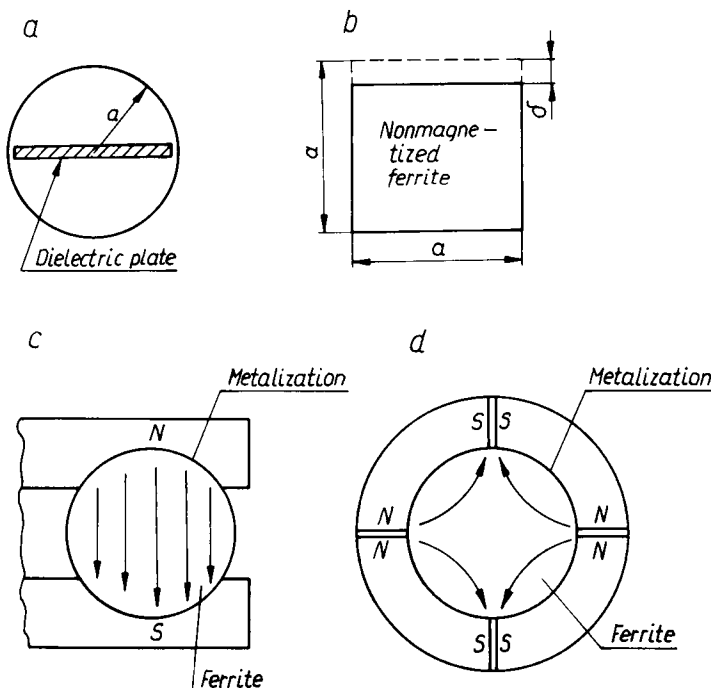


Figure 8. Different constructions of quarter-wave plates: (a) dielectric plate in a cylindrical waveguide, (b) perturbation in square geometry of a square nonmagnetized ferrite waveguide, (c) transversely magnetized cylindrical ferrite waveguide, and (d) transversely four-pole magnetized cylindrical ferrite waveguide.

Faraday rotator in the variable phase shift section. These expressions can be written after Reference [31] as follows.

$$\beta^{\pm} = \beta_0 \left[\epsilon_r \mu_{dr} \left(\mu \pm \frac{8}{\pi^2} \kappa \right) \right]^{0.5}, \quad (18)$$

where

$$\beta_0 = \omega \left[\epsilon_0 \mu_0 \left(1 - (\omega_c / \omega)^2 \right) \right]^{0.5}$$

$$\omega_c = \pi / \left[a(\epsilon \mu_d)^{0.5} \right]$$

$$\epsilon_r = \epsilon / \epsilon_0, \quad \mu_{dr} = \mu_d / \mu_0.$$

Rectangular Waveguide Reciprocal Phase Shifters with Longitudinally Magnetized Ferrite Elements (Reggia–Spencer Phase Shifters)

In rectangular waveguide reciprocal phase shifters with longitudinally magnetized ferrite elements (Reggia–Spencer phase shifters), a ferrite rod or slab is centered in a rectangular waveguide, as sketched in Figure 9 [43]. A solenoid is wound around the waveguide to produce longitudinal magnetic field biasing ferrite. Reggia–Spencer phase shifters are not as popular as dual-mode ones but still find applications in various low- or

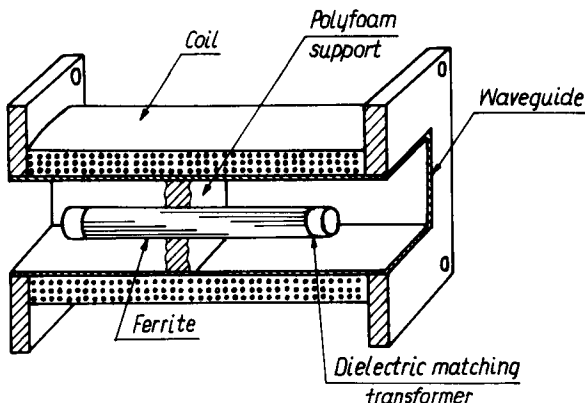


Figure 9. Cross section of a Reggia–Spencer phase shifter.

medium-power systems as easy to make reciprocal devices. Exact expressions enabling the design of Reggia–Spencer phase shifters are not available; however, one can use approximate design theory. It is based on computations of propagation constants for the dominant HE_{11} modes of a ferrite rod in free space [6]. As it was proved by Bardash and Maune, the optimum diameter of a ferrite rod, computed on the ground of this approximate theory, is in the range $0.18 < D_f/\lambda < 0.24$ and agrees well with experiments. Modifications of Reggia–Spencer phase shifters containing longitudinally a magnetized ferrite double toroid can also operate as latching devices [44].

Stripline and Microstrip Phase Shifters

Stripline and microstrip phase shifters offer such advantages over waveguide phase shifters, at low- and medium-power levels, as their low cost, small size, and compatibility with other MIC devices. Principles of operation of such devices are based on variations of the propagation constants for the quasi-TEM modes in striplines and microstrips on magnetized ferrite substrates. Different directions of magnetization can be employed in stripline and microstrip phasers: longitudinal magnetization, transverse magnetization in the plane of the substrate, and transverse magnetization perpendicular to the plane of the substrate. Hofmann [30] analyzed the propagation constants of ferrite-filled microstrip lines magnetized in such directions using simplified quasi-isotropic approximation. He has shown that dispersion of the propagation constants is similar for magnetizations: longitudinal and transverse perpendicular to the plane of the substrate. It is because the main part of the magnetic field in microstrip is orthogonal to these directions. The approximate value of the propagation constant for the quasi-TEM modes in magnetized substrates for such directions of magnetization can be calculated from Equation (13). For transverse magnetization parallel to the ferrite–air interface, propagation constants weakly depend on the static field magnetizing ferrite, and at first approximation can be calculated as for the dielectric medium. Roome and Hair [45] proposed an analog reciprocal phase shifter as in Figure 10, whose phase changes are obtained by changes in the direction of magnetization. The center conductor in this phase shifter is loosely meandered in order to minimize the physical size of the device. Nonreciprocal stripline or microstrip phase shifters usually employ tightly coupled meander lines. In this kind of phase shifter coupling between meander lines is essential for its operation. Such constructions were used by many authors, (e.g., Jones [34], Roome and Hair [45], and Hansson *et al.* [23]). The typical construc-

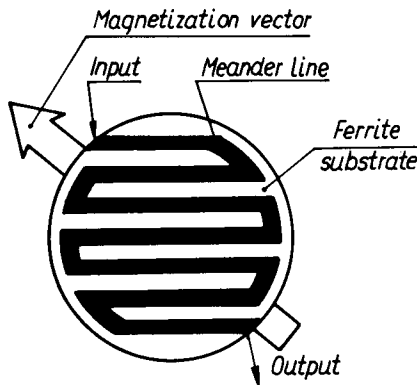


Figure 10. Phase changer with a loosely meandered microstrip line.

tion of a meander line latching nonreciprocal phase shifter is shown in Figure 11. The design of microstrip and stripline phase shifters described above relies on qualitative rather than rigorous theories.

Bolle and Talisa [8] described a model of the edge-guided stripline nonreciprocal phase shifter, consisting of a ferrite stripline loaded at one side with a high permittivity dielectric. They have shown the influence of permittivity and width of the dielectric on differential phase shift for such a model.

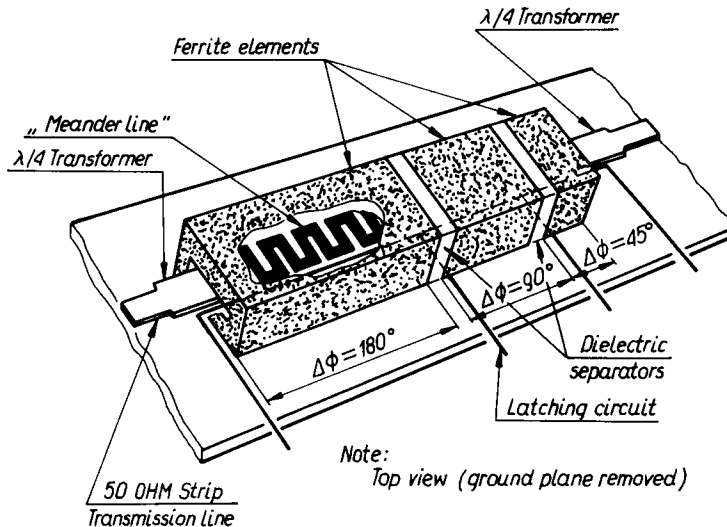


Figure 11. Typical geometry of a three-bit latching meander line phase shifter. Reproduced with permission from Ref. [34], © 1966 IEEE.

4. Ferrite Circulators and Isolators

Basic Geometries and Parameters of Ferrite Element Circulators

A circulator is a multiport nonreciprocal device with ports arranged such that the electromagnetic energy entering a certain port is coupled to an adjacent port and not coupled to the other ports. The most commonly used circulators are three-port symmetrical devices. The circuit symbol for a three-port circulator is shown in Figure 12. This is the model which is used to explain how a circulator operates. If all ports of a circulator are matched, then a signal applied to one port, for instance, to port 1, will emerge from port 2 with a loss called the insertion loss. The insertion loss is usually expressed in decibels according to the following formula:

$$IL \text{ (dB)} = -10 \log_{10} \left(\frac{P_{\text{out}_2}}{P_{\text{inp}_1}} \right). \quad (19)$$

A small part of the input signal also emerges from port 3, and the ratio of this signal to the input signal is called isolation (it is assumed in this definition that port 2 is terminated by a matched load). Isolation is expressed in decibels according to Equation (20).

$$I \text{ (dB)} = 10 \log_{10} \left(\frac{P_{\text{out}_3}}{P_{\text{inp}_1}} \right). \quad (20)$$

The next parameter which characterizes the reflective property of each port of a circulator is the magnitude of the reflection coefficient $|\Gamma|$ or VSWR. Other important circulator parameters are frequency range or

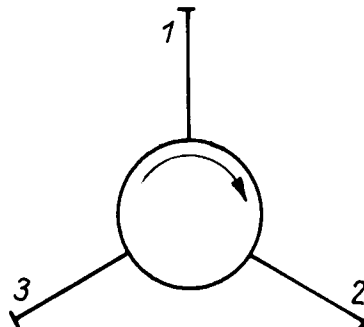


Figure 12. Circuit representation of a three-port circulator.

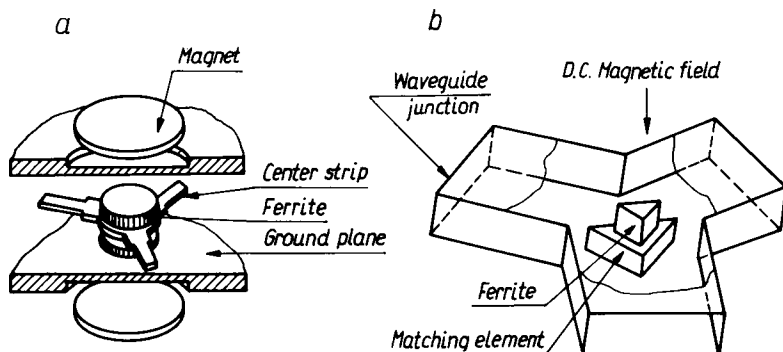


Figure 13. Junction-type circulators: (a) stripline and (b) waveguide. Reproduced with permission from Ref. [39], © 1989 Artech House, Inc.

center frequency and bandwidth, number of ports and configuration, continuous wave and pulse power handling capability, temperature range, phase linearity, type of transmission medium (waveguide, coaxial line, or microstrip), size and weight, and environmental factors.

Principally circulators are designed as three or four port devices. If a multiport circulator is needed it is usually designed as an interconnection of three-port circulators. The most common are the junction-type circulators (Figure 13), designed in a coaxial, microstrip, or waveguide configuration. For very high power levels waveguide differential phase shift circulators are designed (Figure 14). In the low-frequency region (VHF and

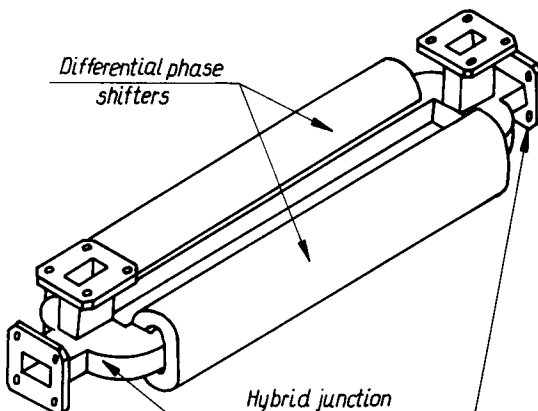


Figure 14. Differential phase shift circulator. Reproduced with permission from Ref. [39], © 1989 Artech House, Inc.

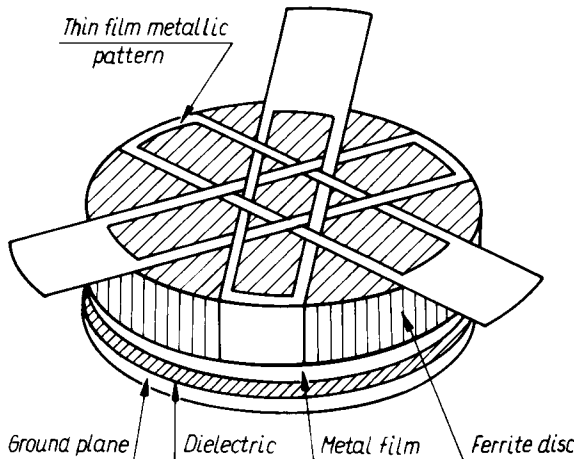


Figure 15. Lumped constant circulator. Reproduced with permission from Ref. [34], © 1966 IEEE.

UHF) the lumped constant circulators are used (Figure 15). Farady rotation circulators (Figure 16) have somewhat greater dimensions than other devices and therefore they are usually used for millimeter waves for which dimensions are not so important.

Y-Junction Circulators

Y-junction circulators are constructed as waveguide, coaxial line, microstrip, coplanar, or lumped-element devices. The existing design concepts of such circulators can be classified into three groups:

- (a) network theory,
- (b) resonance theory, and
- (c) rigorous electromagnetic field theory.

Network theory, developed by many authors (e.g., Auld [4] and Butterweck [11]), explains the general behavior of circulators; however, design procedure, based on this theory, relies on experimental results. A good tutorial paper on the application of network theory for the design of circulators was written by Helszajn and Tan [26].

Resonance theory relies on simplified solutions for the so-called “constituent cavity” corresponding to the internal structure of the junction. It has been shown by many authors (e.g., Bosma [10], Owen [41], and Krupka *et al.* [36]) that the center frequency of circulator operation

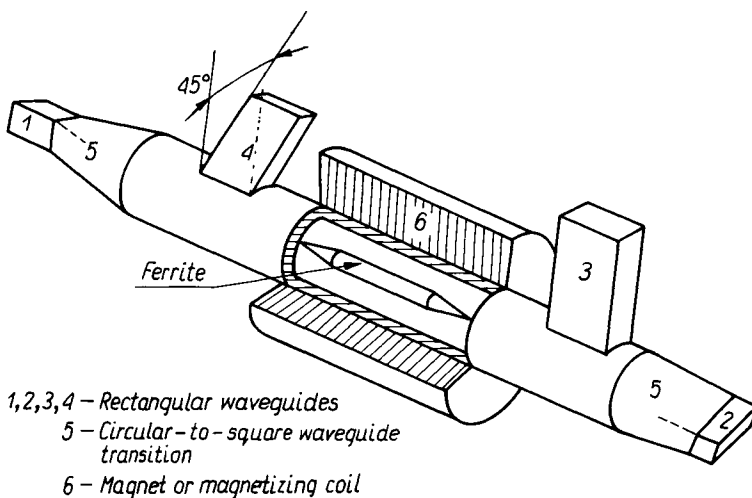


Figure 16. Faraday rotation circulator.

approximately corresponds to the mean value of the resonant frequencies of the TM_{110}^{\pm} or quasi- EH_{110}^{\pm} (hybrid) modes. Such a theory is useful for the design of ferrite dimensions and for predicting spurious modes which often limit the circulator bandwidth. Resonance theory does not allow us to predict circulator characteristics and therefore has limited applications.

The rigorous field theory approach gives the most reliable results and is suitable for automatic design. Several design procedures based on this theory have been developed. Most of them refer to microstrip and stripline circulators [35, 57], or waveguide circulators with full-height ferrite [13, 18]. Some of them refer to more complicated structures which required 3D field analysis (e.g., waveguide circulators containing partial-height ferrite) [22, 53].

The selection of ferrite material is one of the most critical aspects of circulator design and is substantially independent of the microwave transmission medium. The selection depends on the operating frequency, the bandwidth of the circulator, the RF power level, the desired insertion loss, and the ambient temperature range. Generally, for broadband operation the saturation magnetization of the ferrite material should be relatively high and preferably temperature stable, and the effective linewidth and the dielectric loss tangent should be as low as possible to minimize the insertion loss of a circulator.

One can consider two magnetic operating points of circulators: below and above ferromagnetic resonance. The above-resonance operating point

is often chosen for low frequency, high power circulators, or both to avoid low field losses or to avoid nonlinear losses in ferrite at high-power levels. The below-resonance operating point is usually chosen for higher frequency circulators. Usually permanent magnets are applied for operation point selection; however, using hexagonal ferrites, one can use the anisotropy field for biasing the circulator [62].

As was mentioned earlier, approximate formulas for ferrite dimensions are usually derived from approximate expressions on the resonant frequencies of ferrite terminated by perfect electric and magnetic walls [1, 9, 25]. According to this theory, the radius of the ferrite disc for microstrip and stripline circulators should satisfy the following equation [9]:

$$R = 1.84 / \left[\omega_c (\epsilon \mu_d)^{1/2} \right]. \quad (21)$$

The ferrite radius calculated from Equation (21) is in good agreement with experiments [9]. More accurate rigorous theory for analysis of complicated microstrip resonators has been also successfully applied [59]. For millimeter-wave applications higher order mode circulators are also applied [61].

For waveguide circulators, approximate expressions for the dimensioning of partial-height circular and triangular ferrite posts also exist [1, 27]; however, they are not always sufficiently accurate, since in real waveguide

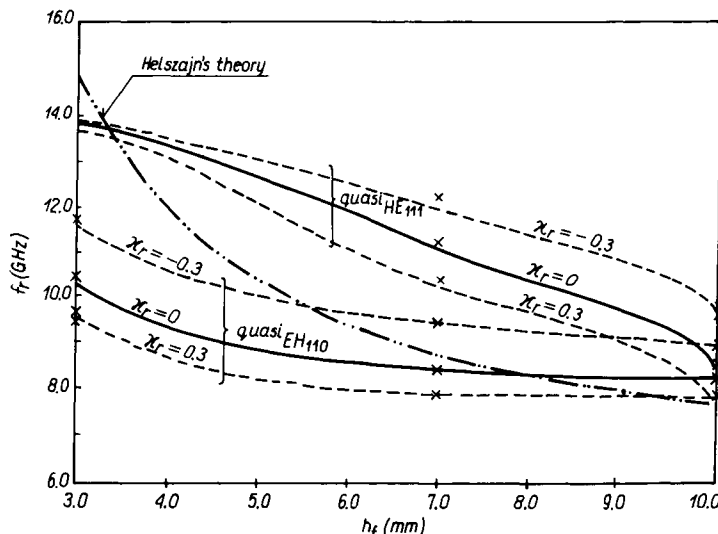


Figure 17. Resonant frequencies for the first two hybrid modes of the constituent cavity for a Y-junction H-plane waveguide circulator.

circulators magnetic walls on the ferrite surfaces provide a rather poor approximation for physically existing boundary conditions. More accurate results can be obtained using the rigorous theory of resonances for "constituent cavity" [36]. In Figure 17 there are the results of rigorous computations of the resonant frequencies for the first two hybrid modes of the constituent cavity for the Y-junction *H*-plane waveguide circulator versus ferrite height. Results of experiments for demagnetized ferrite approximately correspond to the central frequencies of circulation. It is seen from this figure that the central frequency of circulation is properly calculated by the rigorous theory of resonances for any ferrite height. It also can be observed that for full ferrite height the quasi- HE_{111} mode would disturb circulation which takes place on the dominant quasi EH_{110} mode. Results of computations of the resonant frequencies based on Helszajn's formula [27] marked in Figure 17 show limitations of approximate theories.

Isolators

An isolator is a two-port device which passes energy through in one direction and absorbs energy in the reverse direction. Important parameters of isolators are isolation, insertion loss, and power handling capability.

A large class of isolators (isocirculators) can be made from the three-port circulators by termination of one of their ports by a matched

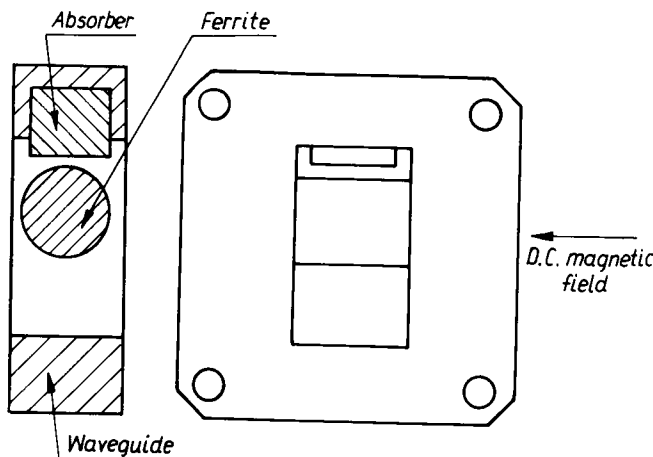


Figure 18. Flange-type waveguide isocirculator. Reproduced with permission from Ref. [5], © 1987 Peter Peregrinus Ltd., London.

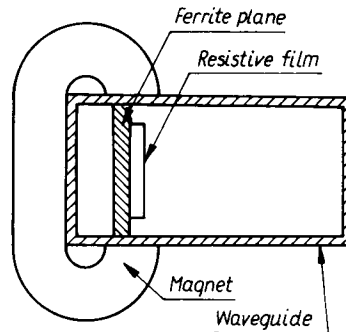


Figure 19. Field displacement isolator.

load. Sometimes isocirculators are specially designed to minimize their dimensions, as shown in Figure 18.

Another category of isolators which are often used in practice are the field displacement and resonance isolators.

The field displacement isolators shown in Figure 19 [16, 54] can be designed on the grounds of theory for transversely magnetized rectangular waveguides containing one ferrite slab. Such isolators are inexpensive, but they are suitable only for low- and moderate-power application.

More suitable for higher power application are the resonance isolators (Figure 20) [5, 37, 46]. Their operation is connected with phenomena of ferromagnetic resonance. Ferrite materials used for the design of such a circulator should have a broad linewidth to ensure a relatively broad isolator bandwidth.

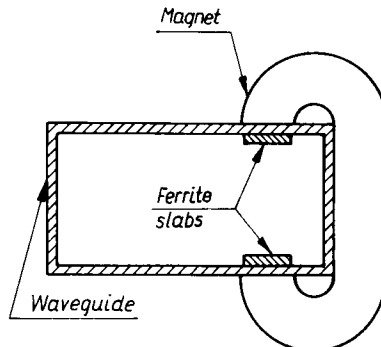


Figure 20. Resonance isolator. Reproduced with permission from Ref. [39], © 1989 Artech House, Inc.

5. YIG Devices

YIG Filters

Single crystals of yttrium-iron garnet (YIG) placed in an RF coupling structure in a DC magnetic field show extremely low linewidths when they are used as resonant elements in bandpass or band-rejection filters. The ferrite resonators are small in comparison with the wavelength of the RF field to ensure a uniform field throughout the volume of the ferrite sample (in order to avoid higher modes excitation). The most often used ferrite resonators are spheres because of their linear tuning characteristics. In practice, the diameter of the sphere is about 0.05–0.6 mm, and its unloaded Q -factor (Q_u) is typically between 2,000 and 10,000. The value of Q_u is critically dependent on the achievement of a high surface polish of a sphere [38]. The analytical formula for Q_u was derived by Carter *et al.* [12] from the equivalent circuit of a magnetic resonance filter. This formula predicts that Q_u for a spherical resonator filter will reach zero at the value of RF frequency given by $f_0 = \omega_m / 4\pi$. It is about 1670 MHz for a spherical YIG resonator, and this is its low cutoff frequency. Figure 21 shows a typical YIG bandpass filter setup with RF-coupling loops, a YIG sphere, and a magnet. Important circuit parameters of the YIG filter are shown in Figure 22. P_0 is the output power, P_a is the available power, BF is the 3-dB bandwidth, f_0 is the center resonant frequency, IL_{min} is the lowest insertion loss, R is the ripple in the passband. S is the amplitude of a spurious magnetostatic mode, ORS is the resonant spurious amplitude,

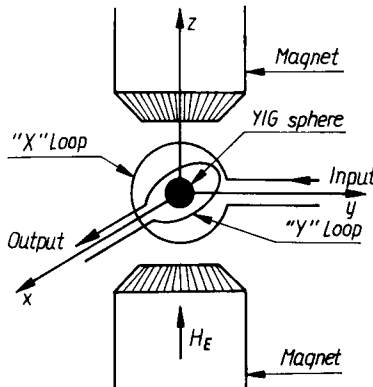


Figure 21. Basic elements of a YIG bandpass filter, showing RF coupling loops, a sphere, and a magnet.

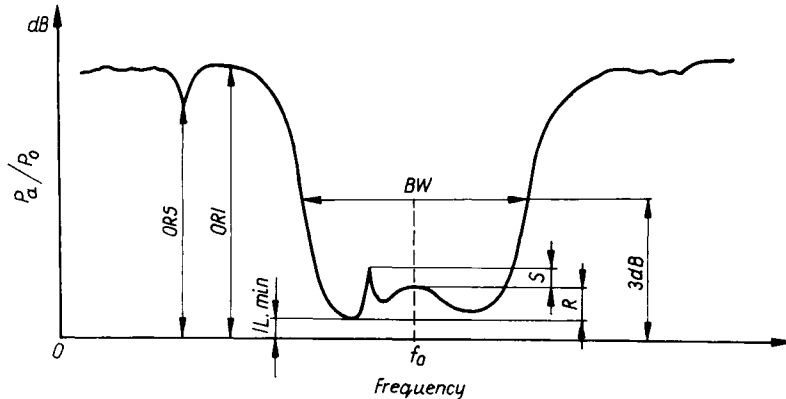


Figure 22. Bandpass YIG filter characteristics.

and ORI is the off-resonance isolation. More details on YIG filters and resonators can be found in a book published by Helszajn [29].

YIG Power Limiters

As was shown by Suhl [50], the resonance susceptibility of a ferrite decreases above some critical value of transverse magnetization due to parametric excitation of spin waves. The decline in susceptibility leads to power limiting. One can distinguish three types of limiters: those which use the saturation of the uniform precession resonance, coincident type limiters, and subsidiary-resonance limiters. The best limiting properties at low-power levels possess coincident-type limiters [3, 17]. The subsidiary-resonance limiters are used when moderately large levels in the RF magnetic field are required [2]. The critical RF magnetic field value for coincidence limiters is given by Equation (22):

$$H_c = \frac{\Delta H \Delta H_k}{M_s}. \quad (22)$$

6. Ferrite Switches

The ferrite switches employ usually switchable circulators. There are two types of switchable circulators—those with an internal and those with an external magnetizing circuit. The internal magnetizing circuit is placed

within the ferrite junction. The external magnetic circuit consists of an external electromagnet. Designs employing electromagnets require a relatively large amount of power [7]. Switching rates for such switches are low, approximately 10–50 μs . Switches with internal magnetizing circuits are more difficult in design, but offer advantages such as low-power consumption and switching rates below 1 μs [42]. High-power switches are usually built using switchable differential phase shift circulators [49].

References

- [1] Y. Akaiwa, Mode classification of a triangular ferrite post for Y-circulator operation, *IEEE Trans. Microwave Theory Tech.*, Vol. MTT-25, pp. 59–61, Jan. 1977.
- [2] J. L. Allen, Compact subsidiary-resonance limiter, *IEEE Trans. Microwave Theory Tech.*, Vol. MTT-17, pp. 193–194, Feb. 1972.
- [3] F. R. Arams, M. Grace, and S. Okwit, Low-level garnet limiters, *Proc. IRE*, Vol. 49, pp. 1308–1313, Aug. 1961.
- [4] B. A. Auld, The synthesis of symmetrical waveguide circulators, *IRE Trans. Microwave Theory Tech.*, Vol. MTT-7, pp. 238–246, Apr. 1959.
- [5] A. J. Baden Fuller, *Ferrites at Microwave Frequencies*. London: Perter Peregrinus, 1987.
- [6] I. Bardash and J. J. Maune, A waveguide reciprocal latching ferrite phase shifter, *IEEE GMMT—Int. Microwave Symp. Dig.*, pp. 274–281, 1968.
- [7] F. Betts, D. Temme, and J. A. Weiss, A switching circulator: S-band; stripline; remanent; 15 kilowatts; 10 microseconds; temperature stable, *IEEE Trans. Microwave Theory Tech.*, Vol. MTT-14, pp. 665–669, Dec. 1966.
- [8] D. M. Bolle and S. H. Talisa, The edge-guided mode nonreciprocal phase shifter, *IEEE Trans. Microwave Theory Tech.*, Vol. MTT-27, pp. 878–882, Nov. 1979.
- [9] H. Bosma, On the principle of stripline circulation, *IEE Proc.*, Part B, Vol. 109, Suppl. No. 21, pp. 137–146, Jan. 1962.
- [10] H. Bosma, On stripline Y-circulation at UHF, *IEEE Trans. Microwave Theory Tech.*, Vol. MTT-12, pp. 61–72, 1964.
- [11] H. J. Butterweck, Der Y Zirkulator, *Arch. Elektron. Uebertragungstech.*, Vol. 17, pp. 163–176, Apr. 1963.
- [12] P. S. Carter, Magnetically-tunable microwave filters using single-crystal yttrium-iron-garnet resonators, *IRE Trans. Microwave Theory Tech.*, Vol. MTT-9, pp. 252–260, May 1961.
- [13] J. B. Castillo and L. E. Davis, Computer-aided design of three-port waveguide junction circulators, *IEEE Trans. Microwave Theory Tech.*, Vol. MTT-18, pp. 25–34, Jan. 1970.
- [14] W. P. Clark, K. H. Hering, and D. A. Charlton, TE-mode solutions for partially ferrite filled rectangular waveguide using ABCD matrices, *IEEE Int. Conv. Rec.* Vol. 14, Part 5, pp. 39–48, Mar. 1966.
- [15] P. J. B. Clarricoats, *Microwave Ferrites*, pp. 213–228. London: Chapman & Hall, 1961.
- [16] R. L. Comstock and C. E. Fay, Operation of the field displacement isolator in rectangular waveguide, *IRE Trans. Microwave Theory Tech.*, Vol. MTT-8, pp. 605–611, 1960.
- [17] R. L. Comstock and M. Loewy, An X-band coincidence ferrimagnetic limiter using lithium ferrite, *Proc. IEEE*, Vol. 51, p. 1769, Dec. 1963.

- [18] J. B. Davies, An analysis of the m-port symmetrical H-plane waveguide junction with central ferrite post, *IRE Trans. Microwave Theory Tech.*, Vol. MTT-10, pp. 596–604, Nov. 1962.
- [19] J. DiBartollo, W. J. Ince, and D. H. Temme, A solid state “flux-drive” control circuit for latching ferrite-phaser applications, *Microwave J.*, Vol. 9, pp. 59–64, Sept. 1972.
- [20] J. J. Green and F. Sandy, Microwave characterization of partially magnetized ferrites, *IEEE Trans. Microwave Theory Tech.*, Vol. MTT-22, pp. 641–645, June 1974.
- [21] A. G. Gurevich, *Ferrites at Microwave Frequencies* (in Russ.). Moscow: State Press, 1960. (Engl. transl., Heywood, London, 1963.)
- [22] D. Hahn, Exact calculation of partial-height waveguide Y-junction circulator using mode-matching technique, *Electron. Lett.*, Vol. 24, pp. 966–968, 1988.
- [23] E. R. B. Hansson, S. Aditya, and M. S. Larsson, Planar meander-line ferrite-dielectric phase shifter, *IEEE Trans. Microwave Theory Tech.*, Vol. MTT-29, pp. 209–215, Mar. 1981.
- [24] J. Helszajn, *Nonreciprocal Microwave Junctions and Circulators*. New York: Wiley, 1975.
- [25] J. Helszajn and F. C. F. Tan, Mode charts for partial-height ferrite waveguide circulators, *IEE Proc.*, Vol. 122, pp. 34–36, Jan. 1975.
- [26] J. Helszajn and F. C. F. Tan, Design data for radial waveguide circulators using partial-height ferrite resonators, *IEEE Trans. Microwave Theory Tech.*, Vol. MTT-23, pp. 288–298, Mar. 1975.
- [27] J. Helszajn and J. Sharp, Resonant frequencies, Q-factor, and susceptance slope parameter of waveguide circulators using weakly magnetized open resonators, *IEEE Trans. Microwave Theory Tech.*, Vol. MTT-31, pp. 434–441, June 1983.
- [28] J. Helszajn, Design of waveguide circulators with Chebyshev characteristics using partial-height ferrite resonators, *IEEE Trans. Microwave Theory Tech.*, Vol. MTT-32, pp. 908–917, Aug. 1984.
- [29] J. Helszajn, *YIG Resonators and Filters*. New York: Wiley, 1985.
- [30] H. Hofmann, Dispersion of the ferrite-filled microstrip-line, *Arch. Elektron. Uebertragungstechn.*, Vol. 28, pp. 223–227, May 1974.
- [31] W. E. Hord, F. J. Rosenbaum, and J. A. Benet, Theory and operation of a reciprocal Faraday-rotation phase shifter, *IEEE Trans. Microwave Theory Tech.*, Vol. MTT-20, pp. 112–119, Feb. 1972.
- [32] W. E. Hord, C. R. Boyd, and D. Diaz, A new type of fast-switching dual-mode ferrite phase shifter, *IEEE Trans. Microwave Theory Tech.*, Vol. MTT-35, pp. 1219–1225, Dec. 1987.
- [33] W. J. Ince and E. Stern, Nonreciprocal remanence phase shifters in rectangular waveguide, *IEEE Trans. Microwave Theory Tech.*, Vol. MTT-15, pp. 87–95, Feb. 1967.
- [34] R. R. Jones, A slow wave digital ferrite strip transmission line phase shifter, *IEEE Trans. Microwave Theory Tech.*, Vol. MTT-14, pp. 684–688, Dec. 1966.
- [35] A. M. Khilla, Dimensionierung breitbandiger Mikrowellen Streifenleitungs Zirkulatoren, *Mikrowellen Mag.* Vol. 10, pp. 528–537, May 1984.
- [36] J. Krupka, W. Glogier, and J. Modelska, Rigorous theory of resonances in waveguide Y-junction circulators, *Proc. 20th Eur. Microwave Conf., Budapest*, pp. 1151–1156, Sept. 1990.
- [37] B. Lax and K. J. Button, *Microwave Ferrites and Ferrimagnetics*. New York: McGraw-Hill, 1962.
- [38] R. C. LeCrew, E. G. Spencer, and C. S. Porter, Ferromagnetic resonance line in yttrium-iron-garnet single crystals, *Phys. Rev.*, Vol. 110, pp. 1311–1313, June 1958.
- [39] D. K. Linkhart, *Microwave Circulator Design*. Norwood, MA: Artech House, 1989.

- [40] J. Nicolas, in *Ferromagnetic Materials* (E. P. Wohlfarth, ed.), Vol. II, Amsterdam: North-Holland, 1980.
- [41] B. Owen, The identification of modal resonances in ferrite loaded waveguide Y-junctions and their adjustment for circulation, *Bell Syst. Tech. J.*, Vol. 51, pp. 595–627, Mar. 1972.
- [42] W. G. Passaro and J. W. McManus, A 35 GHz latching switch, *IEEE Trans. Microwave Theory Tech.*, Vol. MTT-14, pp. 669–672, Dec. 1966.
- [43] F. Reggia and E. G. Spencer, A new technique in ferrite phase shifting for beam scanning of microwave antennas, *Proc. IRE*, Vol. 45, pp. 1510–1517, Nov. 1957.
- [44] F. Reggia and T. Mak, Reciprocal latching phase modulator for microwave frequencies, *IEEE Trans. Magn.*, Vol. MAG-2, pp. 269–273, Sept. 1966.
- [45] G. T. Roome and H. A. Hair, Thin ferrite devices for microwave integrated circuits, *IEEE Trans. Microwave Theory Tech.*, Vol. MTT-16, pp. 411–420, July 1968.
- [46] E. Schlömann, On the theory of the ferrite resonance isolator, *IRE Trans. Microwave Theory Tech.*, Vol. MTT-8, pp. 199–206, 1960.
- [47] E. Schlömann, Microwave behavior of partially magnetized ferrites, *J. Appl. Phys.*, Vol. 41, pp. 204–214, Jan. 1970.
- [48] E. Stern and W. J. Ince, Design of composite magnetic circuits for temperature stabilization of microwave ferrite devices, *IEEE Trans. Microwave Theory Tech.*, Vol. MTT-15, pp. 295–300, May 1967.
- [49] R. A. Stern and J. P. Agrios, A 500 kW X-band air-cooled ferrite latching switch, *IEEE Trans. Microwave Theory Tech.*, Vol. MTT-16, pp. 1034–1037, Dec. 1968.
- [50] H. Suhl, Nonlinear behavior of ferrites at high microwave signal levels, *Proc. IRE*, Vol. 44, pp. 1270–1284, Oct. 1956.
- [51] J. Uher, F. Arndt, and J. Bornemann, Field theory design of ferrite loaded waveguide nonreciprocal phase shifters with multisection ferrite or dielectric slab impedance transformers, *IEEE Trans. Microwave Theory Tech.*, Vol. MTT-35, pp. 552–560, June 1987.
- [52] Q. H. F. Vrehen, Absorption and dispersion in porous and anisotropic polycrystalline ferrites at microwave frequencies, *J. Appl., Phys.*, Vol. 40, pp. 1849–1860, Mar. 1969.
- [53] W. Lin and W. Dou, An exact electromagnetic field theory for the broadband H-plane waveguide junction circulators, *Alta Freq.*, Vol. 58, pp. 225–237, Mar./Apr. 1989.
- [54] S. Weisbaum and H. Boyet, Field displacement isolators at 4, 6, 11, and 24 KMC, *IRE Trans. Microwave Theory Tech.*, Vol. MTT-5, pp. 194–198, July 1957.
- [55] J. A. Weiss, A phenomenological theory of the Reggia–Spencer phase shifter, *Proc. IRE*, Vol. 47, pp. 1130–1137, June 1959.
- [56] L. R. Whicker, *Ferrite Control Components*, Vol. II. Norwood, MA: Artech House, 1974.
- [57] Y. S. Wu, and F. J. Rosenbaum, Wide band operation of microstrip circulators, *IEEE Trans. Microwave Theory Tech.*, Vol. MTT-22, pp. 849–856, Oct. 1970.
- [58] Y. Xu and G. Zhang, A rigorous method for computation of ferrite toroidal phase shifters, *IEEE Trans. Microwave Theory Tech.*, Vol. MTT-36, pp. 929–933, June 1988.
- [59] T. Nagao, Ferromagnetic tree-disk stripline Y circulator, *IEEE Trans. Microwave Theory Tech.*, Vol. MTT-40, pp. 1812–1820, 1992.
- [60] E. El-Sharawy and C. J. Koza, Dual ferrite slot-line for broad-band, high nonreciprocity phase shifters, *IEEE Trans. Microwave Theory Tech.*, Vol. MTT-39, pp. 2204–2210, Dec. 1991.
- [61] A. M. Borjak and L. E. Davis, Mode 1 and mode 2 designs for 94 GHz microstrip circulators, *IEEE Microwave Guided Wave Lett.*, Vol. 3, pp. 310–312, Sept. 1993.
- [62] Dorado International Corp., Seattle, WA (Product Feature), 18 to 95 GHz microstrip ferrite devices, *Microwave J.*, Vol. 36, No. 9, pp. 158–160, Sept. 1993.

Microwave Solid-State Devices

Cam Nguyen

I. Microwave Mixer and Detector Diodes

Introduction

Microwave mixer and detector diodes are normally metal–semiconductor junction rectifying diodes. They consist of Schottky-barrier [1–3], point-contact [1–3], backward [1, 2, 4], superconductor–insulator–superconductor (SIS) junction [5], Josephson junction [5], and barrier injection transit time (BARITT) [6] diodes. Schottky-barrier diodes generally produce the highest mixer and detector performances (Figures 1 and 2) and, currently, are the most widely used devices for mixers and detectors. Schottky-barrier diodes consist of *n*-type semiconductor chips [usually silicon (Si) or gallium arsenide (GaAs)], contacted by an evaporated metal film. Currently available beam-lead and whisker-contacted Schottky-barrier diodes can have cutoff frequencies of about 1800 and 5500 GHz, respectively (Table 1) and are capable of operation well into the millimeter-wave region. Detailed device description can be found in References [1–3, 7, 8].

Structure and Characteristics

The cross-sectional structure of a typical GaAs Schottky-barrier diode is shown in Figure 3. A depletion or space charge region is created under-

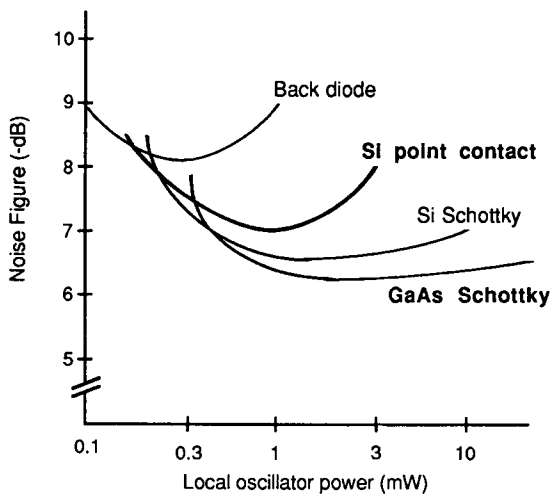


Figure 1. Mixer noise figure (including a 1.5-dB IF amplifier noise figure) as a function of the local oscillator power level [2].

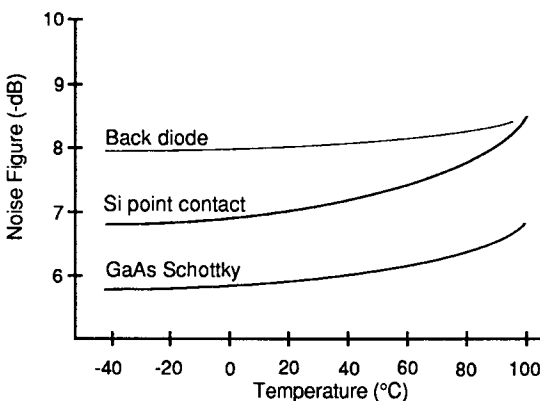


Figure 2. Detector noise figure (including a 1.5-dB IF amplifier noise figure) versus temperature [2].

neath the rectifying junction, formed by the contact of the metal anode to the epitaxial layer. Contact with the diode anode is normally made by metal lead (beam-lead diodes) or whisker (whisker diodes). Typical diameters of anodes are 1.5–5 μm and 10–20 μm for millimeter-wave and microwave diodes, respectively. The cathode is an ohmic contact formed at the top (beam-lead diodes) or bottom (whisker diodes) of the substrate. The whisker diodes (Figure 4a), although providing essentially no parasitic

TABLE I
Typical Characteristics of GaAs Schottky-Barrier Diodes

Parameter	Beam-lead diode	Whisker diode
Anode diameter (μm)	3	1.5
Junction capacitance, C_j (pF)	0.015	0.006
Parasitic capacitance, C_p (pF)	0.010	0.005
Total capacitance, C_t (pF)	0.025	0.011
Series resistance, R_s (Ω)	6	5
Parasitic inductance, L_s (nH)	0.2	0.2
Cutoff frequency, f_c (GHz)	1,770	5,300
Ideality factor, n	1.15	1.20

capacitances and minimized parasitic inductances, resulting in the highest cutoff frequencies and best performance at millimeter wavelengths, are not mechanically rugged and suitable for mass production. The beam-lead diodes (Figure 4b), planar surface-oriented devices, are highly rugged and compatible with hybrid as well as monolithic integrated circuit (MMIC) techniques. The beam-lead diodes can also have high cutoff frequencies due to the small junction areas and parasitic capacitances obtained from photolithographic techniques and the beam-lead arrangement, respectively. The important device parameters are the diode series resistance (R_s), junction capacitance (C_j) and resistance (R_j), and ideality factor (n). R_s is a function of the diode junction area and the epitaxial layer thickness. C_j and R_j are related to the depletion region width, the semiconductor dielectric constant, and the diode area, whereas n depends primarily on the quality of the metal–semiconductor interface. The actual mixing and detection in mixers and detectors, respectively, are accomplished by R_j , with R_s and C_j acting as parasitics degrading the mixer

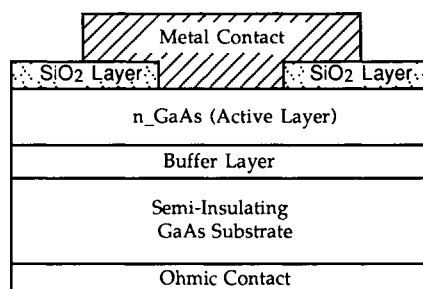


Figure 3. Cross-sectional channel structure of a typical GaAs Schottky-barrier diode.

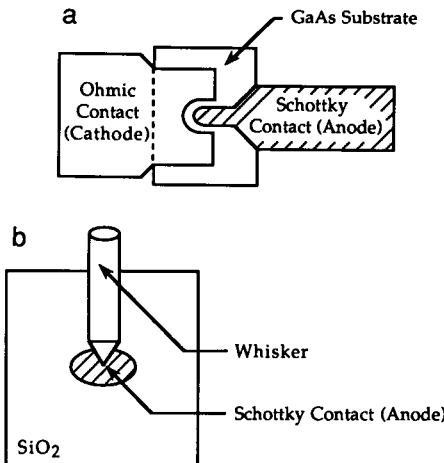


Figure 4. Top view of typical beam-lead (a) and whisker (b) GaAs Schottky-barrier diodes.

conversion loss and detector sensitivity. Increasing R_j and minimizing R_s and C_j will improve the mixer conversion loss, detector sensitivity, and operating frequency. Diodes with n approaching the ideal unity value have low internal noise generation, resulting in low noise performance. Another important device characteristic is the barrier potential (V_b), directly proportional to the barrier height of the metal–semiconductor contact. Lowering V_b , by properly selecting the metal that forms the contact, will result in the low local oscillator power levels needed in mixers and detectors. Detailed discussion of the device structures can be found in References [1, 2, 7–10].

The important characteristics of microwave mixer and detector diodes are f_c , the cutoff frequency,

$$f_c = \frac{1}{2\pi R_s C_j},$$

L_c , the mixer conversion loss,

$$L_c = L_{DC} \left[1 + \frac{R_s}{R_j} + \omega^2 C_j^2 R_s R_j \right],$$

$L_{c,\min}$, the minimum mixer conversion loss,

$$L_{c,\min} = L_{DC}(1 + 2\omega R_s C_j),$$

η , the mixer rectification efficiency,

$$\eta = 1 - \frac{1}{\omega C_j R_j},$$

N_r , the mixer and detector noise temperature ratio (sum of thermal, shot, and flicker noise),

$$N_r = \frac{Z_v N_b + R_s}{Z_v + R_s} \quad N_b = \frac{1}{2} \left[1 + \frac{nI_s + (n-1)I}{nI_s + I} \right],$$

Z_v , the detector video impedance,

$$Z_v \Delta \frac{dV}{dI} = \frac{1}{\alpha(I + I_s)} = R_j + R_s,$$

β_{DC} , the detector DC current sensitivity (rectification efficiency),

$$\beta_{CD} = \frac{\alpha}{2},$$

β , the detector microwave current sensitivity (rectification efficiency),

$$\begin{aligned} \beta &= \frac{\alpha R_j^2}{2(R_s + R_j)(1 + \omega^2 C_j^2 R_j^2 R_s)} \\ &\approx \frac{\beta_{DC}}{1 + \omega^2 C_j^2 R_j} \quad \text{for } R_j \gg R_s, \end{aligned}$$

and δ , the detector microwave voltage sensitivity (rectification efficiency),

$$\delta = \beta Z_v,$$

where ω is the angular operating frequency; L_{DC} is the DC conversion loss determined by the diode I-V characteristics; I is the current at the operating point; I_s is the saturation current; $\alpha = q/nkT$, with q being the electron charge, k being the Boltzmann's constant, and T being the absolute temperature ($\alpha = 40V^{-1}$ at room temperature). Details of device characteristics can be found in References [2, 11].

Fabrication

A typical device fabrication consists of the following steps.

1. Formation of a buffer layer and an *n*-type epitaxial (active) layer on the semi-insulating GaAs substrate.
2. Deposition of the SiO₂ layer.
3. Definition of the active anode area in the SiO₂.
4. Formation of the cathode ohmic contact by deposition and liftoff of a metal layer (usually Ni/Au/Ge).
5. Deposition of the Schottky-barrier metal.
6. Thinning the wafer to the desired thickness.

Detailed information on device processing can be found in References [2, 10, 12–14].

Operation

Microwave mixer and detector diodes operate as nonlinear rectifying elements, formed by the metal–semiconductor contact. In contrast with the *p*–*n* junction diode, the rectification is mainly based on the electron (majority carrier) conduction occurring across a barrier between a metal and a semiconductor, and, in normal operation, there is virtually no storage of holes (minority carriers). These characteristics result in more efficient diode rectification at high frequencies, leading to high sensitivity for mixers and detectors. Details on the operation of these diodes can be found in References [1, 2, 7].

Models

An equivalent-circuit model (Figure 5) for GaAs Schottky-barrier diodes is normally employed in the design of diodes as well as mixers and detectors. The two main nonlinear elements are the voltage-dependent junction capacitance, C_j , and the current-dependent junction resistance, R_j , which is responsible for the mixing and detection in mixers and detectors, respectively. They are given as

$$C_j(V_j) = C_j(0) \left(1 - \frac{V_j}{V_b}\right)^{-\gamma} \quad R_j = \frac{n k T}{q} I(V_j),$$

where $C_j(0)$ is the zero-voltage junction capacitance which can be determined from the device physics [10] or measurement; $V_b \approx 0.95$ for GaAs; and γ is a parameter relating to the semiconductor geometry and doping

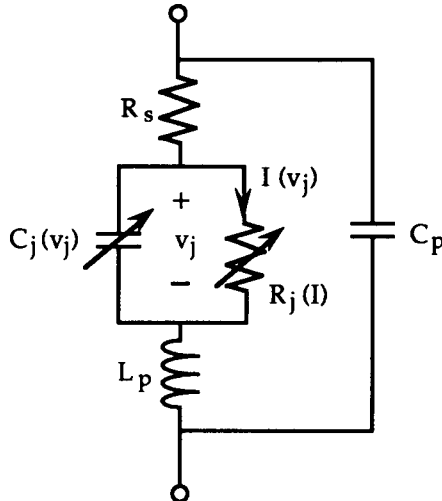


Figure 5. An equivalent-circuit model of GaAs Schottky-barrier diodes.

profile ($\gamma = 0.33$ and 0.5 for the respective linearly graded, abrupt planar junctions). γ can also be obtained as the negative of the slope of $\log(C_j/C_j(0))$ versus $\log(1 - V_j/V_b)$. The diode series resistance, R_s , representing losses in the ohmic contact, the substrate, and the undepleted epitaxial layer, normally determined by extrapolating the measured I-V characteristics [8, 15], is not accurate due to thermal effects in the diode junction. These effects can be accounted for by performing measurements at 10 MHz or higher using the technique described in Reference [15]. At microwave or millimeter-wave frequencies R_s increases substantially due to the skin effect. This effect can be approximately taken into account by using the following equations [15].

$$R_s = \begin{cases} R_{DC} \sqrt{\frac{f}{f_s}} & (f \ll f_s) \\ R_{DC} + \frac{R_{DC} \sqrt{\frac{f}{f_s}}}{2 \left(2 - \sqrt{\frac{f}{f_s}} \right)} (1 + 2j) & (f \gg f_s), \end{cases}$$

where R_{DC} is the low-frequency series resistance and f_s is a function of

the conductor resistivity and geometry and can be determined from the known values of R_{DC} and R_s at any frequency. The approximate value for R_s at high frequencies can also be found using equations in References [8, 10]. All the model parameters' values, including the parasitic elements, L_p and C_p , due to packaging, which produce closely the actual performance of the devices, can be obtained by fitting measured RF S-parameter data of the actual devices to those calculated from the equivalent-circuit model until a closed matched between them is achieved. A comprehensive model in which model parameters are approximated by closed-form equations using the device physical parameters is presented in Reference [16].

2. Microwave Varactor Diodes

Introduction

A microwave varactor diode is a variable-reactance semiconductor device. The variable reactance is provided by the junction capacitance that varies nonlinearly as a function of the applied reverse voltage. This nonlinear feature is useful for various applications such as a voltage-controlled oscillator, a continuous (analog) phase shifter, modulation, a frequency multiplier (harmonic generator), a parametric amplifier, and an up-converter. Varactors may be classified into two general groups: the $p-n$ junction varactor and the Schottky varactor, usually employed at microwave and millimeter-wave frequencies, respectively. For a given voltage range, varactors of increasing capacitance range are the linearly graded, abrupt, and hyperabrupt junctions. The two most commonly used semiconductors for varactors are GaAs and Si, with the former being of greatest interest at microwave and millimeter-wave frequencies due to its high cutoff frequency and quality (Q) factor. GaAs Schottky-barrier varactors

TABLE 2
Typical Characteristics of GaAs Beam-Lead Varactor Diodes

Parameter	Beam-lead varactor
Junction capacitance at 0 V, C_{j0} (pF)	0.4
Parasite capacitance, C_p (pF)	0.02
Capacitance tuning ratio	3 to 1
Series resistance, R_s (Ω)	3
Q factor at 40 MHz	3300

have been used extensively to generate power at millimeter-wave frequencies. Typical electrical parameters of currently available beam-lead varactors are listed in Table 2. GaAs FET-compatible monolithic Schottky-barrier diodes, with a capacitance ratio as large as 49:1, were also developed [17]. Detailed device description can be found in References [18, 19].

Structure and Characteristics

The cross-sectional structure of typical junction and Schottky-barrier varactor diodes is shown in Figure 6. A depletion layer is created in the epitaxial layer. In the junction varactor, ohmic contacts are formed at the *p* and *n* sides for electrical connections to circuits. For the Schottky varactor, contact with the diode anode is made by metal lead (beam-lead diodes) or whisker (whisker diodes), whereas the cathode is an ohmic contact formed at the top (beam-lead diodes) or bottom (whisker diodes) of the substrate. The important device parameters are the diode series resistance (R_s), zero-bias junction capacitance ($C_j(0)$), and capacitance at

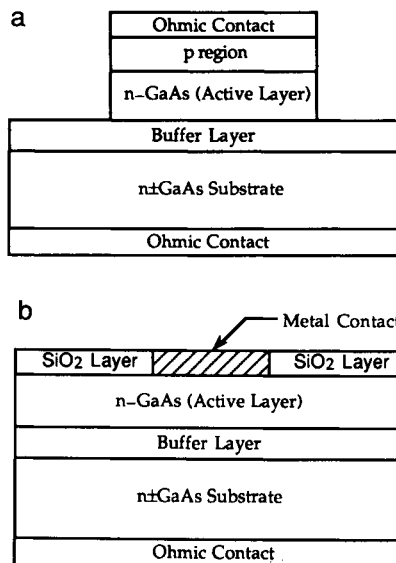


Figure 6. Cross-sectional channel structure of typical *p*–*n* junction (a) and Schottky-barrier (b) varactor diodes.

the pinch-off (punch-through) voltage $V_p(C_j(V_p))$. R_s is a function of the diode junction area and the epitaxial layer thickness and doping profile. R_s can be minimized by increasing the junction area and doping concentration while reducing the epitaxial layer thickness. $C_j(0)$ and $C_j(V_p)$ are related to the semiconductor dielectric constant, the diode area, and, most importantly, the depletion region thickness. To achieve a minimum value for $C_j(0)$, the diode area needs to be increased. $C_j(V_p)$, together with $C_j(0)$, determines the range of the capacitance variation which is the most important characteristic of varactor diodes. In general, a small value for R_s and $C_j(V_p)$ and a large value for $C_j(0)/C_j(V_p)$ are desired.

The important characteristics of varactor diodes are $f_c(V)$, the cutoff frequency at junction bias voltage V_j ,

$$f_c(V) = \frac{1}{2\pi R_s C_j(V_j)},$$

$Q(V)$, the quality factor at V_j and frequency f ,

$$Q(V) = f_c(V)/f,$$

f_{cd} , the dynamic cutoff frequency,

$$f_{cd} = \frac{1}{2\pi R_s} \left(\frac{1}{C_{j,\min}} - \frac{1}{C_{j,\max}} \right),$$

and Q_d , the dynamic quality factor at frequency f ,

$$Q_d = \frac{S_1}{2\pi f R_s} \approx \gamma \frac{C_j(0)}{C_j(V_j)} \frac{f_c(0)}{f}$$

$$\gamma = \frac{C_1}{C_0} \approx 0.25 \text{ (abrupt junction) or } 0.17 \text{ (graded junction)},$$

where $C_j(V_j)$ is the junction capacitance at V_j ; $C_{j,\min}$ and $C_{j,\max}$ are usually the junction capacitances at the pinch-off and zero voltages, respectively; S_1 is the first Fourier coefficient of the time-dependent elastance (reciprocal of capacitance); and C_0 and C_1 are the Fourier coefficients of the junction capacitance. Details of the device characteristics can be found in References [18, 19].

Fabrication

A typical device fabrication consists of the following steps [18, 19].

1. Formation of a buffer layer and an *n*-type epitaxial (active) layer on a heavily doped (n^+) GaAs substrate.
2. Diffusion of a *p*-type dopant such as boron (junction diode) or deposition of the Schottky-barrier metal (Schottky diode) into the epitaxial layer.
3. Formation of ohmic contacts at the top and bottom (junction diode) or an ohmic contact at the bottom (Schottky diode).

Operation

The varactor diode is usually operated under reverse-biased conditions under which it behaves as a voltage-controlled capacitor. As the reverse-biased voltage is increased, the width of the depletion layer increases toward the semi-insulating substrate, resulting in a reduction of the capacitance from a maximum value at 0 V to a minimum value at the pinch-off voltage. Beyond the pinch-off level, the capacitance is essentially independent of the applied voltage and R_s reaches a minimum value. To obtain a large reactance variation, the rate of change of capacitance with bias voltage should be high. Details of the varactor principle of operation can be found in References [18, 19].

Models

Under the normal reverse-bias operation, the varactor diode is modeled as a lumped-element equivalent circuit (Figure 7), in which the junction resistance is neglected due to its large value compared with the junction capacitive reactance at microwave frequencies. The forward-biased varactor equivalent circuit at microwave frequencies includes the diffusion capacitance of the injected carriers as well as the effect of these carriers on the conductance of the semiconductor material and thus is more complicated. The diode junction capacitance $C_j(V_j)$, series resistance R_s , and parasitic elements L_p and C_p , due to packaging, can be evaluated as those for the Schottky-barrier mixer and detector diodes (Section 1). The most widely used measurement technique for R_s is the transmission resonance method [20]. Detailed discussion of the model can be found in References [18, 19]. An equivalent circuit model for a planar GaAs Schottky-barrier varactor diode, based on its physical parameters, has also been developed [21].

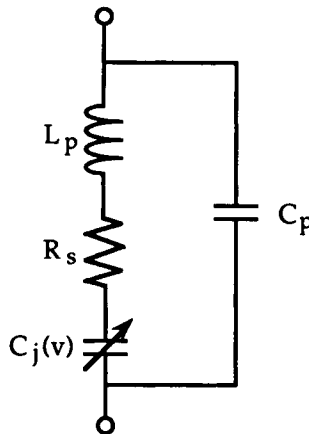


Figure 7. An equivalent circuit model for varactor diodes.

3. Microwave PIN Diodes

Introduction

The PIN diode is a semiconductor diode that consists of a heavily doped p -region (p^+) and a heavily doped n -region (n^+) separated by an extremely high resistivity intrinsic (I) material. Its special features, very high and low impedances under respective reverse- and forward-biased voltages, continuous variation of resistance versus bias, and high-frequency rectification, can be utilized for various applications such as a switch, variable attenuator, phase shifter, limiter, and duplexer. Present PIN diodes can have cutoff frequency of around 2500 GHz (Table 3) and are capable of operation well into the millimeter-wave area. Details of the device can be found in References [22–24].

Structure and Characteristics

The cross-sectional structure of a typical PIN diode is shown in Figure 8. The I layer of a practical diode is either the high-resistivity p - or the high-resistivity n -type (Si or GaAs), referred to as the π - or ν -type, respectively, and have a typical resistivity of about 100 to 10,000 Ω/cm . Its parameters, resistivity, thickness, and cross-sectional area, affect the diode performance. High resistivity results in low RF loss under reverse bias and the least variation of junction capacitance with reverse-biased voltage. A wide I region, although producing a high breakdown voltage, has a low

TABLE 3
Parameters of a PIN Diode

Parameter	Beam-lead PIN
Junction capacitance, C_j (pF)	0.020
Parasitic capacitance, C_p (pF)	0.010
Total capacitance, C_t (pF)	0.030
Series resistance, R_s (Ω)	3
Reverse series resistance, R_r (Ω)	3.5
Forward series resistance, R_f (Ω)	3.5
Parasite inductance, L_p (nH)	0.2
Cutoff frequency, f_c (GHz)	2650
Switching cutoff frequency, f_{cs} (GHz)	2270

transition frequency and a high resistance (diode junction resistance) and requires a large bias voltage and current. A large area, although increasing the power handling capability, has a large capacitance (diode junction capacitance), resulting in narrow circuit bandwidth and a low diode cutoff frequency. The p and n sides have metallic contacts for external electrical connections to circuits. In a well-made PIN diode, the resistances in the p^+ and n^+ regions and the diode ohmic contacts are responsible for RF loss. The packaged PIN diode is used at low microwave frequencies, whereas the beam-lead and chip diodes are usually employed at high microwave and millimeter-wave frequencies due to the high cutoff frequency, resulting from small junction area and parasitics, and the compatibility with hybrid as well as MMIC techniques. Detailed discussion of the device structure can be found in References [22–24].

The important characteristics of PIN diodes are f_c , the cutoff frequency,

$$f_c = \frac{1}{2\pi C_j R_r},$$

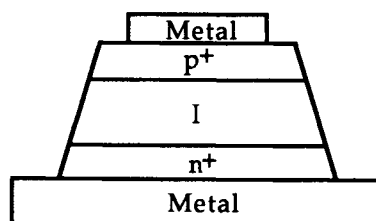


Figure 8. Cross-sectional channel structure of a typical PIN diode.

f_{cs} , the switching cutoff frequency,

$$f_{cs} = \frac{1}{2\pi C_j \sqrt{R_r R_f}},$$

and f_T , the transition frequency,

$$f_T = \frac{D_p}{W^2},$$

where R_r and R_f are the series resistances under reverse- and forward-bias conditions, respectively; C_j is the junction capacitance; D_p is the diffusion constant for holes; and W is the I-layer thickness. Details of device characteristics can be found in References [22–24].

Fabrication

A typical device processing consists of the following steps.

1. Diffusion of p^+ and n^+ into an intrinsic material.
2. Formation of contact material (usually TiAu) at p^+ and n^+ sides.
3. Deposition of contact material (usually Au) at top and bottom contacts.

Operation

The PIN diode behaves principally as an electrically variable resistor. As reverse-biased voltage is applied, the depletion region, formed at the junction between the n^+ -layer and the π -layer (I layer) or between the p^+ -layer and the n -layer (I layer), penetrates across the I layer toward the p^+ or n^+ region, respectively, leading to a reduction in the junction capacitance and an increase in the junction resistance. At a sufficient reverse-bias level, referred to as punch-through voltage, the I layer is fully depleted of carriers and the PIN diode appears essentially as a small constant capacitance with respect to bias variations, producing a nearly open circuit across the device terminals. The punch-through voltage is, in general, approximately $\frac{1}{10}$ of the breakdown voltage. When increasing forward bias is applied across the diode, the depletion layer width is reduced and electrons and holes are injected into the I layer from the n^+ and p^+ layers, respectively, rapidly decreasing the resistivity of the I layer and hence the device junction resistance. At a sufficient forward bias, the diode exhibits a very low resistance (nearly a short circuit) across its terminals. The short- and open-circuited behavior is useful for switch and

phase shifter applications, whereas the effect of changing the device junction resistance versus forward-biased voltage, known as conductivity modulation, is used in applications such as a variable attenuator. Detailed principles of operation can be found in References [22–24].

Models

The PIN diode is normally modeled by lumped-element equivalent circuits as shown in Figure 9a for various bias conditions and in Figure 9b for the forward (f)- and reverse (r)-bias conditions. R_s represents the resistances in the diode ohmic contacts and the p^+ and n^+ regions. R_r and R_f account for the losses due to R_s as well as the I-layer under reverse- and forward-bias conditions, respectively, and can be measured using techniques described in Reference [23]. R_i is the I-layer resistance that varies substantially versus bias current as described in Reference [25]

$$R_i = \frac{kT}{qI_0} \frac{W}{L} \tanh(W/2L) \quad L = \text{diffusion length} = \sqrt{D\tau},$$

where k is the Boltzman's constant; T is the absolute temperature; q is the electron charge; I_0 is the forward bias current, τ is the carrier lifetime, and $D = 2D_n D_p / (D_n + D_p)$, with D_n and D_p representing the respective electron and hole diffusion constants, is the ambipolar diffusion constant. At microwave and millimeter-wave frequencies, all these resistances are expected to increase due to the skin effect. The junction capacitance C_j is

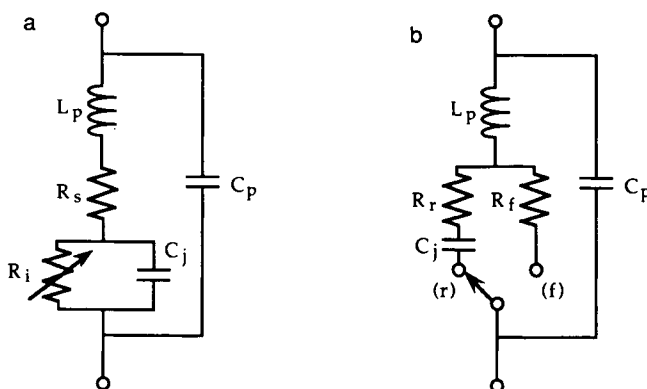


Figure 9. PIN diode equivalent-circuit models under various bias (a) and reverse and forward bias (b).

approximately given by

$$C_j \approx \frac{\epsilon \pi d^2}{4W},$$

where ϵ and d are the permittivity and junction diameter of the intrinsic region, respectively. C_j is normally obtained from measurements at 1 MHz at a reverse bias exceeding the punch-through voltage. All the model parameters' values, including the parasitic elements, L_p and C_p , due to packaging, which produce closely the actual performance of the devices, can be obtained by fitting the device-measured RF S-parameter data to those calculated from the equivalent-circuit model. Detailed discussion on model can be found in Reference [22–24].

4. Microwave GUNN Diodes

Introduction

A microwave Gunn diode is a transferred electron device that utilizes the negative differential resistance property, referred to as the transferred electron or Gunn effect. The negative resistance mechanism is achieved by a reduction in electron velocity caused by an increased electric field, resulting from an applied voltage, beyond a threshold value. This negative resistance feature is used in Gunn oscillators and amplifiers to achieve oscillation and amplification at microwave and millimeter-wave frequencies. Among GaAs, InP, ZnSe, CdTe, and GaAsP compound materials that exhibit the transferred electron effect, GaAs is the most frequently used material due to its maturity and potential for integration with GaAs MMICs, although InP Gunn possesses a higher efficiency, power, and frequency of operation due to its high peak-to-valley velocity ratio and fast energy-transfer-time constant. Currently available GaAs Gunn diodes can produce continuous wave (CW) output power levels from several hundred milliwatts in X-, Ku-, and Ka-band frequency ranges to about 50 mW in W-band frequencies (75–110 GHz). Compared with GaAs and Si IMPATT diodes, Gunn devices have lower output power and efficiency. However, Gunn exhibits lower AM noise than GaAs and Si IMPATTs, FM noise comparable to GaAs IMPATTs, and much lower FM noise than Si IMPATTs. Typical characteristics of a W-band GaAs Gunn diode are listed in Table 4. Details of the device description can be found in References [7, 26–28].

TABLE 4
Typical Characteristics of a W-Band GaAs Gunn Diode

Parameter	GaAs Gunn diode
Operating frequency (GHz)	94
CW output power (mW)	30
Bias voltage (V)	4
Bias current (A)	1
Package capacitance, C_p (pF)	0.15
Package inductance, L_p (nH)	0.12

Structure and Characteristics

The cross-sectional structure of a typical Gunn diode is shown in Figure 10. Ohmic contacts are formed at the epitaxial contact layer and the back of the heavily doped (n^+) substrate for electrical connections to circuits. The important parameters are the electron (carrier) transit time, t_t , across the length of the material and the negative differential resistance. t_t , approximately equal to the reciprocal of the frequency of operation, is proportional to the active layer length, L , and the reciprocal of the electron saturation velocity, v_s . Increasing v_s , by using high-electron-mobility materials, and decreasing L will improve the device operating frequency. Negative resistance is the result of the transfer of conduction currents from a low-energy, high-mobility valley to a high-energy, low-mobility satellite valley, referred to as the transferred electron effect, and depends on the property of the semiconductor. Gunn diodes are normally available in packages. Monolithic Gunn diodes, fabricated on a semi-insulating substrate, have also been developed [29].

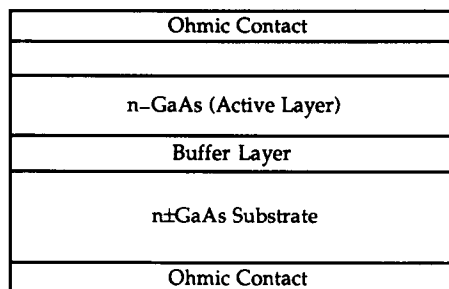


Figure 10. Cross-sectional channel structure of a typical GaAs Gunn diode.

The important characteristics of Gunn diodes are f_{Gunn} , the frequency of oscillation for the Gunn mode,

$$f_{\text{Gunn}} = \frac{1}{t_t} = \frac{v_s}{L},$$

and f_{LSA} , the frequency of oscillation for the LSA mode,

$$f_{\text{LSA}} = 2\pi\sqrt{LC} + \frac{L}{R_0(V/V_{th})},$$

where L and C are the external circuit's resonance parameters and R_0 is the low-field resistance, resulting when the bias voltage V is less than the threshold voltage V_{th} .

Fabrication

A typical device fabrication consists of the following steps [7, 26–28].

1. Formation of a buffer layer, an n -type epitaxial (active) layer, and a contact layer on a heavily doped (n^+) substrate.
2. Formation of ohmic contacts at the contact layer and bottom of substrate.

Operation

The Gunn diode behaves as a negative-resistance device under an appropriate bias voltage. It operates in various oscillation modes, depending on device doping concentration and uniformity, active region length, cathode contact properties, operating bias voltage, and the type of external resonant circuit. The most common modes of operation are the Gunn mode, the limited space-charge accumulation (LSA) mode, and the hybrid mode. The Gunn mode is the fundamental transit-time mode, in which a dipole region, consisting of an accumulation of charge, is formed at the cathode side, with a depletion of charge on the anode side. The dipole grows and drifts toward the anode. After the initial growth of the dipole, a stable condition is eventually reached and the electrons move at a constant velocity. The frequency of operation, which is the reciprocal of the electron transit time, is determined by the length of the active layer and

the electron saturation velocity. The Gunn mode operation is very simple, yet has low efficiency, and the frequency of operation is limited by the length of the active region. The LSA mode operates in a Gunn diode in which only a small accumulation layer of charge is formed near the cathode before it is quenched by the RF voltage resulting from an external resonant circuit. The LSA mode has high efficiency and output power, and its operating frequency depends on the external resonant circuit rather than the active layer length and the electron velocity. The hybrid mode operates between the LSA and other modes, with efficiency inbetween. Gunn diodes can also operate as reflection amplifiers. This mode of operation, however, is becoming less popular due to the availability of low-noise, high-efficiency FET devices at microwave and millimeter-wave frequencies. Details of the operation can be found in References [7, 26–28].

Models

The Gunn diode is normally represented by lumped-element equivalent circuits as shown in Figure 11a for the Gunn mode and Figure 11b for the LSA mode [26]. C_D and $-R$, representing the diode under a high-field operation, are the domain capacitance and the device negative resistance, respectively. C_D can be approximated as

$$C_D = \frac{\epsilon A}{W},$$

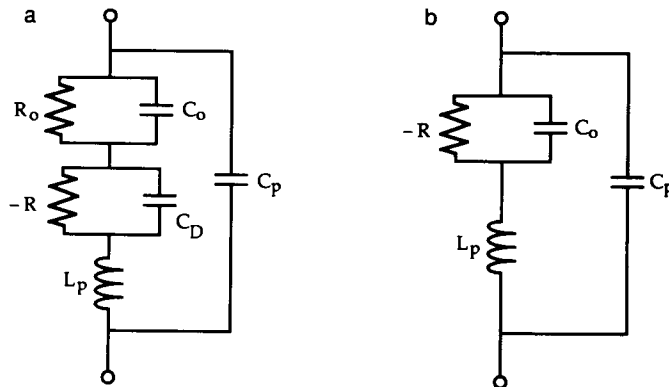


Figure 11. Gunn diode equivalent circuit models in the Gunn mode (a) and the LSA mode (b).

where ϵ is the dielectric constant of the semiconductor material; A is the diode area; and W is the width of the domain. C_0 and R_0 account for the low-field behavior of the diode and can be expressed as

$$C_0 = \frac{\epsilon A}{L}$$

$$R_0 = \frac{EL}{qN_d Av(E_0)},$$

where E is the electric field resulted from the applied voltage; q is the electron charge; N_d is the doping density; and $v(E_0)$ is the electron velocity outside the domain. L_p and C_p are the package parasitic elements. For accurate circuit design, the model parameters are usually evaluated by fitting the diode measured RF S-parameter data to those calculated from the equivalent-circuit model. The diode impedance can be obtained from the difference in the magnitude and phase of the incident and reflected signals, measured using a network analyzer.

5. Microwave IMPATT Diodes

Introduction

A microwave impact-ionization avalanche transit time (IMPATT) diode is a semiconductor diode that operates with a reverse bias sufficient to cause avalanche breakdown. The IMPATT diode employs the carrier impact-ionization and transit-time properties of a semiconductor structure to produce a negative resistance for microwave oscillation and amplification applications. The negative resistance results from the avalanche and transit-time delays that cause the phase delay between the voltage and the current. The negative resistance property is utilized to produce oscillation and amplification at microwave and millimeter-wave frequencies. The most commonly used semiconductor materials for IMPATT devices are Si and GaAs. Si IMPATT diodes, although having a higher frequency of operation and power output than their GaAs counterparts, possess lower efficiency and significantly higher noise. GaAs IMPATTS have the potential for integration with GaAs MMICs. The most popular structures for Si IMPATTs are single and double drift. Structures used for GaAs IMPATTs are single- and double-drift and hybrid Read diodes. At microwave and low-millimeter-wave frequencies, IMPATT diodes have been replaced by GaAs MESFETs, HEMTs, and HBTs for many applications. Yet they are still the most powerful solid-state sources of millimeter-wave

TABLE 5
Typical Characteristics of a W-Band Double-Drift Si IMPATT Diode

Parameter	Double-drift Si IMPATT
Operating frequency (GHz)	94
CW output power (W)	0.3
Bias voltage (V)	20
Bias current (A)	2
Package capacitance, C_p (pF)	0.2
Package inductance, L_p (pF)	0.15

power. Currently available Si IMPATT diodes can have CW output power levels ranging from more than 1 kW in the Ka-band to about 0.5 kW in the W-band. Typical characteristics of a W-band double-drift Si IMPATT diode are shown in Table 5. A detailed description can be found in References [7, 30–33].

Structure and Characteristics

The cross-sectional channel structure of a typical single-drift Si IMPATT device is shown in Figure 12. Other structures are p^+pnn^+ (double-drift Si IMPATT), $p^+n^+nn^+$ or $p^+n^-n^+nn^+$ (single-drift GaAs IMPATT), $p^+pp^+n^+nn^+$ or $p^+pp^+pnn^+nn^+$ (double-drift GaAs IMPATT), and $p^+pn^+nn^+$ or $p^+pnn^+nn^+$ (hybrid GaAs IMPATT). Ohmic contacts are formed at the p^+ and n^+ regions for electrical contacts to external circuits. The double-drift structure can be considered two back-to-back single-drift devices with about twice the breakdown voltage and depletion

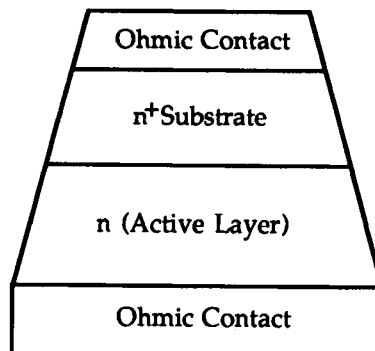


Figure 12. Cross-sectional channel structure of a typical single-drift Si IMPATT diode.

width at a given operating frequency. It has approximately 1.5 and 2 times higher efficiency and output power, respectively, compared with its single-drift counterpart. The n (active) layer of a single-drift diode must be doped so that it is fully depleted at the breakdown voltage and can be divided into two regions: the avalanche region, a narrow high-field zone near the $p^+ - n$ junction at which carriers are generated by impact ionization, and the drift region, a large low-field zone in which the carriers, injected from the avalanche regions, drift at saturated velocity. The avalanche region is an important parameter of IMPATT. Reducing the avalanche region width will increase the magnitude of the device conductance and hence the power capability and efficiency. IMPATT diodes are normally available in packages. Monolithic IMPATT diodes have been developed [34]. Details of structures of IMPATTs can be found in References [7, 30–32].

Fabrication

A typical fabrication process for single-drift Si IMPATT diodes consists of the following steps.

1. Growth of n -type Si epitaxial (active) layer on an n^+ substrate.
2. Formation of ohmic contacts at the top and bottom of the n^+ substrate and epitaxial layer, respectively.

Operation

The IMPATT diode is a negative-resistance device operated in reverse-biased voltages beyond the avalanche breakdown. When a large reverse-biased voltage, less than the breakdown voltage, is applied to the IMPATT diode, negligible current flows, and there exists a narrow high-electric-field region and a long low-electric-field region in the diode. As the bias voltage reaches the breakdown level, the introduction of an AC voltage will cause the electron-hole pairs to grow exponentially, resulting in an avalanche breakdown in the high-field region (avalanche region) with increasing current, causing a substantial increase in current and the number of carriers. Carriers generated in the avalanche region are then swept out continuously by the electric field into either the ohmic region or the low-field region (drift region), depending upon their charge. Due to the time delay in the avalanche and drift states, a phase shift between the voltage and the current exists. It is this phase delay that produces the negative resistance responsible for microwave signal oscillation and amplification. Details of the device operational principle can be found in References [7, 30, 31, 35].

Models

The IMPATT diode is normally modeled by a lumped-element equivalent circuit (Figure 13). The effective inductance L_A and the avalanche capacitance C_A , representing the avalanche region, are given by [30]

$$L_A = \frac{\tau_A}{2J_0\alpha' A}$$

$$C_A = \frac{\epsilon A}{x_A},$$

where τ_A is the time delay due to the impact ionization; J_0 is the DC current density; $\alpha' = \partial\alpha/\partial E$, with α being the ionization rate and E being the total electric field; A is a constant depending on the material; ϵ is the dielectric constant of the semiconductor; and x_A is the avalanche region width. The impedance of the avalanche region is

$$Z_A = \frac{1}{j\omega C_A} \left[\frac{1}{1 - (f_r/f)^2} \right],$$

where $f_r = 1/2\pi\sqrt{L_A C_A}$, representing the avalanche resonance frequency. R_d and X_d constitute the impedance of the drift region given as

$$\begin{aligned} Z_d = R_d + jX_d &= \frac{1}{\omega C_d} \left[\frac{1}{1 - (f/f_r)^2} \left(\frac{1 - \cos \theta_d}{\theta_d} \right) \right] \\ &\quad + \frac{j}{\omega C_d} \left[-1 + \frac{1}{1 - (f/f_r)^2} \left(\frac{\sin \theta_d}{\theta_d} \right) \right], \end{aligned}$$

where $C_d = A\epsilon/(W - x_A)$, with W being the depletion layer width, and

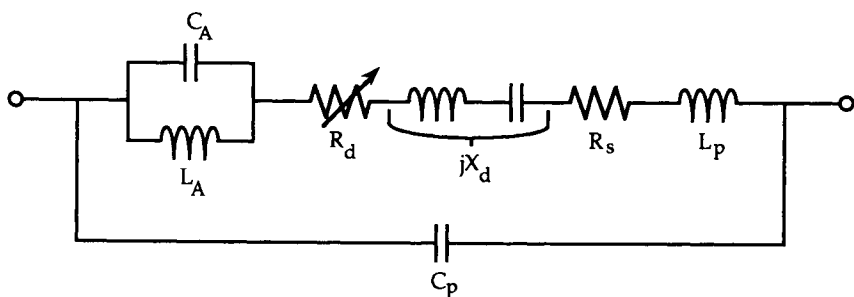


Figure 13. IMPATT equivalent circuit model.

$\theta_d = \omega(W - x_A)/v_s$, with v_s being the saturation velocity. L_p and C_p are the package parasitic elements. R_s represents the sum of the resistances of the semiconductor and the ohmic regions. The total device impedance, without the parasitics, is

$$Z = Z_A + Z_d + R_s.$$

Similar equations are presented in Reference [32]. For accurate circuit design, the model parameters' values are normally obtained by fitting the device's measured RF *S*-parameter data to those calculated from the equivalent-circuit model. The diode impedance can also be determined from the difference in the magnitude and phase of the incident and reflected signals, measured using a network analyzer.

6. Microwave Bipolar Junction Transistors

Introduction

Microwave bipolar junction transistors (BJTs) consist of Si BJTs and heterojunction bipolar transistors (HBTs). They operate at lower frequencies than microwave field effect transistors (FETs). Microwave BJTs find numerous applications in the microwave and millimeter-wave regions, including power amplifiers, low-phase noise oscillators, mixers, and frequency multipliers.

A microwave Si BJT is a conventional Si homojunction *n-p-n* BJT with very small dimensions for the active area. State-of-the-art microwave Si BJTs with an about $0.5\text{-}\mu\text{m}$ emitter can have a cutoff frequency, f_T , in the 20- to 40-GHz range (Table 6). They are used at lower frequencies compared with HBTs and microwave FETs. Detailed description of microwave Si BJTs can be found in References [7, 33, 36–38].

HBT is an otherwise conventional microwave Si BJT with a heterostructure emitter–base junction fabrication on III–V compound materials. The *n*-type emitter is formed in the wide-band-gap AlGaAs, whereas the *p*-type base and *n*-type collector are formed in the lower band-gap GaAs. HBTs have a higher speed and frequency of operation with relaxed geometrical dimensions than do Si BJTs. Other advantages, compared with Si BJTs, include a higher emitter efficiency, decreased base resistance, wider temperature range of operation, lower output conductance, reduced parasitic substrate capacitance, reduced electron transit time, reduced base–emitter capacitance, and higher linearity and lower harmonic distortion performance. Compared with microwave FETs, HBTs offer the highest linearity to DC power and excellent capabilities for

TABLE 6
Comparison of Intrinsic Device Characteristics of HBTs, Si BJTs [Super Self-Aligned Technology (SST)], GaAs MESFETs, and HEMTs [39]

Intrinsic device characteristics	GaAs HBT	Advanced Si bipolar	GaAs HEMT/MESFET
Device speed (f_T, f_{max})	~ 50–200 GHz, ~ 1- to 3- μ m emitter	~ 20–40 GHz, $\leq 0.5 \mu$ m	~ 0.2- to 0.5- μ m gate
Current/effective chip area	~ 50 kA/cm ²	~ 2–5 \times lower	~ 5–10 \times lower
Device matching	$V_{be} \sim 1$ –2 mV	Comparable	~ 3–5 \times worse
Transconductance (g_m)	~ 5–10 K mS/mm	Comparable	~ 20–100 \times lower
Output conductance (g_0)	~ 0.2 mS/mm	~ 10–20 \times higher	~ 25–100 \times higher
Trapping effects	1/f corner < 100 kHz	~ 10–100 \times lower	~ 10–100 \times higher
Input impedance	Base input current	Same	Voltage-controlled gate
White noise (10–20 GHz)	~ 4–6 dB	Comparable	~ 2–7 \times lower
Radiation hardness	> 500 Mrad; > 1×10^{14} neutrons/cm ²	~ 20–50 \times lower	Comparable
Substrate capacitance	No	Yes	No
Power consumption	High	High	Medium
Integration level	MSI–LSI	LSI–VLSI	LSI

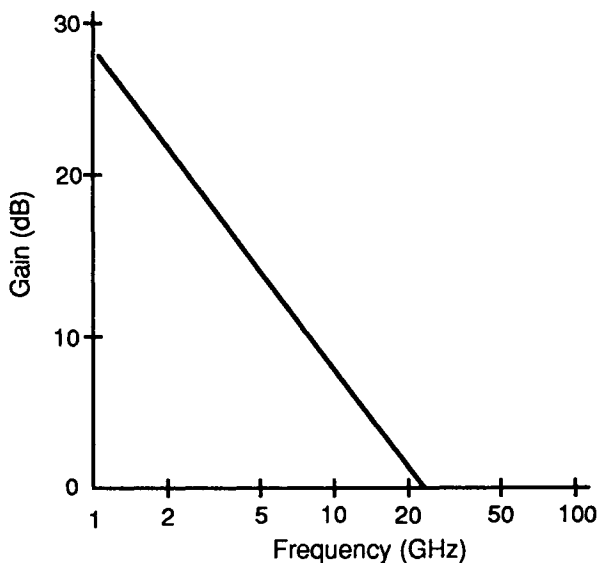


Figure 14. Gain versus frequency of an HBT [43, 44].

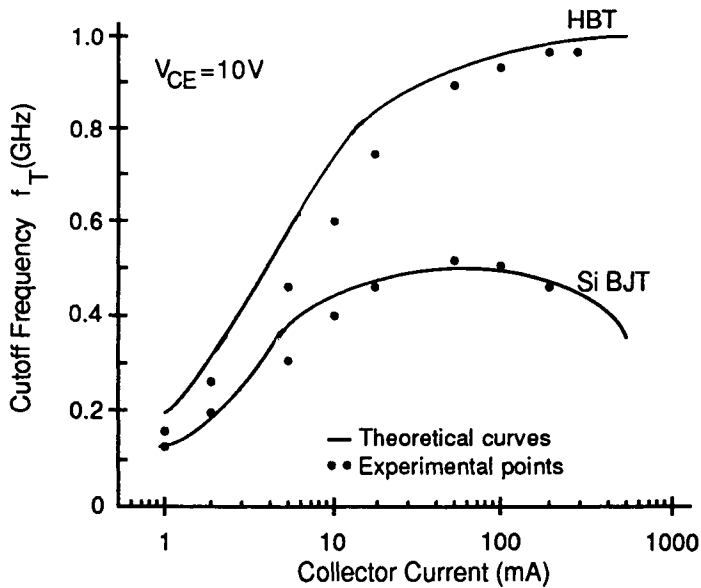


Figure 15. Comparison of cutoff frequencies of an HBT and a Si BJT of similar geometry [43, 45].

TABLE 7
Comparison of Transistors, with Respect to GaAs MESFETs, for Microwave and Millimeter-Wave Power Applications [57]

Characteristics	MESFET	PM HEMT	Conventional HEMT	HBT	InP HEMT
Current density	0	+	+	++	++
Breakdown voltage	0	-	-	0	--
Efficiency	0	+	0	+	+
Gain	0	++	+	+	++
Process complexity	0	-	-	--	-
Thermal impedance	0	0	0	-	+
MMIC compatibility	GaAs	GaAs	GaAs	GaAs	InP
Application frequency	Microwave/ low millimeter-wave	Microwave/ millimeter-wave	Microwave/ millimeter-wave	Microwave	Millimeter-wave

Note. +, better; -, worse.

TABLE 8
Comparison of Merit Parameters for GaAs MESFETs, HEMTs, and HBTs [46]

Merit parameter	MESFET	HEMT	HBT	Conclusion
Small signal				
f_t	L	M	H	HBT is the highest speed.
f_{\max}	M	H	L	HEMT is the highest frequency.
Gain BW	M	H	H	HEMT is the best for the wideband at high frequency.
Noise figure	M	L	H	HEMT is the best for LNAs.
Phase noise	M	H	L	HBT is the best for VCOs.
g_m/g_0	L	M	H	HBT is the best for highly linear amplifiers.
$IP3/P_{DC}$	H	M	H	MESFET is the best at high frequency; HBT is the best at low frequency.
V_{TH} uniformity	L	M	H	HBT is the best for analog LSI circuits.
Hysteresis	H	M	L	HBT is the best for S/H.
Large signal				
Collector efficiency	M	H	H	HBT potentially is the best power device, but the jury is still out.
Power density	M	M	H	HBT potentially is the best power device, but the jury is still out.

Note. H, high; M, medium; L, low.

multipunction microwave/digital applications. Measured f_T and f_{\max} (maximum frequency of oscillation) of 165 and 100 GHz, respectively, have been reported [40]. At 18 GHz, a 3.3-dB noise figure has been achieved [41]. At 10 GHz, 1.25-W output power and 37% power-added efficiency have also been demonstrated [42]. Figure 14 shows the gain performance of an HBT. Cutoff frequencies of an HBT and a Si BJT of similar geometry are compared in Figure 15. Comparisons among HBT, Si BJT, GaAs MESFET, and HEMT are listed in Tables 7 and 8. Most current HBT applications are limited to about 20 GHz with a projected extension into the millimeter-wave region. Details of device description and performances can be found in References [39, 43, 47].

Structure and Characteristics

Cross-sectional structures of typical microwave Si BJTs and HBTs are shown in Figure 16. They are similar to those of low-frequency $n-p-n$ Si BJTs with very small active areas. The two critical dimensions are the emitter stripe width and the base thickness. Reducing these dimensions will increase the gain, noise figure, and frequency of operation. The power output is proportional to the emitter periphery. Current devices can have

an emitter stripe width in the submicrometer region with the base thickness as small as a few hundred angstroms. The key difference between a microwave Si BJT and an HBT is the materials used to fabricate the emitter, base, and collector. The former uses Si, whereas the latter employs III-V materials that lead to a higher emitter efficiency and lower parasitic resistances and capacitances. In HBTs, emitter and base doping levels can be optimized for improved device performance while still maintaining a good common-emitter current gain due to the emitter-base heterojunction. In contrast to BJTs, the emitter doping is not required to be much higher than the base doping to produce high emitter efficiency. Detailed structures for microwave Si BJTs and HBTs can be found in References in [7, 36, 38] and [39, 43, 47], respectively.

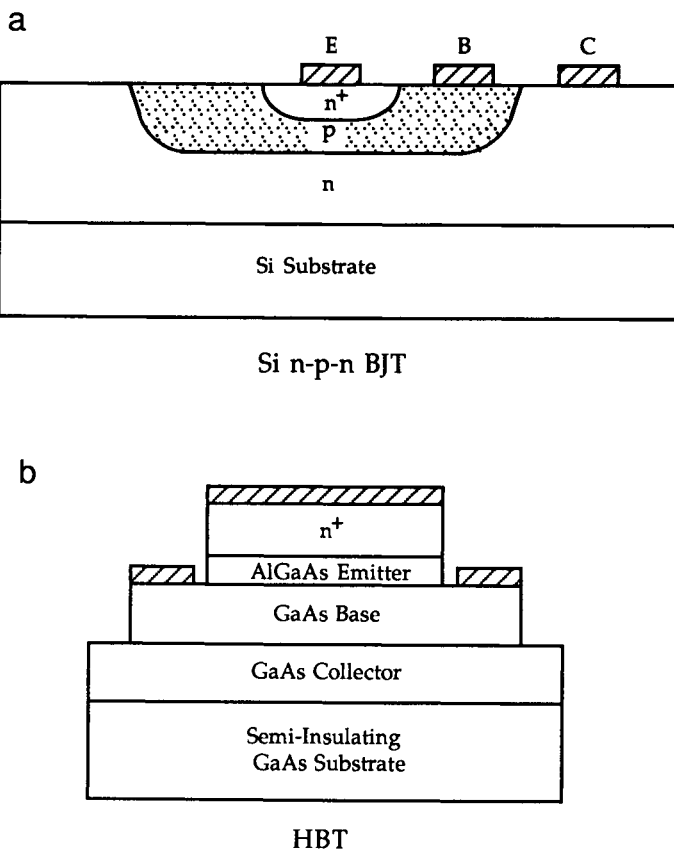


Figure 16. Cross-sectional channel structures of typical Si BJTs (a) and HBTs (b).

The critical characteristics of microwave BJTs are f_T , the cutoff frequency or the frequency of unity current gain,

$$f_T \approx \frac{1}{2\pi\tau_{ec}},$$

f_{max} , the maximum frequency of oscillation or the frequency at which the maximum available gain is 0 dB,

$$f_{max} \approx \left(\frac{\alpha_0 f_T}{8\pi R_b C_{bc}} \right)^{\frac{1}{2}},$$

G_{max} , the maximum available gain at frequency f ,

$$G_{max} \approx \frac{f_T}{f} \left[\frac{\alpha_0}{8\pi(R_b + R_e + 2\pi f_T L_e)C_{bc}} \right],$$

G_u , the unilateral gain, the power gain with no reverse transmission,

$$G_u \approx (f_{max}/f)^2,$$

F_{min} , the minimum noise figure,

$$F_{min} \approx 1 + u + (2u + u^2)^{\frac{1}{2}}$$

$$u = \left[1 - \alpha_0 + \left(\frac{f}{f_\alpha} \right)^2 \right] 2\pi R_b f_T C_{be},$$

and η_{add} , the power-added efficiency,

$$\eta_{add} = \frac{P_0 - P_{in}}{P_{DC}},$$

where τ_{ec} is the total emitter-to-collector (transit) delay time, comprised of the emitter-base, base layer, and collector charging times, and the collector depletion-layer transit time; α_0 is the low-frequency common-base current gain; f_α is the cutoff frequency due solely to the base delay time; P_0 , P_{in} , and P_{DC} are the RF output power, RF input power, and DC input power, respectively. Remaining parameters are defined in the device equivalent-circuit model (Figure 17). Other important parameters include the power output at the 1-dB compression point, its associated gain, and

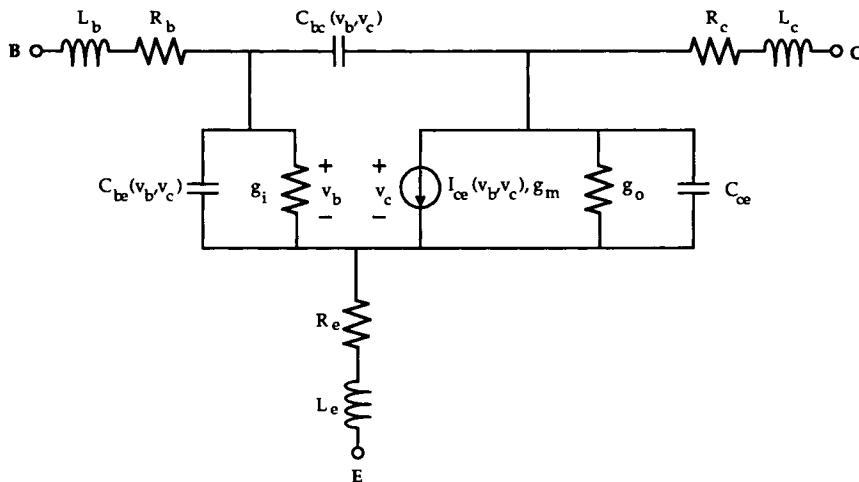


Figure 17. An equivalent-circuit model for microwave BJTs. g_m , transconductance; C_{bc} , C_{be} , and C_{ce} , base–collector, base–emitter, and collector–emitter capacitances; R_b , R_e , and R_c , base, emitter, and collector resistances; g_i and g_o , input base–emitter and output collector conductances; L_b , L_e , and L_c , base, emitter, and collector electrode inductances.

the associated gain corresponding to F_{\min} . Details of the device characteristics can be found in References [7, 33, 36–39, 47].

Fabrication

Several approaches can be employed to fabricate microwave bipolar transistors such as the planar diffusion, ion-implantation, and isoplanar processes. Typically, processing consists of the following steps.

1. Formation of an n -type epitaxial layer (active layer) on the Si substrate and deposition of a silicon dioxide layer.
2. Formation of the base and emitter regions.
3. Formation of the base and emitter ohmic contacts by deposition and liftoff of a metal layer.
4. Formation of the collector region and ohmic contact.
5. Formation of gold-plated air bridge interconnections between device regions.
6. Thinning the wafer to the desired thickness.
7. Formation of the via holes for low-inductance ground connections.
8. Metallization of the wafer backside.

Details of device fabrication can be found in References [36, 37, 39, 47].

Operation

Microwave Si BJT and HBT behave very similarly to a low-frequency $n-p-n$ bipolar transistor. They operate by the injection and collection of minority carriers. In normal biasing (normal active mode), the emitter and collector junctions are forward and reverse biased, respectively. The forward-biased emitter junction injects electrons into the center p region, and the reverse-biased collector junction collects the injected electrons. The emitter current consists of an electron current (due to electrons crossing from the emitter into the base) and a hole current (due to holes crossing from the base into the emitter). In a well-designed microwave transistor, the emitter current consists almost entirely of electrons and is approximately equal to the collector current, whereas the base current is a very small fraction of the emitter current. Besides the normal active mode, there are two other operation regimes: the cutoff regime, in which the emitter and collector junctions are reverse biased and the collector current is negligible, and the saturation regime, in which the emitter and collector junctions are both forward biased, resulting in a large collector current. Details of the principle of operation can be found in References [7, 36, 39, 43, 47].

Models

Microwave BJT linear and nonlinear models are needed for both circuit and device designs. These models can be developed from either measured data or device physics. Modeling based on the device physics [39, 47, 48], by solving the two-dimensional nonlinear equations governing the physical properties of the device, is time consuming and does not produce very accurate results at microwave frequencies, especially in the millimeter-wave region. Accurate models at microwave frequencies can be obtained by incorporating the distributed effects of the device structure, but with increasing difficulty and computational time. Accurate physics-based models, whereas very useful for understanding the operation and design of the device, are therefore of limited use for computer-aided design (CAD) of microwave circuits. The equivalent-circuit model (Figure 17) is very suitable for CAD purpose. The model parameters can be obtained by fitting measured DC and RF S -parameter data of the actual devices to those calculated from the equivalent-circuit models until a close match between them is achieved. This approach needs no knowledge of the device physics and can produce accurate models due to the direct relation between the model and device measured performance. Approximated closed-form equations for its elements were also derived using the device physical

parameters [36–39, 47]. A modified Gummel–Poon nonlinear model for SPICE circuit simulation has also been developed from DC and RF measurements [49].

7. Microwave Field Effect Transistors

Introduction

FETs consist of four different types: the GaAs metal semiconductor field effect transistor (GaAs MESFET), Si MESFET, InP MESFET, and heterostructure FET (HFET). They can be employed for various circuit applications such as mixers, oscillators, amplifiers, phase shifters, switches, frequency multipliers, discriminators, and isolators.

GaAs, Si, and InP MESFETs are junction field effect transistors (JFETs) with a Schottky-junction gate made from GaAs, Si, and InP substrates, respectively. The Si- and InP-based MESFETs have disadvantages, such as a lower operating frequency and gain, respectively, and are thus not popular, compared with GaAs MESFETs. Currently GaAs MESFETs can operate up to millimeter wavelengths. Detailed description of GaAs MESFET can be found in References [7, 8, 43, 50, 51].

HFET, also known as the high electron mobility transistor (HEMT), modulation-doped FET (MODFET), two-dimensional electron gas FET

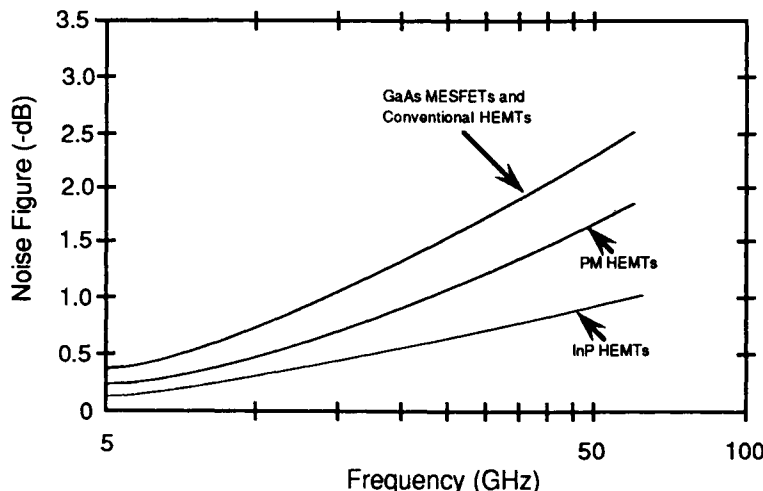


Figure 18. Minimum noise figures achieved for GaAs MESFETs, conventional PM HEMTs, and InP HEMTs [56, 57].

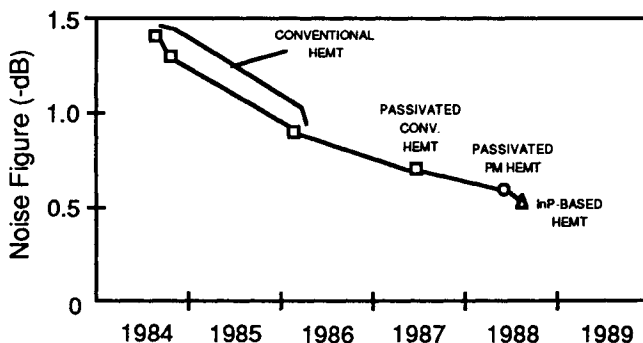


Figure 19. Progress of General Electric 0.25- μm HEMT noise figures at 18 GHz [52].

(TEGFET), or selectively doped heterostructure FET (SDHT), is a conventional MESFET fabricated on an AlGaAs/GaAs heterostructure. Pseudomorphic HEMT (PM HEMT) is based on an AlGaAs/InGaAs/GaAs heterojunction. InP-based HEMT, containing an InAlAs/InGaAs heterojunction, is fabricated on an InP substrate. These devices outperform GaAs MESFETs in many aspects, such as the noise figure, gain, noise bandwidth, gain bandwidth product, operating fre-

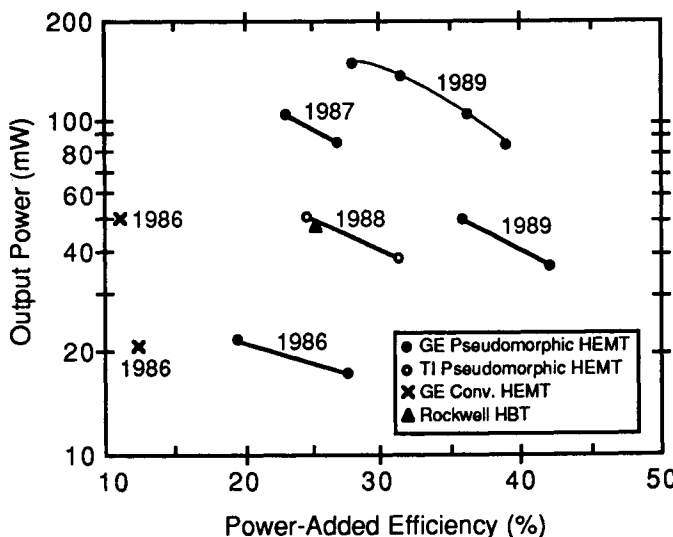


Figure 20. State-of-the-art power output and power-added efficiency of millimeter-wave transistors at 60 GHz [57].

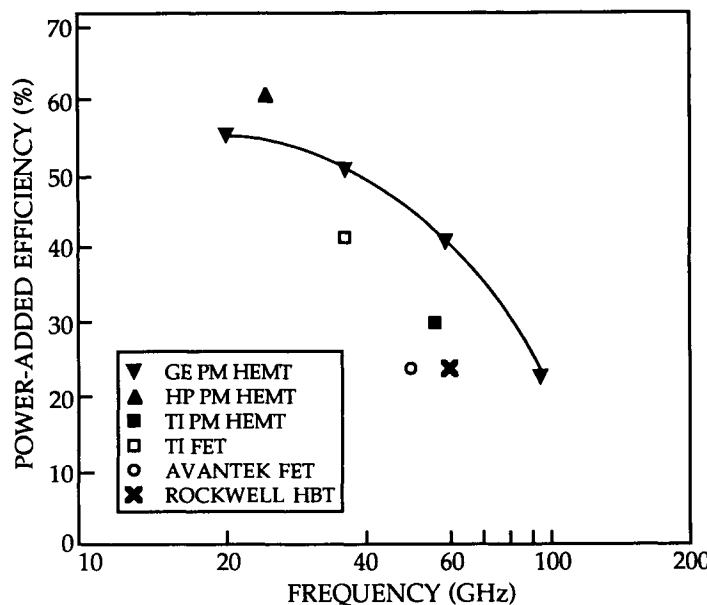


Figure 21. State-of-the-art power-added efficiencies of transistors in the 20- to 94-GHz range [53].

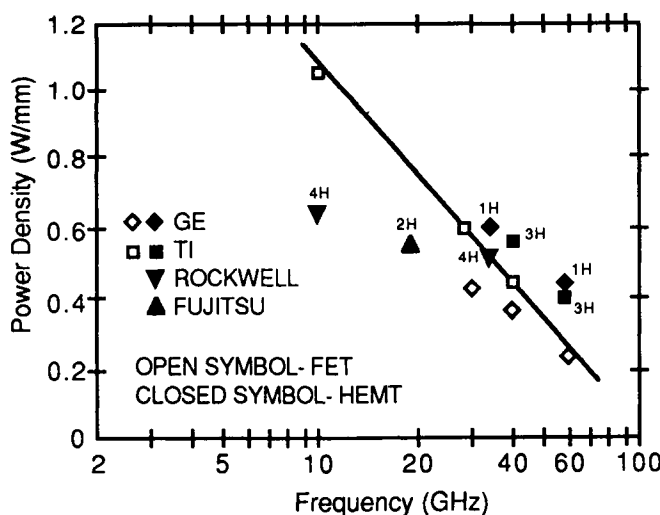


Figure 22. State-of-the-art power densities of HEMTs and GaAs MESFETs [54]. iH ($i = 1, 2, 3$, or 4) refers to the number of heterojunctions in the devices.

TABLE 9
Measured Noise Figures for 0.25- μm General Electric HEMTs at 300 K [54]

Frequency (GHz)	Device type	F_{\min} (dB)	G_a (dB)	F_∞ (dB)
8	Conventional HEMT	0.4	15.2	0.41
18	Conventional HEMT	0.7	13.2	0.73
30	Conventional HEMT	1.5	10.0	1.6
40	Conventional HEMT	1.8	7.5	2.1
62	Conventional HEMT	2.6	5.7	3.3
62	PM HEMT	2.3	4.0	3.3

Note. F_{\min} , minimum noise figure; G_a , associated gain; F_∞ , noise figure of an infinite-stage lossless amplifier, approximating the noise figure of a high-gain (> 15 dB), multistage amplifier.

TABLE 10
Comparison of Noise Figures of 0.15- μm PM and InP HEMTs [57]

Device type	Frequency (GHz)	F_{\min} (dB)	G_a (dB)	F_∞ (dB)
PM HEMT	18	0.55	15.0	0.57
	60	1.6	7.6	1.87
	94	2.4	5.4	3.09
InP HEMT	18	0.3	17.1	0.31
	60	0.9	8.6	1.03
	94	1.4	6.5	1.73

TABLE 11
Comparison of Conventional, PM, and InP HEMTs (as of 1989) [52]

Device type	Age with good RF performance (years)	Performance	Applications	Reliability	MMIC compatibility
Conventional HEMT	6	Good NF	Low noise, 1–60 GHz	Established for low noise	GaAs
PM HEMT	3	Better NF	Low noise, 1–100 GHz	Established for low noise	GaAs
		Best power	Power, 10–100 GHz		
InP HEMT	1	Best NF	Low noise, 1–100 GHz	Poor initially	InP

TABLE 12
**Comparison of the Power Performance of GaAs MESFET and Conventional, PM,
and InP HEMTs at 60 GHz [53]**

Year Reported	Device type	Gate length (μm)	Power density (W/mm)	Maximum power-added efficiency (%)	Associated gain (dB)
1986	GaAs MESFET	0.25	0.25	9	3
	Conventional HEMT	0.25	0.41	14	3
	PM HEMT	0.25	0.43	28	3
1989	PM HEMT	0.15	0.84	41	6

TABLE 13
State-of-the-Art Power Performance of Millimeter-Wave Power PM HEMTs [42]

Gate width (μm)	Frequency (GHz)	Output power (mW)	Power-added efficiency (%)	Power gain (dB)
400	35	216	26	5.3
400	55	184	25	4.6
160	94	62.7	13	4.0

quency, power density, and power-added efficiency (Figures 18 through 22 and Tables 7 through 13). Current InP-based and PM HEMTs exhibit the lowest noise figure and highest gain (1.7-dB noise figure and 7.7-dB gain at 94 GHz) and the highest power performance (62 mW and 13% efficiency at 94 GHz) up to 140 GHz, respectively, whereas the conventional HEMTs are useful through about 60 GHz. Detailed descriptions can be found in References [53–59].

Structure and Characteristics

Cross-sectional structures of typical GaAs MESFETs and HEMTs are shown in Figure 23. The drain (D) and source (S) electrodes form ohmic contacts to the active layer, whereas the gate (G) electrode forms a Schottky barrier which creates a depletion or space charge region underneath the gate. The two most important parameters are the gate length and width. A reduction in the gate length will improve the gain, noise figure, and frequency of operation; typical millimeter-wave low-noise FETs have gate lengths of around $0.25 \mu\text{m}$. Increasing the gate width will increase the RF power capability; typical power FETs have multiple gate

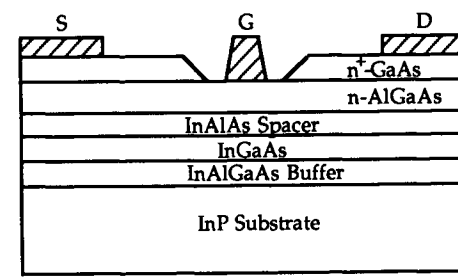
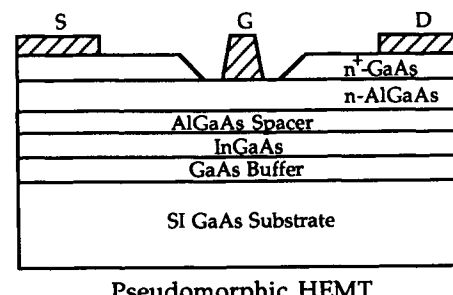
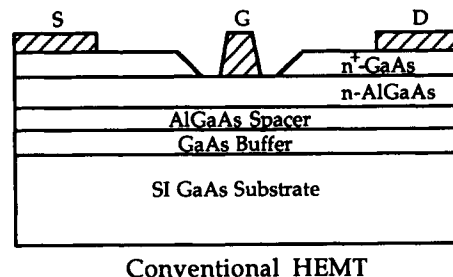
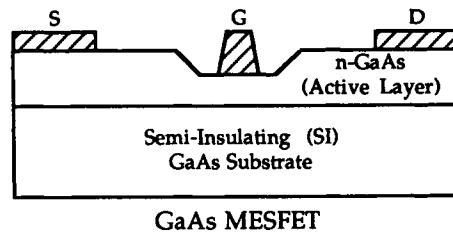


Figure 23. Cross-sectional channel structures of typical GaAs MESFETs and conventional, PM, and InP HEMTs.

fingers, interconnected via air bridges, with a total width of about 400–1000 μm .

The important parameters characterizing the microwave FET performance are f_T , the cutoff frequency or the frequency of unity current gain,

$$f_T \approx \frac{g_m}{2\pi C_{gs}} = \frac{v_s}{2\pi L},$$

f_{\max} , the maximum frequency of oscillation or the frequency at which the maximum available gain is 0 dB,

$$f_{\max} \approx \frac{f_T}{2\sqrt{r_1 + f_T \tau_3}}$$

$$r_1 = \frac{R_g + R_i + R_s}{R_{ds}} \quad \tau_3 = 2\pi R_g C_{dg},$$

G_{\max} , the maximum available gain at frequency f ,

$$G_{\max} = \left(\frac{f_T}{f} \right)^2 \left[\frac{4}{R_{ds}} (R_i + R_s + R_g + \pi f_T L_s) + 4\pi f_T C_{dg} (R_i + R_s + 2R_g + 2\pi f_T L_s) \right]^{-1},$$

G_u , the unilateral gain or the power gain with no reverse transmission,

$$G_u \approx (f_{\max}/f)^2,$$

F_{\min} , the minimum noise figure,

$$\begin{aligned} F_{\min} &= 1 + 2\pi K_f f C_{gs} \sqrt{\frac{R_g + R_s}{g_m}} \times 10^{-3} \\ &= 1 + K_f \frac{f}{f_T} \sqrt{g_m (R_g + R_s)} \\ &= 1 + K_1 L f \sqrt{g_m (R_g + R_s)}, \end{aligned}$$

and η_{add} , the power-added efficiency,

$$\eta_{\text{add}} = \frac{P_0 - P_{\text{in}}}{P_{\text{DC}}},$$

where v_s is the saturation velocity ($\approx 1.2 \times 10^7$ cm/s at 300°K for GaAs); L is the gate length; $K_f = 2.5$; $K_1 = 0.27$ when L is in micrometers; and P_0 , P_{in} , and P_{dc} are the RF output power, RF input power, and DC input power, respectively. Remaining parameters are defined in the device equivalent-circuit model (Figure 24). Other important parameters include the power output at the 1-dB compression point, its associated power gain, and the associated gain corresponding to F_{min} . Details of all important device characteristics can be found in References [7, 8, 43, 50, 51, 59].

Fabrication

Several techniques can be used to fabricate GaAs MESFETs and HEMTs such as the self-aligned, etched-channel, and ion-implantation techniques. Typically, processing consists of the following important steps.

1. Formation of an *n*-type GaAs epitaxial layer (active layer) and a buffer layer over the semi-insulating GaAs substrate.
2. Formation of the source and drain ohmic contacts by deposition and liftoff of an Ni/Au/Ge metal layer.
3. Formation of the Schottky-gate metal stripe by electron-beam (E-beam) lithography.
4. Deposition of silicon nitride as a protective layer.
5. Formation of gold-plated air bridge interconnects between device regions.
6. Thinning the wafer to the desired thickness.
7. Formation of the via holes for low-inductance source grounds.
8. Metallization of the wafer backside.

Detailed device processing is discussed in References [50, 57].

Operation

Microwave FET operation is generally based on the modulation of the channel or drain-source current, I_{ds} , by a longitudinal electric field resulting from applied gate-source (V_{gs}) and drain-source (V_{ds}) voltages. The widths of the depletion region and the conducting channel are controlled by V_{gs} at a fixed V_{ds} . A larger negative V_{gs} results in a wider depletion region, and hence a narrower channel, and decreases I_{ds} . There are three operation regions: the linear region, in which I_{ds} is small and proportional to V_{ds} ; the saturation region, in which I_{ds} remains constant with respect to V_{ds} ; and the breakdown region, in which I_{ds} increases rapidly with a slight increase of V_{ds} . The FET is turned off or pinched off at a value of V_{gs} corresponding to zero I_{ds} , which indicates that the depletion region is

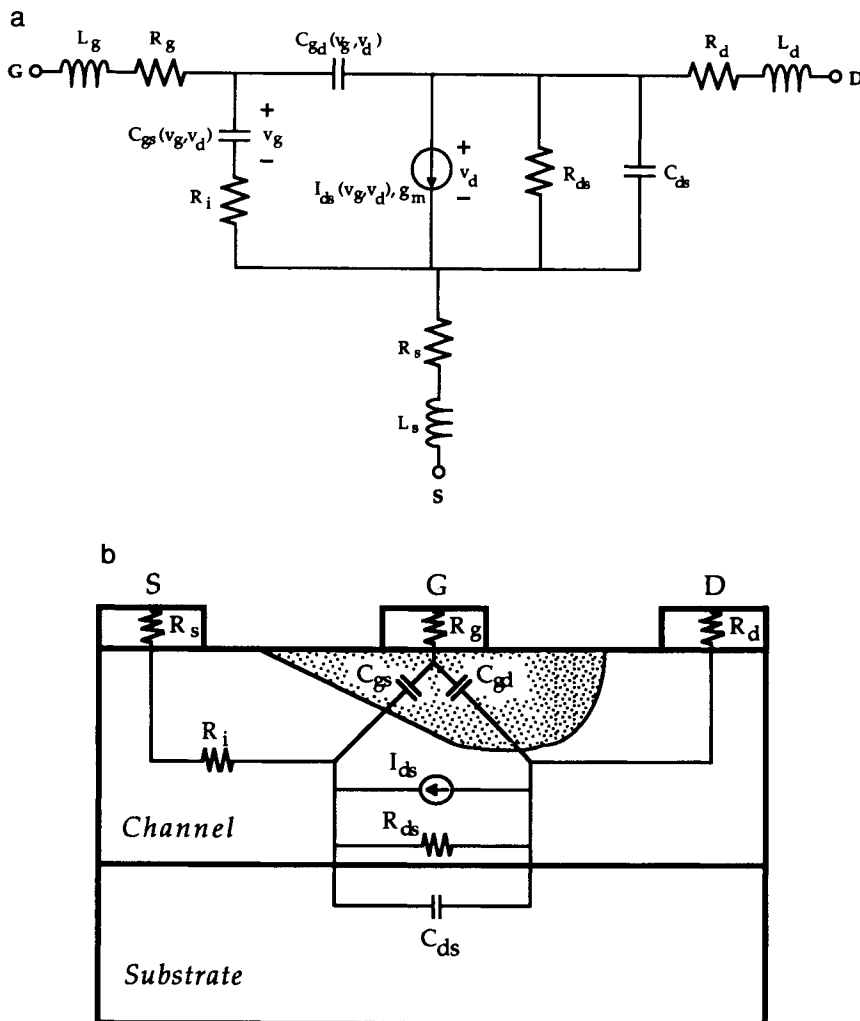


Figure 24. An equivalent-circuit model for microwave FETs (a) and its physical origin (b). g_m , transconductance; C_{gs} , C_{gd} , and C_{ds} , gate-source, gate-drain, and substrate capacitances; R_g , R_d , R_s , R_i , and R_{ds} , gate, drain, source, intrinsic channel, and output resistances; I_{ds} , drain-source current; L_g , L_d , and L_s , gate, drain, and source electrode inductances.

extended completely across the channel. I_{ds} is maximal when V_{gs} is zero at a fixed V_{ds} . For small-signal FETs, typical values for V_{gs} and V_{ds} are from -0.5 to -3 V and from 2 to 5 V, respectively, and for power FETs are from -2 to -5 V and from 5 to 10 V, respectively. Details of the

principles of operation of GaAs MESFETs and HEMTs can be found in References [7, 8, 43, 50, 51, 59] and [57, 58], respectively. The main difference between GaAs MESFET and HEMT operations is the electron flow. The electron transport in HEMTs, occurring in the two-dimensional electron gas (2DEG), resembles that of the undoped GaAs which has little ionized impurity scattering. The electrons thus travel at about twice the velocity ($\approx 2 \times 10^7$ cm/s) and mobility (≈ 8000 cm²/v-s) of those in GaAs MESFETs, resulting in superior RF performance. They can be employed for various circuit applications such as mixers, oscillators, amplifiers, phase shifters, switches, frequency multipliers, discriminators, and isolators.

Models

Microwave FET linear and nonlinear models are needed for circuit as well as device design purposes. Models can be derived from either measured data in the form of equivalent circuits [60–73] or device physics for GaAs MESFETs [74–77] and for HEMTs [78–89]. The latter involves extensive numerical computations and, although very useful for the device design, is of limited use for CAD of microwave circuits. The equivalent-circuit models (Figure 24), on the other hand, are very suitable for CAD. Approximated closed-form equations for its elements, based on the device physics, have been developed for GaAs MESFETs [50, 90]. The model parameters can also be evaluated by fitting measured DC and RF S-parameter data of the actual devices to those calculated from the equivalent-circuit models. Detailed descriptions of these models can be found in References [60–73]. The Curtice–Ettenberg nonlinear model [64] gives reasonably good results for power amplifiers and frequency multipliers. Mass' model [71] can accurately model the harmonic and intermodulation in the device transconductance, and hence the intermodulation of mixers and amplifiers, by fitting the modeled I/V characteristic and its derivatives to those measured.

References

- [1] T. Oxley, in *Microwave Solid-State Devices and Applications* (D. V. Morgan and M. J. Howes, eds.), pp. 222–247. New York: Peter Peregrinus, 1980.
- [2] T. Oxley, in *Variable Impedance Devices* (M. J. Howes and D. V. Morgan, eds.), pp. 155–251. New York: John Wiley & Sons, 1978.

- [3] J. Bahl and P. Bhartia, eds., *Microwave Solid-State Circuit Design*, pp. 420–473. New York, John Wiley and Sons, 1988.
- [4] C. A. Burrus, Jr., *IEEE Trans. Microwave Theory Tech.*, Vol. MTT-24, pp. 706–709, 1963.
- [5] J. H. Hinken, *Superconductor Electronics, Fundamentals and Microwave Applications*. New York: Springer-Verlag, 1989.
- [6] J. Chen *et al.*, *IEEE Int. Microwave Symp. Dig.*, pp. 367–368, 1982.
- [7] S. M. Sze, *Physics of Semiconductor Devices*, 2nd ed. New York: John Wiley and Sons, 1981.
- [8] S. Mass, *Microwave Mixers*. Pedham, MA: Artech House, 1986.
- [9] J. L. Heaton *et al.*, *Electron. Lett.*, Vol. 19, pp. 749–750, 1983.
- [10] M. J. Sisson, *Radio Electron. Eng.*, Vol. 52, pp. 534–542, 1982.
- [11] G. Gradinaru and A. N. Dorobantu, *Proc. Eur. Microwave Conf.*, pp. 657–661, 1980.
- [12] J. L. Heaton *et al.*, *Electron. Lett.*, Vol. 19, pp. 749–750, 1983.
- [13] K. Mills *et al.*, *Electron. Lett.*, Vol. 20, pp. 787–788, 1984.
- [14] P. A. Verlangieri *et al.*, *Int. J. Infrared Millimeter-Waves*, Vol. 6, pp. 1191–1202, 1985.
- [15] D. N. Held, “Analysis of Room Temperature Millimeter-Wave Mixers Using Gallium-Arsenide Schottky Barrier Diodes,” Ph.D. Thesis, Columbia Univ., New York.
- [16] J. L. Heaton, *Microwaves RF*, pp. 102–110, Sept. 1984.
- [17] G. E. Brehm *et al.*, *Proc. 8th Bienn. Cornell Electr. Eng. Conf.*, pp. 53–63, 1981.
- [18] J. C. Irvin *et al.*, in *Microwave Semiconductor Devices and Their Circuit Applications* (H. A. Watson, ed.), pp. 149–193. New York: McGraw-Hill, 1969.
- [19] J. W. Archer and R. A. Batchelor, in *Microwave Solid-State Components* (K. Chang, ed.), pp. 142–191. New York: John Wiley & Sons, 1990.
- [20] B. C. DeLoach, Jr., *IEEE Trans. Microwave Theory Tech.*, Vol. MTT-12, pp. 15–20, 1964.
- [21] P. Philippe *et al.*, *IEEE Trans. Microwave Theory Tech.*, Vol. MTT-26, pp. 250–255, 1988.
- [22] H. M. Olson, in *Microwave Semiconductor Devices and Their Circuit Applications* (H. A. Watson, ed.), pp. 27–339. New York: McGraw-Hill, 1969.
- [23] J. F. White, *Semiconductor Control*. Dedham, MA: Artech House, 1977.
- [24] J. F. White, in *Semiconductor Control Devices: PIN Diodes* (K. Chang, ed.), pp. 192–229. New York: John Wiley & Sons, 1990.
- [25] R. H. Caverly and G. Hiller, *IEEE Int. Microwave Symp. Dig.*, pp. 591–594, 1987.
- [26] C. Sun, in *Microwave Solid-State Components* (K. Chang, ed.), pp. 203–304. New York: John Wiley & Sons, 1990.
- [27] L. F. Eastman, in *Microwave Devices* (M. J. Howes and D. V. Morgan, eds.), pp. 11–39. New York: John Wiley & Sons, 1976.
- [28] J. Pattison, in *Microwave Solid-State Devices and Applications* (D. V. Morgan and M. J. Howes, eds.), pp. 14–18. New York: Peter Peregrinus, 1980.
- [29] A. Chu *et al.*, *IEEE Int. Microwave Millimeter-Wave Monolithic Circuits Symp. Dig.*, pp. 63–67, 1987.
- [30] K. Chang and H. J. Kuno, in *Microwave Solid-State Components* (K. Chang, ed.), pp. 305–391. New York: John Wiley & Sons, 1990.
- [31] B. C. De Loach, Jr., in *Microwave Semiconductor Devices and Their Circuit Applications* (H. A. Watson, ed.), pp. 464–496. New York: McGraw-Hill, 1969.
- [32] P. Brook, in *Microwave Solid-State Devices and Applications*. (D. V. Morgan and M. J. Howes, eds.), pp. 20–28. New York: Peter Peregrinus, 1980.
- [33] J. T. Coleman, *Microwave Devices*. Reston, VA: Reston Publishing Co., 1982.
- [34] J. F. Luy *et al.*, *Microwave Opt. Technol. Lett.*, Vol. 1, pp. 117–119, June 1988.

- [35] G. I. Haddad *et al.*, *IEEE Trans. Microwave Theory Tech.*, Vol. MTT-18, pp. 752–772, 1970.
- [36] L. E. Miller, in *Microwave Semiconductor Devices and Their Circuit Applications* (H. A. Watson, ed.), pp. 539–582. New York: McGraw-Hill, 1969.
- [37] J. S. Lamming, in *Microwave Devices: Device Circuit Interactions* (M. J. Howes and D. V. Morgan, eds.), pp. 117–207. New York: John Wiley & Sons, 1976.
- [38] J. S. Lamming, in *Microwave Solid-State Devices and Applications* (D. V. Morgan and M. J. Howes, eds.), pp. 30–40. New York: Peter Peregrinus, 1980.
- [39] M. E. Kim *et al.*, in *HEMTs and HBTs: Devices, Fabrication, and Circuits* (F. Ali and A. Gupta, eds.), pp. 253–369. Norwood, MA: Artech House, 1991.
- [40] Y. K. Chen *et al.*, *IEEE Electron Device Lett.*, Vol. EDL-10, pp. 267–269, 1989.
- [41] Y. K. Chen *et al.*, *IEEE Electron Device Lett.*, Vol. EDL-10, pp. 470–472, 1989.
- [42] B. Allen, TRW, private communication.
- [43] M. Shur, *GaAs Devices and Circuits*. New York: Plenum Press, 1987.
- [44] H. Ito *et al.*, *IEEE Electron Device Lett.*, Vol. EDL-5, pp. 214–216, 1984.
- [45] J. P. Bailbe *et al.*, *IEEE Trans. Electron Devices*, Vol. ED-27, pp. 1160–1164, 1980.
- [46] J. Berenz and B. Dunbridge, *Microwave J.*, pp. 115–131, Apr. 1988.
- [47] M. B. Das, in *HEMTs and HBTs: Devices, Fabrication, and Circuits* (F. Ali and A. Gupta, eds.), pp. 191–251. Norwood, MA: Artech House, 1991.
- [48] H. K. Gummel and H. C. Poon, *Bell Syst. Tech. J.*, Vol. 49, p. 827, 1970.
- [49] P. C. Grossman and A. K. Oki, *IEEE Bipolar Circuits Technol. Meet. Dig.*, pp. 258–261, 1989.
- [50] R. S. Pengelly, *Microwave Field-Effect Transistors—Theory, Design and Applications*, 2nd ed. Chichester: Research Studies Press, 1986.
- [51] C. A. Liechti, *IEEE Trans. Microwave Theory Tech.*, Vol. MTT-24, pp. 279–300, 1976.
- [52] P. M. Smith and A. W. Swanson, *Appl. Microwave*, pp. 63–72, May 1989.
- [53] P. M. Smith *et al.*, *Microwave J.*, pp. 71–86, May 1990.
- [54] P. M. Smith *et al.*, *IEEE Int. Microwave Symp. Dig.*, pp. 749–752, 1987.
- [55] J. J. Berenz, *IEEE MTT—S Newslet.*, pp. 43–52, Summer 1984.
- [56] U. K. Mishra *et al.*, *Device Res. Conf., Boston*, 1989.
- [57] P. C. Chao *et al.*, in *HEMTs and HBTs: Devices, Fabrication, and Circuits* (F. Ali and A. Gupta, eds.), pp. 77–190. Norwood, MA: Artech House, 1991.
- [58] M. B. Das in *HEMTs and HBTs: Devices, Fabrication, and Circuits* (F. Ali and A. Gupta, eds.), pp. 11–75. Norwood, MA: Artech House, 1991.
- [59] R. J. Hamilton, *Microwave Syst. News*, pp. 115–142, Oct. 1982.
- [60] W. R. Curtice and R. L. Camisa, *IEEE Trans. Microwave Theory Tech.*, Vol. MTT-32, pp. 1573–1578, 1984.
- [61] K. B. Kumar and V. M. Pandharipande, *IEEE Proc., Part H*, Vol. 135, pp. 171–179, 1988.
- [62] G. Dambrine *et al.*, *IEEE Trans. Microwave Theory Tech.*, Vol. MTT-36, pp. 1151–1159, 1988.
- [63] G. D. Vendelin and M. Omori, *Microwaves*, pp. 58–70, June 1975.
- [64] W. R. Curtice and M. Ettenberg, *IEEE Trans. Microwave Theory Tech.*, Vol. MTT-33, pp. 1383–1394, 1985.
- [65] W. R. Curtice, *IEEE Trans. Microwave Theory Tech.*, Vol. MTT-28, pp. 448–456, 1980.
- [66] S. E. Sussman-Fort *et al.*, *IEEE Trans. Microwave Theory Tech.*, Vol. MTT-32, pp. 471–473, 1984.
- [67] A. Materka and T. Kacprzak, *IEEE Trans. Microwave Theory Tech.*, Vol. MTT-33, pp. 129–135, 1985.

- [68] D. L. Peterson, A. M. Pavio, and B. Kim, *IEEE Trans. Microwave Theory Tech.*, Vol. MTT-32, pp. 276–281, 1984.
- [69] H. Statz *et al.*, *IEEE Trans. Electron Devices*, Vol. ED-34, pp. 160–169, 1987.
- [70] H. A. Willing, C. Rauschet, and P. De Santiz, *IEEE Trans. Microwave Theory Tech.*, Vol. MTT-26, pp. 1017–1023, 1978.
- [71] S. A. Maas and D. Neilson, *IEEE Int. Microwave Symp. Dig.*, pp. 1291–1294, 1990.
- [72] W. R. Curtice, *IEEE Trans. Microwave Theory Tech.*, Vol. MTT-36, pp. 220–230, 1988.
- [73] V. D. Hwang and T. Itoh, *IEEE Trans. Microwave Theory Tech.*, Vol. MTT-35, pp. 396–402, 1987.
- [74] K. Yamaguchi, S. Asai, and K. Kodera, *IEEE Trans. Electron Devices*, Vol. ED-23, pp. 1283–1290, 1976.
- [75] N. V. Song and T. Itoh, *Proc. Eur. Microwave Conf.*, pp. 245–250, 1985.
- [76] A. Madjar and F. J. Rosenbaum, *IEEE Trans. Microwave Theory Tech.*, Vol. MTT-29, pp. 781–788, 1981.
- [77] M. A. Khatibzadeh and R. J. Trew, *IEEE Trans. Microwave Theory Tech.*, Vol. MTT-36, pp. 231–238, 1988.
- [78] P. Roblin *et al.*, *IEEE Trans. Electron Devices*, Vol. ED-34, pp. 1919–1928, 1987.
- [79] M. Weiss and D. Pavlidis, *IEEE Trans. Microwave Theory Tech.*, Vol. MTT-36, pp. 239–249, 1988.
- [80] K. Park and K. D. Kwack, *IEEE Trans. Electron Devices*, Vol. ED-33, pp. 673–676, 1986.
- [81] Y. M. Kim and P. Roblin, *IEEE Trans. Electron Devices*, Vol. ED-33, pp. 1644–1651, 1986.
- [82] T. J. Drummond *et al.*, *IEEE Electron Device Lett.*, Vol. EDL-3, pp. 338–341, 1982.
- [83] K. Park *et al.*, *IEEE Trans. Electron Devices*, Vol. ED-34, pp. 2422–2427, 1987.
- [84] M. L. Majewski, *IEEE Trans. Electron Devices*, Vol. ED-34, pp. 1902–1910, 1987.
- [85] H. Hilda *et al.*, *IEEE Trans. Electron Devices*, Vol. ED-33, pp. 1580–1586, 1986.
- [86] M. H. Weiler and Y. Ayasli, *IEEE Trans. Electron Devices*, Vol. ED-31, pp. 1854–1861, 1984.
- [87] A. Cappy *et al.*, *IEEE GaAs Integr. Circuit Symp. Dig.*, pp. 79–82, 1982.
- [88] H. R. Yeager and R. W. Dutton, *IEEE Trans. Electron Devices*, Vol. ED-33, pp. 682–692, 1986.
- [89] H. Hida *et al.*, *IEEE Electron Device Lett.*, Vol. EDL-7, pp. 393–395, 1986.
- [90] H. Fukui, *Bell Syst. Tech. J.*, Vol. 58, pp. 771–797, 1979.

This Page Intentionally Left Blank

Transferred Electron Devices

S. J. Jerome Teng

I. Introduction

Transferred-electron diodes, or Gunn diodes as they are more popularly called, are not truly diodes because a “diode” is usually defined as a device having an asymmetrical current-voltage characteristic. Since Gunn diodes possess a current-voltage characteristic similar to that of resistors, the terms “transferred-electron device” or “Gunn device” are more formerly used.

Gunn diode oscillators have proved a reliable microwave and millimeter-wave solid-state frequency source. The GaAs Gunn diodes have been used extensively in microwave and millimeter-wave systems from 3 to 120 GHz. They are used in a wide range of commercial and military applications such as intruder alarms, local oscillators, low-power radar transmitters, and frequency sweepers. Gunn diodes are preferred for applications such as local oscillators in low-noise receiver front ends due to their low AM/FM noise properties. They also can be used, in addition to broadband oscillator applications, as amplifiers with more than an octave bandwidth. Although the construction of Gunn oscillator circuits could be deceptively simple, a good understanding of them and a sound device technology are two important factors in achieving successful device applications.

In this chapter we review and discuss the Gunn device mechanism, fabrication technology, and applications. In Section 2, an overview of negative differential mobility and device modeling is presented. Gunn device design and its fabrication are described in Section 3. In Section 4, we review and discuss the construction of various forms of Gunn oscillators and circuits. Gunn amplifiers and noise characteristics are presented in sections 5 and 6, respectively. Power combining techniques of Gunn devices are described in Section 7.

Historical Background

In 1963 J. B. Gunn reported the discovery of microwave current oscillations which were produced when an electric field of a few thousand volts per centimeter was applied to a piece of an n -GaAs semiconductor [1]. He indicated that the period of oscillation was inversely proportional to the specimen length and approximately equal to the transit time of electrons between the electrodes. This discovery was later proved, unknown to Gunn at the time, as a successful culmination of some 10 years of worldwide speculation on the possibility of obtaining negative differential bulk conductivity in semiconductors. Gunn's subsequent demonstration of the spatial variation of the electric field within the semiconductor using probe measurements showed that each current oscillation was accompanied by a high-electric-field region which propagated from the cathode to the anode [2, 3].

Shockley [4] in 1954 first indicated the potential importance of two-terminal semiconductor devices having negative resistance at frequencies properly related to the transit time of carriers through them. He pointed out that such negative resistances may be combined with other components to form amplifiers that operate at high frequencies. Some time before the observation of the Gunn effect in GaAs, Ridley and Watkins [5] and Hilsum [6] had independently predicted that a negative differential resistivity could result from the progressive transfer of hot electrons from a high-mobility valley in the conduction band to a low-mobility valley at higher energy. In particular III-V compounds such as GaAs, InP, and InSb were considered to have the necessary band structure for exhibiting the transferred electron effect. Ridley [7] subsequently, a few months after Gunn's discovery, reported that a high-field domain would develop and propagate through the sample when the sample was biased in the negative-resistance region. Kroemer [8] later pointed out that the electron transfer mechanism and the emergence of high- and low-field regions account for the Gunn effect. The theory was finally confirmed by a crucial experiment carried out by Hutson *et al.* [9] By applying hydrostatic

pressure to a sample of GaAs, they lowered the energy of the low-mobility valley relative to the high-mobility valley and found that the threshold field for the Gunn effect decreased and the Gunn effect disappeared totally at very high pressures.

2. Device Physics

Negative Differential Mobility (NDM)

The negative differential mobility effect has been observed in various compound semiconductor materials such as n -GaAs, n -InP [1], n -InAs [10], GaAsP [11], n -CdTe [12, 13], ZnSe [14], and InSb [15]. Most of these materials are III-V compounds. This effect is due to the multivalley conduction band structure of these semiconductors. Figure 1 shows a simplified energy band diagram of GaAs and InP with crystal directions, energy values, and effective masses. In both GaAs and InP the lowest electron energies occur at $k = 0$; thus they are called direct-gap semiconductors. It is typical for many direct-gap semiconductors that this effective mass of the central valley is considerably lower than the free-electron mass. Despite the strong electron scattering in the semiconductor, these electrons are therefore more readily accelerated than free-space electrons, which leads to high electron mobilities.

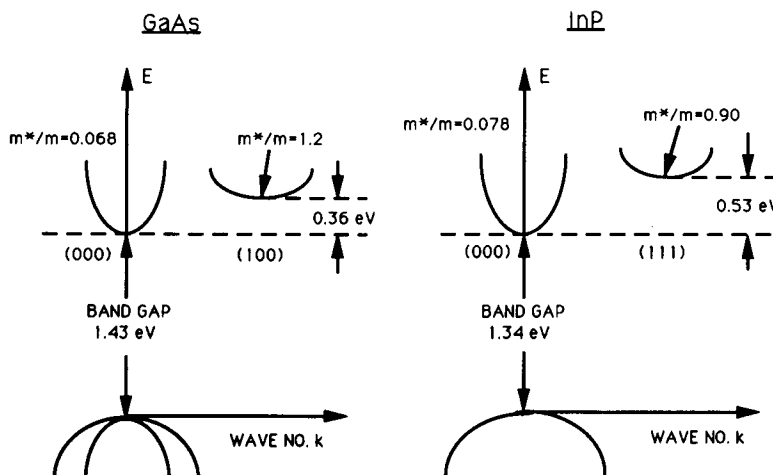


Figure 1. Simplified energy band diagrams of GaAs and InP.

In GaAs, at room temperature, electrons in the lower (000) valley have an effective mass $m^* \approx 0.068m_e$ and mobility $\mu_L \approx 8000 \text{ cm}^2/\text{V-s}$, whereas electrons in the upper, or satellite (100), valleys have $m^* \approx 1.2m_e$ and $\mu_L \approx 180 \text{ cm}^2/\text{V-s}$. The effective masses in the upper valley are much larger. The energy difference ΔE between the two valleys is about 0.36 eV. The relative populations of the two valleys are determined by the energy difference ΔE and the lattice temperature T_o . In GaAs the energy difference $\Delta E = 0.36 \text{ eV}$ is much larger than the thermal energy kT ($\approx 0.026 \text{ eV}$) at room temperature. At zero electric field most electrons are in the low-energy, low-effective-mass states near the lower valley of the conduction band.

As the voltage across a bulk of n -GaAs is increased, the electrons are accelerated by the electric field and their kinetic energy increases. When the energy gained by the electrons is comparable to ΔE , the rate of electron transfer into the upper low-mobility valley increases. As the electric field is raised to threshold of 3.2 kV/cm in GaAs, and 10.5 kV/cm in InP, the average electron velocity starts to saturate [16]. In GaAs the maximum drift velocity is about $2.2 \times 10^7 \text{ cm/s}$ at $E \approx 3.2 \text{ kV/cm}$. Further increase in the electric field results in more electrons in the low-mobility state. This electron drift velocity decrease with increasing electric field leads to a negative differential mobility.

For a semiconductor to exhibit NDM, the energy difference between the upper and the lower valleys must be smaller than the semiconductor bandgap so that avalanche breakdown does not occur before the transfer of electrons into the upper valleys. For example, NDM was observed in InAs only under hydrostatic pressure [10]. In InAs under normal pressures, the low-mobility valleys in the (111) directions are about 1 eV higher in energy than the (000) valley. The direct energy gap is 0.35 eV. NDM is not normally observed because impact ionization occurs before the transfer to the (111) valleys can take place. When pressure is applied to InAs, the lower-upper valley separation decreases while the direct energy gap increases. At high enough pressures NDM is observed.

Velocity-Field Characteristics

The characteristics of drift velocity versus electric field in GaAs, or other NDM material, is of primary importance to the study of microwave oscillations observed in the material. The electron distribution function in GaAs changes as the applied field makes the electrons more energetic. Diffusion and field effects force the electrons away from its unperturbed equilibrium state, whereas the scattering effects due to collisions with lattice and impurities tend to restore this equilibrium. The Boltzmann

transport equation sums up these three processes. Calculation of the velocity-field characteristics $\nu(E)$ of GaAs requires solving the Boltzmann transport equation. Several calculated $\nu(E)$ characteristics of GaAs have been reported [17, 18].

A direct measurement of the velocity-field characteristics in high-conductivity material is difficult because the sample normally oscillates when the average field rises above the threshold. To measure the $\nu(E)$ curve directly, it is necessary to do the experiment in such a short time that the field remains relatively uniform. Gunn and Elliott [19] first reported the measured $\nu(E)$ curve of a GaAs sample 110 μm long, 10 Ω/cm , with a Hall mobility of $8000 \text{ cm}^2/\text{V-s}$, using a voltage pulse of 250 ps duration. Their measured threshold field was 3.8 kV/cm with a peak velocity about $1.8 \times 10^7 \text{ cm/s}$. Their measured negative differential mobility beyond threshold was $300 \text{ cm}^2/\text{V-s}$.

The $\nu(E)$ curve can also be measured by a time-of-flight experiment in which electrons are injected into the sample. Chang and Moll [20] were able to measure the $\nu(E)$ curve of GaAs directly by studying the response of a reverse-biased Schottky-barrier GaAs photodetector to a step input of light. Electrons were injected into the semi-insulating ($10^8 \Omega/\text{cm}$) GaAs through a thin ($\approx 150 \text{ \AA}$) gold film by means of the pulsed laser beam. Then the injected electrons were swept from the cathode to the anode of the GaAs sample by an applied field. A measured threshold field of 2.2 kV/cm was reported by Chang and Moll [20].

This time-of-flight technique was also exploited by Ruch and Kino [21] using pulsed (0.1 ns) high-energy electrons and a gold film of 1000 \AA . They used a 300- μm -long, high-resistivity (10^6 – $10^8 \Omega/\text{cm}$) GaAs sample. Their measured low-field mobility was $7500 \text{ cm}^2/\text{V-s}$, with an initial negative differential mobility of $2400 \text{ cm}^2/\text{V-s}$ at a threshold field of 3.2 kV/cm. The experimental results of Ruch and Kino are in good agreement with the theory of Butcher and Fawcett [17]. The $\nu(E)$ curve of GaAs measured by Fay and Kino [22] using a space-charge wave measurement also agrees well with that of Ruch and Kino. Temperature effects on GaAs transport properties have also been studied [23]. The measured velocity-field relationship of GaAs can be approximated by the following analytical expression [24].

$$\nu(E) = \frac{\mu_o E + \nu_\infty \left(\frac{E}{E_a} \right)^4}{1 + \left(\frac{E}{E_a} \right)^4}, \quad (1)$$

where the low-field mobility $\mu_o = 8000 \text{ cm}^2/\text{V-s}$, the asymptotic velocity

($E = \infty$) $\nu_\infty = 8.5 \times 10^6$ cm/s, and $E_a = 4$ kV/cm. Equation (1) yields a peak velocity of $\nu_p = 2.08 \times 10^7$ cm/s at $E_p = 3.46$ kV/cm. The $\nu(E, T)$ relationship may be empirically expressed as the following which includes a practical temperature range from 300 to 600 K.

$$\nu(E, T) = \frac{2.3 \times 10^9 E + \frac{2.4 \times 10^9 \left(\frac{E}{E_a}\right)^4}{1 - 5.3 \times 10^{-4} T}}{\left[1 + \left(\frac{E}{E_a}\right)^4\right] T}, \quad (2)$$

where $E_a = 4$ kV/cm. Equation (2) can be used in computer simulation of practical Gunn device operation.

Electron Dynamics of NDM

The properties of the propagating space charge instability largely determine the behavior of transferred electron oscillators and amplifiers. The circuit surrounding the device also influences the device behavior. Although the instabilities caused by the electron transfer are well known, the properties of the instabilities cannot be determined by simple means [25]. In a uniformly doped n -type semiconductor of positive differential mobility, a local perturbation of the majority-carrier concentration causes the space-charge inhomogeneity Q to decay exponentially. From Maxwell's equations, the decay can be characterized by the dielectric relaxation time τ_r as

$$Q(t) = Q(0) \cdot e^{-t/\tau_r}, \quad (3)$$

where

$$\tau_r = \frac{\epsilon}{\sigma} = \frac{\epsilon}{qn_o\mu}$$

and

$$\mu = \frac{d\nu}{dE}.$$

n_o is the doping concentration and μ is the differential mobility. τ_r is the time constant for the decay of the excess space-charge $Q(0)$ to neutrality. For GaAs with $n = 10^{15}$ cm⁻³ and at 300 K, τ_r is about 10^{-12} s which is a very short time interval. If the differential mobility μ is negative, then τ_r is

negative and the space-charge inhomogeneity in Equation (3) will grow as a function of time instead of decaying.

In a semiconductor of length L , having an external voltage bias, the transit time t_o for a space-charge layer traveling through the semiconductor is $t_o = L/v_o$. v_o is the average, or saturated, drift velocity which is about 10^7 cm/s in GaAs. If the relationship of Equation (3) that the space-charge layer grows during the entire transit time remains true, the maximum growth factor in Equation (3) can be expressed as $\exp[L/v_o\tau_r]$. For a significant space-charge growth, this growth factor must be larger than unity and the transit time must be larger than the negative dielectric relaxation time. Then we have

$$n_o L > \frac{\epsilon v}{q|\mu|}. \quad (4)$$

For n -type GaAs, the $\epsilon v/q|\mu|$ value is on the order of 10^{12} cm $^{-2}$. Thus $n_o L \geq 10^{12}$ cm $^{-2}$ is an approximated criterion under which a space-charge layer can grow and propagate through a GaAs sample of length L . Dipole domains may be formed during the transit of the space charges due to electric field nonuniformity. It is due to these periodically sweeping space charges, synchronized with a resonant circuit, that microwave signals are generated or amplified. The relationship of Equation (4) ($nL \geq 10^{12}$ cm $^{-2}$) was found to be empirically true in GaAs diodes designed for use in various frequency bands.

The Gunn diode is known as a nonlinear and wide-band device. The device-circuit parameters include the diode doping profile, cathode contact, bias voltage, temperature effect, thermal resistance, resonant cavity, and output coupling. All these factors play a part in diode operation. Some of these factors are interdependent. Thus it is not an easy task to use a computer model to acquire a clear-cut picture in terms of the field-charge distribution of a Gunn diode in operation. However, device modeling helps to illustrate the behavior and relationship of the electric field and charge inside an NDM element and thus facilitate the understanding of device operation [26, 27].

3. Device Design and Fabrication

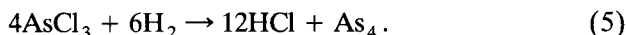
Material Growth

The active region of Gunn devices is usually prepared by epitaxial growth techniques. It is because epitaxial grown layers have the purity, homogeneity, and a positive temperature coefficient of resistivity that are desirable

for the transferred-electron device operation. The epitaxial layers are grown on bulk-grown polished highly-doped ($n > 10^{18} \text{ cm}^{-3}$) GaAs or InP substrates for fabricating discrete devices. Semi-insulating GaAs substrates are used to fabricate planar or integrated Gunn devices. Two early established methods of growing GaAs epitaxial layers are the Vapor Phase Epitaxy (VPE) [28–30] and the Liquid Phase Epitaxy (LPE) [31, 32]. In the VPE growth, two standard methods are the arsenic trichloride (AsCl_3) [28, 33] system and the arsine (AsH_3) system [29, 34].

Vapor Phase Epitaxy

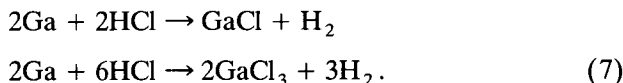
The AsCl_3 VPE system can grow high-purity GaAs material because high-purity AsCl_3 and gallium (Ga) are commercially available. In this system, palladium-diffused hydrogen carries the AsCl_3 into the Ga source region of a two-zone reactor. The dissociated AsCl_3 is then used as the arsenic source. It is also used to transport Ga to the GaAs growth region. Good quality polycrystalline GaAs which can replace Ga as a source material is now commercially available. The initial reaction taking place when the gas mixture heats up is



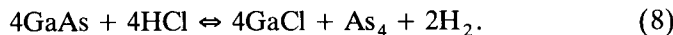
After adding AsCl_3 into the reactor, arsenic is continuously dissolving into the liquid Ga source,



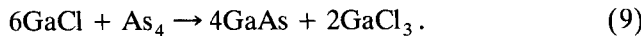
while Ga is simultaneously removed by reaction with HCl to form volatile gallium chlorides (GaCl and GaCl_3) according to



When the Ga source becomes saturated, a GaAs crust is formed over the Ga source. The system is now ready for epitaxial growth. In the growth process, the polycrystalline GaAs in the source region reacts with HCl around 840°C and the following reaction takes place:



At a lower temperature (e.g., 750°C), in the GaAs substrate region, solid GaAs is deposited partly by the inverse reaction of Equation (8) and partly by the reaction



Since hydrogen is used as a carrier gas, the reaction of Equation (8) will be

dominant. When the carrier gas is an inert gas (e.g., argon), the dominant reaction will be Equation (9). The uniformity of GaAs epitaxial layers using the VPE system depends on the growth temperature, AsCl_3 mole fraction, gas flow dynamics, and reactor design. The thickness variation of grown layers can be as low as 3 to 6% across a 3-in. GaAs wafer.

In the arsine (AsH_3) VPE system, a three-zone furnace reactor is required. Purified hydrogen gas carries the HCl into the Ga source region, whereas the AsH_3 bypasses the Ga source and enters the high-temperature middle zone for dissociation. Thus no saturation of the Ga source with As is necessary. Another advantage of this system is that various doping impurities in gaseous form can be easily and swiftly introduced into the growth region. Both AsCl_3 and AsH_3 VPE systems can produce high-quality GaAs with background dopings of $n = 10^{14}$ to 10^{15} cm^{-3} for microwave devices [30, 35, 36].

The epitaxial growth of InP using the $\text{PCl}_3\text{-H}_2$ VPE system has been shown to be a reliable technique to grow device-quality InP [37, 38]. The structure of this InP VPE system is almost identical to that of the GaAs AsCl_3 VPE system except for the sources and reactor temperatures. Efforts of using this InP VPE technique have been concentrated mostly on fabricating millimeter-wave Gunn oscillators and amplifiers [39, 40]. The InP wafer is more fragile and thus more difficult to handle than the GaAs wafer. Lattice-mismatched epitaxial growth has become a field of research and application. Epitaxial growth of good-quality InP on GaAs using this InP VPE system, despite the 4% lattice mismatch, was demonstrated by Teng [41, 42].

Liquid Phase Epitaxy

The GaAs LPE technique was first reported by Nelson [31] to show its advantage over VPE in achieving high-doped epitaxial films and high-quality $p\text{-}n$ junctions intended for tunnel and laser diode applications. This process was then refined to grow high-purity GaAs layers capable of producing microwave oscillators. The LPE technique has the advantage of growing thicker layers in shorter times. For Gunn devices, VPE is preferred over LPE because VPE's doping profile and layer thickness can be better controlled. It is also easier to grow multiple VPE wafers in each run which is suitable for volume production.

Molecular Beam Epitaxy (MBE)

MBE is a new epitaxy technology which has been established. Among many of its applications, MBE is capable of growing device-quality GaAs for transferred electron device applications [43]. MBE achieves the growth by using elemental source evaporation in an ultra-high vacuum chamber

with a pressure of 10^{-10} T. The wafer holder rotates during growth to ensure epitaxial layer uniformity. MBE can grow sophisticated epitaxial layers or heterojunctions as thin as the semiconductor lattice size. However, the inherent slow growth rate of MBE makes it impractical for producing microwave Gunn devices which require active layer thicknesses of 4 to 20 μm . In addition, the MBE setup is more expensive than that of VPE.

Metal–Organic Chemical Vapor Deposition (MOCVD)

MOCVD is another relatively new epitaxy technology. Sometimes, it is referred to MOVPE because MOCVD also uses the vapor phase. The MOCVD method has been shown to be a promising replacement for the VPE [44, 45]. MOCVD has a growth rate similar to that of VPE, but the MOCVD's capability of growing multiple wafers has increased. With a reactor design having both the susceptor and wafers rotated during growth, MOCVD can achieve an epitaxial layer uniformity on 3-in. GaAs wafers comparable to that of MBE. This makes MOCVD an attractive method for volume production of Gunn device wafers.

Device Design

Design Guidelines

The basic device structure of a Gunn diode can be characterized by an active layer length, L , a free carrier concentration, n , and a diode cross-sectional area. Figure 2 shows a typical Gunn diode doping profile in which three n -type epitaxial layers were grown on a highly conducting n^+ substrate. There is no p -type Gunn diode because the NDM effect exists only for electrons. The n^+ cap epitaxial layer is used to facilitate the fabrication of a stable ohmic contact. The ohmic metal contacts can also be fabricated directly on the n -type active layer. Diodes made with low-contact and substrate resistances are preferred because series resistance degrades directly the diode DC-to-RF conversion efficiency.

The diode active layer length corresponds to the electron transit-time frequency of the device. The first design consideration of the Gunn diode is the active layer length versus the operating frequency. The electron transit speed in the active region may vary under different operating conditions and diode properties. Gunn diodes are also known to have an extremely wide operating frequency [46]. An optimum active layer length exists for a given diode application. Figure 3 shows a design guideline of active layer length versus operating frequency for GaAs Gunn diodes. As frequency increases, the active layer length decreases and the doping

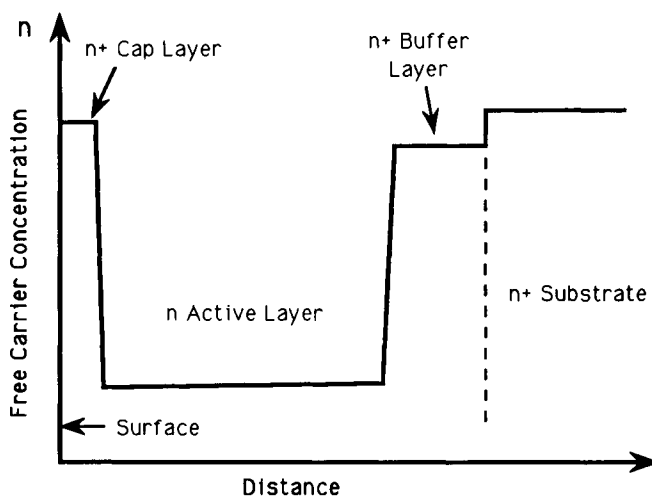


Figure 2. A Gunn diode doping profile.

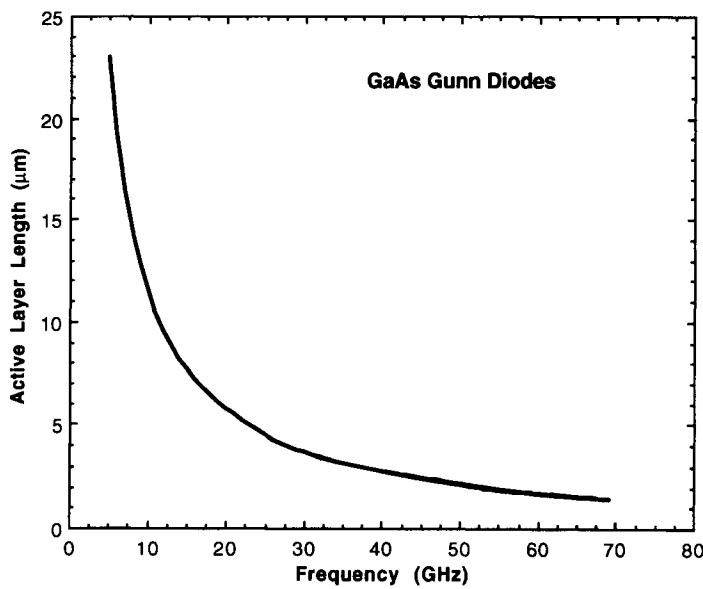


Figure 3. A design guideline of active layer length versus operating frequency for GaAs Gunn diodes.

concentration increases. The active layer length determines the diode threshold voltage. The diode DC operating voltage is about three to five times the diode threshold voltage. The peak-power voltage is usually considered the optimum operating voltage. The same diode operating at different frequencies will have different optimum operating voltages. It is better, in terms of reliability, for a low-frequency diode to operate in a high-frequency cavity than the reverse. The CW operation of InP Gunn diodes is preferred, if not limited, in the millimeter-wave frequency range (> 30 GHz) due to device thermal constraints. The InP Gunn device requires a higher operating voltage than the GaAs Gunn device. For example, typical operating voltages of GaAs and InP Gunn diodes at the Ka band are 6 and 12 V, respectively.

Cathode Contact

In Gunn diode operation, accumulated excess electrons are formed and injected into the active region at the cathode contact. Changes in electron dynamics at the cathode affect the nature of the electron supply. Thus the characteristics of the cathode contact can significantly influence the diode's operation. For example, Gunn diodes made with a metal to n -type ohmic contact are usually more efficient than those made with metal to n^+ sandwiched contact. The first commercial GaAs Gunn diodes in the United States had this metal to n -type contact. On the other hand, the regrown n^+ epitaxial contact is a more reproducible cathode contact. It has the advantage of making diodes suitable for wide-band tuning. Another example is that Gunn diodes made with current-limited cathode contacts are often less inclined to oscillate in an RF cavity. The distinctive features of a current-limited contact is its nondrop-back I-V characteristics and that the threshold voltage is not clearly shown. Gunn diodes, made of GaAs or InP, having a current-limited contact, are inherently suitable for Gunn amplifier applications. Such contacts can be fabricated using the metal to n -type contact but often the fabrication process, such as metalization and alloying, is an art form. The metal to n -type contact can be made equally stable and reliable compared with the regrown n^+ contact.

Optimum barrier heights at the cathode contact for high-efficiency microwave TED devices have been calculated by Hariu and Shibata [47]. They predicted that the optimum barrier height in the thermionic emission mode was about 0.3 to 0.4 eV. The cathode contact plays an especially important role in InP Gunn diode operation. It has been shown that both the power and the efficiency of InP Gunn diodes can be increased by using a current-limiting cathode contact instead of the conventional ohmic

contact [48, 49]. Cathode contacts can be modified using epitaxial grown layers. For example, a two-zone cathode comprising a thin n^+ layer and a high-resistance contact layer has been shown to improve the efficiency of InP Gunn diodes [50]. The current-limited cathode contacts can also be achieved using epitaxial thin n^- or p^- layers or using a graded gap GaAs/AlGaAs heterostructure [51]. One of the drawbacks of current-limited contacts is their reproducibility.

Not only does the cathode contact change the Gunn diode's electrical characteristics, but it also affects the diode's thermal property. Thermal resistance contributed from cathode contact layers (e.g., the n^+ cap layer or the n^- notch layer) may degrade diode performance due to a higher operating temperature in the active region. In general, a good diode design keeps the cathode contact region as thin and abrupt as possible.

Temperature Effect

Gunn diodes operate at power densities as high as 200 kW/cm^3 , especially at higher frequencies at which the diode doping level is increased and the active layer thickness and diode area become smaller. This results in an excessive amount of heat generated in a small area. The generated heat degrades the diode's NDM property. It reduces the diode's optimum operating voltage and the DC-to-RF conversion efficiency. In order for diodes to operate efficiently and reliably, it is important to remove the heat from the diode. This requires that the active region of the diode be in intimate contact with a good thermal conductor such as copper.

The capacity to dissipate heat is usually measured by thermal resistance. Following an example given by Knight [52], for a flip-chip diode of radius a and active layer thickness L directly in contact with a semi-infinite heat sink, the maximum device temperature is determined by

$$T_{\max} = \left(T_{\infty} + \frac{QLa}{K_{st}} \right) \exp \left[QL \left(\frac{L}{2K_1} + \frac{\delta}{K_2} \right) \right], \quad (10)$$

where T_{\max} is the maximum device temperature (K), T_{∞} is the ambient temperature (K), Q is the diode power density (W/cm^3), δ is the thickness of the n^+ contact layer, K_{st} is the thermal conductivity of the heat sink, and K_1 and K_2 are the thermal conductivities of the n and n^+ layers, respectively. Gold-plated copper is frequently used as heat sink for the Gunn diode package. For copper, $K_{st} = 3.88 \text{ W/cm}\cdot\text{K}$. For n -GaAs, $K_1 \approx 150/T_{\max}$ and $K_2 \approx 120/T_{\max}$. QL is the heat flux passing through the area πa^2 . In such a flip-chip device, the maximum temperature occurs

at the interface between the active layer and the n^+ substrate. The power density Q is inversely proportional to the active layer's resistivity. Thus high-frequency diodes would have a higher power density. It is shown in Equation (10) that the maximum device temperature is exponentially proportional to the square of active layer thickness L . This indicates that the active layer thickness and the heat flow paths in GaAs should be made as small as possible. In practical devices, voids between the heat sink and the GaAs ohmic contact will substantially increase the device operating temperature. Poor diode thermal resistance can be detected using a curve tracer when a thermal loop appears on the I-V characteristics. To improve the diode performance and reliability, it is necessary to obtain good thermal bonds and thus to minimize the diode thermal resistance. Gunn cavity blocks are often made with OFHC copper or brass to assist in the heat sink. Aluminum blocks can be used for height-weight requirement.

The pulsed operation of Gunn diodes has a higher DC-to-RF conversion efficiency than that of the CW. This is largely due to temperature effects on the material. The peak-to-valley velocity ratio of GaAs is a strong function of temperature, and it degrades with increasing temperature. The DC-to-RF conversion efficiency remains high if the amount of charge accumulation traveling through the active region is high which in turn depends on the material's peak-to-valley velocity ratio and the carrier concentration. Gunn diodes in pulse operation also have higher operating voltages than those in CW operation.

Doping Profile Slope

In a flip-chip Gunn device in which the heat sink is usually on the cathode side, a thermal gradient across the device is formed due to the thermal resistance of the active layer. The thermal gradient has the effect of reducing the accumulation in the active layer region. This nonuniform accumulation results in the degradation of efficiency, output power, and bandwidth. To optimize the diode performance, the doping profile can be sloped from the cathode to the anode to compensate for the thermal gradient. Such a sloped profile has a lower doping level near the cathode. This doping slope also results in a higher electric field near the cathode which is desirable in diode operation.

Likewise, the diode doping slope can be reversed to achieve the same beneficial effects provided the diode bias polarity is also reversed [53]. Depending on the operating frequency and other operating requirements, the optimum combination of doping profile slope and active layer length is often empirically determined. The beneficial effect of the sloped doping

profile is usually more noticeable in millimeter-wave frequency diodes. A comparison between the uniform and the graded doping concentration profiles of Gunn diodes has been performed by Batchelor [54].

Device Fabrication

The Gunn diode structure usually comes in three forms: (a) flip-chip, (b) integral-heat-sink (IHS), and (c) low-power structures. The cross-sectional views of these three device structures are shown in Figure 4. Their fabrication processes are described in the following section.

Device Processing

The substrates used to fabricate GaAs or InP Gunn diodes are mostly $\langle 100 \rangle$ oriented. Such wafers can be easily cleaved along the two perpendicular $\langle 110 \rangle$ directions. The diode fabrication basically consists of two ohmic contact metalizations. The AuGe/Ni/Au-alloyed ohmic contact is the contact mostly used [55, 56]. First, the wafer's active layer side is metallized with ohmic metals. Mesa-etched structures are frequently used on the active layer side. Then the substrate side is lapped and polished to a desired thickness. The thickness is normally 50 to 100 μm depending on the diode's mechanical and thermal requirements. The alloyed ohmic contacts are then electroplated with gold. The extra gold facilitates the diode packaging in chip and wire bonding. Wafers are then separated into discrete diode chips. The above processing description is mainly for the flip-chip and the low-power devices. Table 1 lists the comparison in terms of device processing and application among the flip-chip, IHS, and low-power diode structures.

Flip-Chip Device

Commercial GaAs Gunn diodes are mostly fabricated using the flip-chip technique. The diode chip thickness ranges from 50 to 100 μm depending on chip size. The size of high-frequency diodes is smaller and thus thinner. The chip size of a Q-band GaAs diode, for example, can be as small as $150 \times 150 \times 50 \mu\text{m}$. In flip-chip diode packaging, the chip is thermocompressionally bonded into a diode package so that the active layer is in close contact with the heat sink. The diode is then wire bonded and sealed with a metal cap. The low thermal resistance reduces the diode operating temperature which in turn allows a higher operating current and a higher output power. The flip-chip device, applicable to all frequency bands for GaAs diodes, is a cost-effective manufacturing method, as described in Table 1. High-performance fundamental-mode V-band to

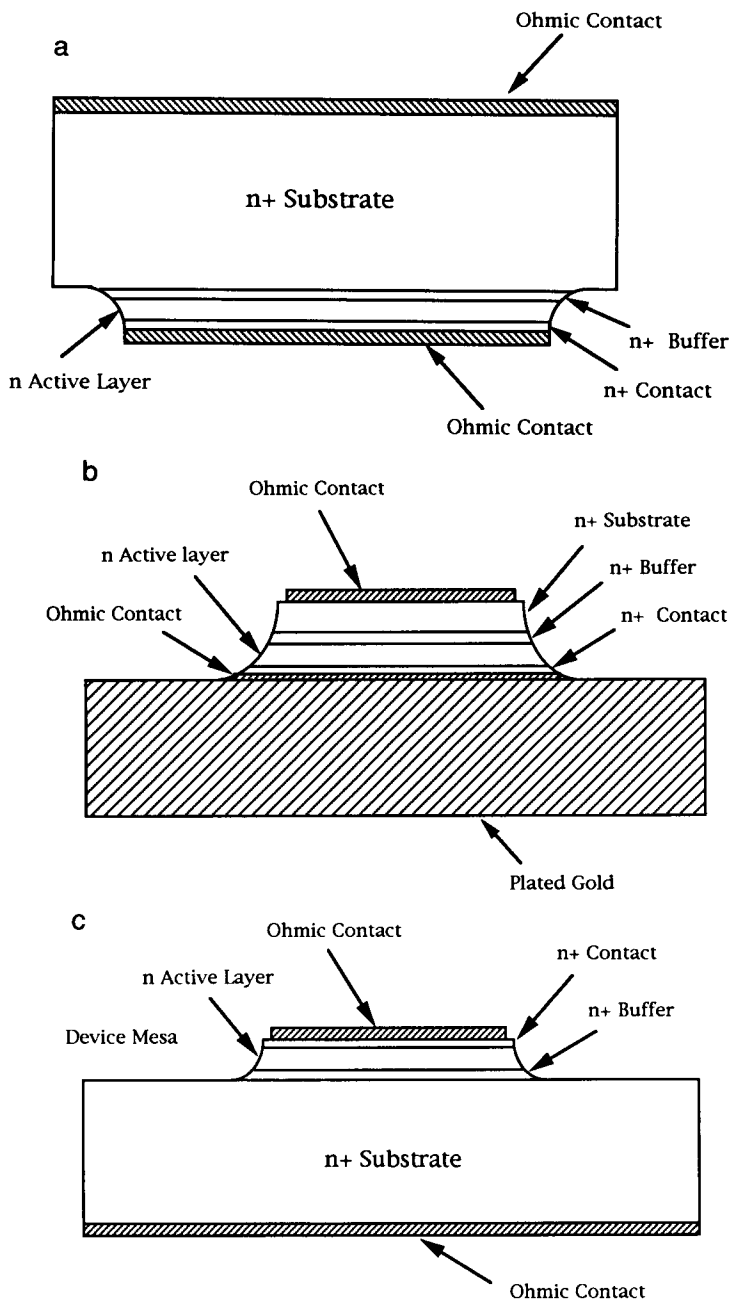


Figure 4. Cross-sectional views of (a) flip-chip, (b) integral-heat-sink, and (c) low-power device structures.

TABLE I
Comparison of Gunn Diode Device Structures

Comparison	Flip-chip device	Integral-heat-sink device	Low-power device
1. Substrate material	GaAs	GaAs or InP	GaAs
2. Frequency band	C- to W-band	Ka- to W-band	C- to K-band
3. Fabrication steps	Fewer	More	Fewer
4. Chip separation	Scribe and Break	Chemical etch	Scribe and break
5. Chips per unit area	High	Low	Medium to high
6. Die attach	Thermal compression	Solder perform	Thermal compression
7. Thermal resistance	Low	Low	High
8. DC-to-RF efficiency	Fair to good	Good	Poor
9. Diode current etch	Extensive	Less	Less
10. Process/packaging cost	Medium	High	Low

second-harmonic W-band GaAs Gunn diodes can be achieved using the flip-chip technique [57].

Integral-Heat-Sink (IHS) Device

The fabrication process of the IHS device structure is more laborious and uses more wafer area than that of the flip-chip device. The IHS fabrication process uses mechanical lapping and chemical thinning techniques to achieve an extremely thin substrate thickness ($\approx 5\text{--}20 \mu\text{m}$) so that the diodes are thus separated and the parasitic resistance is minimized. This substantially reduced substrate thickness, compared with that of the flip-chip device, is an important advantage of the IHS device. A thick-plated gold ($\approx 25\text{--}50 \mu\text{m}$) is used as a diode mechanical support and an immediate heat sink. Instead of using thermocompression die bonding, the IHS diodes are usually soldered into a diode package. The diode is then wire bonded and the ceramic ring is sealed with a metal cap. Having avoided the die bonding, the chance of mechanical damage to the device is greatly reduced. Because InP material is more fragile and damage prone than GaAs material, InP Gunn diodes are mostly, if not exclusively, fabricated using the IHS device structure. GaAs Gunn diodes can also be made with the IHS structure to improve performance, but usually in the millimeter-wave frequency range.

Low-Power Device

The low-power device structure is similar to that of the flip-chip. The difference lies in the size of the mesa area. The low-power device has such

a small predetermined diode area that little or no etch is required after the wire bonding. This is feasible because the low-power device is mounted with the substrate side in contact with the diode package. The heat generated in the diode-active region has to dissipate through the thick GaAs substrate. This results in a high thermal resistance and it degrades the diode performance. The diode's safe operating current level is thus substantially reduced. Diodes for low-power applications can be produced in this epitaxy-side-up configuration. This configuration also prefers the diode heat sink to be biased as an anode for improved thermal dissipation inside the diode.

The low-power device structure is suitable for automated volume production. The diode mounting and wire bonding can be accomplished using an automated machine equipped with TV cameras. Such diodes are mostly used for low-cost, low-power commercial applications, such as door openers, intrusion alarms, and radar/motion detectors. Having performed quality assurances in visual/dimensional inspection and DC/RF screening, GaAs Gunn diodes thus produced can exhibit a mean time between failures (MTBF) of $> 10^6$ hr. Figure 5 shows a schematic diagram of a microwave motion detector module in which a transceiver is built using a Gunn oscillator [58].

Device Package

Two typical Gunn diode packages are shown in Figure 6. Diode packages are mostly made with a copper base having gold-plated surfaces. Diode packages with threaded heat sinks provide the lowest thermal resistance. Low thermal resistance can also be achieved by soldering the

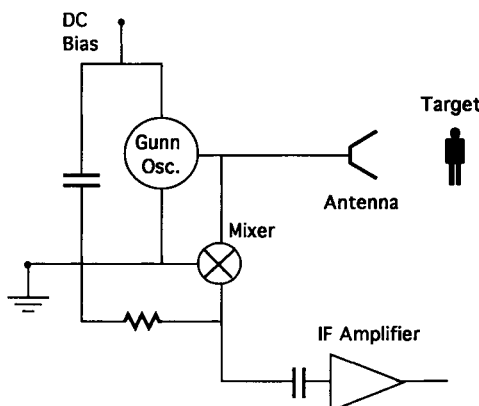


Figure 5. A microwave motion detector module.

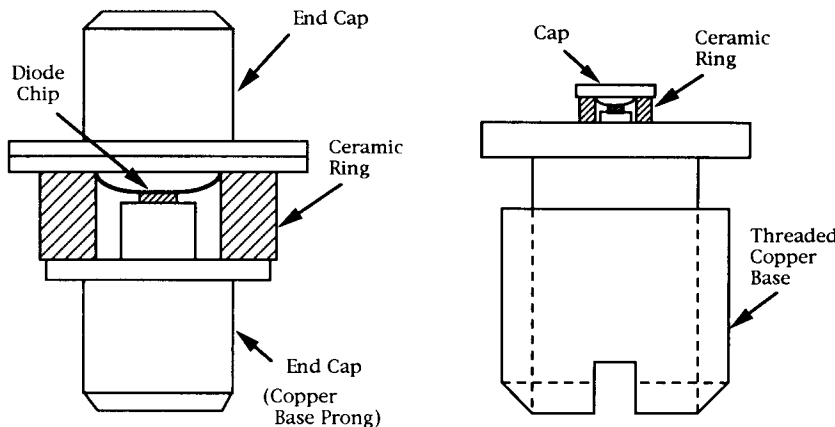


Figure 6. Gunn diode packages.

diode package into another heat sink. Diode reliability depends strongly on the packaging process which includes die mounting, etching, and wire/ribbon bonding. Unlike the Si IMPATT diodes, GaAs Gunn diodes packaged with an embedded diamond heat sink showed no clear advantage in terms of performance versus cost. For low-power microwave applications, a package with a pin-shaped heat sink, as shown in Figure 6, is adequate for the heat sink and easy to assemble. The ceramic ring is usually made with alumina which offers good mechanical strength compared with that of quartz ring. Quartz has a lower dielectric constant than alumina. To lessen diode parasitics such as shunt capacitance, the ceramic ring size is reduced in high-frequency diodes. For example, the ceramic ring sizes of a Q- or V-band diode package are 30 mil in diameter and 20 mil in height. An analysis of microwave equivalent-circuit parameters of Gunn diode packages was reported by Owens and Cawsey [59].

4. Gunn Oscillator and Circuits

Mechanically Tuned Gunn Oscillator

A Gunn diode oscillator comprises a resonant cavity, a Gunn diode inside or near the cavity, a bias circuitry, and an output coupling. Figure 7 shows the basic construction of a commonly used mechanically tuned Gunn oscillator. The oscillator body includes a resonator cavity, a feed-through post for the diode bias, a frequency tuner, and an output coupling tuner.

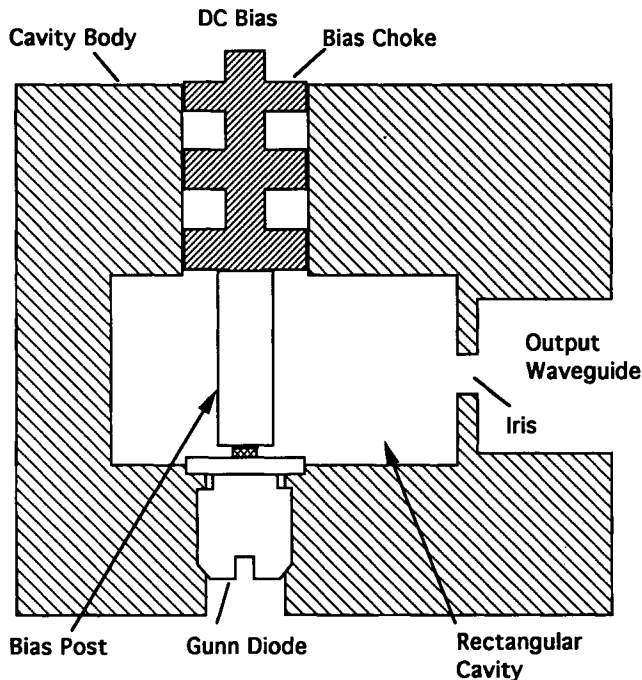


Figure 7. A mechanically tuned rectangular-cavity Gunn oscillator.

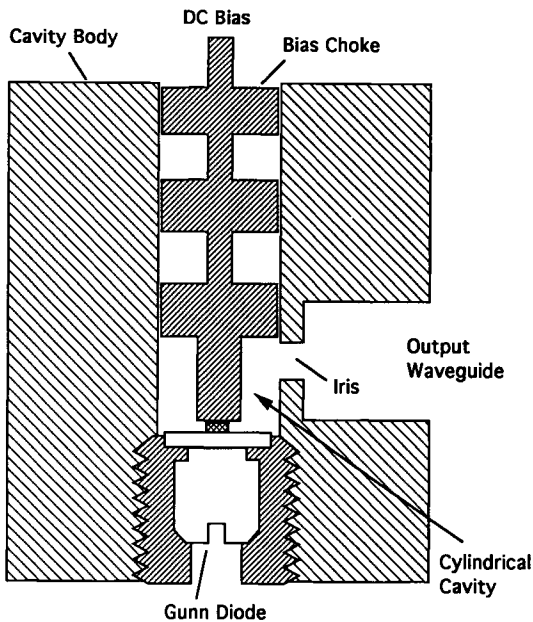


Figure 8. A coaxial-cavity Gunn oscillator.

The frequency and coupling tuners are usually made with a low-loss dielectric material such as sapphire. The output coupling tuner adjusts the output power level. The oscillator frequency can be fine-tuned by adjusting an inserted tuner screw. The tuning range is determined by the tuner location in the cavity. Too much insertion of the tuner screw lowers the cavity's Q value. The frequency tuning using such a tuner screw is usually smooth but in a minor range. There are numerous other ways to construct a mechanically tuned oscillator. Wider tuning ranges, for example, can be achieved by adjusting the length of the resonator [60]. As reported by Tsai and Rosenbaum [61], an RC circuit is generally used in Gunn bias to eliminate the undesired bias circuit oscillation. A Gunn oscillator may have more than one output port. A dual-output Gunn oscillator, for example, generates two separate outputs having the same frequency. This saves the use of a directional coupler, otherwise required.

The unloaded and loaded Q factors of a resonant cavity are expressed as

$$Q_o = \frac{2\pi \text{ (energy stored in the cavity)}}{\text{ (energy dissipated in the cavity per cycle)}} \quad (11)$$

$$Q_L = \frac{2\pi \text{ (energy stored in the cavity)}}{\text{ (energy dissipated in both the cavity and the external circuit per cycle)}}. \quad (12)$$

Gunn oscillator cavities having a high loaded Q result in a better frequency stability but a lower output power. On the other hand, cavities with a low Q value may achieve a higher output power but worse noise properties. The particular choice of a resonant cavity depends on the application requirement. For example, transmission-line resonators, such as a microstrip cavity, become lossy and have relative low Q values at frequencies above 3 GHz. It is thus preferable to use enclosed cavities for Gunn frequency sources. Several commonly used Gunn oscillator cavities are described in this section.

Coaxial Cavity

A coaxial cavity is built like a cylindrical cavity having a center conductor. Gunn diodes are usually mounted at the base of the center conductor. Figure 8 shows the cross-sectional view of a typical coaxial cavity. Coaxial cavities have a relatively low Q value and are widely used in most frequency bands. The oscillator frequency can be fine-tuned by

inserting a dielectric rod into the cavity. A coaxial cavity may have a wider tuning range by varying the length of the cavity using a sliding dielectric or metal washer.

In a coaxial cavity which has a half-wavelength cavity length, unloaded Q can be expressed as

$$Q_o = \frac{\lambda_o}{\delta \left[4 + \frac{2L_1 \left(1 + \frac{b}{a} \right)}{b \ln \left(\frac{b}{a} \right)} \right]}, \quad (13)$$

where a and b are the diameters of inner and outer conductors, respectively, δ is the skin depth, λ_o is the free-space wavelength, and L_1 is the cavity length ($L = \lambda_o/2$). The Q value of Equation (13) reaches a maximum when $b/a = 3.6$ and then

$$Q_{o(\max)} = \frac{\lambda_0}{\delta \left(4 + \frac{7.2L_1}{b} \right)}. \quad (14)$$

Given $b/a = 3.6$, the lowest cutoff wavelength of the TE_{11} mode is given by

$$\lambda_c = 1.43(a + b). \quad (15)$$

Rectangular Cavity

The rectangular cavity is also often used for Gunn oscillators. Given an enclosed rectangular resonant cavity, the free-space resonant frequency λ_o can be expressed as

$$\lambda_o = \frac{2}{\sqrt{\left(\frac{l}{a} \right)^2 + \left(\frac{m}{b} \right)^2 + \left(\frac{n}{c} \right)^2}}, \quad (16)$$

where a , b , and c are the width, height, and length of the cavity, respectively, and l , m , and n are the TE_{lmn} -mode subscripts related to the half-sinusoid number in the standing-wave pattern along the x , y , and z axes, respectively. For example, the resonator frequency of a copper cavity having $a = b = c = 3$ cm is about 7 GHz. The mode lattice for square rectangular resonators (i.e., $b = c$) can be found in Reference [62]. Rectangular cavities in general have a much higher impedance and Q value. The high impedance prevents a strong coupling between the low-impedance Gunn diode and the cavity. Its tuning range is thus not as wide as the coaxial cavity.

In practical applications, a rectangular cavity is often designed in the configuration as shown in Figure 9. The cavity may be considered a section of waveguide terminated with a short circuit at a distance of multiple $\lambda_o/2$. The output waveguide couples to the rectangular cavity through an inductive iris. The diode is mounted on a bias post near the short-circuit back wall and about $\lambda_o/2$ from the iris. The resonator usually operates in the TE_{101} mode. The oscillator frequency can be tuned by adjusting an inserted dielectric or metal rod. The tuning range increases as the tuning rod diameter increases. A bias post having a larger diameter improves the oscillator's turn-on performance but reduces the cavity Q value.

A rectangular high- Q Gunn cavity has a limited tuning bandwidth. The cavity tuning bandwidth can be increased by using a reduced-height waveguide cavity, as shown in Figure 10. This cavity has no coupling iris. It is thus easier to build and modify. Step transformers are used to match the impedance of the diode and the output waveguide. The movable back short is mainly used for the output power coupling. Such a cavity is especially suitable for constructing wide-band Gunn amplifiers. Likewise, a

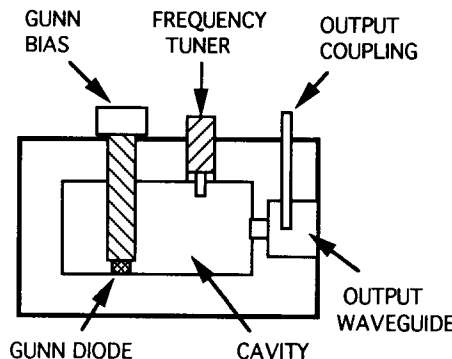


Figure 9. A mechanically tuned rectangular-cavity Gunn oscillator.

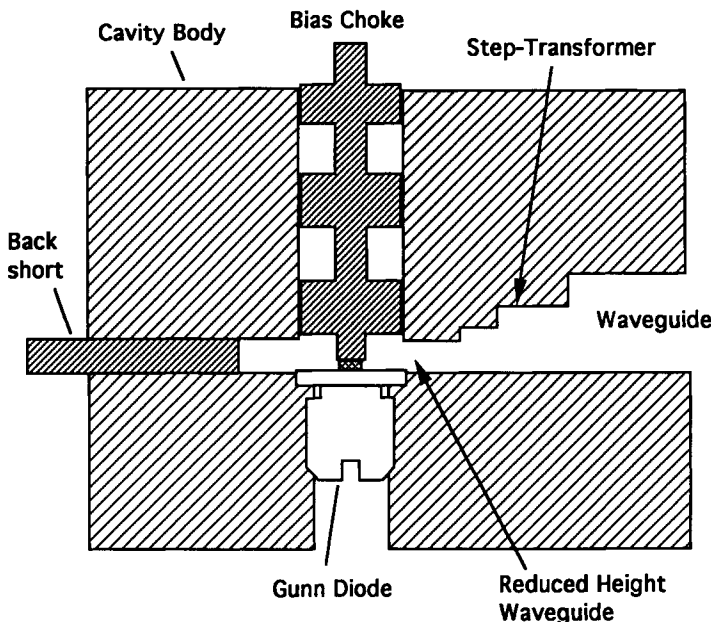


Figure 10. A reduced-height waveguide cavity.

ridged-waveguide cavity also has a wide-band tuning capability. A ridged-waveguide-cavity Gunn oscillator having a wide-band tuning from 8 to 18 GHz was reported by Mizushina and Ohsuka [63].

Microstrip Cavity

Microstrip resonator cavities have a lower Q value than most enclosed cavities. Gunn oscillators made with microstrip cavities are thus noisier and less stable. But they are easier to build and more compatible with the widely used microwave integrated circuits (MIC) [64]. They are manufactured on substrates such as ferrite, alumina, quartz, or sapphire that have a high dielectric constant and low loss. Because tuning screws are not readily available, mechanical tunings can be achieved using abrasive jets or a laser to adjust the conductor size. Electrical tunings are usually done with a varactor or the Gunn bias voltage. Figure 11 shows a microstrip Gunn resonator cavity. The low-pass bias filter is designed with $\lambda/4$ stubs. Output power coupling can be accomplished in various ways. One often-used method is through magnetic field coupling, in which an output

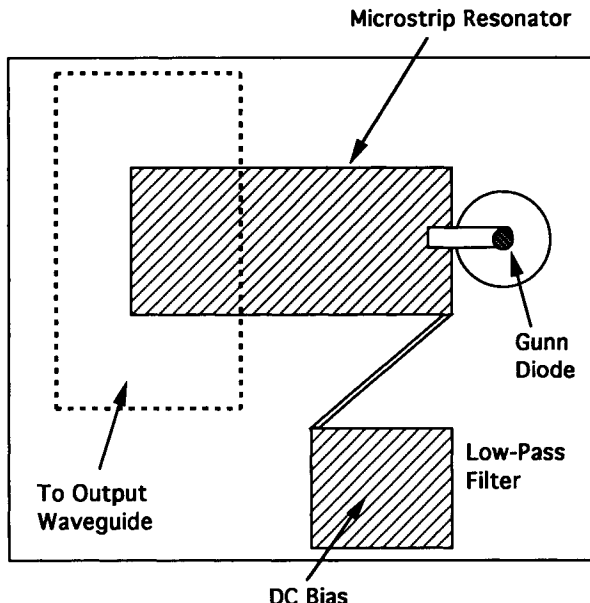


Figure 11. A microstrip Gunn resonator cavity.

microstrip line is placed parallel to the cavity. In Figure 11, the microstrip cavity also acts like an antenna; the RF power is coupled out to the end of a waveguide. Other than $\lambda/4$ length resonators, microstrip cavities can be designed in other configurations such as the resonant-cap cavity as shown in Figure 12. A high Q dielectric resonator can be used together with the microstrip cavity for frequency stabilization [65].

Temperature Compensation

The output frequency of Gunn oscillators is sensitive to temperature change. The frequency drift is due to the changes in cavity dimensions and diode characteristics. In high- Q cavities such as the waveguide cavity with Q s on the order of several hundred units, the frequency drift contributed from the diode is small. In microstrip or coaxial cavities, the change of diode characteristics contributes more to the frequency drift. Depending on applications, temperature compensation schemes sometimes are required to build the oscillator. One commonly used scheme is to construct the oscillator cavity body with two different metals which have different temperature expansion coefficients. The objective is to keep the cavity

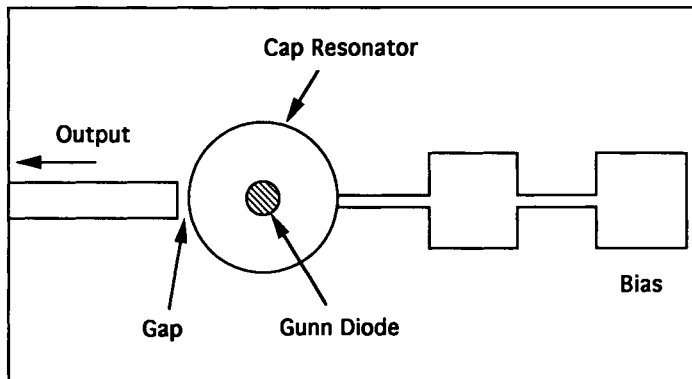


Figure 12. A microstrip Gunn resonant-cap cavity.

resonance frequency independent of temperature. Another technique is to use a dielectric tuning rod which has a negative temperature coefficient of the dielectric constant. This compensates for the cavity expansion. The dielectric tuning rod can also be mounted on a support material such as nylon which withdraws the tuning rod away from the cavity as temperature increases.

The above-mentioned techniques are designed to compensate for frequency drifts due to ambient temperature change. A heater-controlled Gunn cavity is another simple but effective technique to stabilize the frequency against temperature change. Figure 13 shows the schematic of a heater-controlled Gunn oscillator. A temperature-controlled heater keeps the temperature of the Gunn cavity constant (e.g., at 55°C). The oscillator output frequency is then stabilized in any ambient temperature below 55°C. Another advantage of the heater is that the Gunn diode will not have a cold turn-on problem.

Harmonic Operation

Gunn sources are often used in millimeter-wave applications. Experimental results have shown that the operating frequency of GaAs Gunn diodes in the fundamental mode exceeded 80 GHz. The oscillator output power decreases rapidly as the operating frequency goes up. Second-harmonic mode operation is commonly used for frequencies higher than about 70 GHz for GaAs Gunn diodes. Figure 14 shows the CW output power capability versus frequency of single GaAs Gunn diodes. The output power and the diode's DC-to-RF conversion efficiency are in a

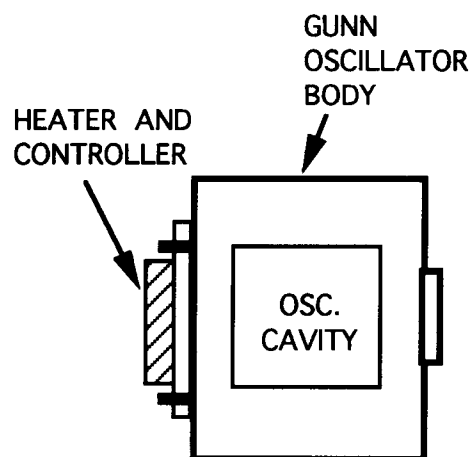


Figure 13. A heater-controlled Gunn oscillator.

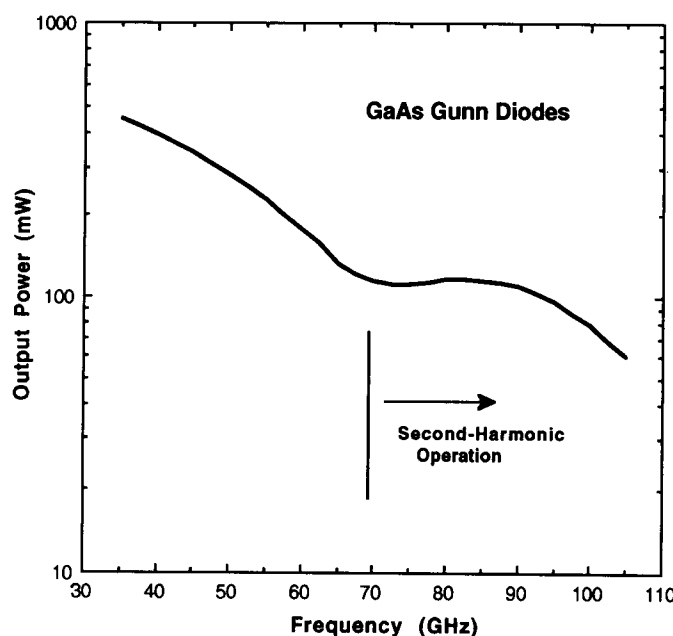


Figure 14. Output power versus frequency of GaAs Gunn diodes.

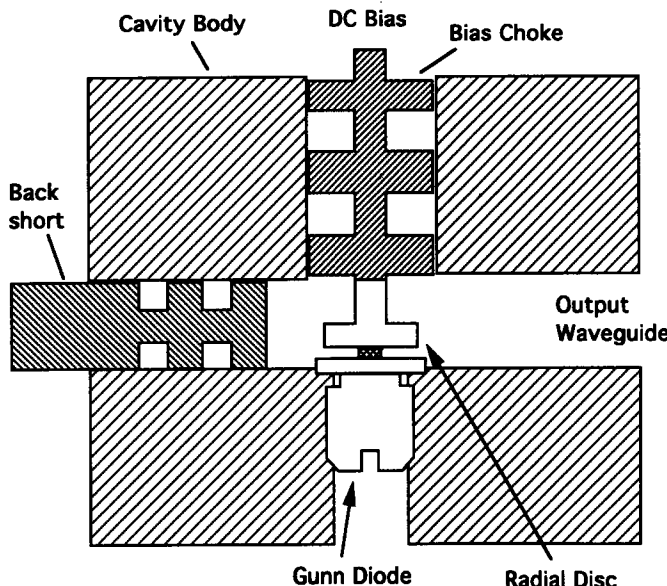


Figure 15. A disc or radial-line cap resonator.

trade-off relationship. Diodes having a reduced current achieve a higher DC-to-RF conversion efficiency at the expense of the output power. As shown in Figure 14, the output power from the second-harmonic mode of GaAs diodes is actually higher than that of the fundamental mode beyond a frequency of about 70 GHz. This is because the constraint in diode structure and cavity design increases as the frequency increases.

Second-harmonic operation offers a practical and viable alternative in manufacturing W-band (75–110 GHz) GaAs Gunn oscillators [57, 66, 67]. Figure 15 shows a cavity having a disc, or radial-line cap, resonator which is routinely used for second-harmonic Gunn operation. In Figure 15, the output waveguide acts as a high-pass filter that allows only the second-harmonic frequency to be extracted. The same principle similarly applies to oscillators using the third-harmonic operation. A ceramic tuning rod near the resonator can be used for frequency adjustment. The movable back short adjusts the coupling of the output power. Output powers of 96 and 48 mW at 94 and 103 GHz with a DC-to-RF conversion efficiency of 2.7 and 2.3%, respectively, have been achieved using Q-band GaAs Gunn diodes in second-harmonic operation [57].

The harmonic operation is also useful to InP Gunn sources [68]. Second-harmonic operation is often used for InP diodes in W-band frequencies. However, the operating voltage of InP Gunn diodes at a given frequency is typically twice as high as that of the GaAs diodes. This built-in characteristic of a high threshold field, and thus a high operating voltage, poses a reliability issue for the InP diodes. To ensure a reliable operation, the operating current levels of InP diodes are usually made between $\frac{1}{5}$ and $\frac{1}{3}$ of that of GaAs diodes. Current-limited cathode contacts, instead of plain ohmic contacts, are also required for the InP diodes to achieve an efficient low-current operation [48, 49]. Otherwise, low current would mean a reduced diode area and a smaller output power.

Frequency Multiplier

In the frequency range from about 100 to 160 GHz, a frequency multiplier can be used to multiply the frequency from a lower frequency Gunn source. Figure 16 shows the circuit diagram of a Gunn-driven frequency multiplier source. No DC bias is required for the passive multiplier device. Frequency tuning can be achieved using a mechanical tuning screw in the Gunn cavity. The multiplication factor is typically 2 or 3. For example, a 130-GHz multiplier source can be built using a Gunn oscillator having an output frequency of either 65 or 43.3 GHz. The output powers of such multiplier sources are high enough to drive an LO circuit for most applications.

Electronically Tuned Gunn Oscillator

Varactor Tuned

A Gunn oscillator can be tuned electronically over a wide frequency range by using a varactor diode mounted inside the resonator [69]. Varactors are rather simple and inexpensive semiconductor devices and have high modulation rates. Often varactor-tuned oscillators are called voltage-controlled oscillators (VCO). Gunn VCOs are widely used for either

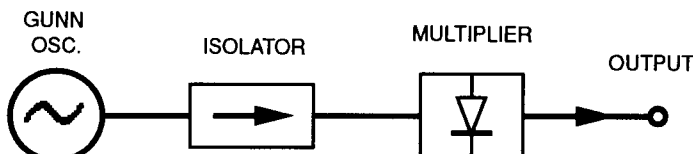


Figure 16. A Gunn-driven frequency multiplier source.

single- or swept-frequency sources. The electronic tuning range depends on the location of the varactor inside the resonator, the capacitance, and device parasitics [70]. There are typically two tuning configurations of varactor-tuned Gunn VCOs: (1) series tuned and (2) parallel tuned. An analytical circuit evaluation for the series and parallel tuning of VCOs was reported by Cawsey [71]. Figure 17 and Figure 18 show the cross-sectional views of series- and parallel-tuned Gunn VCOs either in a coaxial or in a rectangular cavity. The designs of the VCO cavities are similar to those of mechanically tuned Gunn oscillators except for the addition of the varactor. The frequency tuning range is directly proportional to the amount of RF power coupled to the varactor, but inversely to the loaded Q of the cavity. A series-tuned Gunn VCO has more power coupled to the varactor and thus a wider tuning range than those of the parallel-tuned Gunn VCO. The oscillator frequency usually increases as the varactor reverse-biased voltage increases. This is considered a positive frequency tuning.

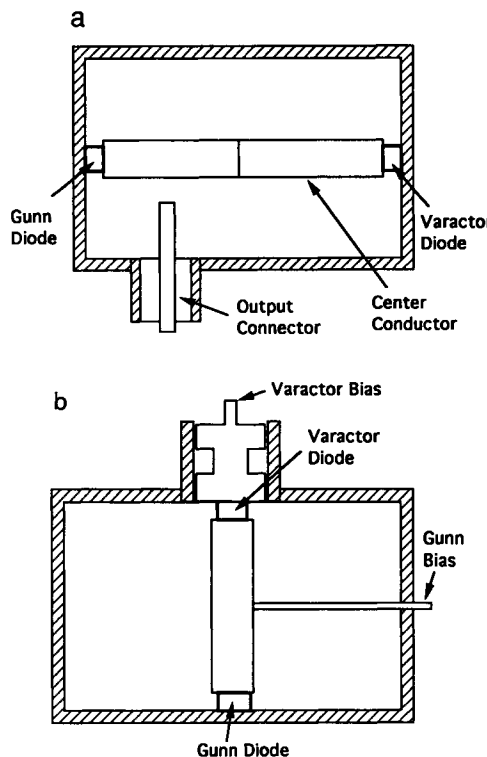


Figure 17. Series-tuned Gunn VCOs: (a) coaxial cavity and (b) rectangular cavity.

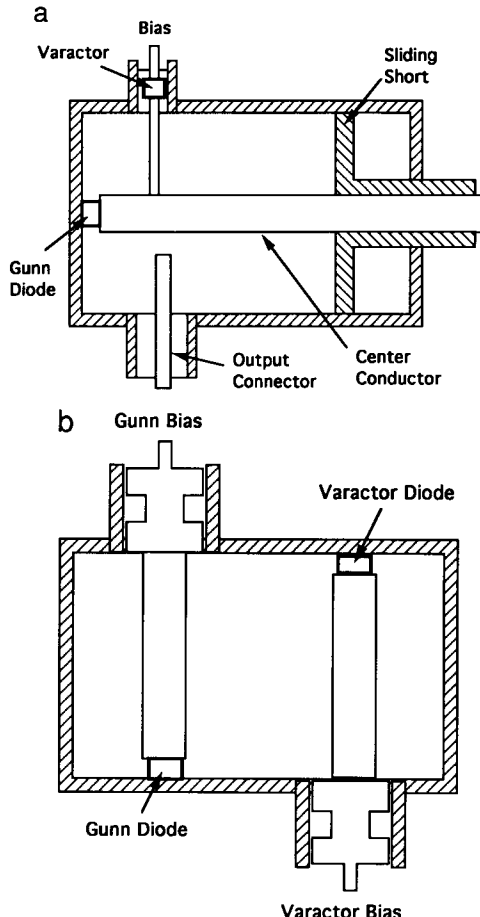


Figure 18. Parallel-tuned Gunn VCOs: (a) coaxial cavity and (b) rectangular cavity.

In millimeter-wave frequency VCOs, the diode capacitance and the package size of the varactor are designed to be smaller. Figure 19 shows a commonly used coaxial-cavity Gunn VCO in which the varactor diode is in series and direct contact with the Gunn diode. In this case, a hyperabrupt-junction GaAs varactor diode is usually soldered into the Gunn bias choke. The output power is coupled through an iris to the waveguide port. Figure 20 shows an example of output power and frequency versus varactor bias voltage of a series-tuned Ka-band Gunn VCO. A tuning bandwidth of 1 GHz at a center frequency of 35 GHz was shown in this VCO. A temperature-controlled heater of 55°C was attached to the

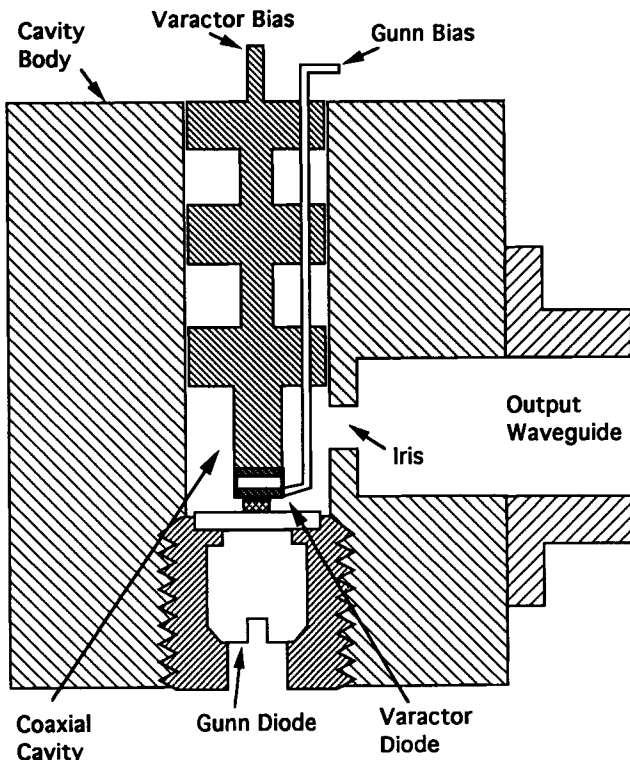


Figure 19. A varactor-tuned coaxial-cavity Gunn oscillator.

Gunn cavity to stabilize the output power and frequency against ambient temperature change. However, as illustrated in Figure 20, the frequency–voltage characteristics of varactor-tuned Gunn sources are inherently nonlinear. An electronic linearizer designed for the varactor bias can be used to correct the frequency-bias nonlinearity.

Another commonly used Gunn VCO design for the millimeter-wave frequency is shown in Figure 21. The varactor is connected in series with the Gunn diode through a disc resonator. The second-harmonic frequency of the Gunn oscillator is extracted to the output waveguide. The back short is used strictly for output power coupling. A tuning bandwidth of 10 GHz with a center frequency of 94 GHz has been achieved using such a GaAs Gunn VCO. The tuning bandwidth and output power in a varactor-tuned Gunn oscillator are in a trade-off relationship. A series-tuned Gunn VCO, which has more power coupled to the varactor, has a wider tuning range but a higher power loss compared with that of the parallel-tuned Gunn VCO. Thus a high-performance Gunn diode is beneficial, if not

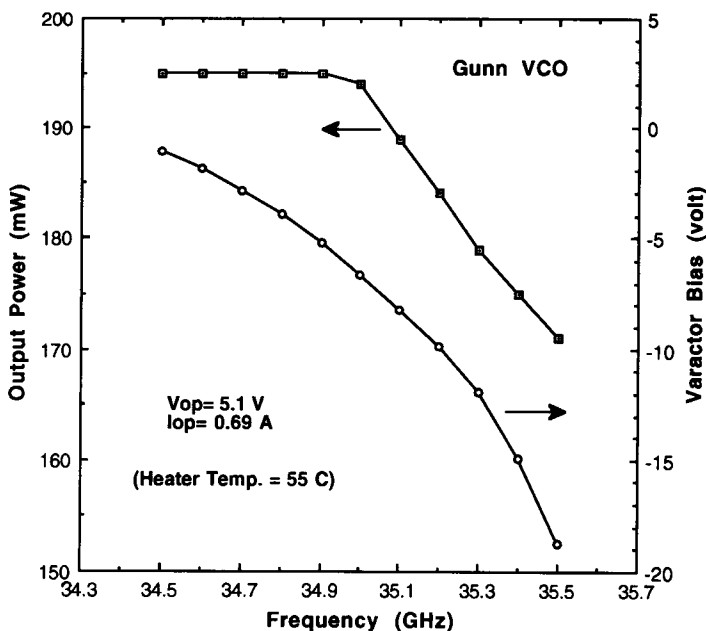


Figure 20. Output power and frequency vs varactor voltage of a Ka-band Gunn VCO.

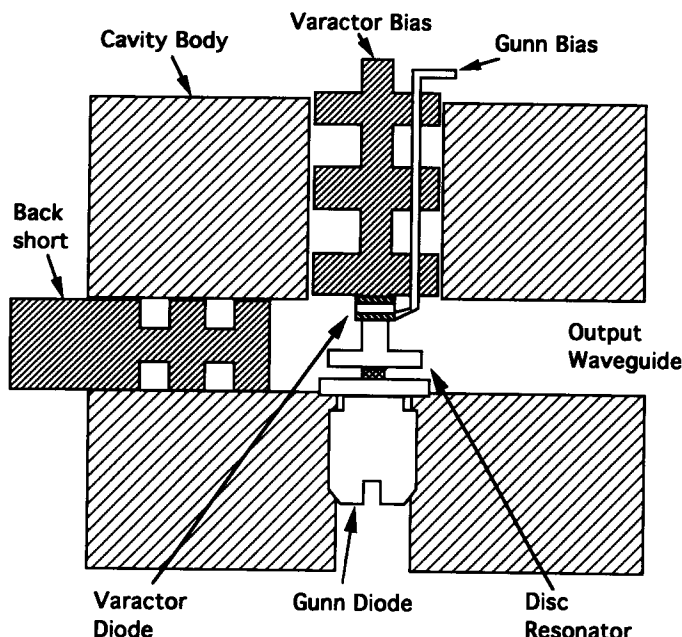


Figure 21. A varactor-tuned second-harmonic Gunn VCO.

essential, in designing wide-band Gunn VCOs for applications. Likewise, the above-described techniques for series- and parallel-tuned Gunn oscillators can be used in microstrip MIC circuits [72, 73].

Bias Tuned

The Gunn oscillator frequency can be tuned simply by varying the bias voltage on the Gunn diode. A bias-tuned Gunn oscillator prefers the diode to have a wide operating voltage range. Gunn diodes that have a low thermal resistance and good DC-to-RF conversion efficiency are ideal for bias-tuned application. The bias tuning characteristics also depend on the oscillator circuit. A discontinuity in frequency or power may occur due to circuit property change such as bias circuit oscillation. Oscillators using second-harmonic operation usually achieve a wider tuning range than those in the fundamental operation mode. Bias-tuned Gunn oscillators generally have a narrower tuning range compared with that of the varactor tuned. The advantage of the bias tune lies in its simplicity. A bias-tuned Gunn oscillator can be used in a phase-locked source simply by using the Gunn bias voltage as the feedback. Figure 22 shows an example of the output power and frequency versus the Gunn bias voltage of a second-

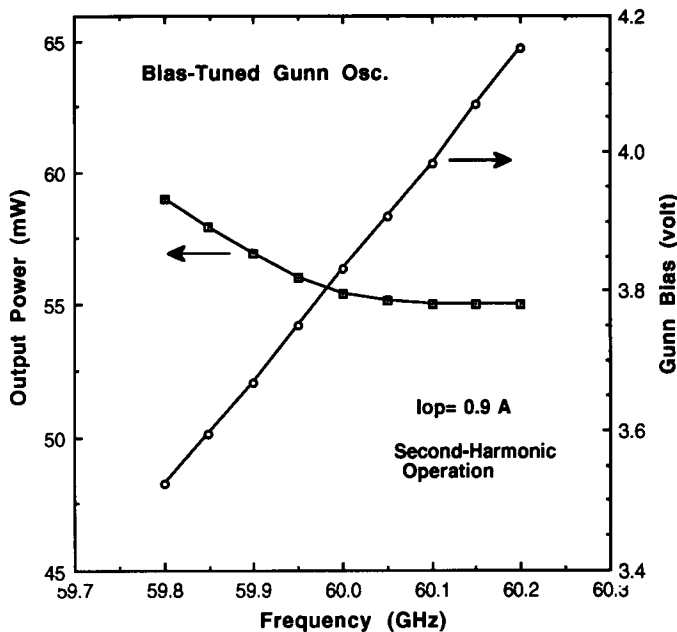


Figure 22. Output power and frequency vs bias voltage of a bias-tuned V-band Gunn oscillator.

harmonic V-band GaAs Gunn oscillator. A tuning bandwidth of 400 MHz at a center frequency of 60 GHz was achieved in this example. The output power usually decreases and the frequency increases as the diode bias voltage increases.

Magnetically Tuned

The frequency tuning of Gunn oscillator can also be achieved by using a magnetically tuned ferrite sphere. The YIG (yttrium–iron garnet)-tuned pulsed Gunn oscillator was first reported by Chang *et al.* [74]. They observed a frequency tuning from 3.2 to 2.4 GHz. The YIG sphere is used as a tunable ferrimagnetic resonator and as a narrow-band bandpass filter. The sphere is loop coupled to the Gunn diode and the load. The resonance frequency and unloaded Q of the resonator can be expressed as [75]

$$f_o = \frac{1}{2\pi\sqrt{LC}} \cong 2.8 \times 10^6 \times H_o \quad (\text{oersteds})$$

$$Q_u = \frac{\omega L}{R}. \quad (17)$$

The unloaded Q_u for single-crystal YIG is about 2000–4000. Wide-band frequency tuning is electrically achieved by varying an applied magnetic field. The YIG-tuned Gunn oscillator achieves a wider bandwidth, a better linearity, and a superior FM noise performance than the varactor-tuned Gunn oscillator. The drawback of the YIG-tuned oscillator is its lower output power, due to weaker coupling. Octave electronic tuning from 6 to 18 GHz using a YIG-tuned CW Gunn oscillator was demonstrated by Omori [76].

The YIG-tuned oscillator is limited to the high end of the microwave frequency band due to the high magnetic fields required. The barium ferrite (BaFe) sphere offers a high uniaxial anisotropy which provides an internal magnetic field. This built-in field thus reduces the external magnetic field required for resonance at millimeter-wave frequencies. A tuning range of 3.2 GHz from a 65-GHz barium–ferrite-tuned Gunn oscillator was reported by Lemke [77]. Barium–ferrite-tuned InP Gunn oscillators tuned from 40.5 to 50 GHz with a 6- to 13-dBm power output were also reported [78].

Gunn Sweeper

Several Gunn VCOs can be combined through electronic control to make wide-band frequency sweepers. This is especially desirable in the millimeter-wave frequency range due to the lack of other comparable

solid-state sweepers. The Gunn frequency sweepers can cover a frequency range of up to 15 GHz either in the V (50–75 GHz) or in the W (75–100 GHz) band [79]. The sweepers can deliver more than 10 dBm of output power in the V-band and 7 dBm in the W-band. The sweeper output is controlled using PIN diodes with a switching time between oscillators of less than 10 ms in the autosweep mode. These sweep generators include a sweep source and the HP-8350B mainframe. The mainframe allows the control of full-sweep function through front-panel data entry or via the IEEE-488 bus. An improved output power flatness can be achieved by using a leveling loop. These broadband frequency sources are ideal for applications, such as local oscillators, that require a low AM and FM noise signal level.

MMIC Gunn Oscillator

The fabrication of Gunn diodes may be integrated into the GaAs monolithic MIC chips. Such Gunn diodes are grown on a semi-insulating GaAs substrate, and the oscillators are designed with low- Q microstrip resonators. The diode has to be electrically isolated from other circuit elements while achieving an adequately low parasitic resistance and thermal resistance. It is not easy to achieve a good heat sink for the diode using an epitaxy-up structure. The generated heat has to be dissipated through the thick GaAs substrate or a thick plated gold. Nor is it easy to fabricate Gunn diodes with good DC-to-RF efficiency using an epitaxy-down structure [80]. One potential advantage of an MMIC Gunn source is its ability to integrate electronic tuning elements, such as a varactor, into the Gunn resonators. A GaAs MMIC Gunn VCO design which incorporates 14 Gunn diodes, a varactor, and a power combiner was demonstrated to have delivered 125 mW at 32 GHz and 70 mW at 40 GHz by Goldwasser *et al.* [81]. The tuning bandwidth was 60 MHz at a center frequency of 32 GHz. The feasibility and reproductibility in terms of diode performance and frequency control, thus the yield and cost, of fabricating MMIC Gunn oscillators remain a challenging task.

Cavity-Stabilized Gunn Oscillators (CSGO)

Microwave communication systems require a highly stabilized low-noise local oscillator (LO). The FM noise in the local oscillator degrades the sensitivity of a receiver. The frequency stability of an ordinary Gunn oscillator and the required stability in the communication systems are on the order of 10^{-3} and 10^{-5} , respectively, over a temperature range of 0 to 50°C. Oscillators made from multiplying the frequency of a quartz crystal have a good long-term stability but a bad short-term stability. The long-term

stability of an oscillator measures the frequency shift versus temperature drift. The short-term stability correlates to the FM noise. The cavity stabilization technique offers an efficient and cost-effective solution for improving both the short-term and the long-term stability of Gunn oscillators. The stabilization of microwave oscillators using an external cavity has been known since the early days of microwave application [82, 83]. The Gunn oscillator is coupled to an external high- Q cavity which in turn determines the oscillator stability. Substantial FM noise reductions (> 20 dB) can be readily achieved using cavity stabilization [84].

Depending on the cavity arrangement and the coupling scheme, cavity-stabilized Gunn oscillators (CSGO) may be classified into the following three types: the (a) reflection type, (b) transmission type, and (c) reaction type. Figure 23 shows the circuit diagram of the three types of CSGO. The reflection- and reaction-type cavities are both one-port circuits, whereas the transmission-type cavity is a two-port circuit. The degree of frequency stability can be measured by a stabilization factor S [84, 85], which is expressed as

$$S = \frac{W_s}{W_{us}} = \frac{Q_{ls}}{Q_{lus}}, \quad (18)$$

where W_s , W_{us} , Q_{ls} , and Q_{lus} are the stored energies and loaded Q

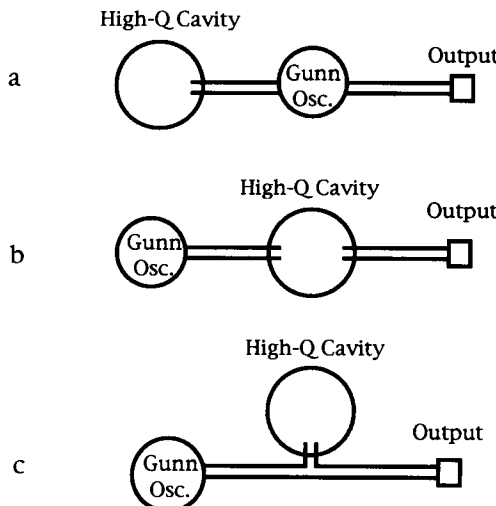


Figure 23. Diagrams of a cavity-stabilized oscillator. (a) Reflection type, (b) transmission type, and (c) reaction type.

factors of the stabilized and unstabilized oscillators, respectively. S is inversely proportional to the loaded factor of the unstabilized oscillator Q_{LUS} . The stabilization factor S , the ratio of Q_{LS} and Q_{LUS} , is thus a relative measure of frequency stabilization. The loaded Q -factor Q_{LS} is a more absolute indication of the degree of frequency stabilization. However, the FM noise reduction is directly determined by the stabilization factor S . The FM noise reduction in decibels can be calculated approximately as $\approx 20 \log S$.

Reflection-Type CSGO

Figure 24 shows the cross-sectional schematic of a reflection-type CSGO in which the Gunn cavity is coupled to a cylindrical high- Q cavity for stabilization. The output power is extracted from the Gunn cavity. The body of the high- Q cavity is usually made of Invar which has a small temperature expansion coefficient. An Invar cavity may use a brass plug at one end. Brass has a higher expansion coefficient than that of invar. As temperature increases, the brass plug extends into the Invar cavity. The brass plug then compensates for the dimensional change of the cavity due to temperature variation [86]. The resonant mode and frequency can be designed using a mode chart in which various TE or TM modes are plotted against the cavity's dimensional ratio D/L , where D is the diameter and L is the length of a right circular cylindrical cavity. It is desirable to design a stabilization cavity having a smooth interior surface, a small volume, and no undesired modes near the resonant frequency. The cavity unloaded Q can easily reach the 10^4 range. The achieved cavity Q value is usually 80–90% of the theoretical Q value. The resonator fre-

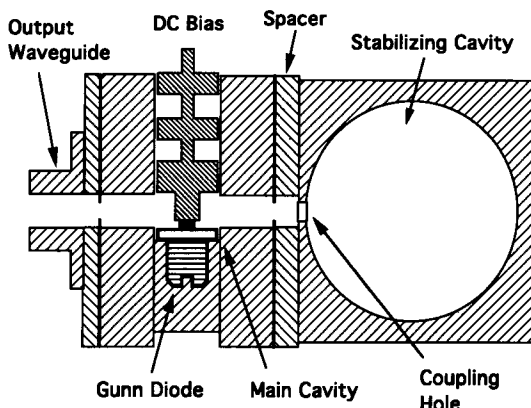


Figure 24. A reflection-type cavity-stabilized Gunn oscillator.

quency can be adjusted by using a tuning screw or changing the spacer size [87, 88]. The reflection-type CSGO is often used for applications such as local oscillators because it has a wide tunable frequency range, a higher output power, and a medium but sufficient loaded Q factor. The reflection-type CSGO with a cylindrical cavity is readily applicable up to millimeter-wave frequencies such as the Q-band [89, 90]. The FM noise thus obtained is about -120 to -100 dBc/Hz at an offset frequency of 1 MHz in K-band to W-band frequencies.

Transmission-Type CSGO

The transmission-type cavity was the first one developed with the frequency stabilization technique [82, 84]. Figure 25 shows the cross-sectional schematic of a transmission-type CSGO in which the output power is extracted from the high- Q cavity. The transmission-type CSGO has a wide frequency range of stabilization. A high loaded Q factor can be readily achieved at the expense of the output power [91]. On the other hand, the increase of the cavity coupling leads to a lower loaded Q factor and a higher output power. The transmission-type CSGO is suitable in applications that require a high loaded Q and a low FM noise; meanwhile the output power level is not as important. Instead of using Invar or copper, a metalized glass cavity may be used for a low-cost but highly stable CSGO. A low FM noise transmission-type CSGO can also be achieved by closely coupling a coaxial Gunn cavity with a cylindrical cavity while the output waveguide port is loosely coupled [92].

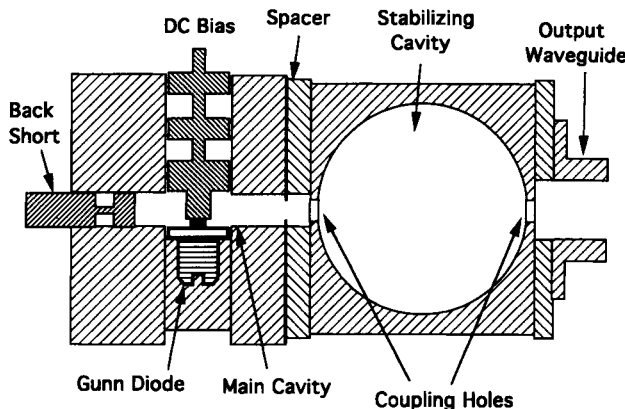


Figure 25. A transmission-type cavity-stabilized Gunn oscillator.

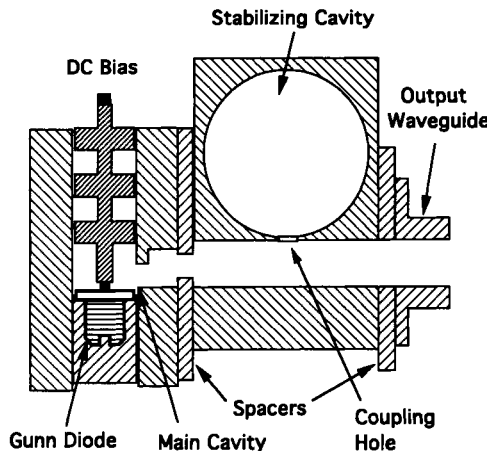


Figure 26. A reaction-type cavity-stabilized Gunn oscillator.

Reaction-Type CSGO

The reaction-cavity-stabilized oscillator was introduced by Goldstein [83]. Figure 26 shows the cross-sectional schematic of a reaction-type CSGO in which the stabilization cavity is inserted between the oscillator and the output port. The tunable stabilization frequency range of the reaction type is small compared with that of the reflection and transmission types. In a reaction-type CSGO, a high loaded Q factor can be achieved at a higher output power than that of the reflection type [85]. As the coupling between the cavities increases, the output power decreases, but the loaded Q factor increases until a maximum value is reached at a very small output power level. Dielectric resonators with high Q factors have been widely used in microwave component applications [93]. Frequency stabilization using a dielectric resonator in an MIC Gunn oscillator is another form of the reaction-type CSGO [65].

5. Gunn Amplifiers

Gunn amplifiers are useful in applications such as driving stages which require a moderate power level over a wide bandwidth. Due to the rapid progress made by microwave FETs, Gunn amplifiers are used more often in the millimeter-wave frequency range. Microwave amplifications of a DC-biased Gunn device was first reported by Thim *et al.* [94, 95]. A diagram of a Gunn amplifier is shown in Figure 27, where a one-port

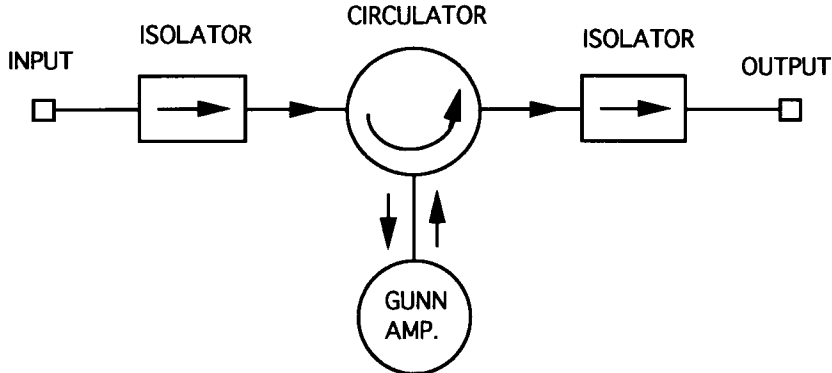


Figure 27. Diagram of a Gunn reflection amplifier.

reflection-type amplification is used. A ferrite circulator serves to isolate the incident and reflected waves. The reflection coefficient, or reflection gain, at the diode is defined as

$$\Gamma = \frac{Z_L - Z_D^*}{Z_L + Z_D}, \quad (19)$$

where Z_L is the load impedance seen by the diode, and Z_D and Z_D^* are the diode impedance and its conjugate, respectively. The Z_L is controlled by a coupling circuit such as an iris or a step transformer. The condition for stability is $Z_L > | - Z_D |$. In order to achieve stability, the coupling circuit must be adjusted to the point at which $Z_L > | - Z_D |$. The power gain G for such a reflection amplifier is given as

$$G = \left| \frac{Z_L - Z_D^*}{Z_L + Z_D} \right|^2. \quad (20)$$

A reduced-height waveguide cavity combined with waveguide circuits is ideally suitable to build a Gunn amplifier [96, 97]. Figure 28 shows a cross-sectional schematic of a reduced-height waveguide cavity having a diode spacer. The cavity is coupled to the output waveguide using step transformers. In this example, a Q-band Gunn diode is mounted on a copper heat sink which is then screwed into the cavity. The sliding back short is used to adjust the gain and suppress the self-excited oscillation. The cavity's resonance frequency and the output coupling can be adjusted

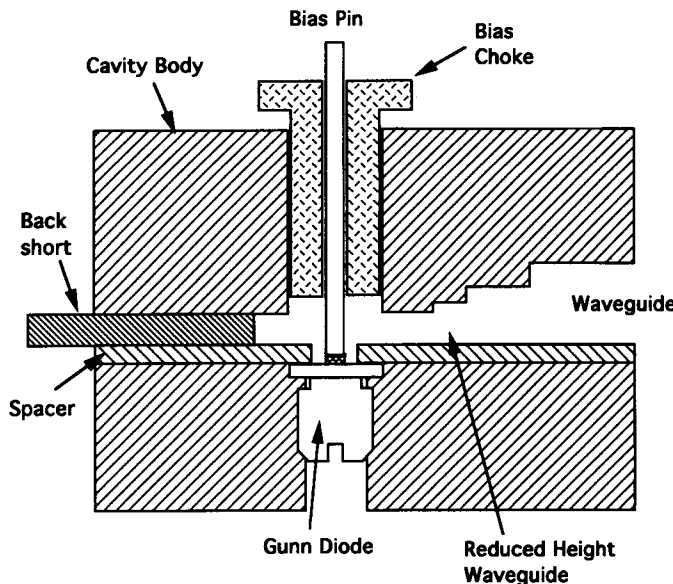


Figure 28. A reduced-height waveguide cavity with a diode spacer.

by adjusting the spacer size and the bias choke location. Figure 29 shows the measured gain curve of such a single-stage GaAs Gunn amplifier at a swept frequency of 43–45 GHz. The gain compression down to 5 dB is clearly shown in Figure 29. Two or more such Gunn amplifiers can be cascaded to increase the gain, but the final output power is limited by the power capability at the last stage. The diagram of a two-stage Gunn reflection amplifier is shown in Figure 30. Higher-power IMPATT diode amplifiers are often used in the latter stages. The design and performance of multistage GaAs Gunn amplifiers for FM-CW communication systems in X, Ku, and Ka bands have been reported [97–99]. InP diodes are also suitable for making millimeter-wave Gunn amplifiers [100, 101].

The main difficulty of making a stable Gunn amplifier lies in the suppression of the diode's self-excited oscillations when there is no input signal. Otherwise, the amplifier would behave like an injection-locked oscillator (ILO). An ILO is easier to optimize because it has fewer stability requirements. Other than circuit-related factors, the diode itself plays an important role in suppressing the amplifier's tendency to oscillate on its own. It has been shown that diodes having a properly designed doping notch near the cathode produced the best frequency stability and optimum noise figure in Gunn amplifiers [102, 103]. The cathode doping notch

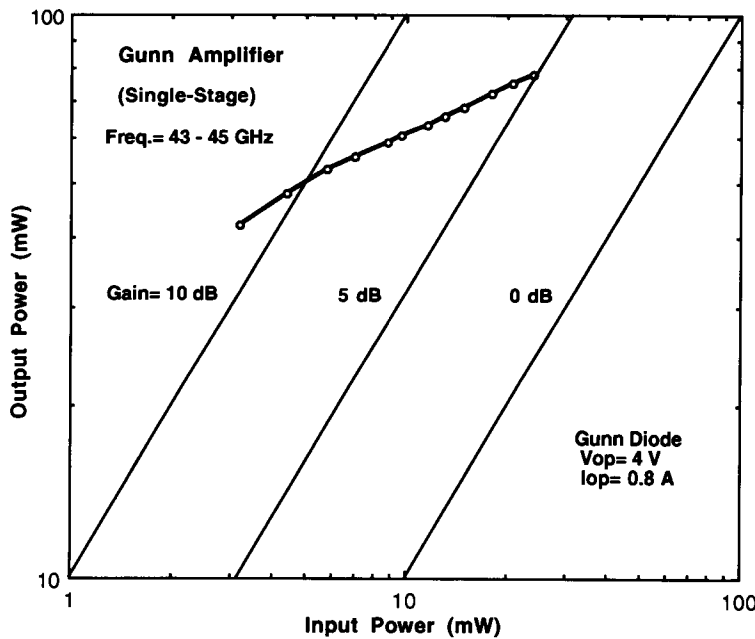


Figure 29. Gain curve of a single-stage Q-band GaAs Gunn amplifier.

creates a flat electric-field distribution at a high enough bias to allow stable amplification. This feature also can be identified by a positive slope of diode I-V curves above threshold. Experiences have shown that, with or without a cathode doping notch, Gunn diodes made with a positive I-V slope above threshold are more inclined to allow stable amplification than those of a negative I-V slope. The shape of the diode I-V curves strongly depends on the fabrication of the cathode contact. Often it is the case that

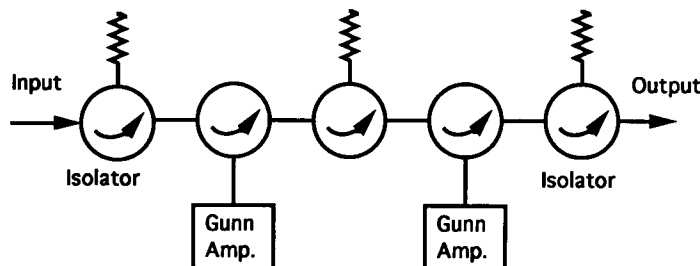


Figure 30. Diagram of a two-stage Gunn amplifier.

an optimized positive diode I-V slope is less than easy to reproduce. This applies to both GaAs and InP Gunn diodes.

6. Noise Characteristics

Gunn Oscillator Noise

Gunn oscillators are known to exhibit noise figures 10 dB or more lower than those of avalanche oscillators [104]. In a negative-resistance oscillator, AM noise is usually weaker than FM noise. The sideband noise power of AM noise is about 20 dB lower than that of FM noise in Gunn oscillators. A general expression for FM noise or root-mean-square (rms) frequency deviation of a negative-resistance oscillator is given as [105, 106]

$$\Delta f_{\text{rms}} = \frac{f_o}{Q_{\text{ex}}} \sqrt{\frac{kTB}{P_o}}, \quad (21)$$

where Δf_{rms} is the rms frequency deviation in hertz in bandwidth B , k is the Boltzmann constant, T is the equivalent noise temperature of the noise source, and P_o is the RF output power of the oscillator. The oscillator external Q_{ex} can be experimentally measured by the frequency pulling technique. The Q_{ex} is determined by the following locking equation [107],

$$Q_{\text{ex}} = \frac{f_o}{\Delta f} \sqrt{\frac{P_i}{P_o}}, \quad (22)$$

where Δf is the total locking range, P_o is the free-running output power, and P_i is the injected signal power.

Both AM and FM noise spectra have been found to depend inversely on the resonator external Q_{ex} . Figure 31 shows the measured AM and FM noise spectra of the three X-band Gunn oscillators having different Q_{ex} as reported by Ohtomo [104]. The same diode was used in the three oscillators and in noise measurements. The FM noise was much improved by the increase of Q_{ex} , whereas the AM noise spectra did not change appreciably. The types of oscillator cavities used are shown in Figure 32, in which type A corresponds to the Q_{ex} curves 2 and 3, and type B the Q_{ex} of curve 1, as shown in Figure 31. It is also seen in Figure 31b that the output power is inversely proportional to the cavity's Q_{ex} .

The FM noise spectrum of a Gunn oscillator consists of two components. The first is the thermal component which depends on loaded Q and

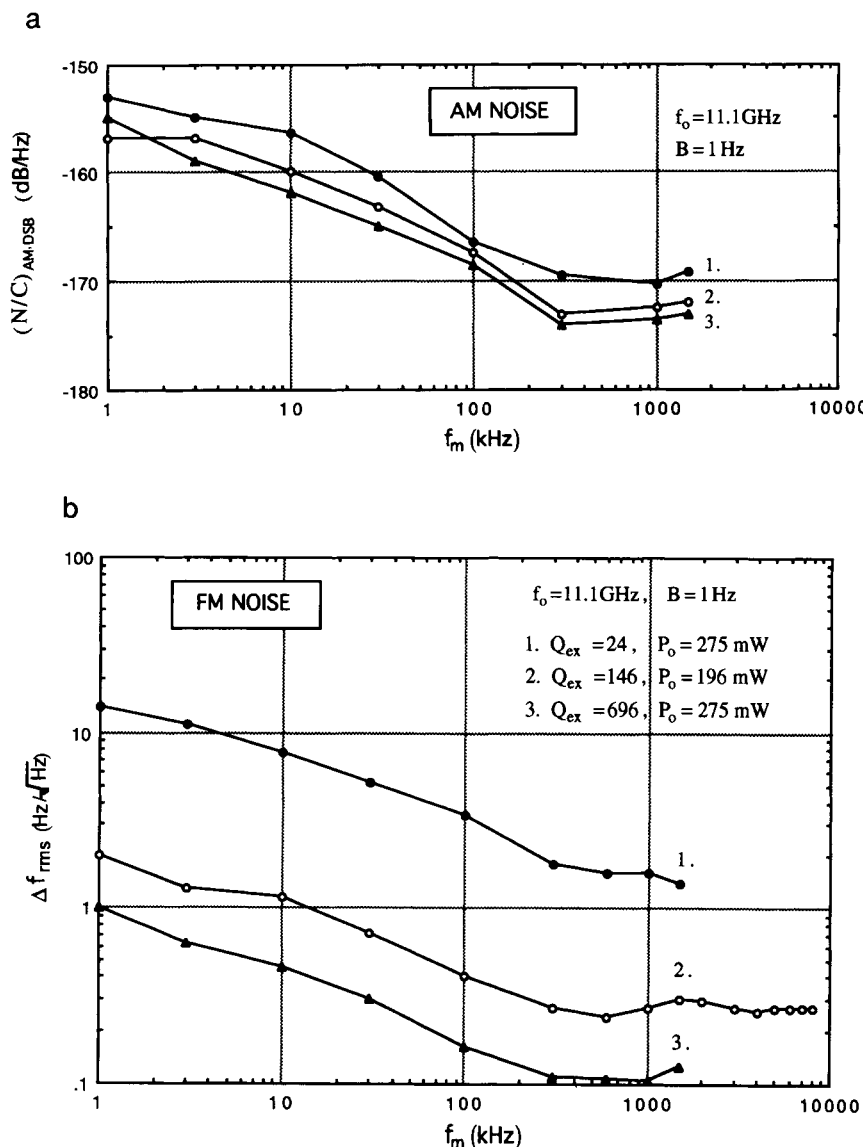


Figure 31. Measured noise spectra of three Gunn oscillators containing the same diode, but having different Q_{ex} . (a) AM noise spectra and (b) FM noise spectra. (From Ohtomo [104], reproduced with permission.)

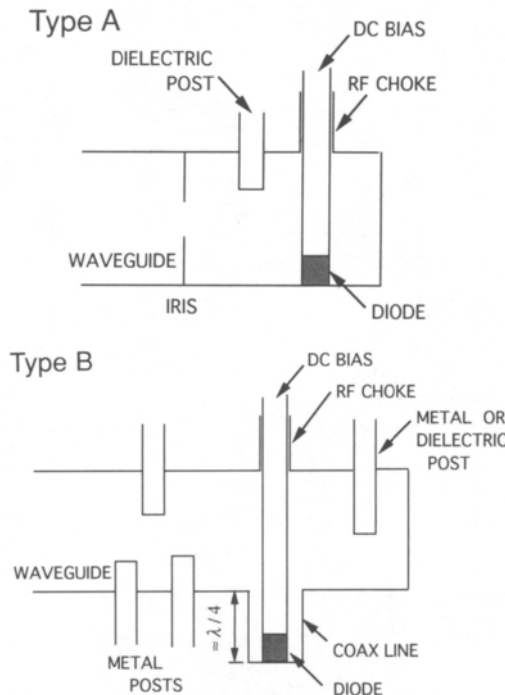


Figure 32. Circuit types used for Gunn oscillator AM and FM noise measurements. (From Ohtomo [104], reproduced with permission.)

the carrier output power. The relationship is shown in Equation (21). The second is the flicker component which depends on the oscillator's "voltage pushing" [108]. The current fluctuations in the oscillator modify the diode bias voltage and thus produce frequency fluctuations.

Oscillator applications generally place a limit on the output noise. Radar and communication systems, for example, require a low FM noise. Parametric amplifier pumps require a low AM noise. The noise of Gunn oscillators can be reduced by the following techniques.

1. Use a regulated stable DC power supply.
2. Increase the loaded Q of the resonator.
3. Optimize the bias circuitry to reduce bias oscillation.
4. Bias the diode at its peak power or the least voltage pushing point.
5. Improve the epitaxial layer quality and ohmic contact technique.
6. Improve the diode packaging to reduce the diode thermal resistance.

In addition, there are two circuit techniques that can be used to reduce the oscillator noise. The first is the external high- Q cavity-stabilized oscillator which was described earlier. The second is the injection-locked or phase-locked oscillator, in which a low-noise external frequency source is used. The latter is described in the following section.

Phase-Locked Gunn Oscillator

Gunn oscillators can be phased locked to an injected RF source provided that the locking frequency is close to that of the free-running oscillator. The FM noise of Gunn oscillators can be considerably improved by injection locking, whereas the AM noise degrades slightly [106, 109]. The injected signal from the output side tends to shift the oscillator frequency f_o toward the injected frequency f_i until the f_o and f_i are equal. The phase difference ϕ between f_i and f_o may be expressed as [107]

$$\phi = \sin^{-1} \left(2Q_{\text{ex}} \sqrt{\frac{P_o}{P_i}} \frac{\Delta f}{f_o} \right), \quad (23)$$

where P_i is the power of the injected signal, P_o is the oscillator output power, and $\Delta f = f_i - f_o$ is the frequency shift. As shown in Equation (23), the phase difference ϕ increases as the frequency shift Δf increases. The maximum frequency shift allowed for locking is at $\phi = \pi/2$. The locking bandwidth of the oscillator equals twice the maximum frequency shift. The locking bandwidth (BW) is therefore

$$\text{BW} = \frac{f_o}{Q_{\text{ex}}} \sqrt{\frac{P_i}{P_o}}. \quad (24)$$

It is seen in Equation (24) that a higher injection signal power P_i achieves a wider locking bandwidth. A higher P_i also produces the lower FM noise of an ILO [109].

In designing a phased-locked Gunn oscillator, an error signal proportional to the frequency deviation Δf is produced using a phase detector. This error signal is then used as a feedback to adjust the frequency of a free-running oscillator. Figure 33 shows the block diagram of a phase-locked Gunn oscillator. The locking reference signal is usually obtained from a master quartz-controlled oscillator multiplied up to the desired frequency. The Gunn oscillator can be a varactor-tuned or bias-tuned VCO. In such an ILO circuit having a phase stabilization feedback, the output noise is further reduced compared with that of a simple ILO.

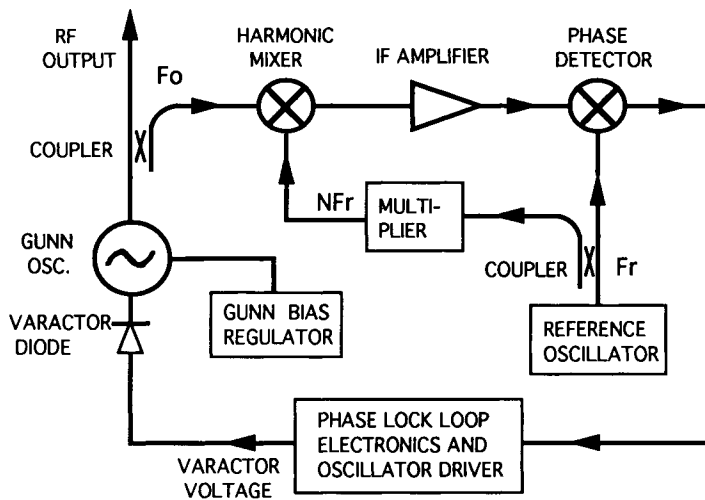


Figure 33. Block diagram of a phase-locked Gunn oscillator.

7. Power Combining Techniques

The output power from a single Gunn diode is sometimes inadequate for application. Some applications use a Gunn source as a transceiver which requires a higher output power. There are various power combining techniques to combine solid-state power sources [110, 111]. Most of the reported techniques were based on IMPATT diodes. In principle, they can be similarly applied to that of Gunn diodes. A power combiner coherently combines the powers from a number of Gunn diodes. The combining techniques generally fall into two categories: the device level and the circuit level. Device level combining is achieved by grouping several devices, in series or in parallel, in an area smaller than a wavelength. Circuit level combining utilizes the resonant circuit to combine the powers contributed from each diode. The degree of difficulty in power combining generally increases as the diode number increases. The following section presents some practical combining techniques used for the Gunn oscillator.

Resonant Cavity Combiners

A resonant cavity combiner was first demonstrated by Kurokawa [112] with 12 IMPATT diodes in a single rectangular waveguide cavity at the X-band. The resonant cavity combiner circuit can be a rectangular-type cavity

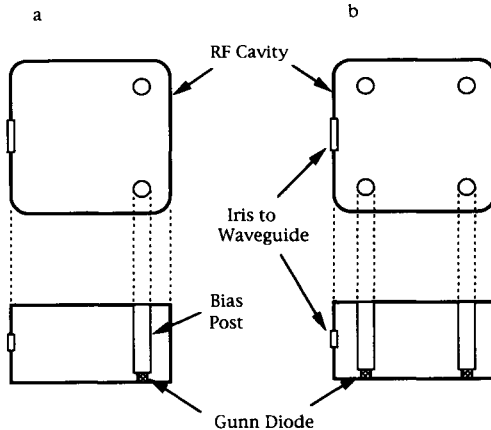


Figure 34. Rectangular resonant cavity combiners: (a) two-diode combiner and (b) for diode combiner.

[112–114] or a cylindrical-type cavity [115, 116]. The rectangular cavity combiners are often used for Gunn diodes up to millimeter-wave frequencies (W-band). Figure 34 shows a typical rectangular cavity structure used for power combining. The cavity can be a two-diode or a four-diode combiner. The diodes are mounted in the corners of the rectangular cavity under bias posts. The oscillator frequency can be tuned by inserting ceramic rods into the cavity. For example, a two-diode Q-band combiner cavity having a second-harmonic W-band output frequency can be constructed in such a manner. Because two or more diodes are being operated in one cavity, problems of frequency jumping may occur. Diodes having similar dc characteristics are often preselected for matching purposes. Gunn diodes made from the same wafer lot are preferred, if not required, in most power combining applications.

Series-Operation Combiners

The device-level power combining of Gunn diodes can be accomplished by series operation. The output power of the Gunn oscillator usually increases as the diode current increases, until the diode temperature becomes too high and the diode impedance becomes too low. One way to increase the output power is to raise the dc and rf impedance of the Gunn diode through the series operation of several diodes. Carroll [117] first reported the pulsed series operation of four Gunn diodes spaced a half-wavelength apart in a coaxial circuit at 2 GHz. Another effective method of series operation is to mount the diodes close together. The

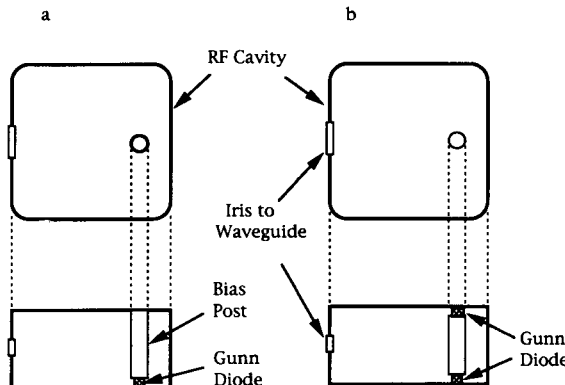


Figure 35. Power combining using a series operation in a rectangular cavity: (a) one-diode structure and (b) two-diode structure.

successful series operation of two Gunn diodes at the X-band was demonstrated by Steele *et al.* [118]. The series operation of multiple stacked Gunn diodes, up to 10 diode chips, with a total pulsed output power of 116 W at the X-band, was also reported [119]. The series operation of Gunn diodes in the millimeter-wave frequency range was reported by Teng and Goldwasser [120]. A pulsed output power of 4.4 W was obtained by series operation of two Gunn diodes at 33.2 GHz. Such a setup can be used in lightweight or hand-held transmitter applications such as ship-based or airborne transponder. Figure 35 shows an example of an oscillator cavity structure for power combining using a rectangular cavity: (a) the one-diode structure and (b) two diodes in series operation. In the case of the one-diode structure, the diode may consist of two stacked diode chips in series. Likewise, the stacked diode structure may be used (as in Figure 33) to further increase the power combining factor. However, CW operation using a stacked diode structure is difficult to achieve due to the unequal thermal resistance of the diodes.

References

- [1] J. B. Gunn, Microwave oscillations of current in III-V semiconductors, *Solid State Commun.*, Vol. 1, pp. 89–91, 1963.
- [2] J. B. Gunn, Instabilities of current in III-V semiconductors, *IBM J. Res. Dev.*, Vol. 8, pp. 141–159, 1964.
- [3] J. B. Gunn, The Gunn effect, *Int. Sci. Technol.*, p. 43, Oct. 1965.

- [4] W. Shockley, Negative resistance arising from transit time in semiconductor diodes, *Bell Syst. Tech. J.*, Vol. 33, pp. 799–826, 1954.
- [5] B. K. Ridley and T. B. Watkins, The possibility of negative resistance effects in semiconductors, *Proc. Phys. Soc., London*, Vol. 78, pp. 293–304, 1961.
- [6] C. Hilsum, Transferred electron amplifiers and oscillators, *Proc. IEEE*, Vol. 50, pp. 185–189, 1962.
- [7] B. K. Ridley, Specific negative resistance in solids, *Proc. Phys. Soc., London*, Vol. 82, pp. 954–966, 1963.
- [8] H. Kroemer, Theory of the Gunn effect, *Proc. IEEE*, Vol. 52, p. 1736, 1964.
- [9] A. R. Hutson *et al.*, Mechanism of the Gunn effect from a pressure experiment, *Phys. Rev. Lett.*, Vol. 14, pp. 639–641, 1965.
- [10] J. W. Allen, M. Shyam, and G. L. Pearson, Gunn oscillations in InAs, *Appl. Phys. Lett.*, Vol. 9, pp. 39–41, 1966.
- [11] J. W. Allen *et al.*, Microwave oscillations in $\text{GaAs}_x\text{P}_{1-x}$ alloys, *Appl. Phys. Lett.*, Vol. 7, pp. 78–80, 1965.
- [12] M. R. Oliver and A. G. Foyt, The Gunn effect in n-CdTe, *IEEE Trans. Electron Devices*, Vol. ED-14, pp. 617–618, 1967.
- [13] G. W. Ludwig, Gunn Effect in CdTe, *IEEE Trans. Electron Devices*, Vol. ED-13, p. 547, 1967.
- [14] G. W. Ludwig, R. E. Halsted, and M. S. Aven, Current saturation and instability in CdTe and ZnSe, *IEEE Trans. Electron Devices*, Vol. ED-13, p. 671, 1966.
- [15] J. E. Smith, Jr. *et al.*, Gunn effect in n-type InSb, *Appl. Phys. Lett.*, Vol. 15, pp. 242–245, 1969.
- [16] P. N. Butcher, W. Fawcett, and C. Hilsum, The dependence of threshold field on intervalley separation in transferred electron oscillators, *IEEE Trans. Electron Devices*, Vol. ED-13, pp. 192–193, 1966.
- [17] P. N. Butcher and W. Fawcett, Calculation of the velocity-field characteristics for gallium arsenide, *Phys. Lett.*, Vol. 21, pp. 489–490, 1966.
- [18] E. M. Conwell and M. O. Vassell, High-field distribution function in GaAs, *IEEE Trans. Electron Devices*, Vol. ED-13, pp. 22–26, 1966.
- [19] J. B. Gunn and B. J. Elliott, Measurement of the negative differential mobility of electrons in GaAs, *Phys. Lett.*, Vol. 22, pp. 369–372, 1966.
- [20] D. M. Chang and J. L. Moll, Direct observation of the drift velocity as a function of the electric field in gallium arsenide, *Appl. Phys. Lett.*, Vol. 9, pp. 283–285, 1966.
- [21] J. G. Ruch and G. S. Kino, Measurement of the velocity-field characteristic of gallium arsenide, *Appl. Phys. Lett.*, Vol. 10, pp. 40–42, 1967.
- [22] B. Fay and G. S. Kino, A new measurement of the velocity-field characteristics of GaAs, *Appl. Phys. Lett.*, Vol. 15, pp. 337–339, 1969.
- [23] J. G. Ruch and W. Fawcett, Temperature dependence of the transport properties of gallium arsenide determined by a Monte Carlo method, *J. Appl. Phys.*, Vol. 41, pp. 3843–3849, 1970.
- [24] H. W. Thim, Computer study of bulk GaAs devices with random one-dimensional doping fluctuations, *J. Appl. Phys.*, Vol. 39, p. 3897, 1968.
- [25] H. Kroemer, Nonlinear space-charge domain dynamics in a semiconductor with negative differential mobility, *IEEE Trans. Electron Devices*, Vol. ED-13, pp. 27–40, 1966.
- [26] H. L. Grubin, M. P. Shaw, and P. R. Solomon, On the form and stability of electric-field profiles within a negative differential mobility semiconductor, *IEEE Trans. Electron Devices*, Vol. ED-20, pp. 63–78, 1973.

- [27] A. Aishima, K. Yokoo, and S. Ono, An analysis of wide-band transferred electron devices, *IEEE Trans. Electron Devices*, Vol. ED-25, pp. 640–645, 1978.
- [28] J. R. Knight, D. Effer, and P. R. Evans, The preparation of high purity gallium arsenide by vapor phase epitaxial growth, *Solid-State Electron.*, Vol. 8, pp. 178–180, 1965.
- [29] J. T. Tietjen and J. A. Amick, The preparation and properties of vapor-deposited epitaxial GaAs_{1-x}P_x using arsine and phosphine, *J. Electrochem. Soc.*, Vol. 113, pp. 724–728, 1966.
- [30] C. M. Wolfe, A. G. Foyt, and W. T. Lindley, Epitaxial GaAs for high-efficiency Gunn oscillators, *Electrochem. Technol.*, Vol. 6, p. 208, 1968.
- [31] H. Nelson, Epitaxial growth from the liquid state and its application the fabrication of tunnel and laser diodes, *RCA Rev.*, Vol. 24, pp. 603–615, 1963.
- [32] C. S. Kang and P. E. Greene, Preparation and properties of high-purity epitaxial GaAs grown from Ga solution, *Appl. Phys. Lett.*, Vol. 11, pp. 171–173, 1967.
- [33] C. M. Wolfe, G. E. Stillman, and E. B. Owens, Residual impurity in high-purity GaAs, *J. Appl. Phys.*, Vol. 41, p. 3088, 1970.
- [34] R. E. Enstrom and C. C. Peterson, Vapor phase growth and properties of GaAs Gunn devices, *Trans. Metall. Soc. AIME*, Vol. 239, pp. 413–418, 1967.
- [35] F. J. Reid and L. B. Robinson, Preparation of epitaxial GaAs for microwave applications, *Proc. 2nd Int. Symp. Gallium Arsenide, Dallas*, pp. 59–65, 1968 (London: Institute of Physics and Physical Society, 1969.)
- [36] B. E. Berson, R. E. Enstrom, and J. E. Reynolds, High-power L- and S-band transferred electron oscillators, *RCA Rev.*, Vol. 31, p. 20, 1970.
- [37] R. C. Clark, B. D. Joyce, and W. H. E. Wilgoss, The preparation of high purity InP, *Solid State Commun.*, Vol. 8, pp. 1125–1128, 1970.
- [38] R. C. Clark, InP vapor phase epitaxy: A review, *J. Cryst. Growth*, Vol. 54, pp. 88–100, 1981.
- [39] R. J. Hamilton *et al.*, InP Gunn-effect devices for millimeter-wave amplifiers and oscillators, *IEEE Trans. Microwave Theory Tech.*, Vol. MTT-24, pp. 775–780, 1976.
- [40] N. Apsley *et al.*, InP millimeter wave transferred electron oscillators, *Gallium Arsenide Relat. Compd.*, 1980, Inst. Phys. Conf. Ser. No. 56, pp. 483–492, 1981.
- [41] S. J. J. Teng, Indium phosphide devices on gallium arsenide substrates, *Microwave J.*, Vol. 28, No. 12, pp. 138–140, 1985.
- [42] S. J. J. Teng, J. M. Ballingall, and F. J. Rosenbaum, Vapor phase epitaxial growth and characterization of InP on GaAs, *Appl. Phys. Lett.*, Vol. 48, pp. 1217–1219, 1986.
- [43] W. H. Yaydl, R. S. Smity, and R. Bosch, 50–100 GHz Gunn diodes using molecular beam epitaxy, *IEEE Trans. Electron Device Lett.*, Vol. EDL-1, pp. 224–226, 1980.
- [44] S. J. Bass and P. E. Oliver, Controlled doping of GaAs produced by vapor phase, using trimethylgallium and arsine, *Gallium Arsenide Relat. Compd.*, Inst. Phys. Conf. Ser. No. 33b, pp. 1–10, 1977.
- [45] M. A. di Forte-Poisson *et al.*, High-power high-efficiency LP-MOCVD Gunn diodes for 94 GHz, *Electron Lett.*, Vol. 20, pp. 1061–1062, 1984.
- [46] J. E. Carroll, Oscillations covering 4 Gc/s to 31 Gc/s from a single Gunn diode, *Electron. Lett.*, Vol. 2, p. 141, 1966.
- [47] T. Hariu and Y. Shibata, Optimum Schottky-barrier height for high-efficiency microwave transferred-electron diodes, *Proc. IEEE*, Vol. 63, pp. 823–824, 1975.
- [48] D. J. Colliver *et al.*, Cathode contact effects in InP transferred-electron oscillators, *Inst. Phys. Phys. Soc. Symp. GaAs*, pp. 286–293, 1972.

- [49] J. D. Crowley, J. J. Sowers, B. A. Janis, and F. B. Fank, High efficiency 90 GHz in InP Gunn oscillators, *Electron. Lett.*, Vol. 16, pp. 705–706, 1980.
- [50] K. W. Gray *et al.*, InP microwave oscillators with 2 zone cathodes, *Electron. Lett.*, Vol. 11, pp. 402–403, 1975.
- [51] S. Neylon *et al.*, State-of-the-art performance millimeter wave GaAs Gunn diodes using ballistically hot electron injectors, *IEEE MTT—S Int. Microwave Symp. Dig.*, pp. 519–522, 1989.
- [52] S. Knight, Heat flow in n^{++} - n^-n^+ epitaxial GaAs bulk effect devices, *Proc. IEEE*, Vol. 55, pp. 112–113, 1967.
- [53] J. Ondria and R. L. Ross, Improved performance of fundamental and second harmonic MMW oscillators through active layer doping concentration contouring, *IEEE MTT—S Dig.*, Vol. 2, pp. 977–980, 1987.
- [54] A. R. Batchelor, On the design of doping concentration profiles for GaAs transferred-electron device layers, *Solid-State Electron.*, Vol. 35, pp. 735–741, 1992.
- [55] N. Braslau, J. B. Gunn, and J. L. Staples, Metal-Semiconductor contacts for GaAs bulk effect devices, *Solid-State Electron.*, Vol. 10, pp. 381–383, 1967.
- [56] G. Y. Robinson, Metallurgical and electrical properties of alloyed Ni/Au-Ge films on n-type GaAs, *Solid-State Electron.*, Vol. 18, pp. 331–342, 1975.
- [57] S. J. J. Teng and R. E. Goldwasser, High-performance second-harmonic operation W-band GaAs Gunn diodes, *IEEE Electron Device Lett.*, Vol. EDL-10, pp. 412–414, 1989.
- [58] Alpha Catalog, “Microwave Semiconductor Products Manual.” Alpha Industries, Inc., Woburn, MA.
- [59] R. P. Owens and D. Cawsey, Microwave equivalent-circuit parameters of Gunn-effect-device packages, *IEEE Trans. Microwave Theory Tech.*, Vol. MTT-18, pp. 780–798, 1970.
- [60] J. S. Joshi and J. A. F. Cornick, Some general observations on the tuning conductors of “electromechanically” tuned Gunn oscillators, *IEEE Trans. Microwave Theory Tech.*, Vol. MTT-21, pp. 582–586, 1973.
- [61] W. C. Tsai and F. J. Rosenbaum, Bias circuit oscillations in Gunn devices, *IEEE Trans. Electron Devices*, Vol. ED-16, pp. 196–202, 1969.
- [62] R. N. Bracewell, Mode lattice for square prism resonators, *Proc. IRE*, Aug. 1947.
- [63] S. Mizushima and T. Ohsuka, The ridged-waveguide-cavity Gunn oscillator for wide-band tuning, *IEEE Trans. Microwave Theory Tech.*, Vol. MTT-24, pp. 257–259, 1976.
- [64] H. C. Okean, E. W. Sardand, and R. H. Pflieger, Microwave integrated oscillators for broad-band high-performance receivers, *IEEE Trans. Microwave Theory Tech.*, Vol. MTT-20, pp. 155–164.
- [65] T. Makino and A. Hashima, A highly stabilized MIC Gunn oscillator using a dielectric resonator, *IEEE Trans. Microwave Theory Tech.*, Vol. MTT-27, pp. 633–638, 1979.
- [66] T. G. Ruttan, Gunn diode oscillator at 95 GHz, *Electron. Lett.*, Vol. 11, pp. 293–294, 1975.
- [67] W. H. Haydl, Fundamental and harmonic operation of millimeter-wave Gunn diodes, *IEEE Trans. Microwave Theory Tech.*, Vol. MTT-31, pp. 879–889, 1983.
- [68] A. Rydberg, High efficiency and output power from second- and third-harmonic millimeter-wave InP-TED oscillators at frequencies above 170 GHz, *IEEE Electron Device Lett.*, Vol. EDL-11, pp. 439–441, 1990.
- [69] D. Large, Octave and varactor-tuned Gunn diode sources, *Microwave J.*, Vol. 13, pp. 49–51, Oct. 1970.

- [70] M. Dean and M. J. Howes, Electronic tuning of stable transferred electron oscillators, *IEEE Trans. Electron Devices*, Vol. ED-21, pp. 563–570, 1974.
- [71] D. Cawsey, Wide-range tuning of solid-state microwave oscillators, *IEEE J. Solid-State Circuits*, Vol. SC-5, pp. 82–84, 1970.
- [72] H. C. Okean, E. W. Sardand, and R. H. Pflieger, Microwave integrated oscillators for broad-band high-performance receivers, *IEEE Trans. Microwave Theory Tech.*, Vol. MTT-20, pp. 155–164, 1972.
- [73] D. Rubin, Varactor-tuned millimeter-wave MIC oscillator, *IEEE Trans. Microwave Theory Tech.*, Vol. MTT-24, pp. 866–867, 1976.
- [74] N. S. Chang, T. Hayamizu, and Y. Matsuo, YIG-tuned Gunn effect oscillator, *Proc. IEEE*, Vol. 55, p. 1621, 1967.
- [75] P. S. Carter, Magnetically-tunable microwave filters using single-crystal yttrium-iron-garnet resonators, *IEEE Trans. Microwave Theory Tech.*, Vol. MTT-9, pp. 252–260, 1961.
- [76] M. Omori, Octave electronic tuning of a CW Gunn diode using a YIG sphere, *Proc. IEEE*, Vol. 57, p. 97, 1969.
- [77] M. Lemke, A millimeter-wave Gunn oscillator, tunable with a barium-ferrite sphere, *Proc. 9th Eur. Microwave Conf.*, pp. 617–620, 1979.
- [78] Y. S. Lau and D. Nicholson, Barium ferrite tuned indium phosphide Gunn millimeter wave oscillators, *IEEE MTT—S Int. Microwave Symp. Dig.*, pp. 183–186, 1986.
- [79] Hughes Catalog, “Gunn Sweeper Products Information.” Hughes Aircraft Co., Torrance, CA.
- [80] J. C. Chen, C. K. Pao, and D. W. Wong, Millimeter wave monolithic Gunn oscillators, *IEEE Microwave Millimeter Wave Monolithic Circuits Symp. Dig.*, pp. 11–13, 1987.
- [81] R. E. Goldwasser *et al.*, Monolithic Ka-band VCOs, *IEEE Microwave Millimeter-Wave Monolithic Circuits Symp.*, pp. 55–58, 1988.
- [82] E. J. Shelton, Stabilization of microwave oscillators, *IRE Trans. Electron Devices*, Vol. ED-1, pp. 30–40, 1954.
- [83] I. Goldstein, Frequency stabilization of a microwave oscillator with an external cavity, *IEEE Trans. Microwave Theory Tech.*, Vol. MTT-5, pp. 57–62, 1957.
- [84] J. R. Ashley and C. B. Searles, Microwave oscillator noise reduction by a transmission stabilizing cavity, *IEEE Trans. Microwave Theory Tech.*, Vol. MTT-16, pp. 743–748, 1968.
- [85] R. Knochel, K. Schunemann, and J.-D. Buchs, Theory and performance of cavity stabilized microwave oscillators, *IEE J. Microwaves, Opt. Acoust.*, Vol. 1, pp. 143–155, 1977.
- [86] S. Nagano and H. Kondo, Highly stabilized half-watt IMPATT oscillator, *IEEE Trans. Microwave Theory Tech.*, Vol. MTT-18, pp. 885–890, 1970.
- [87] Y. Ito, H. Komizo, and S. Sasagawa, Cavity stabilized X-band Gunn oscillator, *IEEE Trans. Microwave Theory Tech.*, Vol. MTT-18, pp. 890–897, 1970.
- [88] S. Nagano and S. Ohnaka, A highly stabilized Ka-band Gunn oscillator, *IEEE Trans. Microwave Theory Tech.*, Vol. MTT-20, pp. 174–176, 1972.
- [89] H. Barth, A high Q cavity stabilized Gunn oscillator at 94 GHz, *IEEE MTT—S Dig.*, pp. 179–182, 1986.
- [90] T. Cutsinger, Millimeter-wave cavity-stabilized GaAs Gunn oscillator, *Microwave J.*, Vol. 17, No. 13, pp. 8–16, 1987.
- [91] K. Schunemann and R. Knochel, On the matching of transmission cavity stabilized microwave oscillators, *IEEE Trans. Microwave Theory Tech.*, Vol. MTT-26, pp. 147–155, 1978.

- [92] R. A. Strangeway, T. K. Ishii, and J. S. Hyde, Low-phase-noise Gunn diode oscillator design, *IEEE Trans. Microwave Theory Tech.*, Vol. MTT-36, pp. 792–794, 1988.
- [93] J. K. Plourde and C. L. Ren, Application of dielectric resonators in microwave components, *IEEE Trans. Microwave Theory Tech.*, Vol. MTT-29, pp. 754–770, 1981.
- [94] H. W. Thim *et al.*, Microwave amplification in a DC-biased bulk semiconductor, *Appl. Phys. Lett.*, Vol. 7, pp. 167–168, 1965.
- [95] H. W. Thim and M. R. Barber, Microwave amplification in a GaAs bulk semiconductor, *IEEE Trans. Electron Devices*, Vol. ED-13, pp. 110–114, 1966.
- [96] A. Sene and F. J. Rosenbaum, A wide-band Gunn-effect CW waveguide amplifier, *IEEE Trans. Microwave Theory Tech.*, Vol. MTT-20, pp. 645–650, 1972.
- [97] A. A. Sweet, J. R. Collinet, and R. N. Wallace, Multistage Gunn amplifiers for FM-CW systems, *IEEE J. Solid-State Circuits*, Vol. SC-8, pp. 20–28, 1973.
- [98] R. E. Goldwasser and F. E. Rosztoczy, 35 GHz-transferred electron amplifiers, *Proc. IEEE*, Vol. 61, pp. 1502–1503, 1973.
- [99] J. G. de Koning *et al.*, Gunn-effect amplifiers for microwave communication system in X, Ku, and Ka bands, *IEEE Trans. Microwave Theory Tech.*, Vol. MTT-23, pp. 367–374, 1975.
- [100] P. H. Wolfert, J. D. Crowley, and F. B. Fank, A medium power solid state amplifier for V-band, *IEEE MTT—S Dig.*, pp. 500–502, 1982.
- [101] F. B. Fank, Indium phosphide mm-wave devices and components, *Microwave J.*, pp. 95–101, Apr. 1984.
- [102] J. Magarshack, A. Rabier, and R. Spitalnik, Optimum design of transferred-electron amplifier devices in GaAs, *IEEE Trans. Microwave Theory Tech.*, Vol. MTT-22, pp. 652–654, 1974.
- [103] C. Barry *et al.*, Design of transferred-electron amplifiers with good frequency stability, *IEEE Trans. Electron Devices*, Vol. ED-24, pp. 270–274, 1977.
- [104] M. Ohtomo, Experimental evaluation of noise parameters in Gunn and avalanche oscillators, *IEEE Trans. Microwave Theory Tech.*, MTT-20, pp. 425–437, 1972.
- [105] W. A. Edson, Noise in oscillators, *Proc. IEEE*, Vol. 48, pp. 1454–1466, 1960.
- [106] K. Kurokawa, Noise in synchronized oscillators, *IEEE Trans. Microwave Theory Tech.*, Vol. MTT-16, pp. 234–240, 1968.
- [107] R. Adler, A study of locking phenomena in oscillator, *Proc. IRE*, Vol. 34, pp. 351–357, 1946.
- [108] A. A. Sweet and L. A. MacKenzie, The FM noise of a CW Gunn oscillator, *Proc. IEEE*, Vol. 58, pp. 822–823, 1970.
- [109] T. Sugiura and S. Sugimoto, FM noise reduction of Gunn-effect oscillators by injection locking, *Proc. IEEE*, Vol. 57, pp. 77–78, 1969.
- [110] K. Chang and C. Sun, Millimeter-wave power-combining techniques, *IEEE Trans. Microwave Theory Tech.*, Vol. MTT-31, pp. 91–107, 1983.
- [111] K. J. Russel, Microwave power combining techniques, *IEEE Trans. Microwave Theory Tech.*, Vol. MTT-27, p. 472, 1979.
- [112] K. Kurokawa, The single-cavity multiple-device oscillator, *IEEE Trans. Microwave Theory Tech.*, Vol. MTT-19, pp. 793–801, 1971.
- [113] T. G. Ruttan, 42-GHz push-pull Gunn oscillator, *Proc. IEEE*, Vol. 60, pp. 1441–1442, 1972.
- [114] Y. Ma and C. Sun, 1-W millimeter-wave Gunn diode combiner, *IEEE Trans. Microwave Theory Tech.*, Vol. MTT-28, pp. 1460–1463, 1980.
- [115] R. S. Harp and H. L. Stover, Power combining of X-band IMPATT circuit modules, *IEEE Int. Solid-State Circuits Conf.*, pp. 118–119, 1974.

- [116] M. Dydyk, Efficient power combining, *IEEE Trans. Microwave Theory Tech.*, Vol. MTT-28, pp. 755–762, 1980.
- [117] J. E. Carroll, Series operation of Gunn diodes for high r.f. power, *Electron. Lett.*, Vol. 3, pp. 455–456, 1967.
- [118] M. C. Steele, F. P. Califano, and R. D. Larrabee, High-efficiency series operation of Gunn devices, *Electron. Lett.*, Vol. 5, pp. 81–81, 1969.
- [119] K. M. Baughan and F. A. Myers, Multiple series operation of Gunn-effect oscillators, *Electron. Lett.*, Vol. 5, pp. 371–372, 1969.
- [120] S. J. J. Teng and R. E. Goldwasser, Millimeter-wave Gunn oscillator in series operation, *IEEE Electron Device Lett.*, Vol. EDL-8, pp. 324–325, 1987.

Microwave IMPATT Diode Amplifiers and Oscillators

David P. Klemer

I. IMPATT Diode Principles

The generation of charge carriers by impact ionization in a region of semiconductor material, and the subsequent transit of those carriers through a drift region within the semiconductor form the underlying basis of operation for the IMPATT diode (*impact ionization avalanche transit-time diode*). The IMPATT device, originally proposed by Read [33] and experimentally demonstrated by Johnston *et al.* [17], is one of a family of two-terminal devices which utilize the transit-time delay of carriers to achieve a terminal negative resistance. This negative resistance may be exploited in active microwave and millimeter-wave circuits such as oscillators and amplifiers; in particular, the IMPATT is capable of generating relatively large amounts of pulsed and continuous-wave power in the millimeter-wave spectrum compared with other solid-state sources. Figure 1 illustrates the device structure originally considered by Read. The avalanche occurs in the vicinity of the $n^+ - p$ junction, and the charge carriers generated by the avalanche process transit the drift zone with saturated velocity under the influence of an electric field.

There are two considerations which relate to the particular mode of operation for a member of the general family of negative-resistance transit-time devices: (1) the mechanism by which charge carriers are generated within the semiconductor and (2) the means by which the phase

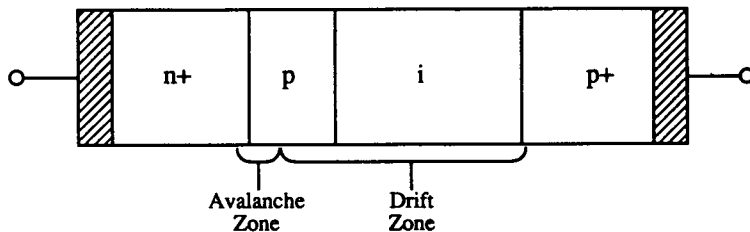


Figure 1. The IMPATT diode structure proposed by Read [33].

of the RF current external to the device is delayed with respect to the voltage, resulting in an effective terminal impedance with a negative real part. The phase delay is established in part by the travel time of carriers through the drift region, although the mechanism of carrier generation may itself inherently introduce an additional significant phase delay, as in those devices which are based on impact avalanche generation. The family of transit-time devices can therefore be delineated primarily according to the means by which carriers are generated; for example, IMPATT devices utilize *impact ionization* for carrier generation, TUNNETT devices depend on carrier injection by *tunneling* [29], and BARITT diodes employ injection across a forward-biased *barrier* region [6]. Table 1 illustrates the family of transit-time devices, indicating the mechanism by which carriers are generated and the predicted or experimentally measured DC-to-RF conversion efficiencies of these devices. The efficiency values in Table 1 are given for illustrative purposes only and should be used with caution, since efficiency is a function of many factors, including the RF voltage amplitude level and operating frequency. The IMPATT is currently the device of choice for efficient, wide-band, high-power millimeter-wave signal generation, whereas other related transit-time devices (such as the TUNNETT diode) have been proposed for operation to terahertz frequencies [43].

As will be discussed in Sections 4 and 5, IMPATT diodes are designed into a microwave circuit which presents a well-defined embedding impedance to the device in order to achieve a desired stable amplifier gain or free-running oscillation frequency. In addition, the circuit design must provide a mechanism for supplying the proper DC current to reverse bias the device in the breakdown region. The value of DC current is important in establishing various performance parameters at the circuit level: the added RF power level, DC-to-RF conversion efficiency, device junction temperature, and median time to failure. At the device level, however, the DC current can be thought of as providing a baseline level of carrier

TABLE I
The Family of Two-Terminal Negative-Resistance Transit-Time Devices

Device type	Injection mechanism	Characteristics	Efficiency ^a	Reference
IMPATT	Impact avalanche	High power High noise	21% Si double drift C 15% Si single drift C	[36]
BARITT	Barrier injection	Low noise Low power	10% C	[40]
TUNNETT	Tunnel injection	Low noise, high frequency Low bias voltage requirement	6% C	[12]
MITATT	Mixed tunnel–avalanche	High-frequency (> 100 GHz) GaAs device	26% C	[12]
QWITT	Quantum-well injection	Wide-bandwidth heterostructure diode	5% M	[20]
<i>Related devices or operating modes</i>				
TRAPATT	Trapped-plasma/ avalanche-triggered transit (related to IMPATT)	High power High efficiency	75% M	[22]
DOVETT	Double-velocity transit time (related to BARITT)	High efficiency High-negative-resistance heterostructure diode	25% C	[38]

^aC, calculated; M, measured. See the text.

generation through impact ionization. The RF voltage waveform which is superposed across a biased IMPATT diode perturbs the generation of carriers in a nonlinear manner, greatly increasing the number of generated carriers as the total device voltage instantaneously swings above the DC level. Figure 2 illustrates the voltage and current waveforms for an avalanche diode, indicating the nonlinear generation of avalanche current; this injected current reaches a maximum at the midpoint of the RF cycle. The external current which flows in response to the drift of the avalanche-generated carriers has a fundamental Fourier component which is displaced in phase by greater than 90° with respect to the applied RF signal. This results in an effective device terminal impedance which has the desired negative real part.

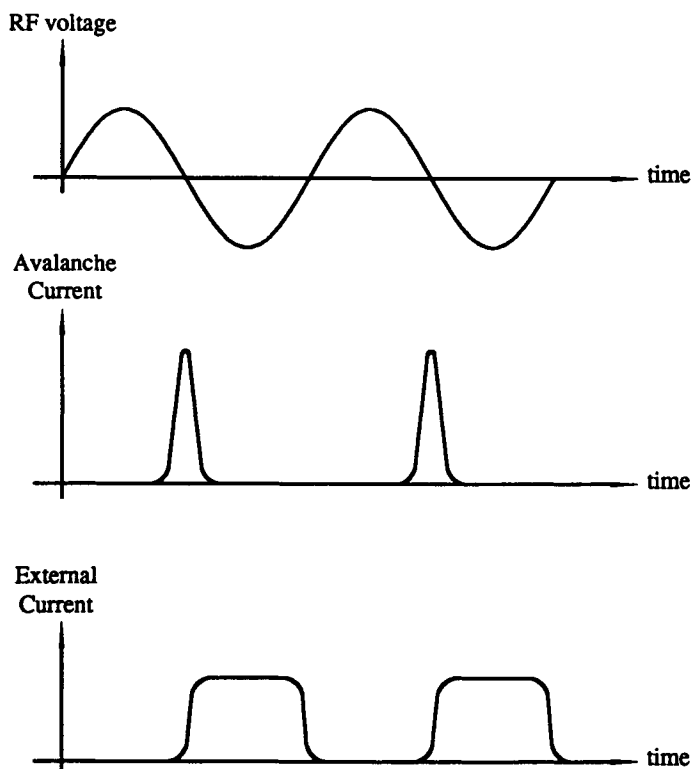


Figure 2. Idealized waveforms which apply to an IMPATT device biased for negative resistance. (After Figure 3 in Haddad et al. [14], © 1970 IEEE, used with permission.)

Avalanche breakdown occurs when the peak electric field in the device is increased to the point at which the so-called ionization integral [40, p. 568] reaches unity,

$$\int_0^W \alpha_n \exp \left[- \int_x^W (\alpha_n - \alpha_p) dx' \right] dx = 1, \quad (1)$$

where W is the width of the depletion region, and α_n and α_p are rates of ionization for electrons and holes, respectively. The electric field distributions within two typical IMPATT device structures are shown in Figure 3; the maximum field (and the region of maximum thermal stress) occurs at the device junction.

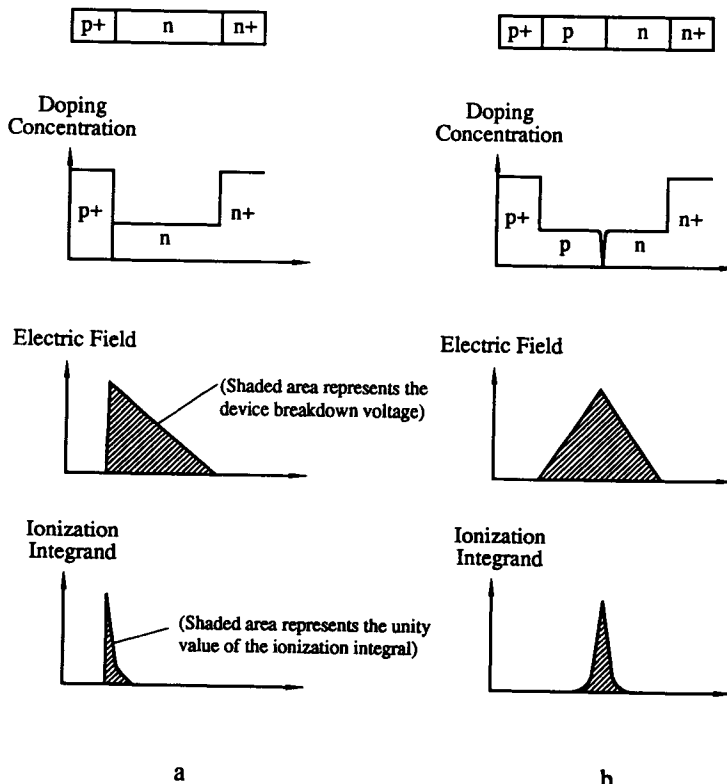


Figure 3. Sketch of the doping profile, electric-field distribution, and ionization integrand associated with a DC-biased IMPATT. (a) Single drift; (b) double drift. (After Figure 2, p. 570, in Sze [40]. *Physics of Semiconductor Devices*, 2nd Edition, Copyright © 1981 by John Wiley & Sons, Inc., reprinted by permission of John Wiley & Sons, Inc.)

2. IMPATT Diode Fabrication

From a device point of view, obtaining the optimum performance characteristics from an IMPATT diode depends on two primary considerations: proper device design and optimum packaging. Device design considerations require that the material profile and device geometry be correctly chosen to provide maximum generated microwave power at the operating frequency. Packaging considerations dictate that the thermal resistance from the device junction to the ambient environment be as low as possible to increase device reliability. These considerations require that materials with very high thermal conductivity such as diamond be used in mounting the device. This is an especially important concern with IMPATTs fabricated from gallium arsenide (GaAs), for example, which has an approximate thermal conductivity of 0.55 W/cm-K at 300 K [3], less than half that of silicon (1.24 W/cm-K). Values of thermal conductivity, along with other relevant material properties, are tabulated in Table 2 for materials typically used in the fabrication of IMPATT devices.

The material profile originally proposed by Read consists of an $n^+ - p - i - p^+$ structure (the so-called "Read diode"); state-of-the-art commercial devices, however, are most commonly fabricated with single-drift or double-drift profiles. Figure 4 illustrates various typical IMPATT profiles which have been discussed in the literature [44]. (Other related variations, such as the so-called hybrid-Read profile, have also been investigated experimentally [45].) If the device area is held constant, the double-drift profile offers the advantage of lower device capacitance and higher-frequency operation compared with single-drift designs, due to greater interelectrode spacing. Alternatively, if the device capacitance (i.e., impedance) is fixed, the double-drift device can be fabricated with a greater junction area and the capability of higher power dissipation than can the single-drift design.

Device fabrication begins with the growth, implantation, or diffusion of the proper profile onto a semiconductor substrate. A double-drift profile may be created by first growing an n -type epitaxial layer onto an n^+ substrate. A p -layer is subsequently defined by diffusion or ion implantation, followed by a highly doped p^+ cap layer which serves to minimize the resistance to the external metal contact. A number of alternative techniques exist for the creation of the proper device profiles: diffusion and ion-implantation processes are inexpensive techniques, but are incapable of realizing extremely sharp, well-defined profiles. Epitaxial growth techniques, which involve the growth of surface layers onto a substrate, are more precise at the expense of greater cost. Metal-organic chemical vapor deposition (MOCVD) and molecular-beam epitaxy (MBE)

TABLE 2
Properties of Materials Used in the Fabrication of Microwave IMPATT Devices and Circuits

Material	Semiconductor substrate material				Mobility (cm ² /V-s) ^a		Density (g/cm ³) ^a
	Thermal conductivity (W/cm-K) ^a	Electrical resistivity (Ω-cm) ^{a, b}	Dielectric constant	Bandgap (eV) ^a	Electrons	Holes	
Silicon	1.24	2.3×10^5	11.9	1.12	1500	450	2.33
Gallium arsenide	0.55	1.0×10^8	13.1	1.42	8500	400	5.32
Indium phosphide	0.80	8×10^{-3}	12.4	1.35	4600	150	4.79
Germanium	0.64	47	16.0	0.66	3900	1900	5.32
Other materials							
Material	Thermal conductivity (W/cm-K) ^a	Electrical resistivity (10^{-8} Ω-m) ^{a, b, c}	Melting point (°C)	Boiling point (°C)	Specific gravity ^a		
Ohmic contact metals							
Copper	4.01	1.71	1085	2563	8.96		
Germanium	0.60	See above	938	2834	5.32		
Gold	3.18	2.26	1064	2857	~ 19.3		
Nickel	0.91	7.12	1455	2914	8.90		
Palladium	0.72	10.73	1555	2964	12.02		
Platinum	0.72	10.70	1769	3827	21.45		
Titanium	0.22	39	1670	3289	4.54		
Zinc	1.16	6.01	420	907	7.13		
Heat sinking / packaging materials							
Aluminum	2.37	2.71	660	2520	2.70		
Copper	4.01	1.71	1085	2563	8.96		
Diamond (Type IIa)	23.20	^d	~ 3550	—	3.51		

Note. Data tabulated from Lide [25], Dean [8], and Williams [42].

^aValues assume a temperature of 298 K.

^bNote the different units for semiconductors /metals.

^cSemiconductor resistivities for intrinsic material.

^dRelative dielectric constant, 5.5 at 0.1 GHz; intrinsic resistivity, 2.7 Ω-m.

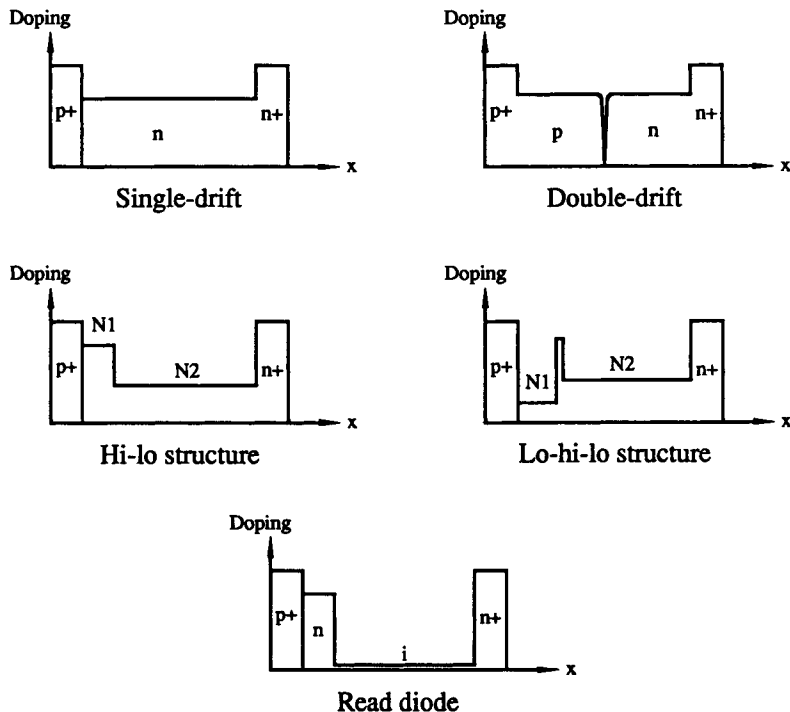


Figure 4. Typical IMPATT device profiles.

are two major epitaxial growth processes frequently used in the gallium arsenide industry. An MBE growth process is used in the design of a related transit-time device, the quantum-well-injection and transit-time (QWITT) diode, which depends on the growth of a very thin (50 Å) GaAs layer sandwiched between two 17 Å AlAs barrier layers [20]. Recent experimental IMPATT designs based on MBE-grown multiquantum well structures [46] and heterojunction IMPATTs [47] have been fabricated and characterized. It may be expected that similar complex IMPATT profiles and heterojunction-based designs will offer future advantages in frequency and RF-power generating capability. Table 3 is a table of various technologies which have been employed in the growth or fabrication of IMPATT-active layers. In addition, donor and acceptor impurity elements are also listed for GaAs and Si.

After the device profile has been established, external ohmic contacts are metalized onto the material by a thin-film metal evaporation process (such as electron-beam or thermal evaporation) or RF sputtering. For

TABLE 3
Technologies Used in IMPATT Active-Layer Fabrication and Donor/Acceptor
Elements for GaAs and Si

Substrate fabrication technology	Material	Reference
Diffusion/implantation		
Diffusion	Silicon	[23]
Ion implantation	Silicon	[35]
	Gallium arsenide	[40, p. 605]
Epitaxial growth		
Molecular-beam epitaxy (MBE)	Silicon	[26]
	Gallium arsenide	[1]
Low-temperature vapor-phase epitaxy (LTVPE)	Gallium arsenide	[24]
Metallorganic chemical vapor deposition (MOCVD)	Gallium arsenide	[4]
Material	Donor element (<i>n</i> -type)	Acceptor element (<i>p</i> -type)
Gallium arsenide	Silicon Selenium	Beryllium Zinc Carbon
Silicon	Phosphorus Arsenic Antimony	Boron Aluminum Gallium Indium

silicon devices, chrome–platinum–gold, copper–platinum–gold, or titanium–gold metalizations have been used to form ohmic contacts to *n*-type silicon, and platinum silicide may be used to create a *p*-type ohmic contact [35]. For gallium arsenide devices a number of metal systems are available; examples are given in Table 4. Two common systems for GaAs microwave devices are gold–germanium (88% Au, 12% Ge by weight) for *n*-type ohmic contacts and gold–zinc (99% Au, 1% Zn) for *p*-type ohmic contacts, although high-temperature refractory metalizations may be chosen to avoid undesirable semiconductor/contact-metal interdiffusion for high-temperature IMPATT operation. After deposition, the metal film is heated to the eutectic temperature to alloy the ohmic metal to the semiconductor. Because of the important relationship between contact resistance and device performance at millimeter-wave frequencies, extensive efforts—many of which are of a proprietary nature—have been

TABLE 4
Example Metal Systems Used in Ohmic Contact Formation on GaAs

Metal system	Composition	Alloy/ sinter temperature (°C)	Comments	Reference
Ohmic contacts to <i>n</i> -type GaAs				
Ag-In	75% Ag, 25% In	500		[28]
Ag-In-Ge	90% Ag, 5% In, 5% Ge	600		[7]
Ag-Sn	98% Ag, 2% Sn	550–650		[21]
Au-Ge-Ni	12% Ge alloy; Ni	480		[9]
Au-Sn	20% Sn	450		[34]
Au-Te	2% Te	500		[34]
In-Au	90% In	550		[31]
Pd-Ge		500 (2 h)	High-temperature ohmic	[37]
Ohmic contacts to <i>p</i> -type GaAs				
Ag-In	25% In	500		[28]
Ag-In-Zn	80% Ag, 10% In, 10% Zn	600		[7]
Au-Be	1% Be			[16]
Au-Zn				[13]
Pt-Ti			High temperature (500°C)	[19]

Note. Adapted from Williams [42, Table 11.2, p. 219], used with permission of Artech House, Inc.

undertaken in the study of optimum materials and processes for providing minimum ohmic contact resistance at the device/contact interface.

An overlayer of gold may be evaporated, electroplated, or both onto the device contacts to improve the ability for successful wire or ribbon bonding to the device contact pads and to reduce the total contact pad resistance. In many cases, additional metal layers (such as nickel) may be used between the ohmic contact metal film and the gold overlayer.

The individual IMPATT devices are next diced from the wafer and thermocompression bonded onto an appropriate heat sink, such as copper or diamond. Ribbon bonds are used to connect the isolated device terminal to a metallic cap, which may be insulated from the heat sink by a ring or standoff fabricated from ceramic or quartz (for higher frequency operation, above 50 GHz). Mounting, bonding, and assembly of the

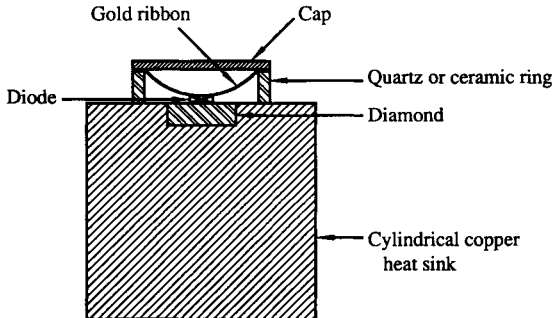


Figure 5. Cross-section of a typical packaged IMPATT device. (From Kuno [23, Figure 24, p. 91], used with permission.)

cathode (or anode) cap onto the insulating ring completes the device fabrication. Figure 5 illustrates a packaged device cross-section which is typical for microwave and millimeter-wave IMPATTs [23].

A number of other experimental processes have been used to fabricate novel IMPATT devices and device geometries for use in monolithic or planar circuits. A monolithic IMPATT design by Bayraktaroglu [1] of Texas Instruments incorporates a varactor diode into a monolithic IMPATT voltage-controlled oscillator; the circuit was fabricated on an MBE-grown gallium arsenide epitaxial layer. A planar silicon ion-implanted IMPATT device was described by Stabile and Lalevic [39]. These experimental devices have comparatively low RF added-power levels; additional developmental effort would be required for these approaches to successfully compete with commercially available discrete IMPATTs.

Other novel semiconductors have been proposed for use as substrate material in the fabrication of IMPATT devices. For example, diamond and silicon carbide (SiC) have been examined as high-temperature materials for the fabrication of high-power IMPATT devices [48], although experimental results are limited.

3. Commercial IMPATT Diode Specifications

Extensive efforts have been applied to the development of commercial IMPATT diodes over the past 20 years, particularly with respect to silicon devices. Gallium arsenide devices have become commercially available in the millimeter-wave range and promise greater DC-to-RF conversion effi-

ciencies than those available with silicon devices; nonetheless, silicon diodes still compete very favorably if one compares overall circuit-level efficiency. Gallium arsenide exhibits an electron mobility and peak electron velocity which are higher than those for silicon. However, it is interesting to note that the delay time between electric field buildup and carrier ionization (the intrinsic response time) is greater for GaAs by an order of magnitude. For this reason it had been suggested [12] that silicon IMPATTs could operate efficiently to over 300 GHz, whereas GaAs devices would be limited to 100 GHz or lower operating frequencies. Experimental investigation [49] suggests that properly designed GaAs IMPATTs may be used at millimeter-wave frequencies of 90 GHz and higher.

IMPATT diode manufacturers use various specifications to describe IMPATT performance. Output power and diode DC-to-RF conversion efficiency are two parameters which are of primary interest. The median time to failure is also usually indicated as a function of junction temperature, determined by the DC voltage and current bias values. Finally, the device junction capacitance must be considered in the design of the microwave circuit.

Table 5 is a summary of IMPATT diode specifications for some commercial devices produced by several of the major diode manufacturers. This table is by no means exhaustive and includes primarily millimeter-wave devices, since IMPATTs remain the preferred solid-state source of continuous-wave power for millimeter-wave frequencies. Caution should be exercised in interpreting or comparing specifications: for example, the DC-to-RF conversion efficiency is strongly dependent on the embedding circuit, and the table entries may reflect an extrapolation of device efficiency from external circuit measurements.

Table 6 is a summary of IMPATT specifications for some commercial devices designed for pulsed operation. This operating mode provides power levels which may exceed CW specifications by an order of magnitude. Numerical simulations suggest that this order-of-magnitude relationship continues into the 100- to 200-GHz range for high-power pulsed silicon IMPATTs [50]; experimental measurements on laboratory devices have yielded power levels as high as 42 W at 96 GHz [51]. Note, however, that pulsed operation requires that careful accounting be made for thermal transients which may occur during operation. A pulsed IMPATT oscillator, for example, may exhibit a frequency chirp as the IMPATT device junction temperature changes significantly over the duration of the pulse.

As mentioned earlier, thermal considerations play an important role in IMPATT circuit design. Complete thermal models for diamond-mounted

TABLE 5
Example Commercial IMPATT Specifications for Continuous-Wave (CW) Devices

	Manufacturer				
	Hughes	Hughes	M/A-COM	Raytheon	Raytheon
Material/profile	Si Double drift	Si Double drift	GaAs Lo-hi-lo	GaAs Double drift	GaAs Double drift
Operating frequency (GHz)	42–46	58–62	14–17	42–46	58–62
CW power (W)	1.0 minimum ^a	1.0 minimum ^a	2.5 minimum	1.4 minimum	1.0 minimum
Efficiency			15% minimum	13% minimum	10% minimum
Junction temperature (°C)	250	250	225 maximum	200 ^b	225 ^b
Operating voltage (V dc)	30–42	24–34	30–40	24.0 typical	20.0 typical
Operating current (mA dc)	—	—	550 maximum	450 typical	500 typical
Breakdown voltage (V dc)	—	—	13–23	13.0 ± 1.0	11.6 ± 0.5
Thermal resistance (°C/W)	—	—	12 maximum	21 maximum	25 maximum
Zero-bias junction capacitance (pF)	1.0–3.0	0.8–3.0	10.0–15.0	3.4 ± 0.1	2.3 ± 0.1

^aDepends on the embedding circuit.

^bJunction temperature rise.

TABLE 6
Example Commercial IMPATT Specifications for Pulsed Devices

	Manufacturer				
	Hughes	Hughes	M/A-COM	Raytheon	GEC-Plessey
Material/profile	Si	Si	GaAs	GaAs	
Operating frequency (GHz)	Double drift 34–36	Double drift 92–96	(lo-)Hi-lo 16.5–17.5	Double drift 33–38	Double drift 31–38
Peak power output (W)	20.0 minimum	20.0 minimum	10.0 minimum	7.0 minimum	20–25
Pulse width (μ s)	—	—	5.0–15.0	0.5 typical	0.25 maximum
Duty cycle	—	—	1.0–10.0%	0.42 typical	1% maximum
Efficiency	^a	^a	14% minimum	12% minimum	4–5%
Junction temperature (°C)	—	—	225 maximum	—	—
Operating voltage (V dc)	—	—	40 nominal	32.0 typical	55 typical
Operating current (A dc)	—	—	2.0 maximum	2.0 typical	14 typical
Breakdown voltage (V dc)	—	—	30 nominal	16.3 \pm 1.1	40 typical
Thermal resistance (°C/W)	—	—	10 maximum	10.5 maximum	—
Zero-bias junction capacitance (pF)	3.5–5.0	2.5–6.5	40 nominal	13.5 \pm 0.5	5.5 maximum ^b

^aDepends on the embedding circuit.

^bAt breakdown.

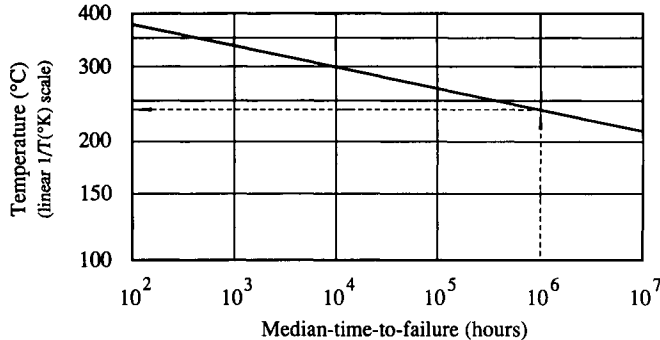


Figure 6. Arrhenius plot for GaAs IMPATT diodes. (After Figure 4 in Hierl et al., High efficiency pulsed GaAs Read IMPATT diodes, Vol. 14, No. 5, 2 March 1978, pp. 155–157, © 1978, IEEE, used with permission.)

IMPATT diodes have been described in the literature [52]. Figure 6 is an example of an Arrhenius plot of diode junction temperature plotted against median time to failure for GaAs IMPATT diodes. The mechanisms responsible for IMPATT failure result in a median time to failure, τ , which satisfies a relationship of the form

$$\tau = \tau_0 \exp(E_A/kT), \quad (2)$$

where the activation energy E_A is about 1.9 eV for GaAs [40, p. 612] and 1.6 eV for silicon [2, p. 107].

4. IMPATT Diode Amplifier Design

The negative resistance associated with a DC-biased IMPATT is commonly used in the design of one-port reflection amplifiers for high-power millimeter-wave applications. Figure 7 illustrates a simplified model of the circuit under consideration; an active one-port amplifier has a reflection gain given by

$$|\Gamma_{in}|^2 = \left| \frac{\Gamma_D - \Gamma_C^*}{1 - \Gamma_D \Gamma_C} \right|^2, \quad (3)$$

where Γ_D denotes the reflection coefficient of the active IMPATT device measured in a system with positive-real normalization impedance Z_0 , and Γ_C represents the circuit reflection coefficient at the device/circuit refer-

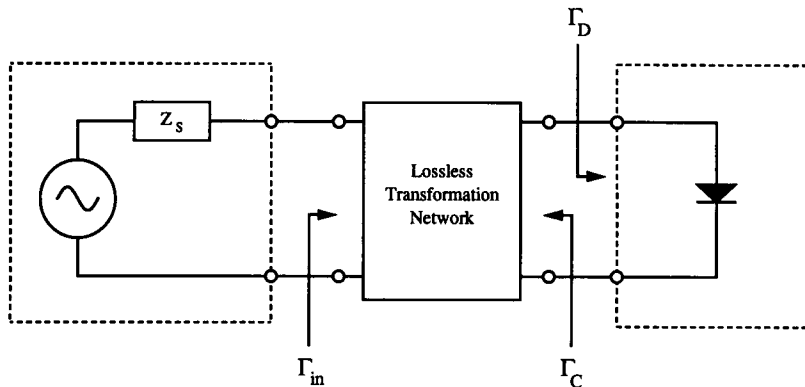


Figure 7. Schematic representation of the device/circuit interface.

ence plane, measured using the same normalization:

$$\Gamma_D = \frac{Z_D - Z_0^*}{Z_D + Z_0} \quad \text{and} \quad \Gamma_C = \frac{Z_C - Z_0^*}{Z_C + Z_0}. \quad (4)$$

Here Z_D and Z_C represent the device impedance and circuit impedance, respectively. Note that $|\Gamma_D| > 1$ for an active device, corresponding to the fact that $\text{Re}(Z_D) < 0$. Furthermore, because IMPATTs are most often used in high-power applications, Z_D should properly be viewed as a large-signal “impedance” (or, more appropriately, describing function) which varies with frequency as well as the amplitude of the RF signal applied to the device, $Z_D \equiv Z_D(\omega, A)$, where ω is the radian frequency and A is the amplitude of the RF signal incident on the device. The impedance of the linear embedding circuit Z_C is a function only of frequency, $Z_C(\omega)$.

It is possible to show that the gain $|\Gamma_{in}|$ is independent of the choice of normalization impedance Z_0 . This implies that the normalization impedance of the measurement system used to characterize the device and circuit is arbitrary—a fortuitous result, as it may allow unstable interaction between the active one-port and the measurement system to be suppressed by the appropriate choice of Z_0 .

Equation (3) indicates that a desired reflection gain may be realized by proper design of circuit impedance Z_C once $Z_D(\omega, A)$ is known. Broad-band amplifier design oftentimes requires the use of wide-band lossless impedance transforming techniques in order to transform a given source impedance Z_S , to the desired Z_C . A single-diode amplifier may consist of an IMPATT one-port reflection amplifier attached to a three-port circula-

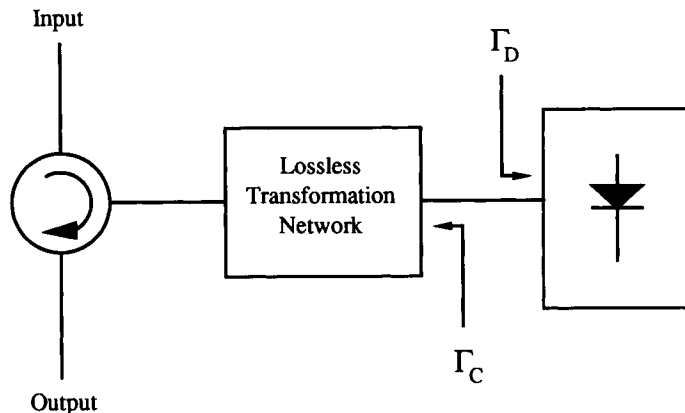


Figure 8. Two-port IMPATT amplifier.

tor to separate incident and amplified reflected waves as shown in Figure 8. In this case the source impedance Z_s is the impedance at the amplifier port of the circulator (ideally a match); the lossless transformation is used to establish the proper circuit impedance Z_c to realize a desired gain. Figure 9 illustrates various cross-sections of typical waveguide-mounting arrangements for millimeter-wave IMPATT diodes. Stepped-waveguide transitions shown in this figure are employed to effect

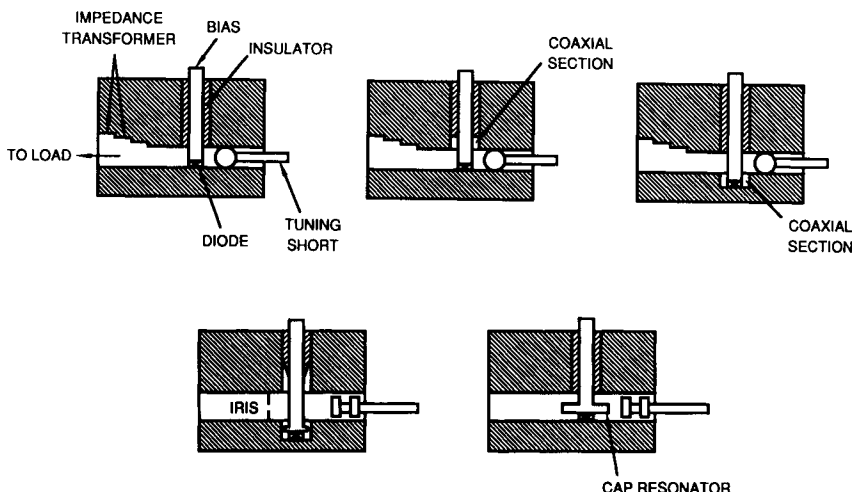


Figure 9. Waveguide mounting configurations for millimeter-wave IMPATTs. (After Kuno [23, Figure 26, p. 95], used with permission.)

the desired impedance transformation from a standard full-height waveguide. Other fixturing schemes have also been proposed. Coaxial fixtures have been employed, for example, in the microwave impedance characterization of IMPATT diodes [53].

Assuming that the measurement system is stable when used to determine the negative-real IMPATT impedance, it will be possible to determine the reflection coefficient Γ_D of the active IMPATT ($|\Gamma_D| > 1$) as a function of frequency and the incident RF amplitude level. The active IMPATT reflection coefficient may be plotted on the reciprocal reflection-coefficient ($1/\Gamma_D$) plane, and constant-gain circles may be plotted as a function of frequency and the RF signal level. The center and radii of these constant-gain circles are given by [32]:

$$C = \left(\left| \frac{|\Gamma_D|^2 |\Gamma_{in}|^2 - |\Gamma_D|^2}{|\Gamma_D|^2 |\Gamma_{in}|^2 - 1} \right| \right) \left[\frac{1}{\Gamma_D} \right] \quad (5)$$

$$R = \left(\left| \frac{|\Gamma_D|^2 - 1}{|\Gamma_D|^2 |\Gamma_{in}|^2 - 1} \right| \right) |\Gamma_{in}|, \quad (6)$$

where $|\Gamma_{in}|$ is the desired gain and Γ_D is the device reflection coefficient, $\Gamma_D \equiv \Gamma_D(\omega, A)$.

If it is desired to maximize the DC-to-RF conversion efficiency, values for RF added power (or generated power), defined as the difference between reflected and incident RF power,

$$\begin{aligned} P_{\text{added}} &= P_{\text{rf, reflected}} - P_{\text{rf, incident}} \\ &= P_{\text{rf, incident}} (|\Gamma_D|^2 - 1), \end{aligned} \quad (7)$$

can be measured as a function of frequency and RF amplitude. At a given frequency a maximum for P_{added} will occur as $P_{\text{rf, incident}}$ is increased, and a corresponding locus $\Gamma_{D,\max}(\omega)$ can be constructed along which added power is maximum. An amplifier design for maximum efficiency consists of using this locus to construct an appropriate impedance-transforming network which provides the desired gain over the frequency range of interest.

Throughout this discussion, the effect of IMPATT bias on device negative-real impedance has been ignored. In the practical design of a high-power amplifier, the choice of DC bias current is not arbitrary; instead the DC current is chosen to be the maximum value consistent with a specified device operating lifetime determined by thermal considerations. Knowledge of the thermal impedances associated with the physical IMPATT circuit environment along with the DC dissipation allows the

junction temperature and median time to failure to be established (Figure 6). The preferred method for providing IMPATT DC bias uses a DC source with high source impedance (i.e., constant-current biasing). However, investigation suggests that reducing the DC source impedance (so-called "loadline biasing") results in improved circuit performance over variations in temperature [54].

In Section 3 specifications of typical RF generated power levels are given for some commercial devices. The generation of higher power levels than are available from a single IMPATT diode requires combining the added power from several devices, using one of a number of techniques. A series cascade of individual amplifiers may suffice for relatively low levels of power (using typically no more than two to four single-IMPATT amplifier stages in series). Parallel (hybrid) combining techniques at the circuit level are quite common for generating significant amounts of power; these techniques can be categorized as either resonant or nonresonant and are included in the summary in Figure 10.

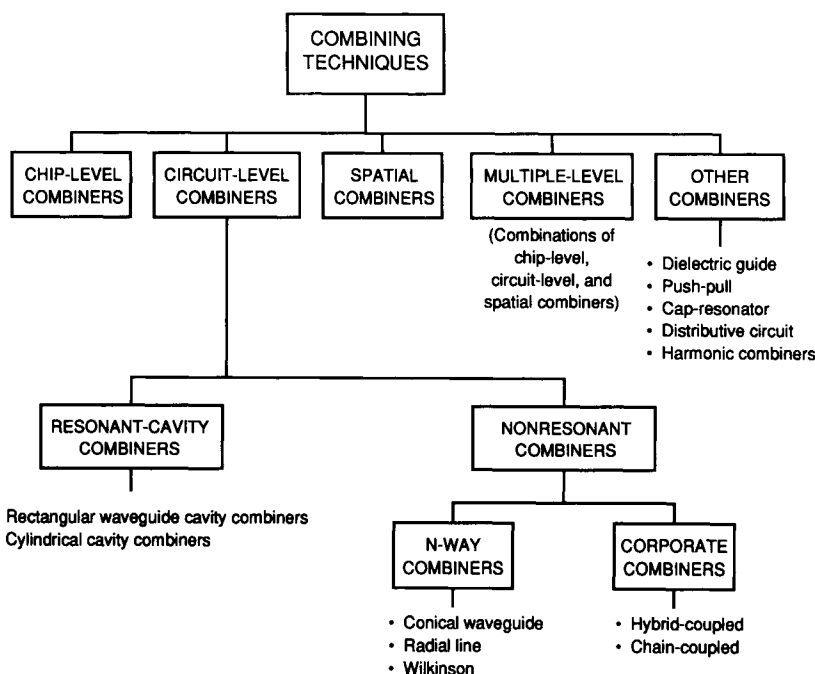


Figure 10. Power-combining techniques. (After Figure 1 in Chang and Sun [5], © 1983 IEEE, used with permission.)

5. IMPATT Diode Oscillator Design

IMPATT diodes also find common use as the active element in high-power microwave and millimeter-wave oscillators. The design of these circuits closely parallels that of IMPATT-based reflection amplifiers; in fact, injection-locked IMPATT oscillators (ILOs) are often considered an acceptable alternative to stable power amplifiers if free-running ILO output power can be tolerated in the absence of an input signal.

The circuit representation of the interface between the circuit and the active device (Figure 7) also applies to the simple negative-resistance oscillator circuit. From the expression for the gain of an active one-port IMPATT,

$$|\Gamma_{in}|^2 = \left| \frac{\Gamma_D - \Gamma_C^*}{1 - \Gamma_D \Gamma_C} \right|^2, \quad (8)$$

it is evident that choosing $\Gamma_C = 1/\Gamma_D$ at a specific frequency will result in a finite output signal in the absence of a driving incident signal. As discussed in the previous section, IMPATT large signal impedance is a function of frequency and RF amplitude; hence the value of Γ_C will establish both the oscillator frequency and the signal amplitude. For maximum DC-to-RF conversion efficiency, the appropriate choice for $\Gamma_C = 1/\Gamma_D$ would correspond to the point on the device characteristics associated with maximum P_{added} [defined in Equation (7)] at the given operating frequency.

In Figure 11, the inverse reflection coefficient $1/\Gamma_D$ for the device is plotted on the reflection coefficient plane as a function of frequency and incident signal level A ; note that $|1/\Gamma_D| < 1$ for an active device. The negative of the device impedance, $-Z_D(\omega, A)$, is plotted along with circuit impedance, $Z_C(\omega)$, on the impedance plane. The intersection of the circuit and device characteristics establishes the operating frequency and amplitude for the oscillator.

The behavior of the impedance loci near the intersection point determines the stability and noise properties of an IMPATT oscillator, as well as the injection-locking characteristics of an IMPATT ILO. For small injection signals, the total locking bandwidth $\delta\omega_L$ of an ILO is given by [41, 60]

$$\delta\omega_L = \frac{2\omega_0}{Q_e} \sqrt{\frac{P_i}{P_o}} \frac{1}{\sin \theta}, \quad (9)$$

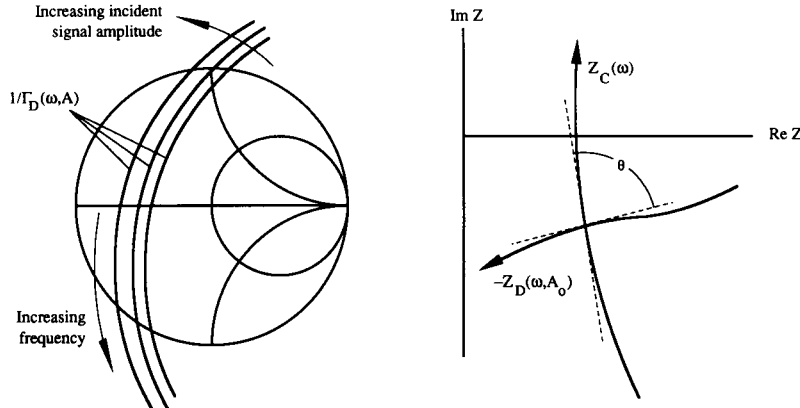


Figure 11. Sketch of the inverse reflection coefficient and impedance characteristics for IMPATT one-port reflection oscillator design.

where P_i is the injected power, P_o is the oscillator output power, and Q_e is the quality factor of the external resonant circuit. The angle θ is defined in Figure 11.

A number of modern numerical approaches have been used in computer-aided IMPATT oscillator design; these techniques are typically based on a solution of the equations describing the IMPATT device physics, subject to circuit-imposed boundary conditions [55]. The device/circuit equations may be solved generally by using a time-domain approach [56] or by a nonlinear hybrid time-domain/frequency-domain algorithm [57].

Figure 12 illustrates the maximum power capability of state-of-the-art IMPATT continuous-wave (CW) oscillators as a function of frequency. Below 100 GHz, output power is limited by thermal considerations, resulting in an f^{-1} frequency dependence. Above 100 GHz, limitations due to electronic constraints such as packaging and parasitic effects result in an f^{-2} frequency behavior.

Pulsed IMPATT oscillators are capable of providing power levels over an order of magnitude higher than those for CW oscillators. Earlier discussions which described the importance of thermal considerations also apply to pulsed oscillators; in particular, these oscillators will exhibit a frequency chirp over the duration of the pulse as the IMPATT device junction increases in temperature. Bias circuits which increase DC bias current during the “on” pulse can be designed to shift the device impedance in such a manner so as to compensate for thermal effects, resulting in a minimum frequency chirp.

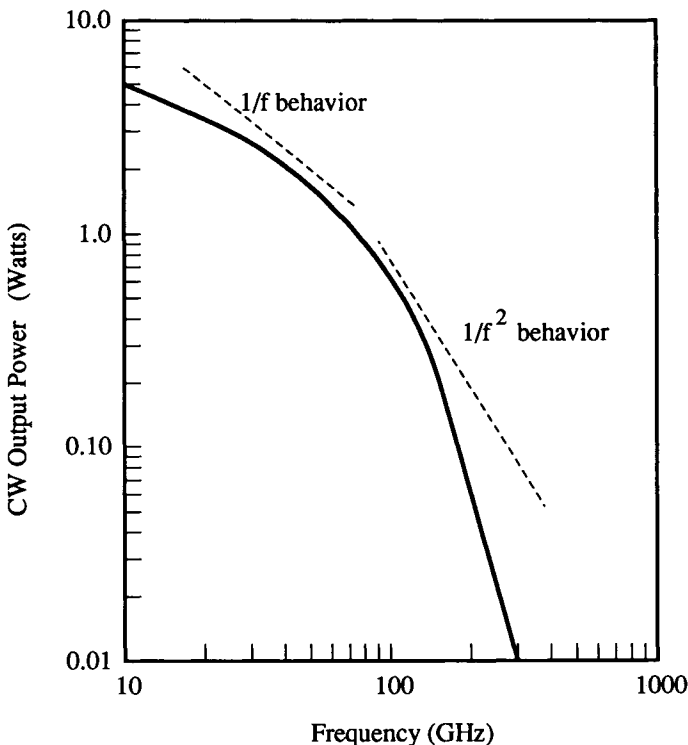


Figure 12. Maximum power capability for IMPATT CW oscillators. (From Figure 3.14 in Bhartia and Bahl, *Millimeter Wave Engineering and Applications*, p. 100 Copyright © 1984 by John Wiley & Sons, Inc., reprinted by permission of John Wiley & Sons, Inc.)

6. Noise Characteristics of IMPATT Diode Oscillators and Amplifiers

The avalanche process used to generate charge carriers in an IMPATT is an inherently noisy process; hence IMPATTs are traditionally used in high-power applications for which low-noise, low-power solid-state devices such as Gunn diodes are inappropriate. As indicated in Table 1, a number of transit-time devices are capable of providing superior (lower) noise performance by virtue of alternate carrier generation mechanisms. In fact, IMPATT devices have been studied both theoretically and experimentally as solid-state *sources* of noise for use at millimeter-wave frequencies. Such sources are capable of broad bandwidths and high excess noise ratios [58, 59].

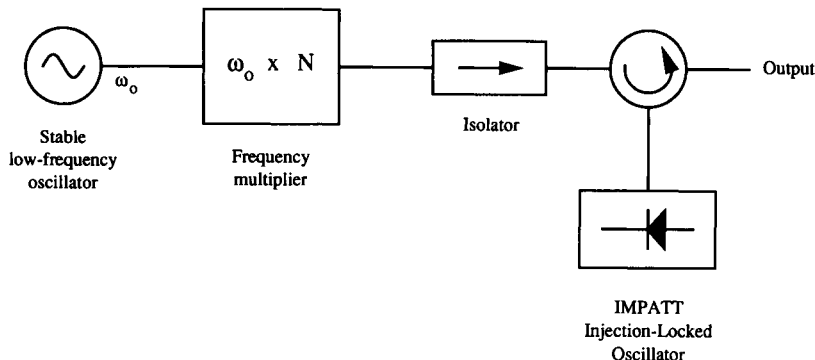


Figure 13. Block diagram of an injection-locked IMPATT oscillator.

The noise properties of a millimeter-wave IMPATT oscillator can be improved by phase or injection locking, as is also possible with low-frequency oscillators. Figure 13 illustrates the block diagram of a low-noise injection-locked system; the harmonic of a stable low-noise reference tone is used as the injection signal for locking the IMPATT ILO. Improvements in the signal-to-noise-ratio of over 30 dB are indicated for a phase-locked IMPATT oscillator [23].

Measured FM noise deviation for a low-noise W-band (75–110 GHz) IMPATT oscillator is illustrated in Figure 14 [10]; the circuit is based on a single-drift GaAs IMPATT diode. From the discussion on oscillator design, it is evident that the noise behavior of these oscillators is influenced by the circuit quality factor. The noise measure of an IMPATT oscillator may be defined as [18, 30]

$$M \equiv \frac{\Delta f_{\text{rms}}^2 Q_{\text{ex}}^2}{f_0^2 k T_0 B} P_0, \quad (10)$$

where Q_{ex} is the external circuit quality factor, Δf_{rms} is the FM noise deviation, B is the measurement bandwidth, and k and T_0 are, respectively, Boltzmann's constant and the effective device temperature in Kelvins. P_0 and f_0 are, respectively, the oscillator output power and frequency. The noise measure increases with output power and is greater for silicon diodes than for GaAs devices. Noise measure values recorded for a 50-mW, 94-GHz IMPATT oscillator are 23 dB for GaAs diodes and 33 dB for silicon diodes [10]. This agrees with the trend observed for 50-GHz oscillators which exhibit the same 10-dB degradation in the noise measure for silicon devices [30]. Other authors indicate similar higher

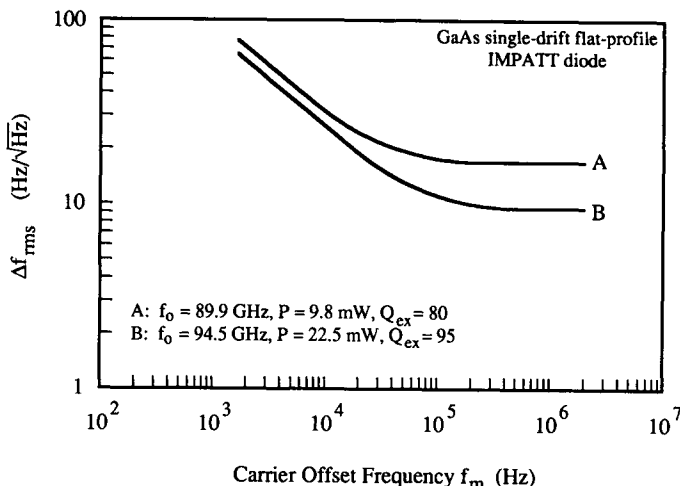


Figure 14. Measured FM noise deviation as a function of carrier offset frequency. (After Figure 2 in Eisele [10], © 1990, IEE, used with permission.)

noise characteristics with silicon devices: 40 dB versus 25 dB (silicon versus GaAs) for small-signal amplifiers and 55 dB versus 35 dB (silicon versus GaAs) for oscillators [40].

Measurements of AM noise characteristics are available for the M/A-COM commercial CW devices described in Section 3. The double-sideband AM noise-to-signal ratio in a 100-Hz bandwidth is typically –136 dB and is flat for frequencies 1 to 100 kHz away from the carrier frequency [27].

References

- [1] B. Bayraktaroglu, V-Band monolithic IMPATT VCO, *IEEE MTT—S Int. Microwave Symp. Dig.*, New York, Vol. II, pp. 687–690, 1988.
- [2] P. Bhartia and I. J. Bahl, “Millimeter Wave Engineering and Applications.” New York: John Wiley & Sons, 1984.
- [3] J. S. Blakemore, Semiconducting and other major properties of gallium arsenide, *J. Appl. Phys.*, 53, No. 10, pp. R123–R181, 1982.
- [4] N. Camilleri and B. Bayraktaroglu, Monolithic millimeter-wave IMPATT oscillator and active antenna, *IEEE MTT—S Int. Microwave Symp. Dig.*, New York, Vol. II, pp. 955–958, 1988.
- [5] K. Chang and C. Sun, Millimeter-wave power-combining techniques, *IEEE Trans. Microwave Theory Tech.*, Vol. MTT-31, pp. 91–107, 1983.
- [6] D. J. Coleman, Jr. and S. M. Sze, A low-noise metal-semiconductor-metal (MSM) microwave oscillator, *Bell Syst. Tech. J.*, Vol. 50, pp. 1695–1699, 1971.

- [7] R. H. Cox and H. Strack, Ohmic contacts for GaAs devices, *Solid-State Electron.*, Vol. 10, pp. 1213–1218, 1967.
- [8] J. A. Dean, ed., *Lange's Handbook of Chemistry*, 13th Ed. New York: McGraw-Hill, 1985.
- [9] W. D. Edwards, W. A. Hartman, and A. B. Torrens, Specific contact resistance of ohmic contacts to gallium arsenide, *Solid-State Electron.*, Vol. 15, pp. 387–392, 1972.
- [10] H. Eisele, GaAs W-band IMPATT diodes for very low-noise oscillators, *Electron. Lett.*, Vol. 26, pp. 109–110, 1990.
- [11] M. E. Elta, H. R. Fetterman, W. V. Macropoulos, and J. J. Lambert, 150 GHz GaAs MITATT source, *IEEE Electron Device Lett.*, Vol. EDL-1, pp. 115–116, 1980.
- [12] M. E. Elta and G. I. Haddad, High-frequency limitations of IMPATT, MITATT, and TUNNETT mode devices, *IEEE Trans. Microwave Theory Tech.*, Vol. MTT-27, pp. 442–449, 1979.
- [13] H. J. Gopen and A. Y. C. Yu, Ohmic contacts to epitaxial pGaAs, *Solid-State Electron.*, Vol. 14, pp. 515–517, 1971.
- [14] G. I. Haddad, P. T. Greiling, and W. E. Schroeder, Basic principles and properties of avalanche transit-time devices, *IEEE Trans. Microwave Theory Tech.*, Vol. MTT-18, pp. 752–772, 1970.
- [15] T. L. Hierl, J. J. Berenz, J. Kinoshita, and I. V. Zubeck, High efficiency pulsed GaAs Read IMPATT diodes, *Electron. Lett.*, Vol. 14, pp. 155–157, 1978.
- [16] T. Ishida, S. Wako, and S. Ushio, Contact and interconnect formation on compound semiconductor devices by ionized-cluster beam deposition, *Thin Solid Films*, Vol. 39, pp. 227–235, 1976.
- [17] R. L. Johnston, B. C. DeLoach, Jr., and B. G. Cohen, A silicon diode microwave oscillator, *Bell Syst. Tech. J.*, Vol. 44, pp. 369–372, 1965.
- [18] J. Josenhans, Noise spectra of Read diode and Gunn oscillators, *Proc. IEEE*, Vol. 54, pp. 1478–1479, 1966.
- [19] A. Katz, C. R. Abernathy, and S. J. Pearton, Pt/Ti ohmic contacts to ultrahigh carbon-doped p-GaAs formed by rapid thermal processing, *Appl. Phys. Lett.*, Vol. 56, pp. 1028–1030, 1990.
- [20] V. P. Kesan, A. Mortazawi, D. R. Miller, V. K. Reddy, D. P. Neikirk, and T. Itoh, Microwave and millimeter-wave QWITT diode oscillators, *IEEE Trans. Microwave Theory Tech.*, Vol. 37, pp. 1933–1941, 1989.
- [21] S. Knight and C. Paola, in *Ohmic Contacts to Semiconductors* (B. Schwartz, ed.), p. 102. New York: Electrochem. Soc., 1969.
- [22] D. F. Kostishack, UHF avalanche diode oscillator providing 400 watts peak power and 75 percent efficiency, *Proc. IEEE*, Vol. 58, pp. 1282–1283, 1970.
- [23] H. J. Kuno, in *Infrared and Millimeter Waves*, Vol. 1: *Sources of Radiation* (K. J. Button, ed.), pp. 55–128. New York: Academic Press, 1979.
- [24] B. D. Lauterwasser, Growth of GaAs millimeter wave IMPATT diode material using low temperature vapor phase epitaxy, *J. Cryst. Growth*, Vol. 88, pp. 527–534, 1988.
- [25] D. R. Lide, ed., *CRC Handbook of Chemistry and Physics*, 72nd Ed. Boca Raton, FL: CRC Press, 1991.
- [26] J.-F. Luy, A. Casel, W. Behr, and E. Kasper, A 90-GHz double-drift IMPATT diode made with Si MBE, *IEEE Trans. Electron Devices*, Vol. ED-34, pp. 1084–1089, 1987.
- [27] M/A-COM, Inc., “Semiconductor Products Master Catalog,” Burlington, MA, 1988.
- [28] H. Matino and M. Tokunaga, Contact resistances of several metals and alloys to GaAs, *J. Electrochem. Soc.*, Vol. 116, pp. 709–711, 1969.
- [29] J.-I. Nishizawa, K. Motoya, and Y. Okuno, GaAs TUNNETT diodes, *IEEE Trans. Microwave Theory Tech.*, Vol. MTT-26, pp. 1029–1035, 1978.

- [30] H. Okamoto, Noise characteristics of GaAs and Si IMPATT diodes for 50-GHz range operation, *IEEE Trans. Electron Devices*, Vol. ED-22, pp. 558–565, 1975.
- [31] C. R. Paola, Metallic contacts for gallium arsenide, *Solid-State Electron.*, Vol. 13, pp. 1189–1197, 1970.
- [32] D. F. Peterson, A device characterization and circuit design procedure for realizing high-power millimeter-wave IMPATT-diode amplifiers, *IEEE Trans. Microwave Theory Tech.*, Vol. MTT-21, pp. 681–689, 1973.
- [33] W. T. Read, Jr., A proposed high-frequency negative-resistance diode, *Bell Syst. Tech. J.*, Vol. 37, pp. 401–446, 1958.
- [34] V. L. Rideout, A review of the theory and technology for ohmic contacts to group III-V compound semiconductors, *Solid-State Electron.*, Vol. 18, pp. 541–550, 1975.
- [35] T. E. Seidel, R. E. Davis, and D. E. Iglesias, Double-drift-region ion-implanted millimeter-wave IMPATT diodes, *Proc. IEEE*, Vol. 59, pp. 1222–1228, 1971.
- [36] T. E. Seidel, W. C. Niehaus, and D. E. Iglesias, Double-drift silicon IMPATT's at X Band, *IEEE Trans. Electron Devices*, Vol. ED-21, pp. 523–531, 1974.
- [37] A. K. Sinha, T. E. Smith, and H. J. Levinstein, Sintered ohmic contacts to *n*- and *p*-type GaAs, *IEEE Trans. Electron Devices*, Vol. ED-22, pp. 218–224, 1975.
- [38] J. E. Sitch, and P. N. Robson, Efficiency of BARITT and DOVETT Oscillators, *Solid State Electron Devices*, Vol. 1, 1976.
- [39] P. J. Stabile and B. Lalevic, Lateral IMPATT diodes, *IEEE Electron Device Lett.*, Vol. 10, pp. 249–251, 1989.
- [40] S. M. Sze, *Physics of Semiconductor Devices*, 2nd Ed. New York: John Wiley & Sons, 1981.
- [41] H.-J. Thaler, G. Ulrich, and G. Weidmann, Noise in IMPATT diode amplifiers and oscillators, *IEEE Trans. Microwave Theory Tech.*, Vol. MTT-19, pp. 692–705, 1971.
- [42] R. Williams, *Modern GaAs Processing Methods*. Norwood, MA: Artech House, 1990.
- [43] G. I. Haddad, J. R. East, and C. Kidner, Tunnel transit-time (TUNNETT) devices for terahertz sources, *Microwave Opt. Technol. Lett.*, Vol. 4, No. 1, pp. 23–29, 1991.
- [44] C. Dalle and P.-A. Rolland, Read versus flat doping profile structures for the realization of reliable high-power, high-efficiency 94-GHz IMPATT sources, *IEEE Trans. Microwave Theory Tech.*, Vol. 38, pp. 366–372, 1990.
- [45] C. K. Pao, J. C. Chen, R. K. Rolph, A. T. Igawa, and M. I. Herman, Millimeter-wave double-drift hybrid Read profile Si IMPATT diodes, *IEEE MTT—S Int. Microwave Symp. Dig.*, Dallas, Vol. 2, pp. 927–930, 1990.
- [46] C. C. Meng, H. R. Fetterman, D. C. Streit, T. R. Block, and Y. Saito, GaAs/AlGaAs multiquantum well structures applied to high frequency IMPATT devices, *IEEE MTT—S Int. Microwave Symp. Dig.*, Atlanta, Vol. 2, pp. 539–542, 1993.
- [47] M. J. Bailey, Heterojunction IMPATT diodes, *IEEE Trans. Electron Devices*, Vol. ED-39, pp. 1829–1834, 1992.
- [48] R. J. Trew, J.-B. Yan, and P. M. Mock, The potential of diamond and SiC electronic devices for microwave and millimeter-wave power applications, *Proc. IEEE*, Vol. 79, pp. 598–620, 1991.
- [49] H. Eisele, GaAs W-Band IMPATT diodes: The first step to higher frequencies, *Microwave J.*, Vol. 34, No. 5, pp. 275–276, 279–282, 1991.
- [50] C.-C. Chen, R. K. Mains, and G. I. Haddad, High-power generation in IMPATT devices in the 100-200-GHz range, *IEEE Trans. Electron Devices*, Vol. 38, pp. 1701–1705, 1991.
- [51] W. Behr and J. F. Luy, High-power operation mode of pulsed IMPATT diodes, *IEEE Electron Device Lett.*, Vol. 11, pp. 206–208, 1990.
- [52] G. Csanyi, Reliability critical thermal model for double-drift IMPATT diodes on diamond heat sinks, *Qual. Reliab. Eng. Int.*, Vol. 6, No. 2, pp. 73–84, 1990.

- [53] G. P. Monahan, A. S. Morris, and M. B. Steer, A coaxial test fixture for characterizing low-impedance microwave two-terminal devices, *Microwave Opt. Technol. Lett.*, Vol. 6, pp. 197–200, 1993.
- [54] R. L. Eisenhart, A better biasing technique for IMPATT diodes, *IEEE MTT—S Int. Microwave Symp. Dig., Boston*, Vol. 3, pp. 1191–1194, 1991.
- [55] V. Stojiljkovic, M. J. Howes, and V. Postoyalko, A new approach in CAD of MM-wave IMPATT oscillators, *IEEE MTT—S Int. Microwave Symp. Dig., Boston*, Vol. 2, pp. 603–605, 1991.
- [56] W. Anzill, T. Goeller, F. X. Kaertner, P. Russer, and J. Buechler, Self-consistent simulation of a high-power 73 GHz integrated IMPATT oscillator, *Electron. Lett.*, Vol. 26, pp. 1697–1698, 1990.
- [57] T. Goeller, M. Schwab, and P. Russer, Efficient simulation of millimeter-wave IMPATT oscillators by FATE, a combined time- and frequency-domain method, *IEEE Microwave Guided Wave Lett.*, Vol. 1, pp. 343–345, 1991.
- [58] M. M. Radmanesh and J. M. Cadwallader, Millimeter-wave noise sources at V-Band (50 to 75 GHz), *Microwave J.*, Vol. 36, No. 9, pp. 128, 130, 132–134, 1993.
- [59] M. M. Radmanesh and J. M. Cadwallader, Solid-state noise sources at mm-waves: theory and experiment, *Microwave J.*, Vol. 34, No. 10, pp. 125–128, 130, 133, 1991.
- [60] K. Kurokawa, Some basic characteristics of broadband negative resistance oscillator circuits, *Bell. Syst. Tech. J.*, Vol. 48, pp. 1937–1955, 1969.

This Page Intentionally Left Blank

Microwave Transistor Oscillators and Amplifiers

Aksel Kiiss

Part A: AMPLIFIERS

I. Introduction — Amplifier Classification

In designing an amplifier for a particular application, the designer has to consider the following amplifier performance parameters:

- Frequency coverage—amplifier bandwidth,
- Gain—gain flatness,
- Noise figure,
- Input/output match—VSWR/return loss,
- Dynamic range,
- Unconditional stability,
- Power consumption,
- Maximum safe input power,
- Amplitude/phase tracking,
- Performance variation as a function of temperature, and
- Size.

There are applications in which all of the above-listed characteristics are important and critical. There are other applications in which only one

or two key parameters are needed. There are also cases in which not all of the requirements can be met simultaneously and design compromises have to be made.

It is almost impossible to universally classify amplifiers by their noise figure, dynamic range, or frequency coverage. Definitions and terms vary from manufacturer to manufacturer.

For discussion and design purposes we can classify amplifiers by dynamic range and frequency coverage. The dynamic range classification divides the amplifiers into low-noise and power amplifiers. Each of the above amplifier subgroups can, in turn, be classified by bandwidths:

- Moderate,
- Classical octave band,
- Multi octave, and
- Ultra-wide-band designs.

Low-noise amplifiers normally are used for sensitive receiver applications. In these applications the amplifier dynamic range is not a critical requirement. An output power capability on the order of +10 to +13 dBm is sufficient. The amplifier gain requirements normally exceed 30 dB.

2. Low-Noise Amplifiers

Moderate Bandwidth Amplifiers

The frequency allocations for radar, satellite, and terrestrial communications are limited to 5–10% of the center frequency bandwidth. Moderate-bandwidth amplifiers are designed for these applications. These designs require a good input/output match, a low noise figure, and constant gain as a function of frequency. Typically, the input/output return loss is on the order of 14 to 25 dB, and gain ripple ranges from ± 0.15 to ± 0.50 dB for commercially available amplifiers. Noise figures range from less than 0.5 dB in the L band to 3.0 dB in the Ka band.

Octave Band Designs

Octave band amplifier designs perform to somewhat more relaxed specifications when compared with the moderate-bandwidth models. Input/output return loss specifications are in the 10- to 15-dB range, and the amplifier gain ripple increases to ± 1.0 dB. Noise figures increase by a few tenths of a decibel to 0.5 dB in the Ka band when compared with the moderate-bandwidth designs.

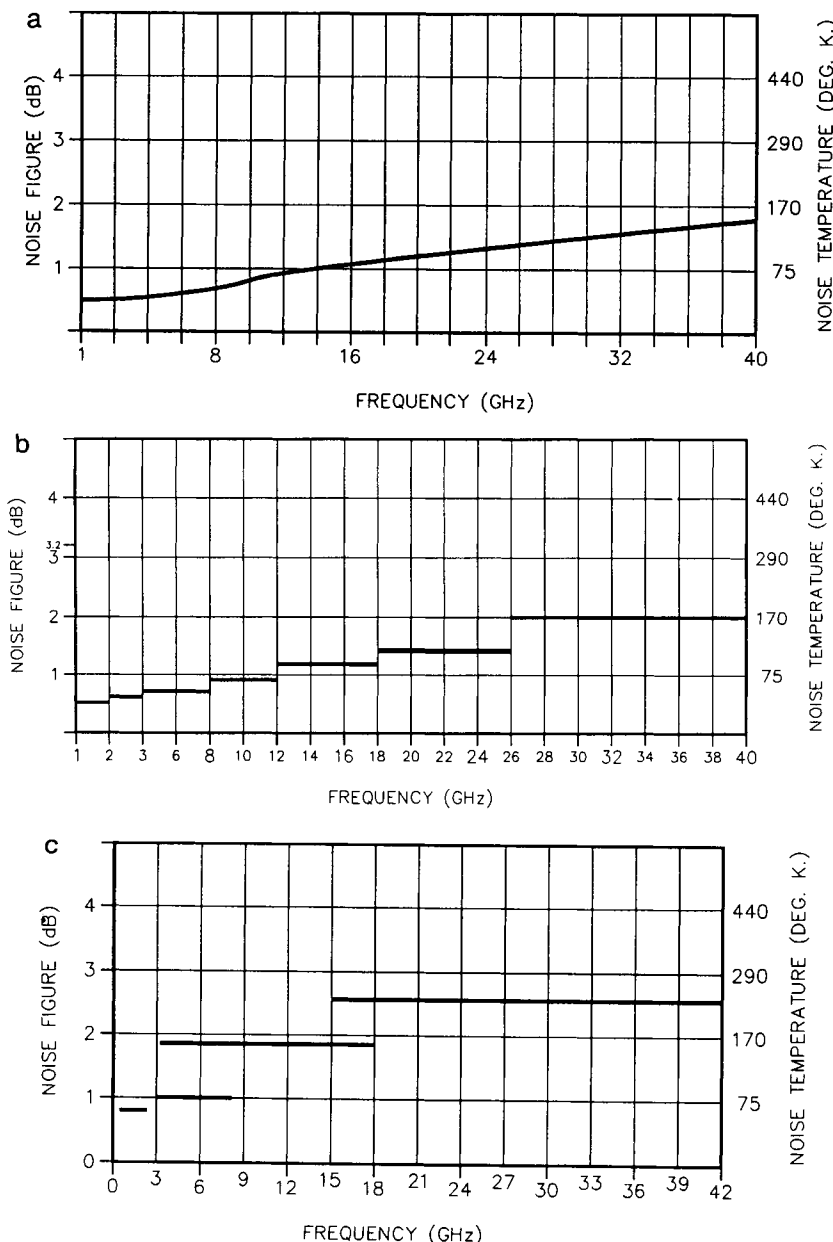


Figure 1. (A) Noise figure vs frequency of moderate band amplifiers. (B) Noise figure vs frequency of classical octave band amplifiers. (C) Noise figure vs frequency of multi octave band amplifiers.

(Continues)

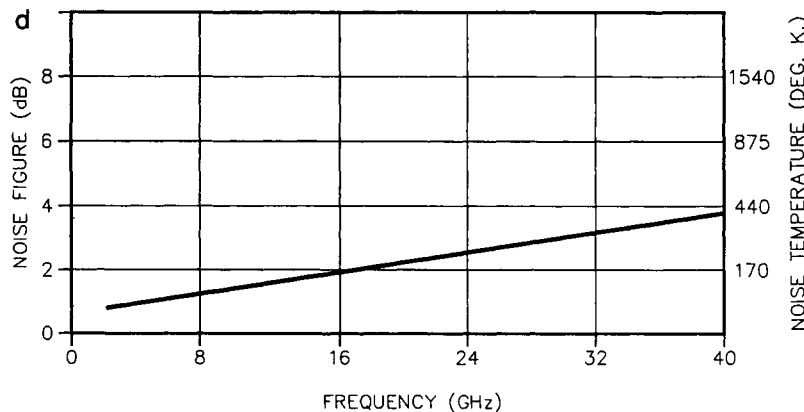


Figure 1. (Continued) (D) Noise figure as a function of the upper cutoff frequency (lower cutoff at 100 MHz) of ultra-wide-band amplifiers.

Multi octave Designs

In the multi octave designs, the input/output return loss specifications are on the order of 10 dB (2:1 VSWR), and the noise figures are approximately 0.5 dB higher than the octave band designs.

Ultra-Wide-Band Designs

Ultra-wide-band designs have their lower cutoff frequency around 100 MHz, and the upper cutoff frequency extends to 40 GHz. Commercially available amplifier noise figures in the 1992 time frame as a function of frequency for the bandwidth classifications are given in Figure 1. Figures 2 to 5 depict the measured S-parameter and noise figure performance of amplifiers with various bandwidths.

3. Amplifier Design

Amplifier design starts with the selection of the proper transistor for the intended application. In the case of a low-noise amplifier design, the input stages require the use of low-noise transistors. The transistor can be selected from the generic performance data supplied by the transistor

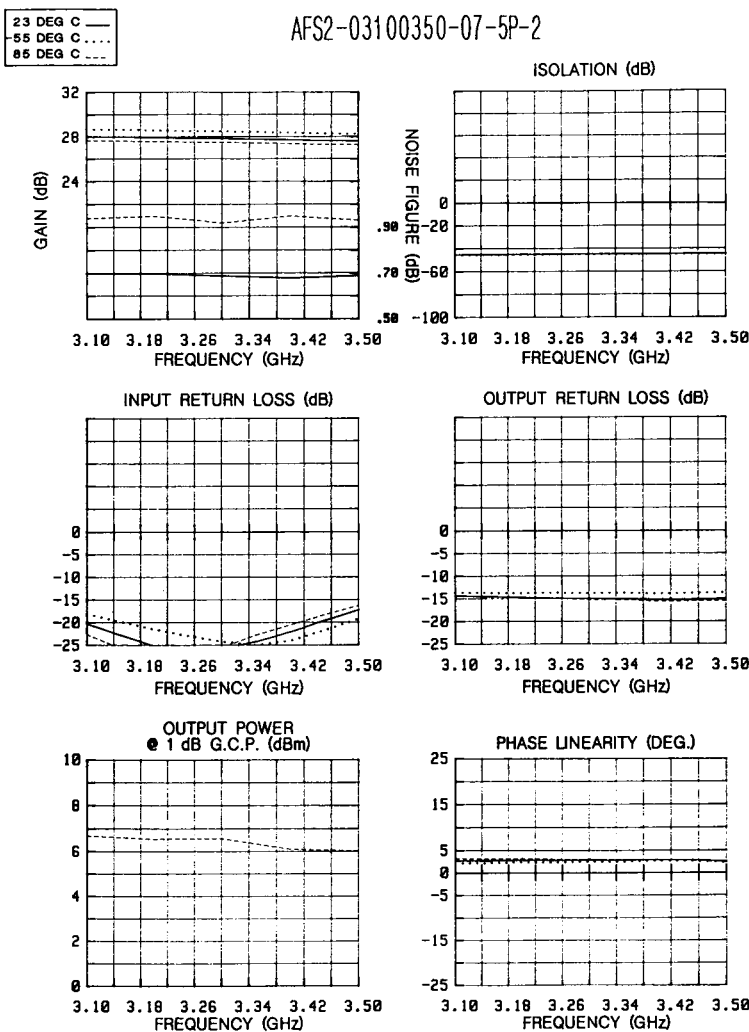


Figure 2. Performance of a two-stage, moderate-bandwidth, low-noise amplifier.

manufacturer or, if one is using a packaged transistor, by performing actual *S*-parameter measurements on the transistor itself. In wideband amplifier designs, unpackaged transistor chips are used almost exclusively. Unfortunately, the chips cannot be evaluated prior to their use in the actual amplifier. Instead, samples are taken from a given wafer, and the data are used as representative for the lot.

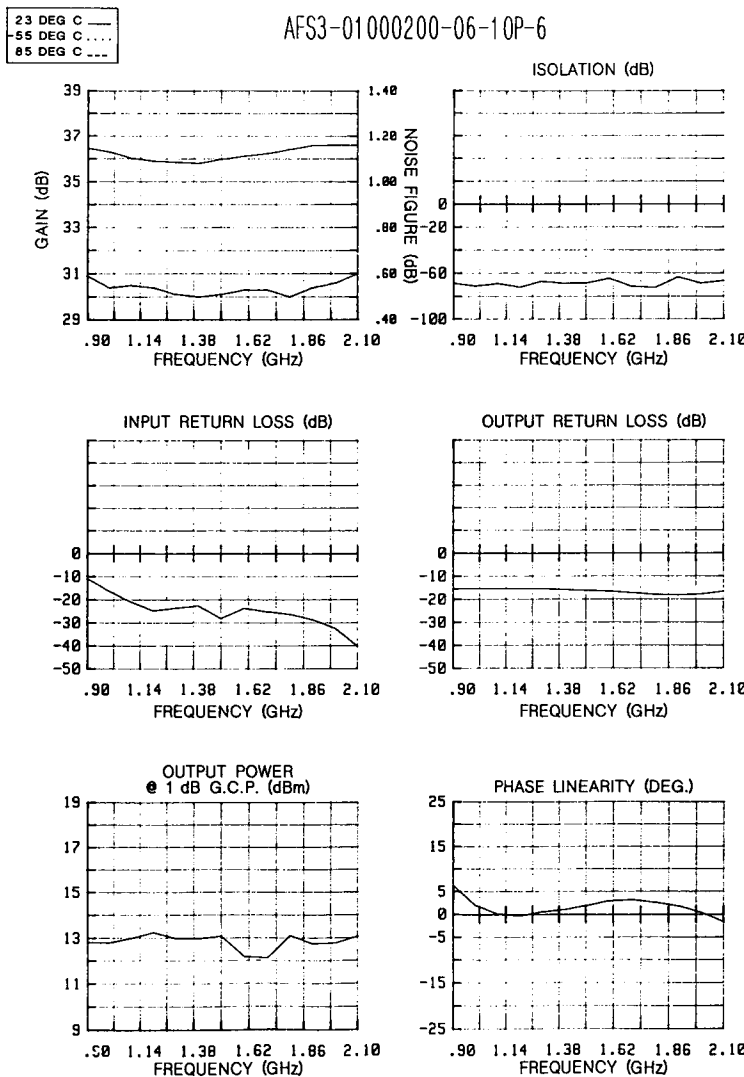


Figure 3. Performance of a three-stage, 1- to 2-GHz, low-noise amplifier.

Transistor Biasing

Transistor manufacturers normally provide information for the transistor's proper bias conditions. Both the transistor gain and the noise figure are a function of the transistor bias current. In general, the bias current is lower

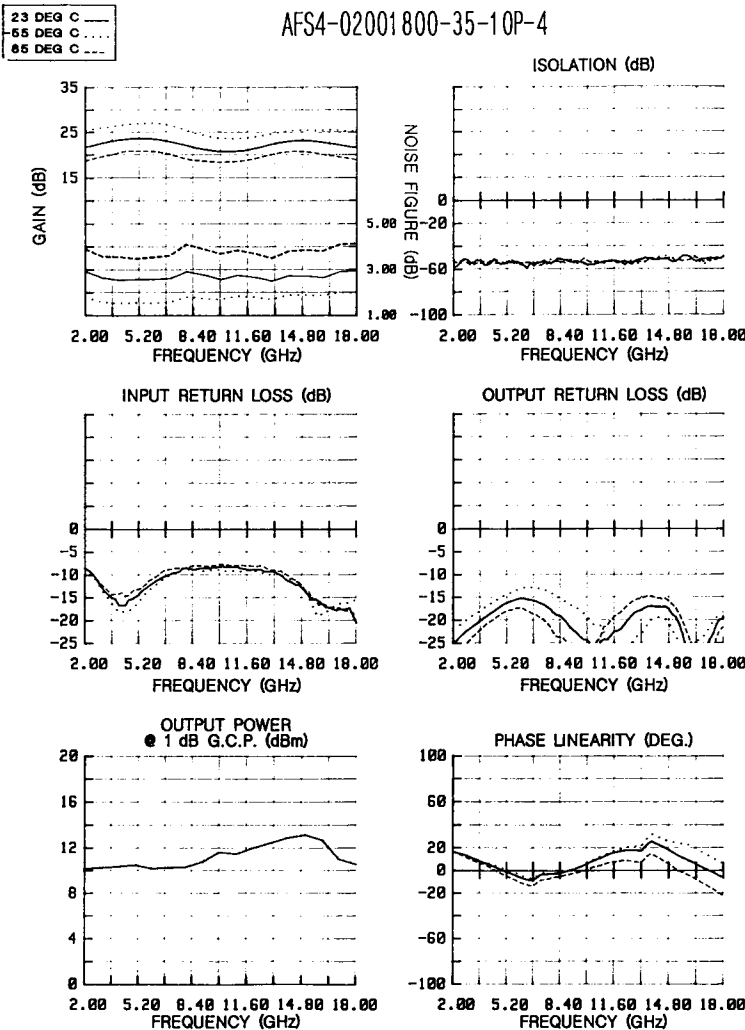


Figure 4. Performance of a four-stage, multi octave, low-noise amplifier.

for minimum noise figure conditions than for the amplifier maximum gain design. Figure 6 shows the Fujitsu FHX13XULTRAHEMT gain and noise figure as a function of the bias current. Also, in biasing the transistor, one has to take into consideration the environmental conditions under which the amplifier is expected to operate. Typical transistor derating information as a function of temperature is shown in Figure 7.

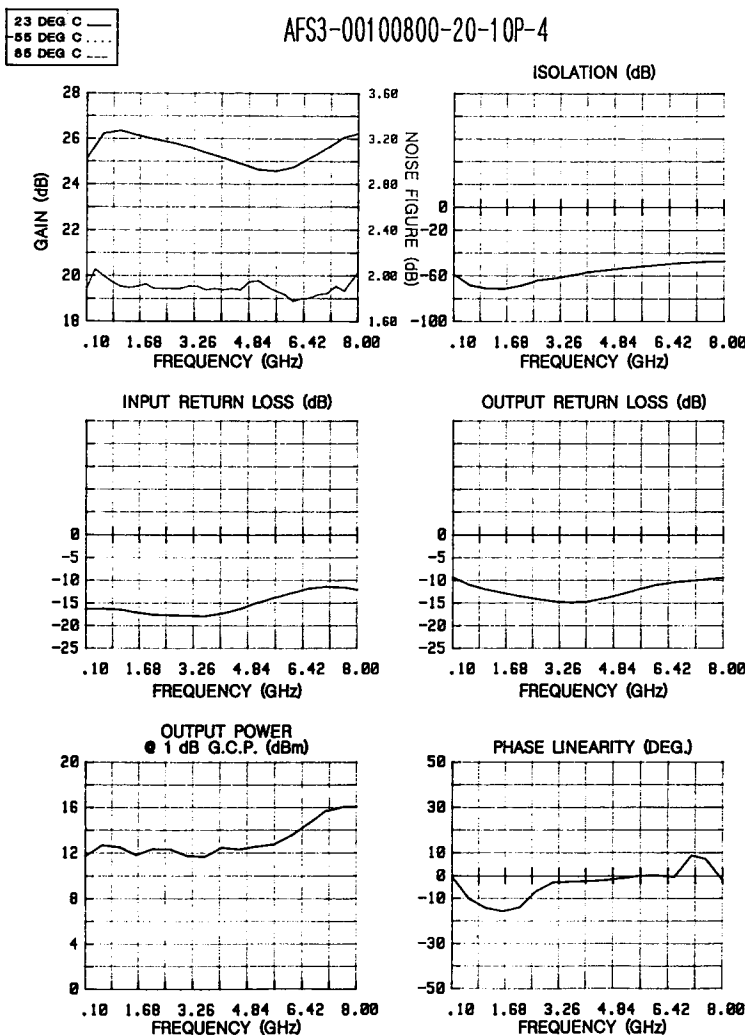


Figure 5. Performance parameters of a three-stage, 0.1- to 8.0-GHz, low-noise amplifier.

Characterizing the Transistor by Its S-Parameters

Modern microwave amplifier design and its performance characterization are almost universally based on *S*-parameter technology. A major reason for the preference for using *S*-parameters is that *y* (admittance)- and *z* (impedance)-parameters require measurements to be performed with open and short circuits, conditions that are difficult to achieve at microwave

frequencies. S-parameter measurements are made at a characteristic impedance level, normally 50Ω at microwave frequencies, thereby easing the measurement problem.

S-parameter theory is discussed in great detail in most circuit theory textbooks and will not be repeated. We refer to them here to the extent required to characterize the transistor and amplifier.

$$b_1 = s_{11}a_1 + s_{12}a_2$$

$$b_2 = s_{21}a_1 + s_{12}a_2$$

$$s_{11} = \frac{b_1}{a_1}; \quad a_2 = 0, \quad \text{input return loss}$$

$$s_{21} = \frac{b_2}{a_1}; \quad a_2 = 0, \quad \text{forward gain}$$

$$s_{22} = \frac{b_2}{a_2}; \quad a_1 = 0 \quad \text{output return loss}$$

$$s_{12} = \frac{b_1}{a_2}; \quad a_1 = 0 \quad \text{reverse gain/loss.}$$

When the transistor is correctly biased, either for the lowest noise figure or for the highest gain, the transistor S-parameters (Figure 8) can be measured as a function of frequency. They can be expressed in complex form, or we can plot their magnitude on a logarithmic scale as a function of frequency. The complex impedance data are given in Figures 9A and 9B, and the magnitude is given in Figure 10. As the logarithmic amplitude data show, the S-parameters are extremely frequency sensitive. Practical amplifiers, however, require constant gain and well-matched input/output ports. In addition, low-noise designs also require the lowest possible amplifier noise figure. To achieve this, amplifier designs use additional circuitry (e.g., input, interstage, and output matching networks). The input/output matching networks are functionally shown in Figure 11.

To increase the amplifier gain, one can simultaneously conjugately match the input and output ports by use of low-loss matching elements. Mathematically

$$\Gamma_S^* = S'_{11} = S_{11} + \frac{S_{12}S_{21}\Gamma_L}{1 - S_{22}\Gamma_L}$$

$$\Gamma_L^* = S'_{22} = S_{22} + \frac{S_{12}S_{21}\Gamma_S}{1 - S_{11}\Gamma_S},$$

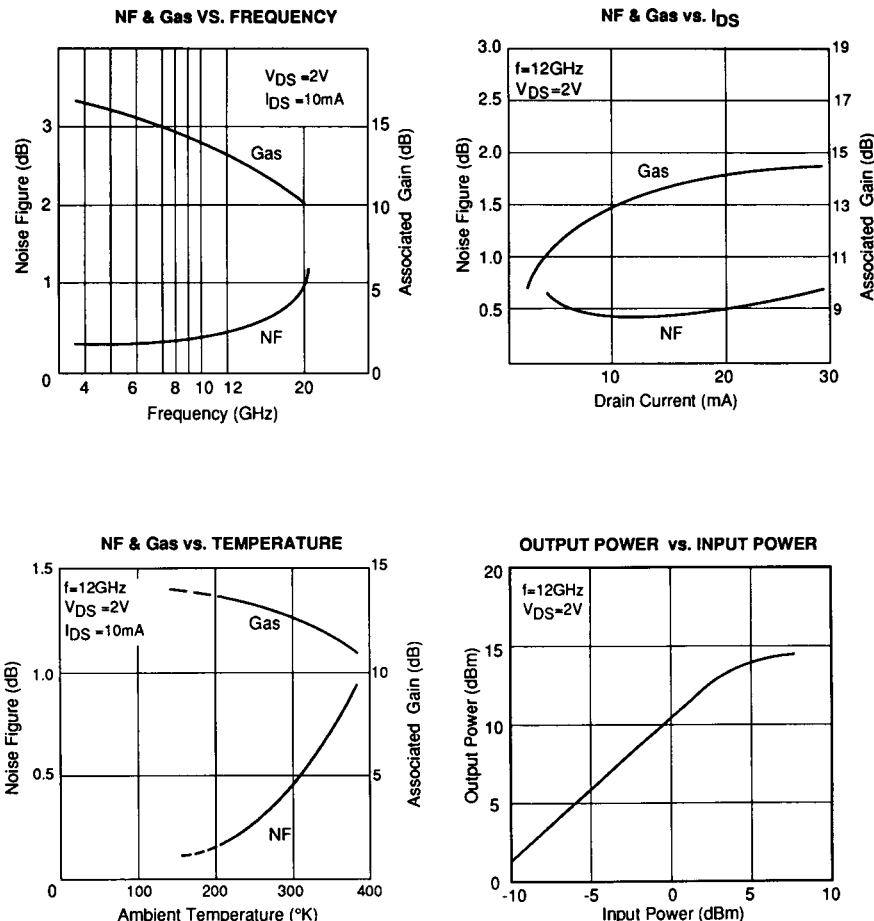


Figure 6. Transistor parameter dependence on frequency, drain current, and temperature.

where the asterisk denotes complex conjugate values. For the amplifier to be unconditionally stable $S'_{11} \leq 1$ and $S'_{22} \leq 1$.

If we define the amplifier insertion gain (transistor) as the ratio of power delivered to the load to that available from the generator, we can rewrite the above equations:

$$G_T = \frac{(1 - |\Gamma_L|^2)|S_{21}|^2(1 - |\Gamma_S|^2)}{|(1 - S_{22}\Gamma_L)(1 - S_{11}\Gamma_S) - S_{12}S_{21}\Gamma_L\Gamma_S|^2}.$$

ABSOLUTE MAXIMUM RATINGS (Ambient Temperature $T_a = 25^\circ C$)

Item	Symbol	Condition	Rating	Unit
Drain-Source Voltage	V_{DS}		3.5	V
Gate-Source Voltage	V_{GS}		-3.0	V
Total Power Dissipation	P_t		180	mW
Storage Temperature	T_{STG}		-65 to +175	$^\circ C$
Channel Temperature	T_{CH}		150	$^\circ C$

ELECTRICAL CHARACTERISTICS (Ambient Temperature $T_a = 25^\circ C$)

Item	Symbol	Test Conditions	Limit			Unit
			Min.	Typ.	Max.	
Drain Current	I_{DS}	$V_{DS} = 2V, V_{GS} = 0V$	10	30	60	mA
Transconductance	gm	$V_{DS} = 2V, I_{DS} = 10mA$	35	50	-	mS
Pinch-off Voltage	V_p	$V_{DS} = 2V, I_{DS} = 1mA$	-0.1	-0.7	-1.5	V
Gate-Source Breakdown Voltage	V_{GSO}	$I_{GSO} = -10\mu A$	-3.0	-	-	V
Noise Figure	NF	$V_{DS} = 2V, I_{DS} = 10mA$	-	0.45	0.50	dB
Associated Gain	Gas		11	12.5	-	dB
Noise Figure	NF	$f = 12GHz$	-	0.60	0.65	dB
Associated Gain	Gas		11	12.5	-	dB

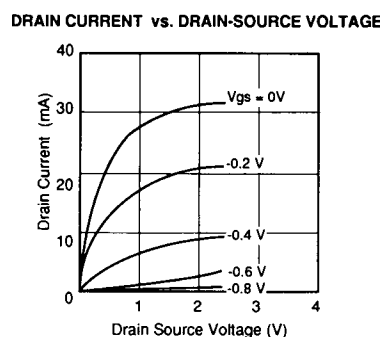
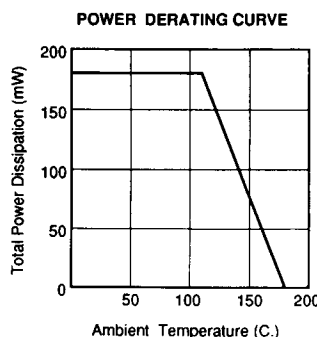


Figure 7. Transistor derating as a function of ambient temperature.

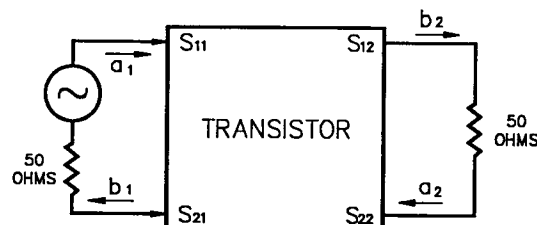
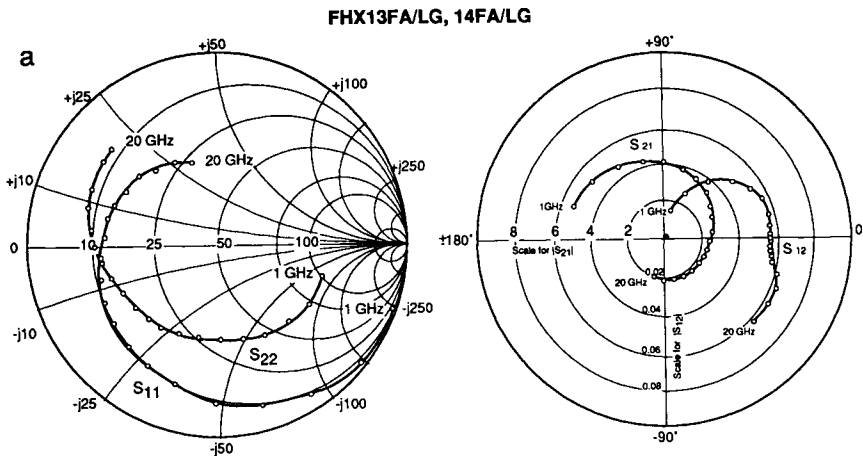


Figure 8. Transistor S-parameter definition.



S-Parameters
V_{DS}=2V, I_{DS}=10mA

FREQ. GHz	S11			S21			S12			S22		
	MAG	ANG		MAG	ANG		MAG	ANG		MAG	ANG	
1.0	.988	-20.0		5.327	160.1	.015	75.7	.574	-.16.3			
2.0	.956	-39.5		5.133	141.0	.028	63.3	.560	-.32.1			
3.0	.908	-58.1		4.851	123.0	.039	50.1	.539	-.47.3			
4.0	.862	-75.5		4.534	105.9	.048	39.0	.522	-.62.0			
5.0	.811	-91.6		4.213	89.7	.053	29.3	.502	-.75.6			
6.0	.763	-107.1		3.886	74.4	.056	21.0	.488	-.89.6			
7.0	.727	-121.1		3.582	60.0	.057	13.2	.487	-.103.0			
8.0	.701	-133.3		3.300	46.4	.056	7.9	.498	-.114.9			
9.0	.682	-144.1		3.078	33.8	.055	3.5	.515	-.125.0			
10.0	.659	-154.2		2.899	21.4	.055	-0.0	.531	-.134.4			
11.0	.636	-164.4		2.748	9.3	.054	-2.6	.544	-.144.0			
12.0	.618	-175.4		2.593	-3.3	.054	-5.2	.561	-.155.1			
13.0	.608	-175.5		2.466	-14.8	.054	-5.7	.590	-.164.0			
14.0	.596	166.6		2.366	-26.6	.055	-7.8	.619	-.172.4			
15.0	.585	158.3		2.279	-38.3	.056	-9.7	.654	-.179.7			
16.0	.564	148.8		2.244	-50.7	.058	-12.8	.677	-.172.6			
17.0	.543	138.2		2.217	-63.6	.061	-17.6	.701	-.163.4			
18.0	.525	127.3		2.185	-77.1	.063	-24.7	.727	-.154.1			
19.0	.506	116.2		2.143	-91.4	.063	-33.1	.748	-.143.6			
20.0	.470	106.5		2.089	-105.4	.061	-43.1	.763	-.137.2			

Figure 9. (A) Packaged transistor complex S-parameter data.

To gain a greater insight into the amplification process, it is often assumed for initial amplifier design that $S_{12} = 0$. This assumption means that the transistor output port is isolated from the input; i.e., there is no feedback.

The gain equation then reduces to

$$G_T = \frac{1 - |\Gamma_S|^2}{1 - |S_{11}\Gamma_S|^2} |S_{21}|^2 \frac{|1 - \Gamma_L|^2}{1 - |S_{22}\Gamma_L|^2}.$$

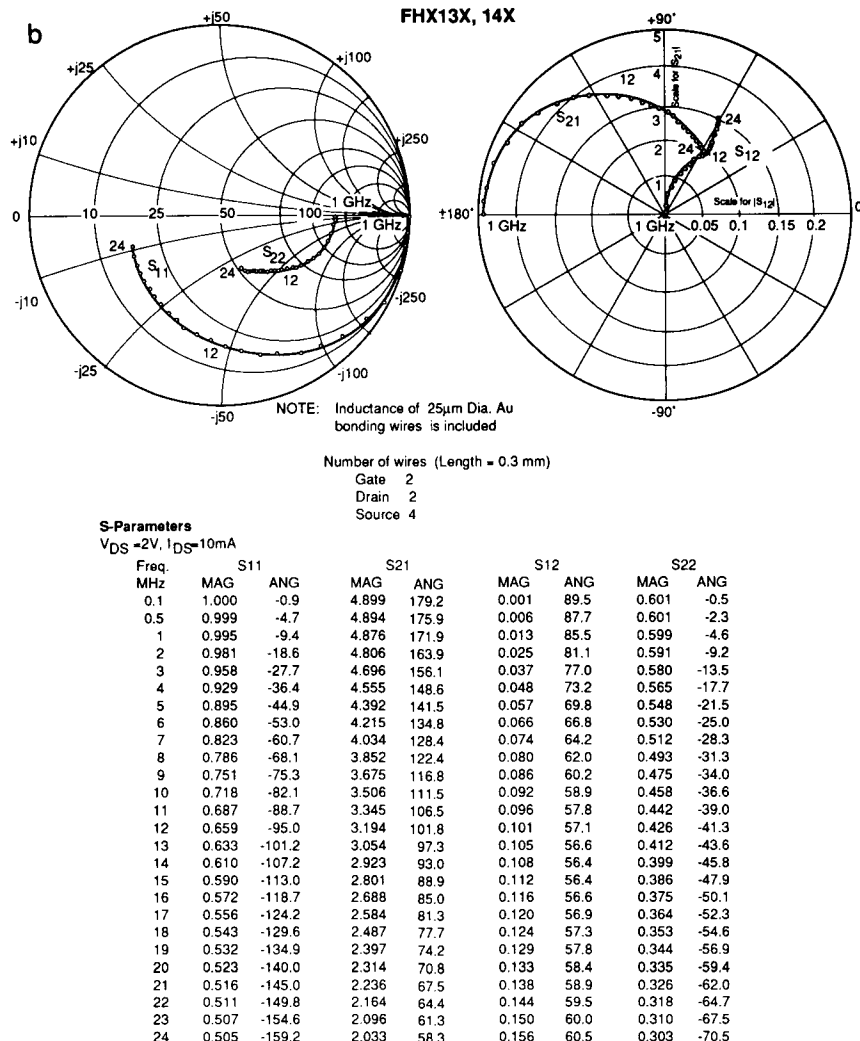


Figure 9. (Continued) (B) Chip transistor complex S-parameter data.

In the case of a conjugate input/output match (for $S_{12} = 0$), the equation further reduces to

$$G_T = \frac{1}{1 - |S_{11}|^2} \times |S_{21}|^2 \frac{1}{1 - |S_{22}|^2}.$$

There are three parts to the amplifier gain: S_{21} from the transistor, the gain realized by matching the input port, and the output port.

FUJI30X 2 IN PAR. $V_{ds}=1.5V$ $I_{ds}=31\text{ mA}$

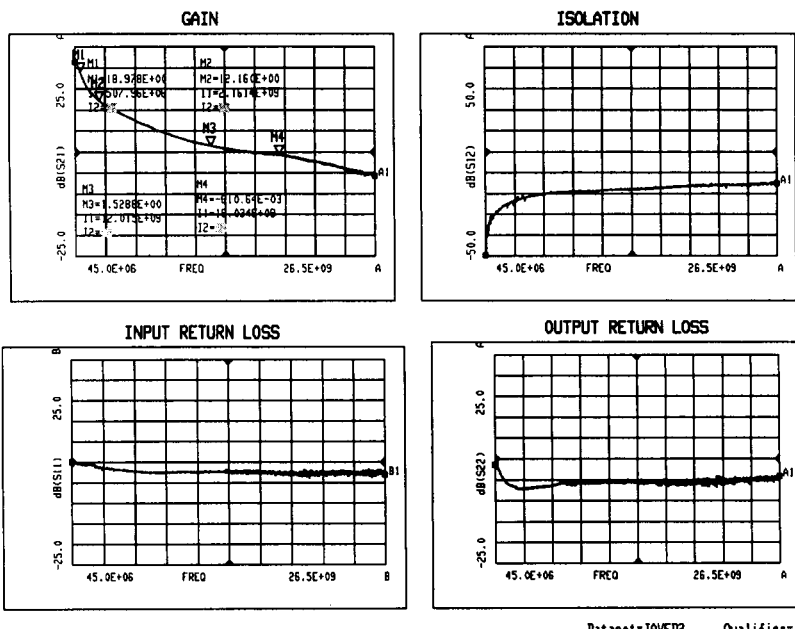


Figure 10. S-parameter magnitude logarithmic presentation.

Theoretically at least it is possible to design lossless matching networks that satisfy the complex conjugate match conditions over the frequency range of interest. In a practical amplifier other conditions, such as gain flatness and the low-noise figure, make these designs impractical. The amplifier design engineer resorts to different design techniques to alleviate the problem. We will discuss some of these methods under Low-Noise Amplifier Design.

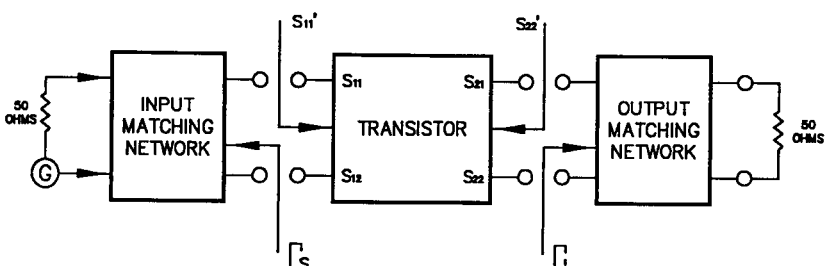


Figure 11. Functional presentation of amplifier input/output matching networks.

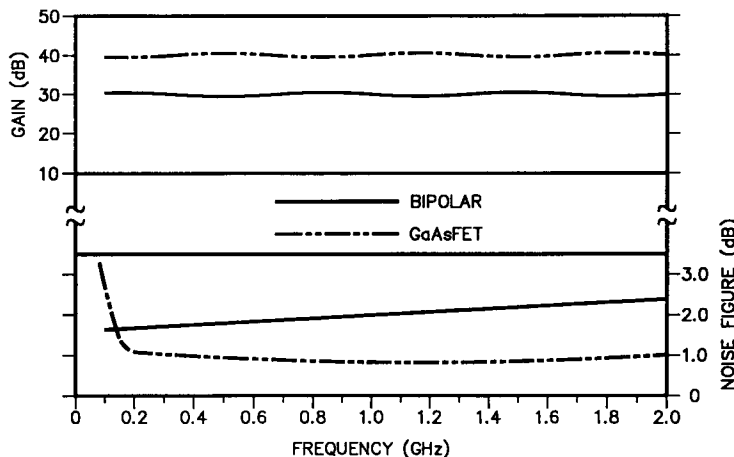


Figure 12. Comparative gain and noise figure performance of bipolar and GaAs FET amplifiers in the 1- to 2000-MHz frequency band.

Amplifier Characterization

Low-noise amplifier designs use bipolar junction, GaAs FET, HEMT, and more recently PHEMT and ULTRA HEMT transistors. Bipolar transistors offer lower noise figures for applications in which the amplifier lower cutoff frequency extends below approximately 50 MHz. The comparative noise figure and gain performance of 1- to 2000-MHz bipolar and GaAs FET amplifiers are shown in Figure 12.

Bipolar Amplifiers

Bipolar transistor technology matured about 10 years ago; thus there has not been any substantial improvement in the noise figure or gain performance in bipolar amplifier designs. Wide-band bipolar transistor amplifiers extend from a few kilohertz to approximately 2000 MHz. A 0.01- to 100-MHz amplifier schematic and test data are shown in Figures 13 and 14.

GaAs FET Amplifiers

Most low-noise microwave amplifier designs are based on GaAs FET technology. We have selected the Fujitsu ULTRA HEMT™ FHX13 and

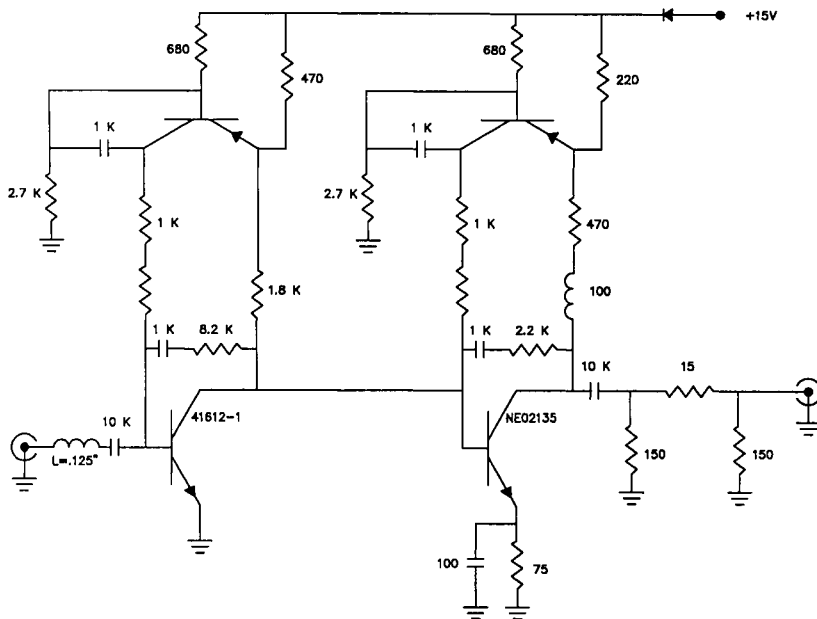


Figure 13. Schematic diagram of 0.01- to 100-MHz, low-noise bipolar amplifier.

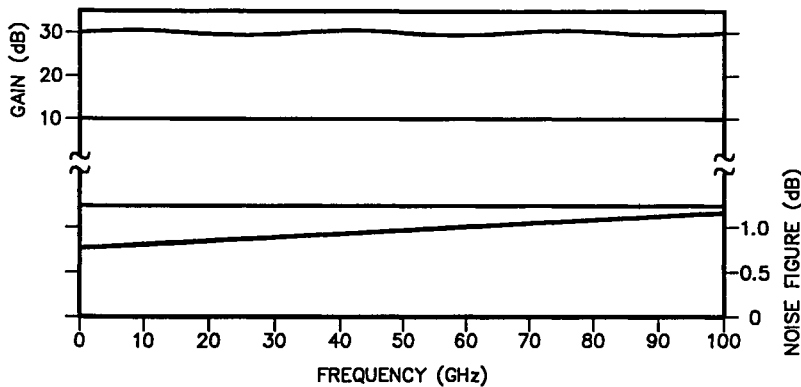


Figure 14. Noise figure and gain vs frequency of a 0.01- to 100-MHz wide-band, low-noise, two-stage bipolar amplifier.

14 series, as presenting the state of the art in a mid-1992 time frame. One would expect improvements in the noise figure, gain, etc., especially at higher microwave frequencies, as a function of time.

Low-Noise Amplifier Design

If we take a transistor, conjugately match the output port for maximum gain, and then adjust the input network for the amplifier's lowest noise figure, we find that the input reflection coefficient differs greatly from the conjugate match conditions obtained for the maximum gain design. Plotting the reflection coefficient as a function of frequency for the lowest noise figure can be practically implemented by use of test setups designed for that purpose and manufactured by companies such as Maury Microwave and Focus, among others. The test setup consists of a low-loss input tuner, a section in which to embed the transistor, and a low-loss output tuner. The setup is microprocessor controlled, and the complex impedance can be recorded from the digital display.

Theoretically the noise figure of an amplifier, or for that matter any noisy two-port amplifier, can be expressed mathematically by

$$F = F_{\min} + \frac{4r_N[\Gamma_s - \Gamma_{\text{opt}}]^2}{(1 - |\Gamma_s|^2)(1 + \Gamma_{\text{opt}})^2},$$

where F_{\min} is the amplifier minimum noise figure, Γ_s is the source reflection coefficient, r_N is the equivalent normalized amplifier noise resistance, and Γ_{opt} is the source reflection coefficient for the minimum noise figure (F_{\min}). The equation has four unknowns: r_N , F_{\min} , and the real and imaginary parts of Γ_{opt} . By measuring the amplifier noise figure at four different values, including F_{\min} , and determining the corresponding source reflection coefficient for these noise figures, one can calculate the four unknowns by simultaneously solving the four equations. In practice, up to seven noise figure measurements are taken. It is interesting to note that if the source impedance differs from Γ_{opt} , one can plot so-called constant noise figure circles for which the same noise figure can be obtained for impedances that correspond to constant noise figures on a circle. Generic Γ_{opt} , constant noise figure circles, and the noise parameters are shown in Figures 15A and 15B.

Single-Stage Amplifier Design

Customer-dictated performance conditions of a simultaneous input noise and power match, constant amplifier gain, low-gain ripple, and good output match impose formidable design difficulties on the amplifier designer. Below we will discuss some of the design techniques used to overcome some of the difficulties.

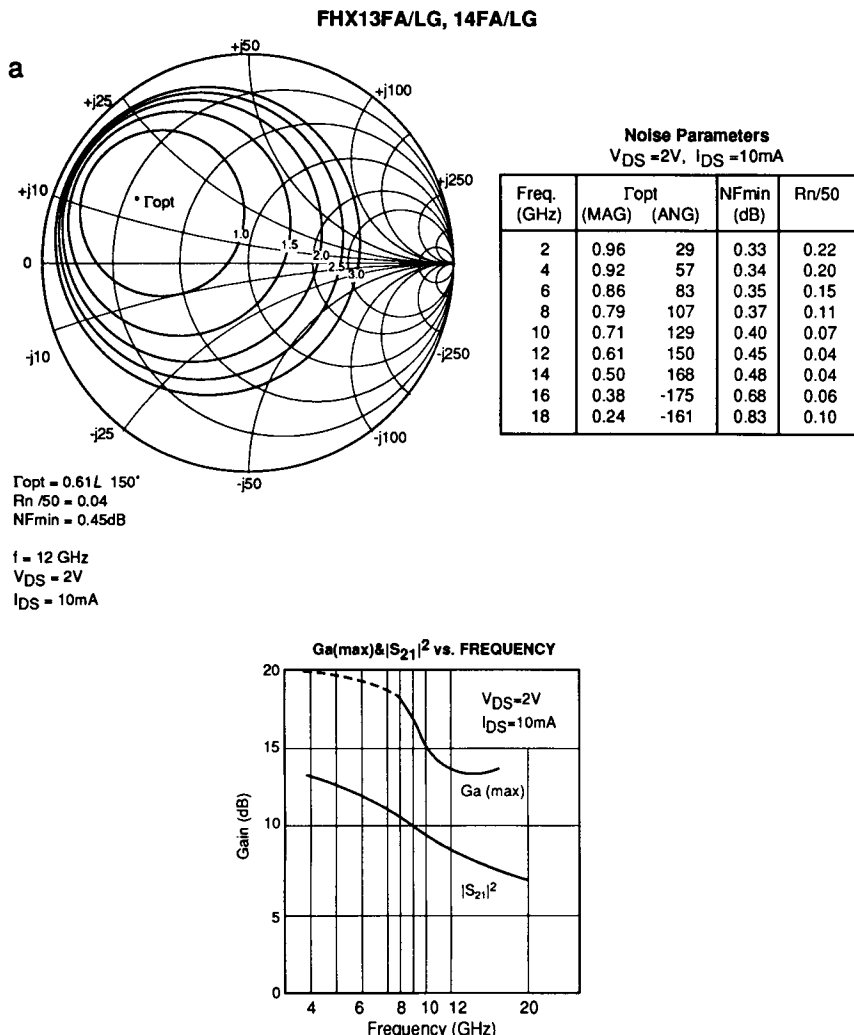


Figure 15. (A) Noise figure circles of a packaged transistor.

Low-Noise Amplifiers Using Low-Loss Isolators

The isolator is a three-port ferrite circuit element, shown in Figure 16. Signals incident on the input port of the circulator are transmitted to the output port through one of the three isolator junctions. Any signals reflected at the output port further circulate through the second junction and are absorbed in the internal 50Ω resistive termination. Ideally, no

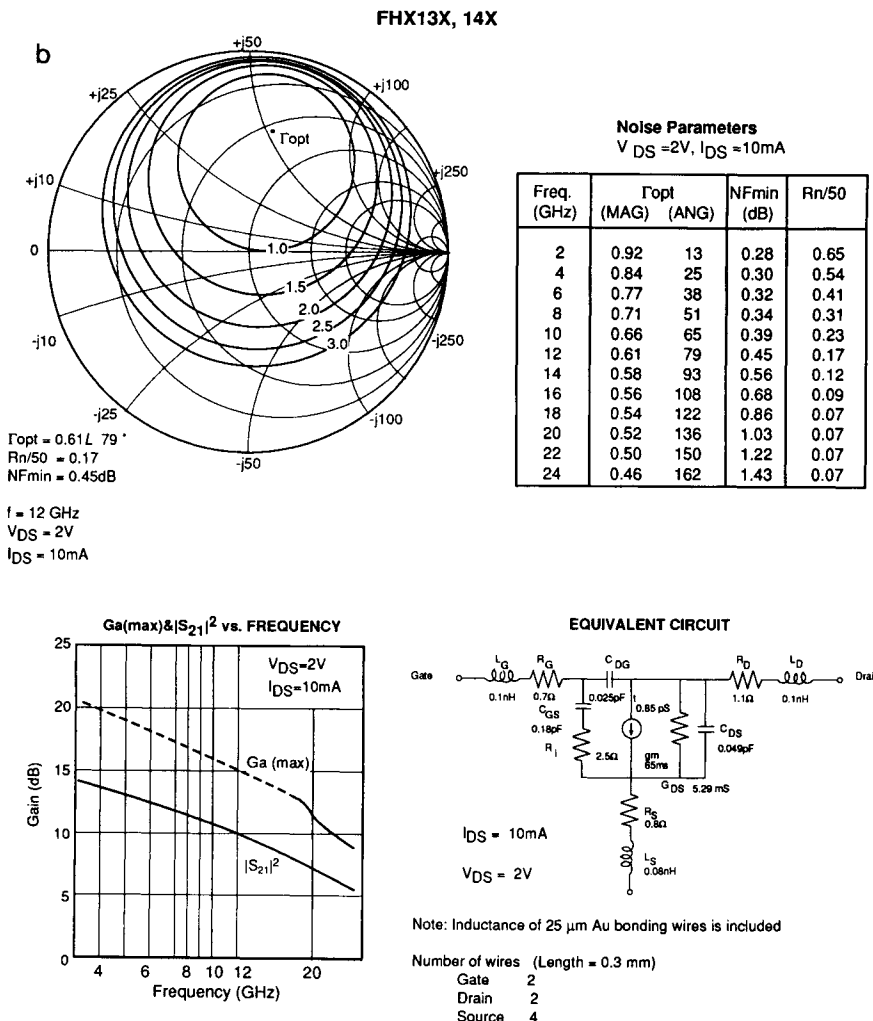


Figure 15. (Continued) (B) Noise figure circles of a transistor chip.

signal is reflected back to the input port, thus creating a perfect power match at the input port. Practically, moderate-bandwidth low-loss isolators have input return losses on the order of 20–25 dB, insertion losses of 0.1–0.2 dB per junction, and reverse isolation on the order of 30 dB. In octave band isolators the return loss is reduced to 15–20 dB, and the insertion loss increases to 0.4–0.5 dB per junction. When such isolators are placed at the input and output ports of a single-stage amplifier, they

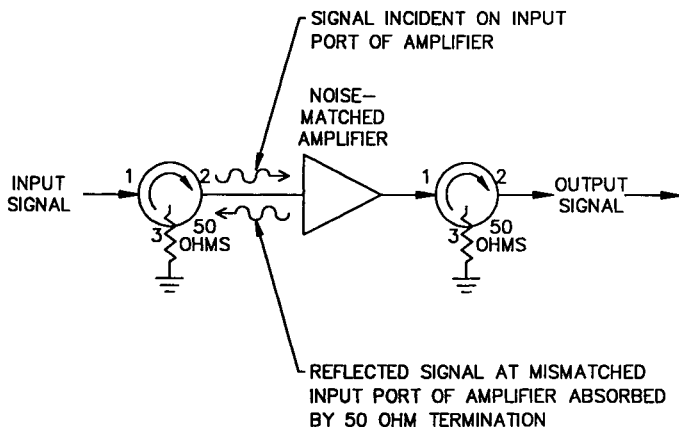


Figure 16. Low-noise amplifier using low-loss isolators for input power matching.

automatically provide good input and output return loss for the amplifiers regardless of the impedances of the amplifier itself. Thus the amplifier designer can design the amplifier input for optimum noise match and can use the output matching network for gain shaping the amplifier frequency response. The penalties the amplifier designer pays are the added cost of the isolators and an increase in the amplifier physical size. In addition, the insertion loss of the isolator increases the amplifier noise figure.

Balanced Amplifier Design

The apparent input power match can also be simulated by the use of a 3-dB 90° hybrid coupler. Signals entering the coupler input port are split and exit at ports 3 and 4 with equal amplitude, but 90° out of phase. The reflected signals at ports 3 and 4 are 180° out of phase at the input port and cancel, thus creating an apparent power match. They add in-phase at port 2 and are dissipated in the 50- Ω termination. To achieve this condition, the terminating impedances at ports 3 and 4 have to be identical as a function of frequency. If one now connects two identical amplifiers to ports 3 and 4 and connects the output ports of these amplifiers to an identical output coupler, one obtains well-matched amplifier input and output ports. Now the transistor inputs can be noise matched and the output matching network can be used for gain shaping without affecting the overall amplifier input impedances. Again, for this performance to be achieved, the two transistors and their ancillary circuitry have to be well matched.

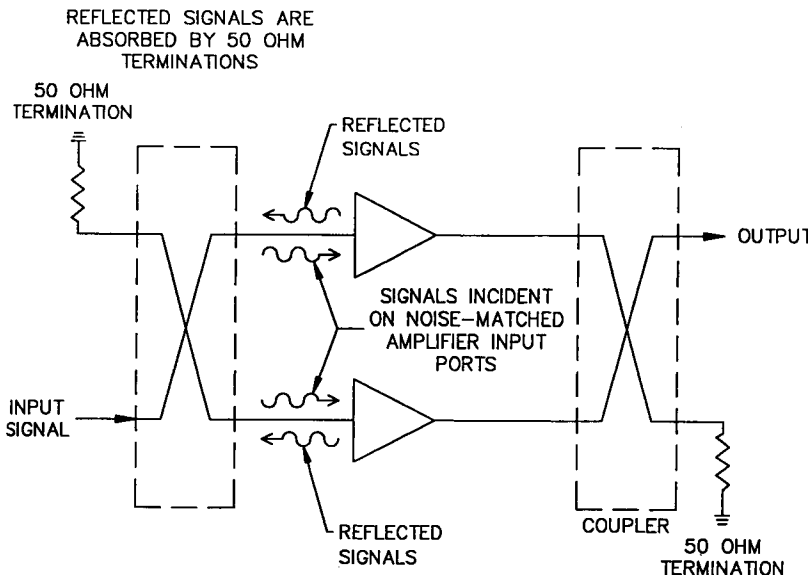


Figure 17. Low-noise amplifier using the balanced design approach.

The disadvantages of the balanced amplifier design are the use of the couplers, doubling the number of transistors, and doubling the amplifier power dissipation. Advantages include a 3-dB increase in the amplifier output power.

In a practical amplifier the coupler losses, on the order of 0.3–0.5 dB, add directly to the amplifier overall noise figure. For that reason the balanced design is not universally used for ultra-low-noise amplifier designs.

Performance degradation results when the transistors' optimum noise impedances are not the same or if the coupler amplitude and phase performance (equal amplitude and constant 90° phase difference with frequency) are not the same. Typically, the amplifier noise figure is degraded by up to 0.5 dB from that achievable without the use of the coupler. This circuit configuration is depicted in Figure 17.

Lossless Feedback

The third design approach uses shunt and series lossless feedback in various combinations. The feedback is used to convert the transistor input impedance to the complex conjugate of the optimum source impedance for the minimum noise figure (F_{\min}). Once that condition is reached, it is

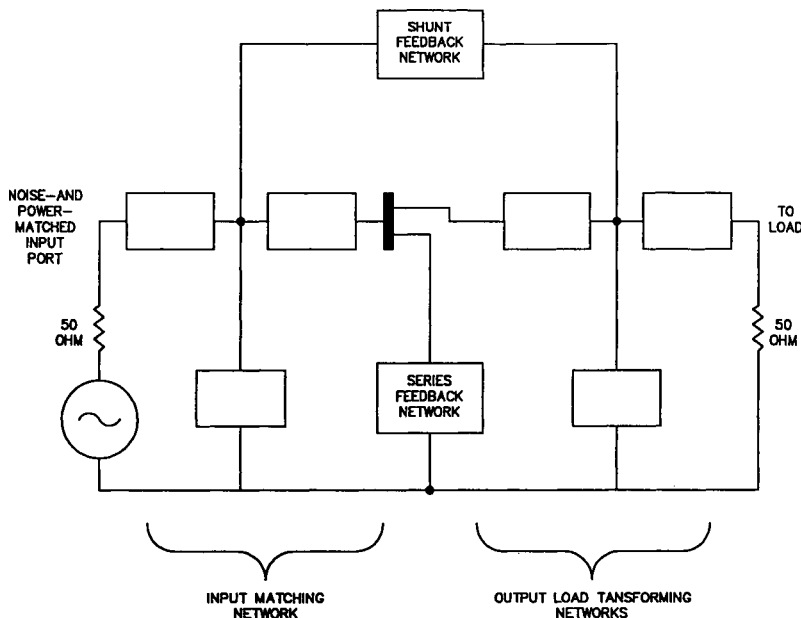


Figure 18. Lossless feedback, low-noise amplifier design.

possible, at least theoretically, to design a lossless matching network that transforms that transistor input impedance to a $50\text{-}\Omega$ power match at the source. Of course, the ideal condition is to have both a $50\text{-}\Omega$ input impedance and a $50\text{-}\Omega$ optimum noise source impedance. Unfortunately, in a practical world one always has to compromise. The generally accepted standard for multi octave amplifiers is a maximum input VSWR of 2 with the possible lowest noise figure.

In order not to degrade F_{\min} substantially with the matching network, the feedback elements should be substantially lossless. However, the use of lossless feedback introduces potential amplifier instabilities, and extreme care must be taken to make sure that the resultant amplifier has unconditional stability. Additionally, feedback inherently reduces the overall available gain from the transistor, increases the second-stage noise contributions, and degrades the amplifier's overall noise figure. The functional block diagram is shown in Figure 18.

The Fundamentals of Distributed Amplifier Design

The concept of distributed amplification has been extensively analyzed since it was first proposed by W. S. Percival in 1935 [1]. Distributed

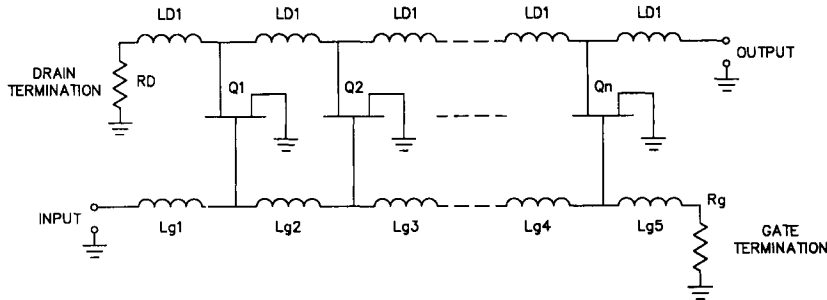


Figure 19. Fundamental schematic of a distributed GaAs FET amplifier.

amplification has been successfully demonstrated in both hybrid and monolithic solid-state amplifiers.

A schematic representation of a FET-distributed amplifier is shown in Figure 19. The input and output parasitic capacitances of the transistors are combined with lumped inductors to form artificial transmission lines. They are referred to as gate and drain lines. These lines are coupled by the transconductances of the active devices. The ability to absorb the capacitances and to add the transconductances increases the gain-bandwidth product and power handling capabilities.

Distributed amplifiers can be optimized for ultra-wide bandwidth, low-input and -output VSWR, and flat gain response. The idle port resistor absorbs RF signals to reduce low-frequency signal gain in order to flatten the overall gain response. Low VSWR is partly due to signals being dissipated at the resistors. Resistive loss at gate line termination is a major contributing factor to a higher noise figure in distributed amplifiers. The noise figure can be reduced by increasing the gate line terminating resistance. Negative feedback can be applied to reduce the input VSWR and gain of lower frequency signals.

The inner working of distributed amplifiers is rather complex. In addition, ultra-wide bandwidth performance requires that matching networks be optimized across the entire frequency band. Therefore, computer-derived designs are attractive for these designs.

The four design methods described above are all used in low-noise amplifier designs. Below 4 GHz the lossless feedback design approach offers the best results. In the 4- to 8-GHz frequency region the lossless feedback and low-loss isolator design up to the octave bandwidth compete almost on an equal footing. Above 8 GHz in the moderate-band to octave band designs the low-loss isolator design approach offers a better input match and a slightly lower noise figure when compared with the lossless

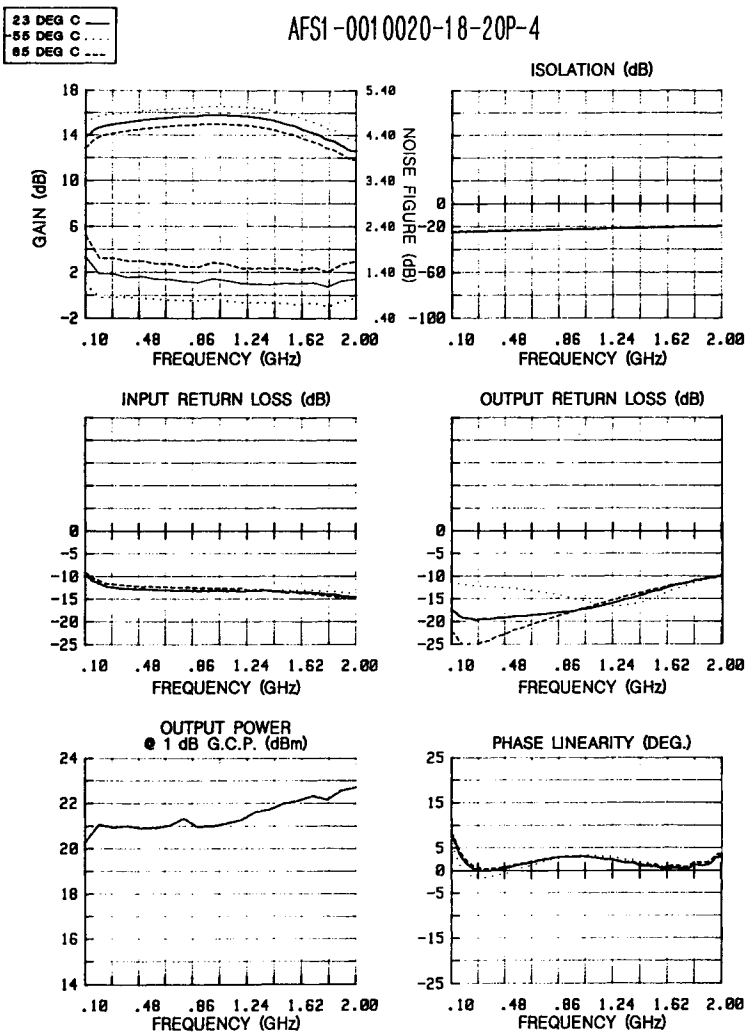


Figure 20. Performance parameters of a single-stage, ultra-wide-band amplifier.

feedback designs. For amplifiers that require wider than octave frequency coverage, the lossless feedback and the distributed design offer the best results. The balanced or the distributed design can be used for low-gain requirements that also need a higher dynamic range. Figure 20 presents the test results of a single-stage wide-band amplifier using the lossless feedback design approach.

Multistage Amplifier Design

Ultra-low-noise amplifiers are almost universally multistage designs. In system applications that require high sensitivity, a low-noise requirement is coupled with sufficient amplifier gain to mask any second-stage noise contribution that may degrade the system sensitivity. Typical amplifier gains range from 30 to 50 dB. A multistage amplifier design offers the

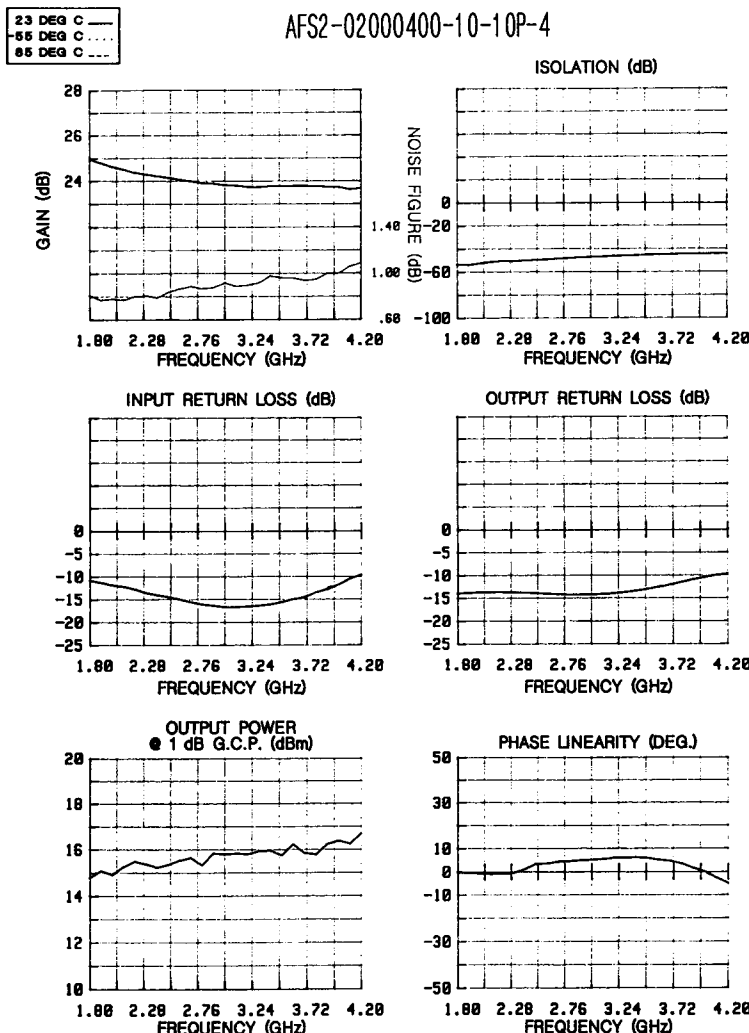


Figure 21. Performance parameters of a two-stage, 2- to 4-GHz, low-noise amplifier.

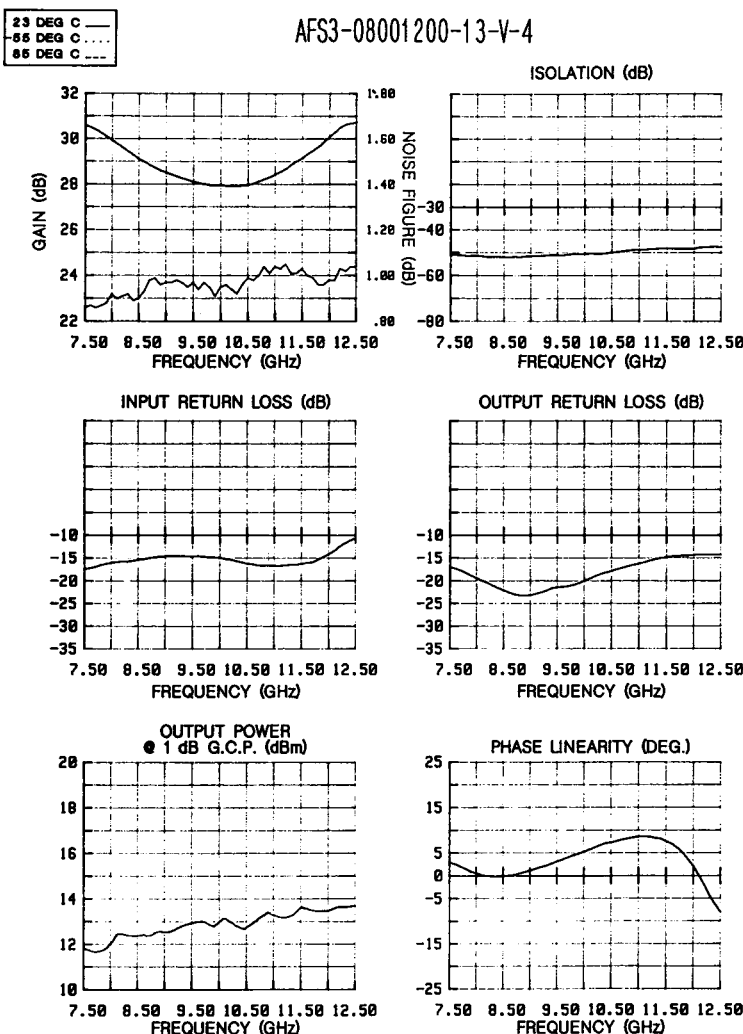


Figure 22. Performance parameters of a three-stage, 8- to 12-GHz, low-noise amplifier.

design engineer more degrees of freedom than a single-stage amplifier design. For example, one can optimize the input and the first and second amplifier interstages for the amplifier's lowest noise figure and use the remaining interstages and the output network for frequency shaping and output matching. Figures 21 to 23 present performance parameters of two-, three-, and four-stage classical octave band amplifier designs.

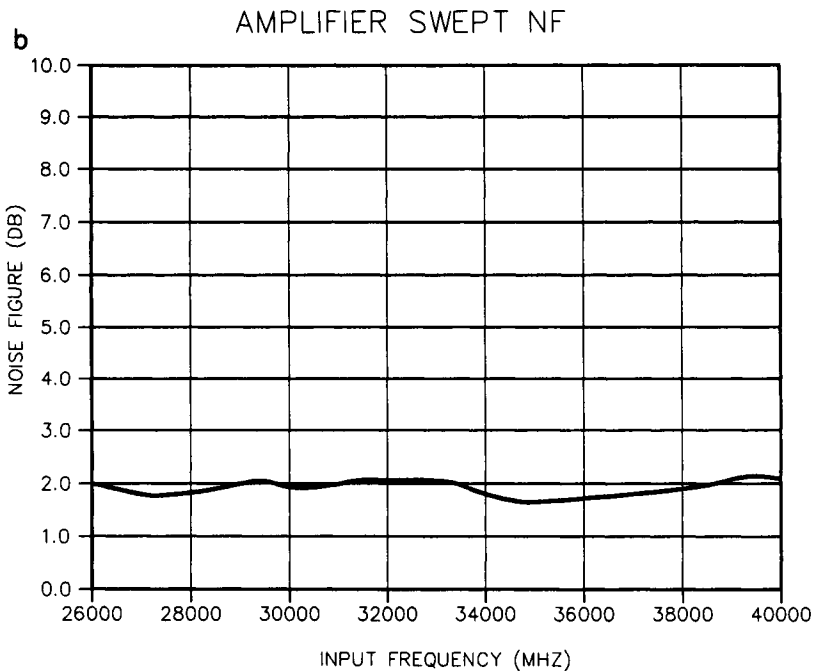
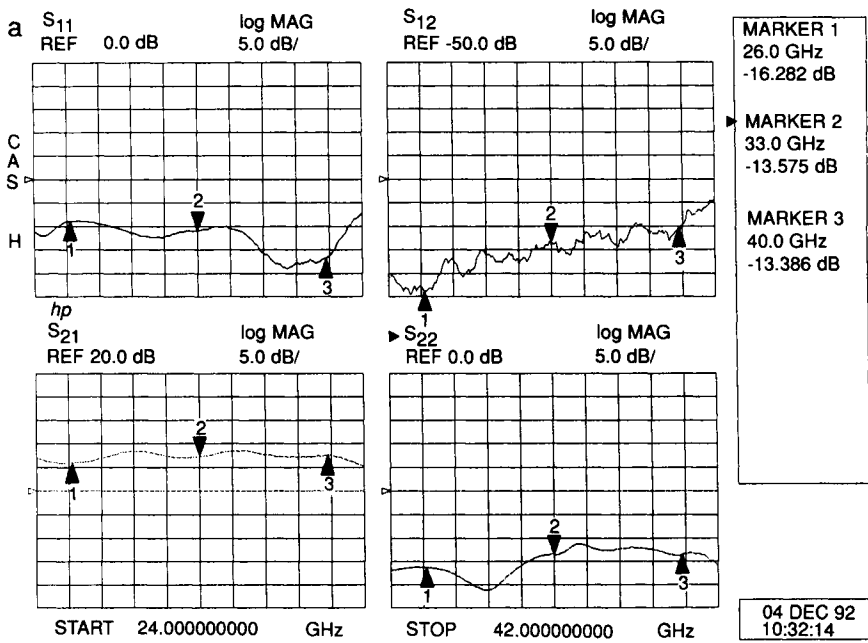


Figure 23. (A) S-parameters of a 26- to 40-GHz, low-noise amplifier. (B) Noise figure vs frequency of a 26- to 40-GHz, low-noise amplifier. Datapoint spacing equals 1000 MHz.

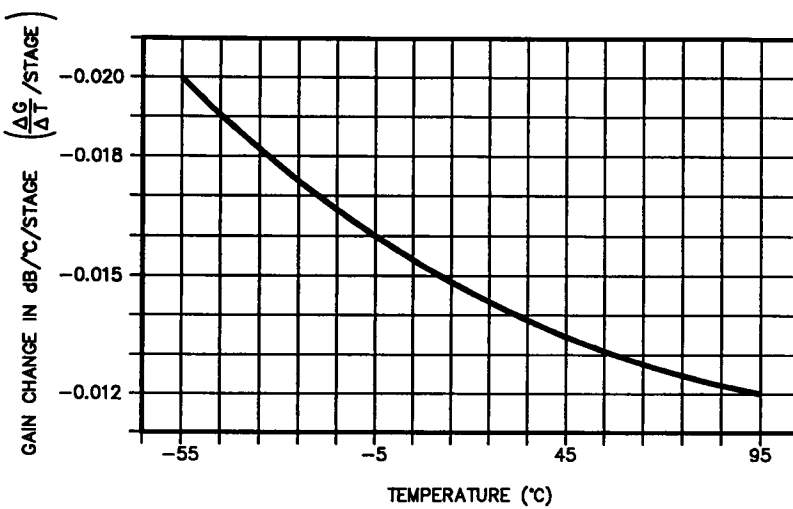


Figure 24. Gain vs temperature.

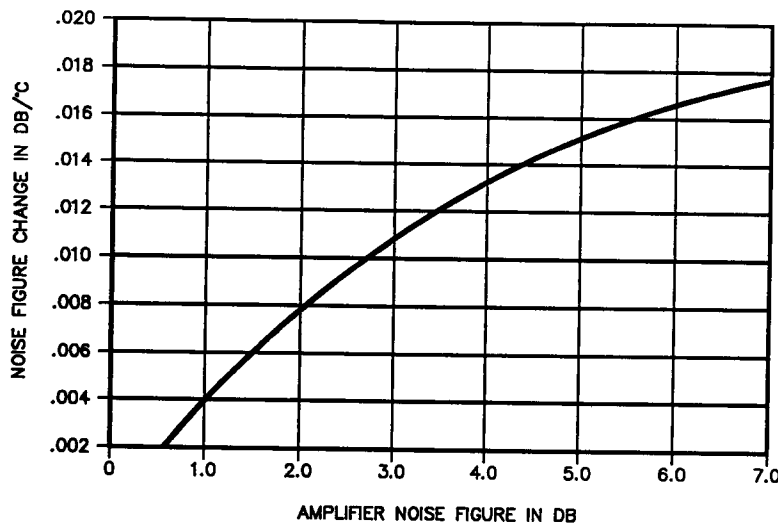


Figure 25. Noise figure change vs temperature.

Temperature Dependence of the Amplifier Gain and Noise Figure

Both the amplifier gain and the noise figure are functions of the environmental temperature. As the temperature increases, the amplifier gain

decreases and the noise figure increases. With decreasing temperature the noise figure decreases and the gain increases. GaAs bipolar transistor performance varies less than the performances of GaAs FET and HEMT. The typical temperature dependence is shown in Figures 24 and 25.

Temperature Compensation

Amplifier gain variation with temperature can be minimized by using temperature compensation. Standard techniques include bias compensation and the use of dual gate transistors or PIN diode attenuators. All of these methods are designed to increase the amplifier gain with increasing temperature and decrease it with decreasing temperature. A commonly used element is a temperature-dependent resistor, such as a sensistor, whose value decreases with increasing temperature and increases with decreasing temperature. When used in the amplifier bias circuit, this resistor change varies the bias of the transistor and compensates for the temperature-dependent gain variations over the operating temperature range. A temperature-compensated, low-noise, 1- to 2-GHz amplifier gain as a function of temperature is shown in Figure 26. The amplifier has a 38-dB gain, and the gain stays within a 1-dB window from -55 to 85°C . For comparison purposes the uncompensated amplifier gain variation over the temperature range would have been on the order of 3–4 dB. Although one can compensate for the gain variation, one cannot eliminate the temperature dependance of the amplifier noise figure.

Cryogenically Cooled Low-Noise Amplifiers

One of the appealing characteristics of the GaAs FET and HEMT transistors is that noise figures decrease with temperature down to almost absolute 0 K. This phenomenon is used in applications in which extremely low noise performance is required. The simplest cooling method is the use of Peltier cooling. This works almost like a home refrigerator by removing heat from the amplifier and lowering its operating temperature—thus improving the noise performance. For other applications, liquid nitrogen (77 K) or liquid helium (20 K) temperatures are used. These last two design approaches require closed-cycle refrigeration systems. A typical

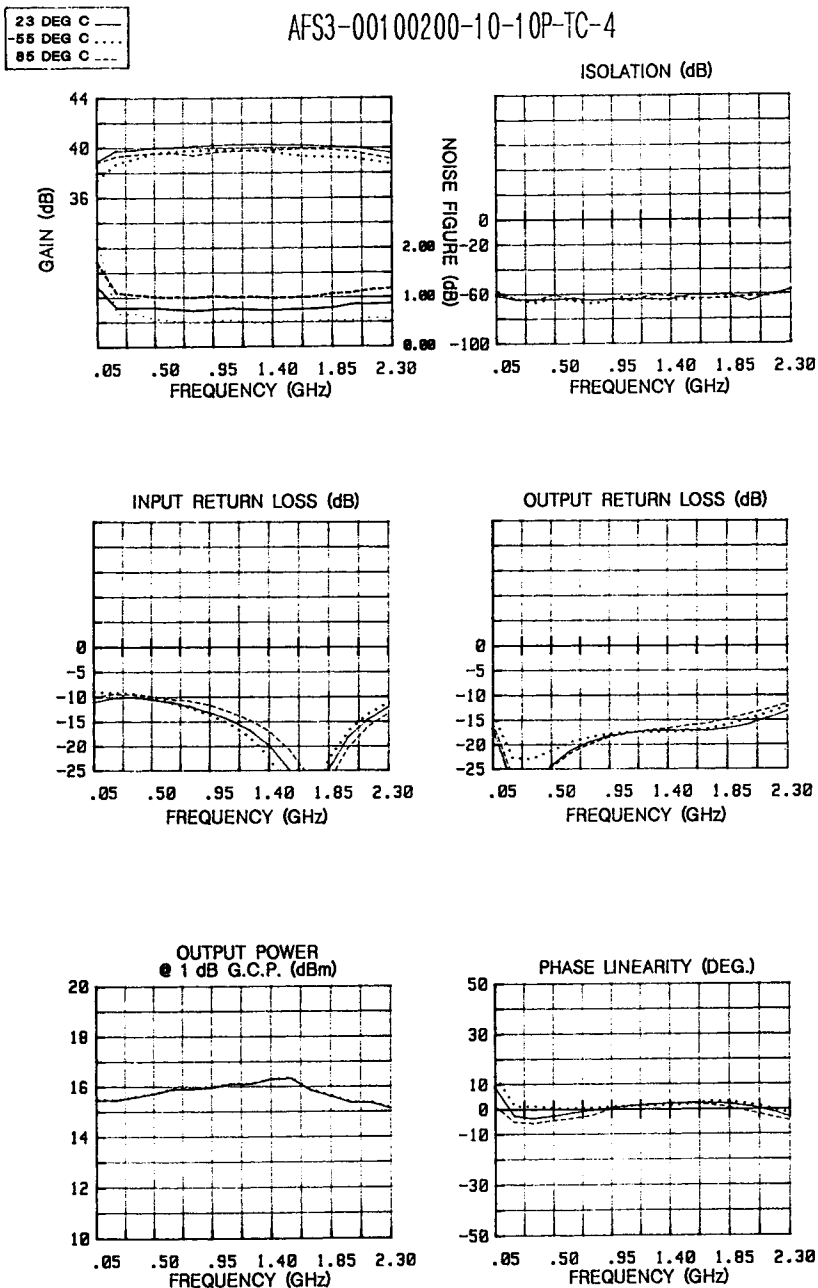


Figure 26. Temperature-compensated, 0.1- to 2.0-GHz, low-noise amplifier.

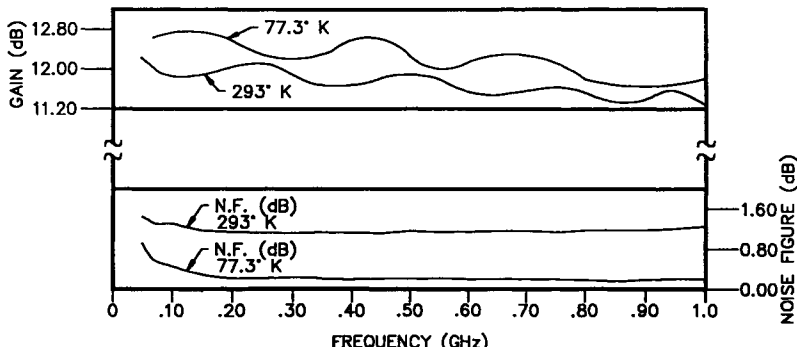


Figure 27. Cryogenically (77 K) cooled, single-stage amplifier noise: noise figure and gain as a function of temperature and frequency.

gain and noise figure performance of 0.1- to 1.0-GHz cooled amplifiers is shown in Figure 27.

Computer-Aided Amplifier Design

Over the last 20 years computers have emerged as important tools for the amplifier design engineer. Commercially available programs, such as EEsof, Super Compact, and HP8510B Microwave Design Systems, are complemented with in-house proprietary design programs by various amplifier manufacturers. The biggest drawback to computer-aided design is the engineer's inability to accurately model his circuit. The ever-present stray circuit parasitics complicate easy characterization, especially at higher microwave frequencies, and lead to incorrect results. Experienced microwave amplifier engineers find it more cost-effective to resort to their past experience in scaling their well-proven designs to their new frequency requirements. Quite often the computer modeling is done after the actual amplifier is designed and the design physically proven. However, component tolerance analysis by the computer saves time and takes out the drudgery of monotonous computations. The following amplifier performance data represent both computer-aided and noncomputerized designs that have been optimized by the design engineers on the bench. Figure 28 presents a single-stage, 0.1- to 8.5-GHz distributed amplifier design using EEsof, and Figure 29 presents the measured S-parameter data.

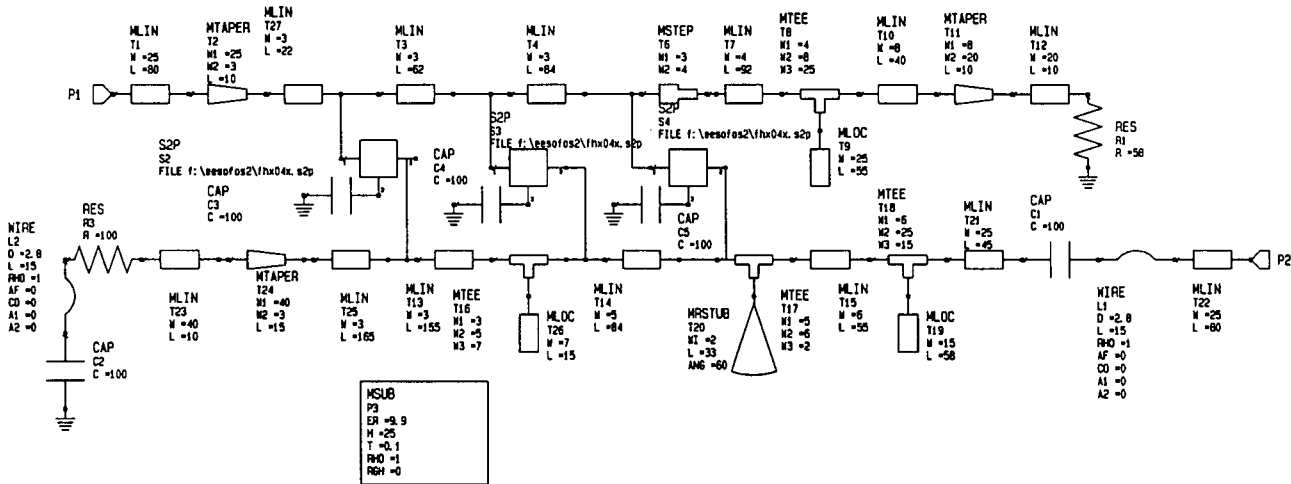


Figure 28. A 0.1- to 8.5-GHz distributed amplifier.

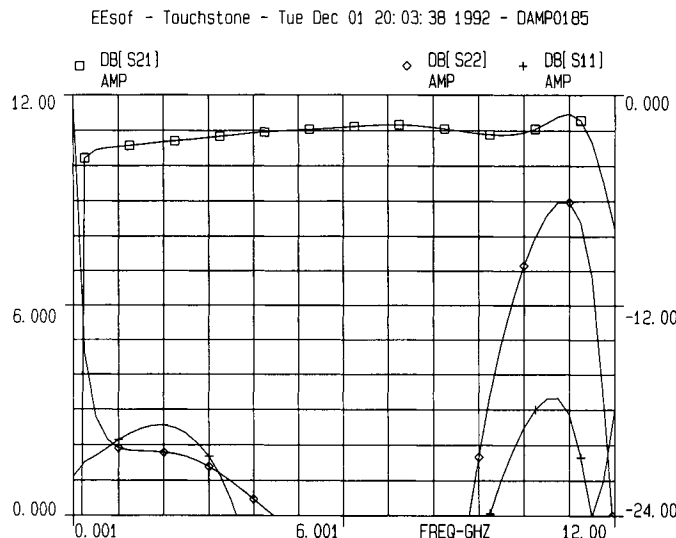


Figure 29. S-parameters of a distributed amplifier.

4. Power Amplifiers

Power amplifier design, very much like low-noise amplifier design, starts with the selection of the proper power transistor for the intended purpose. Besides the output power capability, other amplifier parameters, such as intermodulation products and AM/PM conversion, must be considered by the designer. When a single transistor does not satisfy the output power requirements, power enhancement is achieved by power-combining multiple transistors. To achieve stability and a wide bandwidth, the transistors have to be isolated from each other. The isolation is achieved by use of either 3-dB 90° hybrids that were discussed under Balanced Amplifier Design or by using Wilkinson power dividers of various designs. The simplest in-phase Wilkinson power divider consists of two $\lambda/4$ 70- Ω transmission lines and a 100- Ω resistor, as shown in Figure 30A. The signal incident on port 1 is divided equally into the two 70- Ω lines. As long as the two loads on ports 2 and 3 are equal, no power is dissipated in the 100- Ω resistor. If the loads are not equal, there will be a potential difference between the two ports and power will be dissipated in the resistor, thus minimizing gain ripples caused by mismatches.

To minimize gain ripple caused by reflections at the amplifier input and output ports in moderate-bandwidth designs, one can add an additional $\lambda/4$ line to one arm of the power divider, as shown in Figure 30B.

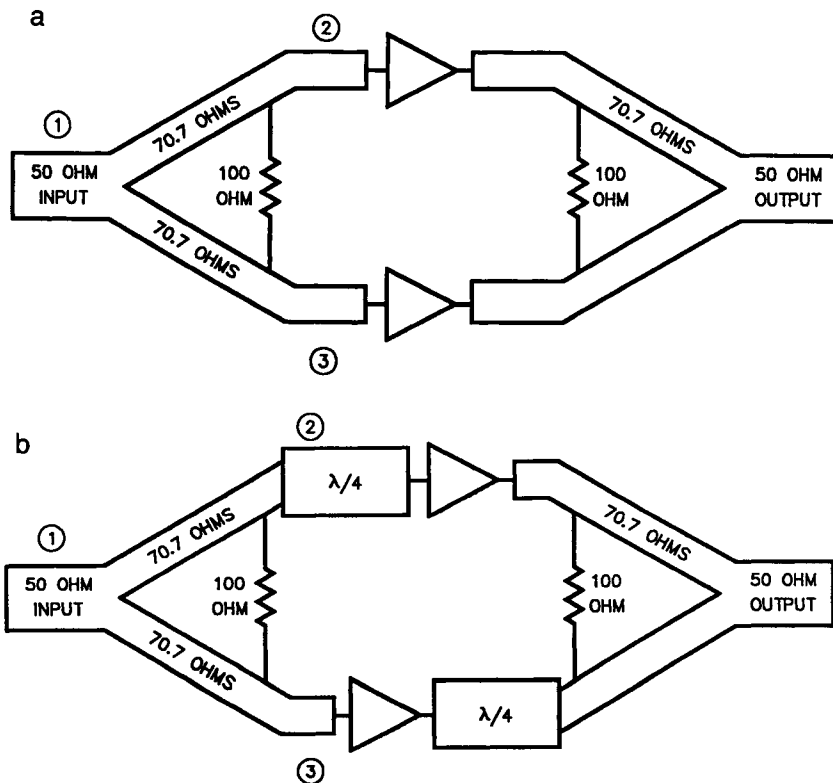


Figure 30. (a) Power combining with an in-phase Wilkinson power divider. (b) Power combining with a 90° Wilkinson power divider.

Power reflected at the amplifier input ports will arrive at the 100- Ω resistor 180° out of phase and will be dissipated in the resistor. This design approach simulates the 3-dB 90° hybrid performance and is applicable for 5–10% bandwidth designs.

The two-way power divider can be extended to multi octave frequency coverage by using multisection designs of different impedance levels and different resistance values. The power dividers can be used for both division and power combining. Normally the port-to-port isolation of a two-way power divider is on the order of 15–20 dB and decreases somewhat in a multiport device. One of the critical parameters of the divider/combiners is low insertion loss and good heat transfer characteristics. Duroid normally offers lower loss when compared with alumina substrates.

TPM1617-8 and TPM1617-16 are partially matched

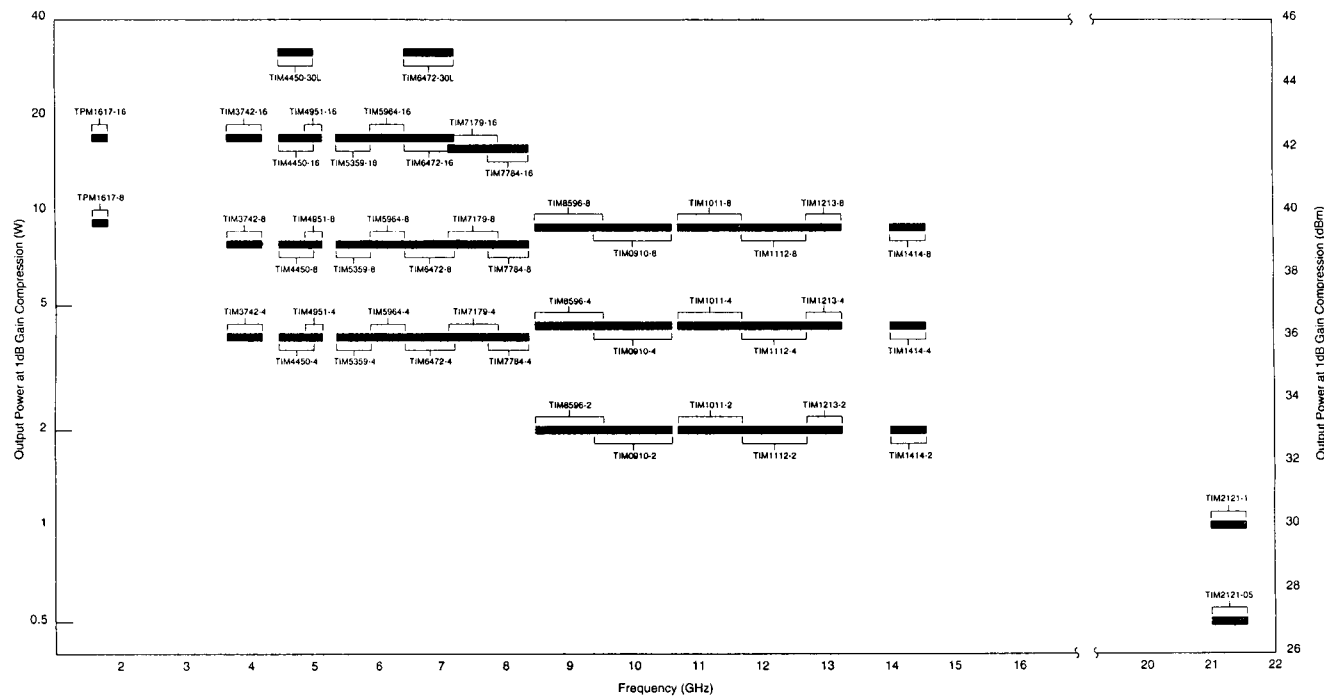


Figure 31. Toshiba IMFETs: P_{out} vs. f_{map} . TPM1617-8 and TPM1617-16 are partially matched.

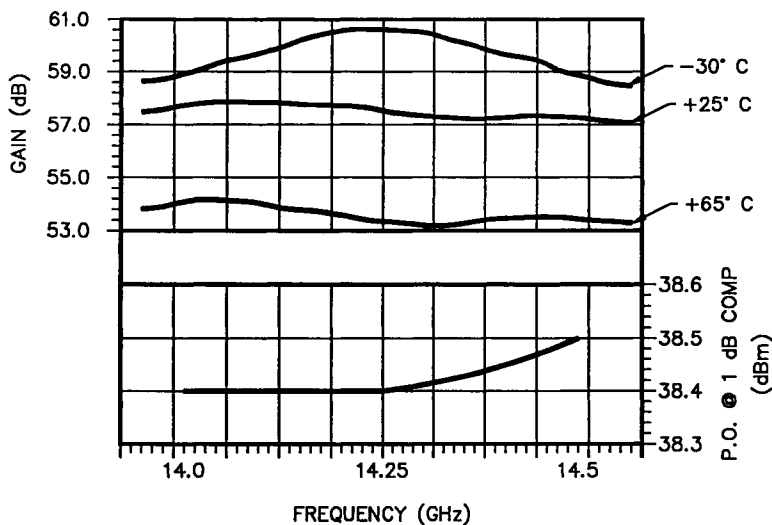


Figure 32. Gain vs frequency and temperature, and output power vs frequency of a 14.0- to 14.5-GHz, 5-W power amplifier.

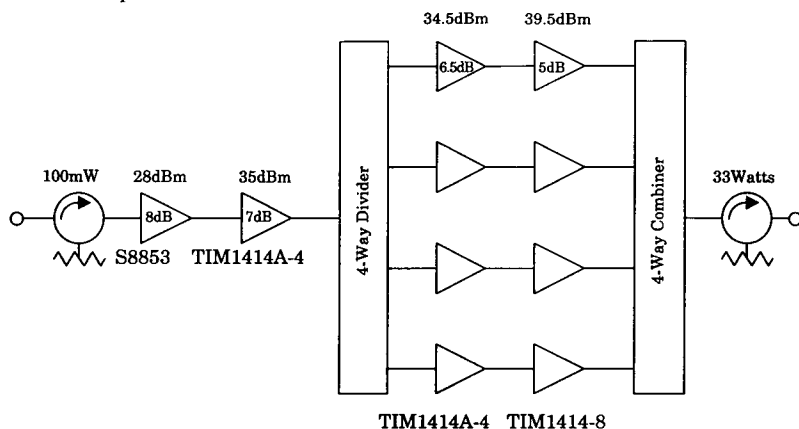
Moderate Bandwidth Amplifiers

Various power transistor manufacturers have introduced internally matched transistor modules, called TIMs. The modules are designed to work from a $50\text{-}\Omega$ source into a $50\text{-}\Omega$ load with the specified output power capability. The modules can also be cascaded for higher amplifier gain. Figure 31 lists the frequency ranges and the output power capabilities of Toshiba internally matched transistors. Figure 32 shows a 5-W 14.0- to 14.5-GHz amplifier, and Figure 33 shows various manufacturer-suggested combinations of internally matched transistors to achieve higher output power.

Octave Band Power Amplifiers

By using balanced amplifier designs, power outputs on the order of +33 dBm up to 8 GHz and of +30 dBm to 18 GHz are available. For higher power outputs, additional power combining is required and can be achieved by combinations of Lang couplers and Wilkinson power dividers. Figure 34 shows the gain and output power of a 2-W, 4- to 8-GHz amplifier.

$f = 14.0$ to 14.5 GHz
 $P_{out} = 33$ watts
 $P_{in} = 100\text{mW}$
Combining Efficiency = 93%
Total D.C. Input = 180 watts



	S8853	TIM1414A-4	TIM1414A-4	TIM1414-8
$V_{DS}(\text{V})$	9	9	9	9
$I_{DS}(\text{A})$	0.2	1.4	1.4	3.4

Figure 33. Functional block diagram of a 14-GHz power amplifier.

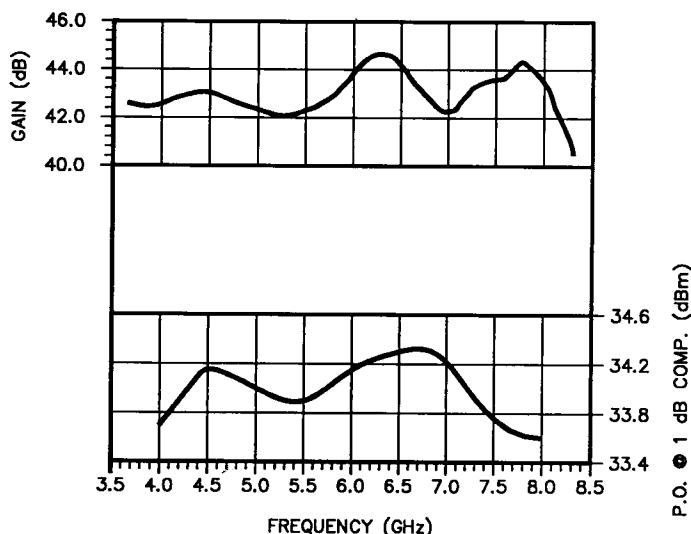


Figure 34. Gain and output power vs frequency of a 2-W, 4- to 8-GHz power amplifier.

Multioctave and Ultra-Wide-Band Power Amplifiers

Multioctave and ultra-wide-band power amplifiers using distributed MMIC designs have 1-W output power capability up to 26 GHz.

Part B: OSCILLATORS

I. Introduction

Rapid growth in telecommunications and an almost exponential increase in the use of the available electromagnetic frequency spectrum have imposed more stringent requirements on the microwave oscillator designer. Only a few years ago free-running oscillators were widely used in microwave systems and in test instrumentations. In today's applications free-running oscillators have been replaced by phase-locked designs and frequency synthesizers. In the past, phase and amplitude noise were hardly mentioned as important oscillator design parameters. With the rapid increase in digital data transmission, coupled with ever-increasing data rates, oscillator phase noise spectral density has become one of the important design parameters. In this part we will investigate the various design methods deployed by oscillator manufacturers to achieve frequency accuracy, stability, and spectral purity. Key performance parameters of oscillators are

- Frequency accuracy,
- Frequency stability vs time and temperature,
- Level stability vs time and temperature,
- Tunability,
- Spectral purity,
- Spurious outputs,
- Sensitivity to supply voltage changes, and
- Sensitivity to load impedance variations.

To facilitate the general discussion of oscillator performance, we will classify the oscillators by frequency control. This in turn can be further subdivided into free-running oscillators and externally or internally con-

trolled oscillators. The free-running oscillators can be categorized by voltage/current tuning oscillators and mechanically tuned oscillators. Under the voltage/current-controlled oscillators, we will discuss varactor-tuned oscillators and current-tuned YIG oscillators. Under mechanically tuned oscillators we have

- LC-tuned oscillators,
- Cavity-tuned oscillators,
- Coaxial-resonator-controlled oscillators, and
- Dielectric-resonator-controlled (DRO) oscillators.

Under externally controlled we have

- Phase-locked frequency sources,
- Frequency synthesizers, and
- Frequency multipliers.

Table 1 summarizes the most pertinent performance characteristics of the various types of oscillators. Phase noise spectral density is depicted separately on the following pages.

2. Free-Running Oscillators

Electronically Tuned Oscillators

Voltage-Tuned VCOs

Voltage-tuned oscillators use varactors to control the frequency of a parallel or series resonant circuit. Varactors are voltage-variable capacitors formed by reverse-biased semiconductor diodes. A total change in the capacitance limits the tuning range to octave band designs. By limiting the oscillator tuning range, the oscillator designer can improve the oscillator phase noise performance. The functional schematic diagram of an oscillator in the 2- to 4-GHz range is given in Figure 1. Figure 2 compares the phase noise performance of a 2- to 4-GHz octave band design with that of an oscillator with a 10% tuning range in the same frequency range.

Current-Tuned YIG Oscillators

YIG-tuned oscillators use the resonance characteristics of a ferromagnetic YIG sphere (yttrium–iron garnet) as the frequency determining element. A magnetic field across the YIG sphere controls the resonance frequency. The frequency of oscillation is directly proportional to the magnetic field across the YIG sphere. The magnetic field, in turn, is directly proportional to the current passed through the magnet's tuning

TABLE I
Summary of Various Oscillator Performance Parameters

Oscillator	Tunability		Frequency range	Temperature range (°C)	Temperature stability (ppm/°C)	Frequency pulling	Frequency pushing
Voltage tuned		From moderate to octave bands	40 GHz	−20–70	50–200 1.5 : 1 VSWR	0.2%	8 MHz/V
YIG tuned		Octave to multi octave	0.5–40 GHz	−50–85	10–100	1 MHz/1.5 1.5 : 1 VSWR	1 MHz/V
Cavity tuned	20%	1%	0.5–6 GHz	0–60	5–10	0.4%	0.4 MHz/V
Coaxial resonator	—	10%	0.5–3.0 GHz	−25–75	5–10	0.0002% 1.5 : 1 VSWR	0.2 MHz/V
DRO	Typical, 1% Maximum, 5%	Typical, 1% Maximum, 5%	3–20 GHz	−55–85	1–10 2 MHz maximum 500 kHz minimum 1.5 : 1 VSWR	15 kHz/V	
PLDROs	3%	0.1%	3.0–26 GHz	−20–70	same as that in reference	—	—

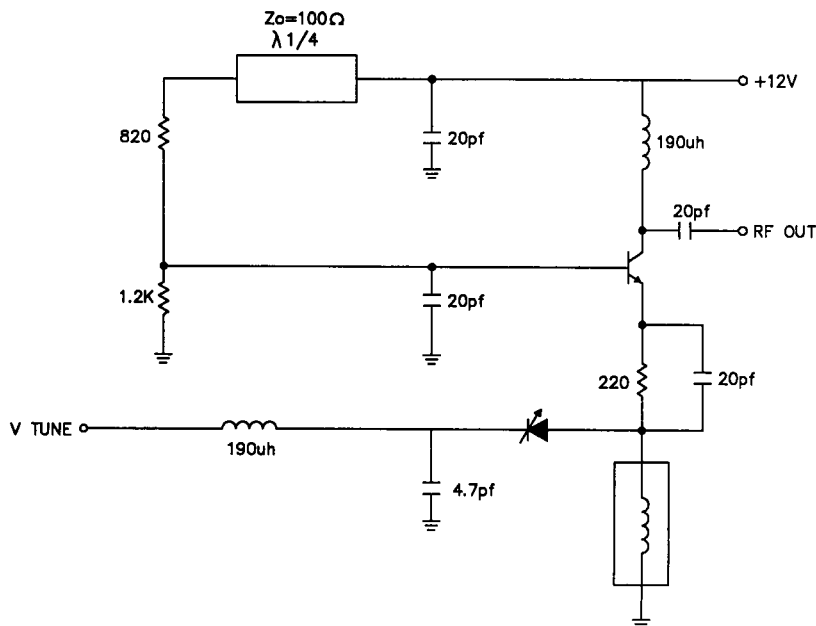


Figure 1. Schematic diagram of a 2.5- to 2.8-GHz, varactor-tuned oscillator.

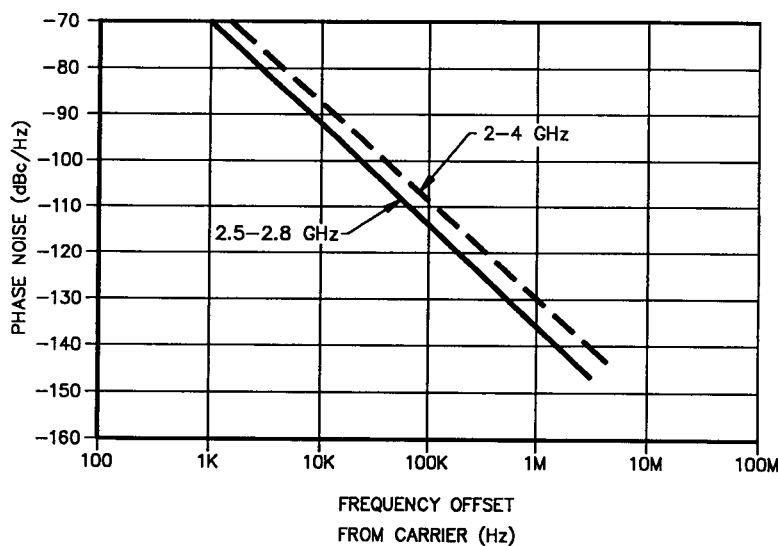


Figure 2. Phase noise spectral density of a varactor-tuned oscillator

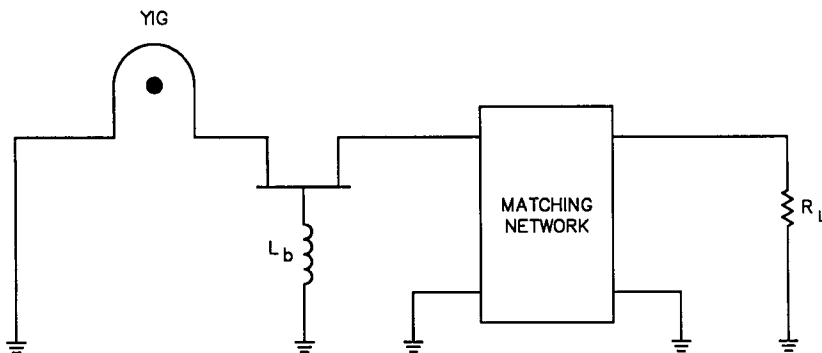


Figure 3. Common-gate GAS - FET YIG-tuned oscillator.

coil. Consequently, YIG-tuned oscillators are current-tuned devices—the frequency of oscillation is directly proportional to the current through the tuning coil—thus they exhibit better linearity than varactor-tuned oscillators.

Also, YIG oscillators have a multi octave frequency coverage compared with the varactor-tuned oscillators that are limited to an octave coverage. The YIG oscillators have much lower tuning speeds than the varactor-tuned oscillators and also exhibit hysteresis characteristics. Both bipolar and GaAs FET transistors are used. The bipolar transistors are used up to 20 GHz, and the GaAs FET devices are used up to 40 GHz. The bipolar designs offer a 15- to 20-dB improvement in phase noise performance when compared with the GaAs FET devices. The functional schematics of 2- to 8-GHz bipolar and GaAs FET YIG-tuned oscillators

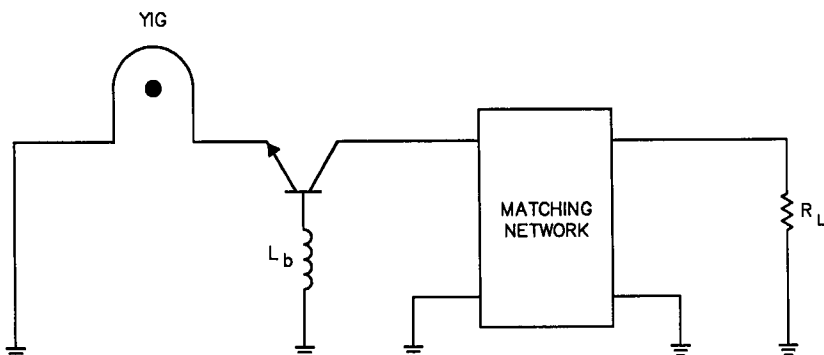


Figure 4. Common-base bipolar YIG-tuned oscillator.

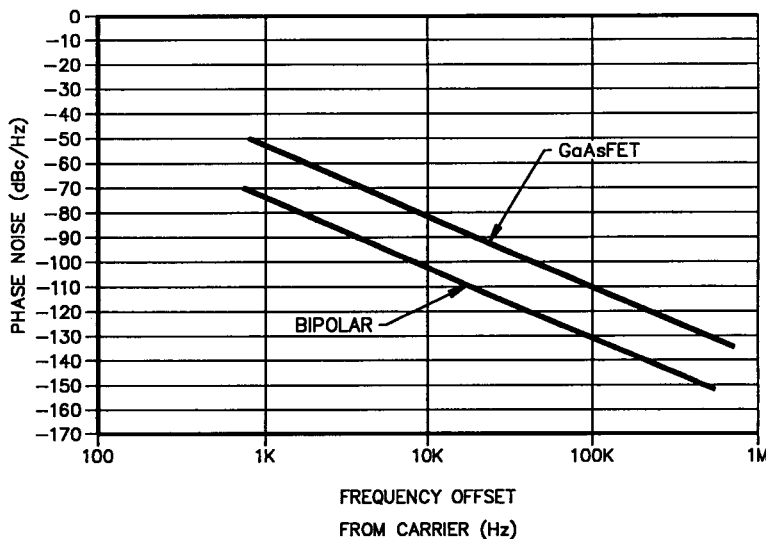


Figure 5. Typical phase noise power spectral density of a YIG-tuned oscillator at 2 GHz.

are shown in Figures 3 and 4, and typical phase noise spectral density is shown in Figure 5.

Mechanically Tuned Oscillators

LC-Tuned Oscillators

The LC-tuned oscillators are lumped-element inductors and mechanically tunable capacitors as the frequency determining elements. They are used in the 50- to 1000-MHz frequency range and are tunable over an approximately 40% bandwidth. The schematic diagram is shown in Figure 6, and the typical phase noise performance is shown in Figure 7.

Cavity-Tuned Oscillators

Cavity-tuned oscillators use a quarter-wave coaxial resonator as the frequency determining element. They are used mostly in the 0.5- to 6.0-GHz frequency range. At frequencies above 6 GHz the physical dimensions of the coaxial cavity become too small for good resonator performance, whereas below 500 MHz, on the other hand, the physical dimensions are too large for most applications. With proper mechanical design the cavity-tuned oscillators can be tuned up to an octave in the tuning range. Figure 8 shows the schematic diagram of a 2- to 4-GHz

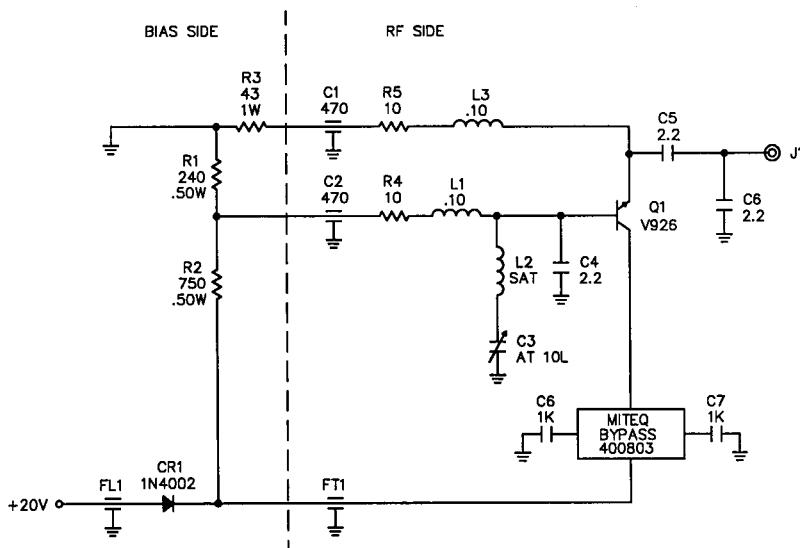


Figure 6. Schematic diagram of a 0.67- to 1.0-GC-MHz mechanically tuned oscillator.

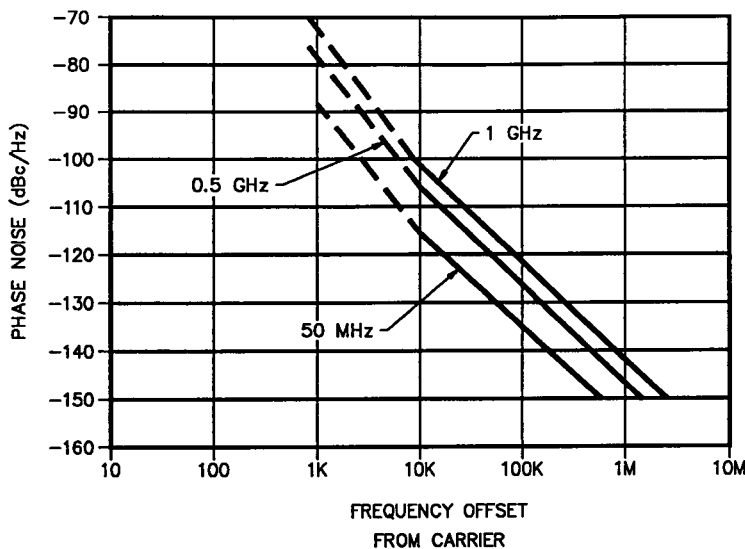


Figure 7. Typical phase noise spectral density of mechanically tuned LC oscillators.

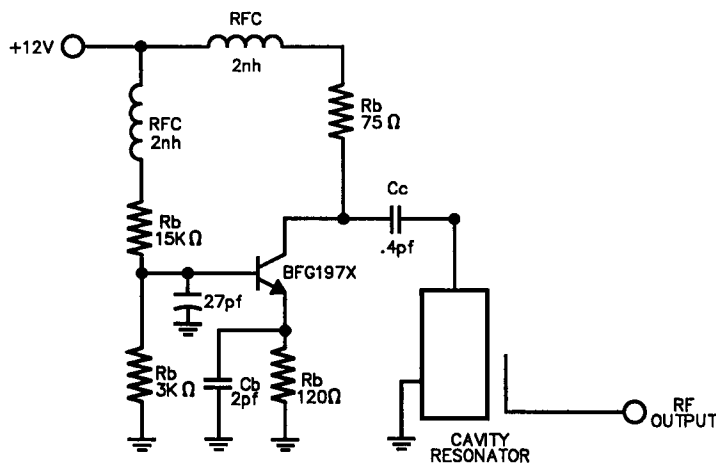


Figure 8. Schematic diagram of a cavity-tuned oscillator.

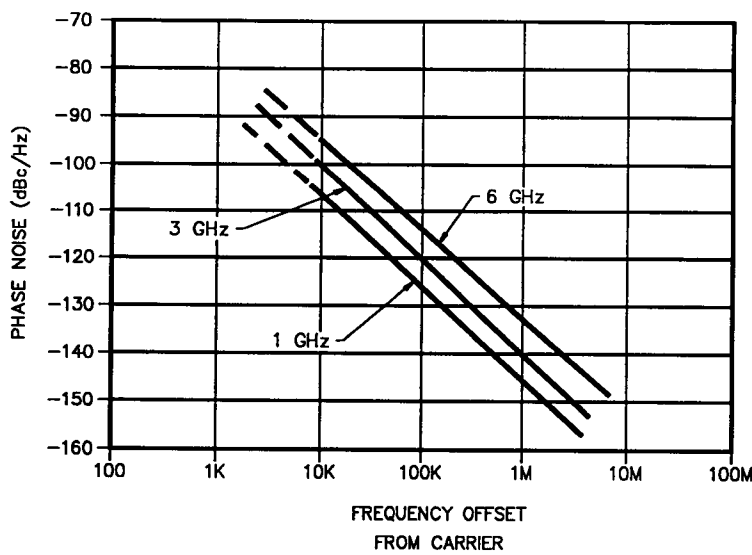


Figure 9. Typical phase noise spectral density of cavity-tuned oscillators.

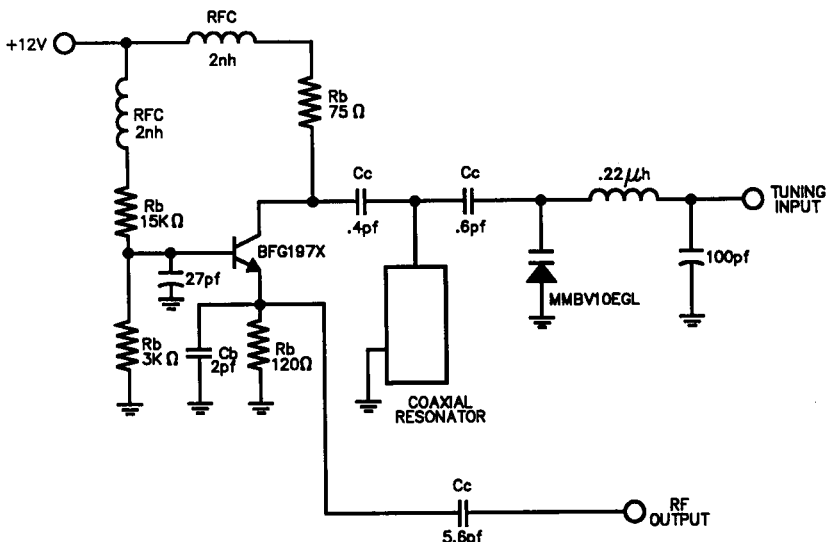


Figure 10. Schematic diagram of a coaxial resonator oscillator.

cavity-tuned oscillator. Figure 9 shows the phase noise spectral density of cavity-tuned oscillators at various frequencies.

Coaxial-Resonator-Stabilized Oscillators

Coaxial resonator designs are used in the 0.5- to 3-GHz frequency range. The frequency determining element is usually a quarter-wave or half-wave high-dielectric resonator. The dielectric constant of the resonator ranges from approximately 40 to 90. A schematic of a 900-MHz oscillator is shown in Figure 10. Phase noise spectral density is plotted in Figure 11.

Dielectric-Resonator-Stabilized Oscillators

Dielectric resonator oscillator design uses a high-dielectric resonator (sometimes called a puck) as the frequency determining and stabilizing element. Dielectric resonators are used primarily in the 3- to 20-GHz frequency range. Below 3 GHz the physical size of the resonator becomes prohibitively large for most applications. The oscillators can be mechanically tuned by approximately 1% around their center frequency by varying the air gap between the dielectric resonator and the ground plane. Figure 12 shows a schematic diagram of a typical oscillator. Figure 13 presents the phase noise power spectral density of a 10.5-GHz dielectric

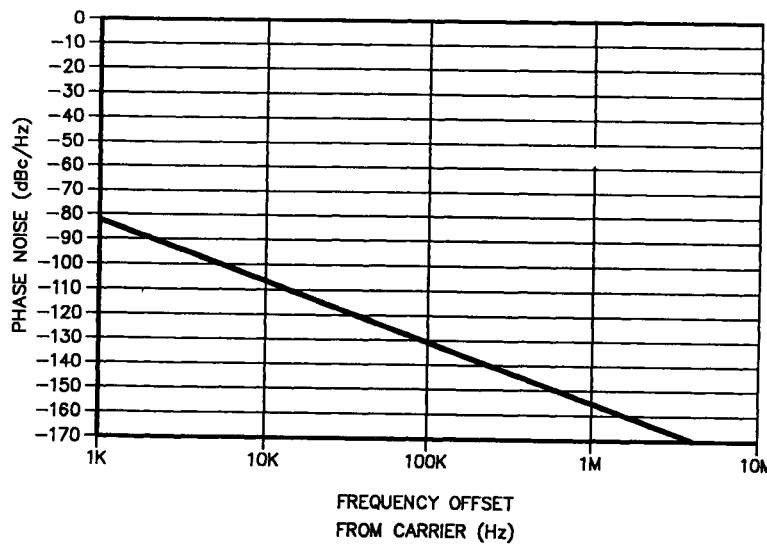


Figure 11. Typical phase noise spectral density of a coaxial resonator oscillator at 1.24 GHz.

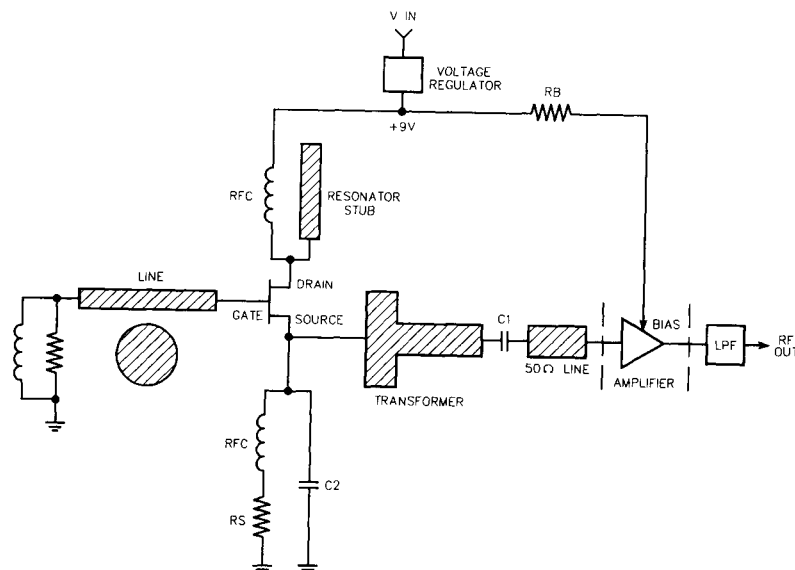


Figure 12. Schematic diagram of a dielectrically controlled oscillator.

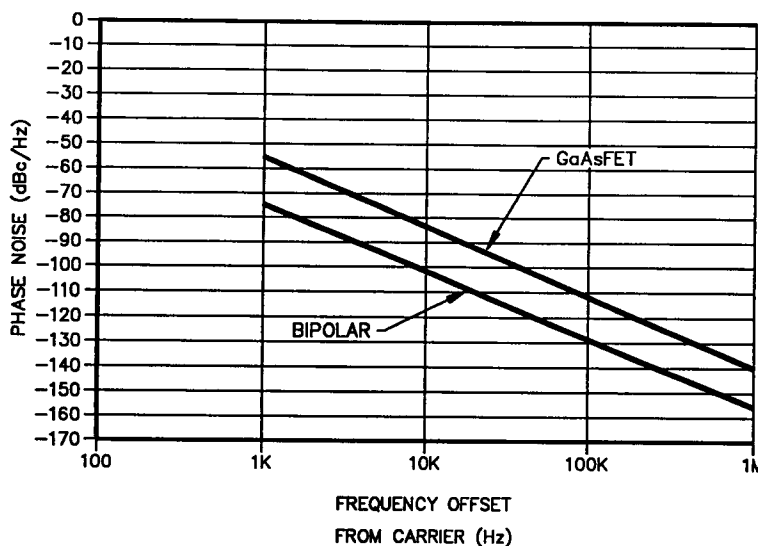


Figure 13. Typical phase noise spectral density of bipolar and GaAs FET dielectric resonator oscillators (DRO) at 10.5 GHz.

resonator oscillator using both the GaAs FET and bipolar transistors. As we can see the bipolar design offers a 10- to 15-dB phase noise improvement over the GaAs designs.

3. Internally or Externally Controlled Oscillators

Phase-Locked Frequency Sources

A properly designed phase-locked oscillator is an accurate and stable frequency source. Its stability and accuracy are directly related to the stability and accuracy of a lower frequency reference. The lower frequency reference can take many forms. It can be a fixed-frequency, high-stability crystal oscillator supplied as an integral part of the phase-locked oscillator assembly, or it can be an externally supplied crystal reference, a bank of multiple switchable crystal oscillators, or an externally supplied low-frequency synthesizer. The reference source is sometimes a phase-locked oscillator, locked to a low-frequency 1- to 20-MHz standard.

Fixed-frequency dedicated sources consist of cavity-controlled or dielectrically controlled oscillators. Multifrequency sources use cavity oscillators for applications that can tolerate the time required for cavity adjustments or use automatic frequency-agile oscillators for which a short

acquisition time or remote frequency control is required. For high-shock and -vibration environments that cannot tolerate mechanical changes, dielectric resonator oscillators are often used.

Sources of Noise in Phase-Locked Oscillators

A phase-locked frequency source offers two distinct advantages to the system designer:

1. It stabilizes the microwave oscillator to the stability of a high-performance, high-stability reference.
2. It shapes the phase noise spectral density of the microwave oscillator to approximately that of the reference within the loop bandwidth. Since normally the phase noise spectral density of the reference is orders of magnitude better than that of the free-running microwave oscillator, the phase-locked oscillator offers improved performance over the free-running oscillator. Of course, this is accomplished at the expense of a considerably more complex circuitry in comparison with that of the free-running oscillator.

A typical phase noise spectral density as a function of offset from the carrier is shown in Figure 5 in Chapter 33. The graph has four distinct regions. Very close to the carrier, the slope of the spectral density varies as $1/f^3$, followed by $1/f^2$ and $1/f$ to the constant thermal noise floor far away from the carrier. In a practical phase-locked loop, there are additional sources of noise that degrade the phase noise performance of the output. In an analog phase-locked loop, the additional sources of noise result from the phase detector and from the operational amplifiers used in the loop. In the digital phase-locked loops, digital dividers and the digital phase detector add to the phase noise. Figure 14 depicts the major sources of noise in cavity-controlled and frequency-agile phase-locked oscillators with digital and analog loop designs.

Phase-Locked Oscillator Design Approaches

Industry uses both analog and digital phase-locked loop designs. An analog design multiplies the reference signal up to the output frequency of the microwave oscillator and uses conventional analog phase detectors or sample-and-hold circuits for phase detection at microwave frequencies. A digital phase-locked oscillator uses a fixed division ratio prescaler to divide the microwave output to a lower frequency and then uses digital frequency dividers for the main signal as well as for the reference signal. Low-frequency digital phase detectors form the final link of the phase-locked loop.

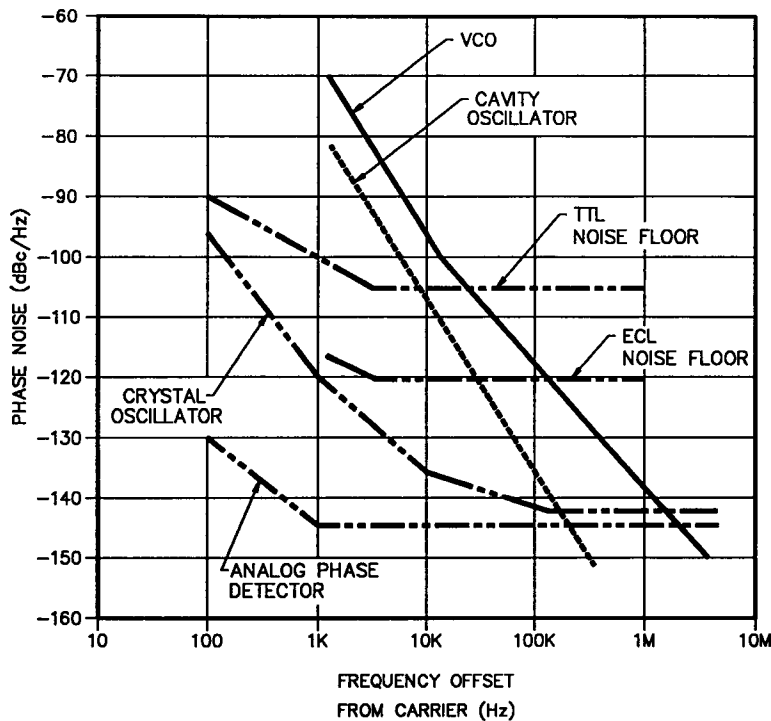


Figure 14. Various sources of noise in analog and digital phase-locked loops at 1 GHz.

The upper frequency bound in phase-locking fundamental oscillators to a lower frequency reference is limited, in the comb generator design approach, by the ability to generate sufficient comb power in the desired combline for a proper lock. With the frequency divider approach, the upper frequency bound is determined by the frequency limitation of available digital prescalers. The highest fundamental frequency is approximately 20 GHz in analog (combline) designs and 10 GHz in the digital divider approach. Functional block diagrams of the two design approaches are depicted in Figures 15 and 16.

The figures below show the major components of a phase-locked frequency source. They are

- Frequency standard (external or internal),
- Phase detector/loop filter/acquisition circuit,
- Main signal oscillator,
- Frequency dividers, and
- Frequency multipliers.

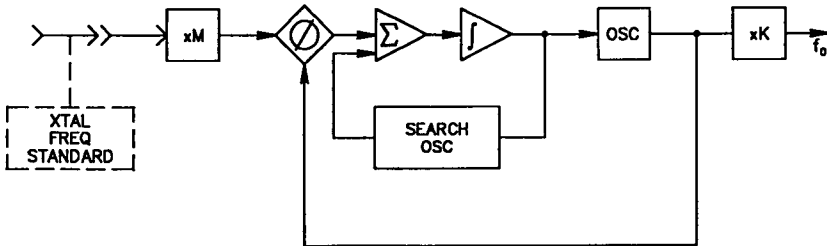


Figure 15. Analog phase-locked oscillator.

Each of these components must be tailored for a particular output frequency and desired performance. The desired output frequency F_0 is

$$F_0 = K \times \frac{F_r}{M} \times N.$$

Phase-Locked Oscillator Classification

A fixed-tuned phase-locked oscillator uses either a reference oscillator internal to the phase-lock structure or one that is supplied externally. A change of frequency for a fixed-tuned phase-locked oscillator requires readjustment of the fundamental oscillator frequency and a change in the input reference frequency. A frequency-agile phase-locked oscillator will change the output frequency when the input reference frequency is changed (within its design range).

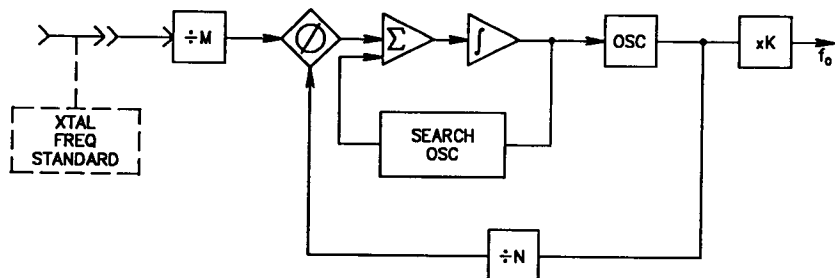


Figure 16. Digital phase-locked oscillator.

Fixed-Frequency Phase-Locked Oscillators

Four basic fixed-frequency phase-locked oscillator designs will be discussed:

1. Voltage-controlled crystal oscillators (VCXOs) phase-locked to a 1- to 20-MHz frequency standard,
2. Cavity-tuned phase-locked oscillators with internal or external reference oscillators,
3. Fixed-tuned coaxial resonator oscillators with internal or external reference sources, and

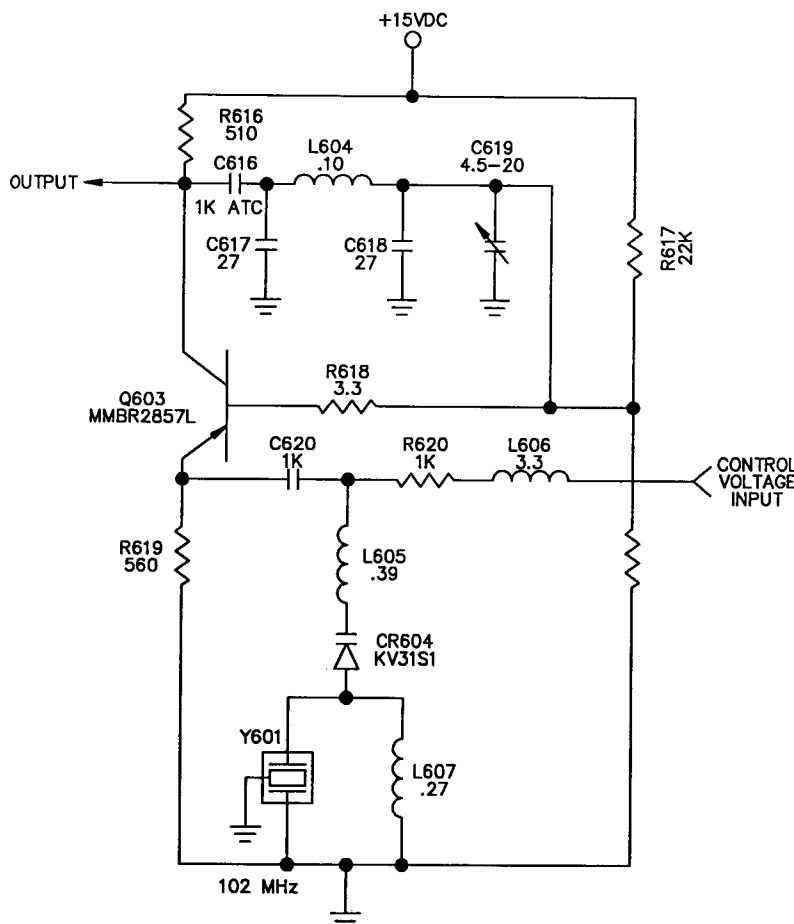


Figure 17. VCXO.

4. Fixed-tuned dielectric-resonator-controlled oscillators with internal or external reference sources.

Phase-Locked VCXOs

Current system designs often require coherency among the multiple frequency sources used in the system. For that reason, a common high-stability and high-accuracy station standard, usually in the 1- to 20-MHz range, is provided as the reference frequency for all of the frequency sources used at the station. However, using a low-frequency reference (5 MHz) in a high-frequency phase-locked oscillator makes the rejection of the reference sidebands and other spurious outputs extremely difficult.

Use of a VCXO offers an ideal solution to the problem. Within the narrow-loop bandwidth, the digital noise and the phase noise of the reference oscillator are of the same order of magnitude; consequently no degradation results from the frequency division by digital dividers. Outside the loop bandwidth, the phase noise is that of a high-*Q* crystal oscillator in the 100- to 200-MHz frequency region. In addition, the spurious outputs are filtered by the active high-*Q* output resonant circuit of the crystal oscillator. Thus the resultant oscillator exhibits the high stability and

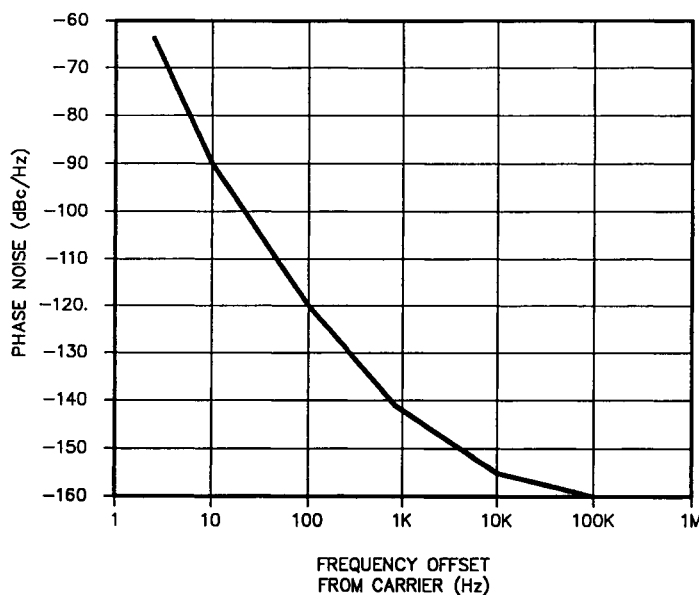


Figure 18. Typical phase noise spectral density of a VCXO phase-locked oscillator at 102 MHz (5 MHz reference).

accuracy of the low-frequency oscillator. If this source is used as a reference for a higher frequency oscillator, coherency as well as low-phase noise performance results. Typically all nonharmonically related spurious signals are rejected by more than 100 dB.

When the VCXO is used as a reference source for a higher frequency oscillator, the approach is known as a dual phase-locked loop design. Figure 17 shows a schematic of a typical VCXO at 102 MHz, and Figure 18 depicts the phase noise spectral density.

Phase-Locked Cavity Oscillators

Phase-locked cavity oscillators can be used with fundamental crystal oscillators or with phase-locked VCXOs as frequency references for fixed frequency applications. In addition, they can be used with a variable frequency reference or with multicrystal oscillators as a reference source. The variable reference frequency or multiple-crystal oscillator approaches can be used only in applications in which time allows the cavity oscillator to be returned to reacquire a lock. A schematic diagram of a cavity-tuned phase-locked oscillator is shown in Figure 19, and typical phase noise performance is shown in Figure 20.

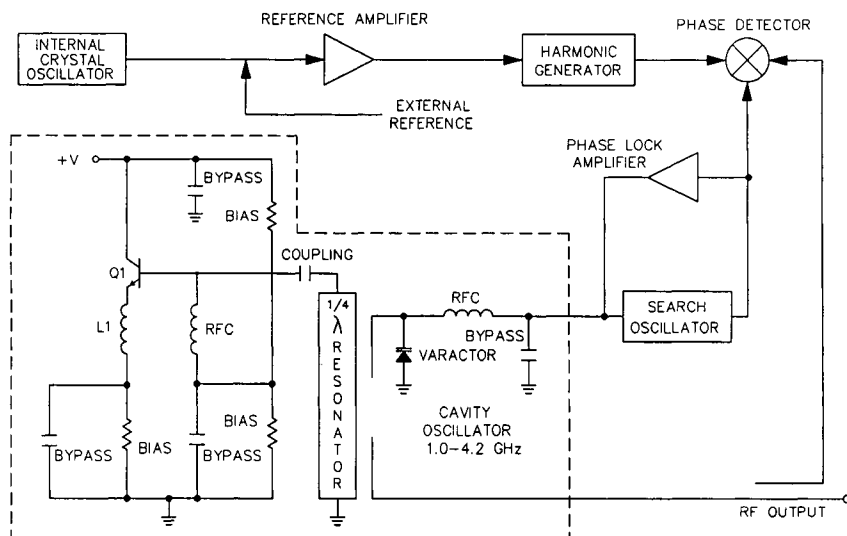


Figure 19. Phase-locked cavity oscillator.

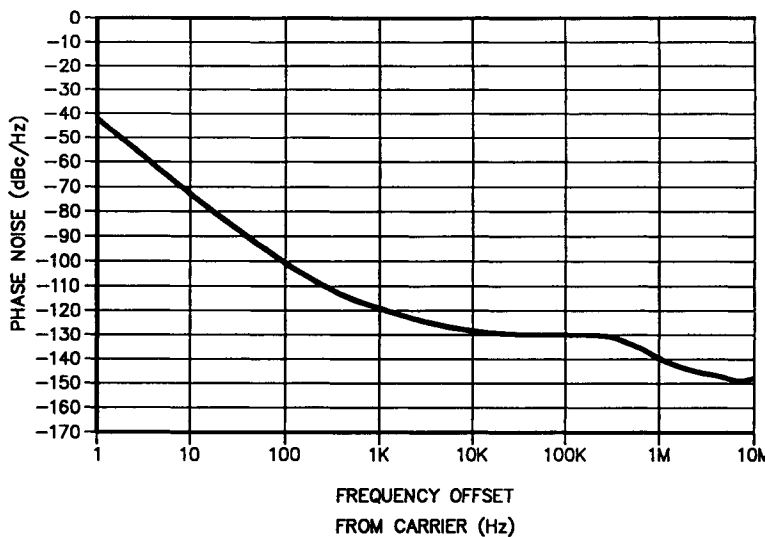


Figure 20. Typical phase noise spectral density of a phase-locked cavity oscillator at 1 GHz.

Phase-Locked Coaxial Resonator Oscillators

When a varactor tuning port is added to the free-running coaxial resonator oscillator, it can be phase-locked like the cavity oscillator to a stable crystal reference source. Figure 21 shows a schematic diagram of a coaxial resonator oscillator, and Figure 22 depicts the phase noise spectral density.

Dielectric Resonator Phase-Locked Oscillators

When a voltage control port is added to a free-running DRO, it can then be used as a phase-locked frequency source. Figure 23 shows a functional block diagram of a phase-locked DRO, and Figure 24 presents phase noise data at various frequencies.

Variable-Frequency Phase-Locked Sources

For applications that require a highly stable but variable-frequency microwave signal source, frequency-agile phase-locked oscillators are used. The frequency-agile oscillator can be phase locked to a multiple-crystal source or to a low-frequency, high-performance frequency synthesizer. These sources use fundamental high-performance voltage-controlled oscillators with a 10% nominal bandwidth up to 1.5 GHz in frequency. At

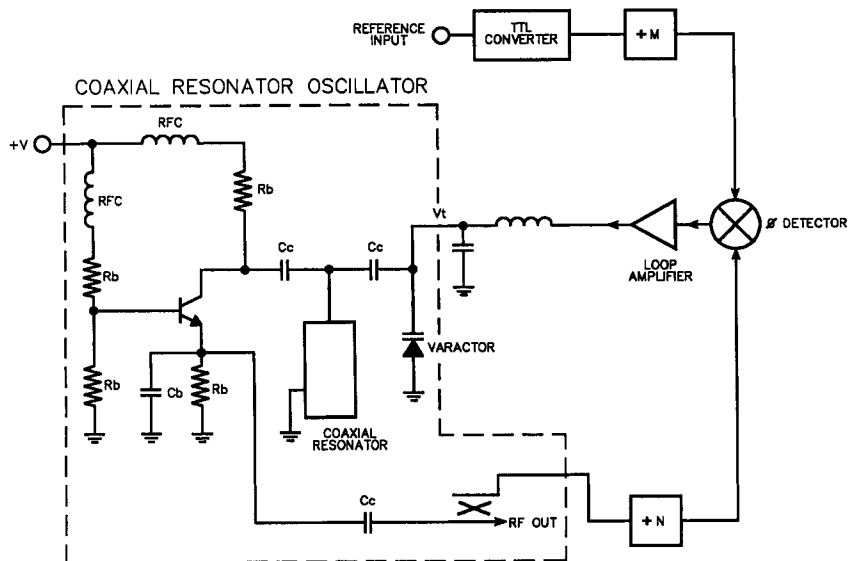


Figure 21. Coaxial resonator phase-locked oscillator.

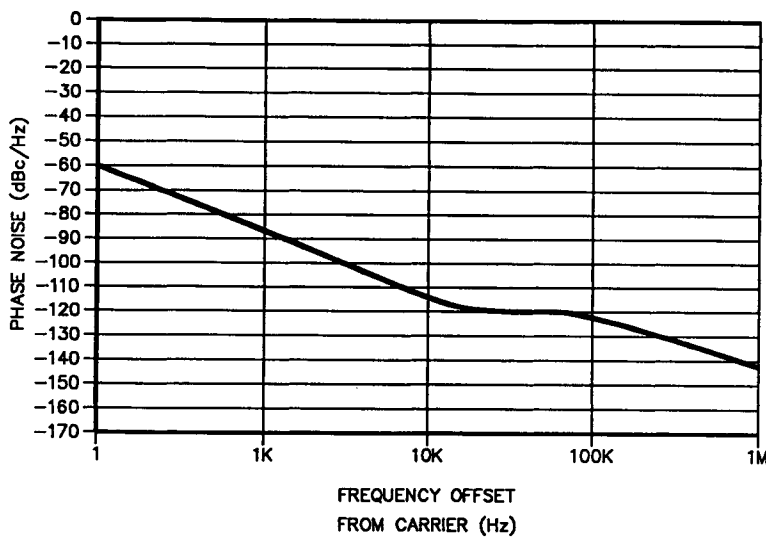


Figure 22. Typical phase noise spectral density of a coaxial resonator phase-locked oscillator at 1.26 GHz.

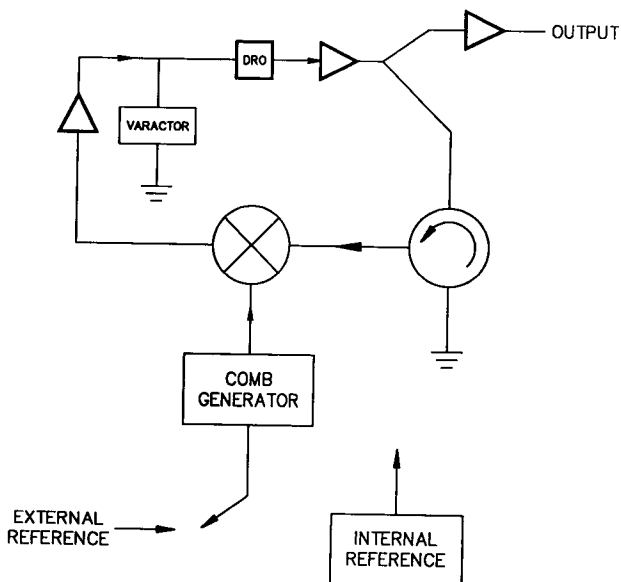


Figure 23. Functional block diagram of a phase-locked DRO oscillator.

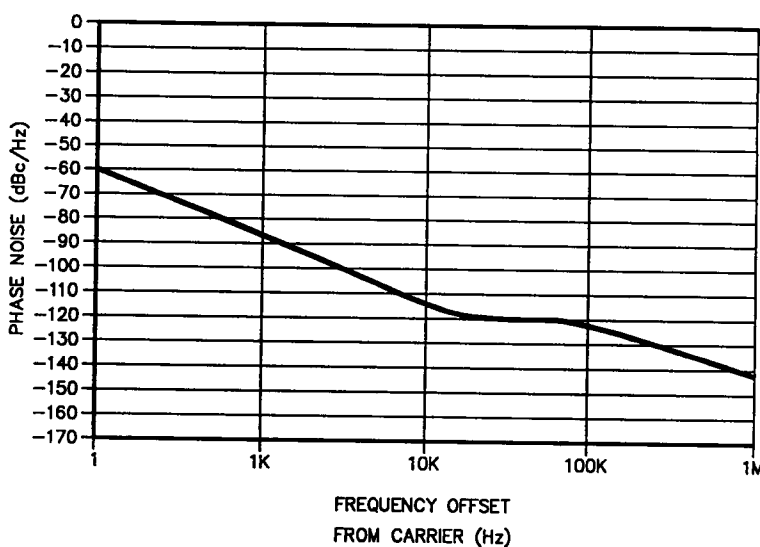


Figure 24. Typical phase noise spectral density of a 10.5-GHz, bipolar transistor DRO phase-locked oscillator.

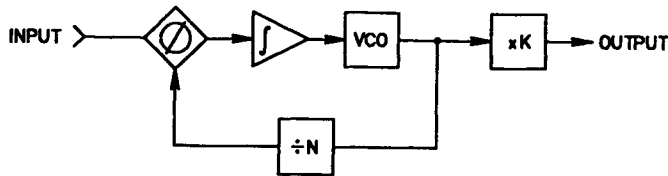


Figure 25. Functional block diagram of a frequency-agile phase-locked oscillator.

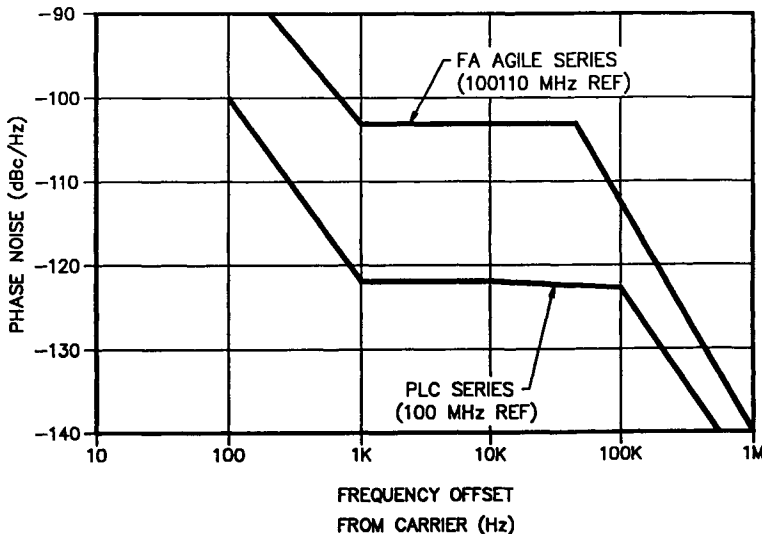


Figure 26. Typical phase noise spectral density of cavity- and voltage-tuned phase-locked oscillators at 1 GHz.

frequencies above 1.5 GHz, either passive or active frequency multipliers are used.

The phase-locked oscillators use both analog and digital loop design approaches. A functional block diagram of a frequency-agile phase-locked oscillator is shown in Figure 25 and Figure 26 gives the comparative phase noise performance of the fixed-frequency and frequency-agile sources.

4. Frequency Synthesizers

The ever-increasing complexity and sophistication of today's systems are imposing more stringent performance requirements on the frequency sources that are used as system building blocks. Frequency stability, frequency agility, coherency, and good spectral purity are only a few of

these new demands. Frequency agility itself requires either the output frequency of the transmitter or the local oscillator frequency of the receiver to be changed in a preprogrammed or predetermined manner. If the number of required frequency steps is small and if coherency among the outputs is not required, the design can be accomplished in a mechanically tuned cavity oscillator or in a frequency-agile oscillator phase locked to a bank of switched crystal oscillators. The former can be used only if the time allocated for a change of frequency permits the mechanical retuning of the cavity. As the number of required frequency steps increases or if coherency among the output frequencies is required, the multiple-crystal oscillator design approach becomes uneconomical. In most of these instances the system designer uses the frequency synthesizers. There are two design alternatives:

1. A frequency-agile oscillator phase locked to a low-frequency synthesizer or
2. A self-contained microwave synthesizer with a step size small enough to meet the frequency accuracy and frequency resolution requirements of the application.

Frequency synthesizers have a wide range of applications. For instance, they are used in superheterodyne receivers and transmitters that require reception or transmission of multiple carriers over a specified frequency range, frequency hopping radars, and frequency generators that require extreme frequency stability, setability (resolution), and accuracy. The performance requirements of the synthesizers vary greatly. For example, a synthesizer for satellite telephony or video transmission requires only coarse frequency steps, and close-to-the-carrier phase noise performance is not of the utmost importance. On the other hand, synthesizers for single-channel-per-carrier applications and for high-data-rate digital transmissions require very good close-in phase noise performance. Synthesizers for military applications require fast switching times in addition to the spectral purity and low-phase-noise requirements. Therefore, the detailed specifications for these sources are as varied as differences in the specific systems themselves and require different design approaches. Below we will discuss the theory and performance of direct and indirect frequency synthesizers.

Direct Frequency Synthesis

Direct analog frequency synthesis can be implemented by a large variety of frequency generation blocks. The specific requirements, such as frequency range, step size, spurious output, and phase noise, influence the design

approach. Direct synthesis is implemented by use of the following basic design techniques.

Integer frequency multiplication. This is accomplished by generating and selecting a desired harmonic of a reference signal.

Integer frequency division. Digital dividers are used for frequency division.

Addition and subtraction. Double balanced mixers are used to generate sum and difference frequencies. Filters are used to eliminate the unwanted mixed output signals.

Direct synthesis can be implemented using any arithmetic base, such as 2, 4, 8, or 10.

The following simplified example illustrates a base 10 iterative design technique. Refer to Figure 27 to supplement the following discussion.

The frequency generation block is composed of three major subsections, fixed frequency generation, variable frequency generation (synthesis), and frequency translation. The last translates the synthesized frequency range to the output frequency range. The fixed frequency generation part of the block generates 10 fixed frequencies. 18–27 MHz. Each of these frequencies is connected to a series of 10-pole single-throw switches. The switches, S_1 , S_2 , and S_3 , select one of the 10 frequencies and connects it to a mixer input. The following example illustrates the operation of the frequency plan. Let S_1 , S_2 , and S_3 select 18 MHz. The 2-MHz input to M_1 , the first mixer, mixes with the 18 MHz from S_1 to produce a 20-MHz sum frequency. The 20-MHz sum output is divided by 10 in the divider D_1 to generate 2 MHz. Since the remainder of the block is iterative, the last

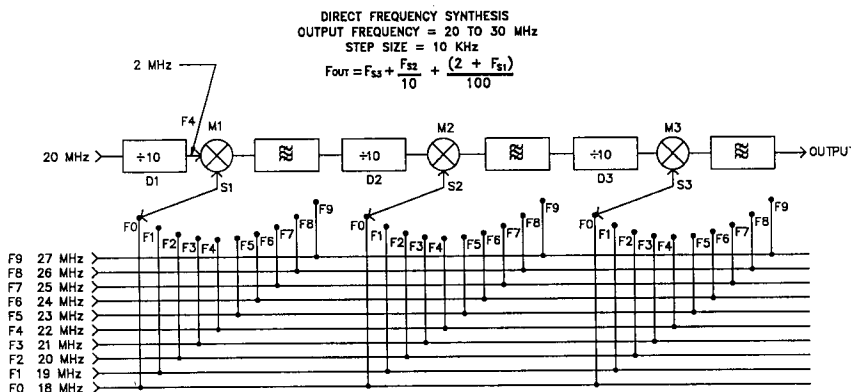


Figure 27. VHF section of a direct frequency synthesizer.

mixer, M_3 , will also generate a 20-MHz output. Since the last mixer, M_2 , is not followed by a divider, 20 MHz is the output frequency. Let the first selector switch, S_1 , now select 19 MHz, whereas S_2 and S_3 remain connected to the 18-MHz bus. The output of the first mixer is now 20 MHz. The output of the second mixer is now 20.1 MHz ($21/10 + 18$). The output of the third mixer is 20.01 MHz. For each iterative stage that the signal passes through, the frequency slip resolution is enhanced by an additional decade. The equation for the output frequency is:

$$F_{\text{out}} = F_{S_3} + \frac{F_{S_2}}{10} + \frac{(2 + F_{S_1})}{100},$$

where F_{S_N} is the frequency ($F_0 - F_9$) selected by the selector switches.

This output signal is known as the VHF fine-tune frequency. The VHF selection is shown in Figure 28. A switched oscillator is mixed with a comb signal, producing a fixed output frequency. This is normally stepped in 10-MHz increments. This new frequency is then mixed with the VHF signal. The mixed output signal is then mixed with another signal (f_1) which is stepped normally in 1-MHz increments. These are the medium-tune steps for the synthesizer. The signal and the switched oscillator are multiplied by 10 and mixed to produce the desired output frequency.

The switchable oscillator can be a good nonlocked unit, since its stability and phase noise are cancelled out theoretically due to up and down conversion. The reference frequency generators can be locked oscillators, comb generator filter combinations, or both.

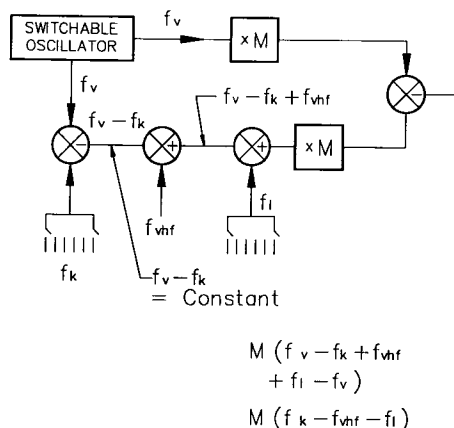


Figure 28. UHF section of a direct frequency synthesizer.

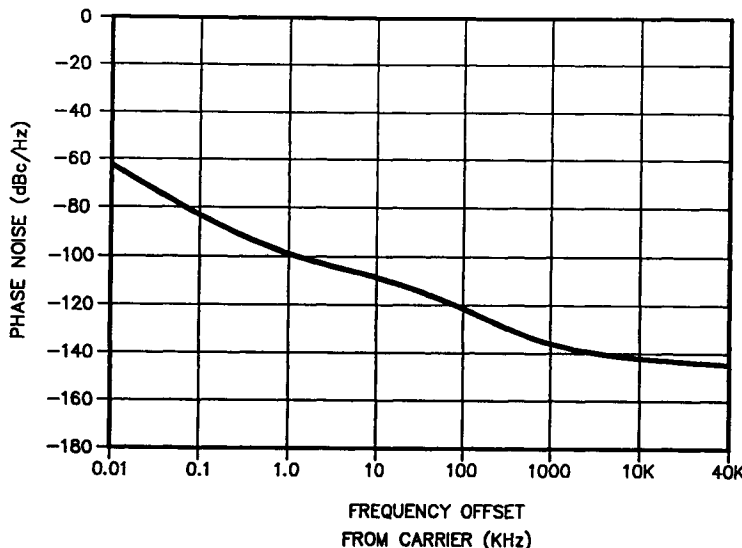


Figure 29. Phase noise power spectral density of a direct frequency synthesizer at 8 GHz.

Direct synthesis has the advantage of fast switching and high spectral purity. Its disadvantages are size and cost. The typical phase noise spectral density of a direct frequency synthesizer is shown in Figure 29.

Indirect Frequency Synthesis

Phase Noise as a Function of Synthesizer Bandwidth

The phase noise power spectral density of the frequency synthesizer depends on the synthesizer frequency coverage. As the tuning range of the synthesizer increases, so does the phase noise power spectral density. This degradation to phase noise performance is caused by the lower Q of the tuned circuits associated with the more widely tunable oscillators. A typical L-band oscillator phase noise as a function of tuning range is shown in Figure 30. This performance degradation can be overcome by the use of the multiple switched oscillators, each with a narrow tuning range.

Spurious Outputs

Spurious outputs are the undesired by-products of the various frequency divisions, multiplications, and frequency translations. They can be suppressed and their numbers minimized, but cannot be completely eliminated. Techniques of spurious minimization include judicious frequency

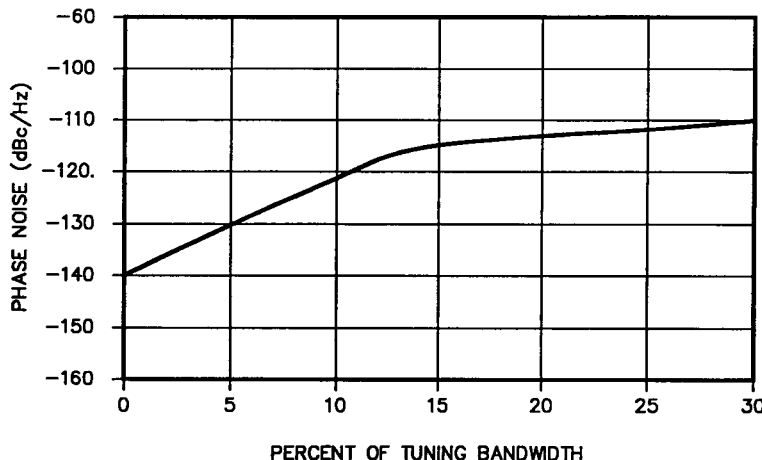


Figure 30. Typical phase noise power density of an L-band oscillator as a function of tuning bandwidth at 100 kHz from the carrier.

selections for the various subloops, proper frequency division and multiplication ratios, sufficient selectivity in the loop filters, and, of course, sufficient filtering, decoupling, and regulation of the power supplies. Elimination of ground loops diminishes the level of spurious sidebands caused by the power-line frequencies and their harmonics. The most troublesome are the in-band spurious outputs, because they cannot be filtered by additional output filters. The level of out-of-band spurious signals can be decreased by additional filtering.

Indirect Frequency Synthesizers

Single-Loop Designs

A functional block diagram of the basic single-loop frequency synthesizer is shown in Figure 31. Although single-loop synthesizers are very cost-effective frequency sources, they have performance limitations in more stringent system applications. The basic design limitations of a single-loop synthesizer are its close-in phase noise and relatively high spurious outputs close to the carrier. These limitations are the result of high-order multiplication of the reference noise and narrow-loop bandwidth. Even though the final output of the synthesizer is locked to the reference and has the same frequency stability, the narrow-loop bandwidth required for small frequency steps makes the output sensitive to outside perturbances, such as line voltage pickup, vibrations, shock, etc. Phase

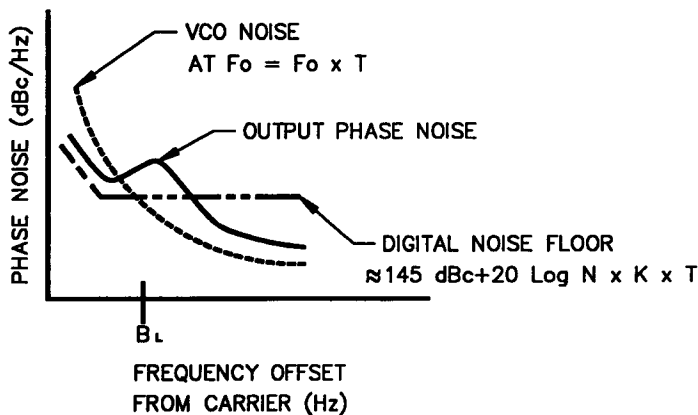
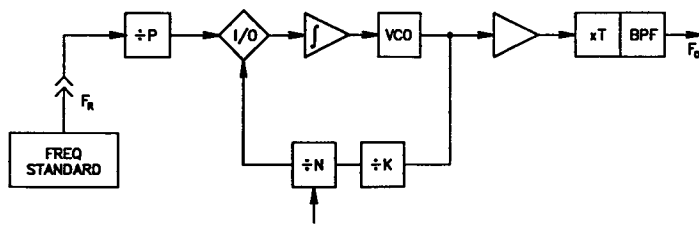


Figure 31. Functional block diagram and sources of phase noise in a single-loop frequency synthesizer.

noise also depends on the step size. This design is useful for analog video transmitter and receiver applications.

Multiloop Designs

The limitations of the single-loop frequency synthesizer are overcome with a multiloop synthesizer design. The multiloop frequency synthesizer consists of three basic subassemblies, as shown in Figure 32:

1. The fine frequency synthesizer,
2. The coarse frequency synthesizer, and
3. The output summing phase-locked loop.

The output frequency is generated in the output summing phase-locked loop by adding the outputs of the fine- and coarse-step subassemblies. The coarse-step synthesizer divides the output frequency range into several equal frequency intervals, whereas the fine-frequency synthesizer provides the desired step resolution within each coarse-frequency segment. The fine-frequency section of the synthesizer can itself have finer frequency

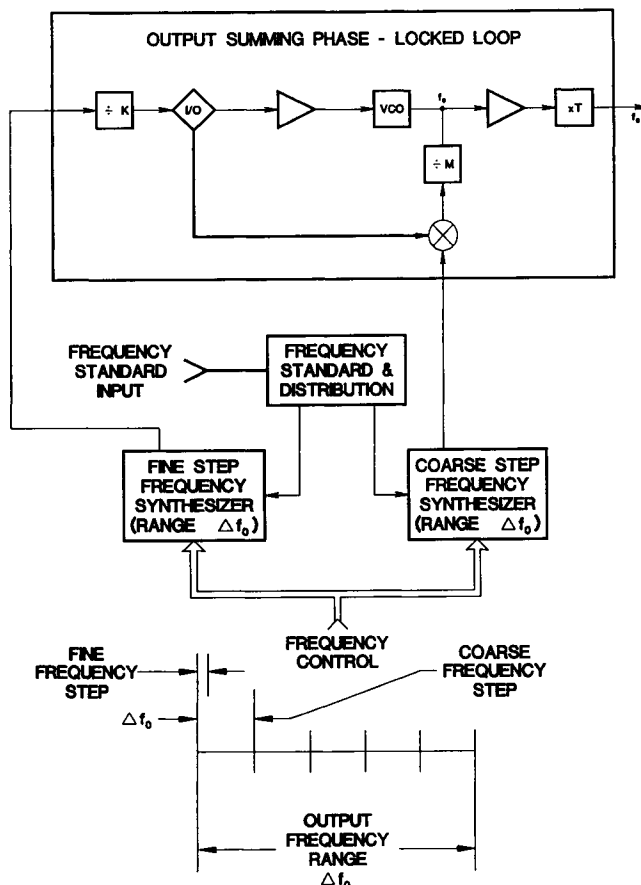


Figure 32. Functional block diagram of the multiloop frequency synthesizer.

subloops. The coarse-frequency synthesizer has a large frequency step size, and quasidirect synthesis techniques can be used to obtain good spectral purity and fast output switching. The comparative phase noise performance of the various synthesizer designs in the 4.7- to 5.3-GHz frequency range, with a 125-kHz frequency step size, is shown in Figure 33.

1. The single-loop synthesizer (Figure 31) normally has a low-loop bandwidth since its reference frequency is less than 10 kHz; thus, VCO noise predominates.

2. Noise is primarily generated in the coarse loop which uses digital dividers to obtain the desired frequency. These dividers limit the achievable noise reduction.

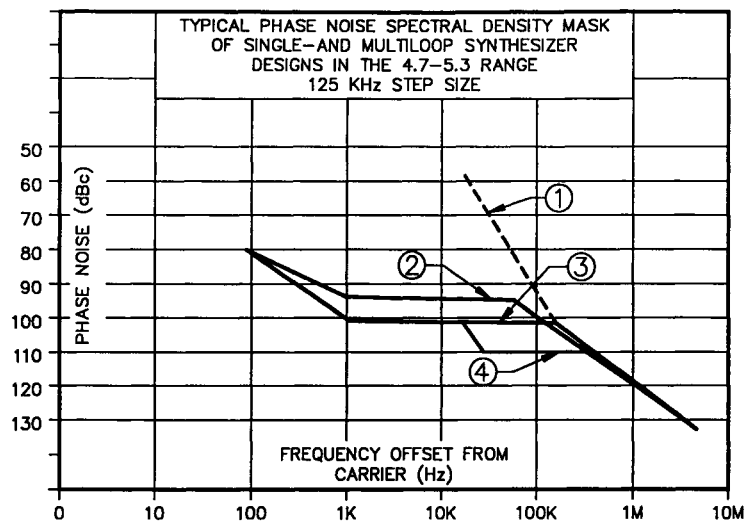


Figure 33. Typical phase noise spectral density mask of single- and multiloop synthesizer designs in the 4.7- to 5.3-GHz range, with a 125-kHz step size.

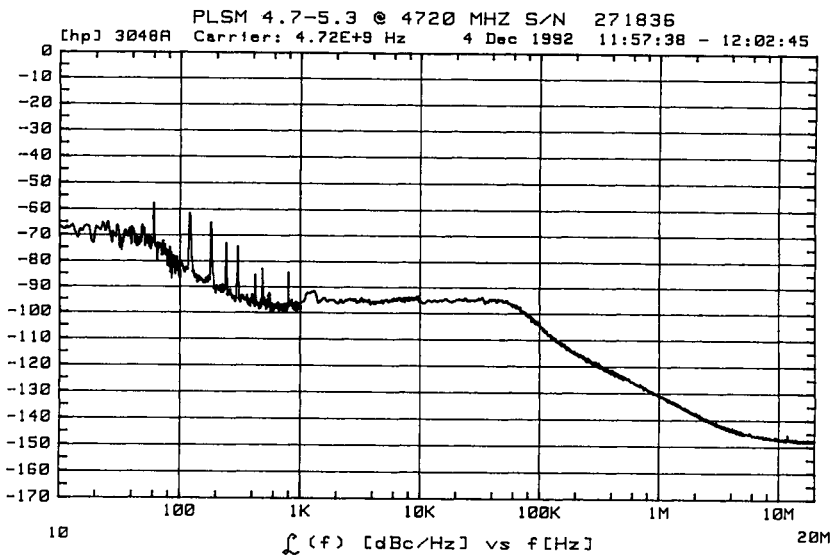


Figure 34. Phase noise power spectral density of a 4.7- to 5.3-GHz, 125-kHz-step frequency synthesizer at 4.72 GHz.

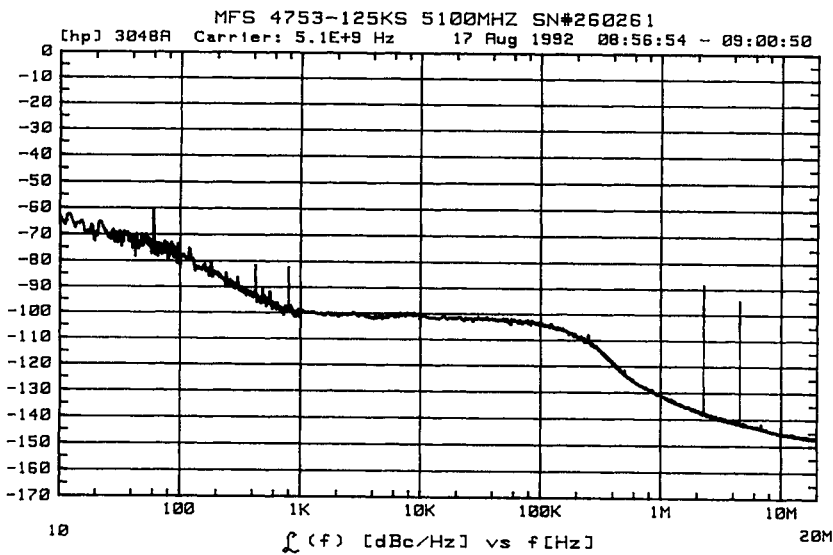


Figure 35. Phase noise power spectral density of a 4.7- to 5.3-GHz, 125-kHz-step frequency synthesizer at 5.1 GHz.

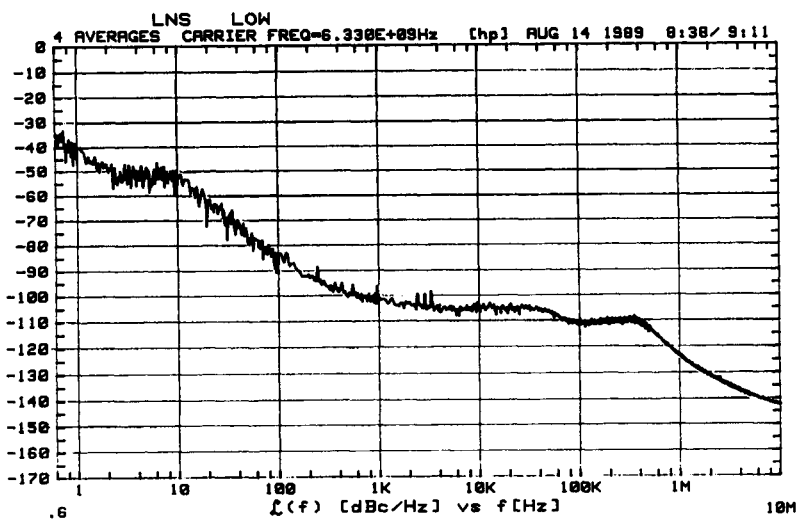


Figure 36. Phase noise power spectral density of a 6.0- to 6.5-GHz, 1-kHz-step frequency synthesizer at 6.33 GHz.

3. Through the use of crystal oscillators in the coarse loop, the digital phase noise is eliminated. The noise floor is primarily due to main-loop and fine-loop noise.

4. Similar to the previous synthesizer, except that the initial mixing frequency is four times higher than before ($M \times T$ is $\frac{1}{4}$ of the above $M \times T$). This reduces the noise floor contribution of the main loop by 10 dB.

Figures 34, 35, and 36 show measured phase noise data of the various multiloop synthesizer designs.

5. Frequency Multipliers

Frequency multipliers extend the frequency range of fundamental frequency sources. Multipliers are used either to obtain improved performance compared with fundamental sources at the multiplied frequency or to provide signal sources at frequency ranges in which fundamental oscillators are not available.

In most frequency multiplier designs, the multiplier output contains, besides the desired harmonic output, unwanted signals. These include the fundamental input signal leakage, as well as lower and higher order harmonics generated in the multiplier. Quite often with odd-order multipliers, the undesired signals are higher in level than the desired signal. In even-order ($\times 2$ and $\times 4$) multipliers, the undesired outputs are normally 10–20 dB below the desired output. Thus, the output signals can be amplified before the output is filtered. This is not possible with odd-order multipliers, because the unwanted signals will cause the amplifier to saturate and suppress the desired output.

Frequency Doublers

Both passive and active frequency doublers are commercially available. The passive doubler is a full-wave rectifier that has the second harmonic as the highest output Fourier component. The conversion loss range is 10–15 dB, and the fundamental rejection is approximately 15–20 dB. Frequency doublers can be designed to cover multioctave frequency bands. Active frequency doublers combine passive doublers with wide-band medium-power amplifiers. Figure 37 shows the output power and fundamental rejection of a 10- to 20-GHz-input and 20- to 40-GHz-output passive frequency doubler. The input power in the 10- to 20-GHz range was nominally +22 dBm. An active doubler performance in the same

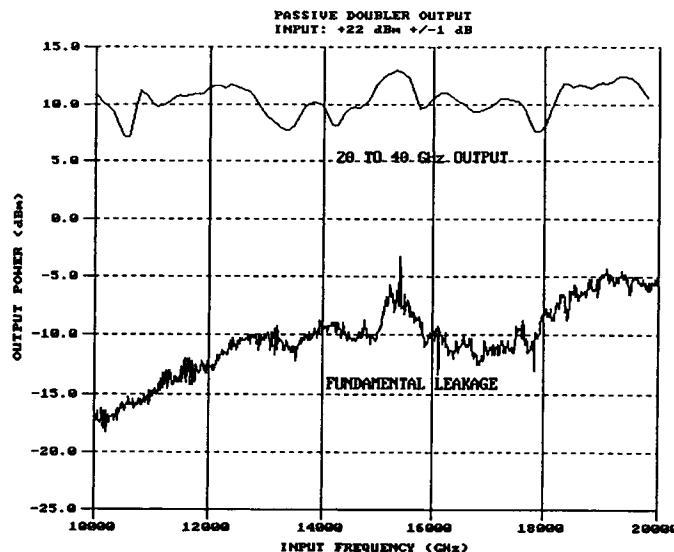


Figure 37. Output power and fundamental leakage vs frequency of a 20- to 40-GHz, passive frequency doubler at +22 dBm of nominal input. Datapoint spacing equals 100 MHz.

frequency band is shown in Figure 38. The doubler consists of a passive doubler and a three-stage, 20- to 40-GHz amplifier. The input power to the doubler was +10 dBm nominal.

Higher Order Frequency Multipliers

In addition to the frequency doublers described previously, MITEQ also manufactures wide-band frequency triplers, quadruplers, and quintuplers. The bandwidth of these multipliers is limited by the existence of higher order harmonics within the desired frequency band. The maximum spurious-free bandwidth for the various orders of multiplication can be expressed mathematically as

$$\text{tripplers: } \frac{f_H}{f_L} = \frac{4}{3}$$

$$\text{quadruplers: } \frac{f_H}{f_L} = \frac{5}{4}$$

$$\text{quintuplers: } \frac{f_H}{f_L} = \frac{6}{5},$$

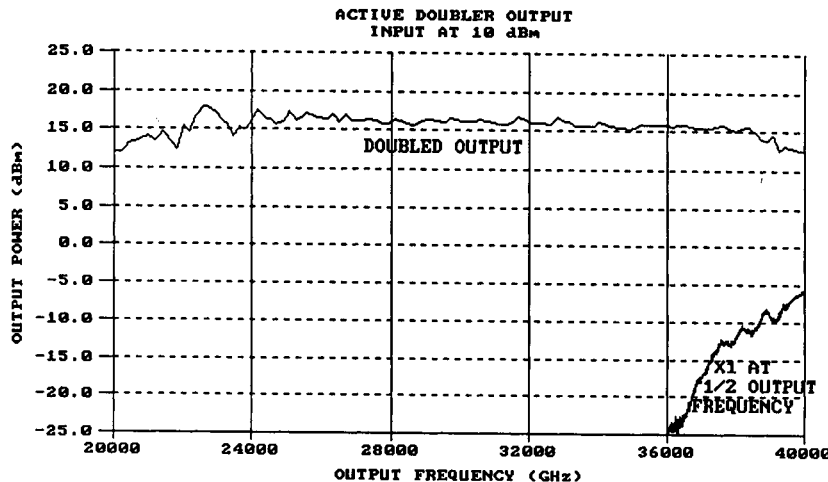


Figure 38. Output power and fundamental leakage vs frequency of a 20- to 40-GHz, active frequency doubler at +10 dBm of nominal input. Datapoint spacing equals 180.1 MHz.

where f_H is the high end of the spurious free band and f_L is the low end of the spurious free band.

In a practical situation, the operable bands are narrower because filters do not have infinite skirt selectivity. The actual bandwidth depends on the desired out-of-band spurious rejection, the relative level of the undesired harmonic power closest to that of the desired harmonic, etc. Also, for higher multiplication ratios that can be factored into cascadable multipliers with intermediate filters, the multiplier bandwidth can be increased over that of a single-step multiplier.

Reference

- [1] W. S. Percival, "Thermionic Valve Circuits," Br. Pat. 460,562, Jan. 25, 1937.

Microwave Detectors, Mixers, Converters, and Harmonic Generators

T. Koryu Ishii

I. Microwave Amplitude Modulation Detectors

Basic Circuit

The principle of AM detection is rectification. With the rectifier and accompanying filters, the AM detector recovers the envelope of AM microwaves. Therefore, AM detectors are also called envelope detectors. The objective of the AM detector is to recover the modulating signals from modulated microwaves. This recovering process is also termed de-modulation [1, 2].

A basic schematic diagram of an AM detector circuit is shown in Figure 1. Most microwave detection is performed using semiconductor detector diodes. Detector diodes are basically microwave rectifying diodes. They open for the negative half-cycle of microwaves and close for the positive half-cycle of microwaves.

As seen in Figure 1, there are two types of AM microwave detectors. The diode detector can be mounted either in series with the output circuit or in parallel with the output circuit. In the series diode detector circuit shown in Figure 1a, the detected voltage appears for positive half-cycles of microwaves across the load resistance R . During the negative half-cycles

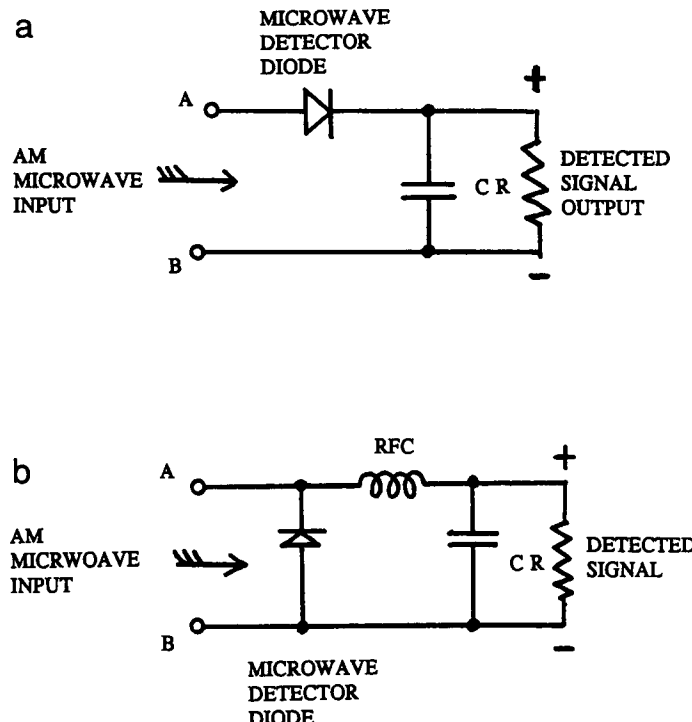


Figure 1. Basic AM detector circuits. (a) Series diode detector circuit. (b) Shunt diode detector circuit.

the diode is open. Thus, during that period, the microwave circuit is open. The capacitance C is for the cycle-to-cycle voltage smoothing. In the case of the shunt diode detector circuit, the detected voltage appears across the load resistance R for the negative half-cycles of microwaves. During positive half-cycles, the microwave source circuit is short-circuited and no microwave voltage is available to the detector output resistance R . The shunt capacitance C is for the cycle-to-cycle detected voltage smoothing. The choke coil RFC shown is for the isolation of the detector load from microwave leakage by preventing microwaves from entering the demodulation signal circuit. In both detector circuits, if the polarity of the diode reverses, then the polarity of demodulated signals also reverses.

After all, a microwave detector is a microwave rectifier. Therefore the microwave quadruple detector shown in Figure 2 is also used. The diodes are often developed monolithically and packaged as an integrated circuit chip [3–5]. These are also called the ring detector or the bridge detector.

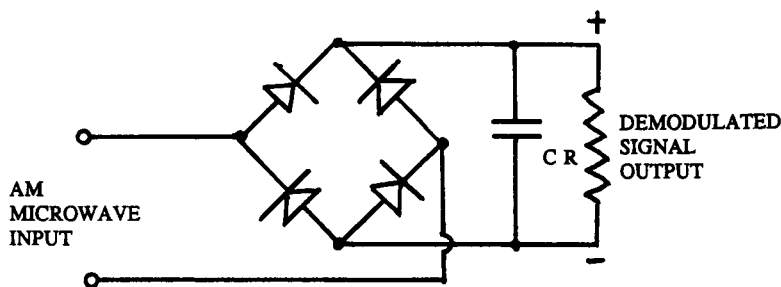


Figure 2. Basic AM quadruple detector.

In Figure 2, C is the capacitance for the cycle-to-cycle detected voltage smoothing and R is the detector load resistance across which the detected voltage appears. The quadruple detector is a full-wave rectifier or full-wave detector [1].

Two-Wire Line AM Detector Circuit

Examples of schematic diagrams of two-wire line (TWL) AM detector circuits are shown in Figure 3. All detector circuits must have an impedance matching network between the TWL and the detector. If the operating wavelength is short, a short-circuited stub or open circuited stub impedance matching transformer, as shown in Figure 3a, may be practical. If the operating wavelength is too long, then a lumped parameter impedance matching transformer, as shown in Figure 3b, is practical. DC blocking capacitors are necessary to prevent detected signals from going back to the microwave transmission line at the input side and DC isolation toward the demodulation signal circuit at the detector output side. The blocking capacitors on the output side should not be used in the case of microwave CW (continuous unmodulated wave) detection. Most two-wire line detector circuits must be fabricated from discrete circuit components. Therefore the microwave detector diodes for this application should be packaged in such a way that two solderable lead wires come out of both ends of the detector diode package. Some examples of such packaged microwave detector diodes are listed in Table 1. These diodes are glass packaged and ready to be soldered onto a circuit board. In this table, tangential signal sensitivity (TSS) is the microwave input signal power level which is 2.6 dB over the noise at the input [6]. Most detector diodes listed in Table 1 are silicon Schottky barrier diodes [3–5].

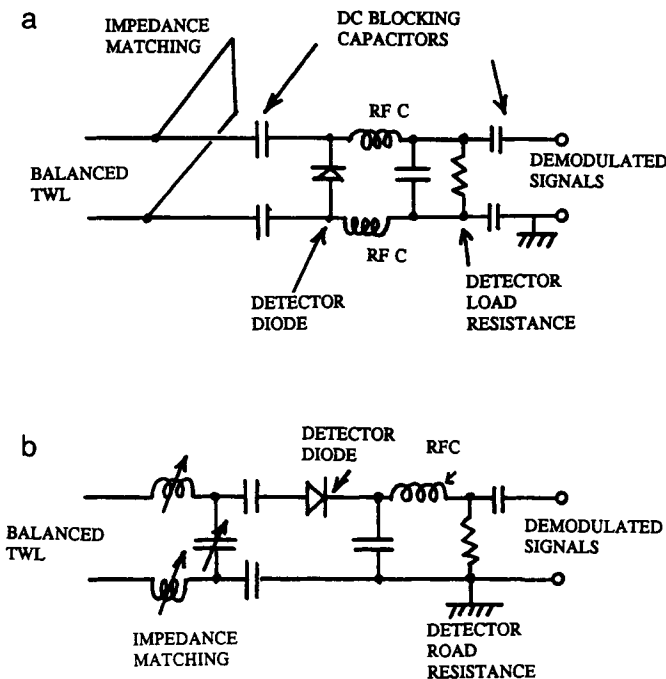


Figure 3. Two-wire line (TWL) AM detector circuit. (a) TWL shunt AM detection. (b) TWL series AM detection.

Coaxial Line AM Detector Circuit

Examples of schematic diagrams of coaxial line AM detector circuits are shown in Figure 4. The detector diode can be mounted in series with the coaxial line as shown in Figure 4a or in parallel with the coaxial line as shown in Figure 4b. The radio frequency choke (RFC) is a low-pass filter. It passes demodulated low-frequency signals but it stops microwave frequency signals from leaking. The tuners shown in Figure 4 concentrate the maximum available microwave power on the detector diode by sliding a contact- or noncontact-type shorting plunger by taking an impedance matching. For that matter, selection of distances l_1 and l_2 in Figure 4a and distance l_1 in Figure 4b is important. In addition to the line end tuner, an additional input impedance matching transformer at the input before the entrance to this detecting structure will be helpful for better sensitivity. Normally, the detected signal output is terminated by the load impedance which also provides a DC return for the detector diode.

TABLE I
Examples of TWL AM Detector Diodes [3 – 5]

Microwave detector diode	Package size		Operating frequency range (GHz)	Nominal TSS (dBm)
	Diameter (mm)	Length (mm)		
40052L	1.72 ~ 1.91	3.68 ~ 4.19	1–3	–50
40053L	1.72 ~ 1.91	3.68 ~ 4.19	1–3	–55
40072L	1.72 ~ 1.91	3.68 ~ 4.19	3–12	–50
40204L	1.72 ~ 1.91	3.68 ~ 4.19	3–12	–52
40202L	1.72 ~ 1.91	3.68 ~ 4.19	3–12	–55
4E928	1.72 ~ 1.91	3.68 ~ 4.19	1–12	–49
4E928A	1.72 ~ 1.91	3.68 ~ 4.19	1–12	–52
4E928B	1.72 ~ 1.91	3.68 ~ 4.19	1–12	–55
4E928C	1.72 ~ 1.91	3.68 ~ 4.19	1–12	–56
4E928D	1.72 ~ 1.91	3.68 ~ 4.19	1–12	–56
DDL6672	1.73 ~ 1.91	3.81 ~ 4.44	3.95–12.4	–48
DDC4562	1.73 ~ 1.91	3.81 ~ 4.44	8.2–12.4	–56
5082-2755	1.73 ~ 1.91	3.81 ~ 4.32	1–12	–55
5082-2787	1.73 ~ 1.91	3.81 ~ 4.32	1–12	–52
5082-2824	1.73 ~ 1.91	3.81 ~ 4.32	1–12	–56

In the case of Figure 4b, the end cap of the short circuit can be a screwed cap which provides access to the diode mounting, and the diode can be spring loaded. Then adjusting the screwed cap itself can help the impedance matching of the diode. This effect is apparent in higher microwave frequencies.

The detector diodes are packaged in a cartridge type, a pill type, or a coaxial type depending on the detector mount design [7]. Some examples of commercially available coaxial line AM detector diodes are listed in Table 2. In this table, X-band means a frequency range of 8.2 ~ 12.4 GHz, S-band means 2.6 ~ 3.95 GHz, KU-band means 12.4 ~ 18 GHz, and Q-band means 33 ~ 50 GHz.

Waveguide AM Detector Circuit

Schematic diagrams of waveguide AM detector circuits are shown in Figure 5. As seen in Figure 5a, a packaged detector diode is mounted often directly inside a waveguide. Impedance matching between the waveguide and the diode is performed by both the screw tuners and the waveguide shorting plunger in this example. Detected output appears

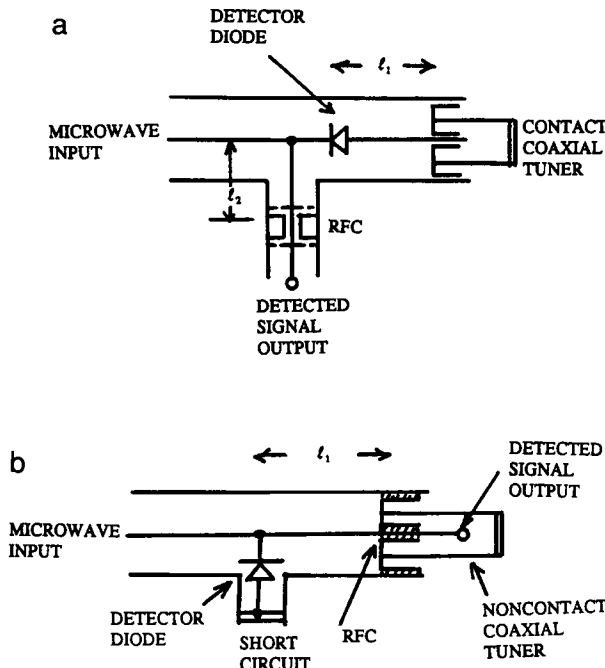


Figure 4. Schematic diagrams of coaxial line AM detector circuits. (a) Series detector. (b) Shunt detector.

across the load resistance R . The load resistance to the detector diode also provides a DC detector current return path.

In the example shown in Figure 5b, a packaged coaxial line type detector diode is mounted outside the waveguide. This configuration is advantageous in a frequency range of millimeter wavelengths. In millimeter wavelengths, the package of the detector diode is often larger than the waveguide itself. In such cases, it is impossible to mount a packaged detector diode inside a waveguide. In this case, the diode package is mounted outside the waveguide and the diode detector is connected or coupled to the waveguide by an antenna wire as seen in Figure 5b.

In Figures 5a and 5b, the RFC is an important component of the microwave detector circuit. The RFC is basically a feed-through capacitor. It allows detected or demodulated signals to pass through but it stops microwave from coming out of the RFC. Microwaves are confined in the waveguide, and they do not come out to the detector output circuit. Most RFCs are commercially available as circuit components.

The packaged detector diodes listed in Table 2 are usable in waveguide systems. Some of the coaxial-type packaged detector diodes are also

TABLE 2
Microwave AM Detector Diodes for Coaxial and Waveguide Applications [3 – 5]

Microwave detector diode	Packaging			Operating frequency range (GHz)	Nominal TSS (dBm)
	Type	Diameter (mm)	Length (mm)		
MA40041	Cartridge	7.42 ~ 7.52	20.32 ~ 21.34	S-band	-55
MA40040	Cartridge	7.42 ~ 7.52	20.32 ~ 21.34	S-band	-50
MA40064	Cartridge	1.98 ~ 2.18	4.83 ~ 5.33	S-band	-55
MA40063	Cartridge	1.98 ~ 2.18	4.83 ~ 5.33	S-band	-50
MA40043	Cartridge	7.42 ~ 7.52	20.32 ~ 21.34	X-band	-52
MA40043	Cartridge	7.41 ~ 7.52	20.32 ~ 21.34	X-band	-50
MA40201	Cartridge	1.98 ~ 2.18	4.83 ~ 5.33	X-band	-55
MA40203	Cartridge	1.98 ~ 2.18	4.83 ~ 5.33	X-band	-52
MA40065	Cartridge	1.98 ~ 2.18	4.83 ~ 5.33	X-band	-50
MA40207	Pill	1.30 ~ 1.40	1.02 ~ 1.27	X-band	-55
MA40208	Pill	1.30 ~ 1.40	1.02 ~ 1.27	X-band	-52
MA40205	Cartridge	1.98 ~ 2.18	4.83 ~ 5.33	KU-band	-52
MA40206	Cartridge	1.98 ~ 2.18	4.83 ~ 5.33	KU-band	-50
MA40215	Pill	1.30 ~ 1.40	1.02 ~ 1.27	KU-band	-52
MA40216	Pill	1.30 ~ 1.40	1.02 ~ 1.27	KU-band	-50
MA40267	Cartridge	1.98 ~ 2.18	4.83 ~ 5.33	Q-band	-49
MA40268	Pill	1.30 ~ 1.40	1.02 ~ 1.27	Q-band	-49
MA40251	Cartridge	1.98 ~ 2.18	4.83 ~ 5.33	X-band	-55
MA40253	Cartridge	1.98 ~ 2.18	4.83 ~ 5.33	X-band	-52
MA40257	Pill	1.30 ~ 1.40	1.02 ~ 1.27	X-band	-55
MA40257	Pill	1.30 ~ 1.40	1.02 ~ 1.27	X-band	-52
MA40255	Cartridge	1.98 ~ 2.18	4.83 ~ 5.33	KU-band	-52
MA40256	Cartridge	1.98 ~ 2.18	4.83 ~ 5.33	KU-band	-50
MA40265	Pill	1.30 ~ 1.40	1.02 ~ 1.27	KU-band	-52
MA40266	Pill	1.30 ~ 1.40	1.02 ~ 1.27	KU-band	-50
DDL6725	Cartridge	7.42 ~ 7.52	20.3 ~ 21.3	X-band	-48
DDC4561	Cartridge	7.42 ~ 7.52	20.3 ~ 21.3	X-band	-49 ~ -56
5082-2750	Pill	1.3 ~ 1.4	1.02 ~ 1.27	X-band	-55
HSCH-3207	Pill	1.3 ~ 1.4	1.02 ~ 1.27	2-10	-50 ~ -53
5082-2751	Cartridge	1.53 ~ 1.63	4.83 ~ 5.33	X-band	-55
HSCH-3206	Cartridge	1.53 ~ 1.63	4.83 ~ 5.33	2-10	-50 ~ -53

tabulated in Table 3 [4]. In this table, *R* signifies the reverse polarity of detected signals.

Microstrip-Line AM Detector Circuit

Schematic diagrams of microstrip-line microwave AM detector circuits are shown in Figure 6. The microstrip-line circuit can be monolithically

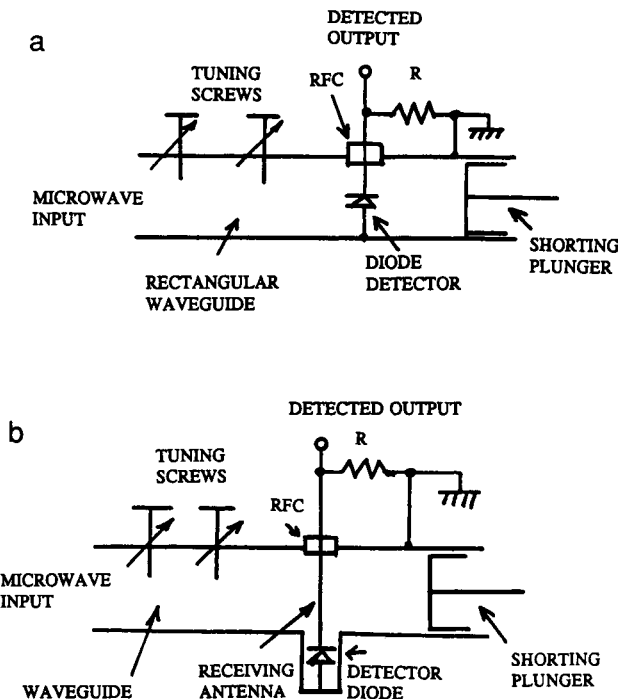


Figure 5. Schematic diagrams of a waveguide AM detector. (a) Detector diode mounted internally. (b) Detector diode mounted externally.

TABLE 3
Coaxial Cartridge Packaged Microwave Detectors for Waveguide Applications

Microwave detector diode	Packaging			Operating frequency range (GHz)	Nominal TSS (dBm)
	Type	Diameter (mm)	Length (mm)		
DDA5360	Coaxial	5.46 ~ 5.59	18.7 ~ 19.4	KU	-58
DDA5360R	Coaxial	5.46 ~ 5.59	18.7 ~ 19.4	KU	-58
DDA5361	Coaxial	5.46 ~ 5.59	18.7 ~ 19.4	K	-58
DDA5361R	Coaxial	5.46 ~ 5.59	18.7 ~ 19.4	K	-58
DDA5365	Coaxial	4.01 ~ 4.11	13.8 ~ 14.1	Millimeter waves	-50
DDA5365R	Coaxial	4.01 ~ 4.11	13.8 ~ 14.1	Millimeter waves	-50
DDA5367	Coaxial	4.01 ~ 4.11	13.8 ~ 14.1	Millimeter waves	-45
DDA5367R	Coaxial	4.01 ~ 4.11	13.8 ~ 14.1	Millimeter waves	-45

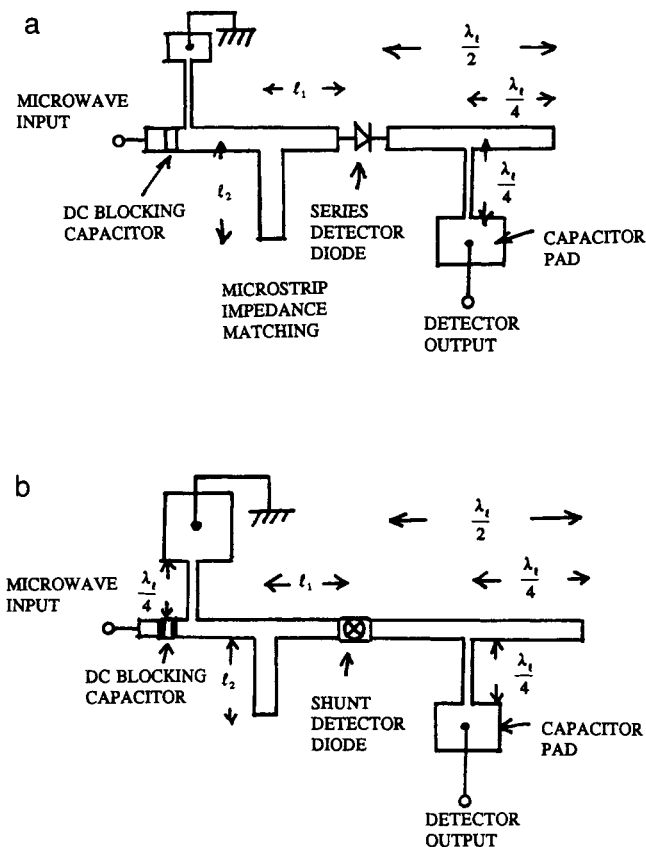


Figure 6. Schematic diagrams of microstrip-line circuits. (a) Microstrip-line series detector circuit. (b) Microstrip-line parallel detector circuit.

developed or fabricated by the use of surface mountable circuit components and microstrip lines.

In Figure 6a a packaged microstrip-line detector diode is connected in series with the microstrip line. The diode is impedance matched with the single stub matching technique [8] in this example. The lengths l_1 and l_2 are determined for the impedance matching. A section of a microstrip line with the length of one-half wavelength, $\lambda_l/2$, produces the maximum microwave voltage at the detector diode [8]. Detected output is taken out from the circuit board through an RFC consisting of an extremely thin or high-impedance quarter-wavelength ($\lambda_l/4$) microstrip line and a capacitor

pad. The capacitor pad creates a microwave capacitive short circuit to the ground plate, and the $\lambda_1/4$ thin line creates extremely high impedance at the joint to the original microstrip line, preventing microwaves from escaping to the detector output circuit, thus forming microwave RFC. A similar RFC is seen at the left of the system shown in Figure 6a. In this RFC, as seen in the figure, the capacitor pad is physically conductively short circuited to the ground plate. This provides a DC return path to the detector diode. If the main microstrip-line characteristic impedance is in a 50Ω system, then the characteristic impedance of the thin line section would be $200 \sim 300\Omega$ to create a good RFC effect. A DC blocking capacitor isolates the detector circuit from the rest of the microwave systems at the input.

In Figure 6b the detector diode is mounted parallel to the stripline. A packaged diode is mounted between the microstrip and the ground plate.

Some commercially available surface mountable packaged or unpackaged chip-type microwave detector diodes are listed in Table 4 [3–5]. In this table, chip-type package is convenient for parallel mounting to the microstrip lines and the series package is for the series mount.

2. Microwave Frequency Modulation Detectors

Basic Principles

FM detection at microwave frequencies is rare. Usually, microwave frequencies are converted using a heterodyne mixing technique, and FM detection is performed at the VHF or HF frequency. FM detection at VHF or HF is out of the scope of this chapter. Therefore details can be found elsewhere. Many IC chips are commercially available from various manufacturers.

One of the most popular FM detectors in VHF or HF is the PLL IC (phase lock loop integrated circuit) chip. In a PLL, a VCO (voltage-controlled oscillator) follows the incoming RF (radio-frequency) signals using the control voltage to the VCO. This means that the frequency modulation is now converted into the voltage variation of the VCO. Therefore by monitoring the variation of control voltage of the VCO, FM signals can be demodulated.

In special cases of microwave application, FM detection must be performed at microwave frequencies. In this case, FM microwaves are fed to a frequency-sensitive circuit such as a resonator or a hybrid circuit. The circuit's throughput is then amplitude modulated microwaves. In other

TABLE 4
Surface Mount Microwave Detector Diodes [3–5]

Microwave detector diode	Package size	Package type	Operating frequency range (GHz)	Nominal TSS (dBm)
HSCH-5300	(250 ~ 320) × (180 ~ 270) × (40 ~ 60) μm	Series	1–26	(–44) ~ (–54)
5082-0023	380 × 380 × 10 μm	Chip	1–26	–54
5082-0029	380 × 380 × 10 μm	Chip	1–26	–54
5082-0013	380 × 380 × 10 μm	Chip	1–26	–42
5082-0009	380 × 380 × 10 μm	Chip	1–26	–55
5082-200D	(2.24 ~ 2.64) × (2.34 ~ 2.64) × (0.74 ~ 1.09) mm	Series	To 12	–44 ~ –54
5082-2765	(1.14 ~ 1.40) × (1.14 ~ 1.40) mm	Series	To 12	–44 ~ –54
5082-2207	× 1.27 mm maximum	Series	To 12	–44 ~ –54
DDC4582	2.41 ~ 2.67 mm diameter	Series	8.2–12.4	–49 ~ –56
DDB4719	2.41 ~ 2.67 mm diameter	Series	8.2–12.4	–50
DDB3263	2.41 ~ 2.67 mm diameter	Series	12.4–18	–48
DDB5098	2.41 ~ 2.67 mm diameter	Series	18–26.5	–50
DDC6980	(1.14 ~ 1.40) ² × 1.02 mm maximum	Series	8.2–12.4	–55
DDB3221	(1.14 ~ 1.40) ² × 1.02 mm maximum	Series	8.2–12.4	–50
DDB3266	(1.14 ~ 1.40) ² × 1.02 mm maximum	Series	12.4–18	–48
DDB3267	(1.14 ~ 1.40) ² × 1.02 mm maximum	Series	18–26.5	–50
DDC4722	(2.34 ~ 2.64) ² × (0.71 ~ 1.06) mm	Series	8.2–12.4	–55
DDB3268	(2.34 ~ 2.64) ² × (0.71 ~ 1.06) mm	Series	8.2–12.4	–50
DDB4393	(2.34 ~ 2.64) ² × (0.71 ~ 1.06) mm	Series	12.4–18	–48
DDB3269	(2.34 ~ 2.64) ² × (0.71 ~ 1.06) mm	Series	18–26.5	–50
DDC4717	(2.34 ~ 2.64) ² × (0.71 ~ 1.06) mm	Series	8.2–12.4	–49 ~ –56
DDB4371	(2.34 ~ 2.64) ² × (0.71 ~ 1.06) mm	Series	12.4–18	–49 ~ –56
DDC3218	(1.73 ~ 1.83) ² × (0.71 ~ 1.06) mm	Series	8.2–12.4	–49 ~ –56
[DCDC7609	(0.46 ~ 0.56) ² mm	Chip	8.2–12.4	–49 ~ –56
CDB7605	(0.46 ~ 0.56) ² mm	Chip	8.2–12.4	–50
CDB7606	(0.46 ~ 0.56) ² mm	Chip	12.4–18	–48
DDB4585	(1.30 ~ 1.40) ² mm	Chip	18–26.5	–49 ~ –56
MA40265-276	(1.02 ~ 1.27) × (1.29 ~ 1.39) ²	Series	Up to 18	–52
MA40268-276	(1.02 ~ 1.27) × (1.29 ~ 1.39) ²	Series	Up to 18	–50
MA402170	(0.330 ~ 0.431) ² × (0.102 ~ 0.152)	Chip	Up to 12.4	–52
MA40272	(0.330 ~ 0.431) ² × (0.102 ~ 0.152)	Chip	Up to 18	–52
MA40257-2176	(1.02 ~ 1.27) × (1.29 ~ 1.39) ²	Series	Up to 12.4	–55
MA40258-276	(1.02 ~ 1.27) × (1.29 ~ 1.39) ²	Series	Up to 12.4	–52
MA40207-276	(1.02 ~ 1.27) × (1.29 ~ 1.39) ²	Series	Up to 12.4	–55
MA40208-276	(1.02 ~ 1.27) × (1.29 ~ 1.39) ²	Series	Up to 12.4	–52
MA4215-276	(1.02 ~ 1.27) × (1.29 ~ 1.39) ²	Series	Up to 18	–52
MA4216-276	(1.02 ~ 1.27) × (1.29 ~ 1.39) ²	Series	Up to 18	–50
MA40220	(0.330 ~ 0.431) ² × (0.102 ~ 0.152) mm	Chip	Up to 12.4	–52
MA40222	(0.330 ~ 0.431) ² × (0.102 ~ 0.152) mm	Chip	Up to 18	–52

words, the frequency-sensitive microwave circuits convert FM microwaves to AM microwaves. After this conversion is performed, the various AM detectors presented in Section 1 are used, depending on the frequency-sensitive network formed of TWLs, coaxial lines, waveguides, or microstrip lines.

VHF or HF PLL or Long-Wave IC

In most microwave FM communication systems, microwaves are converted to long waves (0.3 ~ 3 MHz), HF (3–30 MHz), or VHF (30 ~ 300 MHz), at which FM detection is performed. One of the most popular FM detectors is a PLL IC. A block diagram of the inside of the PLL IC chip is shown in Figure 7. FM microwave signals are converted to long-wave frequency (LWF), HF, or VHF by mixing them in a constant frequency local oscillator. The FM LWF, HF, or VHF is fed to a PLL IC. This signal and a VCO output are fed to the phase comparator within the PLL IC. The phase comparator puts out zero volts if the frequency and the phase of the two inputs are identical and in phase. If the phase angles of the two

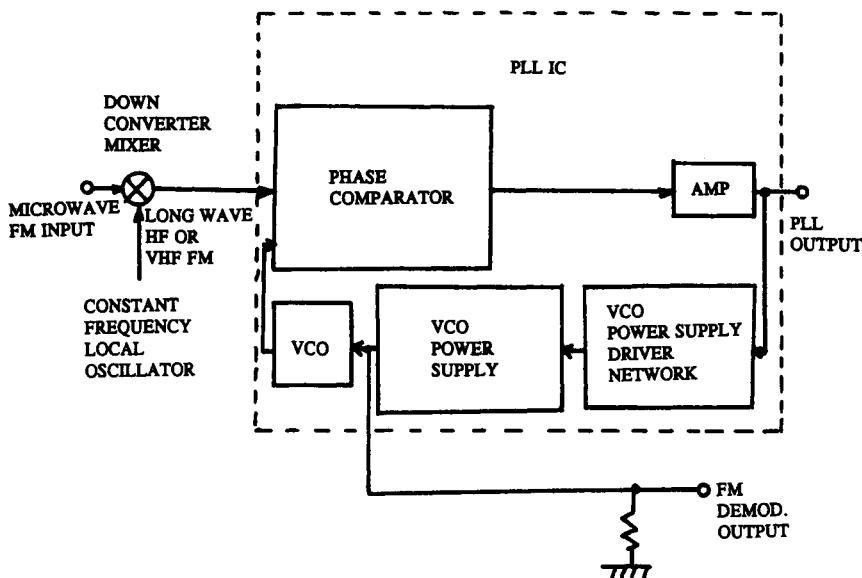


Figure 7. A block diagram of phase lock loop (PLL) FM detection of microwave FM input.

TABLE 5
Example of a Commercial PLL IC Chip [26]

PLL IC	Supply voltage	Supply current	Operating frequency	Detector output voltage	Adjustment tracking range
XR-211	4.5 ~ 20 V	4 ~ 5 mA	300 KHz maximum	15 V	$\pm 1 \sim \pm 80\%$

inputs are different due to the difference in frequency, the phase comparator produces an output voltage proportional to the phase angle difference. The phase comparator output is basically the PLL output.

A part of the PLL output voltage is used for the negative feedback loop to make the PLL output voltage zero despite the FM input. To do that the VCO frequency must follow the FM input frequency. To make the VCO frequency follow the FM input frequency, the VCO power supply voltage must be varied accordingly. A VCO power supply driver network puts out control signals to the variable voltage VCO power supply according to the PLL output voltage. Therefore the VCO voltage change is proportional to the VCO frequency change which is equal to the FM frequency excursion. Therefore the change in the VCO power supply voltage is demodulation of the input FM signals.

Some characteristics of a commercially available PLL IC chip are presented in Table 5. The phase comparator and VCO are commercially available [9, 10] up to low microwave frequencies. Therefore the PLL FM detector can be fabricated directly at microwave frequencies up to the UHF (0.3 ~ 3 GHz) range [11].

Microwave FM Detector Circuits

FM detection is usually not performed at microwave frequencies. It is usually performed after conversion to a lower frequency to take advantage of a larger modulation index. However, in some microwave applications FM detection must be performed at microwave frequencies. In such special cases, the block diagram of the microwave FM detection circuits is similar to that presented in Figure 8. As seen in this figure, FM microwave signals are amplified and fed to a frequency-sensitive circuit such as a resonator or a hybrid circuit. The output of the frequency-sensitive circuit is AM microwaves. Any frequency-sensitive circuit is essentially an FM to

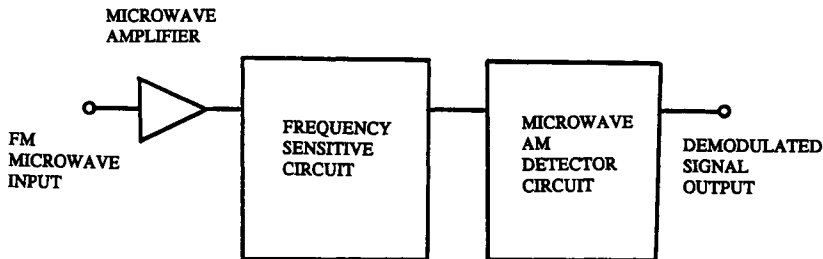


Figure 8. A block diagram of a microwave FM detection system.

AM convertor. Therefore after passage through the frequency-sensitive circuit the signal can be demodulated simply by using an AM detector circuit.

Schematic diagrams of resonator-type microwave FM detector circuits are shown in Figure 9. An example of a waveguide FM detector is shown in Figure 9a. The frequency-sensitive circuit in this case is a high-*Q* cavity resonator. The cavity may be tuned in a transmission mode, reaction mode, or discriminator mode. These modes are illustrated in Figure 10. In the figure are plots of microwave output signal levels versus microwave operating frequency curves. Depending on the tuning of the resonator, it can resonate in the transmission mode as shown in Figure 10a, in the reaction mode as shown in Figure 10b, or in the discriminator mode as shown in Figure 10c. Therefore the quiescent FM frequency f_1 or f_2 can be placed at $f_1 < f_0$ or $f_2 > f_0$ for the transmission mode and the reaction mode as shown in Figures 10a and 10b, respectively, where f_0 is the resonance frequency of the high-*Q* resonator. For discriminator mode operation, $f_1 = f_2 = f_0$. As seen in Figures 10a and 10b, the detected output based on f_1 and that based on f_2 in both the transmission mode and the reaction mode are 180° out of phase with each other.

In Figure 9a, the output of the cavity section is, therefore, AM microwaves. Therefore with a conventional AM detector the modulating signals are demodulated. If the system is a coaxial line system, then the configuration of the detector circuit will be the same as that shown in Figure 9b. In this case the cavity resonator is loop coupled. An example of an FM detector in a microstrip-line system is shown in Figure 9c. In this case the resonator is a side coupled tunable dielectric resonator (DR).

The frequency-sensitive circuit can be built using a hybrid circuit as shown in Figure 11 [8]. A schematic diagram of a waveguide hybrid ring

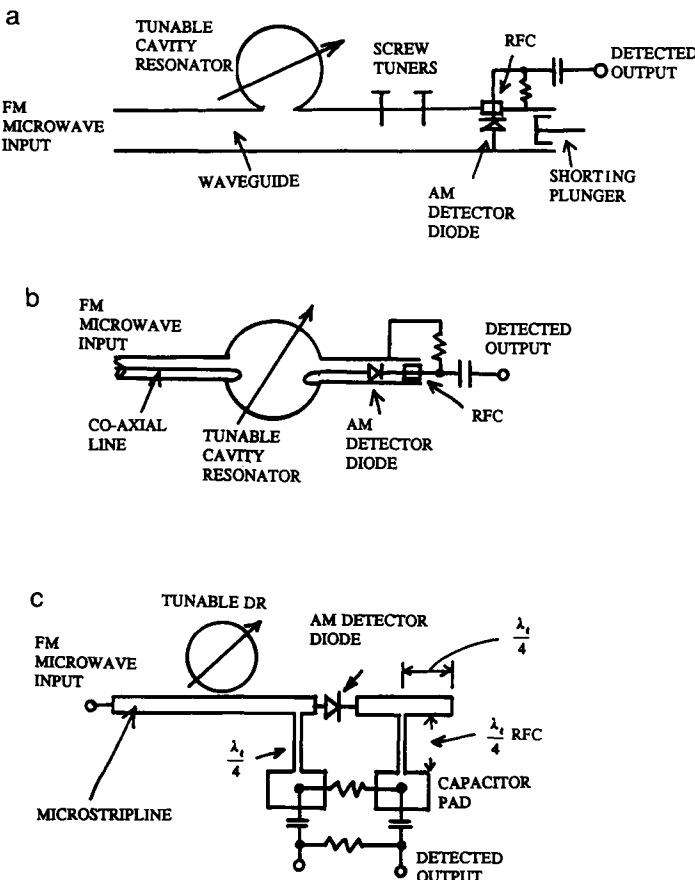


Figure 9. Schematic diagrams of microwave FM detector circuits using microwave resonators.
 (a) Waveguide FM detector. (b) Coaxial line FM detector. (c) Microstrip-line FM detector.

FM detector using an *E*-plane rat-race circuit or a hybrid ring is shown in Figure 11a. Short-circuited waveguide stub lengths l_1 and l_2 and screw tuners Nos. 1 and 2 are adjusted to produce a prescribed quiescent microwave signal level at the detector output waveguide at the center frequency of FM frequency excursion. As the FM microwave frequency deviates from the center frequency, the microwave signal power level changes in the detector waveguide. Thus placing an AM detector in the output waveguide, causes the FM microwave signals to be demodulated.

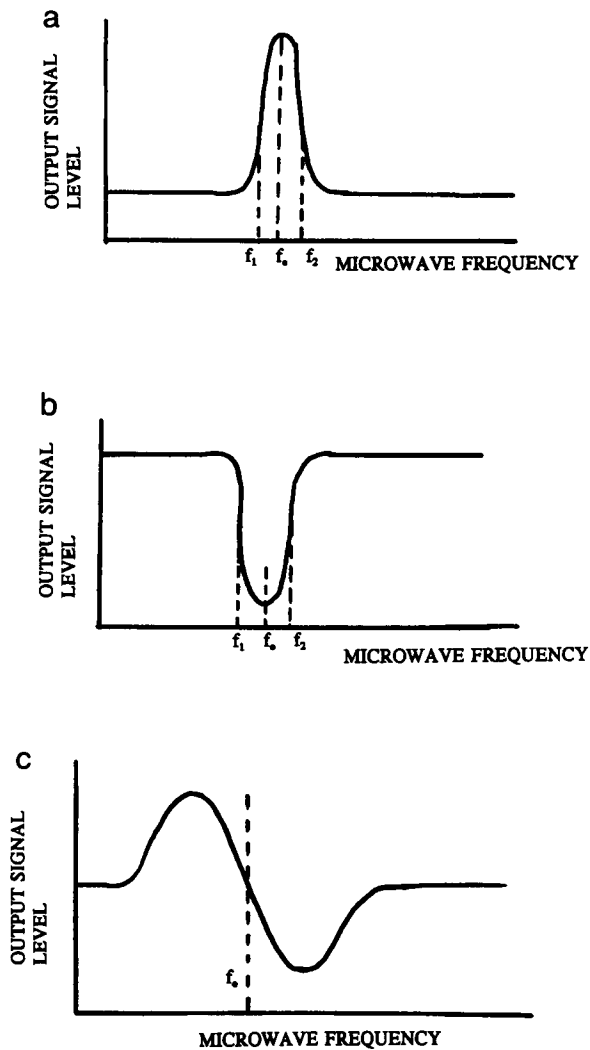


Figure 10. Various modes of resonance. (a) Transmission mode of resonance. (b) Reaction mode of resonance. (c) Discriminator mode of resonance.

The same principles work on a microstrip-line hybrid ring FM detector as shown in Figure 11b [8]. For convenience open circuited stubs are employed in most microstrip-line hybrid ring detectors.

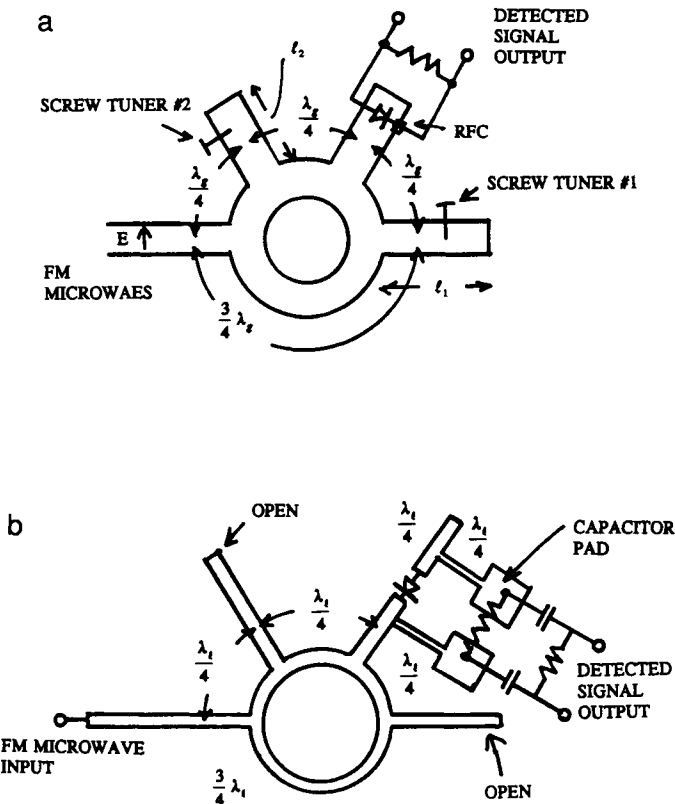


Figure 11. Hybrid circuit microwave FM detectors. (a) A waveguide hybrid ring FM detector. (b) A microstrip-line hybrid ring FM detector.

3. Microwave Phase Modulation Detectors

Generally the circuit configurations of phase modulation (PM) detectors or phase shift keying (PSK) detectors are identical to those of frequency modulation (FM) detectors or frequency shift keying (FSK) detectors, respectively. Therefore, the circuit configurations shown in Figures 7, 8, 9, and 11 are applicable to PM or PSK detectors, except whenever applicable phase-sensitive circuits are utilized instead of frequency sensitive circuits. Any RF bridges and resonators are inherently phase sensitive. The output voltage of RF bridges and resonators is phase sensitive. Therefore it can be used as the phase modulation detector by attaching an AM detector at

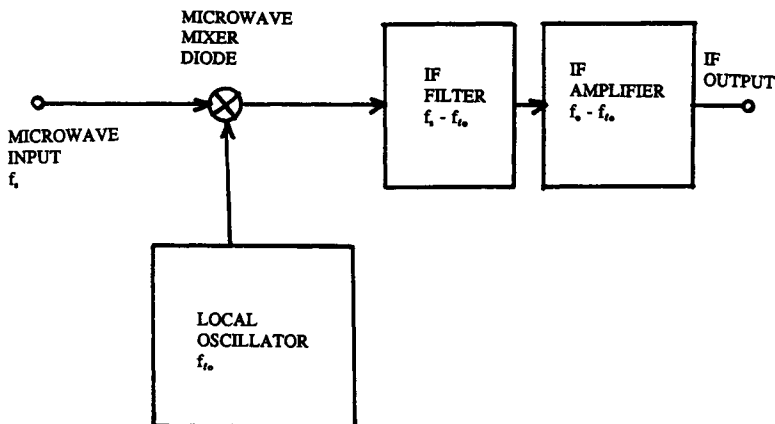


Figure 12. A block diagram of a microwave mixer.

the output. IC chips for PM and PSK detectors are commercially available from major IC makers [11–13].

4. Microwave Mixers

Microwave mixers are microwave devices which convert microwave frequencies to intermediate frequencies. Depending on the frequency of microwaves to be converted, the intermediate frequencies (IF) can be UHF (300–3000 MHz), VHF (30–300 MHz), or HF (3–30 MHz). A block diagram of the general configuration of a microwave mixer circuit is shown in Figure 12 [14]. The IF is a beat frequency between the input signal frequency f_s and the local oscillator (LO) frequency f_{lo} . The IF is $(f_s - f_{lo})$. In microwave mixers, for convenience, $f_s > f_{lo}$, by a designer's choice. It can be $f_s < f_{lo}$. In such a case $IF = f_{lo} - f_s$.

When signals of two frequencies (f_s and f_{lo}) are mixed, usually their harmonics $n(f_{lo} - f_s)$, where n is an integer, will be generated. So are $n(f_{lo} + f_s)$, nf_{lo} , and mf_s , where m is an integer ($nf_{lo} + mf_s$) and ($nf_{lo} \sim mf_s$). Therefore a good filter is needed to accept IF only. If nf_1 is present, then another microwave frequency, f'_s , can be mixed with nf_1 . This produces $IF = f'_s - nf_1 = f_s - f_1$. If this happens, f'_s is received as if it is the signal. In fact, this approach is convenient if the microwave signal frequency is too high and if an adequate LO source is not immediately available.

Equal IF can be produced for $\text{IF} = f_{\text{lo}} - f_s$ when $f_{\text{lo}} > f_s$, and $\text{IF} = f_s - f_{\text{lo}}$ when $f_s > f_{\text{lo}}$ for the same f_s . If this happens, these f_{lo} are called image frequencies.

In microwave frequencies, most mixers utilize a semiconductor diode. The diode mounting configuration is a coaxial line, waveguide, or microstrip-line configuration.

Coaxial Line Microwave Mixers

Examples of schematic diagrams of coaxial line microwave mixers are shown in Figure 13. In Figure 13a, a mixer diode is mounted in series with the center conductor. Both f_s and f_{lo} are fed on the mixer diode. The beat frequency $f_s - f_{\text{lo}}$ (IF) is generated at the diode due to its nonlinearity. The generated IF is taken out through RFCs which stop microwaves but let IF pass through. The RFC must be of the noncontact type. A dc return circuit external to the shown circuit must be provided if the mixer diode is not the zero-bias-type diode. The diode may be packaged as

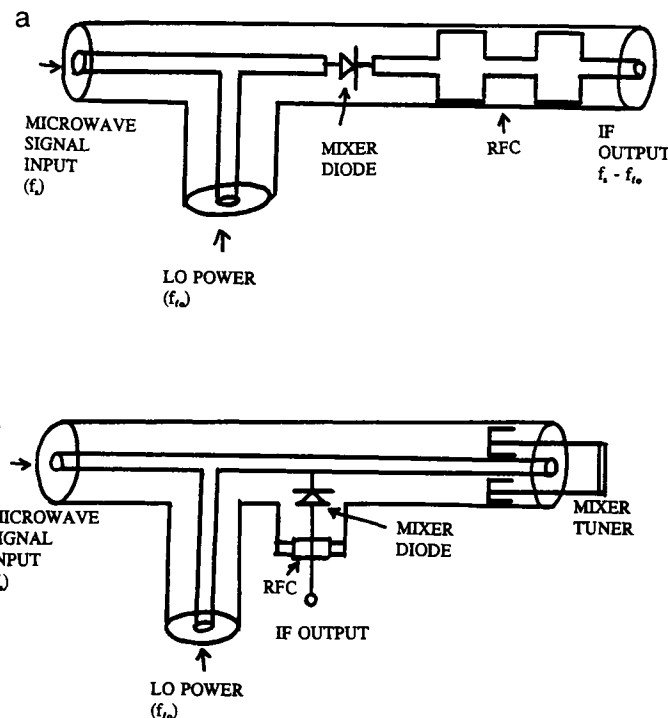


Figure 13. Schematic diagrams of coaxial line microwave mixers. (a) Series mount. (b) Shunt mount.

TABLE 6
Example of Commercial Microwave Mixer Diodes for Both Coaxial and Waveguide Applications

Model number	Package type	Operating frequency	Maximum noise figure (dB)	Nominal IF impedance (Ω)	Conversion loss (dB)
MA40194	Cartridge 3	X-band	12	250	4.8
MA40191	Cartridge 119	X-band	12	250	4.8
MA40183	Cartridge 119	KU-band	12	250	4.8
MA40181	Cartridge 119	K-band	12	350	4.8
MA40408	Pill 120	KA-band	6.5	250/500	—
IN21G	Cartridge	S-band	5.5	350/450	—
IN1132	Coaxial	SX-band	9.5	100/200	—
IN23H	Cartridge	X-band	6.0	335/465	—
IN78G	Coaxial	KU-band	7	400/565	—
IN236C	Coaxial	X-band	9.5	400/600	—
IN53D	Coaxial	KA-band	9.0	400/800	—

either the pill type or the cartridge type depending on the diode mount. The diode can be mounted parallel as shown in Figure 13b. This model has an adjustable tuner.

Some examples of commercially available microwave mixer diodes are listed in Table 6 [3–5]. Some diodes are operated with the local oscillator power as low as $-8 \sim -10$ dBm, but most diodes require $8 \sim 10$ dBm of LO power.

Waveguide Mixers

Examples of schematic diagrams of waveguide mixers are shown in Figure 14. In Figure 14a, a mixer diode is mounted directly in the waveguide using a post or a pedestal. Any cartridge-type or pill-type packaged mixer diode in Table 6 [3–5] can be used for this purpose. These packaged diodes are field replaceable in case of defect. In high millimeter-wave frequencies, these packaged diodes are larger than the waveguide itself. Therefore it is not possible to mount a packaged diode in a waveguide. The semiconductor mixer diode chip must be directly mounted on the waveguide using gold wire bonds. The whole waveguide is now a part of the diode chip. Such a chip is not field replaceable. When broken, the whole mount must be replaced and the defected waveguide mount must be shipped to the factory for repair.

In Figure 14a both LO signals and microwave RF signals are applied to a mixer diode. Conceptually, the structure of the diode mount for

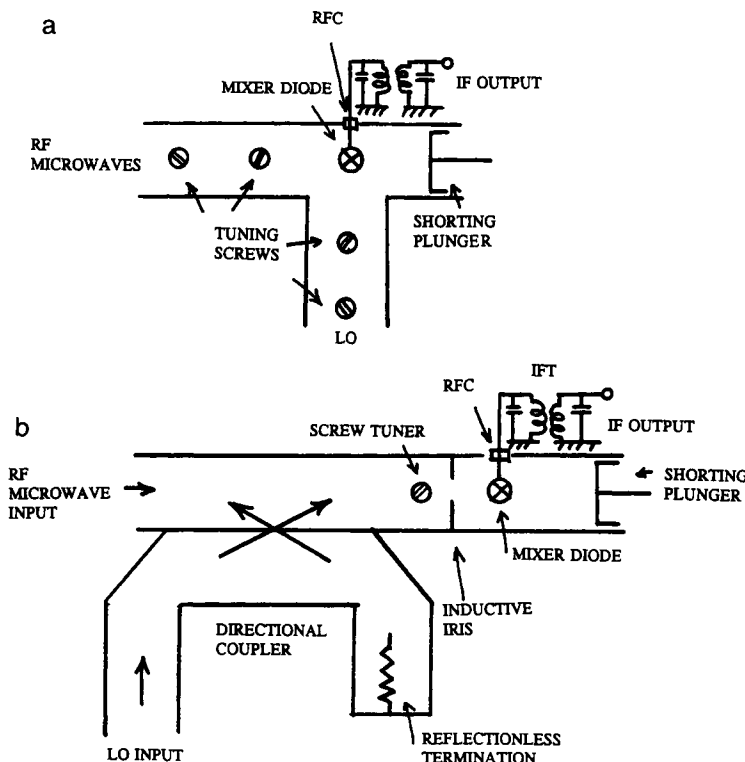


Figure 14. Waveguide mixers. (a) T-junction mixer. (b) Directional coupler mixer.

microwave detection is identical to that in Figure 5. The mixed output is taken out through an RFC which permits IF to pass and stops RF microwaves inside the waveguide.

The RF microwaves and LO output can be mixed through the use of a directional coupler as shown in Figure 14b. Both signals are led to a matched diode mount. The IF output is taken through an RFC to outside the waveguide. Schematic diagrams of balanced mixers are shown in Figure 15. A hybrid ring balanced mixer is shown in Figure 15a, and a hybrid T balanced mixer is shown in Figure 15b. The objective of balanced mixers is to reduce the electrical noise associated with the local oscillator. In both designs, the microwave RF signals are applied to the mixer diodes 180° out of phase so that the signals are added in series or in a "push-pull" configuration to the ground at the IFT input. On the other hand, the LO input is applied in phase to both mixer diodes so that the LO noise appearing in the primary part of the IFT are parallel or in a push-push

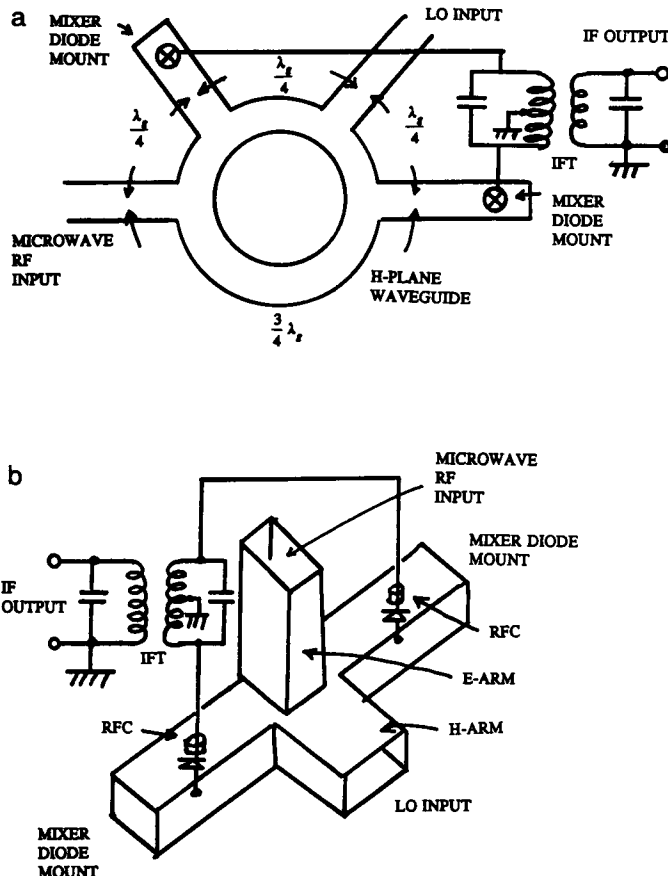


Figure 15. Schematic diagrams of waveguide balanced mixers. (a) Hybrid ring balanced mixer. (b) Hybrid T balanced mixer.

configuration to the ground. Thus the advantage of the balanced mixer is the low conversion loss and low local oscillator noise. The mixer also prevents leakage of the LO output into the microwave RF port. Various manufacturers produce microwave mixers [10].

Microstrip-Line Mixers

Schematic diagrams of examples of microstrip-line mixers are shown in Figure 16. A schematic diagram of a single-ended mixer is shown in Figure 16a. Both the microwave RF signal and the LO power are applied to

the mixer diode, and the beat frequency or the IF signals are taken out of a quarter-wavelength choke. As seen in this figure reradiation of the LO power from the RF input cannot be prevented and the LO noise appearing at the IF terminal is not suppressed.

A schematic diagram of a hybrid ring balanced mixer is shown in Figure 16b. In this circuit both mixer diodes receive in-phase LO power and thus LO noise is in the push-push configuration in the primary winding of the IFT. Thus the LO noise is suppressed. Both mixer diodes receive 180° out-of-phase RF signals. Therefore the push-pull situation is created in the primary winding of the IFT for the modulation signals. Due to the path-length difference from the LO port to the RF port, the LO power cannot leak out of the RF input port.

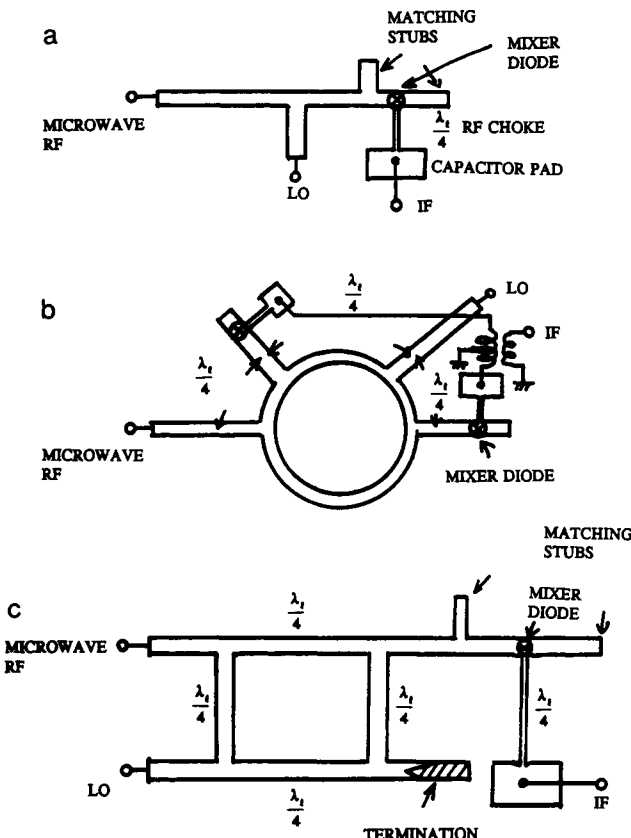


Figure 16. Schematic diagrams of microstrip-line mixers. (a) Single-ended microstrip-line mixer. (b) Hybrid ring microstrip-line mixer. (c) Directional coupler microstrip-line mixer.

A schematic diagram of a directional coupler microstrip-line mixer is shown in Figure 16c. This is basically a single-ended mixer. But reradiation from the LO power is prevented due to the use of the directional coupler. Various manufacturers produce [11, 15–19] packaged microstrip-line mixers.

Lumped Parameter Microwave Mixers

Schematic diagrams of lumped parameter microwave mixers are shown in Figure 17.

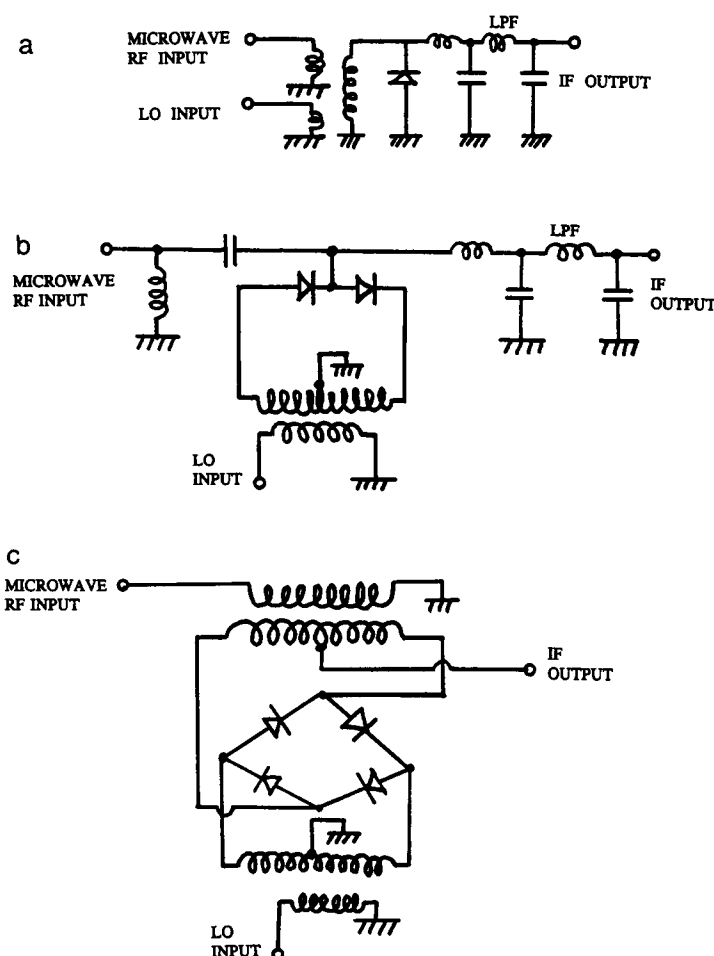


Figure 17. Schematic diagrams of lumped parameter mixers. (a) Single-ended mixer circuit. (b) Single balanced mixer circuit. (c) Double balanced mixer circuit.

A schematic diagram of a single-ended mixer circuit is shown in Figure 17a. Both the voltage at the microwave RF signal frequency and that at the LO frequency are impressed across a single mixer diode. The beat frequency or IF generated is taken out through a low-pass filter. Leakage of the LO output from the RF input is not controlled. LO noise suppression is not provided.

A schematic diagram of a single balanced mixer circuit is shown in Figure 17b. Both LO voltage and RF voltage are impressed across two mixer diodes. The generated beat frequency or the IF singles are taken out through a low-pass filter (LPF). The connecting joint of the two diodes is the neutral point of the LO voltage. Therefore, LO noise will not appear at the IF output. At the same time, LO power will not leak out to the RF or IF terminal. The two diodes are connected in a push-pull configuration or activated alternatively for the input RF signals.

A schematic diagram of a double balanced mixer is shown in Figure 17c. Both RF and LO voltages are applied across four diodes. The beat frequency or the generated IF is taken out between the neutral point of the RF input transformer and the ground. Since this is a neutral point for LO voltage, the LO voltage will not leak to either the RF input circuit or the IF output circuit. So too is the noise associated with LO. These diodes are, however, in the push-pull configuration for the RF input because the right-hand-side pair and the left-hand-side pair of the diodes conduct alternatively for the RF input. These lumped parameter mixers are commercially available from various manufacturers under different configurations of packaging [7, 9].

5. Microwave Up-Converters

Microwave up-converters are a special type of microwave mixer. Instead of IF, the up-converters output the sum frequency signals of the input microwave RF frequency and the LO frequency. Microwave up-converters take the form of waveguide up-converters, microstrip-line up-converters, and lumped parameter up-converters, depending on applications and the operating frequency range. The up-conversion technique is useful if the microwave carrier frequency needs to be altered [20, 21].

Waveguide Up-Converters

Schematic diagrams of waveguide up-converters are similar to those of the mixers shown in Figures 14 and 15 except that all IFTs are replaced by resistors matched to the mixer diode to provide a rectified DC current return path. The diode mount section must have a cavity resonator tuned

to the sum frequency of the RF and the LO. The tuning is done by a shorting plunger at the end of the waveguide cavity resonator as shown in Figure 14b and a screw tuner mounted in proximity to the diode.

Microstrip-Line Up-Converters

Schematic diagrams of microstrip up-converters are similar to those of microstrip-line mixers as shown in Figure 16 except that all IFTs are replaced by resistors matched to the mixer diode to provide a rectified DC return path. The microstrip-line resonators behind each mixer diode mount must be tuned to the sum frequency of the RF and the LO.

Lumped Parameter Up-Converters

Schematic diagrams of lumped parameter up-converters are similar to those shown in Figure 17, except that all LPFs must be replaced by HPFs (high-pass filters) to pass the sum frequency of the RF frequency and the LO frequency only. The IF output is now the sum frequency output. Various manufacturers produce microwave up-converters [10].

6. Microwave Down-Converters

The microwave mixers discussed in Section 4 are a special type of microwave down-converter. If the output of the down-converter is IF, then it is called the microwave mixer. If the output of the down-converter is a difference frequency of the RF and the LO frequencies, then it is called the down-converter. Therefore, all circuit configurations discussed in Section 4 are applicable to the down-converter except that all IFTs must be replaced by the difference frequency tuning circuit [20, 21].

7. Microwave Parametric Amplifiers

Microwave parametric amplifiers are low-noise amplifiers. Generally, if low noise is required, low-noise amplifiers (LNA) are commercially available. These are carefully designed microwave transistor amplifiers. These transistors cannot escape from the shot noise. The microwave parametric amplifier does not rely on transistor current. Therefore, the effect of shot noise is nonexistent or minimal. The active part is not the transistor but the variable capacitance diode (varactors). These varactor diodes are either zero biased or reverse biased. Therefore, there will be very little shot noise.

Circuit configurations of microwave parametric amplifiers are somewhat similar to the circuit configurations of the microwave mixers discussed in Section 4. All IFTs are replaced by a resistor matched to the ground or by a direct ground or should be connected to the reverse biasing DC power supply depending on the varactor design employed. The microwave transmission line section where the varactor diode is mounted must be tuned to the idler frequency which is the difference frequency of the input microwave RF and the LO frequencies. In microwave parametric amplifier terminology, the LO is called the PO (pump oscillator). The difference frequency is called the IF (idler frequency). The cavity resonator may become unreasonably large if the IF is low. Then it takes the form of a lumped parameter circuit.

In the parametric amplifier, the RF is amplified at the IF. The parametric amplifier can be considered a down-converter having a positive conversion gain with low noise. The down-converter has a negative conversion gain with moderate noise. Various manufacturers list the available PIN diodes and tuning varactor diodes [3–5]. In the microwave parametric amplifier, the PO power is transferred to the IF power through the IF channel which is modulated by RF.

8. Amplitude Modulation Noise in Detectors, Mixers, and Converters

The open circuit noise voltages across the detector, mixer, or converter diode [4] are expressed below.

The Thermal Noise

$$V_{NT}^2 = 4KTB(R_s + R_a), \quad (1)$$

where K is Boltzmann's constant, 1.38054×10^{-23} J/K; T is the absolute temperature of the diode in Kelvins; B is the operating frequency bandwidth in Hertz; R_s is the series resistance of the junction in Ohms; and R_a is the output load resistance of the diode in Ohms.

The Shot Noise

At the junction of the diode,

$$V_{NS}^2 = 2KTBR_j \left(1 + \frac{I_s}{I_0 + I_s} \right), \quad (2)$$

where I_s is the reverse saturation current of the diode in Amperes, I_0 is the DC bias quiescent diode current in Amperes, and R_j is the small signal junction resistance in Ohms,

$$R_j = \frac{0.028}{I_0 + I_s}. \quad (3)$$

The (1/f) Noise (Surface Statics and Tap Noise) (Flicker Noise)

$$V_{NF}^2 = 2KTf_N \ln\left(1 + \frac{B}{f_L}\right), \quad (4)$$

where f_N is the noise corner frequency in Hertz which is the frequency at which $V_{NF}^2 = V_{NS}^2$ and f_L is the lowest frequency limit of the system in Hertz.

The Total Amplitude Modulation (AM) Noise [4]

$$V_N^2 = 2KTBR_j \left[1 + \frac{I_s}{I_0 + I_s} + \frac{f_N}{B} \ln\left(1 + \frac{B}{f_L}\right) + 2R_a + 2R_s \right] \quad [4]. \quad (5)$$

The Tangential Signal Sensitivity (TSS)

The TSS is approximately 4 dB above the minimum detectable signal level (MDS, where $S/N = 1$ or 0 dB). The S/N ratio is 2.5/1.

$$\text{TSS} = 10 \log_{10} \frac{\sqrt{4KT}}{\text{FM}} + 5 \log_{10} \frac{2Z_v + 2R_a}{2_v + 2R_a}, \quad (6)$$

where Z_v is the diode series impedance in Ohms and FM is the figure of merit, which is

$$\text{FM} = \frac{E_o}{\sqrt{Z_v + R_j}} \quad (\text{W})^{-1/2}, \quad (7)$$

where E_o is the voltage output per input power,

$$E_o = \frac{3570}{100 + \frac{100}{R_j}} \quad (\text{V/W}). \quad (8)$$

9. Phase Modulation Noise in Detectors, Mixers, and Converters

Inherently, detectors, mixers, and converters do not produce PM noise by themselves. However, these are generally phase-sensitive circuits. Therefore, if the phase instability is involved in microwave RF input or the LO input or if power supply voltage fluctuation causes LO phase instability, then the phase instability or phase fluctuation will be translated by the detector, mixer or converter circuit as the AM noise. Therefore, the appropriate unit of the phase noise is dB/deg phase deviation from the center. Similarly, the frequency modulation noise is defined by dB/Hz frequency deviation from the center. Or, more generally, the unit of the PM noise is dB/unit phase fluctuation and that of the FM noise is dB/unit frequency fluctuation.

10. Microwave Harmonic Generators

A schematic diagram of a waveguide-type harmonic generator is shown in Figure 18. A schematic diagram of a loop coupled PIN diode harmonic generator is shown in Figure 18a. The PIN diodes are mounted in a matched tunable cavity resonator which is resonating at the fundamental frequency f_0 . The PIN diodes' DC return path is provided by a matched resistor mounted outside the waveguide through an RFC, unless the diode is designed as the zero-bias type. A magnetic loop antenna is attached to the diode, and the loop is coupled to a secondary tunable and matched cavity resonator which is resonating at a desirable harmonic frequency, nf_0 , where n is an integer. The loop current contains the diode current rich in harmonics. In this design, the tuning is done by the use of the shorting plungers, and the impedance matching is done by screw tuners.

A schematic diagram of a probe coupled zero-bias varactor diode harmonic generator is shown in Figure 18b. The matched primary cavity is tuned at the fundamental frequency f_0 , and the secondary cavity resonator is tuned at the desirable harmonic frequency nf_0 . The diode has an electric probe antenna which is coupled to the secondary cavity resonator through a coupling hole. Impedance matching is performed using screw tuners. Although this configuration lacks the DC return path for the diode, a microwave displacement current which is rich in harmonics is flowing through the diode and the antenna probe.

Depending on the operating frequency and the power level, the primary cavity resonator can be a coaxial line resonator and the secondary

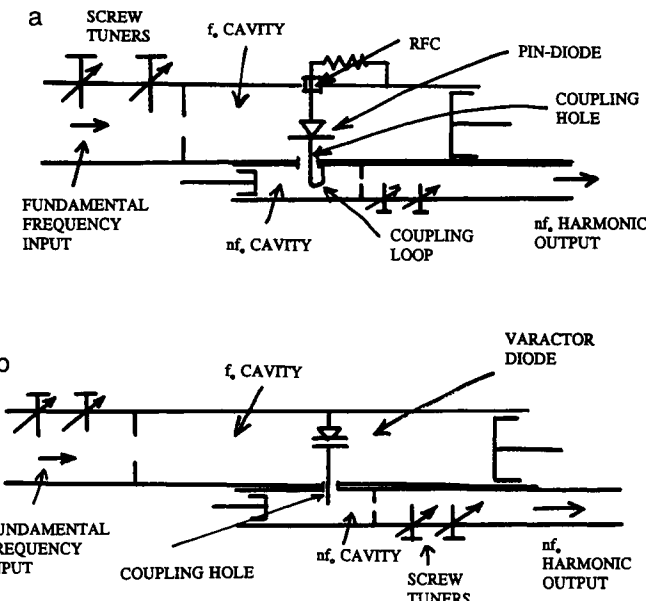


Figure 18. Schematic diagrams of waveguide type microwave harmonic generators. (a) Loop coupled harmonic generator. (b) Probe coupled harmonic generator.

resonator can be a cavity resonator. At any configuration of the harmonic generator, it must have a matched primary cavity resonator which resonates at the fundamental frequency. A nonlinear microwave diode (Schottky barrier diode, varactor diode, PIN diode, step-recover diode, or tunnel diode) must be mounted in the primary cavity resonator. A coupling must be provided between the diode and the secondary cavity resonator which is in resonance at the desired harmonic frequency and matched at that frequency. Various manufacturers produce harmonic generators [9, 10, 16, 22–25].

11. Packaging Configurations of Microwave Detectors, Mixers, Converters, and Harmonic Generators

Microwave Detector Packaging

Microwave detector diodes include Schottky barrier diodes and PN junction diodes. These are packaged in various sizes and styles depending on applications as shown in Figure 19 [4].

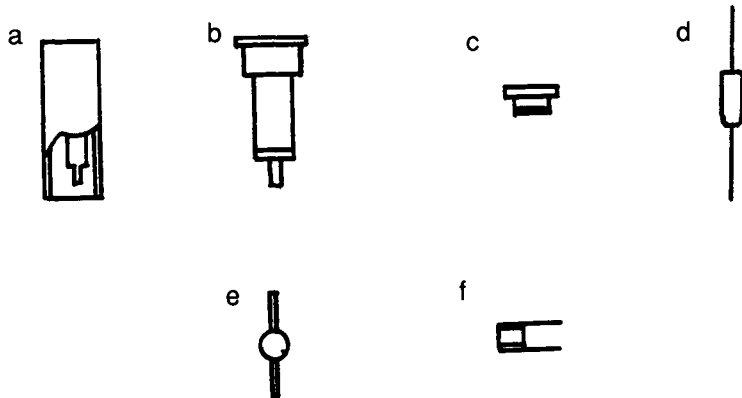


Figure 19. Sketch of some representative styles for microwave detector and mixer diodes [4].
(a) Coaxial package. (b) Cartridge package. (c) Pill package. (d) Bead package. (e) Microstrip package.
(f) Microstrip package.

These diodes are mounted in various styles of microwave detector circuit packages. An example of a waveguide packaged microwave detector is shown in Figure 20 [10]. This is a millimeter-wave detector designed for the 50- to 75-GHz range. The WR-15 rectangular waveguide opening is seen at the lower left. Millimeter-wave signals are fed through this waveguide opening. The detector diode is mounted inside the package, and the detected output is taken out of the SMA coaxial connector at the top. The typical video sensitivity of this detector is 800 mV/mW, and the

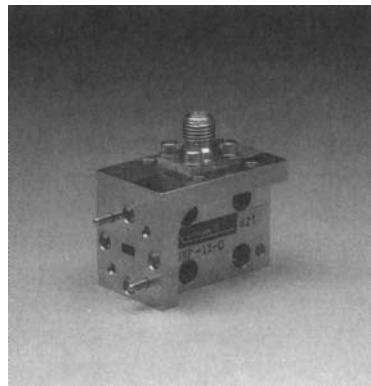


Figure 20. A packaged waveguide style microwave detector [10]. (Courtesy of the Millitech Corporation).

tangential sensitivity is -50 dBm. This detector circuit packaging utilizes a zero-bias detector diode. The packaging can be in an entirely coaxial style. The microwave RF input can be a coaxial line connector. The detected video or audio output can be also a coaxial line connector.

Microwave Mixer Packaging

Microwave mixer diodes are packaged in the same way as microwave detector diodes, as shown in Figure 19. These diodes are mounted in packaged microwave mixer circuits as shown in Figure 21. A waveguide balanced mixer is shown in Figure 21a. This particular model is designed for microwave RF frequencies in the 50- to 75-GHz range with an LO frequency in the same range. Both RF and LO frequencies are fed through WR-15 waveguide openings, RF at the left and LO at the right. The IF can be at any frequency between 10 MHz and 18 GHz depending on the combination of RF and LO frequencies. The typical conversion loss of this device is 5.5 dB, and the noise figure, 6.5 dB. The approximate size of the entire structure is $1.91 \times 2.79 \times 4.0$ cm, including the connector and flanges.

A microstrip balanced mixer is shown in Figure 21b. In this package, microwave RF is fed through an SMA connector at the right. The LO is fed through an SMA connector at the right. The LO is fed through an SMA connector at the left. Both RF and LO in this particular model are in the range of 2–18 GHz. The IF is taken out from the SMA connector in the middle. The IF frequency can be at any frequency between the DC and 500 MHz depending on the combination of the RF and LO frequencies. The typical conversion loss of this device is 6.5 dB. The LO power can be in the range of +7 to +13 dBm. The mixer diodes are in a beam lead ring quad configuration. The size of this package is approximately $2.26 \times 1.38 \times 0.38$ in., including connectors [15].

An example of a lumped parameter balanced mixer package is shown in Figure 21c. This is a surface mountable six-pin package. Pin No. 1 is the LO input. Pin Nos. 2 and 3 are grounded. Pin No. 4 is the microwave RF input, Pin No. 5 is the IF output, and Pin No. 6 is grounded. The RF/LO frequencies are designed in the range of 400 to 1400 MHz, aimed at cellular radio applications [9]. The IF can be DC to 800 MHz depending on the combination of RF and LO frequencies. Only 3 dBm of LO power is needed. A conversion loss of 6 ~ 8 dB is expected. LO–RF port isolation is 22 dB. LO–IF port isolation is 18 dB. The size of this package is $0.25 \times 0.31 \times 0.2$ in. [9]. As seen in Figure 21, all mixers have the RF input, LO input, and IF output, regardless of the type of transmission line systems employed.

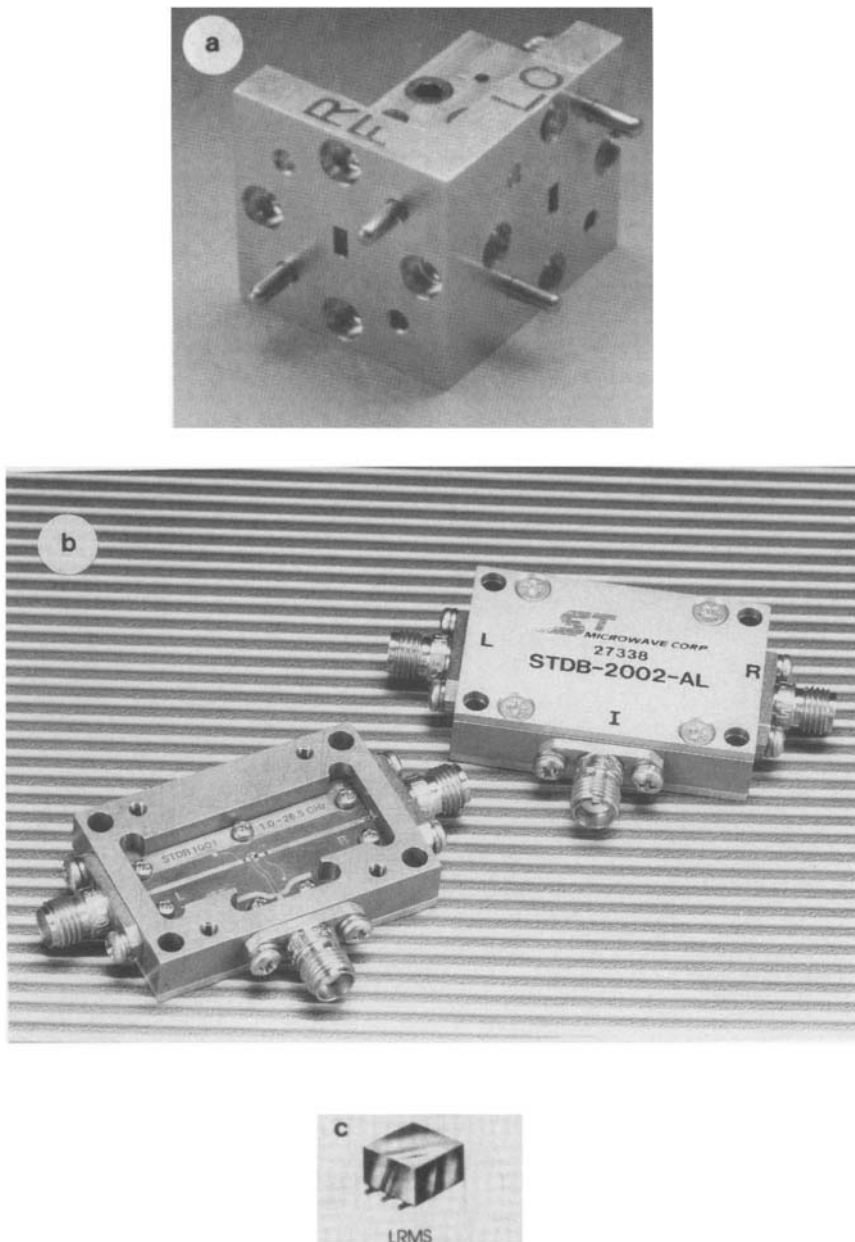


Figure 21. Examples of packaged microwave mixer circuits. (a) A waveguide balanced mixer [10] (courtesy of the Millitech Corporation). (b) A microstrip balanced mixer [15] (courtesy of the Millitech Corporation). (c) A lumped parameter balanced mixer [9].

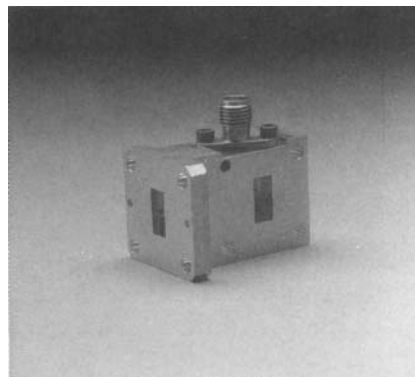


Figure 22. An example of microwave up-converter packaging [10] (courtesy of the Millitech Corporation).

Microwave Converter Packaging

An example of a microwave converter is shown in Figure 22. This converter was originally designed for up-conversion. The input frequency is 10 MHz to 18 GHz, fed to the SMA connector at the top. The LO power of +13 dBm and frequency of 18 ~ 26.5 GHz are fed to the WR-42 waveguide opening below the SMA connector. The up-converted output frequency of 18 ~ 26.5 GHz, depending on the combination of the input frequency and the LO frequency, comes out of the waveguide opening at the left. The typical conversion loss is 5.5 dB [10]. The typical operating output power of the up-converted signal is 1 mW [10].

The same packaging can be used as a down-converter. The signal to be converted will be fed to the waveguide opening at the left. The LO power is fed to the waveguide opening at the right. The down-converted signal can be taken out from the SMA connector at the top.

Microwave Harmonic Generator Packaging

Any nonlinear semiconductor diode, including a Schottky barrier diode, beam lead diode, PIN diode, varactor diode, step-recovery diode, and tunnel diode, can be used as a harmonic generating diode. The diodes are packaged as shown in Figure 23, for example [10]. In this example, the fundamental frequency signal, in the range of 11 to 16 GHz, is fed through an SMA connector, shown at the top of the structure, whereas the tripled frequency signal, in the range of 33 to 48 GHz, comes out of the WR-22

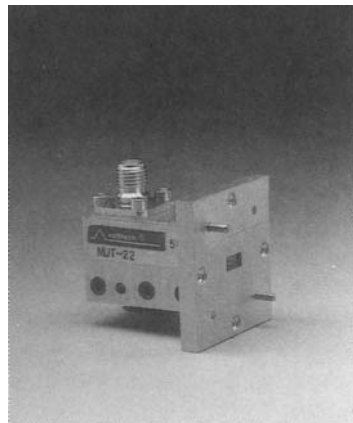


Figure 23. An example of a packaged third harmonic generator [10] (courtesy of the Millitech Corporation).

rectangular waveguide opening. The tripled frequency output power is 0.7 to 1 mW for approximately 40 mW of input fundamental frequency power. The approximate size of the structure is $1.13 \times 1.38 \times 1.13$ in., including the connector and the flange. The second harmonics are suppressed to -30 dB from the third harmonics. The fourth harmonics are suppressed to -20 dB from the third harmonics.

References

- [1] C. Potter and A. Bullock, Nonlinearity correction of microwave diode detectors using a repeatable attenuation step, *Microwave J.*, Vol. 31, No. 5, pp. 272–279, May 1993.
- [2] Alpha Industries, Silicon and GaAs beamless diodes replace beam-leads, *Microwaves RF*, Vol. 32, No. 3, p. 176, Mar. 1993.
- [3] MA/COM, “Semiconductor Products Master Catalog,” Burlington, MA, 1988.
- [4] Alpha Industries, “Diodes, Modules, and MMICs Products Capabilities Application Notes,” Alpha Semiconductor Div., Woburn, MA, 1990.
- [5] Hewlett Packard Co., “Microwave and RF Designer’s Catalog,” Palo Alto, CA, 1990–1991.
- [6] E. A. Wolff and R. Kaul, *Microwave Engineering and Systems Applications*. New York: Wiley (Interscience), 1988.
- [7] A. Jelenski, A. Grüb, V. Krozer, and H. L. Hartnagel, New approach to the design and the fabrication of THz Schottky barrier diodes. *IEEE Trans. Microwave Theory Tech.*, Vol. MTT-41, pp. 549–557, Apr. 1993.
- [8] T. Koryu Ishii, *Microwave Engineering*, 2nd. Ed., Washington, DC: Harcourt Brace Jovanovich, 1989.
- [9] Mini-Circuits, “RF/IF Signal Processing Guide,” SF-91/92, Brooklyn, NY, 1991.

- [10] Millitech Corp., "Millimeter Wave and Submillimeter Wave Components Subassemblies and Assemblies," South Deerfield, MA, 1992.
- [11] Avantek, "Modular and Oscillator Components," Milpitas, CA, 1990.
- [12] K. V. Puglia, Phase-locked DRO uses a sampling phase detector, *Microwaves RF*, Vol. 32, No. 7, pp. 103–111, July 1993.
- [13] D. Rosemarin, Technique provides simple analysis of PLL functions, *Microwaves RF*, Vol. 32, No. 11, pp. 89–192, Nov. 1993.
- [14] J.-X. Yang, R. Agahi, D. Dai, C. F. Musante, W. Grammer, K. M. Lau, and K. S. Yngvesson, Wide-bandwidth electron bolometric mixers, *IEEE Trans. Microwave Theory Tech.*, Vol. MTT-41, pp. 581–589, Apr. 1993.
- [15] ST Microwave Corp., Frequency discriminators use mixer technology, *Microwave J.*, Sept. 1991.
- [16] Vernitron Corp., "RF and IF Signal Processing Components," Catalog No. 911, St. Petersburg, FL, 1992.
- [17] Merrimac, "RF and Microwave Processing M-90," West Caldwell, 1990.
- [18] T. Heil, D. Neuf, and S. Spohrer, A 4 to 20 GHz, doubly-balanced, drop-in microstrip mixer, *Microwave J.*, Vol. 36, No. 8, pp. 106–108, Aug. 1993.
- [19] D. K. Lovelace, Silicon MOSFETs power Gilbert-cell mixers, *Microwaves RF*, Vol. 32, No. 4, pp. 59–60, Apr. 1993.
- [20] Microphase Systems, Inc., Single-drawer SATCOM down- and up-converters, *Microwave J.*, Vol. 36 No. 3, p. 122, Mar. 1993.
- [21] Condor Systems, Inc., A 1 GHz bandwidth frequency conversion system, *Microwave J.*, Vol. 36, No. 8, p. 118, Aug. 1993.
- [22] Milli Wave, 40–60 GHz amplifiers and multipliers, *Microwave J.*, Vol. 36, No. 2, p. 145, Feb. 1993.
- [23] B. K. Kormanyos and G. M. Rebeiz, A 26 to 220 GHz harmonic mixer-receiver, *Microwave J.*, Vol. 36, No. 7, pp. 103–108, July 1993.
- [24] R. J. Hwu, A mm-wave high power monolithic back-to-back varactor diode frequency tripler, *Microwave J.*, Vol. 36, No. 5, pp. 240–253, May 1993.
- [25] S.-W. Chen, T. Ho, R. R. Phelleps, J. L. Singer, K. Pande, P. Rice, J. Adair, and M. Ghahremani, A high-performance 94-GHz MMIC doubler, *IEEE Microwave Guided Wave Lett.*, Vol. 3, No. 6, pp. 167–169, June 1993.
- [26] W. Thomasi, *Electronic Communications Systems*. Englewood Cliffs, NJ: Prentice-Hall, 1988.
- [27] G. Vandersteen and A. Vander Vorst, Nonlinear model and measurement method for microwave mixers, *IEEE Microwave Guided Wave Lett.*, Vol. 3, No. 5, pp. 133–135, May 1993.

Electron Beam Formation, Focusing, and Collection in Microwave Tubes

Richard True

I. Introduction

Powerful electron beams lie at the heart of modern microwave tubes. This chapter describes how such beams are generated, focused, and collected in linear beam tubes. In linear beam tubes the magnetic and tube axes are coincident. Emphasis is placed upon the design of beam optical systems used in traveling wave tubes (TWTs) and high-power klystrons because of their widespread use. Beam optical systems which generate hollow beams are briefly mentioned.

Computers are used extensively in the design process, and a generic description of frequently used codes is included. Many of these codes and much of the technology presented in this chapter are not limited to microwave tubes but can be applied to other devices such as linear accelerators (linacs), free-electron lasers (FELs), and numerous other devices which employ linear beams.

Figure 1 is a block diagram of the major internal elements of a generic linear beam tube. On the left is the electron gun which generates the beam; the center section includes the interaction structure, in which the RF power is developed from the DC beam power; and on the right is the collector, in which the spent beam ends its journey. Customarily, there

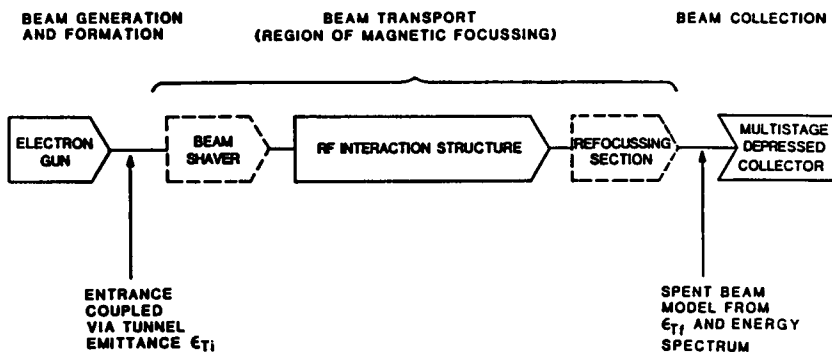


Figure 1. Framework of generalized focusing theory in a linear electron beam device. Reprinted with permission from Ref. [11], © 1987 IEEE.

is a magnetic field throughout the interaction region which focuses the beam so that it can proceed from the gun to the collector with little or no interception on the RF circuit. The dashed blocks show two optional elements which may be present. Beam shavers are thermally robust sections used to protect the input structures of certain high-power tubes. Refocusing sections can be included to condition (that is, reduce the transverse velocity content of) spent beams prior to entry into multistage depressed collectors.

Textbooks which discuss the fundamentals of electron gun and beam focusing design that the author has found useful are cited in References [1–6]. Survey or handbook references include References [7, 8]. This chapter includes theory and techniques to handle nonlaminar beams. This and other subject material covered is expanded upon in the other references listed.

2. Description of Electron Guns

Pierce Gun Basics

Presented in Figure 2 is a schematic diagram of a Pierce gun [7]. It includes a heater to raise the temperature of the cathode surface to a level sufficient for thermionic emission to occur. When the potential of the anode is positive with respect to the cathode, electrons are drawn from the cathode surface and move toward the anode. In space-charge limited flow, beam current is determined by the strength of the electrostatic field at the cathode surface (determined by the geometry of the gun). Gun designs in

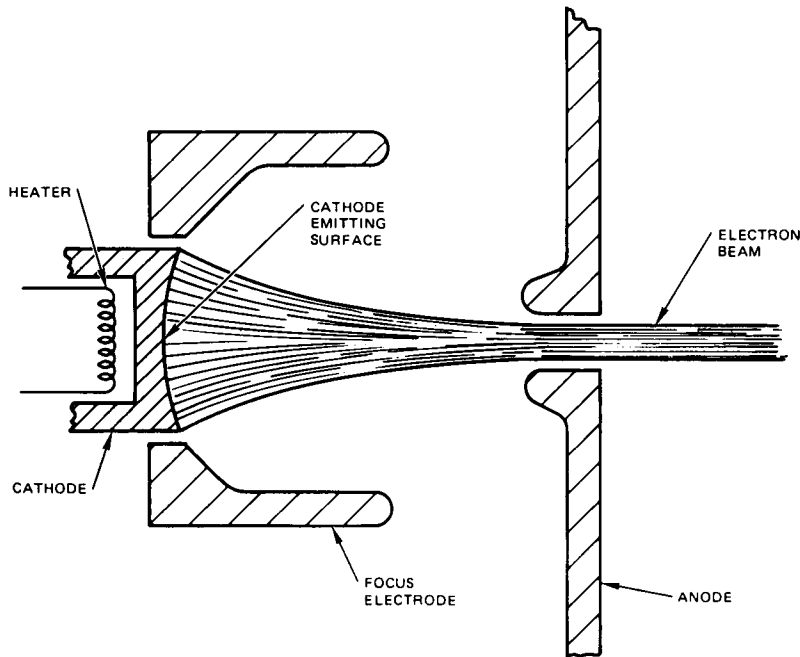


Figure 2. Pierce electron gun. Reprinted with permission from Ref. [7].

this chapter assume space-charge limited emission unless noted otherwise. Cathode emission is discussed more fully in Section 3.

In a Pierce gun, electronic flow in the region between the cathode and the anode resembles that between concentric spheres. The geometry of the cathode, focus electrode, and anode provides an electrostatic field shape which provides this flow pattern. When the beam passes through the anode opening, it encounters a diverging lens. Beyond the anode, the beam spreads due to space-charge repulsive forces.

Available cathode emission density and high-voltage breakdown between the cathode and the anode place practical limits on achievable beam current density without compression of the beam. The Pierce gun provides a means of substantially increasing beam current density by electrostatic beam compression. Current densities in transported TWT beams are typically a few hundred a/cm^2 , whereby klystron beams are often $500 \text{ a}/\text{cm}^2$ or higher. Beams within microwave tubes are thus very intense.

Voltage and current are related in any space-charge limited electron gun by the $\frac{3}{2}$ -power law. Perveance is a measure of the intensity of the

space charge; microperveance is typically used in gun design and is defined as

$$P_\mu = 10^6 I_0 / V_0^{3/2}, \quad (1)$$

where I_0 is the beam current and V_0 is the applied voltage (cathode to anode or body voltage).

In Pierce guns, the half-angle, θ , microperveance, and linear beam compression, r_c/r_{95} , are related approximately as follows [9],

$$\theta^\circ = 12.9 \sqrt{P_\mu r_c / r_{95}}, \quad (2)$$

where the notation is defined in Figure 3. In Equation (2), r_c is the disk radius of the cathode and r_{95} is the radius of the beam enclosing 95% of the beam current at the waist. Equation (2) pertains to gridded guns over the most common parameter space for Pierce guns, $\theta \leq 40^\circ$, $P_\mu \leq 3$, and $2 \leq r_c/r_{95} \leq 8$. It has been found that this equation also works reasonably well for ungridded (diode) guns over this range.

Equation (2) provides useful insight into the behavior of Pierce guns. Namely, it can be seen that it is necessary to deepen the cathode dish (increase θ) to achieve a given degree of beam compression as perveance increases. Further, it is necessary to increase θ to achieve a more highly compressed beam at constant perveance.

Geometrical scaling in guns is easily remembered by reference to Equations (1) and (2). It is generally true that perveance in space-charge limited guns remains constant if all gun dimensions are scaled in equal proportion. Also, the size of the electron beam scales in direct proportion to the given geometrical scaling as well. Of course, if a given gun is scaled down in size, cathode loading, J (a/cm^2), will increase by the linear scaling ratio squared. For a constant size gun, if the applied voltage is increased, current will increase according to Equation (1) and J will increase in direct proportion to the cathode current.

Finally, Equation (2) provides a rationale for cataloguing gun data. The author has found it convenient to file various gun designs in order of

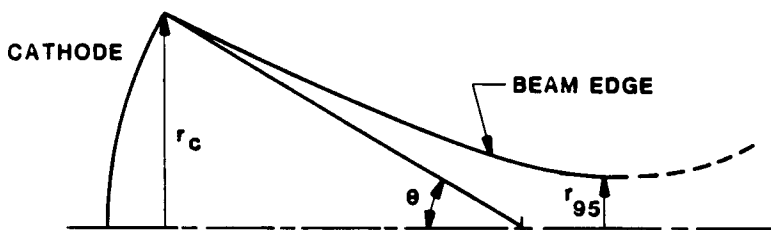


Figure 3. Pierce gun notation.

increasing half-angle, increasing microperveance within each half-angle set, and increasing cathode diameter below this. Computer runs, design calculations, and experimental beam analyzer data can be readily retrieved if filed in this fashion.

It is necessary to electrically isolate the cathode and focus electrode of the gun from ground potential and enclose the gun itself within a vacuum vessel. Normally the interaction structure or body of a tube is at ground potential. Figure 4 shows a picture of a klystron high-voltage gun enclosure [10]. This structure includes features to aid high-voltage standoff such as a high-resistance coating on the inner surface of the ceramic, uncorrugated ceramic (used when the gun is operated in oil dielectric fluid), and an oxidized stainless steel focus electrode. This technology is suitable for guns which run at voltages up to hundreds of kilovolts.

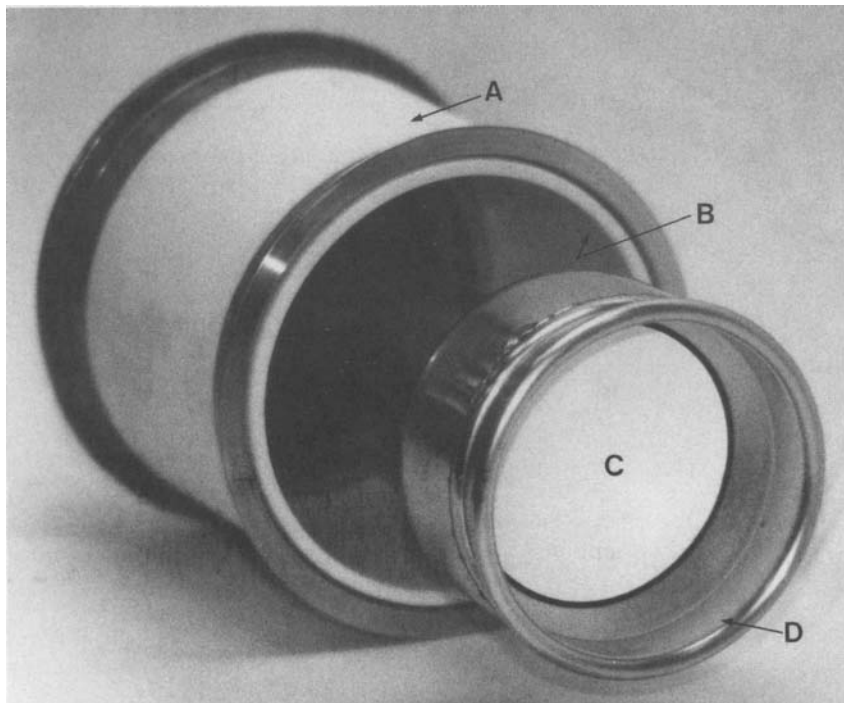


Figure 4. Flashlight configuration used in Litton high-voltage guns. (A) Uncorrugated ceramic; (B) high resistance coating on inner surface of ceramic; (C) cathode; (D) oxidized stainless steel focus electrode. Reprinted with permission from Ref. [10], © 1991 IEEE.

The beam can be switched on and off (modulated) in diode Pierce guns in three ways. First, the voltage of the cathode can be switched from ground to the full negative operational level. The drawback of cathode pulsed guns is that full cathode current must be switched when the negative voltage is applied.

Second, it is possible to electrically isolate the anode in a Pierce gun from ground. In a modulating (mod) anode gun, cathode voltage is fixed at its normal negative operational level. The beam is turned on in this case by switching the mod anode potential from a little below cathode to ground. Current intercepted by the mod anode is typically quite small; thus, guns of this type have an advantage over cathode pulsed guns in terms of required switching power.

Third, it is possible to electrically isolate the focus electrode from the cathode. Beam switching in this case is accomplished by changing the potential of the focus electrode from a negative value (with respect to cathode) sufficient to cut off the beam, to cathode potential. Often the potential of the isolated focus electrode in the on mode is a little below cathode potential to reduce cathode edge emission. Like the mod anode gun, intercepted current is negligibly small; however, switching voltage in this case is much less. This type of modulation scheme is most useful in lower perveance guns (say, $< 0.25 \mu\text{perv}$) since negative voltage required for cutoff generally decreases with perveance. As a calibration point, in a $0.25 \mu\text{perv}$ gun design, the beam is cut off by a voltage of $-0.125V_0$ (with respect to the cathode).

In certain long-life applications, an isolated anode is held at a potential positive with respect to ground. This is done to create a positive ion trap to prevent ionic back-bombardment of the cathode (and subsequent cathode damage). The applied voltage to accomplish this is typically a few percent of V_0 ; thus the high-voltage design in this case is much less severe than the design of a mod anode gun. As with the mod anode gun, intercepted current on the anode is negligible.

Gridded Pierce Guns

Presented in Figure 5 is a computer simulation of a shadow gridded Pierce gun [11]. This plot was obtained using code DEMEOS (see Section 4). The beam in such codes is typically represented by a series of rays. Equipotential contours lie among the cathode, grids, and anode. This simulation shows the development of a halo of electrons outside of the main beam core as the beam compresses. Fortunately, these electrons originate near the shadow grid wires and carry only a small fraction of the total beam current.

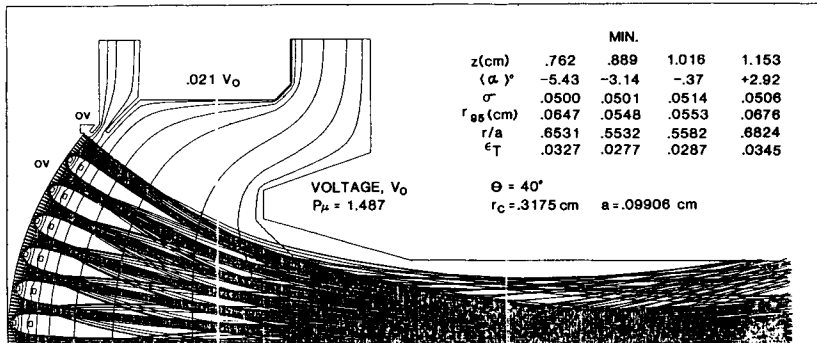


Figure 5. Computer simulation of a shadow gridded gun used in a broadband TWT (thermal beam model). Reprinted with permission from Ref. [11], © 1987 IEEE.

In gridded guns, the grid acts as a gate controlling the flow of current. When the control grid voltage is positive (with respect to the cathode) current flows; conversely, when the grid is biased sufficiently negative, all current ceases to flow. Typically, the grid operating voltage level and negative bias levels are small in comparison with the beam voltage (0.01 – 0.02 times V_0). The electrostatic amplification factor, μ , of gridded guns used in microwave tubes is thus quite high.

Figure 6 shows a zoom view of a shadow gridded gun near the cathode center (nonthermal beam model in this case). It can be seen that electrons are kept away from the control grid due to the presence of the shadow grid at the cathode potential. In this gun design, the control grid is larger than the shadow grid to reduce the total grid voltage swing (increase the μ of the gun). Electrons miss the control grid wires by a substantial margin, and the observed control grid current in actual shadow gridded guns is typically a very small fraction of the total beam current (essentially zero).

Some shadow gridded guns have the shadow grid mounted directly on the cathode surface. In the case of contiguous shadow gridded guns, it is necessary to apply suitable emission suppressive materials to prevent electronic emission from the shadow grid. Lower temperature cathodes are also required when such shadow grids are used, for acceptable tube life.

Intercepting gridded guns do not have any shadow grid to shield the control grid from beam current. These guns typically intercept beam current roughly in proportion to the area of the grid divided by the area of the cathode. Intercepting gridded guns have limited pulse length and duty cycle capabilities due to grid overheating in comparison with shadow gridded guns.

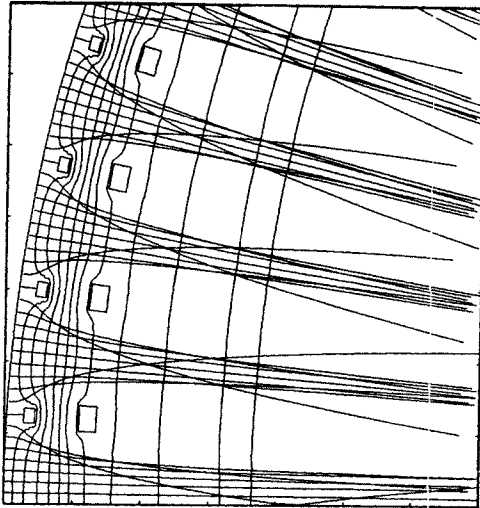


Figure 6. Zoom view of shadow gridded gun simulation near the cathode center. Reprinted with permission from Ref. [12], © 1989 IEEE.

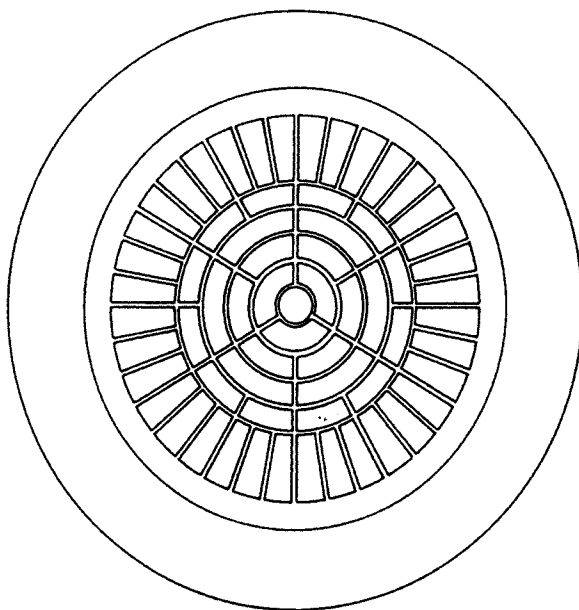


Figure 7. Bore-sight view of a hybrid grid. Reprinted with permission from Ref. [12], © 1989 IEEE.

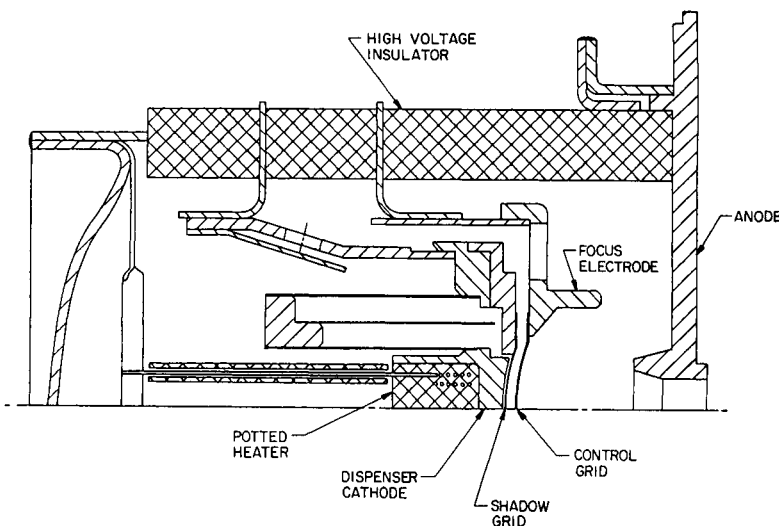


Figure 8. Mechanical layout of a shadow gridded gun.

Figure 7 is a bore-sight view of a hybrid grid (rings and vanes). Grid mesh density can be made quite uniform in this type of grid. The shadow and control grid patterns are similar (not identical) for achievement of grid alignment in the final gun. Other grid patterns are also used in gridded guns. One type consists entirely of vanes, some have a preponderance of vanes and a few rings, some grids have mostly rings, and hexagonal mesh grids are often used in intercepting gridded guns.

A mechanical layout of a medium-voltage shadow gridded gun is presented in Figure 8. In this gun, the control grid and focus electrode form one assembly and have identical voltages. Guns of this type are often used for V_0 levels below, say, 15 kV. In higher voltage gridded guns, the focus electrode is usually electrically isolated from the control grid; it is connected instead to the cathode. This is done to prevent high currents from flowing through the grid pulse modulator in the event of a focus electrode-to-anode arc.

Other Solid Beam Guns

Presented in Figure 9 is a computer simulation of a multielectrode gun used in low-noise tube applications. In this type of gun, the focus electrode is typically run negative to suppress edge emission, and magnetic flux threads the cathode. Tubes having noise figures below 5 dB using guns of this generic type are not uncommon.

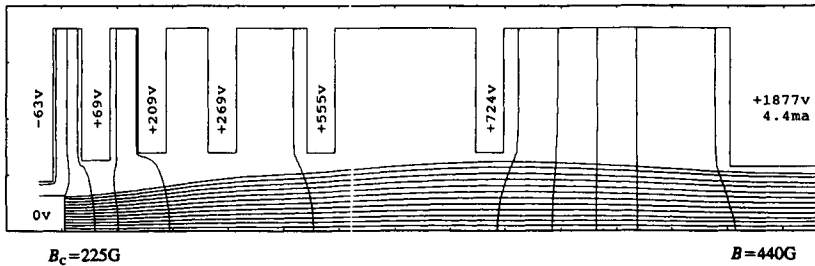


Figure 9. Low-noise gun.

Another electron beam source is shown in Figure 10. This system employs a high-perveance intercepting gridded Pierce gun followed by a beam acceleration section (postaccelerator). Long bursts of very short pulses (on the order of 5 ps) can be generated with this arrangement. Guns of this type have been used to provide beams for linacs which drive FELs, plus other applications.

Another important type of gridded gun is the dual-mode gun [14]. In this type of gun, current is switched by a double set of control grids which provide a beam capable of being focused at two very different levels of current (see Figures 11 and 12). Good focusing is possible if the beam current density at each current level is equal (or, in the notation of Figure 11, if $I_1/b_1^2 = I_2/b_2^2$). Beam current switching enables efficient saturated amplifier operation of a TWT at power levels which can differ by as much as 10 dB. Tubes operating at 10% duty cycle in the high-current mode and cw in the low-current mode have been built. Multimode and other forms of current switched guns have been developed over the years [15]; however, the gun of Figures 11 and 12 is the most widely used of this class.

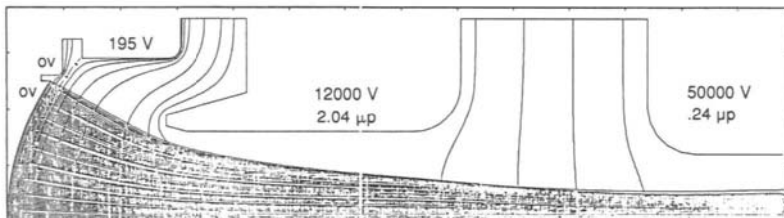


Figure 10. High-perveance intercepting gridded gun with a postaccelerator used in an FEL linac injector. Reprinted with permission from Ref. [13], © 1985 IEEE.

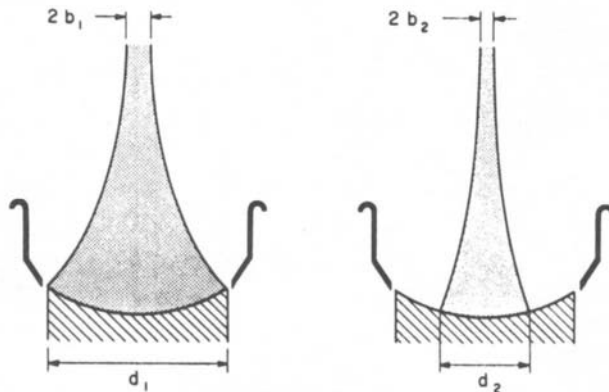


Figure 11. Principle of dual-mode gun operation. Reprinted with permission from Ref. [14], © 1973 IEEE.

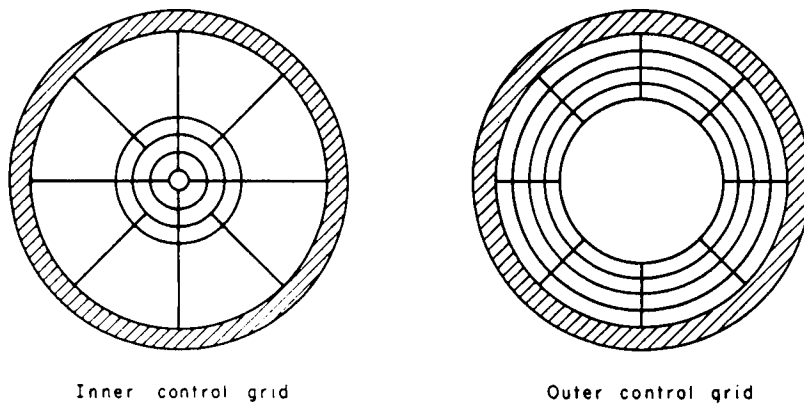


Figure 12. Control grids in a dual-mode gun. Reprinted with permission from Ref. [14], © 1973 IEEE.

Hollow Beam Guns

Figure 13 is a computer plot of a high-perveance hollow beam gun used in certain low-frequency solenoid focused helix TWTs. Flux threads the cathode in this gun. The degree of cathode immersion which determines the ultimate beam size can be adjusted by means of a movable cylindrical shunt element over or by the gun. This shunt also serves to shape the field so that the beam clears the anode.

Presented in Figure 14 is a computer simulation of a standard magnetron injection gun (MIG). This type of gun also provides a high-perveance hollow beam. It can be seen that longitudinal beam compression

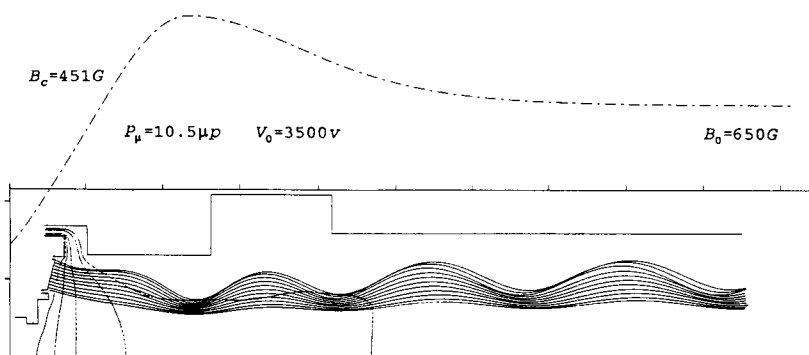


Figure 13. High-perveance hollow beam gun.

can greatly magnify beam current density over that available from the emitter. In this type of gun, electrons are attracted to the positively biased anode around the conical cathode; however, they are constrained to move axially by the applied axial magnetic field. These guns have found use in high-power switch tubes and klystrons.

Another type of MIG (shown in Figure 15) is often used in gyrotrons. Guns of this type are usually run temperature limited rather than space-charge limited. In the simulation of Figure 15, the magnetic field increases along the axis in the downstream direction which compresses the beam. This type of beam possesses a high degree of rotational energy which is critical for the cyclotron resonance maser interaction process. Such rotation is illustrated in the plot by the curling ribbon nature of the flowing beam. One useful reference document on these guns is Reference [18]. This report contains a useful collection of other references.

The final hollow beam guns considered in this section produce axis-encircling beams for gyrotrons and other gyrodevices. Figure 16 presents a schematic diagram of a basic magnetic centerpost gun [19]. Depending on the flux in the centerpost (obtained by energizing the auxiliary coil), final

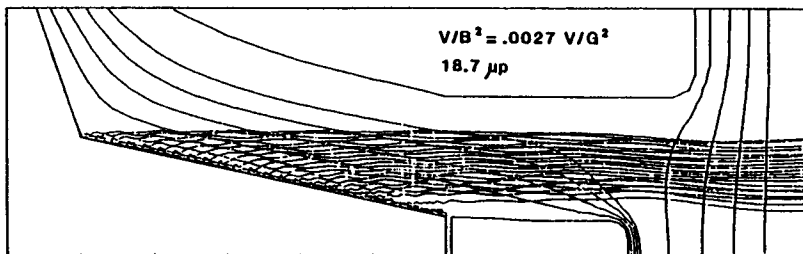


Figure 14. Magnetron injection gun. Reprinted with permission from Ref. [16], © 1983 IEEE.

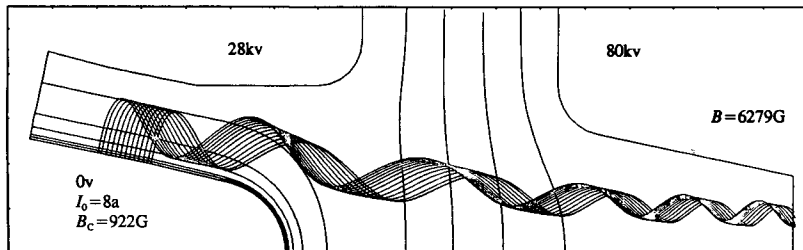


Figure 15. Gyrotron gun simulation. Reprinted with permission from Ref. [17], © 1989 AIP.

rotation of the beam as a whole can be varied from zero to the cyclotron frequency, ω_c .

In beam optical studies of magnetic field reversals, it was found that postreversal beam ripple can be virtually eliminated by a specially shaped magnetic cusp obtained from a triple-pole-piece field reversal element (Figure 17) [20]. This concept has been combined with a convergent beam centerpost gun to produce an advanced centerpost (ACP) gun (Figure 18) [21]. ACP guns provide extremely low transverse and axial velocity spread beams.

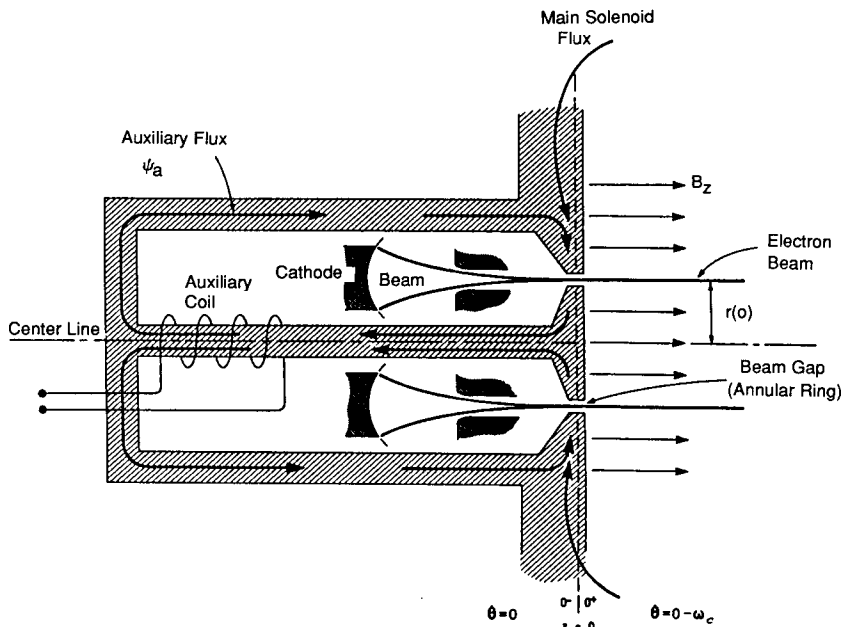
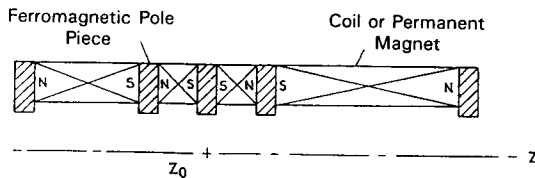
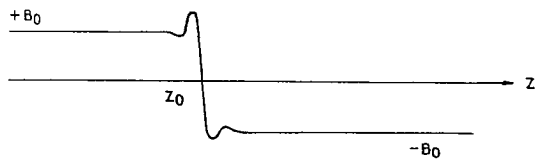


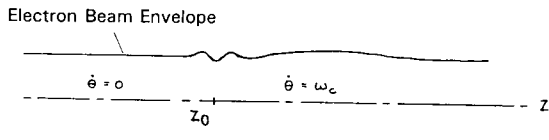
Figure 16. Magnetic centerpost gyrotron gun. Reprinted with permission from Refs. [18] and [19], © 1960 IEEE.



(a) Triple pole piece magnetic field reversal element



(b) Magnetic flux density through field reversal



(c) Behavior of beam passing through reversal

Figure 17. Behavior of a beam passing through triple-pole-piece field reversal. Reprinted with permission from Ref. [20], © 1981 IEEE.

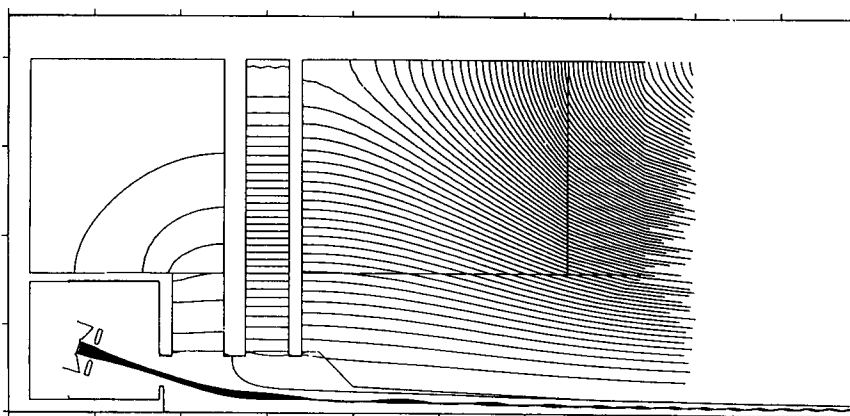


Figure 18. Advanced centerpost gun with flux lines superimposed. Reprinted with permission from Ref. [21], © 1989 IEEE.

3. Electron Emission

Electron Emission Basics

There are three basic mechanisms of electron emission which are of importance in microwave tubes. These are thermionic, field, and secondary emissions. We shall first consider thermionic emission since this is the basic mechanism which governs the creation of electron beams used in microwave tubes. The subject of electronic emission is treated more fully in References [3] and [6], and the interested reader is encouraged to consult them.

In thermionic emission, electrons are emitted according to the Richardson–Dushman (R–D) equation,

$$J = AT^2 e^{-\phi/W_T}, \quad (3)$$

where $A = 120 \text{ a/cm}^2 (\text{°K})^2$, T equals the cathode temperature in kelvins, ϕ is the work function in electron volts (eV), $W_T = T/11,600$ in electron volts, and J has the units of a/cm^2 . This equation gives the potential amount of current which can be drawn from a cathode surface (below the field emission threshold and neglecting the Schottky effect [6]). Cathode emission is said to be temperature limited when it is governed by Equation (3). As a reference point, a typical value of the work function in a type-B dispenser cathode is approximately 2 eV at 1100°C. Note that all temperatures herein are *true*, not brightness.

Figure 19 illustrates the amount of current drawn from the cathode in a typical diode electron gun as a function of anode voltage. In the space-charge limited region, current flow is governed by the $\frac{3}{2}$ -power law [Equation (1)]. Current flow is limited in this region by the buildup of space charge in front of the cathode surface. As voltage is increased, more current can be drawn before space charge builds up to the point at which the electric field in front of the cathode becomes zero (which limits further current flow). In the temperature limited region of the curve (flat upper portion), current is limited per Equation (3).

In the space-charge limited region, current density emerging from a small element of the cathode area can be related to the voltage and distance as follows,

$$J = kV^{3/2}/\zeta^2, \quad (4)$$

where V is the potential (referenced to cathode) a small distance, ζ , from the emitting surface. Equation (4) is essentially the Child–Langmuir (C–L) law (which pertains to planar diodes). This equation in differential form

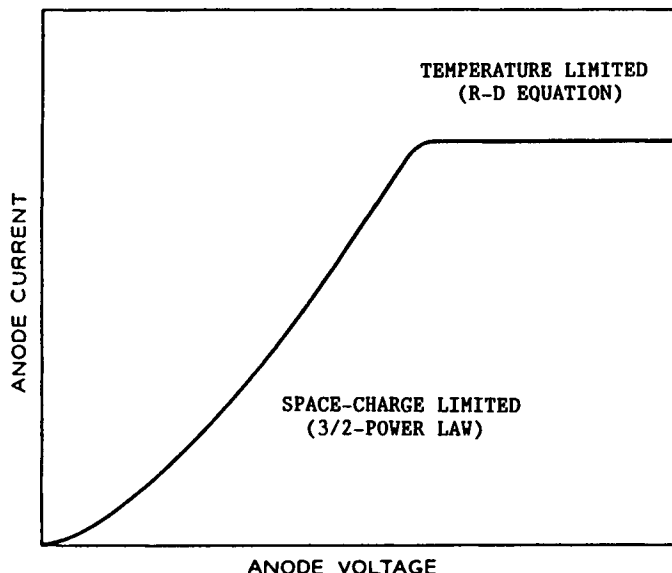


Figure 19. Anode current versus voltage, illustrating space-charge limited and temperature limited regions.

provides a useful approximate means of obtaining the space-charge limited emission density for curved cathodes and other surface shapes. Actually, the zero field point is slightly displaced from the physical surface of the cathode, and the potential at this point (the potential minimum) is slightly lower than the potential of the cathode [4]. These two effects are usually negligible in practical microwave tube guns. A useful treatment of the transition region of the curve of Figure 19 is presented in Reference [22].

The second type of emission which can occur in microwave tubes is field emission. In one instance, small whiskers or protuberances extending from tube elements having electrostatic surface fields (such as the focus electrode) can have fields at their tips higher than the field emission threshold. Field emission can lead to undesirable effects such as unwanted X-ray emission, or it can even incite high-voltage breakdown. This type of emission is generally governed by the Fowler-Nordheim equation, originally published in Reference [23] with corrections in Reference [24]. A useful reference on field emission from small metallic whiskers is Reference [25].

The final type of emission (which is also deleterious in linear beam tubes) is secondary emission [3]. In this type of emission, primary electrons in a given energy range, impinging upon surfaces in positive fields (that is,

fields which accelerate electrons away from the surface), can produce a multiplicity of electrons (secondary electrons) which leave the surface. Secondary emission can lead to multipactor in klystron cavity gaps or it can reduce the collection efficiency of multistage depressed collectors. A new reference [26] provides useful working equations for the calculation of secondary emission current.

Cathode Loading Determination

The electron optics codes provide very accurate values of cathode loading for diode and gridded guns. However, it is often useful to obtain preliminary estimates of cathode loading prior to use of such codes. This can be accomplished as follows. In Pierce guns, current density along the cathode surface varies approximately as

$$J(\alpha) = J_0 / \cos^2 \alpha, \quad (5)$$

where the notation is defined in Figure 20 [12]. This is primarily due to the effect of the anode opening in the gun. Integrating Equation (5) over the cathode surface yields total current from which J_0 can be obtained:

$$J_0 = \frac{I_0}{2\pi \left(\frac{r_c}{\sin \theta} \right)^2 \left(\frac{1}{\cos \theta} - 1 \right)}. \quad (6)$$

Current density at the cathode edge can be computed from Equation (5) by setting α equal to θ .

Average cathode current density calculated by dividing I_0 by the area of the cathode is approximately equal to the value of J from Equation (5)

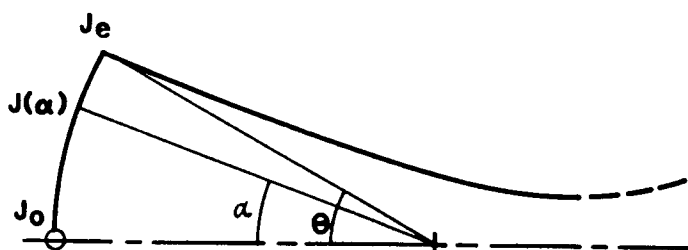


Figure 20. Current density notation.

using the cathode area bisection angle given by

$$\alpha_m = \cos^{-1} \left(\frac{1 + \cos \theta}{2} \right). \quad (7)$$

Clearly, the highest current density occurs at the outer edge of the cathode in Pierce guns. The variation becomes worse for high-half-angle guns.

Cathode loading in gridded guns can be estimated by adjusting the cathode current upward to take into account grid geometrical screening and cathode usage degradation arising from shadow gridding. Peak cathode loading within each grid cell is thus determined by using I in place of I_0 in Equations (6) and (5), where I is given by

$$I = I_0 \left(\frac{1}{1 - S} \right) \frac{1}{U}. \quad (8)$$

In Equation (8), the cathode usage factor, U , is defined as the current passing the grids divided by the uniform current density current, and S is proportional to the geometrical screening factor of the grid [27]. In determination of U , the projected area beneath the grid is excluded, and the highest current density in the cell is used to determine the uniform current density current.

In a shadow gridded gun, U can be reasonably taken as 0.75 and S as 0.15. From Equation (8), I/I_0 is equal to 1.57. In this case, the highest current density, typically about midway between the shadow grid wires, is roughly 1.6 times higher than that of the gridless case. Newer shadow grid designs, including contiguous shadow gridded guns, have lowered this ratio. In intercepting gridded guns, if U is taken as 1 and S is equal to 0.11, the loading increase is only 1.12 over the gridless case.

Dispenser Cathodes

Most modern linear beam tubes use dispenser cathodes as the source of electrons. They can deliver a high level of current density in long-pulse and DC operation, and they are quite resistant to poisoning. Basically, they are made by melting a mix of barium and calcium aluminates into a porous (about 80% dense) sintered tungsten matrix cathode head. Upon cathode activation, a low-work-function surface comprising a monolayer of barium and oxide dipoles is developed. Survey articles on dispenser cathodes include sections in References [3] and [6], as well as papers [28–30].

Emission density capabilities of the type-B dispenser cathode range from 8 to 10 a/cm² for pulsed and from 1.6 to 2 a/cm² for cw operation.

Its typical operational temperature range is roughly 1160–1220°C and its work function is 2–2.1 eV. In high-duty-cycle tubes (duty cycle greater than about 20%), current density averaged over time should not exceed the cw limits. Cathode temperatures in high-performance microwave tubes lie typically at the high end of the range above (sometimes even higher) with emission densities at their maximum. Tubes designed for long life are operated at the lower end and have more modest cathode loading. In gun design, the highest value of cathode loading determined by either approximate methods or numerically using an electron optics code should not exceed the emission density capabilities of the given cathode used.

In general, as cathode temperature is increased, higher current densities can be drawn before the temperature limited level is reached. However, as cathode temperature increases, cathode life decreases due to the increased evaporation rate of the surface layer and loss of the emission mix. If the work function is lowered in Equation (3), on the other hand, higher emission can occur at a lower temperature. Modern cathodes use various means to lower the work function so that they can be run at lower temperatures for longer life.

The type-M cathode is an example of this type of cathode. It is made by sputtering a thin coating of an alloy of osmium and ruthenium (approximately 2000–5000 Å thick) on the surface of a type-B cathode. The work function of type-M cathodes is roughly 1.8–1.9 eV (about 0.2 eV lower than that of type B). They are typically run approximately 100°C cooler than type B, or in the range 1060–1120°C. When operated in this fashion, the emission capabilities of type M equal or exceed those of type B. References [6], [28], and [30] include further information on this type of cathode plus other new lower temperature cathodes such as the mixed metal matrix, cermet (scandate), controlled porosity dispenser (CPD), and others.

Oxide Cathodes

Oxide cathodes are still used in certain klystrons and other microwave tubes. Advantages include their low operating temperature (typically in the range 775–825°C) and low cost. These can be important advantages in very large cathodes. The work function of such cathodes is typically 1.4–1.5 eV. Oxide cathodes can deliver high peak current levels over short pulse lengths (for example, 8–10 a/cm² for 2-μs pulses); however, the emission capability degrades markedly with pulse length (down to about 250 ma/cm² for reliable operation DC).

Oxide cathodes are made by spraying, dipping, or cataphoretically depositing a thin coating of emission mix onto a specially prepared nickel

cathode base. Either double or triple carbonate coatings can be applied to the surface of the cathode; however, double carbonate coatings (comprising barium and strontium carbonates in roughly equal molecular proportions) appear advantageous from a coating adherence and life point of view. During activation of the cathode, carbonates are converted into oxides plus a certain number of free metal atoms. Barium atoms on the surface of the coating are thought to be the main emission sites. The thickness of the coating after activation is typically on the order of 0.05 mm. The chemistry, manufacture, and performance of oxide cathodes are covered further in References [3] and [31].

Cathode Heaters

Cathode temperature must be raised to the desired operational level, then be held invariant, and be uniform along the surface in order to achieve proper emission and reliable cathode life. This is typically accomplished by means of a heater situated behind or inside the cathode. One cathode heater arrangement is shown in Figure 8. In this case, the heater is a double coil of tungsten wire (alloyed with a small percentage of rhenium to increase ductility) held in place by hard-fired alumina potting. Double coils are used in order to reduce stray magnetic fields at the surface of the cathode (which can adversely affect the electron beam).

Another type of potted noninductive heater used to heat Pierce gun cathodes is a toroidal coil with the wire from one end passed back through the center, or a bifilar helical toroid. This type of heater is typically mounted near the periphery of the cathode [28]. Many large dispenser cathodes used in klystrons are made in this fashion. Heater wire in very large cathodes can be quite thick (on the order of 1 mm) and is often molybdenum rather than tungsten.

Current is passed through the heater which raises its temperature due to ohmic heating. Heat is thereupon transferred to the cathode head by conduction through the potting. Applied heater voltage can be either AC or DC. If DC voltage is used to power the heater, the end of the heater not connected to the cathode (the heater leg) should be negative with respect to cathode potential to prevent premature potting failure. Heater voltage in small cathodes (on the order of 1 cm in diameter or less) is often 6.3 V, and heater power is a few watts to a few tens of watts. In large guns (on the order of 10 cm in diameter), heater voltage can be tens of volts and cathode powers can be many hundreds of watts. In general, heater power is small in comparison with the level of RF power generated by the given microwave tube itself.

Oxide cathodes run at lower temperatures, and large cathodes used in klystrons often include pancake (flat) heaters. In one type, tungsten heater wire is threaded through a set of alumina beads used to electrically isolate the heater from the cathode. The wire takes the form of a double spiral (to reduce stray magnetic fields). The wire and bead assembly is then held in place by a rear cover (which also acts as a rear heat shield). In this case, heat is transferred to the cathode head by radiation. In another type of heater, the spiraling heater wire is coiled. It closely resembles a hotplate; thus it is called a hotplate heater. Free-standing heaters (which look somewhat like an unpotted version of the heater in Figure 8) are sometimes used in smaller cathodes. Heat transfer is by radiation in this case.

For certain applications, it is necessary to heat the cathode very rapidly. Small dispenser cathodes which reach their final operating temperature in a matter of seconds can be designed [28, 32, 33]. Three basic types are identified below. All employ a reduced mass cathode head.

The first type includes a pancake heater coated with alumina (or another insulating coating) directly bonded to the back of a thin cathode [32]. Alternately, a toroidal heater mounted near the periphery of a thin cathode head is also capable of very fast warmup [28]. A newer type of cathode heater has been made by depositing anisotropic pyrolytic graphite upon an anisotropic pyrolytic boron nitride insulator [33].

The second basic type includes a thoriated tungsten (or other) directly heated axillary cathode mounted behind the main cathode. Heater current is passed directly through the axillary cathode which heats it in a fraction of a second. Voltage is then applied between the axillary and the main cathodes, causing current to flow. The main cathode is heated by the power carried by the beam from the axillary cathode. This cathode heats somewhat faster than the first type.

The third type is a directly heated dispenser cathode. This cathode has been shown to have the fastest warmup time of the three basic types listed. It does, however, possess mechanical and electrical drawbacks which have limited its general use.

Design of fast warmup cathodes (and cathodes in general) is typically carried out using computer codes such as TBCATH, for example [32]. This code provides cathode temperature versus time given the basic cathode configuration, certain physical dimensions, materials, applied heater voltage, or input power. The analysis includes the nonlinear resistance of the heater with temperature and can be used to design the heater itself. TBCATH has been used to uncover principles of fast warmup cathode design. One example is that, in a potted heater configuration, faster overall warmup speed can be accomplished by making cathode thermal shielding poor (so that the cathode is an effective thermal radiator). This

makes the cathode inefficient from a power consumption point of view but faster.

4. Computer Codes Used in Beam Optical Design

Design Methodology

Heavy use is made of computers and computer codes in the design of beam optical systems for microwave tubes. Hundreds of codes have been written which cover essentially all aspects of the design. Figure 21 presents

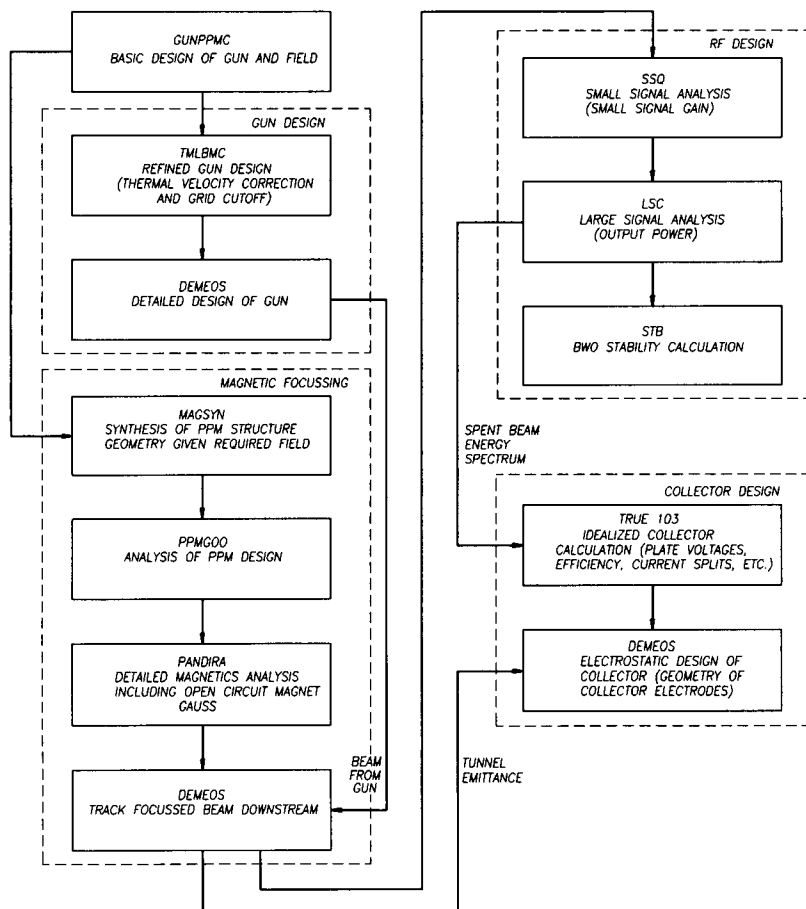


Figure 21. Example of codes used in a helix tube design.

a flow chart showing a sample of Litton codes used in the design of a grid pulsed, periodic permanent magnet (PPM) focused, helix TWT with a multistage depressed collector (MDC).

This figure identifies generic areas of design common to linear beam devices (compare with Figure 1). Further, Figure 21 shows the relationship of one code to another and points out the integrated nature of the design process. One objective here is to provide a global view of the design process. In general, there is a hierarchy of codes running from simple, very user friendly ones to rough out well-balanced, reasonable, beam optical designs and to more complex and accurate codes such as POISSON (PANDIRA) [34, 35] and DEMEOS [36, 37]. Both PANDIRA and DEMEOS are deformable triangular mesh codes.

At the top of the chart is GUNPPMC, used to achieve a basic beam optical design. A sample printout from this code is presented in Figure 22. This code provides design information about the gun, plus a good estimate of the required practical PPM field strength, B^+ (rms) in kilogauss, and whether the chosen periodic length, L , is within acceptable bounds for good beam stability in the periodic focusing system (parameter λ_p/L). Note that a , used herein, is the inner radius of the RF circuit (drift sections in a klystron). This information can be then fed into the gun design and magnetic focusing blocks.

TMLBMC is another small code used to rough out the gun design to a higher level of detail. PIERCE is a Pierce gun synthesis code [38] which is sometimes useful in this phase of the design. Next, DEMEOS can be used to carry out the detailed design of the gridded gun. Note that in designing a gridded gun, it is important to include a representation of the grid (or grids) in the computer simulation. Deformable triangular mesh codes such as DEMEOS allow for the convenient inclusion of grids. AUTOGRID (not listed) is a code which automatically provides a full data set for DEMEOS in the cathode and grid region given a few simple inputs. In nongridded guns, uniform mesh electron optical codes such as EGUN [39–41] can be used with success.

In development of the magnetic focusing design, MAGSYN is shown first. This simple code automatically determines the magnet and pole piece dimensions to provide a given PPM field level on axis. These dimensions can then be entered into code PPMG00, written by Vaughan based on the work of Sterzer and Siekanowicz [42]. This code provides a refined estimate of the peak field on axis and the flux density levels in the pole pieces.

The detailed magnetic design can be carried out next with PANDIRA. PANDIRA handles permanent magnet focusing structures, whereas code POISSON handles electromagnets. Both of these codes include the finite

```

GUNPPMC: Program after Trans. E.D. 1984, 1987; Vers. 2.4; 2-9-89
QBasic pgm for PC or PS/2 by R. True

Case date =11-14-1989    Linear dim in inches

2087 WITH HYPOTHETICAL CIRCUIT AND GRID

disk rc = .125      v0 = 9.6 kv      pmu = .54
r95/a = .45        a = .082        L = .55

i0 = .5079262 a
r95 = .0369      rc/r95 = 3.387534      (rc/r95)^2 = 11.47539
calc th = 17.44731 deg    actual th = 17.4      delta th = 4.730797E-02

cath sph rad = .4180032      cath area = .3241077 cm^2

ungridded:
j0 = 1.49544      ja = 1.567153      je = 1.642304 a/cm^2
beam j = 18.40478 a/cm^2

gridded gun data:
screen factor=.1      cathode usage factor= 1
peak current densities:
j0 = 1.6616      ja = 1.741281      je = 1.824782 a/cm^2

calc sigma = .0261      analyzer sigma = .0113
T (deg C) = 1130      thermal sigma = 8.500937E-03

single period focussing:
factor F= 1.65 [default value=1.65]      B+/Bbr = 1.31419
Bbr = .6364639 kG      B+(rms)= .8364347      B+ pk s.p. = 1.182897

focf1 = 2.920423      lamda_p= 1.812322      lamda_p/L = 3.295131
[pulse lamda_p/L >2.7 and cw lamda_p/L >3.2]
Vs s.p.= 1.155574 (kv) [k=1]      Vs s.p./V0= .1203723
T-emittance = .005085

phase advances (deg):
P0= 50.76252      Pp= 54.62606      P= 9.650225      P/P0= .1901053

emittance growth estimate:
small f= .0386 [.0386 gaussian, 0 uniform]
ef/ei= 1.495806      T-emittance (final)< 7.605154E-03

```

Figure 22. Sample printout from code GUNPPMC (see text).

permeability of the iron. PANDIRA can be used to advantage in designing the magnetic entrance (the point at which the beam from the gun enters the magnetic focusing system). PANDIRA can also solve the problem of an individual focusing magnet in free space. This improves the specification of magnets.

The next step in the procedure is to track the beam from the gun downstream using DEMEOS in order to verify the focusing design and to obtain the characteristics of the focused beam including filling factor, r_{95}/a , and tunnel emittance, ϵ_T . Tunnel emittance is defined as the product of the beam filling factor and the standard deviation of the normalized transverse velocity distribution within the beam, σ . This infor-

mation is used in subsequent collector calculations as shown in the flow chart.

The next block is concerned with the RF design of the tube. Three programs written by Hiramatsu can be used [43]. SSQ is a small signal gain program which computes gain as a function of frequency [44]. A feature of this code is that the physical geometry of the helix and supporting structure is entered, and the interaction impedance and circuit phase velocity are calculated.

LSC is a large signal TWT analysis program used to compute saturated output power as a function of frequency [45]. This code employs a Langrangian approach; that is, the beam is subdivided into a number of disks which are then tracked downstream. LSC is able to accurately model multiple severs, circuit velocity tapers, etc. The energy spectrum of the beam which exits the interaction region is available from this code. This information is necessary for depressed collector calculations.

The final code of this set is STB which is used to determine circuit stability as a function of circuit length [46], beam filling factor, etc. Information from this code makes it possible to design the RF circuit so that it is free of unwanted oscillations (which can lead to severe disruption of the focused beam).

The next block of the procedure is design of the MDC. TRUE103 processes the spent beam data from LSC and can be used to determine single collector or MDC performance. This code has a built-in optimizer routine which determines a set of collector plate voltages for maximum efficiency (for any given spent beam energy spectral distribution). It also accepts collector plate voltages from the user so that the best compromise set of collector voltages can be ascertained. This code sets up a sophisticated 60-ray model of the finite emittance spent beam in the tube and writes the data on a file for use in collector calculations performed using DEMEOS.

Finally, DEMEOS can be used to design the depressed collector and to determine its practical performance. Beam flow within the collector is determined for various injected beams (from TRUE103), as are the geometry and applied voltages of the collector electrodes. This procedure is useful in the design of single-stage collectors and MDCs, and it has been found that computed efficiency and current splits are in good agreement with experimental data.

Beam Optics Codes

In the flow chart of Figure 21, DEMEOS appears in the blocks on gun design, beam focusing, and collection. Because of the importance of this

generic type of code (which we shall hereafter call a gun code) in the design of beam optical systems, a further discussion of them is presented below. Basic principles which apply to both uniform mesh (UM) and deformable triangular mesh (DTM) gun codes are identified below. Reference is made to EGUN and DEMEOS which typify UM and DTM codes, respectively. General references on UM gun codes include References [4], [39], and [47].

Presented in Figure 23 is a flow chart illustrating the overall method used in such codes. Although this diagram pertains to DEMEOS, it also

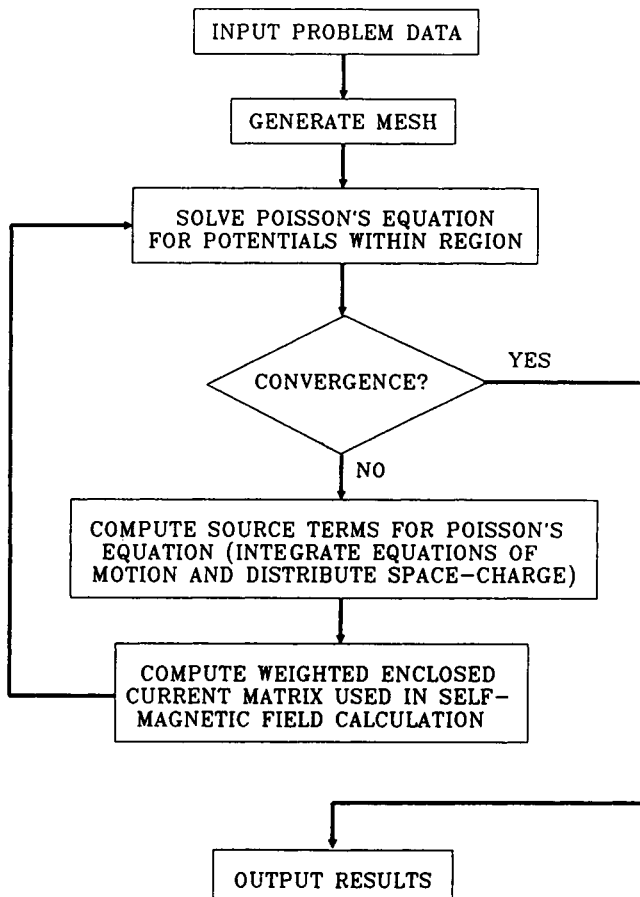


Figure 23. Flow chart of a relativistic version of DEMEOS (see text). Reprinted with permission from Ref. [10], © 1991 IEEE.

applies, in general, to essentially all gun codes. Both DTM and UM codes use the method of self-consistent fields in which Poisson's equation is solved in alternation with the tracing of trajectories and the deposition of space charge. Self-consistency is achieved when the numerical solution of Poisson's equation is essentially stationary as the loop is iterated. The lower block applies only to the relativistic version of DEMEOS which is discussed later.

After input data are entered, the code sets up the mesh. In UM codes, this step includes setting up broken stars through which the boundary passes (see Figure 26). In the DTM code, a logical diagram is prepared as shown in Figure 24. The code accepts logical space coordinates (I, J), real space coordinates (Z, R), and boundary potentials. The interior must be completely enclosed by Dirichlet and Neumann boundaries as is the case in all boundary value problems. The code then generates a topically regular mesh as shown in Figure 25. So-called G -boundary lines interior to the region can be used to control mesh density. G -points are treated as regular interior points in all other respects.

Laplace's equation is solved first rather than Poisson's equation since there is no charge in the region initially. The finite difference or finite element approximation to Poisson's or Laplace's equation can be solved either by successive overrelaxation (as in DEMEOS [35, 36]) or by matrix methods (as in EGUN [40, 47]). Solution by overrelaxation is summarized in Figure 26, where R_0 is the residual in a UM code (square mesh), and F_0 is the residual in the DTM code. Note that the right-hand side of the residual equation represents the finite difference approximation of Poisson's equation in the UM code; in the DTM code, the right-hand side is a finite element formulation. In the equations shown, V refers to potential; S is the source (space-charge) term; e or w is the coupling coefficient associated with a given neighboring node, i ; and β and α are the acceleration factors. A solution is achieved when R_0 or F_0 approaches zero. This state is achieved by sweeping through the mesh repeatedly in a systematic fashion while updating each V by a quantity proportional to the residual. Note that superscript n refers to the current value of V , $n + 1$ refers to the updated value, and $n, n + 1$ indicates current and new values.

As seen in Figure 23, the first time through the self-consistent fields loop, the test for convergence is bypassed. The next major step in the procedure, therefore, is determination of the source terms, S , at each interior node for use in the Poisson solver (which computes V at each interior mesh point). As seen in Figure 27, current from a small section of the cathode (elementary diode) first is computed from Child's Law. J or \bar{C} must be modified by a damping factor, γ , to prevent solution instability.

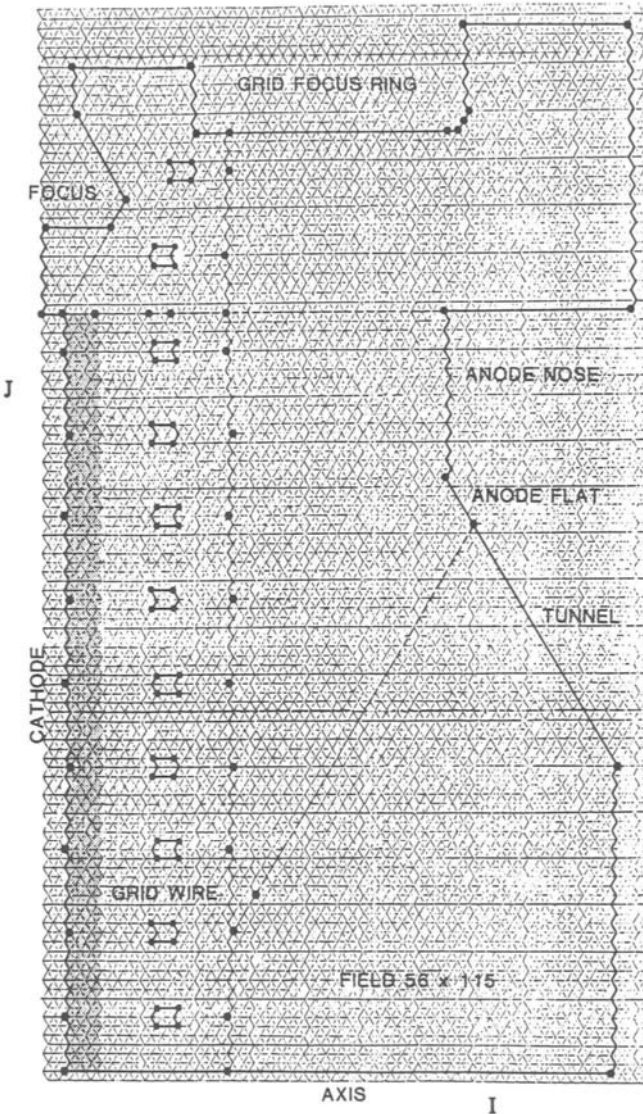


Figure 24. Logical diagram for the gun in Figures 25 and 30. Reprinted with permission from Ref. [13], © 1985 IEEE.

Charge in UM codes is then usually distributed within the mesh by numerical integration of the equations of motion and accumulation of q_j for each ray according to Figure 28. Note that in Figure 27 I_j refers to ring

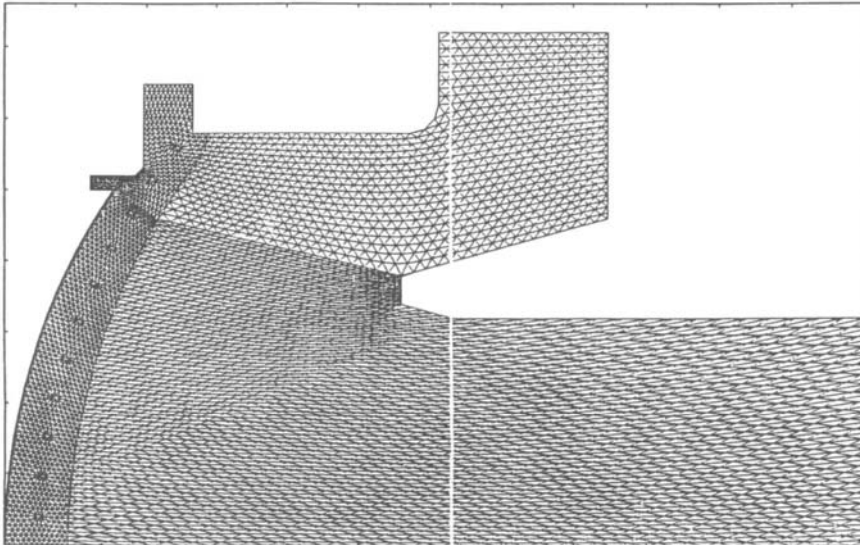


Figure 25. Zoom view of the deformed triangular mesh on which Poisson's equation is solved. Reprinted with permission from Ref. [13], © 1985 IEEE.

current, whereas I_j in Figure 28 refers to current per radian. In the DTM code, charge is assigned directly in the region near the cathode (the open circles in the approximately rectangular mesh region), where M_l represents the space-charge weighting function associated with node l , and ADOD_l is the radially weighted dodecagon area [36]. Outside of this region, charge is assigned by integration of the equations of motion and by accumulation of superelectrons (each carrying charge DQ) associated with a given mesh point depending on whether DQ lies within the cell (dodecagon) boundary. There are n superelectrons per time step.

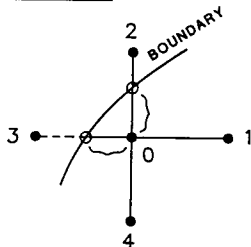
Figure 29 presents the equations of motion for the relativistic version of DEMEOS (called RDEMEOS) [10]. In this figure, θ is angular velocity, γ is the relativistic mass factor, η is the absolute value of the electron-charge-to-mass ratio, A refers to magnetic vector potential, V_r and V_z are potential gradients, B refers to magnetic flux density, and E_0 is the electronic rest energy. The relativistic code integrates pseudovelocities $\gamma\dot{r}$ and $\gamma\dot{z}$ (which are proportional to momentum) [48].

The self-magnetic field, B_θ , is determined from Ampere's circuital law, where μ_0 in the equation is the magnetic permeability of free space. To speed the calculation, a weighted enclosed current matrix is updated every iteration of the self-consistent fields loop as shown in Figure 23. A

$$\nabla^2 V + \sigma = 0$$

$$\sigma = \rho / \epsilon_0$$

SQUARE MESH

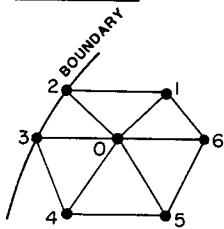


$$R_o = \sum_{i=1}^4 e_i (V_i - V_o) + s_o$$

SOLUTION : $R_o \rightarrow 0$

$$V_o^{n+1} = V_o^n + \beta R_o^{n,n+1} / \sum_{i=1}^4 e$$

DEFORMABLE MESH



$$F_o = \sum_{i=1}^6 w_i (V_i - V_o) + s_o$$

SOLUTION : $F_o \rightarrow 0$

$$V_o^{n+1} = V_o^n + \alpha F_o^{n,n+1} / \sum_{i=1}^6 w_i$$

Figure 26. Solution of Poisson's equation in gun codes.

unique feature of the method is that $\frac{1}{2}$ of the outer ray current is used in the calculation along with the actual position of the ray. This so-called center of gravity approach has led to improved accuracy in computation of the self-magnetic field. In another DTM code (MAGUN), a method for the computation of all three components of the self-magnetic field is used [49].

Figure 30 presents results for an intercepting gridded gun, showing boundaries, electronic trajectories, and equipotential contours. This and other results presented herein are from the standard version of DEMEOS. The nonrelativistic version of the code pertains to a majority of electron optical systems in microwave tubes since most operate at voltages at which relativistic effects are negligible (say less than 50 kV).

Other Codes

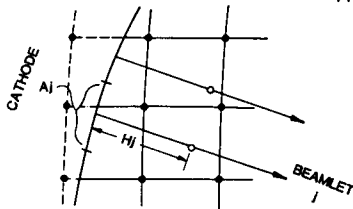
Codes discussed up to this point may be considered, in general, mainline. In addition, there are numerous other codes in the beam optics area

CHILD'S LAW

$$\bar{C} = V(\xi) / \xi^{4/3} \text{ AND } J = k \bar{C}^{3/2} \text{ WHERE } k = 4\epsilon_0 \sqrt{2\eta} / 9$$

SQUARE MESH

MORE THAN ONE BEAMLET
PER CELL OF MESH FOR
ACCURACY

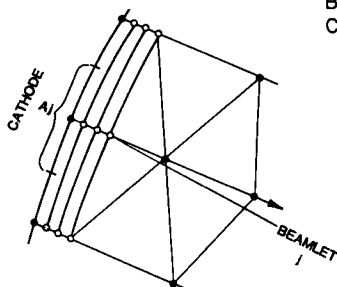


$$J_j = J_j^0 + \gamma (J_j - J_j^0)$$

$$I_j = J_j A_j$$

DEFORMABLE MESH

BEAMLETS FROM NODES
COMPRISING CATHODE



$$\bar{C}_j = \bar{C}_j^0 + \gamma (\bar{C}_j - \bar{C}_j^0)$$

$$J_j = k \bar{C}_j^{3/2}$$

$$I_j = J_j A_j$$

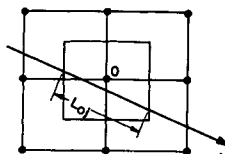
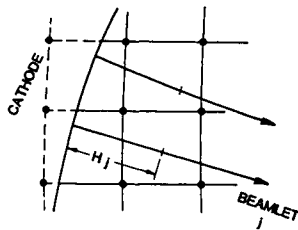
Figure 27. Determination of emitted current in gun codes.

covering almost every imaginable aspect of the design. In essentially every case today, where theory exists, so does a computer code based on the work. Further, there is ample computer hardware to handle even the most complex beam optical problem. In the rest of this chapter, codes other than those already identified will be presented in the context of the discussion.

Linear accelerators are similar to microwave tubes in many respects, and codes used to design them can often be applied to microwave tubes. A compendium of codes used in particle accelerator design has been compiled by workers in the Los Alamos Accelerator Code Group [50]. This compendium includes the gun codes EGUN and DEMEOS, magnet codes POISSON and PANDIRA, particle-in-cell (PIC) and electromagnetic (EM)

INTEGRATION OF EQUATIONS OF MOTION AND
CHARGE ASSIGNMENT

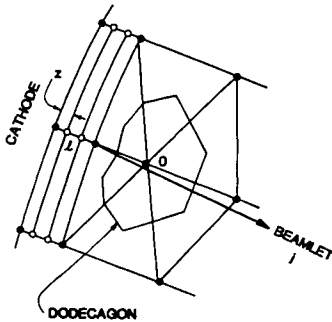
SQUARE MESH



$$q_j = \frac{-l_j L_{0j}}{\epsilon_0 (2\eta V_0)^{1/2}}$$

$$S_o = S_o + q_j$$

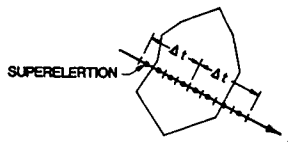
DEFORMABLE MESH



OPEN CIRCLES

$$S_\ell = -M_\ell \frac{4}{9} \bar{C} (\ell_z)^{-2/3} ADOD_\ell$$

REGION BEYOND



$$DQ_j = -l_j \Delta t / n \epsilon_0$$

$$S_o = S_o + DQ_j$$

Figure 28. Determination of source terms in gun codes.

codes MAGIC, SOS, MASK, ARGUS, VARGUS, and numerous others. These PIC and EM codes (or derivatives) have been used in the microwave tube field.

Both DTM and UM three-dimensional (3D) gun codes which are applicable to nonaxisymmetric systems exist [51, 52]. These codes have been used with success in the analysis of certain difficult problems. In general, however, the use of 3D codes in design (including the PIC and EM codes of the last paragraph) remains limited by the difficulty of data input and slower processing speed.

There is also another large group of codes which are useful to the designer of beam optical systems. These include finite element analysis

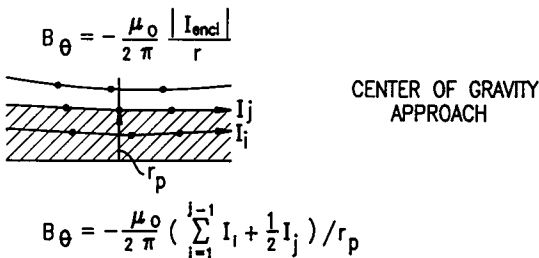
$$\dot{\theta} = \frac{1}{\gamma r^2} (\eta r A_\theta - \eta r_c A_{\theta c})$$

$$\frac{d}{dt}(\gamma \dot{r}) = \eta v_r - \eta (r \dot{\theta}) B_z + \eta \dot{z} B_\theta + \gamma r \dot{\theta}^2$$

$$\frac{d}{dt}(\gamma \dot{z}) = \eta v_z - \eta \dot{r} B_\theta + \eta (r \dot{\theta}) B_r$$

$$\gamma = 1 + V_p / E_0$$

WHERE V_p IS VOLTAGE AT ANY POINT ALONG TRAJECTORY
FROM POTENTIAL MATRIX (2-D TAYLOR SERIES EXPANSION)



DIVISION BY r_p IN PREDICTOR-CORRECTOR LOOP IN RAY TRACING INTEGRATION ROUTINE.

Figure 29. Relativistic trajectory equations used in code RDEMEOS (see text). Reproduced with permission from Ref. [10], © 1991 IEEE.

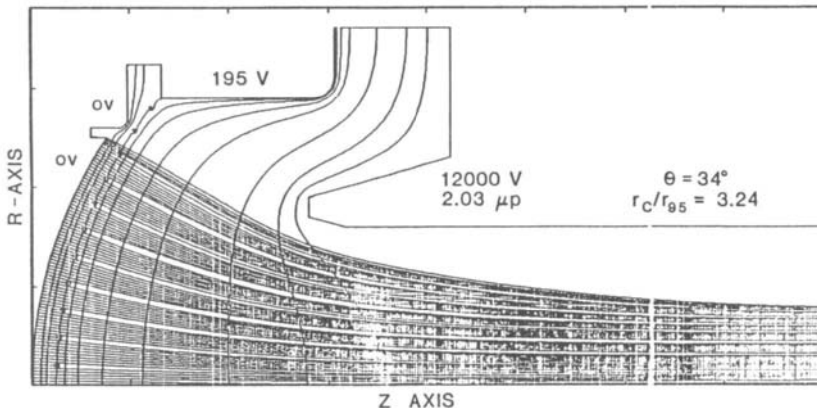


Figure 30. Computer simulation of a triode Pierce gun using a deformable triangular mesh code. Reproduced with permission from Ref. [13], © 1985 IEEE.

(FEA) codes (thermal and mechanical design); computer-aided drafting codes (mechanical layout); computer-aided test codes (acquisition and reduction of cathode, beam, magnetic, and collector data); service routine codes (general mathematical routines, graphics, plots, system); and miscellaneous codes (scientific word processing, spreadsheets, and data base management). Many of the codes in this paragraph are generic insofar as they are commonly used by all practicing engineers and scientists.

5. Optical Design of Electron Guns

Basic Design

This section discusses the optical design of a Pierce gun. Basic principles and methods are presented which can be applied to the design of other types of electron guns. In general, the design proceeds from codes based upon analytic and empirical gun theory to the development of external electrodes by such techniques as beam edge field matching. After cold beam simulations are made using one of the various gun codes, finite emittance beam calculations (which better represent real beams) can be made using these very same codes. High-voltage breakdown is an important aspect of high-voltage gun design.

Presented in Figure 31 is a sample printout from code TMLBMC; this code provides a more complete analysis of the design originally roughed out with GUNPPMC. The notation in this code is similar to that in GUNPPMC. TMLBMC uses the analytic solution of Langmuir and Blodgett (flow between concentric spheres) in the region between the cathode and the anode [53]; anode lens beam divergence per Danielson, Rosenfeld, and Saloom (DRS) [54]; and the universal beam spread curve from this point to the waist. These calculations use the uncompensated value of θ given by

$$\theta_u = \sin^{-1}(k_{oc} \sin \theta), \quad (9)$$

where k_{oc} is the optical compensation factor described in References [38] and [55]. The default value for k_{oc} in this code is 0.9.

Another approach to the problem is to use the synthesis procedure presented by Vaughan in Reference [38]. In this case, one starts with V_0 , I_0 , r_w (waist radius), and J_c (or r_c) and works backward to find r_c (or J_c) and θ which are consistent. Code PIERCE is based on this procedure. Reference [38] is a useful paper to develop a further understanding of the basic design of diode Pierce guns.

```

TMLBMC--Conical Flow; PS/2 Vers. 4.0; R. True; 12-4-88
DRS cap gamma = 1.25
Case date =11-14-1989           Linear dim in inches

* Case title: 2087 WITH HYPOTHETICAL CIRCUIT AND GRID

disk rc = .125      th = 17.4 deg     v0 = 9.6 kv     pmu = .54
opical comp factor = .9
uncomp th = 15.6129 deg used below

i0 = .5079262      jc(a/cm^2) = 1.574259
cath sph rad = .464448   anode sph rad = .2133071
cath-anode dist = .2511409

mean grid spacing = .015
grid sph rad = .449448      vg = 102.1166  volts

thickness of grid = .002      width of grid wires = .002
short grid pitch = .032      long grid pitch = .032
effective linear grid pitch = 2.262742E-02
grid cutoff voltage =-86.09062

Thermal Beam Analysis
Tc(deg C) = 1130      a= .082
check pmu = .5399956

      z        re       re/a      sig      r95      r95/a
0.25114  0.05741  0.70011  0.00174  0.05915  0.72133
0.27626  0.05525  0.67376  0.00181  0.05394  0.65775
0.30137  0.05318  0.64852  0.00189  0.05203  0.63455
0.32648  0.05120  0.62442  0.00198  0.05023  0.61253
0.35160  0.04932  0.60151  0.00208  0.04852  0.59173
0.37671  0.04755  0.57983  0.00219  0.04692  0.57219
0.40183  0.04587  0.55941  0.00231  0.04542  0.55395
0.42694  0.04431  0.54031  0.00244  0.04404  0.53706
0.45205  0.04285  0.52256  0.00257  0.04277  0.52155
0.47717  0.04151  0.50821  0.00272  0.04161  0.50748
0.50228  0.04029  0.49128  0.00289  0.04058  0.49487
0.52740  0.03918  0.47782  0.00306  0.03967  0.48378
0.55251  0.03820  0.46586  0.00324  0.03889  0.47422
0.57762  0.03734  0.45542  0.00344  0.03823  0.46624
0.60274  0.03662  0.44654  0.00365  0.03771  0.45985
0.62785  0.03602  0.43923  0.00388  0.03752  0.45751
0.65297  0.03555  0.43350  0.00411  0.03729  0.45470
0.67808  0.03521  0.42937  0.00436  0.03721  0.45378
0.70319  0.03500  0.42683  0.00463  0.03729  0.45473

```

Figure 31. Sample printout from code TMLBMC (see text). Reproduced with permission from Ref. [12], © 1989 IEEE.

Returning to TMLBMC, the method of successive bisection is used to determine the anode spherical radius, and the cathode-to-anode distance is determined according to Muller [56]. Positive grid voltage is computed from the Langmuir and Blodgett solution, and the grid cutoff by the method explained in Reference [12]. Grid voltage from this code can be used in development of the external electrodes of the gun. Spreading of the cold beam as a function of distance from the cathode center, z , is given by r_e . Thermal beam spreading is given by r_{95} according to theory in

DRS. Parameter sig is the position of the σ electron in DRS here (not the normalized transverse velocity). Thermal and nonthermal beam spread data from this code can be combined with cold beam results from DEMEOS or EGUN to provide realistic estimates of the size of the actual beam from the gun [11].

External Electrodes

Often the designer has access to gun designs similar to those of the new gun. On the other hand, if there is nothing close, a procedure based upon beam edge field matching is sometimes useful [57]. It is summarized in Figures 32–34 [58]. This procedure was adapted from one which originally used an electrolytic tank analog [59].

Figure 32 summarizes the basic method used to determine the position of the anode. Actually, the position of the anode from TMLBMC is

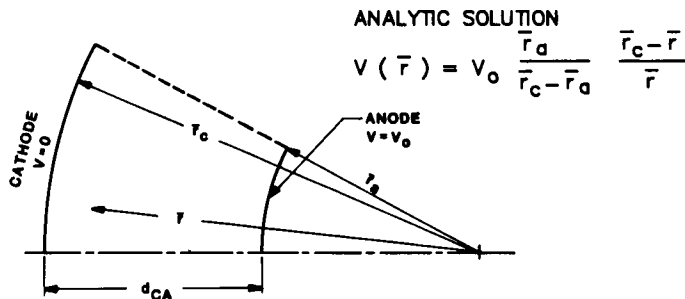
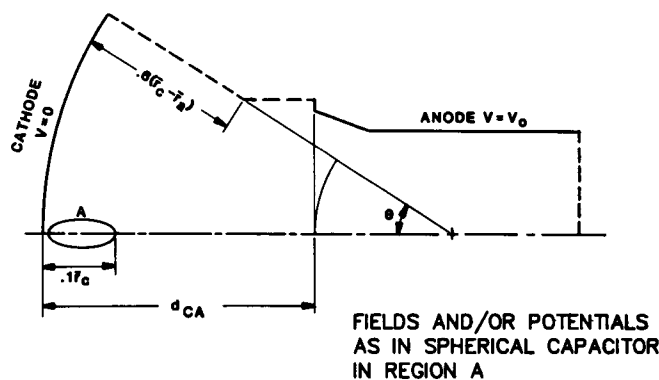


Figure 32. Anode design based on solution of Laplace's equation.

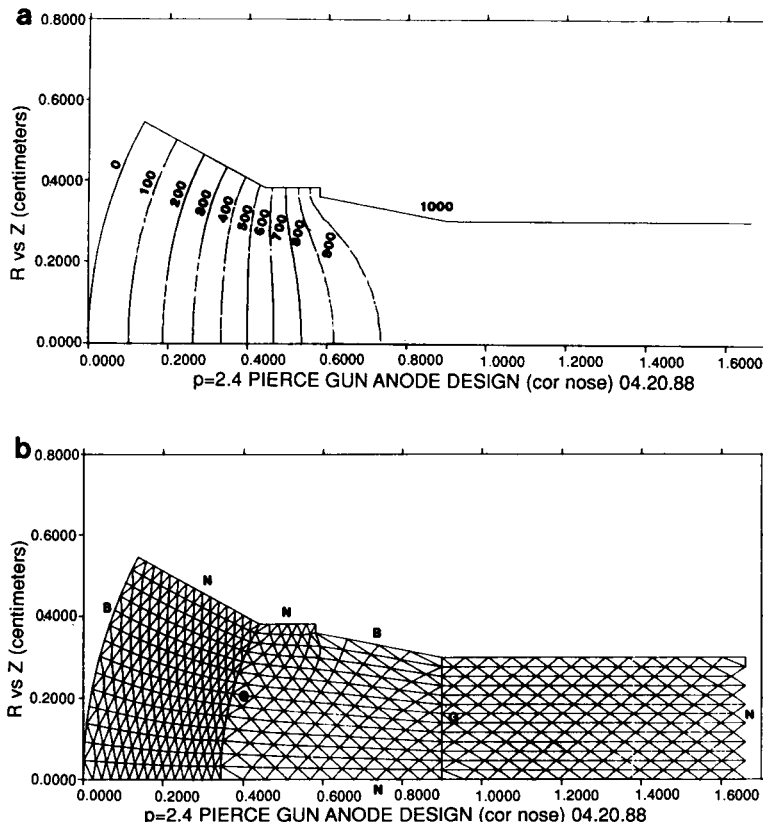


Figure 33. Anode design based on Laplace equation solution. (a) Boundaries and equipotentials; (b) mesh. Reproduced with permission from Ref. [58], © 1989 AIP.

usually not too far off from the final value. In Figures 32–34, the uncompensated value of θ is used. The basic approach is to adjust the position of the anode until the solution of Laplace's equation for the voltage near the center of the cathode matches its theoretical counterpart (see Figure 32). If DEMEOS is used, mesh points can easily be made to lie along the upper Neumann boundary, representing the beam edge. In this case, given the fact that only Laplace's equation is being solved and since the mesh is somewhat coarse, the solution is completed in a few seconds on personal computer (PC) class equipment. Of course the mesh can be made more dense for higher accuracy.

The next step is summarized in Figure 34. In this case, part of the beam flow region is replaced by a beam edge Neumann boundary

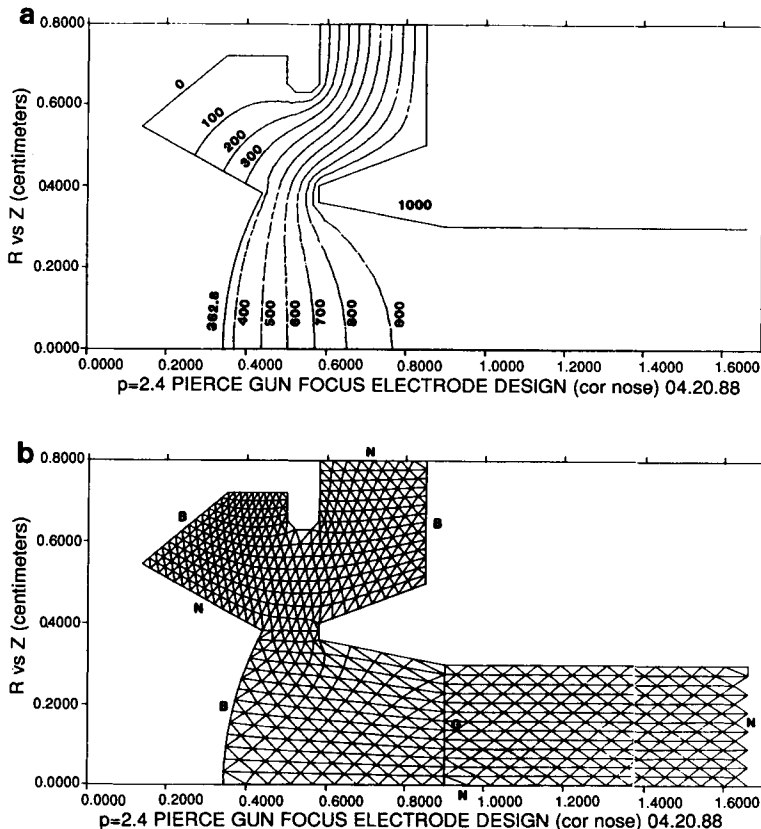


Figure 34. Focus electrode design based on Laplace equation solution. (a) Boundaries and equipotentials; (b) mesh. Reproduced with permission from Ref. [58], © 1989 AIP.

(*N*-boundary) and a fixed potential boundary (*B*-boundary) which begins at the bend point, $0.6(\bar{r}_c - \bar{r}_a)$, in Figure 32. The potential of this boundary can be obtained from the grid voltage routine in TMLBMC. As a first start at the geometry of the external electrodes, the solution in Reference [60] is often helpful. Near the edge of the cathode, the angle of the focus electrode with respect to the beam edge is typically set at the Pierce angle (equal to 67.5°).

External electrodes are then adjusted until the potentials along the beam edge *N*-boundary are in approximate agreement with their theoretical counterparts (again obtained from the grid voltage routine in TMLBMC). Details in the corner region can be accurately represented

(such as the gap between the cathode and the focus electrode) for an improved match to the beam boundary. As in Figure 33, DEMEOS can be used to solve Laplace's equation very efficiently. DEMEOS also allows curved N -boundaries; thus it is possible to use this same technique to develop external electrodes which match curved beam solutions.

The next step is to apply optical compensation (deepen the cathode dish). In this step, θ is now the original design value [see Figure 31 and Equation (9)]. This is done to prevent translaminar streaming, or the crossing of electrons from near the cathode edge into the main body of the beam. Optical compensation improves beam laminarity and makes current density more uniform across the beam at the waist. Further, it is necessary to move the focus electrode forward in relation to its original position after deepening the dish and readjust the position of the anode to achieve the objective perveance.

The final electrode refinement stage is accomplished by solving the problem with a gun code (such as DEMEOS or EGUN). Such a simulation from DEMEOS is shown in Figure 35. It is customary to first solve the problem using a cold beam model and then switch to the more accurate thermal beam model after a reasonable electrode design has been achieved. In this stage of the design, external electrodes can be trimmed to improve beam quality, beam size, cathode loading, beam edge flow (cathode corner design), ease of manufacture, voltage standoff, or other factors.

Using the more advanced design techniques and codes has led to high-quality diode Pierce gun designs which exceed the previously discussed limits. For example, guns with half-angles as high as 50° and area convergences of 100 or more are often found in modern high-power

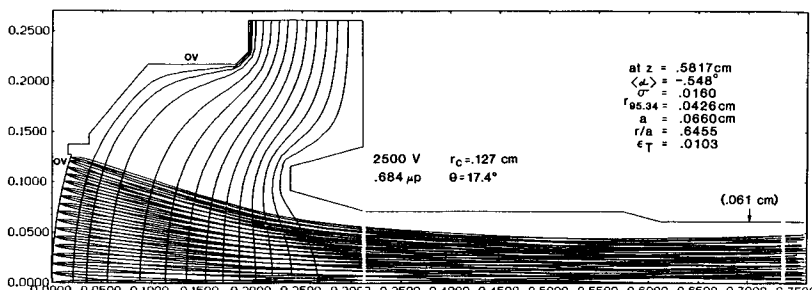


Figure 35. Computer solution for a diode gun using a three-ray model to simulate the thermal electron beam. Reproduced with permission from Ref. [11], © 1987 IEEE.

klystrons. Guns for specialized applications having micropervances greater than 6 have been designed.

Tunnel Emittance and Gridded Guns

In real guns, electrons emerge from the hot cathode with a finite emission velocity [3]. In gun codes, the random velocity distribution of electrons can be represented by the model shown in Figure 36 [11]. Energy parallel to the cathode, V_T in electrovolts, in each side ray is equal to kT/e , where k equals Boltzmann's constant, T is absolute cathode temperature (K), and e is the charge carried by one electron.

The gun shown in Figure 35 uses such a thermal beam model. Typically, finite beam temperature causes beam dilation over the cold beam solution and beam nonlaminarity which impacts the field required to focus the beam (see Section 6).

Tunnel emittance, ϵ_T , is a key parameter for evaluating the quality of electron gun designs. Further, it is indispensable in the design of gridded guns, the prediction of the required focusing field in a PPM focusing system, spent beam modeling for MDC design, and understanding the behavior of electron beam optical systems in general [11]. The basic concept was first introduced in Reference [61]. It is defined as

$$\epsilon_T = \sigma r_{95}/a. \quad (10)$$

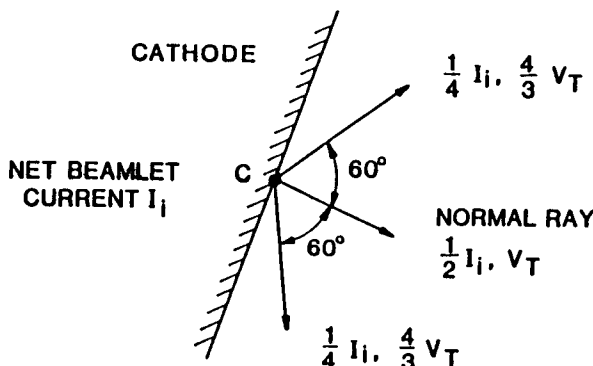


Figure 36. Thermal beam model in which a triplet of rays is launched from the emission site, C. Reproduced with permission from Ref. [11], © 1987 IEEE.

In this definition, σ is the standard deviation of the normalized transverse velocity distribution of the beam which, in gun codes, can be calculated from

$$\sigma = \left[\frac{1}{I_0} \sum_{i=1}^n I_i (\alpha_i - \bar{\alpha})^2 \right]^{1/2}, \quad (11)$$

where, at a given plane, I_0 is the total current crossing the plane, I_i equals beamlet current, α_i equals the beamlet slope, and the weighted mean beam slope is

$$\bar{\alpha} = \frac{1}{I_0} \sum_{i=1}^n I_i \alpha_i. \quad (12)$$

Tunnel emittance differs from standard definitions of emittance [40] in its neglect of second moments and its normalization with respect to tunnel radius a . It is most meaningful when $\bar{\alpha}$ is small which is typically the case. The relationship between standard emittance used in the high-energy physics community and ϵ_T is discussed in Reference [11].

In gridded guns, it has been found by numerical and experimental means that σ is roughly proportional to θ . In Reference [9], σ/θ was reported to be 0.0015. The meaning of this, in general, is that higher half-angle guns have a higher transverse velocity content (are hotter).

The operating permeance in gridded guns can be adjusted by changing the value of the grid voltage; however, there is a best permeance for any given geometrical design. Figure 37 shows a plot of r_{95}/a versus ϵ_T as a function of grid voltage and anode spacing, d , for a 34° intercepting gridded gun. Note that the incremental change in d is not uniform in the plot, and a cold beam model was used in the simulation. Such curves have been called hairpin curves [9]. As grid voltage is lowered, permeance decreases and the beam becomes smaller until a minimum ϵ_T point is reached at the vertex of the curve. This is the best operating point for the gun. As the voltage is lowered further, permeance continues to decrease; however, r_{95}/a levels off (sometimes r_{95}/a actually increases as voltage is lowered). In the upper branch of the hairpin, the grid voltage is higher than that which provides laminar beam flow through the grid cells. This tends to scatter electrons outward, thus dilating the beam. In the horizontal branch of the hairpin curve, the grid voltage is below optimum which overfocuses electrons through the grid cell, leading to a substantially higher value of σ and, of consequence, ϵ_T .

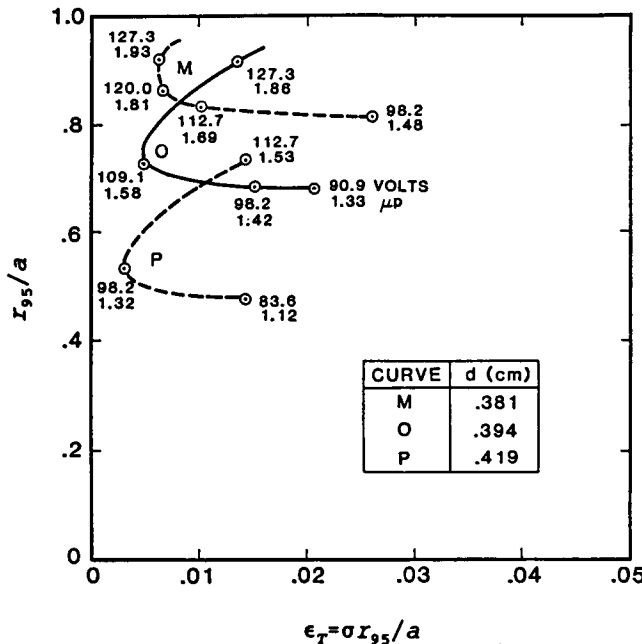


Figure 37. Hairpin curves for a Litton M592 medical accelerator gun, summarizing the effect of cathode-to-anode spacing on performance. Reproduced with permission from Ref. [13], © 1985 IEEE.

Voltage Standoff

Electric field gradients off the electrode surfaces must be low enough or high-voltage breakdown will occur in the gun. An empirical relationship relating maximum operating voltage to minimum interelectrode spacing, L , has been developed by Staprans [62]:

$$V = kL^{0.8}. \quad (13)$$

This relationship pertains to gaps up to about 3 cm. This equation is based upon the assumption that field enhancement above V/L lies in the range 1.3 to 1.7 (average, 1.5). In well-designed Pierce guns, field enhancement is closer to the 1.3 value. In Equation (13), factor k is pulse length dependent and in MKS units is approximately equal to

$$k = 9 \times 10^6 \dots 6 \times 10^6 \dots 4 \times 10^6 \dots 3 \times 10^6 \quad (14)$$

for 1-, 5-, and 100- μ s pulses and DC operation, respectively. Ceramic insulator lengths are typically chosen to be at least 10 times L from

Equation (13). Equation (13) is qualitatively similar to the criterion proposed by Kilpatrick, discussed in Reference [6].

Typically, arcs originate from negative electrodes (such as from the focus electrode in a Pierce gun); thus care must be taken to round and polish such electrode surfaces. Further, it is necessary to include inner and outer corona rings in high-voltage guns to shield triple junctions (metal-to-metalization-to-ceramic) to prevent breakdown along the ceramic insulator. Corona rings should be arranged so that the inner-to-inner distance is less than the inner-to-outer distance between opposing voltage poles to avoid ceramic puncture.

6. Beam Focusing

Magnetic Focusing Basics

The magnetic field required to focus an idealized beam (uniform current density and zero temperature) from a shielded gun (zero magnetic flux at the cathode) is the so-called Brillouin field level [3]. This is given approximately by

$$B_b = 26.2\sqrt{P_\mu \cdot kV} / r_{95}, \quad (15)$$

where B_b is in gauss, kV is V_0 in kilovolts, and r_{95} is in centimeters [9]. A more accurate expression for the Brillouin field uses the axial electronic potential [47]. In typical tubes, the difference in magnetic field between the approximate and the exact expressions amounts to no more than a few percentage points.

Thermal velocity effects and grid scattering (in gridded guns) make the required practical level of the magnetic field significantly higher than the Brillouin field level. It is possible to prescribe the practical rms level of the magnetic field, B^+ , necessary to focus a real electron beam from a shielded gun of normalized transverse velocity, σ , from

$$B^+ = B_b \sqrt{F(1 + 197.6\sigma^2/P_\mu)}, \quad (16)$$

where F is a constant equal to 1.65 [9, 11]. This relationship provides the field at the outer envelope of the beam necessary to hold the nonlaminar beam in equilibrium at that radius. This equation strictly pertains to gaussian beams having a gaussian transverse velocity distribution. It has been found to work for most practical beams, even those having different current density profiles. Further, it provides very accurate results for

beams from gridded guns. Other workers have proposed relationships qualitatively similar to this [63, 64].

It is possible to estimate σ by various means and use Equation (16) to arrive at an initial estimate of the required magnetic focusing field. This technique is used in GUNPPMC during the initial phase of the design (see Figure 22). For example, it was shown that σ in gridded guns is roughly 0.0015θ . If this is combined with Equation (2), then Equation (16) becomes [9]

$$B^+ = B_b \sqrt{1.65(1 + 0.0741r_c/r_{95})}. \quad (17)$$

In gridded guns, the practical magnetic field increase over the Brillouin field is a function of linear beam convergence only. Stated another way, higher convergence guns are hotter and more field needs to be applied to focus them.

In diode guns, it is possible to arrive at an estimate of σ assuming phase space is conserved during beam compression:

$$\sigma = (r_c/r_{95})(kT/2eV_0)^{1/2}. \quad (18)$$

Using finite temperature beam models in gun codes enables σ to be determined more accurately, leading to an improved determination of the required magnetic field from Equation (16).

The equation for the Brillouin field, Equation (15), forms a convenient basis for magnetic field scaling. That is, the required applied magnetic field scales by the square root of perveance and voltage and inversely with beam size. For example, if all gun dimensions are scaled up equally in a diode or gridded gun, σ will remain essentially constant if cathode temperature is unchanged, and required B^+ will decrease by $1/r_{95}$.

Periodic Permanent Magnet Focusing

There are various means of focusing electron beams through the drift tube of a linear beam microwave tube. One popular method is periodic permanent magnet (PPM) focusing which is summarized in Figure 38. This type of focusing scheme is considerably smaller and lighter than a uniform field permanent magnet system capable of focusing an equivalent beam [65]. Further, permanent magnet focusing does not consume any power (in contrast to an electromagnet). This type of focusing is often used in helix and coupled cavity TWTs (CCTWTS).

In a PPM focusing system, the strength of the magnetic focusing field (rms at the beam envelope) should be equal to B^+ . In PPM focused pulsed tubes, r_{95}/a at the waist is often 0.6–0.65 which also forms the basis of the

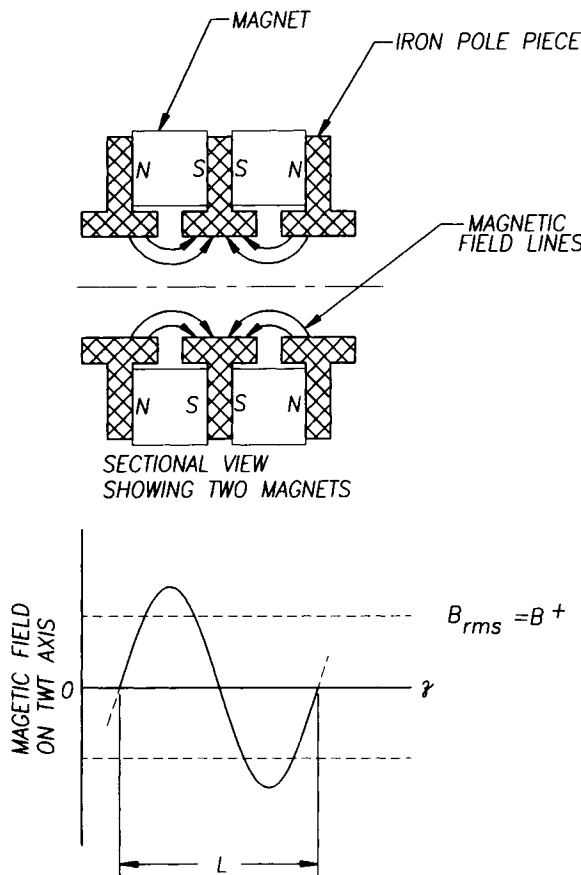


Figure 38. Single-period PPM focusing structure.

magnetic field computation. In the case of cw tubes, r_{95}/a is typically in the range 0.45–0.5.

In addition, an additional criterion for periodic length must be satisfied to achieve adequate beam stability. This can be expressed in terms of a beam stiffness factor, λ_p/L , defined as

$$\lambda_p/L = 36.1r_{95}/\sqrt{P_\mu}L. \quad (19)$$

Practical limits on λ_p/L have been developed and are discussed in References [9] and [11]. For pulsed tubes, it is good practice for λ_p/L to

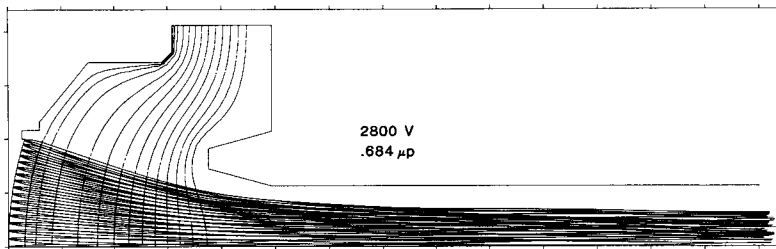


Figure 39. Diode gun of Figure 35 with a PPM focused beam. Reproduced with permission from Ref. [11], © 1987 IEEE.

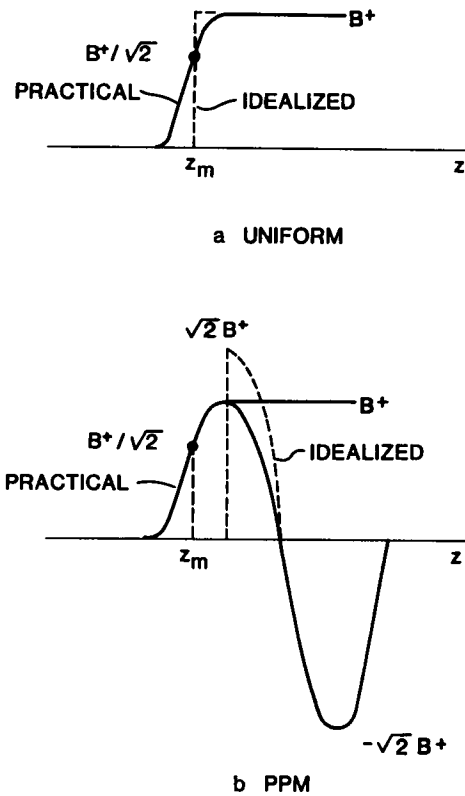


Figure 40. Placement of the beam waist with respect to the entrance magnetic field. (a) Uniform; (b) PPM. Reproduced with permission from Ref. [11], © 1987 IEEE.

exceed 2.7, and in cw tubes λ_p/L should exceed 3.2. In general, the higher λ_p/L is, the better.

Figure 39 presents the gun in Figure 35 with an applied magnetic focusing field determined from Equations (15) and (16). Note that in Figure 35 the value of σ is 0.0151 since V_0 is higher than that of Figure 39. The magnetic entrance is summarized in Figure 40 [11]. The z -value of the beam waist, z_m , is taken as the point of minimum ϵ_T , before (or equal to) the point at which $\bar{\alpha} = 0^\circ$ and before (or equal to) the point at which r_{95} has reached its minimum.

Double period (DPPM) focusing is often used in coupled cavity TWTs to reduce transverse magnetic fields introduced by the kidney slots of the RF structure [6, 66]. Presented in Figure 41 is a simulation of a shadow gridded gun and beam focused by the axial double period field shown in Figure 42 [67]. In DPPM focusing systems, the convention for periodic length, L , is one-half of the full double period (two field peaks).

In a single-period focusing system, the rms magnetic field level increases away from the axis as the modified Bessel function [42]. The variation is similar in DPPM systems as well [68]. Code FVR (field versus radius) computes the rms level of the field off axis (plus other quantities) from the Fourier-Bessel expansion of B_z on axis for DPPM (and

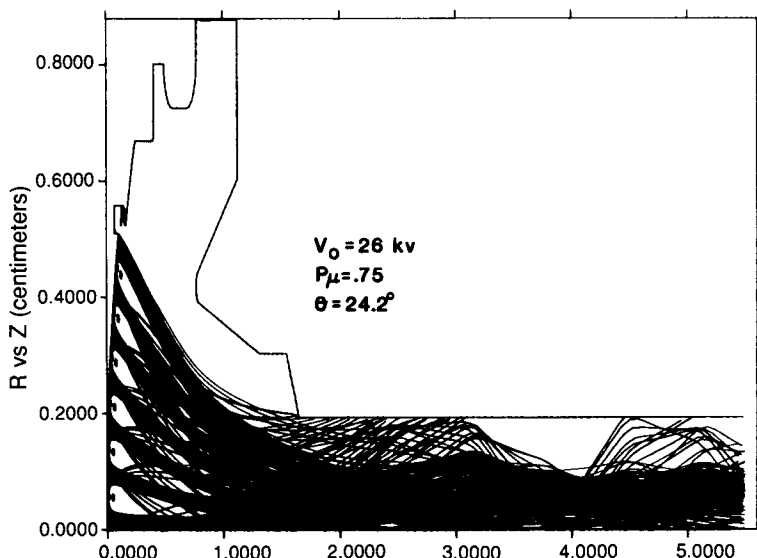


Figure 41. Simulation of L5637 gun used in an emittance growth study (thermal beam model). Beam focused by the DPPM field of Figure 42 (through five peaks). Reproduced with permission from Ref. [58], © 1989 AIP.

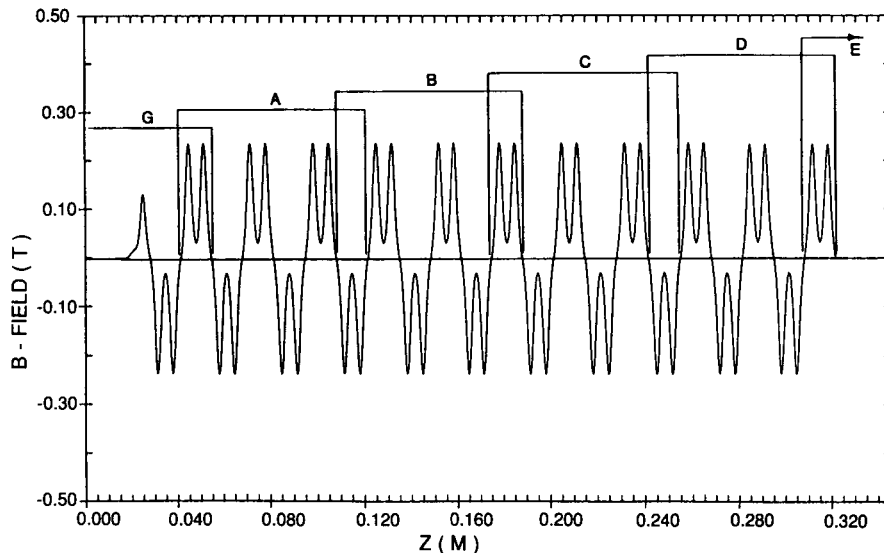


Figure 42. Number of magnetic periods in each overlapping frame of the gun and continuation runs. Reproduced with permission from Ref. [67].

single-period) focusing systems. The increase from axis to envelope in DPPM focusing systems is usually less than roughly 10–15% (single-period focused helix TWTs lie below the bottom of this range). Strictly, the rms field level from FVR at the beam envelope should match that from Equations (15) and (16) in a properly designed focusing system. If Equations (15) and (16) are used for the axial field, on the other hand, the value calculated will be conservative. The example of Figures 41–45 uses the correct envelope field.

Solution Splicing and Emittance Growth

In tracking PPM focused beams over long lengths, it is necessary to break the problem up into a series of overlapping frames as shown in Figures 42 and 43 [67]. This is done to avoid instabilities in gun codes which employ the self-consistent fields procedure. It is possible to improve solution stability by using S -matrix averaging, that is, $S = 0.5(S + S^\circ)$, where \circ denotes the S -matrix from the last iteration of the self-consistent fields loop, and S the current value. This technique helps to extend the length over which stable solutions are possible; however, it does not absolutely guarantee prevention of the long-beam instability.

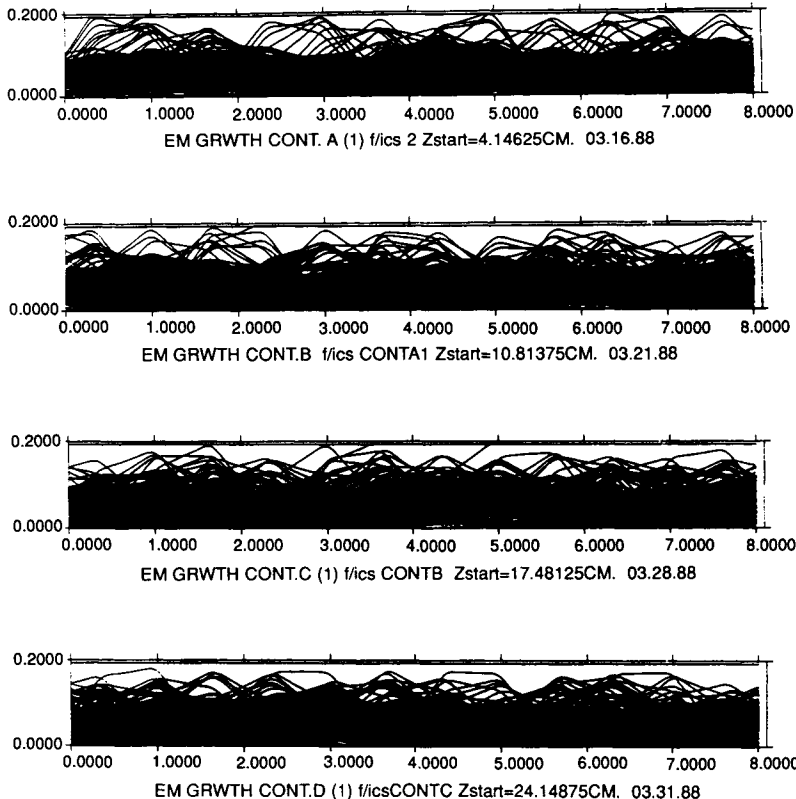


Figure 43. Simulation down to the end of the tube. (Note that the beginning of window E corresponds to $z = 30.8$ cm and circuit length-to-radius = 147.2; 43 cells of the magnetic field to this point.) Reproduced with permission from Ref. [67].

The conventional procedure of splicing solutions is to end the tunnel at the right with a Neumann boundary and then inject the exit beam into the next frame at a left-hand N -boundary. This technique is convenient and generally accurate enough for most simulations. On the other hand, the technique of Figures 42 and 43 has been shown to be necessary for more advanced emittance growth studies [67]. In the technique of Figures 42 and 43, beam data are saved at a plane back from the right-hand N -boundary. Mesh and voltage data are also saved at this plane. The left-hand side of the continuation frame is then set up so that the mesh and fixed boundary potentials exactly replicate those at the last beam exit plane. The beam is then relaunched at the left-hand side of the continuation frame in the conventional fashion.

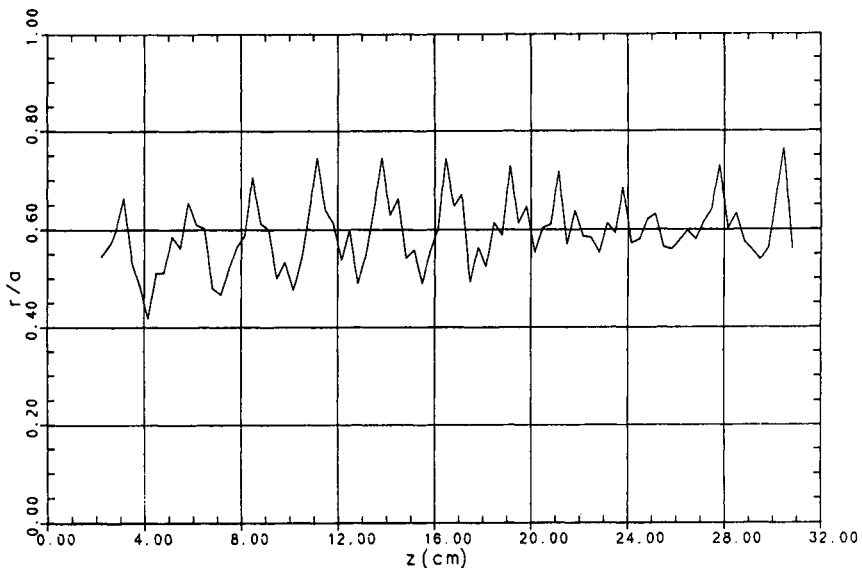


Figure 44. Beam filling factor versus axial distance using the overlapping frame method over the full length of the tube. Reproduced with permission from Ref. [58], © 1989 AIP.

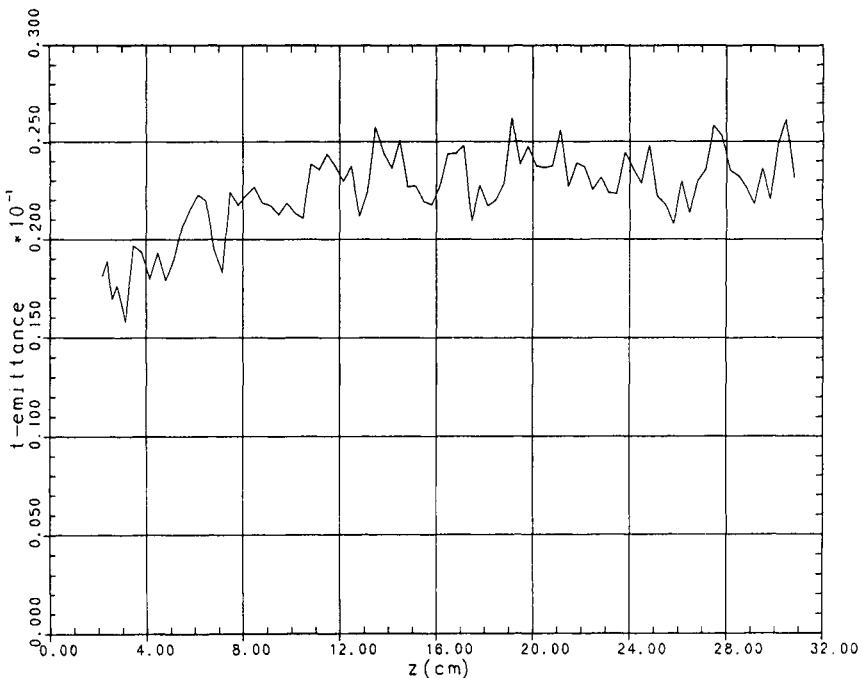


Figure 45. Tunnel emittance versus axial distance using the overlapping frame method. Reproduced with permission from Ref. [58], © 1989 AIP.

In PPM focusing systems, the beam tends to randomize with distance, causing emittance to grow [11, 67]. Figures 44 and 45 are plots of r_{95}/a and ϵ_T versus z , respectively, over the full tube length. In Figure 44, it can be seen that average r_{95}/a is initially somewhat lower than the final value on the right. Growth in ϵ_T is more pronounced due to the fact that both σ and r_{95}/a are increasing as can be seen in Figure 45. Generally, after roughly the first two to three λ_p 's, the initial growth phase ceases, and ϵ_T increases more slowly thereafter.

One of the most important objectives in gun and beam optical design is minimization of ϵ_T since beam transmission is directly related to it [9]. All of the means presented so far in this chapter must be invoked to produce a low-emittance design. Figure 46 shows a plot of beam transmission versus ϵ_T for a group of PPM focused TWTs. This plot can be understood qualitatively from the definition of ϵ_T . That is, as r_{95}/a increases, the beam becomes too large to make it through the tunnel, or,

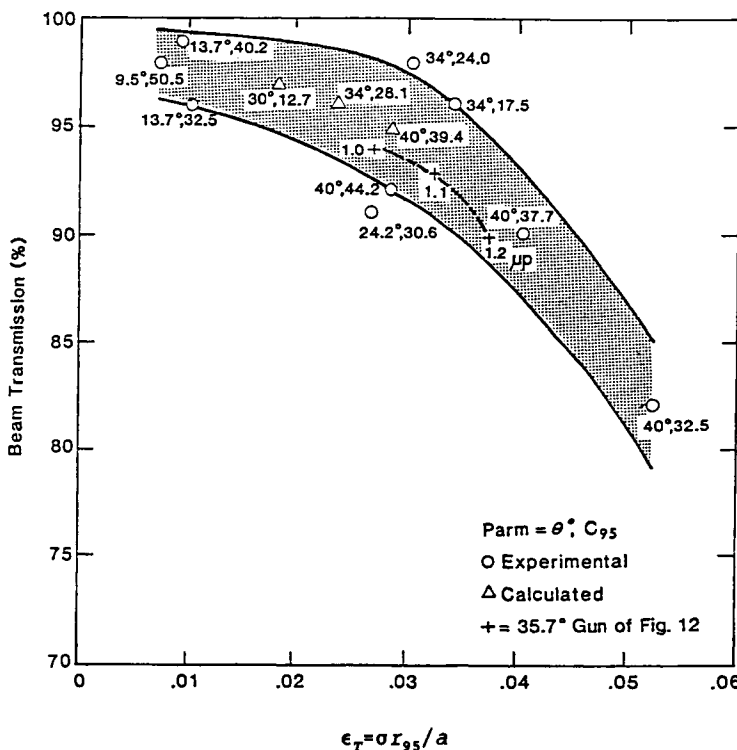


Figure 46. Beam transmission versus tunnel emittance. Reproduced with permission from Ref. [9], © 1984 IEEE.

as σ increases, the beam becomes too hot to be well focused (the width of the transverse velocity distribution expands).

Uniform Field Focusing

Uniform field or solenoidal focusing is another method of beam focusing which is often used in high-average-power TWTs and klystrons. In this case, the main axial magnetic field is uniform (or adiabatically tapered), produced by the arrangements shown schematically in Figure 47. The upper figure shows an electromagnet (solenoid), and the lower shows a permanent magnet structure (used on certain lower power klystrons). Flux usually threads the cathode in this type of focusing, as shown in Figure 48. References on the subject include References [2, 5, 6, 10, 58] plus others listed below.

There are three basic types of uniform field focusing, namely, Brillouin, space-charge balanced flow, and confined flow. In Brillouin

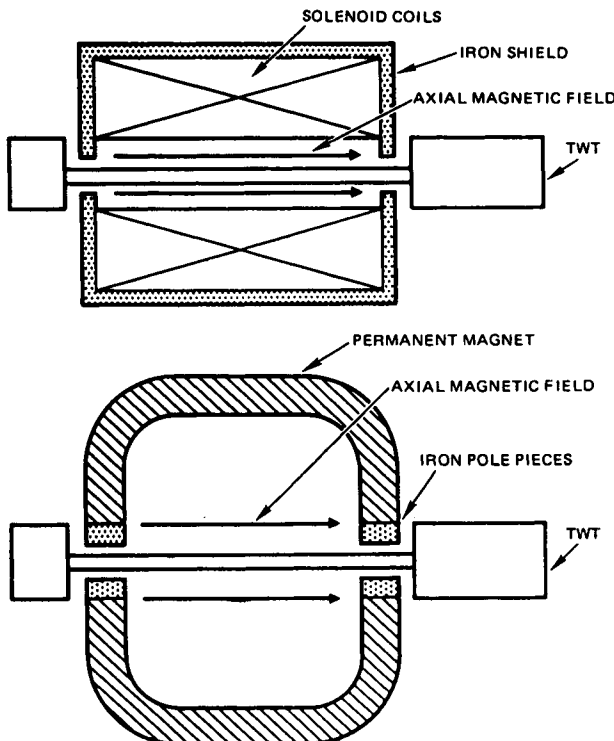


Figure 47. Solenoid and permanent magnet focusing structures (Hansen et al., 1982). Reproduced with permission from Ref. [7].

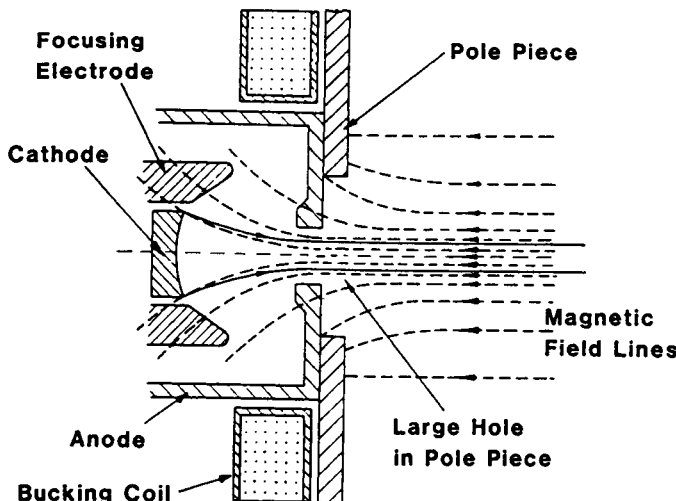


Figure 48. Magnetic circuit configuration for launching smooth flow at field levels above the Brillouin value (Gittins, 1964). Reproduced with permission from Ref. [2], © 1964 Elsevier.

focusing there is zero flux at the cathode. In this case (as in PPM focusing), the main magnetic field is computed from Equations (15) and (16), noting that here the uniform field level is equal to the rms level. Placement of the beam waist with respect to the entrance magnetic field is summarized in Figure 40a. Brillouin focusing is rarely used in high-power tubes due to its generally inferior beam stability in comparison with space-charge balanced or confined flow.

In the second type of focusing, space-charge balanced flow, the cathode is partially immersed and the level of field is less than, say, 1.8 times Brillouin. This method of focusing has been used in certain high-power CCTWTs and klystrons when solenoid power is limited [58]. Beam stiffness in this case is not as good as confined flow; however, it is better than that of Brillouin focusing.

The third type of uniform field focusing is confined flow. In this type of focusing, the main field is typically 2–2.5 times that of Brillouin focusing, and the cathode is heavily immersed. Confined flow focusing provides excellent beam transmission and a very stiffly focused beam which is quite resistant to RF defocusing. It is the preferable method of beam focusing in high-power solenoid focused tubes. Confined flow will constitute the remainder of this subsection.

In the case of high-power klystrons, an r_{95}/a equal to 0.7 is often chosen as a design starting point (assuming that the klystron has a diode gun). Note that this is larger than that used in PPM focused TWTs or that

used with gridded guns. Next, B_b can be computed from Equation (15). After this, the level of immersion can be computed using the ratio of the main field, B , to B_b . Letting $m = B/B_b$, flux at the cathode edge, ψ_c , can be determined from flux in the beam, ψ_0 , as follows,

$$\psi_c = \psi_0 \sqrt{1 - \frac{1}{m^2}}, \quad (20)$$

where, in axisymmetric systems, magnetic flux is equal to

$$\psi = \int \mathbf{B} \cdot d\mathbf{A} = \int_0^r B_z(r) 2\pi r dr. \quad (21)$$

If $m = 2$, flux at the cathode edge from Equation (20) is $0.866\psi_0$. In many tubes, this value is adjusted to reduce the average radius of the focused beam to that desired (since electrons scallop outward in the case of immersed flow [5]). Typically, the reduction of cathode immersion is not more than about 0.9 that computed from Equation (20). In real tubes, bucking coils are usually included on the gun side of the solenoid which can be used to adjust cathode flux (see Figure 48).

Various computer codes are involved in the design of confined flow focusing systems. To start, one can use MMBC (Moster–Molnar B -field code) to determine the basic geometry and location of the input pole piece [69]. MMBC computes axial magnetic field versus distance given the strength of the main magnetic field, the pole piece opening, and the location of the back of the pole piece (the side facing the coils). Note that the magnitude of the magnetic field at the back of the pole piece is approximately 0.5 times the main field level.

MMBC also calculates the field off axis from a second-order power series expansion given a set of (z, r) coordinates specified by the user [70]. Flux at the cathode edge can be computed from code FLUX which evaluates Equation (21) using values from MMBC. FLUX can also be used to conveniently compute the flux in the beam, from which the ratio ψ_c/ψ_0 can be determined for comparison with the objective flux ratio deduced from Equation (20).

In addition to choosing the correct degree of cathode immersion, it is standard practice to match the angle of the flux line passing through the edge of the cathode (available from MMBC) with the beam discharge angle (assumed to be equal to θ) and to match the beam waist according to Figure 40a. If one cannot achieve a perfect match among all three, it is often acceptable to match cathode immersion and the position of the beam waist with respect to the magnetic field and to compromise the angle of the flux line.

Another design method is to represent the field by a set of coils and compute the magnetic field from elliptic integrals [71]. Such a set of coils

can be found by the method in Reference [72]. The option for coils exists in EGUN. This option may possibly be installed in DEMEOS in the future.

The next step of the design process is creation of a practical solenoid design using code POISSON. Often the geometry (that is, the size of the aperture) and the location of the pole piece from MMBC are used in the first cut. SOLENOID, a solenoid design code written from first principles by Laycock, can be used to develop a set of practical field coils, the pole piece, and the return path for further analysis with POISSON. It provides flux density levels in the pole piece and return path, solenoid weight, voltage, current, turns, and power, given as inputs the magnetic field level, size, packing density, number of packs, materials, and tape thickness. After this, the design is typically adjusted to achieve an approximate match between the axial field from POISSON and that from MMBC.

Both EGUN and a version of DEMEOS can import values from POISSON for an improved representation of the magnetic field and hence improved accuracy. Such simulations provide an accurate picture of the beam focused by the practical magnetic field and are helpful in achievement of a solenoid design which provides a smooth well-focused beam. In the design refinement phase, it is often helpful to lay transparencies of flux plots from POISSON over gun simulation plots.

It has been found for typical confined flow focusing systems that axial field values from MMBC imported into DEMEOS provide results which are close to those produced using field data imported from POISSON (assuming that the axial field is similar). This is due to the fact that, in DEMEOS, only terms up to the second order are used in the off-axis expansion of the magnetic field and azimuthal magnetic vector potential A_θ [11]. This simplification provides an important option to the designer.

As a final point, it is possible to increase the magnetic field level adiabatically toward the tube output in order to counteract beam blowup due to beam bunching from the RF interaction process. The increase in output magnetic field can be as high as 1.5 times the main field in confined flow focused klystrons. This technique can also be used in PPM focused TWTs. In such tubes, however, the increase usually does not exceed 15% because the main magnetic field is usually close to (or at) its maximum level already. Further information on adiabatic tapers can be found in Reference [4].

Other Types

Another type of focusing scheme combines confined flow (actually space-charge balanced flow) with PPM (or DPPM). It has been applied to a dual-mode TWT having a solid beam in the high mode and a hollow beam

in the low mode [73]. This was done to equalize the tube gain between the two modes. Confined flow DPPM has been applied to high-power coupled cavity TWTs in order to reduce the level of beam blowup in the output section of the tube [70].

Two other focusing schemes are field reversal focusing and long-period focusing [74]. These basic types combine uniform field focusing with PPM (in the sense that the magnetic field periodically changes sign). In these generic types of focusing the slope and shape of the reversal are critical (see Figure 17). Field reversal focusing has been used in lower power klystrons in order to reduce the magnet size and weight over those of a single permanent magnet (see Figure 47).

Long-period focusing of TWTs has been under investigation for use in millimeter-wave tubes (for which the periodic length cannot be made short enough to satisfy the limit on λ_p/L for good focusing) and for use as a means to reduce cost in standard TWTs [75]. Beam stability is an important issue in long-period focusing schemes.

7. Electron Beam Collection

Single-Stage Collectors

Presented in Figure 49 is a simulation of a confined flow focused beam entering a single-stage depressed collector of a high-power CCTWT [58]. In the simulation, the magnetic field drops toward zero beyond the output pole piece, allowing the beam to expand due to space charge. In confined flow focused tubes, there is an additional dispersal force when the beam crosses flux lines upon exit from the magnetic field. The collector shown in Figure 49 is a so-called Faraday cage collector. In this type of collector, the collector mouth is small in comparison with the size of the collector bucket, causing primary and secondary electrons to be effectively trapped.

The simulation was performed using DEMEOS which allowed modeling of the electron source (a shadow gridded gun), the transport region,

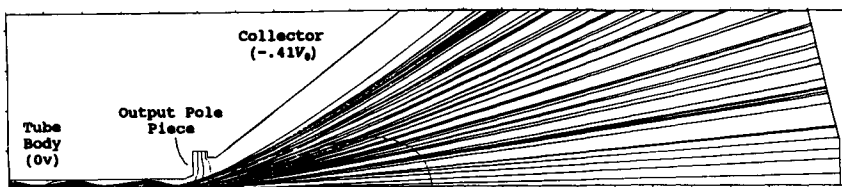


Figure 49. Downstream view of end-to-end simulation (shadow gridded gun-to-collector) of a confined flow focused beam. Reproduced with permission from Ref. [58], © 1989 AIP.

and beam optics within the collector, all in one run. Beam stiffness is high enough in certain confined flow focusing systems for such calculations to converge (in contrast to PPM systems). Confined flow focusing tends to limit emittance growth which is another manifestation of high-beam stiffness [58].

Beam spreading within the collector reduces beam power density at the walls of the collector to a manageable level. In Figure 49, the voltage of the collector is depressed $0.41V_0$ below the ground. This tends to slow the electron beam of energy, approximately V_0 , to an energy of $(1 - 0.41)V_0 = 0.59V_0$ which reduces the thermal power which must be dissipated within the collector. Note that, as the collector voltage is reduced from the ground to its operational level of depression (here, $-0.41V_0$), the beam spreads out more rapidly within the collector due to the higher effective level of space charge [58].

In typical collectors, it is good practice to limit power dissipated on the walls to, say, 1000 W/cm^2 . Collectors which can handle power densities up to roughly 2000 W/cm^2 have been built, however, with great difficulty. The rear of the collector shown in Figure 49 has a relatively flat back end. Sometimes single-stage collectors include a conical taper at the rear to better equalize the thermal power load in this region.

Certain klystrons have collectors which are mounted directly to the body of the tube (undepressible collectors). Advantages include mechanical strength and simplicity plus freedom from RF leakage. Disadvantages include the fact that they cannot be depressed to save power or drain ions, and beam current transported to the collector cannot be directly measured. Current to depressible (isolated) collectors can be conveniently measured which allows adjustment of the magnetic focusing field for optimum beam transmission. This represents an important advantage; hence, a large fraction of microwave tubes include isolated collectors (either a single or a multistage depressed collector).

Spent Beam Models

The simulation of Figure 49 includes an accurate dc model of the beam. This subsection describes finite emittance RF spent beam models for collector (or refocusing section plus collector) simulations. By spent beams we mean beams at the exit of the RF interaction region of the tube.

Presented in Figure 50 is a time sequence simulation of a klystron beam in the RF interaction region from PIC code MASK [50] which illustrates beam bunching due to the RF interaction process [16]. The gun end is at the left and the collector is at the right in the simulation, and the axial scale is compressed. The beam acquires a substantial spread in axial

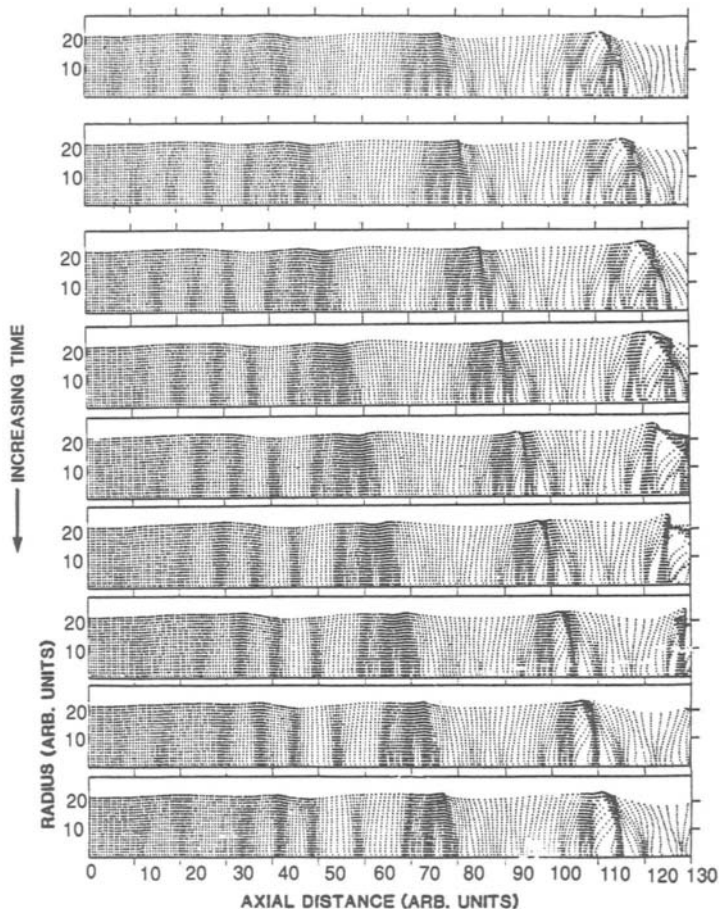


Figure 50. Time sequence simulation of a klystron beam in the RF interaction region from PIC code MASK (see text). Reproduced with permission from Ref. [16], © 1983 IEEE.

energy due to the RF interaction process, as well as a spread in transverse velocity.

Figure 51 shows an example of the energy spread in the beam from a helix TWT operating at the point of maximum RF output power (at saturation). This plot was produced by TRUE103 using data from large-signal code LSC. In Figure 51, at low energy, all of the electrons in the spent beam have energy greater than the voltage of the collector, and all can enter it ($I_J/I_C = 1$, where total spent beam current equals I_C). As the collector voltage is depressed, a point is reached ($V_J/V_0 = 0.38$), beyond

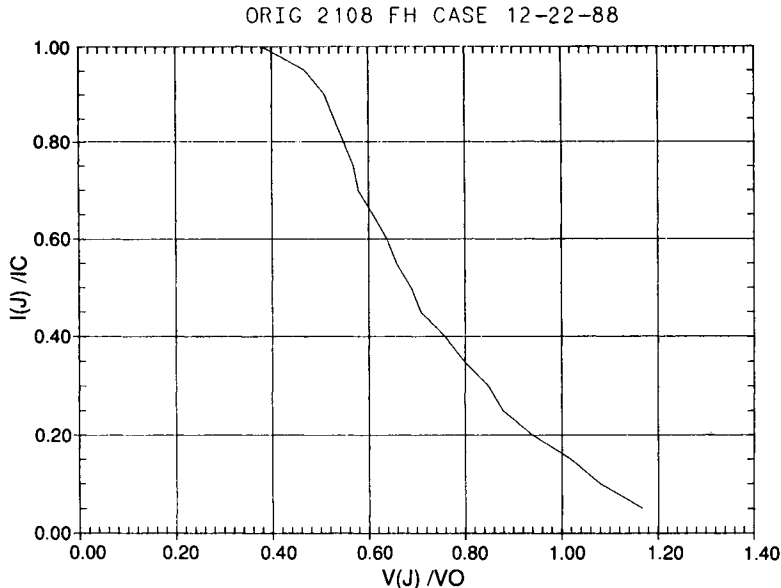


Figure 51. Energy spread in a spent beam of a helix TWT.

which fewer and fewer electrons in the beam have sufficient energy (V_J) to make it into the collector. A certain fraction of the electrons in the beam acquire energy actually greater than V_0 due to the RF interaction process ($V_J/V_0 > 1$).

Various other large-signal codes can be used to obtain the energy spread in the spent beam, including PIC codes and various ring model codes [76–78]. These codes can provide a realistic distribution of exit angles in the spent beam, especially if a finite emittance model of the beam from the gun is used as input. Small codes exist to convert exit beam particle energy and positional information over an RF wavelength into energy and angular distributions at a plane for use in gun codes.

It is possible to use PIC codes to model both the RF interaction process and the collector at once [79, 80]. Wilson has prepared an animated graphical presentation which runs on a PC illustrating particle motion within a single- and a dual-stage depressed collector [80]. Work is in progress to model the gun, beam optical system, RF interaction, and collector all at once [81, 82].

For design purposes, it has been found that one can readily set up a reasonable beam model for collector simulations using results from disk model codes, such as LSC, and the value of ϵ_T at the beam exit plane [11].

Assuming that the beam is launched from a plane on which the voltage and magnetic field are zero for convenience, the beamlet slope can be computed from

$$\alpha_i = \tan^{-1} \left(\sqrt{2} \sigma \sqrt{V_0/V_i} [-\ln(1 - I/I_c)]^{1/2} \right), \quad (22)$$

where I is enclosed current.

Table 1 summarizes a 60-ray finite emittance scrambled beam model based on Equation (22) and set up by TRUE103 for DEMEOS. Additional inputs to TRUE103 to prepare the data file include z , r_{95} , the beam type (uniform or gaussian-like), the number of rays (20, 40, or 60, where 60 is the default value), and spent beam σ from ϵ_T of the dc beam. The radius of the RF beam, r_{95} , is typically taken to be $\frac{4}{3}$ that of the dc beam. This modeling procedure is explained more fully in Reference [11]. The data from DEMEOS simulations using this model agree very well with measured spent beam data [83, 84]. This model with DEMEOS has been used to design dozens of successful MDCs.

Multistage Depressed Collectors

Presented in Figure 52 is a DEMEOS simulation of an MDC using a 60-ray uniform current density beam model. The actual computer plot is in color to distinguish $\frac{1}{2}$ from $\frac{1}{4}$ current rays (see Figure 36) and equipotentials. In a depressed collector, electrons are sorted according to energy class. The lowest energy electrons have only enough energy to make it to the first stage. In this particular collector, a larger fraction of higher voltage electrons make it to the second stage.

This collector includes a dispersing spike or probe at the cathode potential. This probe creates negative fields within the second bucket which prevent secondary emission of electrons. The probe is not always present in all collectors especially those designed for low cost. Collectors which are symmetric about an axis of symmetry are typically used in microwave tubes, and their design and performance are covered in greater depth in References [86–88]. Another generic type of collector is nonaxisymmetric [89, 90]. Such collectors have found limited use in CCTWTs.

Refocusing sections are sometimes included before the entrance of MDCs to cool the spent beam by a controlled adiabatic expansion [85]. Typically the beam is allowed to expand, and then it is refocused by one or more magnetic lenses. The basic idea assumes conservation of phase space or $\epsilon_{T_1} \sim \epsilon_{T_2}$, where 1 refers to the entrance of the refocusing section and 2 to the exit. From the definition of tunnel emittance ($\epsilon_T = \sigma r_{95}/a$), if

TABLE I
Spent Beam Model Set Up by TRUE103

Z (M)	R (M)	Amperes	Volts	Angle (°)
0.000001	0.00018573	0.017200	7488.0000	0.000000
0.000001	0.00032269	0.017200	5440.0000	0.000000
0.000001	0.00041837	0.017200	4224.0000	0.000000
0.000001	0.00049716	0.017200	3520.0000	0.000000
0.000001	0.00056658	0.017200	6912.0000	0.000000
0.000001	0.00063037	0.017200	5120.0000	0.000000
0.000001	0.00069228	0.017200	4096.0000	0.000000
0.000001	0.00075044	0.017200	3392.0000	0.000000
0.000001	0.00080860	0.017200	6528.0000	0.000000
0.000001	0.00086675	0.017200	4864.0000	0.000000
0.000001	0.00092491	0.017200	3904.0000	0.000000
0.000001	0.00098307	0.017200	3264.0000	0.000000
0.000001	0.00104498	0.017200	6016.0000	0.000000
0.000001	0.00111065	0.017200	4544.0000	0.000000
0.000001	0.00118194	0.017200	3712.0000	0.000000
0.000001	0.00126073	0.017200	3008.0000	0.000000
0.000001	0.00135829	0.017200	5632.0000	0.000000
0.000001	0.00147086	0.017200	4416.0000	0.000000
0.000001	0.00158717	0.017200	3648.0000	0.000000
0.000001	0.00170537	0.017200	2432.0000	0.000000
0.000001	0.00018573	0.008600	7488.0000	1.086870
0.000001	0.00018573	0.008600	7488.0000	-1.086870
0.000001	0.00032269	0.008600	3392.0000	5.083340
0.000001	0.00032269	0.008600	3392.0000	-5.083340
0.000001	0.00041837	0.008600	3712.0000	7.974240
0.000001	0.00041837	0.008600	3712.0000	-7.974240
0.000001	0.00049716	0.008600	5440.0000	1.827150
0.000001	0.00049716	0.008600	5440.0000	-1.827150
0.000001	0.00056658	0.008600	6528.0000	3.968150
0.000001	0.00056658	0.008600	6528.0000	-3.968150
0.000001	0.00063037	0.008600	3008.0000	9.518300
0.000001	0.00063037	0.008600	3008.0000	-9.518300
0.000001	0.00069228	0.008600	4224.0000	2.574420
0.000001	0.00069228	0.008600	4224.0000	-2.574420
0.000001	0.00075044	0.008600	4864.0000	4.945590
0.000001	0.00075044	0.008600	4864.0000	-4.945590
0.000001	0.00080860	0.008600	5632.0000	7.578020
0.000001	0.00080860	0.008600	5632.0000	-7.578020
0.000001	0.00086675	0.008600	3520.0000	3.303100
0.000001	0.00086675	0.008600	3520.0000	-3.303100
0.000001	0.00092491	0.008600	3904.0000	5.918590
0.000001	0.00092491	0.008600	3904.0000	-5.918590
0.000001	0.00098307	0.008600	4416.0000	9.398440
0.000001	0.00098307	0.008600	4416.0000	-9.398440
0.000001	0.00104498	0.008600	6912.0000	2.677440
0.000001	0.00104498	0.008600	6912.0000	-2.677440
0.000001	0.00111065	0.008600	3264.0000	6.924720
0.000001	0.00111065	0.008600	3264.0000	-6.924720
0.000001	0.00118194	0.008600	3648.0000	11.734800
0.000001	0.00118194	0.008600	3648.0000	-11.734800
0.000001	0.00126073	0.008600	5120.0000	3.462220
0.000001	0.00126073	0.008600	5120.0000	-3.462220
0.000001	0.00135829	0.008600	6016.0000	5.469710
0.000001	0.00135829	0.008600	6016.0000	-5.469710
0.000001	0.00147086	0.008600	2432.0000	14.273700
0.000001	0.00147086	0.008600	2432.0000	-14.273700
0.000001	0.00158717	0.008600	4096.0000	4.251420
0.000001	0.00158717	0.008600	4096.0000	-4.251420
0.000001	0.00170537	0.008600	4544.0000	6.729270
0.000001	0.00170537	0.008600	4544.0000	-6.729270

Note. L2108; $V_0 = 6400$ V; $I_c = 0.688$ A; $\sigma = 0.06407$.

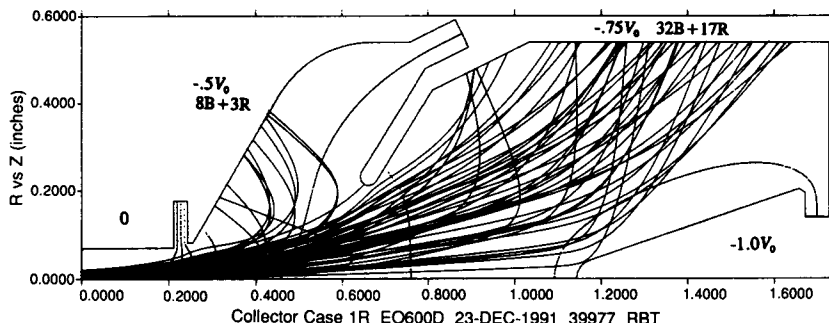


Figure 52. Simulation of a multistage depressed collector. R, red rays; B, blue rays.

$r_{952} > r_{951}$, then $\sigma_2 < \sigma_1$. Refocusing sections are generally not used in tubes in which physical space is limited.

The run of Figure 52 does not include an applied magnetic field. Often, in collector modeling, the spent beam is launched before the final magnetic field peak in a PPM focused tube (two peaks in the case of DPPM focusing). Code PPMFLD can be used to write a data set for DEMEOS for the 0° to 90° portion of the final sine wave, followed by MAGLENS which can be used to generate data from the 90° point to the end of the collector. MAGLENS gives the axial magnetic field distribution of a single magnetic lens [3]. Using a radius in the lens calculation equal to the inner pole piece radius is usually satisfactory. This method creates a realistic profile of the decaying magnetic field at the end of the PPM stack. MAGLENS is also useful in setting up magnetic field data for refocusing section calculations.

Figure 53 shows electrical connections to a typical TWT with a dual-stage depressed collector. The figure can be used to explain how single-stage depressed collectors and MDCs save power. In this case, considering a hypothetical set of voltages and currents (and neglecting heater power), the power supply must furnish $E_k I_w + E_{b_2} I_{b_2} + E_{b_1} I_{b_1} = 3.88$ kW, where $E_k = V_0$ and I_w equals current lost to the tube body (RF structure). From the point of view of the beam, net input power is equal to $10\text{ kV} \times 1a - 5\text{ kV} \times 0.4a - 7.5\text{ kV} \times 0.55a = 3.88$ kW. In the case of an undepressed collector, input power is $E_k I_0 = 10$ kW. Net power saved by the inclusion of an MDC is thus $10 - 3.88 = 6.12$ kW.

If RF output power, P_{rf} , is 1.5 kW, then undepressed efficiency $\eta_0 = P_{rf}/E_k I_0 = 1.5/10 = 0.15$. Depressed efficiency, η_T , on the other hand, is equal to $1.5/3.88 = 0.39$. Efficiency gain due to the MDC is equal to $0.39/0.15 = 2.6$. Efficiency gain is readily determined experimentally in

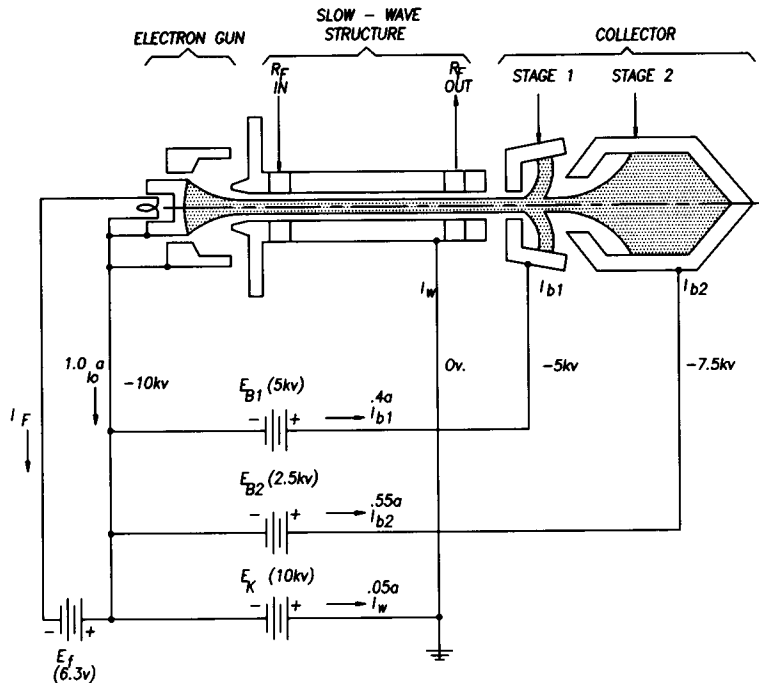


Figure 53. Notation for MDC efficiency calculations.

practical TWTs by comparing depressed efficiency (normal operation) with undepressed efficiency (all stages grounded). Computed and experimental η_T/η_0 data have been assembled for various collector designs and have been plotted as a function of η_0 . In general, for a given number of stages, η_T/η_0 decreases as η_0 increases. The plot provides a useful means of determining the quality of a given collector design.

Secondary Emission and Mechanical Design

It can be seen in the computer plot of Figure 52 that one ray strikes the tip of the second stage. In this collector design, the tip is in a positive field region since the equipotential at $-0.75V_0$ lies to the right. Any secondary electrons which are generated in this region are accelerated toward stage 1 or the body which degrades collection efficiency. It is possible to reshape the electrode contours in many cases or adjust the magnetic field to reduce or eliminate this current.

Collector electrodes are often made from copper because of copper's high thermal conductivity. It is possible to include various surface coatings or condition the collector electrodes to reduce secondary emission [91]. Also, the electrodes themselves can be made from a secondary emission suppressive material such as carbon [92]. Such techniques are mainly used in high-performance collectors such as those in space TWTs, in which overall tube efficiency is critical. A provision has been included in EGUN to launch and follow secondary electrons [93].

Collector electrodes are usually supported on hard fired ceramic insulators such as alumina or beryllia. Because of the high heat loads, careful attention has to be paid to the thermal, electrical, and mechanical design of the plates and insulators. Thermal and mechanical finite element codes are helpful in this regard. Leads from the individual stages to the high-voltage vacuum feed-throughs represent another important area of design.

Typically the spent beam has not completely debunched upon entry into the collector. This can excite collector oscillations. It is possible to employ lossy dielectrics inside or outside the vacuum envelope to damp such oscillations if they occur. Frequently, shielded collector leads include loss to prevent spurious oscillations from being broadcast to the outside world.

8. Gun and Beam Measurement

Experimental measurement techniques are also important in the development of beam optical systems. In the cathode area, cathode quality can be ascertained from Miram plots [94]. Also, techniques are available to determine the work function of cathode surfaces [95]. Life testing of cathodes is ongoing, and much data are available, including theories for the prediction of cathode life [96–99].

Electron beam profiles (current density versus radius) are typically obtained by moving a small pinhole target (current density probe) across the beam. References on beam analyzers and measurement theory include References [5, 11, 55, 100–103]. The motion of the target in modern beam analyzers is typically controlled by a computer, and three-dimensional plots of the electron beam at various axial planes can be produced. Emittance measurements are available from some systems [11]. Further, analyzers can measure the properties of beams within focusing systems. Finally, they can be used to measure the properties of spent beams for collector design and development [83, 84, 104].

Magnetic fields within various magnetic focusing structures can be measured by a computer-controlled movable Hall probe, connected to a gauss meter, interfaced to the computer. Axial, off-axis, and transverse magnetic fields can be measured. Transverse magnetic field measurements are difficult, and usually the focusing structure must be rotated about the axis and a difference method used to obtain accurate readings.

In development of a beam optical system, often the next step is the fabrication of a beam stick to verify the gun and beam optical design. This device includes a gun, magnetic focusing structure, and collector. It typically does not include an RF interaction circuit but merely a dummy beam tunnel. The tunnel should be as long as the interaction structure to properly account for emittance growth. In some cases, the magnetic focusing structure can be moved axially with respect to the gun. Further, the strength of individual magnets can be adjusted on a PPM or DPPM beam stick. Note that it is possible to determine the effective PPM or DPPM focusing field in the sealed beam stick (or tube) by measuring the stop band voltage [68]. Measurements other than DC beam transmission and electrical characteristics of the gun and collector can be made on the beam stick. These include measurement of spurious X-ray emissions from the gun or collector, temperature measurements, and other factors.

9. Summary and Reliability Issues

This chapter has described the means to arrive at reliable beam optical designs in linear beam microwave tubes. The discussion focused upon basic principles and included practical guidelines. Various computer codes and how they interrelate to one another in the design process were discussed. The codes identified represent only a sampling of those which are available.

The microwave tube field possesses highly advanced technology in various areas. Some identified in this chapter include: (1) high-current-density thermionic cathodes; (2) low-emittance diode and gridded guns; (3) focusing of dense space-charge beams; (4) advanced single-stage and multistage depressed collectors; (5) high-voltage techniques; and (6) theoretical and experimental methods.

The proper design of beam optical systems in microwave tubes can favorably affect the tube life and reliability. Modern microwave tubes are made from metal and ceramics and are very tough. They are radiation hard and survive in harsh environments such as space and the military. They have very long lives when properly designed [105]. For example, the transmitter on the intrepid Voyager which visited the outer planets in-

cluded a TWT. This tube functioned flawlessly throughout the duration of the mission (and may be alive and well today).

Most high-performance military aircraft carry TWTs or klystrons, and many advanced guided missiles carry tubes. All of the tubes in these equipments worked admirably during the Desert Storm conflict. Klystrons have been used in airport radars for decades. They provide vision to our aircraft controllers and guide our planes to safety. Finally, microwave tubes power the high-energy accelerators designed to unlock the ultimate secrets of nature, and future systems utilizing tubes will likely be used to help clean up the environment.

Tube reliability is customarily predicted using military handbook MIL-HDBK-217 [106]. This handbook was revised to reflect continuing advances in tube reliability (Notice 1); however, an effort is underway to update it again since even the 1992 version grossly understates actual microwave tube mean-time-between-failure (MTBF) data. This, and tube reliability in general, is discussed in depth by Gilmour [6].

Acknowledgements

In development of this chapter, the author benefited from numerous positive interactions with leaders in the field both at Litton and elsewhere. I thank them for their helpfulness and support. Furthermore, I thank my wife, Sarah, for her patience and encouragement.

References

- [1] J. R. Pierce, *Theory and Design of Electron Beams*. Princeton: Van Nostrand, 1954.
- [2] J. F. Gittins, *Power Travelling-Wave Tubes*. New York: Am. Elsevier, 1964.
- [3] J. W. Gewartowski and H. A. Watson, *Principles of Electron Tubes*. Princeton: Van Nostrand, 1965.
- [4] P. T. Kirstein, G. S. Kino, and W. E. Waters, *Space-Charge Flow*. New York: McGraw-Hill, 1967.
- [5] A. Septier, ed., *Focussing of Charged Particles*, Vols. 1 and 2. New York: Academic Press, 1967.
- [6] A. S. Gilmour, Jr., *Principles of Traveling Wave Tubes*. Norwood, MA: Artech House, 1994.
- [7] J. W. Hansen *et al.*, "System Aspects of Communications TWTA's," Appl. Note, Hughes Aircraft Co., Electron Dynamics Div., Torrance, CA, Aug. 1982.
- [8] J. W. Hansen, US TWTs from 1 to 100 GHz, *Microwave J.*, Suppl., pp. 179–193, Sept. 1989.
- [9] R. True, A theory for coupling gridded gun design with PPM focussing, *IEEE Trans. Electron Devices*, Vol. ED-31, pp. 353–362, Mar. 1984.
- [10] R. True, Beam optics calculations in very high power microwave tubes, *IEDM Tech. Dig.*, pp. 403–406, Dec. 1991.
- [11] R. True, Emittance and the design of beam formation, transport, and collection systems in periodically focussed TWT's, *IEEE Trans. Electron Devices*, Vol. ED-34, pp. 473–485, Feb. 1987.

- [12] R. True, Calculation and design of grids in Pierce guns, *IEDM Tech. Dig.*, pp. 215–218, Dec. 1989.
- [13] R. True, The design of gridded Pierce guns for accelerators, *IEEE Trans. Nucl. Sci.*, Vol. NS-32, pp. 2611–2613, Oct. 1985.
- [14] J. R. Hechtel and B. J. Hamak, A dual mode electron gun having non-intercepting grids, *IEDM Tech. Dig.*, pp. 171–174, Dec. 1973.
- [15] R. True and J. Cooke, An equal emittance dual-mode gun, *IEEE Microwave Power Tube Conf., Monterey, CA, May 1984*.
- [16] R. True, Computers and tubes—Today and tomorrow, *IEDM Tech. Dig.*, pp. 436–439, Dec. 1983.
- [17] R. True, A novel electron source for EBIS machines, *Int. Symp. Electron Beam Ion Sources, AIP Conf. Proc.* No. 188, pp. 259–270, Nov. 1988.
- [18] J. M. Baird and A. C. Attard, “Gyrotron Gun Study Report,” NRL Rep. N000173-79-C-0132, B-K Dynamics, Rockville, MD, Sept. 1981.
- [19] K. K. Chow and R. H. Pantell, The cyclotron resonance backward-wave oscillator, *Proc. IEEE*, Vol. 48, pp. 1865–1867, Nov. 1960.
- [20] G. P. Scheitrum and R. True, A triple-pole-piece magnetic field reversal element for generation of high rotational energy beams, *IEDM Tech. Dig.*, pp. 332–335, Dec. 1981.
- [21] G. P. Scheitrum, R. S. Symons, and R. B. True, Low velocity spread axis encircling electron beam system, *IEDM Tech. Dig.*, pp. 743–746, Dec. 1989.
- [22] J. R. M. Vaughan, A synthesis of the Longo and Eng cathode emission models, *IEEE Trans. Electron Devices*, Vol. ED-33, No. 11, Sept. 1986.
- [23] R. H. Fowler and L. Nordheim, Electron emission in intense electric fields, *Proc. R. Soc. London*, Vol. 119A, pp. 173–181, 1928.
- [24] R. E. Burgess, H. Kroemer, and J. M. Houston, Corrected values of Fowler–Nordheim field emission functions $v(y)$ and $s(y)$, *Phys. Rev.*, Vol. 90, p. 515, May 1953.
- [25] C. A. Spindt *et al.*, Physical properties of thin-film field emission cathodes with molybdenum cones, *J. Appl. Phys.*, Vol. 47, No. 12, Dec. 1976.
- [26] J. R. M. Vaughan, A new formula for secondary emission yield, *IEEE Trans. Electron Devices*, Vol. ED-36, No. 9, Sept. 1989; J. R. M. Vaughan, Secondary emission formulas, *IEEE Trans. Electron Devices*, Vol. ED-40, No. 4, Apr. 1993.
- [27] R. True, An ultra-laminar tetrode gun for high duty cycle applications, *IEDM Tech. Dig.*, pp. 286–289, Dec. 1979.
- [28] J. L. Cronin, Modern dispenser cathodes, *IEE Proc.*, Vol. 128, Part 1, pp. 19–31, Feb. 1981.
- [29] J. L. Cronin, Practical aspects of modern dispenser cathodes, *Microwave J.*, pp. 57–62, Sept. 1979.
- [30] R. E. Thomas *et al.*, Thermionic sources for high-brightness beams, *IEEE Trans. Electron Devices*, Vol. ED-37, pp. 850–861, Mar. 1990.
- [31] G. Herrmann and S. Wagener, *The Oxide-Coated Cathode*, Vols. 1 and 2. London: Chapman & Hall, 1951.
- [32] R. True *et al.*, Design and performance of a three-second-warmup dispenser cathode, *IEEE Microwave Power Tube Conf., Monterey, CA, May 1980*.
- [33] M. J. Cattelino, G. V. Miram, and B. Smith, Fast- and super-fast-warm-up cathodes using novel APG/APBN heaters, *IEEE Trans. Electron Devices*, Vol. ED-38, pp. 2239–2243, Oct. 1991.
- [34] R. K. Cooper *et al.*, “Poisson/Superfish Reference Manual,” Los Alamos Accelerator Code Group (MS H829) LA-UR-87-126, Los Alamos Natl. Lab., Los Alamos, NM, Jan. 1987.

- [35] A. M. Winslow, Numerical solution of the quasilinear Poisson equation in a non-uniform triangle mesh, *J. Comput. Phys.*, Vol. 2, pp. 149–172, 1967.
- [36] R. True, “Space-Charge-Limited Beam Forming Systems Analyzed by the Method of Self-Consistent Fields with Solution of Poisson’s Equation on a Deformable Relaxation Mesh,” Ph.D. Thesis, Univ. of Connecticut, Storrs, 1972.
- [37] R. True, The deformable relaxation mesh technique for solution of electron optics problems, *IEDM Tech. Dig.*, pp. 257–260, Dec. 1975.
- [38] J. R. M. Vaughan, Synthesis of the Pierce gun, *IEEE Trans. Electron Devices*, Vol. ED-28, pp. 37–41, Jan. 1981.
- [39] W. B. Herrmannsfeldt, Electron ray tracing programs for gun design and beam transport, *Workshop Linear Accel. Beam Opt. Codes, AIP Conf. Proc.* No. 177, pp. 45–58, 1988.
- [40] W. B. Herrmannsfeldt, EGUN—An Electron Optics and Gun Design Program, SLAC-331, Stanford Linear Accelerator Center, Stanford, CA, Oct. 1988.
- [41] V. Hamza, Convergence and accuracy criteria of iteration methods for the analysis of axially symmetric and sheet beam electrode shapes with an emitting surface, *IEEE Trans. Electron Devices*, Vol. ED-13, pp. 485–493, May 1966.
- [42] F. Sterzer and W. W. Siekanowicz, The design of periodic permanent magnets for focussing of electron beams, *RCA Rev.*, pp. 39–59, Mar. 1957.
- [43] Y. Hiramatsu, Computer-aided design of helix-type TWT's, *IEDM Tech. Dig.*, pp. 261–262, Dec. 1975.
- [44] J. R. Pierce, *Travelling Wave Tubes*. Princeton: Van Nostrand, 1950.
- [45] J. Reutz, D. Bates, G. Kino, and Y. Hiramatsu, Large signal analysis for “0” type microwave amplifiers, *High-Power Microwave Symp., Fort Monmouth, NJ, May 1965*.
- [46] H. R. Johnson, Backward-wave oscillators, *Proc. IRE*, Vol. 43, pp. 684–697, June 1955.
- [47] K. Amboss, The analysis of dense electron beams, in *Advances in Electronics and Electron Physics* (L. Marton, ed.), Vol. 26, pp. 1–170. New York: Academic Press, 1969.
- [48] M. Caplan and C. Thorington, Improved computer modelling of magnetron injection guns for gyrotrons, *Int. J. Electron.*, Vol. 51, pp. 415–426, 1981.
- [49] C. Thorington, Particle simulation of electron beams with self-consistent magnetic fields, *IEEE Trans. Electron Devices*, Vol. Ed-33, pp. 1883–1889, Nov. 1986.
- [50] H. S. Deaven and K. C. D. Chan, “Computer Codes for Particle Accelerator Design and Analysis: A Compendium,” 2nd Ed., LA-UR-90-1766, Los Alamos Natl. Lab., Los Alamos, NM, May 1990.
- [51] D. M. MacGregor, Three-dimensional analysis of cathode ray tubes for color television, *IEEE Trans. Electron Devices*, Vol. Ed-33, pp. 1098–1106, Aug. 1986.
- [52] N. J. Dionne, H. J. Krahn, and R. Harper, Three dimensional simulation of gridded TWT guns, *IEDM Tech. Dig.*, pp. 479–482, Dec. 1980.
- [53] I. Langmuir and K. B. Blodgett, Currents limited by space-charge between concentric spheres, *Phys. Rev.*, Vol. 24, pp. 49–59, July 1924.
- [54] W. E. Danielson, J. L. Rosenfeld, and J. A. Saloom, A detailed analysis of beam formation with electron guns of the Pierce type, *Bell Syst. Tech. J.*, pp. 375–420, Mar. 1956.
- [55] R. D. Frost, O. T. Purl, and H. R. Johnson, Electron guns for forming solid beams of high perveance and high convergence, *Proc. IRE*, Vol. 50, pp. 1800–1807, Aug. 1962.
- [56] M. Muller, New points of view in the design of electron guns for cylindrical beams of high space charge, *J. Br. IRE*, Vol. 16, pp. 83–94, 1955.
- [57] R. True, “Lecture Notes on Axisymmetric Gun Design,” Stanford Univ. AFTER Program, Stanford, CA, 1979 (unpublished).

- [58] R. True, Advances in *E*-beam formation, focussing and collection, *Int. Symp. Electron Beam Ion Sources, AIP Conf. Proc.* No. 188, pp. 219–232, Nov. 1988.
- [59] R. D. Brooks, “A General Design Method for High Perveance Solid Beam Electron Guns,” Bell Telephone Lab. Memo., Dec. 11, 1964 (unpublished).
- [60] J. R. Hechtel, Zur Bestimmung der Elektrodenformen von Elektronenkanonen nach Pierce, *Telefunken-Ztg.*, Vol. 28, pp. 222–226, Dec. 1955.
- [61] R. True, Gridded gun design and beam focussing using the concept of tunnel emittance, *Microwave Power Tube Conf., Monterey, CA, May 1982*.
- [62] A. Staprans, Electron gun breakdown, *1985 High-Voltage Workshop, Monterey, CA, Feb. 1985*.
- [63] G. Herrmann, Optical theory of thermal velocity effects in cylindrical electron beams, *J. Appl. Phys.*, Vol. 29, pp. 127–136, Feb. 1958.
- [64] J. R. Hechtel, Magnetic focussing of electron beams in the presence of transverse velocity components, *IEEE Trans. Electron Devices*, Vol. Ed-28, pp. 473–482, May 1981.
- [65] J. T. Mendel, C. F. Quate, and W. H. Yokim, Electron beam focussing with periodic permanent magnet fields, *Proc. IRE*, Vol. 42, pp. 800–810, May 1954.
- [66] L. M. Winslow and D. J. Bates, “Periodic Permanent Magnet Electron Beam Focussing Arrangement for Traveling-Wave Tubes Having Plural Interaction Cavities in Bore of Each Annular Magnet,” U. S. Pat. 3,324,339, Feb. 1964.
- [67] R. True and W. B. Reyes, Simulation of long PPM focussed beams in studies of emittance growth, *IEEE Microwave Power Tube Conf., Monterey, CA, May 1988*.
- [68] R. True, The role of the stop band voltage in PPM focussed TWT’s, *IEEE Microwave Power Tube Conf., Monterey, CA, May 1988*.
- [69] C. R. Mosler and J. P. Molnar, “Some Calculations of the Magnetic Field Requirements for Obtaining Brillouin Flow in Cylindrical Electron Beams,” Bell Telephone Lab. Memo., Jan. 16, 1951 (unpublished).
- [70] K. Amboss, “High Power Radar TWT,” U.S. Army Laboratory Command Rep. SL CET-TR-86-0045-1, Hughes Aircraft Co., Torrance, CA, Feb. 1988.
- [71] J. R. M. Vaughan, Representation of axisymmetric magnetic fields in computer programs, *IEEE Trans. Electron Devices*, Vol. ED-19, pp. 144–151, Feb. 1972.
- [72] J. R. M. Vaughan, Methods of finding the parameters of ideal current loops for computer simulation of magnetic fields, *IEEE Trans. Electron Devices*, Vol. ED-21, pp. 310–312, May 1974.
- [73] F. Bjornstad, “Improved Dual-Mode Electron Gun,” RADC Final Rep. F 30602-76-C-0177, Varian Associates, Palo Alto, CA, Oct. 1977.
- [74] W. W. Siekanowicz and J. H. Cash, Focusing of medium- and high-power electron beams by use of long-period magnetic fields, *Proc. 5th Int. Congr. Microwave Tubes, Paris*, pp. 209–214, Sept. 1964.
- [75] J. M. Baird, R. M. Phillips, and S. Snyder, Theory of stability in long period focused (LPF) electron beams with comparison to experiment, *IEEE Microwave Power Tube Conf., Monterey, CA, May 1990*.
- [76] P. Ramins *et al.*, Verification of an improved computational design procedure for TWT dynamic refocuser MDC systems with secondary emission losses, *IEEE Trans. Electron Devices*, Vol. ED-33, pp. 85–90, Jan. 1986.
- [77] J. R. M. Vaughan, “Development of Computer Program TWTVA for Calculation of 3-D Electron Trajectories in Coupled Cavity TWT’s,” Naval Electronic Laboratory Center Final Rep. N00123-76-C-0424, Litton Industries, San Carlos, CA, Mar. 1976.
- [78] C. B. Thorington, FINELGUN, AVBEAM, LSIGPREP, RFCIRC, and LSIG2D: A complex of 2.5-dimensional codes for large signal analysis of coupled-cavity TWTs, *IEEE Microwave Power Tube Conf., Monterey, CA, May 1988*.

- [79] A. Mankofsky, Three-dimensional electromagnetic particle codes and applications to accelerators, *Workshop Linear Accel. Beam Opt. Codes, AIP Conf. Proc.* No. 177, pp. 45–58, 1988.
- [80] Y. Goren, R. Wilson, and P. Lally, 2.5-Dimensional time domain particle-in-cell simulation code for collector design, *IEDM Tech. Dig.*, pp. 877–880, Dec. 1990.
- [81] W. Peter *et al.*, “Simulation of a Klystron Gun,” LA-9571 UC-28, Los Alamos Natl. Lab., Los Alamos, NM, Nov. 1982.
- [82] K. Nguyen *et al.*, Analysis of the 425-Mhz Klystrode, *IEEE Trans. Electron Devices*, Vol. ED-38, pp. 2212–2220, Oct. 1991.
- [83] K. H. Krause, “A Dynamic Refocusing System for Linear Beam Microwave Tubes,” Degree of Engineer Thesis, Stanford Univ., Stanford, CA, 1979.
- [84] J. R. Hechtel, R. Herriott, and J. R. M. Vaughan, Analysis of the spent beam of a high power TWT, *IEDM Tech. Dig.*, pp. 492–495, Dec. 1981.
- [85] H. G. Kosmahl, Modern multistage depressed collectors—A review, *Proc. IEEE*, Vol. 70, pp. 1325–1334, Nov. 1982.
- [86] H. G. Kosmahl, How to quickly predict the overall TWT and multistage depressed collector efficiency, *IEEE Trans. Electron Devices*, Vol. ED-27, pp. 526–529, Mar. 1980.
- [87] H. G. Kosmahl and P. Ramins, Small-size 81 to 83.5 percent efficient 2- and 4-stage depressed collectors for octave bandwidth high performance TWT's, *IEEE Trans. Electron Devices*, Vol. ED-24, pp. 36–44, Jan. 1977.
- [88] A. Schram, TWT efficiency improvement using multistage depressed collectors, *Microwave J.*, pp. 31–34, Aug. 1975.
- [89] I. Tammaru, “Multistage Depressed Collector Investigation for Traveling-Wave Tubes,” NASA Rep. CR-72950, Hughes Aircraft Co., Torrance, CA, June 1971.
- [90] J. R. Hechtel, A novel electrostatic-focussing depressed collector for linear beam tubes, *IEEE Trans. Electron Devices*, Vol. ED-24, pp. 45–52, Jan. 1977.
- [91] A. N. Curren *et al.*, A low-power, high-efficiency Ka-band TWTA, *IEDM Tech. Dig.*, pp. 581–584, Dec. 1991.
- [92] J. D. Wilson *et al.*, A high-efficiency 59- to 64-GHz TWT for intersatellite communications, *IEDM Tech. Dig.*, pp. 585–588, Dec. 1991.
- [93] D. A. Force, “Calculation of Secondary Electron Trajectories in Multistage Depressed Collectors for Microwave Amplifiers,” NASA TP-2664, 1986.
- [94] M. J. Cattelino, G. V. Miram, and W. R. Ayers, A diagnostic technique for evaluation of cathode emission performance and defects in vehicle assembly, *IEDM Tech. Dig.*, pp. 36–39, Dec. 1982.
- [95] T. J. Grant, Emission degradation characteristics of coated dispenser cathodes, *IEDM Tech. Dig.*, pp. 700–703, Dec. 1986.
- [96] R. Batra and D. Marino, “Design, Construction and Long Life Endurance Testing of Cathode Assemblies for Use in Microwave High Power Transmitter Tubes,” NASA Lewis Research Center Rep. CR-175116, Sept. 1986; L. Dombro and J. F. Wilson, “Long Life Endurance Testing of Cathode Assemblies,” Final Rep. to NASA Contract NAS 3-25080, NASA Lewis Research Center Rep. CR-187153, 1994; see also “Cathode Life Test Facility Annual Report,” Naval Surface Warfare Center, Crane Div., Crane, IN, Oct. 1993.
- [97] R. T. Longo, Long life, high current density cathodes, *IEDM Tech. Dig.*, pp. 152–155, Dec. 1978.
- [98] A. M. Shroff, J. C. Tonnerre, and D. Brion, Coverage and work function of dispenser cathodes, *IEDM Tech. Dig.*, pp. 704–707, Dec. 1986.
- [99] R. Forman, Update on thermionic cathode progress, *IEDM Tech. Dig.*, pp. 387–390, Dec. 1991.

- [100] J. R. Hechtel, Analysis of non-laminar electron beams for high-power microwave tubes, *IEDM Tech. Dig.*, pp. 197–200, Dec. 1974.
- [101] R. Harper and M. P. Puri, Characteristics of typical Pierce guns for PPM focussed TWTS, *AIP Conf. Proc.* No. 188, pp. 245–258, Nov. 1988.
- [102] G. V. Miram, Diagnostic techniques with a computer controlled beam analyzer, *IEDM Tech. Dig.*, pp. 708–711, Dec. 1986.
- [103] R. Wilson and R. Rodriguez, A computerized three dimensional approach to beam measurement and analysis, *IEDM Tech. Dig.*, pp. 712–715, Dec. 1986.
- [104] K. J. Moy and T. J. Grant, An experimental test station for multistage depressed collectors, *IEDM Tech. Dig.*, pp. 665–667, Dec. 1984.
- [105] R. Strauss, Reliability of SSPA's and TWTA's, *IEEE Trans. Electron Devices*, Vol. ED-41, pp. 625–626, Apr. 1994.
- [106] Military Handbook, *Reliability Prediction of Electronic Equipment*, MIL-HDBK-217F, Notice 1, July 10, 1992.

This Page Intentionally Left Blank

Microwave Solid-State Switches, Phase Shifters, and Attenuators

T. Koryu Ishii

I. Microwave Solid-State Switches

Basics

A microwave switch is basically a device which turns microwaves on and off. Like any other electrical switch, there are various types of switch, including SPST (single pole single throw), SPDT (single pole double throw), and SPMT (single pole multiple throw), as shown in Figure 1.

As for solid-state switching devices, transistors and diodes are logical candidates. Due to the simplicity and cost effectiveness, most microwave solid-state switching devices practically in use are PIN junction diodes, as shown in Figure 2. The diode is operated under forward DC bias conditions to close the diode switch. When the diode is forward biased sufficiently, the diode resistance is very small and it presents very little loss for microwaves to propagate through. The attenuation of microwave power through the switching diode is termed the insertion loss. The insertion loss is calculated by

$$IL = 10 \log_{10} \frac{P_D}{P_O} \quad (\text{dB}), \quad (1)$$

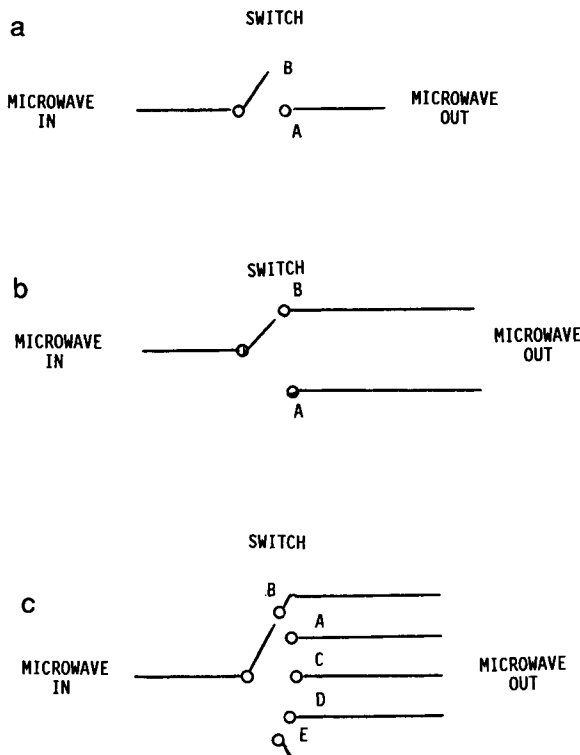


Figure 1. Schematic diagrams of various microwave switches. (a) SPST microwave switch. (b) SPDT microwave switch. (c) SPMT microwave switch.

where P_D is the microwave power output through the switching diode when the diode is on and P_O is the microwave power output with the diode short circuited.

Another important factor of a microwave switch is the isolation. The isolation is a power ratio between the power of the switched output, P_D , and the stray coupled microwave power to the adjacent unswitched circuit, P_S .

$$ISO = 10 \log \frac{P_S}{P_D} \quad (\text{dB}). \quad (2)$$

When the PIN diode is zero biased or reverse DC biased, the diode presents very high resistance which is the equivalent to the open switch condition.

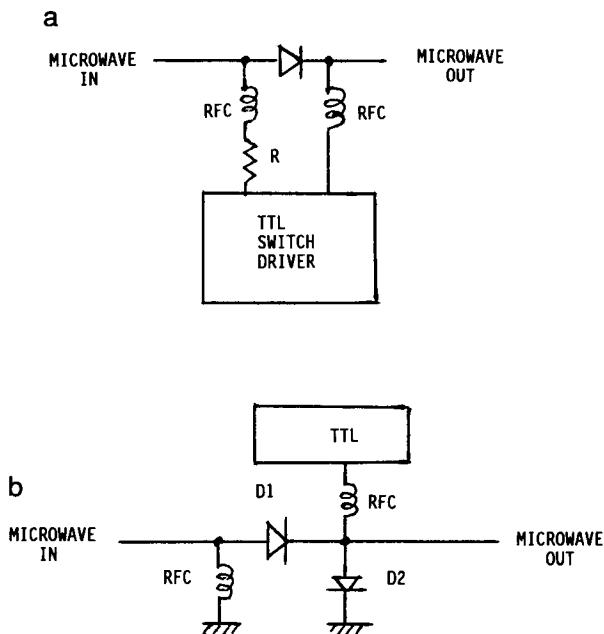


Figure 2. Schematic diagrams of PIN diode microwave switches. (a) SPST single-PIN diode microwave switch. (b) SPST double-PIN diode microwave switch.

A general microwave equivalent circuit and sufficiently forward biased and zero or reverse biased PIN diode microwave equivalent circuits are shown in Figure 3. In this figure, L is the lead inductance, R_s is the series resistance, including the lead resistance and bulk resistance of semiconductors, R_N is the nonlinear junction resistance, C_J is the junction capacitance, and C_p is the package capacitance. If the diode is sufficiently forward biased, the junction resistance is very small and the effects of reactance due to capacitance can be omitted, as shown in Figure 3b. Under these conditions, switch AB is considered closed for microwaves impressed to transmit from either A to B or B to A. Microwave power loss through the conducting state of the switch is the insertion loss of the switch. Most PIN diode switches have few decibels of insertion loss. When the diode is zero biased or reverse biased, there will be a large R_N and the diode can be considered open. C_J will be very small under zero or reverse bias conditions due to the I-layer, as shown in Figure 3c. In this case the diode is considered open between A and B, but in reality, points A and B are connected through small C_J and C_p . Therefore points A and B are not completely isolated. The ratio of microwave power leaked through to the

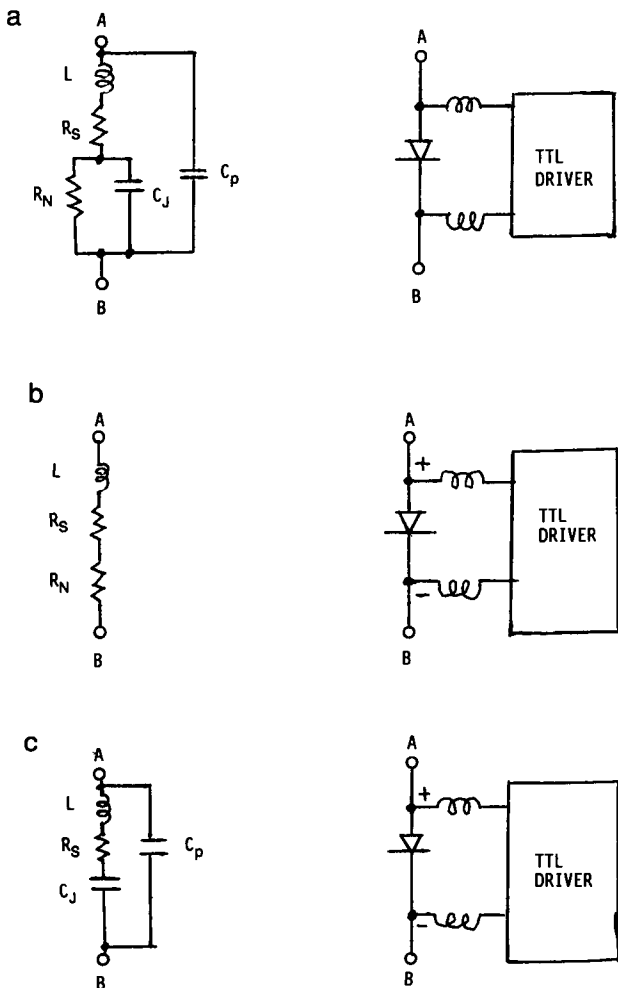


Figure 3. Microwave equivalent circuit of a switching PIN diode. (a) General equivalent circuit. (b) Sufficiently forward biased. (c) Zero or reverse biased.

power input is termed isolation in either the A to B direction or the B to A direction. Most commercial PIN diode switches produce an isolation of -40 to -60 dB.

As seen from Figures 3b and 3c, the switching speed is determined by, besides the TTL switch driver's switching speed, the inherent PIN diode packaging parameters L , R_S , C_J , and C_p . In most commercial microwave switching PIN diodes, L is less than 1 nH [1]. The junction resistance

under forward bias conditions can be calculated by [1]

$$R_N = \frac{w^2}{(\mu_n + \mu_p) I_F \tau}, \quad (3)$$

where w is the thickness of layer I, μ_n is the electron mobility, μ_p is the hole mobility, I_F is the forward bias current, and τ is the carrier lifetime. Equation (3) is valid in a range of frequency which is

$$f > \frac{1300}{w^2}. \quad (4)$$

Under zero or reverse biased conditions,

$$C_J \approx \frac{\epsilon A}{w}, \quad (5)$$

where A is the cross-sectional area of the junction and ϵ is the permittivity of the intrinsic I-layer semiconductor. Equation (5) is valid in a frequency range of [1]

$$f > \frac{1}{2\pi\rho\epsilon}, \quad (6)$$

where ρ is the resistivity of the I-layer.

Switching Configurations of SPST Switches

Various switching configurations of the microwave SPST are shown in Figure 4. Note that each diode is driven by its own TTL switch driver which is not shown in this figure.

For the series connected SPST switch, as shown in Figure 4a, the insertion loss is given by [1]

$$IL = 20 \log_{10} \left[1 + \frac{R_S + R_N}{2Z_0} \right] \text{ (dB)}. \quad (7)$$

The isolation is [1]

$$ISO = 10 \log_{10} \left[1 + \left(\frac{X_c}{2Z_0} \right)^2 \right] \text{ (dB)}, \quad (8)$$

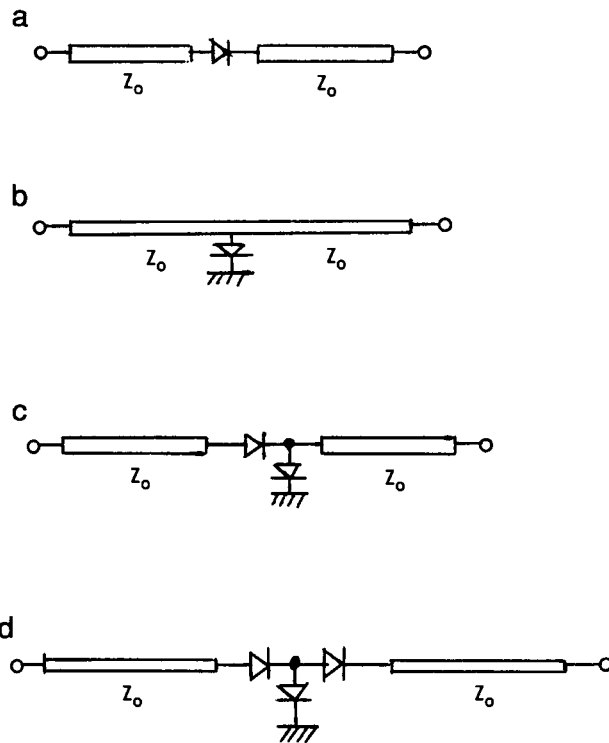


Figure 4. Switching configuration of SPSTs. (a) Series connected SPST. (b) Shunt connected SPST. (c) Series – shunt SPST. (d) T connected SPST.

where

$$X_c = \frac{1}{\omega C_J}. \quad (9)$$

For the shunt connected SPST switch, as shown in Figure 4b, the insertion loss is [1]

$$IL = 10 \log_{10} \left[1 + \left(\frac{Z_0}{2X_c} \right)^2 \right] \text{ (dB)} \quad (10)$$

and the isolation is [1]

$$ISO = 20 \log_{10} \left[1 + \frac{Z_0}{2(R_S + R_N)} \right] \text{ (dB)}. \quad (11)$$

For the series–shunt SPST switch, as shown in Figure 4c, the insertion loss is [1]

$$IL = 10 \log_{10} \left[\left(1 + \frac{R_S + R_N}{2Z_0} \right) + \left(\frac{Z_0 + R_S + R_N}{2X_c} \right)^2 \right] \text{ (dB)} \quad (12)$$

and the isolation is [1]

$$ISO = 10 \log_{10} \left[\left(1 + \frac{Z_0}{2(R_S + R_N)} \right) + \left(\frac{X_c}{2Z_0} \right)^2 \left(1 + \frac{Z_0}{R_S + R_N} \right) \right] \text{ (dB).} \quad (13)$$

For the T connected SPST switch, as shown in Figure 4d, the insertion loss is [1]

$$IL = 20 \log_{10} \left[1 + \frac{R_S + R_N}{Z_0} \right] + 10 \log_{10} \left[1 + \left(\frac{Z_0 + R_S + R_N}{2X_c} \right)^2 \right] \text{ (dB)} \quad (14)$$

and the isolation is [1]

$$ISO = 10 \log_{10} \left[\left\{ 1 + \left(\frac{X_c}{Z_0} \right)^2 \right\} \left\{ \left(1 + \frac{Z_0}{2R_S + R_N} \right)^2 \right\} + \left\{ \left(\frac{X_c}{2(R_S + R_N)} \right)^2 \right\} \right] \text{ (dB).} \quad (15)$$

In a commercial PIN switching diode, with a forward bias current of 10 mA, the series resistance R_S and R_N range from 0.6 to 3 Ω , the junction capacitance at 20 V reverse bias ranges from 0.5 to 1.5 pF, the carrier lifetime τ ranges from 0.3 to 3 μs , the thickness of the I-layer ranges from 0.4 to 3 mil, and the reverse voltage rating ranges from 35 to 200 V.

Switching Configurations of SPDT Switches

Some examples of schematic diagrams of switching configurations of the PIN diode SPDT are shown in Figure 5. These circuits may be the monolithic IC or discrete type. Depending on the TTL command, the microwave input is switched to microwave output port No. 1 or No. 2.

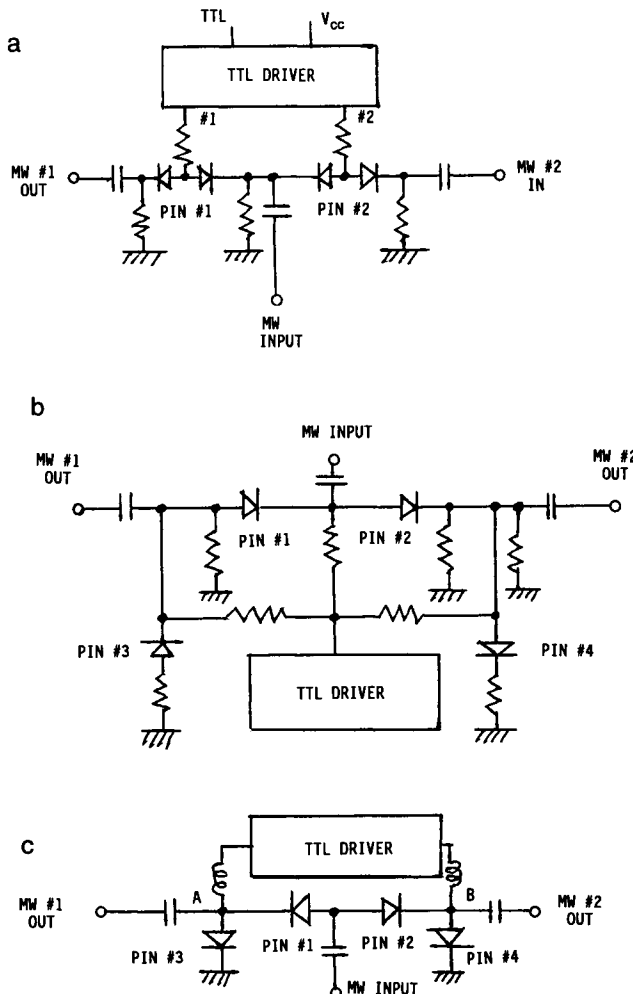


Figure 5. Switching configuration of SPDT switches. (a) Reflective SPDT switch [2]. (b) Nonreflective SPDT switch [3]. (c) Series - shunt SPDT switch [4].

In the case of Figure 5a, when TTL driver port No. 1 is high and No. 2 is low, microwave input couples to the No. 1 output port. When TTL driver port No. 1 is low and No. 2 is high, then the input microwaves couple to the No. 2 output port. "High" means the forward bias to PIN diodes, so that these are in the conduction state. "Low" means the zero bias or reverse bias to PIN diodes, so that these are in the "off" state or in the "high-resistance" state. In this arrangement, shown in Figure 5a, when

the output port is severely mismatched, reflections appear at the input port.

In the case of Figure 5b, when the TTL driver is high, the PIN No. 1 diode is off and the PIN No. 2 diode is on. Therefore the microwave input power goes to microwave output port No. 2. At the same time, both PIN No. 3 is off and PIN No. 4 is on. PIN No. 4 helps provide approximately matched impedance to microwave (MW) input port No. 2 even when the MW No. 2 output port is severely mismatched. When the TTL driver command is low, PIN No. 1 is on and PIN No. 2 is off. To do that the low command must be sufficiently negative. Then the input microwaves go to microwave output port No. 1. PIN No. 3 is off and PIN No. 4 is on. PIN No. 4 helps to absorb reflection from the MW No. 1 output port even if the port is severely mismatched by means of providing a connection to buffer resistors.

In the case of Figure 5c, when TTL drive output A is high and B is low, microwave input goes to the MW No. 2 output port. The reason is that PIN No. 1 is on, PIN No. 2 is off, PIN No. 3 is off, and PIN No. 4 is on.

Switching Configurations of SPMT Switches

Schematic diagrams of examples of single-pole multiple-throw PIN diode switches are shown in Figure 6. A schematic diagram of the reflective SPMT switch [3] is shown in Figure 6a. For any MW output port, if the TTL drive signal is high, then the port is off, and if the TTL drive signal is low, then the port is on. If any output port produces high reflection, the reflected waves go back to the MW input port.

A schematic diagram of the nonreflective SPMT switch [3] is shown in Figure 6b. For any MW output port, if the TTL drive signal is high, then the port is on, and if the TTL drive signal is low, then the port is off. The series resistance in series with the shunt PIN diode is adjusted to absorb excess reflections from the output port when the shunt diode is on.

Switching Configurations of Transfer Switches

Various switching configurations of transfer switches are shown in Figure 7. In Figure 7, when port Nos. 1 and 2 are connected, port Nos. 3 and 4 are connected. At the same time, ports Nos. 1 and 2 are disconnected and ports Nos. 3 and 4 are disconnected. These switching functions are obtained by turning the individual PIN diode on or off as needed using TTL-driven PIN diode drivers. Quarter-wavelength lines are microwave frequency chokes when the diode is turned on or off. For example, in

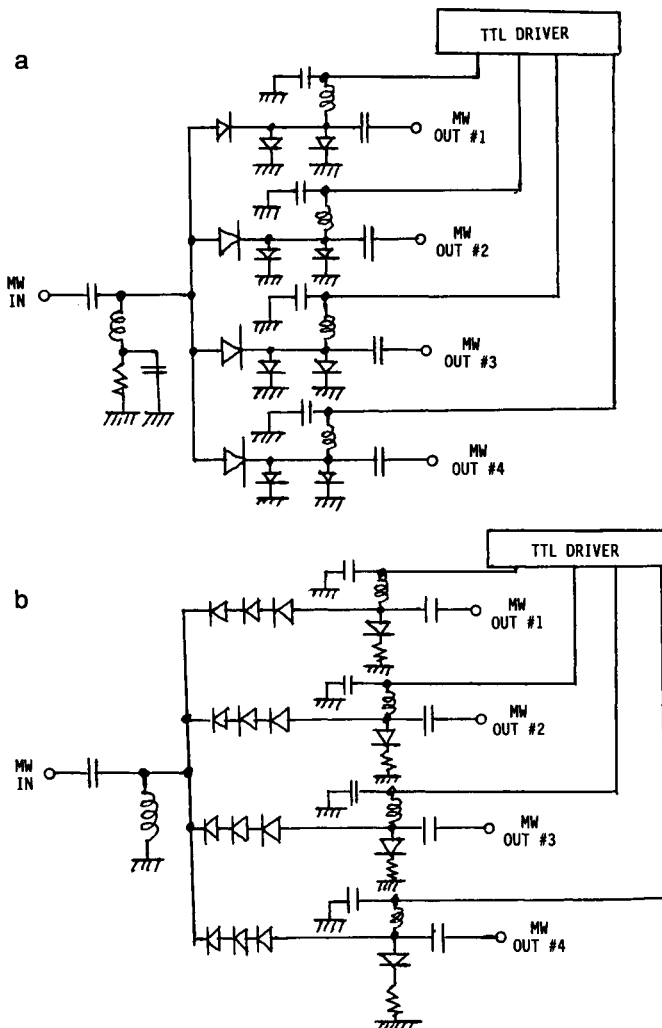


Figure 6. Schematic diagrams of PIN diode SPMT switches. (a) Reflective SPMT switch. (b) Nonreflective SPMT switch.

Figure 7a, if diode No. 1 between port Nos. 1 and 2 is turned on, then the impedance at port No. 1 and port No. 2 becomes extremely high. This makes microwave transmission between port No. 1 and port No. 2 extremely difficult. This means that port No. 1 and port No. 2 are considered to be disconnected. When PIN diode No. 1 is off, then microwave transmission becomes possible and port No. 1 and port No. 2 are connected.

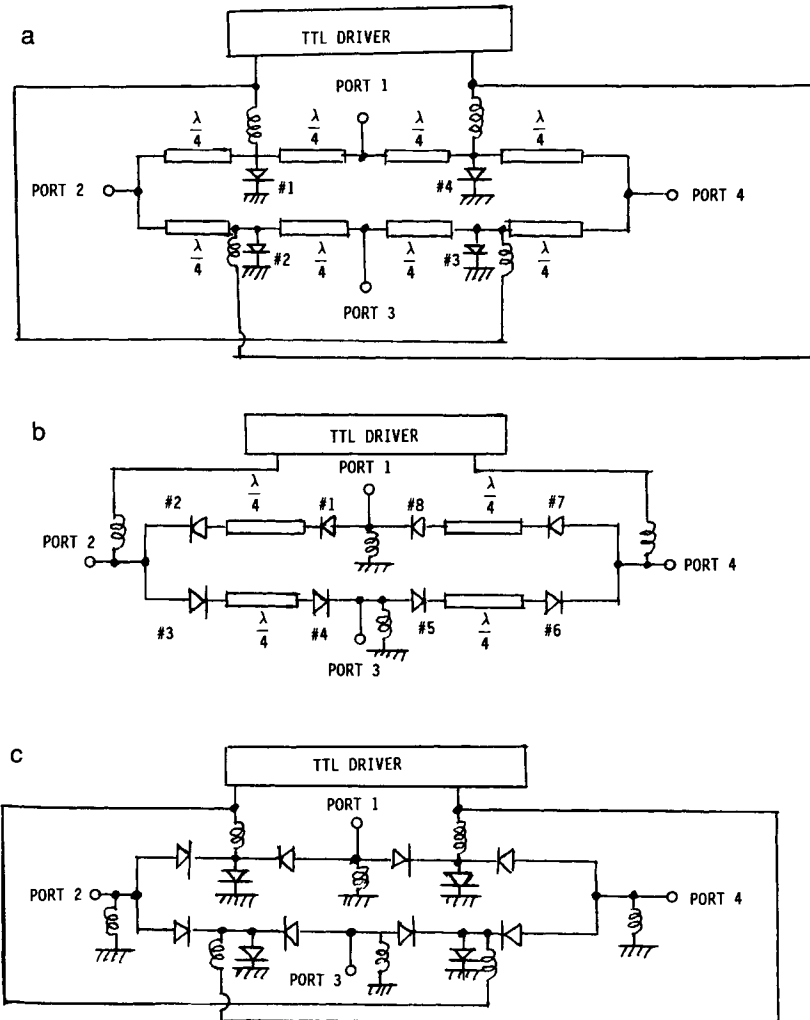


Figure 7. Schematic diagram of transfer switches. (a) All shunt PIN transfer switch. (b) All series PIN transfer switch. (c) Series - shunt PIN transfer switch.

Sample Applications

Sample applications of solid-state SPDT switches are shown in Figure 8 [1]. These are diplexers. The SPDT switches to the antenna either to the transmitter or to the receiver depending on the TTL driver signal. When the TTL driver signal is high, the PIN diodes are on, connecting the antenna to the transmitter. The receiver terminal is grounded and a

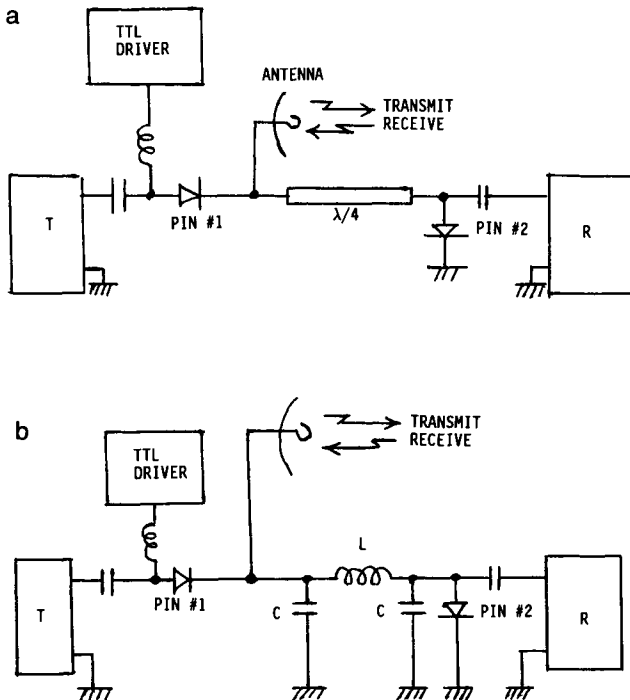


Figure 8. Microwave diplexer circuit. (a) Quarter-wavelength choke TR switch [1]. (b) Lumped choke TR switch [1].

high-input impedance is produced by the $\lambda/4$ choke or the RF choke L at the antenna base toward the receiver. Therefore, the transmitter signals go to the antenna, and very little power leaks to the receiver.

When the TTL driver signal is low, then both PIN diodes are off. The transmitter is now disconnected from the antenna, and the received signal from the antenna goes to the receiver since the receiver terminal is now ungrounded. This time, since the PIN diode is off, the line from the antenna base to the receiver input is matched. Figure 8a is for high microwave frequency applications, and Figure 8b is for low microwave frequency applications in which the quarter-wavelength line becomes too long to be practical.

The switching circuits shown in Figure 8 are used for both the communication mode and the radar mode. For communication mode operation, the TTL driver signal is high only when the transmitter is operated. Normally the TTL driver signal is kept low for receiving. For radar mode operation, the TTL driver signal is high for a short period of

TABLE I
Commercial Microwave Solid-State Data Switches

Type	Model number	Insertion loss (dB)	Isolation (dB)	Switching speed (mS)	Operating frequency (GHZ)	Microwave power (dBm)	Driving requirement
SPST[2]	PSW-1111	1.1–1.7	28–50	4	2.5 maximum	+ 20	5 V, 5 mA
SPDT[2]	TOSW-230	1.3–1.8	35–60	2	3.0 maximum	+ 28	5 V, 10 mA
SP4T[2]	TOSW-425	1.1–1.5	35–60	2	2.5 maximum	+ 28	5 V, 10 mA
SPST[2]	KSWHA-1-20	0.8–1.2	65–75	0.003	2.0 maximum	+ 30	5 V, 200 mA
SPST[3]	AHS1802-0	0.2–2.1	40	0.025	18.0 maximum	+ 30	+ 5.5 V/ – 16.5 V
SPST[3]	AHS1802-1	1.1–2.4	60	0.025	18.0 maximum	+ 30	+ 5.5 V/ – 16.5 V
SPDT[3]	AHD1802	1.3–2.9	50	0.075	18.0 maximum	+ 30	+ 5.5 V/ – 16.5 V
SP3T[3]	AHT1802	1.4–3.1	50	0.075	18.0 maximum	+ 30	+ 5.5 V/ – 16.5 V
SP4T[3]	AHQ1802	1.6–3.4	50	0.075	18.0 maximum	+ 30	+ 5.5 V/ – 16.5 V
SP5T[3]	AHF1802	1.7–3.5	50	0.075	18.0 maximum	+ 30	+ 4.4 V/ – 16.5 V
SPST[1]	MA47206	0.5 maximum	20 minimum	0.010	10.0	—	10V, 10 mA
SPST[1]	MA47220	0.5 maximum	20 minimum	0.1	10.0	—	0V, – 100 mA
SPST[1]	MS103	2.5 maximum	70 minimum	0.02	18.0 maximum	+ 30	- 5V, + 13 mA
SPST[4]	MS104	1.0 maximum	60 minimum	0.04	4.0 maximum	+ 30	- 5V, + 20 mA
SPDT[4]	MS203	2.7 maximum	55 minimum	0.025	18.0 maximum	+ 20 minimum	± 13 mA
SPDT[4]	MS205	1.3 maximum	70 minimum	0.04	4.0 maximum	+ 20 minimum	± 20 mA
SP3T[4]	MSF303	2.7 maximum	55 minimum	0.025	18.0 maximum	+ 20 minimum	5V, 175 mA
SP5T[4]	MSF503	3.1 maximum	65 minimum	0.025	18.0 maximum	+ 20 minimum	5V, 240 mA

time in the form of short pulse train. The rest of the time, the TTL driver signal is kept low. This allows the transmitter to transmit interrogation pulses periodically and at the same time the receivers to receive echoes from the radar targets.

Some Practical Microwave Solid-State Switches

Pertinent data for some of commercial microwave solid-state switches are listed in Table 1 by reference. An example of practical application of solid-state switches can be seen in Reference [5].

2. Microwave Solid-State Phase Shifters

Basics

The important part of a microwave solid-state phase shifter is a reverse biased varactor diode, or the variable capacitance diode. An equivalent circuit of a reverse biased varactor diode is shown in Figure 9. In this figure, L_s is the lead inductance, R_s is the spreading resistance of the lead and bulk parts of the semiconductor, and C_J is the junction capacitance which is a function of reverse bias voltage. The higher the reverse voltage is, the smaller the capacitance. R_J is the junction resistance due to the minority carrier. Therefore, it is very large under reverse biased condition. Generally, under reverse biased conditions,

$$|R_s + j\omega L_s| \ll 1/\omega C_J \quad (16)$$

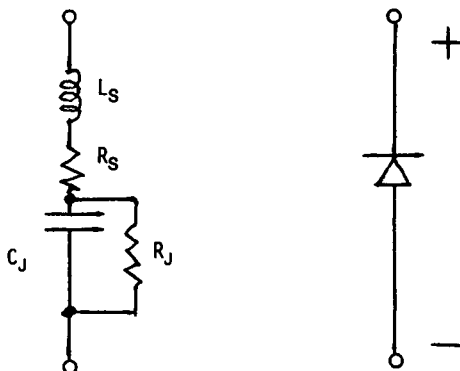


Figure 9. An equivalent circuit of a reverse biased varactor diode.

and

$$R_J \gg 1/\omega C_J. \quad (17)$$

This means that the effect of C_J dominates in a reverse biased varactor diode. In many cases, a varactor diode can be considered a bias voltage controlled variable capacitor or tuning capacitor diode.

When a single varactor diode is used as a phase shifter, the diode can be used in a shunt, as shown in Figure 10a, or in series, as shown in Figure 10b, against the transmission line in which the diode is mounted.

The $ABCD$ matrix of a shunt mounted varactor diode is

$$\begin{bmatrix} A & B \\ C & D \end{bmatrix} = \begin{bmatrix} 1 & 0 \\ -\dot{\gamma} & 1 \end{bmatrix}, \quad (18)$$

where $\dot{\gamma}$ is the diode admittance. For example, if L_S and R_S are very small and R_J is very large,

$$\dot{\gamma} = j\omega C_J. \quad (19)$$

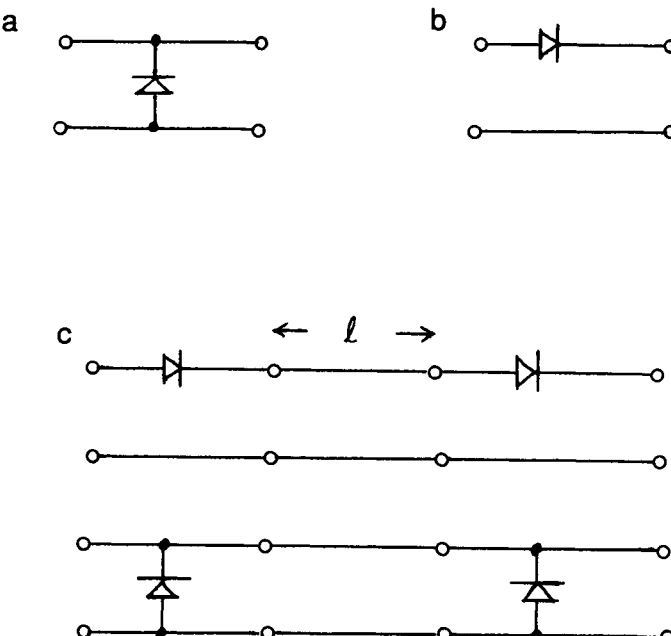


Figure 10. Schematic diagrams of varactor mounted phase shifters. (a) Shunt mounted varactor diode. (b) Series mounted varactor diode. (c) Cascaded varactor diode phase shifter with a transmission line section.

The $ABCD$ matrix of a series mounted varactor diode is

$$\begin{bmatrix} A & B \\ C & D \end{bmatrix} = \begin{bmatrix} 1 & -Z' \\ 0 & 1 \end{bmatrix}, \quad (20)$$

where Z' is the diode impedance. For example, if both L_S and R_S are very small and R_J is very large,

$$Z' = -j \frac{1}{\omega C_J}. \quad (21)$$

The $ABCD$ parameters of any two-port network, including the varactor diode two-port network, is related to S -parameters by [6]

$$S_{11} = \frac{AZ_{02} + B - CZ_{01}Z_{02} - DZ_{01}}{AZ_{02} + B + CZ_{01}Z_{02} + DZ_{01}} \quad (22)$$

$$S_{22} = \frac{Z(AD - BC)\sqrt{Z_{01}Z_{02}}}{AZ_{02} + B + CZ_{01}Z_{01} + DZ_{02}} \quad (23)$$

$$S_{21} = \frac{2\sqrt{Z_{01}Z_{02}}}{AZ_{01} + B + CZ_{01}Z_{02} + DZ_{01}} \quad (24)$$

$$S_{12} = \frac{-AZ_{02} + B - CZ_{01}Z_{02} + DZ_{01}}{AZ_{02} + B + CZ_{01}Z_{02} + DZ_{01}}, \quad (25)$$

where Z_{01} is the source impedance and Z_{02} is the load impedance. The phase shift across this varactor diode two-port network is

$$\Delta\phi = \tan^{-1} \frac{I_m S_{21}}{R_e S_{21}}. \quad (26)$$

The insertion loss across the varactor diode mounted two-port network is

$$L \text{ (dB)} = 10 \log \frac{1}{|S_{21}|^2}. \quad (27)$$

The voltage standing wave ratio (VSWR) of this network is

$$\text{VSWR} = \frac{1 + |S_{11}|}{1 - |S_{11}|}. \quad (28)$$

If a single-stage varactor diode does not produce a desirable phase shift, the several stages of a diode network can be cascaded together with several transmission line sections, as shown in Figure 10c.

The $ABCD$ matrix of a transmission line of length l is

$$\begin{bmatrix} A & B \\ C & D \end{bmatrix} = \begin{bmatrix} \cos \beta l & jZ_0 \sin \beta l \\ j\frac{\sin \beta l}{Z_0} & \cos \beta l \end{bmatrix}, \quad (29)$$

where Z_0 is the characteristic impedance of the transmission line and β is the phase constant of the transmission line, or

$$\beta = \frac{2\pi}{\lambda_1}, \quad (30)$$

where λ_1 is the wavelength on the transmission line.

The overall $ABCD$ matrix of a cascaded transmission network in which the $ABCD$ parameters are A_i , B_i , C_i , and D_i is

$$\begin{bmatrix} A & B \\ C & D \end{bmatrix} = \begin{bmatrix} A_1 & B_1 \\ C_1 & D_1 \end{bmatrix} \begin{bmatrix} A_2 & B_2 \\ C_2 & D_2 \end{bmatrix} \begin{bmatrix} A_3 & B_3 \\ C_3 & D_3 \end{bmatrix} \dots \quad (31)$$

At any rate, the phase shift across the overall two-port network is given by Equation (26), the insertion loss is given by Equation (27), and the VSWR is given by Equation (28).

DC Biasing Configuration

The DC biasing configuration of a varactor diode mounted phase shifter is very similar to that of a PIN diode switch, as shown in Figure 2, except that the varactor diodes must be biased in the reverse direction for the variable shift.

Some Practical Varactor Diodes

To design a varactor diode phase shifter, pertinent diode parameters must be known first. Some practical examples of commercial varactor diodes are shown in Table 2. In this table,

$$Q = \frac{1}{\omega C_J R_J}. \quad (32)$$

Therefore,

$$R_J = \frac{1}{\omega GQ}. \quad (33)$$

3. Microwave Solid-State Attenuators

Basics

For microwave solid-state attenuators, forward biased PIN diodes are employed. An equivalent circuit of a forward biased PIN diode is similar to that depicted in Figure 9. In this case the effect of R_J is more dominant than the effect of C_J , or

$$R_J \ll 1/\omega C_J. \quad (34)$$

In a PIN diode, R_J depends on the forward bias voltage. When the bias voltage is low, R_J can be as high as $10^3 \Omega$. When the bias voltage is high, R_J can be as low as a few ohms. The PIN diode can also be used as shown in Figure 10.

The $ABCD$ matrix of a shunt mounted PIN diode is similar to that in Equation (18). When R_J is dominating,

$$\dot{\gamma} = 1/R_J. \quad (35)$$

The $ABCD$ matrix of a series mounted PIN diode is similar to that in Equation (20). When R_J is the dominating equivalent circuit parameter of the PIN diode,

$$Z' = R_J. \quad (36)$$

The phase shift across this PIN diode two-port network is given by Equation (26), and the attenuation across the network is given by Equation (27). The VSWR of the network is calculated using Equation (28). If the PIN diode attenuator takes the form shown in Figure 10c, the $ABCD$ matrix is calculated using Equations (29)–(31).

DC Biasing Configuration

The DC biasing configuration of a PIN diode mounted attenuator is very similar to that of a PIN diode switch, as shown in Figure 2, except that the bias voltage is varied continuously depending on the amount of attenuation desired.

TABLE 2
Pertinent Parameters of Commercial Varactor Diodes [1, 7]

Model number	Minimum breakdown voltage (V)	Capacitance (pF)	Maximum/minimum capacitance ratio	<i>Q</i>	Operating frequency (GHz)
MA45225	30	0.5	2.7	5500	10–12
MA45242	30	15	4	2000	0.5–1.0
MA45290	90	1.0	6	1500	2.0–4.0
MA45299	90	5.6	8.8	600	0.5–1.0
DVH6760	60	3.3	3.8	2100	0.1–7.0
DVH6730	30	3.3	3.2	4800	0.1–10.0
DVE4500	25	0.5	3.1	4300	3.5–35.0
DKV6550	22	0.22	2.2/1.8	400	0.5–35.0
CVG7965	22	1.0	8.5/5.5	2500	0.5–35.0

Some Practical PIN Diodes

To design a PIN diode attenuator, pertinent diode parameters must be known first. Some practical examples of commercial PIN attenuator diodes are shown in Table 3. Some already built and ready-to-use packaged integrated circuit-type PIN diode attenuators are also commercially available. Some examples of packaged integrated circuit PIN diode attenuators are listed in Table 4.

TABLE 3
Examples of Practical Attenuator PIN Diodes

Model number	Forward resistance (Ω)	Forward current (mA)	Operating frequency (GHz)	Reference
HPND-4001	50/2	0.1/50	1–20	8
HPND-4018	600/3	0.01/100	1–20	8
5082-3900	6000/3	0.0001/100	1–20	8
5082-3305	700/0.5	0.001100	1–20	8
MA47056	17000/1.5	0.001/100	0.1–2	1
MA47057	8000/1	0.001/100	0.1–2	1
MA4PH601	7500/3.5	0.001/100	0.1–2	1
CSB7401-01	15/1.4	1/100	0.1–12	7
CSB7401-02	10/1.2	1/100	0.1–12	7
CSB7401-03	10/1.2	1/100	0.1–12	7
SMP1604-01	1000/5	0.01/10	0.1–3	7
SMP1607-01	2000/8	0.01/10	0.1–3	7
SMP1609-01	3000/15	0.01/10	0.1–3	7
SMP1609-02	3500/10	0.01/10	0.1–3	7

TABLE 4
Examples of Practical Packaged IC Diode Attenuators

Model number	Attenuation (dB)	VSWR	Insertion loss (dB)	Control dc current (mA)	Operating frequency (GHz)	Reference
UTF-015	15	2.0	2.5	0-7	0.005-1	3
UTF-025	20	2.5	3.3	0-7	0.005-2	3
UTF-030	25	2.0	3.5	0-10	1-2	3
UTF-035	23.5	2.1	2.5	10-35	0.05-2	3
UTF-040	30	2.5	2.5	0-75	0.01-1	3
PPF-030	25	2.0	3.5	0-10	1-2	3
PAS-2	35	—	6.5	0-20	0.01-1	2
ZFAS-15	35	—	3.5	0-20	0.01-2.5	2
ZMAS-1	55	—	3.5	0-20	0.005-0.45	2
ZAS-1	55	—	3.5	0-20	0.005-0.45	2
TOAT-3610	19	1.5	4.0	0-6	0.01-1	2
TOAT-51020	35	1.5	4.0	0-6	0.01-1	2
MAT-25	25	1.8	—	—	0-1.5	2
MAT-40	40	1.5	—	—	0-0.5	2

References

- [1] M/A-COM Semiconductor Products Operation, "Semiconductor Products Master Catalog," No. SP101, Burlington, MA, 1988.
- [2] Mini-Circuits, "RF/IF Signal Processing Guide," SF-91/92, New York, 1992.
- [3] Avantek, "Modular and Oscillator Components Data Book," 2nd Ed., A-148/R-4-90, Milpitas, CA, 1990.
- [4] Watkins-Johnson Co., "RF and Microwave Component Designer's Handbook," Palo Alto, CA, 1988-1989.
- [5] A. J. Slobodnik, Jr., R. T. Webster, and G. A. Roberts, A monolithic GaAs 36 GHz phase shifter, *Microwave J.*, Vol. 36, No. 6, pp. 106-111, June 1993.
- [6] K. C. Gupta, R. Garg, and R. Chadha, *Computer-Aided Design of Microwave Circuits*. Dedham, MA: Artech House, 1981.
- [7] Alpha Industries, "Diodes, Modules, and MMICs Products Capabilities Application Notes," Alpha Semiconductor Div., Woburn, MA, 1990.
- [8] Hewlett Packard Co., "Microwave and RF Designer's Catalog," Palo Alto, CA, 1990-1991.

Microwave Thermionic Density Modulated Devices and Applications

T. Koryu Ishii

I. Principles of Microwave Thermionic Triodes

A schematic diagram of a typical structure of a microwave thermionic triode [1–4] is shown in Figure 1a. This is a vacuum tube of cylindrical symmetry. This figure is a cutaway diagram of the tube. The cathode is heated in the vacuum. Thermal electrons are emitted and pulled toward the anode. The electron flow toward the anode is controlled by a negatively biased control grid. Since the shape of the tube resembles a lighthouse, this type of vacuum tube is termed the *lighthouse tube*. All electrodes employ conducting discs to make contact with the circuit.

An equivalent circuit of the tube and an attached amplifier circuit are schematically shown in Figure 1b. This figure shows a schematic diagram of a grid-tuned and an anode-tuned amplifier. The principles of a vacuum tube amplifier resemble the principles of a field effect transistor (FET) [3].

An example of a lighthouse tube installed into microwave resonator cavities is schematically shown in Figure 2. The lighthouse tube is simply pushed into the cavity resonator assembly. The cavity resonators are coaxial to each other in their structure. All cavity cylinders are insulated from each other using a noncontact shorting plunger for the DC biasing purpose. Microwaves to be amplified are fed to the grid cavity through a

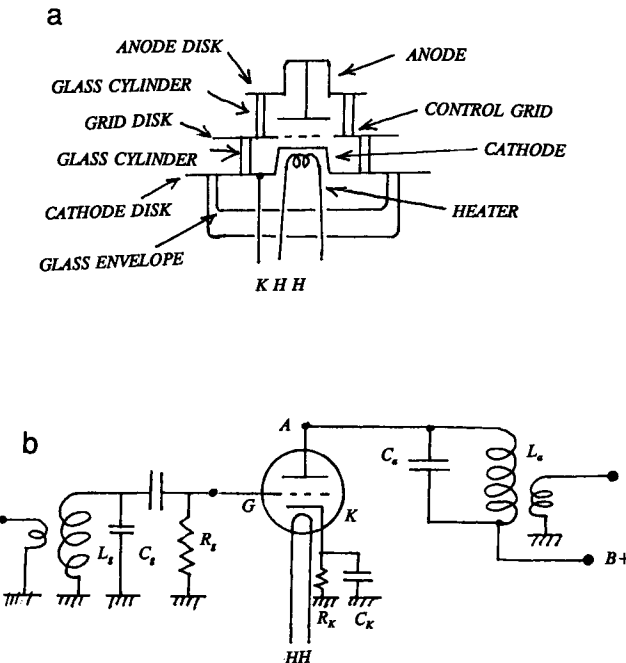


Figure 1. Structural and circuit representations of a microwave thermionic triode. (a) Structural schematic diagram of a microwave thermionic triode. (b) Schematic circuit diagram of a microwave thermionic vacuum triode amplifier.

coaxial magnetic loop coupler. Alternatively, a capacitor probe coupler is also employed. The control grid is excited by the input signals. The amplified microwaves appear in the anode cavity by the triode action. The amplified microwaves are coupled out by an insulated and choked magnetic loop coupler.

Under resonance conditions, the microwave anode current i_a is related to microwave voltage across the grid and the cathode v_g by

$$i_a = g_m v_g, \quad (1)$$

where g_m is the transconductance of the triode. If R_a is the resonance resistance of the anode cavity, then the output power at the anode is

$$P_a = \frac{1}{2} i_a^2 R_a = \frac{1}{2} R_a g_m^2 v_g^2. \quad (2)$$

If R_g is the resonance resistance of the grid cavity, then the input power

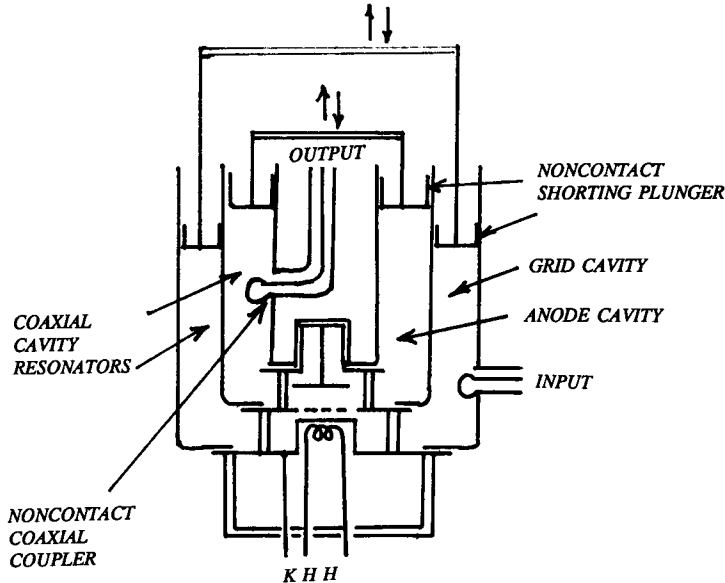


Figure 2. A schematic diagram of a lighthouse tube assembly.

given to the grid cavity is

$$P_g = \frac{1}{2} \frac{v_g^2}{R_g}. \quad (3)$$

Therefore, the power gain of this triode amplifier is

$$G_p = \frac{P_a}{P_g} = R_a R_g g_m^2. \quad (4)$$

By making a feedback loop from the anode cavity to the grid cavity, it is possible to make an oscillator. If the feedback ratio is k , then

$$P_g = k P_a. \quad (5)$$

Using Equations (2) and (3) in Equation (5),

$$\frac{1}{2} \frac{v_g^2}{R_g} = k \frac{1}{2} R_m g_m^2 v_g^2$$

or

$$R_g R_m G_m^2 k = 1. \quad (6)$$

This is the oscillation condition under resonance.

2. Examples of Microwave Thermionic Triodes

An example of a microwave thermionic triode [4], TH 326, is shown in Figure 3. The top part is the anode assembly with cooling fins. The anode dissipation of this tube is 200 W. It requires 280 l/min of forced air cooling. The exhaust cooling air temperature must be less than 100°C for proper anode operation. To produce 280 l/min of forced air cooling, the air pressure difference between the air inlet and the air outlet must be 0.5 mbar. The anode DC bias voltage can be as high as 2 kV. The anode current can be as high as 250 mA. The maximum anode dissipation is 270 W.

The second metallic ring from the top in Figure 3 is a part of the control grid assembly. The control grid is insulated from the anode by a white ceramic ring. The control grid is negatively biased up to -50 V.

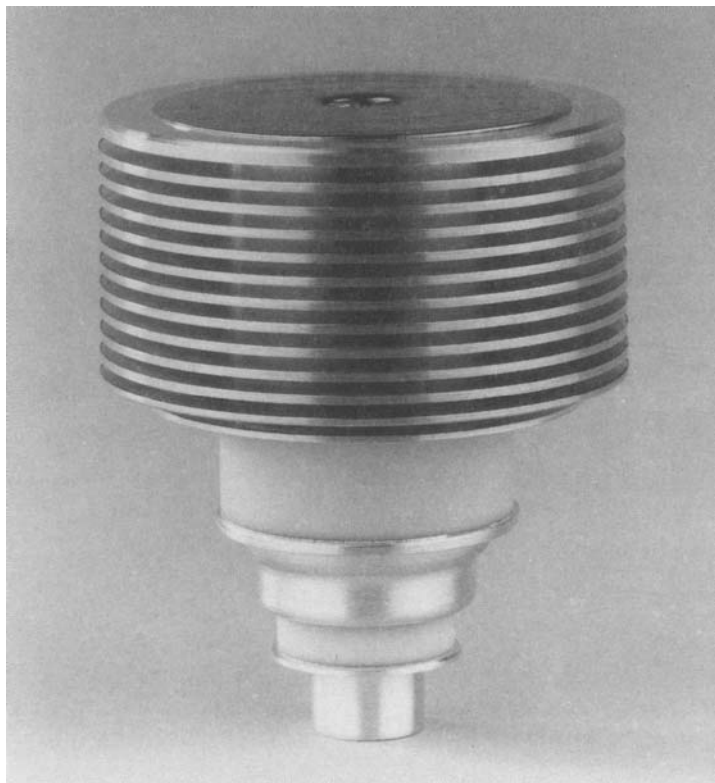


Figure 3. A picture of microwave power triode TH 326 (courtesy Thomson Tubes Electroniques).

The bottom metallic structure is a part of the cathode assembly. The cathode is an indirectly heated oxide cathode. The cathode requires 2 A of heater filament current. The cathode and the grid are insulated from each other by a white ceramic ring.

The interelectrode capacitance between the cathode and the grid is 22 pF. Between the grid and the anode is 3.9 pF, and the capacitance between the cathode and the anode is 0.05 pF.

This tube has a typical power gain of 20 dB with a transconductance of 8 mA/V. The peak output power is 50 W at the maximum operating frequency of 1000 MHz. This tube has a diameter of 54 mm and a height of 63 mm. It weighs 170 g.

A performance chart for microwave triode TH 326 is shown in Figure 4. This chart shows the performance characteristics of TH 326 under various operating anode voltages, V_a ; grid voltage V_g ; or the Q -point (bias point) selected. For example, the anode dissipation is

$$P_A = V_a I_a \quad (\text{at the } Q\text{-point}). \quad (7)$$

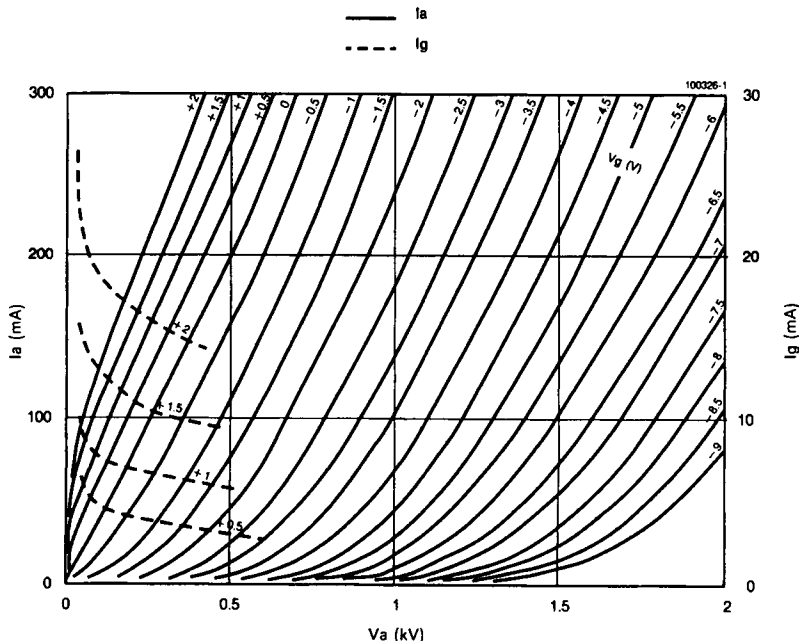


Figure 4. A performance chart of microwave power triode TH 326 (courtesy Thomson Tubes Electroniques).

The transconductance is

$$g_m = \Delta I_a / \Delta V_g \quad (\text{at the } Q\text{-point}), \quad (8)$$

where ΔV_g is a peak-to-peak grid voltage swing and ΔI_a is a corresponding peak-to-peak current swing. The voltage gain is

$$G_v = \Delta V_a / \Delta V_g \quad (\text{at the } Q\text{-point}), \quad (9)$$

where ΔV_a is the peak-to-peak anode voltage swing.

The power gain is

$$G_p = (\Delta V_a / \Delta V_g)^2 \quad (\text{at the } Q\text{-point}). \quad (10)$$

For example, in Figure 4, if the DC bias point (Q -point) is chosen to be $V_a = 1$ kV and $V_g = -3.5$ V, then $I_a = 103$ mA and $I_g \approx 0$ mA. Therefore the DC anode dissipation is 1 kV \times 103 mA = 103 W. If ΔV_g is chosen to be 5.5 V and the DC power supply voltage is chosen to be $V_B = 2$ kV, then the example load line is constructed by connecting point $V_B = 2$ kV and the Q -point, as shown in Figure 4. If ΔV_g is chosen to be 5.5 V, then the

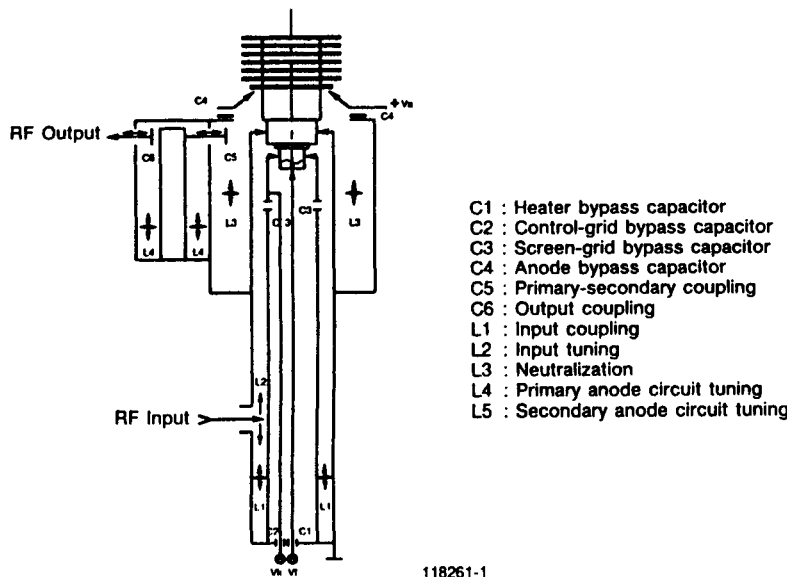


Figure 5. An electrical schematic diagram of cavity mounted microwave power triode TH 326 (courtesy Thomson Tubes Electroniques).

swing of the grid voltage is

$$-9.0 \text{ V} < V_g < +2 \text{ V}. \quad (11)$$

From Figure 4, the corresponding swing of the anode current along the example load line is

$$25 \text{ mA} < I_a < 180 \text{ mA}. \quad (12)$$

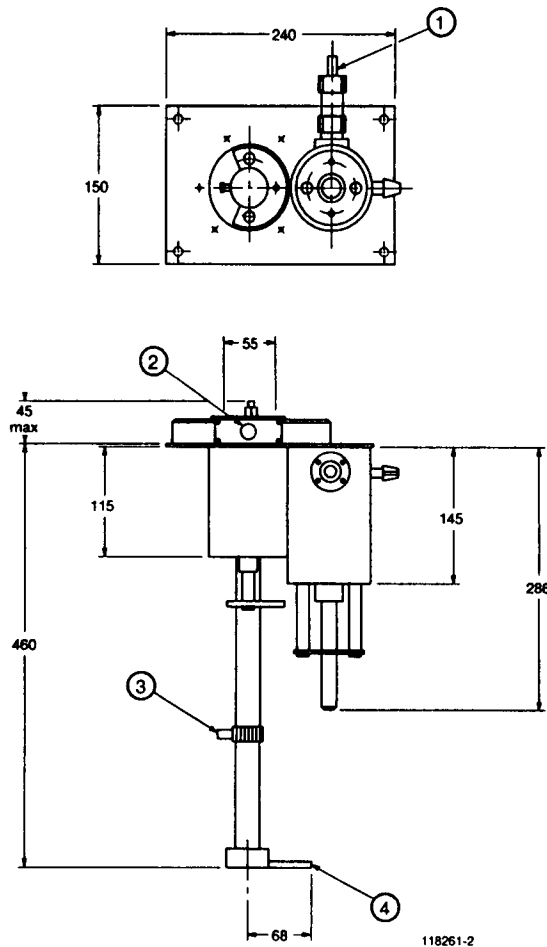


Figure 6. Mechanical outline drawing of a cavity mounted microwave power triode TH 326 (courtesy Thomson Tubes Electroniques).

Therefore

$$\Delta I_a \approx \frac{180 - 25 \text{ mA}}{2} = 77.5 \text{ mA.} \quad (13)$$

The swing of anode voltage V_a along the example load line is

$$0.2 \text{ kV} < V_a < 1.72 \text{ kV.} \quad (14)$$

Therefore

$$\Delta V_a \approx \frac{1.72 - 0.2 \text{ kV}}{2} = 0.76 \text{ kV.} \quad (15)$$

The microwave output power, P , is

$$P = \frac{1}{2} \Delta V_a \Delta I_a = \frac{1}{2} 0.76 \text{ kV} \times 77.5 \text{ mA} \approx 29 \text{ W.} \quad (16)$$

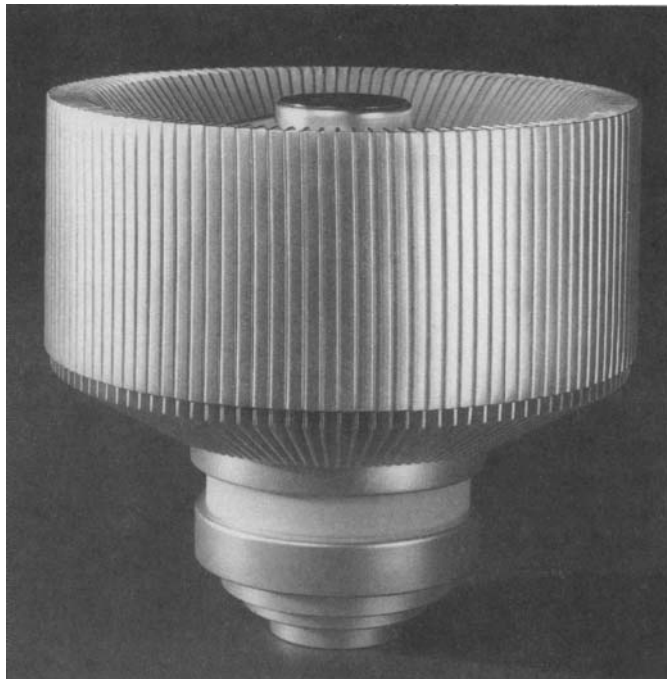


Figure 7. A picture of microwave power triode TH 328 (courtesy Thomson Tubes Electroniques).

The transconductance is

$$g_m = \frac{\Delta I_a}{\Delta V_g} = \frac{77.5 \text{ mA}}{5.5 \text{ V}} \approx 14 \text{ mS.} \quad (17)$$

The voltage gain is

$$G_v = \frac{\Delta V_a}{\Delta V_g} = \frac{0.76 \text{ kV}}{5.5 \text{ V}} \approx 138 \quad (18)$$

or

$$G_v (\text{dB}) = 20 \log_{10} G_v = 20 \log_{10} 138 \approx 43 \text{ (dB).} \quad (19)$$

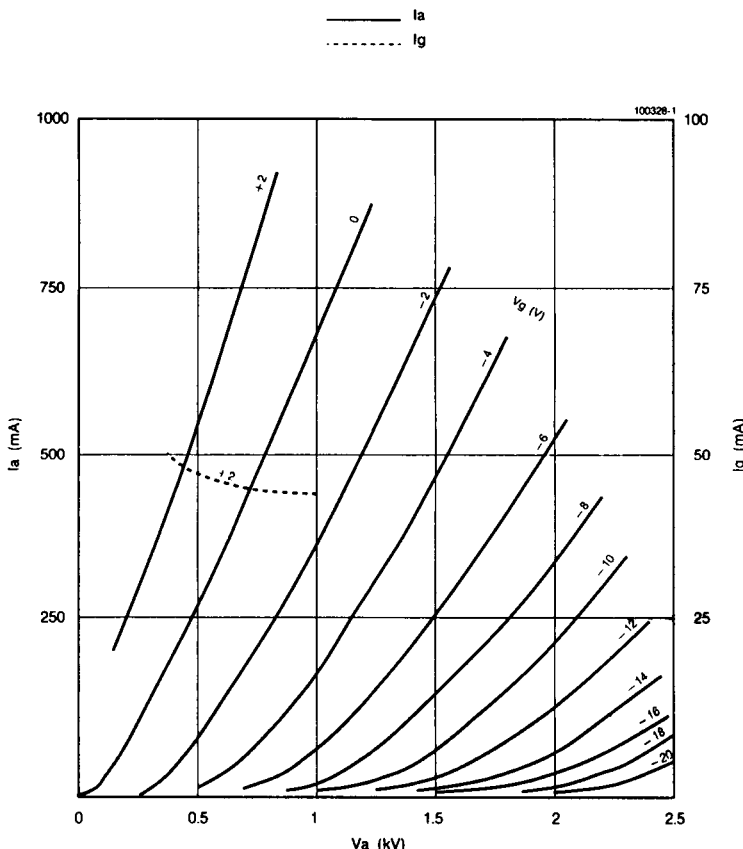


Figure 8. A performance chart of microwave power triode TH 328 (courtesy Thomson Tubes Electroniques).

The power gain is

$$G_p = G_v^2 = (138)^2 = 1.9044 \times 10^4 \quad (20)$$

or

$$G_p (\text{dB}) = 10 \log_{10} G_p = 10 \log_{10} 1.9044 \times 10^4 \approx 43 \text{ (dB)}. \quad (21)$$

A schematic circuit diagram of a cavity mounted microwave triode, TH 326, is shown in Figure 5. Microwave input signals are fed to the grid-cathode coaxial reentrant and tunable cavity resonator through a coaxial cable. The cavity is tunable by a tuning plunger, L_1 . The input coupling position is adjustable by sliding L_2 . The heater and cathode access is provided by C_1 and C_2 through the inner metallic tube for the cathode. The anode cavity is tuned by L_3 and C_5 . This cavity is acting as an impedance matching transformer. Real resonance to the anode cavity is provided by separate reentrant coaxial cavity L_4 and C_6 . The microwave output is taken out of C_6 .

A mechanical drawing of the TH 326 microwave vacuum triode is shown in Figure 6. The microwave coaxial cable input is at Port 3. The amplified output comes out of a coaxial output at Port 1. This is attached to the separate coaxial reentrant cavity resonator. The cylindrical structure

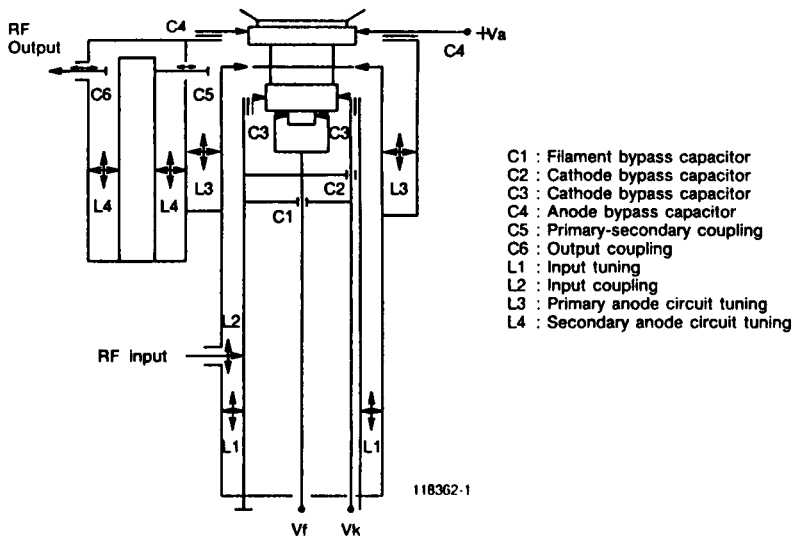


Figure 9. An electrical schematic diagram of cavity mounted microwave power triode TH 328 (courtesy Thomson Tubes Electroniques).

next to it houses the TH 326 microwave vacuum triode. Cooling air to the anode is provided through Port 2, and the cooling air for the rest of the tube is provided through Port 4. The structure is 505 mm tall, 240 mm wide, and 165 mm deep.

A second example of microwave vacuum triode TH 328 is shown in Figure 7. The top metallic structure with the cooling fin is the anode structure. The middle metallic ring is the grid access, and the bottom metallic structure houses the cathode and heater assembly. This is 110 W with an operating frequency up to 1000 MHz. The typical microwave

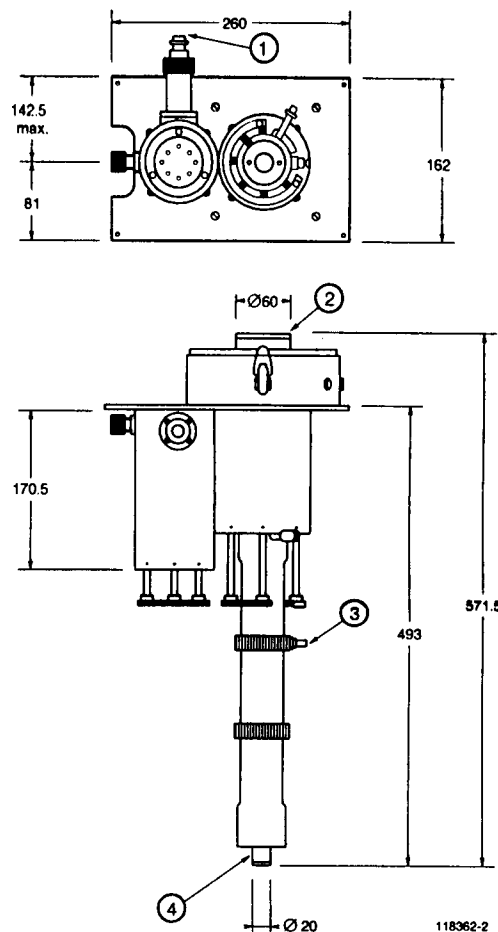


Figure 10. Mechanical outline drawing of activity mounted microwave power triode TH 328 (courtesy Thomson Tubes Electroniques).

power gain is 20 dB, and the anode power dissipation is up to 750 W, with forced air cooling to make the tube's operating temperature less than 250°C. The air flow should be at least 470 l/min. The air pressure difference of 1 mbar is required between the air inlet and the air outlet. The maximum outlet air temperature is 100°C. This tube is an oxide cathode with indirect heating. The approximate heater current is 5.4 A. The cathode-grid capacitance is 19 pF, the cathode-anode capacitance is 0.07 pF, and the grid-anode capacitance is 8.2 pF. The average amplification factor is 180 and the transconductance is 85 mA/V when the anode current is 400 mA.

The DC operating anode voltage can be as high as 2.2 kV, and the maximum DC anode current is 0.6 A. The DC grid bias voltage is up to -6 V. This tube can be operated at any orientation, and it weighs 950 g. A performance chart for TH 328 is shown in Figure 8.

A schematic diagram of TH 328 mounted on a cavity resonator system is shown in Figure 9. The grid-cathode coaxial reentrant cavity resonator is tuned by a coaxial shorting plunger, L_1 . The microwave input signal to



Figure 11. A picture of microwave power triode TH 339 (courtesy Thomson Tubes Electroniques).

be amplified is sent in through a coaxial coupling, L_2 . The anode-grid cavity is tuned by L_3 , and the output cavity resonator is tuned by a coaxial resonator, L_4 . The anode cavity and the output cavity are coupled by a coupling electrical probe, C_5 . The amplified microwave output is coupled out through the output coupling C_6 . The access to the cathode and the heater is obtained by the innermost cylinder. The filament heating lead V_f is connected to the heater structure through the microwave bypass filter capacitor C_1 . The cathode lead V_K is connected to the cathode through a microwave bypass capacitor, C_2 , and the cathode cylinder is DC insulated by C_3 , a bypass capacitor.

An outline drawing of a TH 328 microwave power amplifier assembly is shown in Figure 10. The microwave input is fed at Port 3. The amplified output comes out at Port 1. The anode cooling forced air is fed from the top at Port 2. The rest of the tube is cooled by forced air fed in Port 4. The assembly is 571.5 mm tall, 260 mm wide, and 192 mm deep.

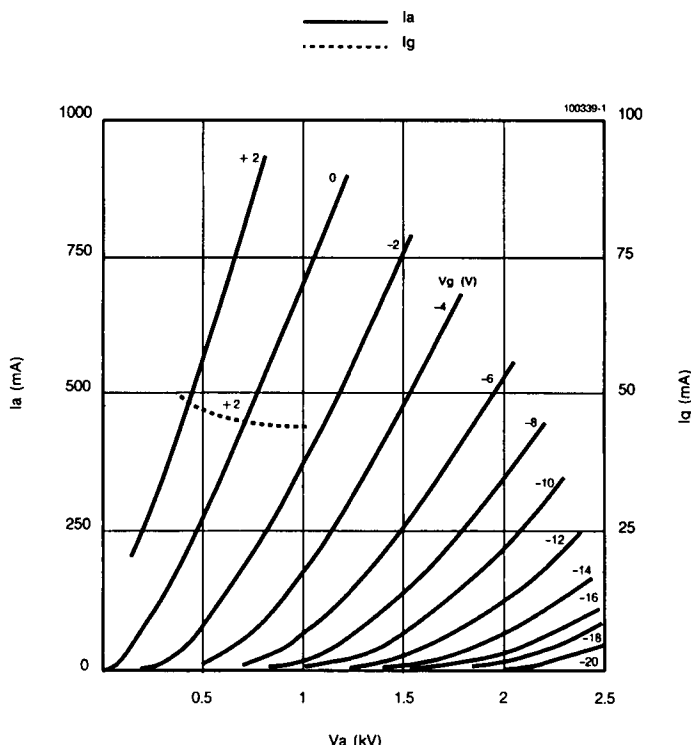


Figure 12. A performance chart of microwave power triode TH 339 (courtesy Thomson Tubes Electroniques).

A third example of a microwave power vacuum tube triode TH 339 is shown in Figure 11. This is a 220-W tube operable at up to 1000 MHz with a typical power gain of 20 dB and an anode dissipation up to 1200 W. The DC anode voltage can be as high as 2.2 kV, and the DC control grid bias voltage can be as high as -100 V. The peak cathode current can be as high as 2.5 A, and the average DC anode current is 600 mA. This tube has an indirect heated oxide cathode which requires a heater current of 5.5 A. The cathode-grid capacitance is 19 pF, the cathode-anode capacitance is 0.07 pF, and the grid-anode capacitance is 8.2 pF. The average amplification factor is 180, and the transconductance at an anode current of 400 mA is 85 mA/V. This tube can be operated at any orientation. It weighs approximately 1.2 kg. Forced air cooling of 1250 l/min to the anode is required for the anode dissipation of 1 kW. The air pressure drop across the air inlet and the air outlet should be 4.5 mbar, and the maximum air temperature at the output should be 100°C. The maximum operating temperature of the tube should be 250°C. A performance chart for TH 339 is shown in Figure 12.

A schematic diagram of TH 339 with its cavity circuit is shown in Figure 13. The grid-cathode cavity resonator is tuned by a coaxial shorting plunger L_1 , and microwave input signals are fed through a coaxial coupling, L_2 . The anode-grid cavity resonator is tuned by a coaxial shorting plunger, L_3 . A separate reentrant cavity resonator is tuned by a coaxial

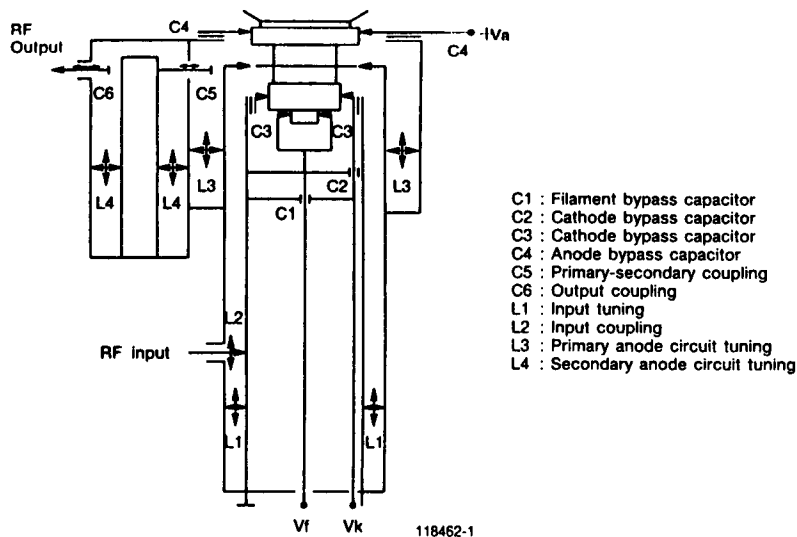


Figure 13. An electrical schematic diagram of cavity mounted microwave power triode TH 339. (courtesy Thomson Tubes Electroniques).

shorting plunger, L_4 . The coupling to the output coaxial line is adjusted by the output coupler C_6 . The whole cavity structure is insulated from the DC anode voltage by a bypass capacitor, C_4 , and from the DC cathode bias voltage by a bypass capacitor C_3 . The access to the heater V_f of the cathode is obtained through the inside of the innermost cylinder through a bypass capacitor, C_1 , and the return of the filament heater current and access to the cathode V_K are also in the inside of the innermost cylinder through a bypass capacitor, C_2 .

A structure drawing of the cavity mounted TH 339 microwave triode power amplifier is shown in Figure 14. Microwave signals are fed in Port 3,

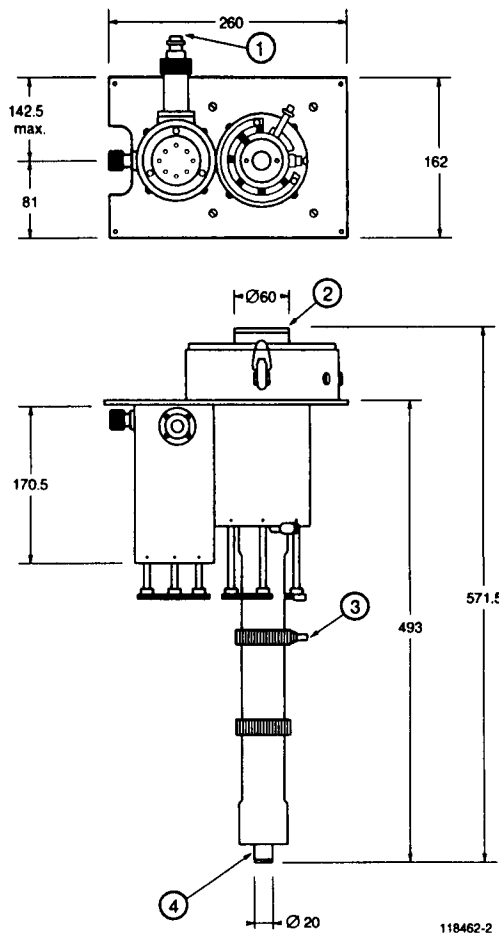


Figure 14. Mechanical outline drawing of a cavity mounted microwave power triode TH 339 (courtesy Thomson Tubes Electroniques).

and the amplified microwave signals come out from Port 1. Forced air cooling for the anode comes in at Port 2, and the rest of the tube is cooled by the forced air fed to Port 4.

3. Principles of Microwave Thermionic Tetrodes

The principles of microwave thermionic tetrodes [1–4] are similar to those of the microwave thermionic triodes as far as the microwave amplification and oscillation are concerned. However, the structures of tetrodes are different from those of the triodes. There is one more grid between the control grid and the anode. A schematic diagram of a microwave tetrode circuit is shown in Figure 15. As seen in this figure, the screen grid is DC biased positively. The screen grid reduces interelectrode capacitance between the anode and the control grid by absorbing space charges. As seen in Figure 15, the screen grid is DC biased positively, yet it is RF grounded by the bypass capacitor. Therefore it shields the control grid from the anode to prevent or reduce the feedback from the anode. The feedback through the interelectrode capacitance may cause instability and oscillation.

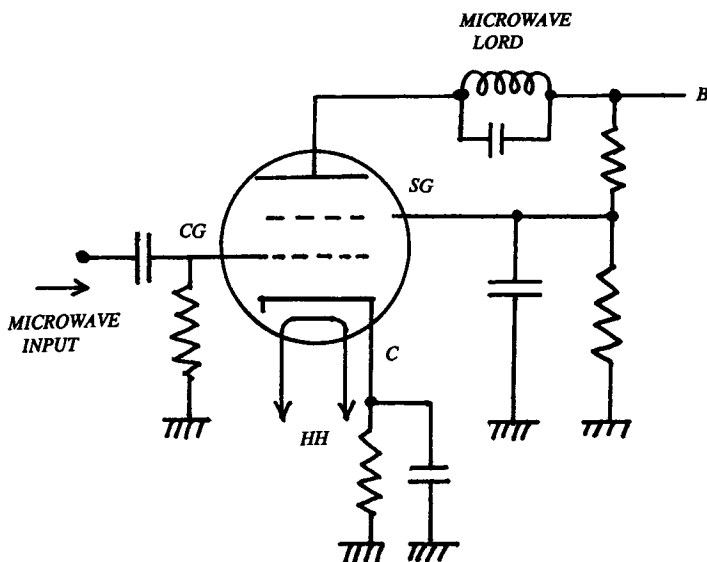


Figure 15. A schematic diagram of a microwave tetrode amplifier.

tion at high-gain operation if it is not properly controlled. The screen grid makes the tube operation stable at high-gain operation. Therefore, generally, microwave thermionic tetrodes are of much higher power than microwave thermionic triodes.

A schematic diagram of a cavity mounted microwave vacuum tetrode is shown in Figure 16. Microwave input power is fed through an input coupler to the cavity between the control grid and the cathode. The cavity itself is grounded and DC insulated using bypass capacitor rings at the contacts between the tube electrodes and the cavity. The grid-cathode cavity resonator is tuned by the use of the grid cavity tuner. The amplified microwave power at the anode is taken out through the output coupler in the anode-screen grid cavity resonator. The cavity resonator is tuned using the anode cavity tuner. Access to the screen grid and the control grid for DC biasing V_{cg} and V_{sg} , respectively, is obtained through a gap between the anode cavity and the cathode cavity, as shown in Figure 16. Access to the heaters and cathode biasing are provided using a cathode socket.

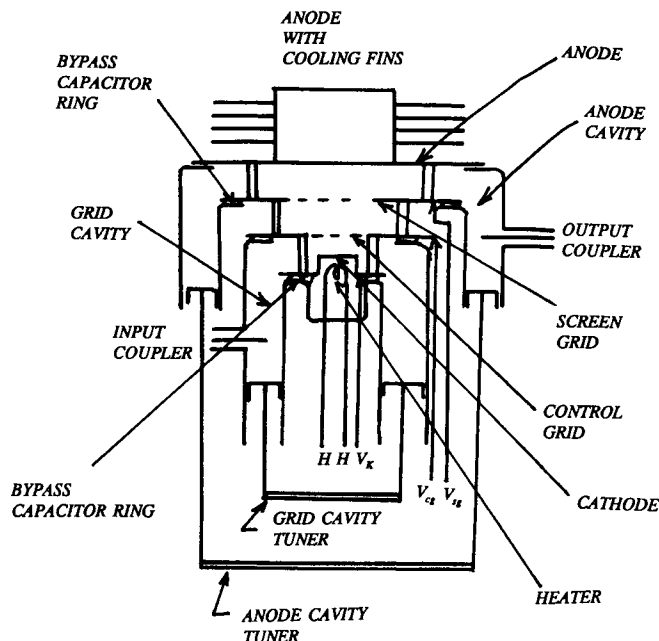


Figure 16. A configuration of a cavity mounted lighthouse type microwave vacuum tetrode.

4. Examples of Microwave Thermionic Tetrodes

An example of 1.1-kW, 1-GHz microwave thermionic tetrode [4, 5] TH 547 is shown in Figure 17. The upper cylindrical structure contains the anode and its cooling structure. This tube has an anode dissipation up to 5 kW. It requires 5 kV to operate, with an anode current of $0.1 \sim 4$ A. A typical power gain of 16 dB is expected. The second ring from the top is for the screen grid. It is DC biased normally up to $V_{g2} = +650$ V. The screen grid current may be as high as $I_{g2} = 200$ mA. The screen grid dissipation can be as high as 25 W. The third ring from the top is for the control grid. The control grid is DC biased at $V_{g1} = -200$ V. The control grid current range is $I_{g1} = 100 \sim 800$ mA, and the control grid power dissipation may be as high as 5 W. The lowest cylindrical structure in Figure 17 is for the cathode and heater assembly for the TH 547 microwave power tetrode.



Figure 17. A picture of microwave power tetrode TH 547 (courtesy Thomson Tubes Electroniques).

This tube uses a thoriated tungsten cathode. The heater requires 34 A of current.

The capacitance between the cathode and the control grid of this tube is 40 pF, and the capacitance between the anode and the cathode is 0.02 pF. The capacitance between the control grid and the screen grid is 50 pF, and the capacitance between the control grid and the anode is 0.18 pF. The capacitance between the screen grid and the anode is 8.2 pF. The average amplification factor is 7. The transconductance of this tube at the anode current $I_a = 1$ A and the screen grid voltage $V_{g2} = 500$ is 40 mA/V. This tube must be operated in a vertical position with the anode up. The anode is water cooled. To combat against 5 kW of anode dissipation, at least 3 l/min of water flow is needed. The water pressure at the water inlet should be 5 bar. The maximum temperature of the outlet water should not exceed 100°C. Electrode-terminal rings and the tube ceramic body must be cooled by forced air. The tube body temperature should not exceed 250°C. The maximum diameter of this tube is 9.4 cm, and the tube is 15.6 cm tall. The weight of the tube is 2.1 kg.

A performance chart for TH 547 is shown in Figure 18. This chart is for the operation of the tube at the screen grid voltage $V_{g2} = 400$ V. The

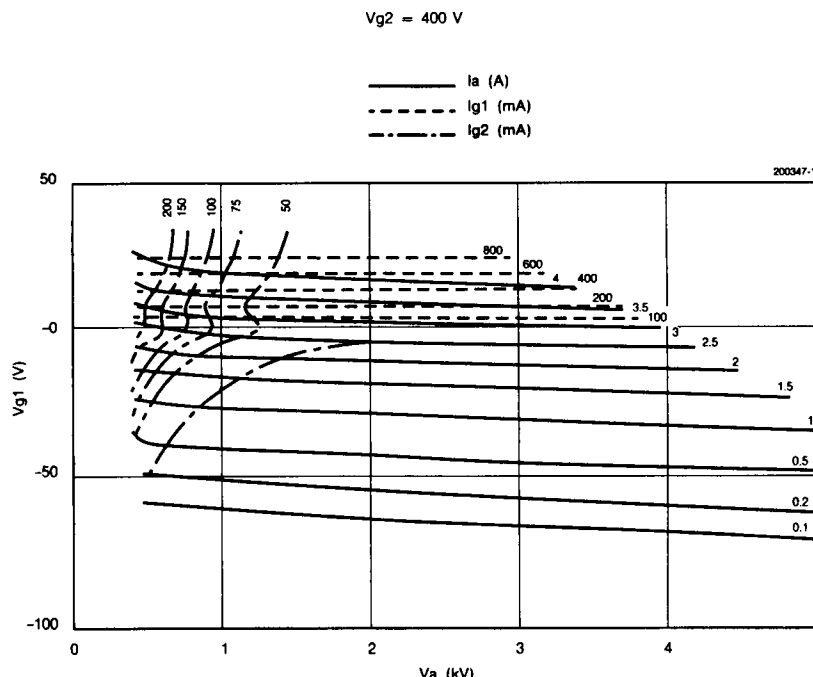


Figure 18. A performance chart of microwave power tetrode TH 547 (courtesy Thomson Tubes Electroniques).

solid line shows the anode current I_a in amperes, the dashed line shows the grid current I_{g1} in milliamperes, and the chain lines represent the screen grid current I_{g2} in milliamperes.

An electrical schematic diagram of cavity mounted TH 547 is shown in Figure 19. Microwave input power is fed to the grid cavity resonator through a tunable input coupler, L_2 . The grid cavity is tuned by a tuner, L_1 . Amplified microwave power is taken out of the tube from the anode cavity by a coupler, C_5 . The anode cavity resonator is tuned by a tuner, L_4 . A secondary high- Q semicoaxial reentrant cavity resonator is tuned by a ring shaped tuner, L_5 . The microwave power is taken to the outside circuit through an output capacitive coupling, C_5 . Cavities are DC insulated through microwave bypass capacitor C_1 at the heater cathode, C_2 at the control grid, C_3 at the screen grid, and C_4 at the anode. Filament heater current is fed through a terminal, V_f , within the cylindrical structure in the cathode socket. The negative bias voltage for the control grid is fed from the terminal $-V_{g1}$ through a lead wire running along the cavity wall of the grid cavity. The screen grid is positively biased from terminal $+V_{g2}$ through a wire running in the cap between the grid cavity and the anode cavity. The anode voltage is fed to the anode through terminal $+V_a$ directly.

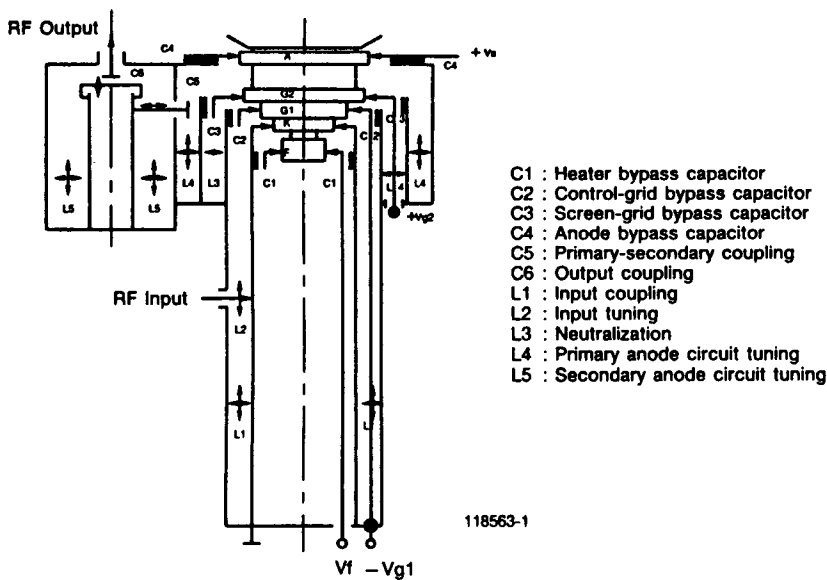


Figure 19. An electrical schematic diagram of cavity mounted power tetrode TH 547 (courtesy Thomson Tubes Electroniques).

A mechanical outline drawing of a cavity mounted TH 547 microwave power tetrode is shown in Figure 20. The microwave input is fed at Port 2, and the amplified power is taken out from a coaxial output at Port 1. The forced air for cooling the tube body comes out at Port 3. This amplifier is 67 cm tall, 28.8 cm wide, and 17.4 cm deep.

Another example of a microwave vacuum power tetrode, TH 584, is shown in Figure 21. This is a 1-GHz, 10.5-kW tube. This tube has a thoriated tungsten cathode, and it requires 130 A of heater current.

This tube must be operated in a vertical position with the anode structure up. The tube itself weighs 4.1 kg. The maximum diameter of this

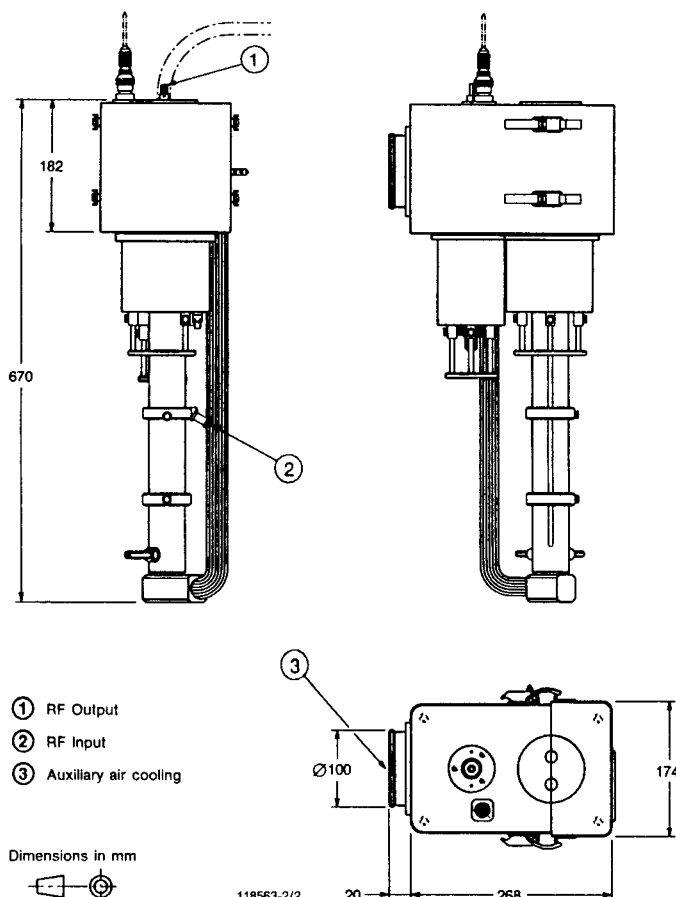


Figure 20. Mechanical outline drawing of cavity mounted microwave power tetrode TH 547 (courtesy Thomson Tubes Electroniques).



Figure 21. A picture of microwave power tetrode TH 584 (courtesy Thomson Tubes Electroniques).

tube is 12.8 cm, and the height is 16.6 cm. The capacitance between the cathode and the control grid is 72 pF, that between the cathode and the anode is 0.03 pF, that between the control grid and the screen grid is 93 pF, that between the control grid and the anode is 0.37 pF, and that between the screen grid and the anode is 13.2 pF. The average amplification factor of this tube is 8, and the transconductance, with an anode

voltage of 7 kV, a screen grid voltage of 300 V, and an anode current of 2 A, is 80 mA/V.

The typical power gain of this tube is 15 dB. The cylindrical structure on the top in Figure 21 is the anode and its cooling structure. The anode dissipation is up to 25 kW, operated at the anode voltage of 7 kV and the anode current of 4.5 A. The tube can stand a maximum anode current of 22 A. Therefore it must be cooled by water. It requires cooling water of 15 l/min with a maximum water pressure of 5 bar at the inlet. The cooling water temperature at the outlet must be less than 100°C. The ring second

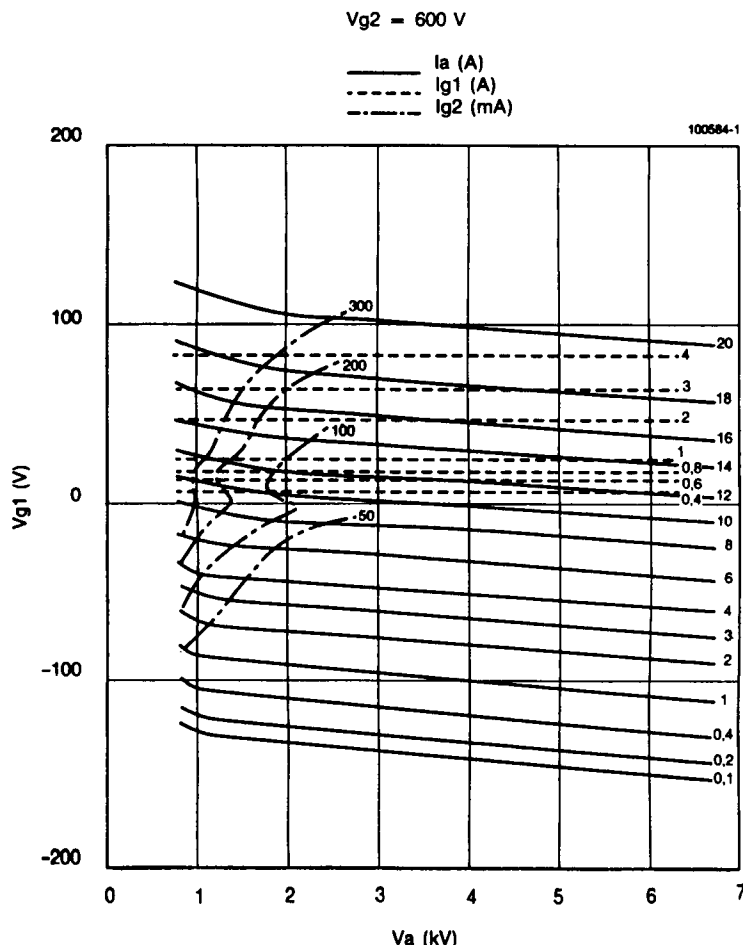


Figure 22. A performance chart of microwave power tetrode TH 584 (courtesy Thomson Tubes Electroniques).

from the top in Figure 21 is for the screen grid. The screen grid is biased at +800 V dc. The operating screen grid current is in a range of 50–300 mA. The screen grid dissipation is up to 120 W. The third ring from the top in Figure 21 is for the control grid. The control grid is dc biased at –200 V. The operating control grid current ranges from 0.4 mA to 4 A. The control grid dissipation can be up to 50 W. The bottom cylindrical structures are for the cathode and heater assembly. A performance chart for power thermionic tetrode TH 584 is shown in Figure 22. In this chart, solid lines show constant anode current curves in amperes. The dashed lines show constant controlled grid current curves in amperes. The chain lines show constant screen grid current curves in milliamperes.

An electrical schematic diagram of a cavity mounted TH 584 microwave power tetrode is shown in Figure 23. Microwave input power is fed to the grid cavity through a coaxial cable and a tunable input coupler, L_1 . The grid cavity is tuned by a tuning ring, L_2 . The amplified microwave power is taken out from the anode cavity through a tunable output coupler, C_6 . The anode cavity is tuned by using tuning rings L_4 and L_5 . The entire cavity is dc insulated from the tube using bypass capacitor rings C_1, C_2, C_3 , and C_4 . Access to the anode to supply the anode voltage is directly from the outside through terminal $+V_a$. Access to the screen grid

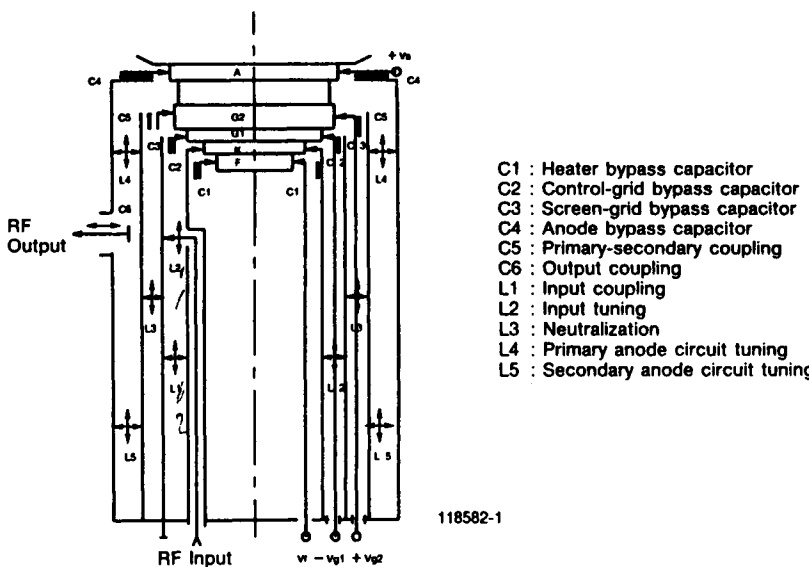


Figure 23. An electrical schematic diagram of cavity mounted microwave power tetrode TH 584 (courtesy Thomson Tubes Electroniques).

G_2 to supply the bias voltage to the screen grid is through the gap between the anode cavity and the grid cavity through terminal $+V_{g2}$. Access to the control grid to supply negative DC control grid bias voltage is obtained using a line along the wall of the grid cavity resonator through the $-V_{g1}$ terminal. Access to the filament is obtained through a socket with a lead wire from terminal V_1 .

A mechanical outline drawing of a cavity resonator mounted microwave power tetrode, TH 584, is shown in Figure 24. The microwave input power is fed at Port 4, and the amplified microwave power comes out at Port 2. The top structure is for water cooling the anode. The tube body is cooled by forced air. The cooling air inlet is at Port 3, and the

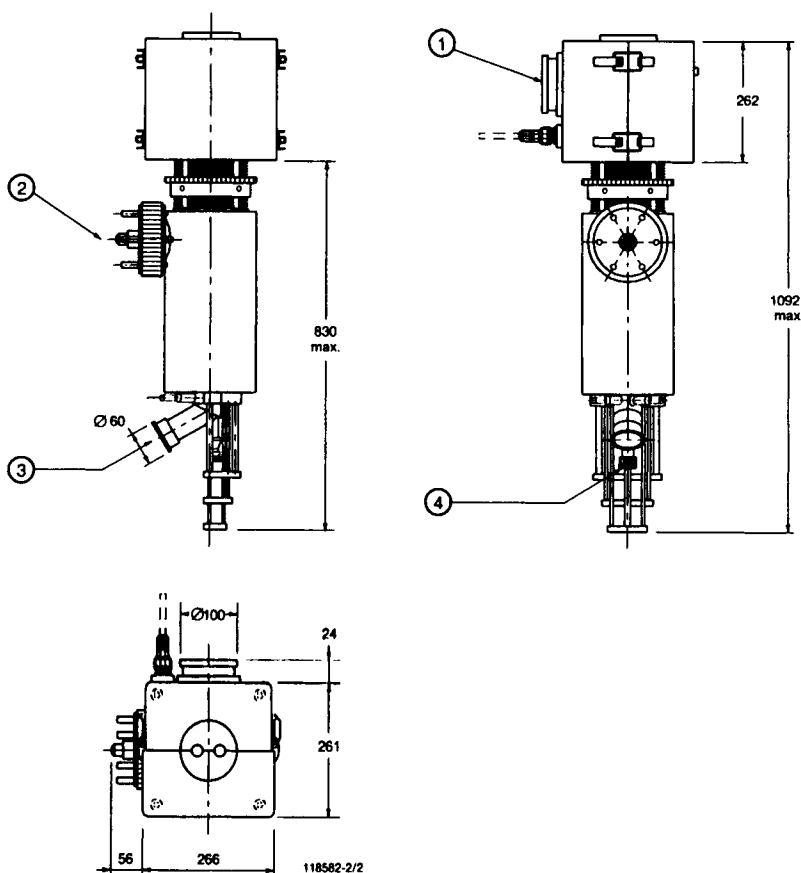


Figure 24. Mechanical outline drawing of cavity mounted microwave power tetrode TH 584 (courtesy Thomson Tubes Electroniques).

cooling air outlet is at Port 4. This structure is 1.092 m high, 32.2 cm wide, and 28.5 cm deep.

An example of a microwave high-power vacuum tetrode, TH 582, is shown in Figure 25. This can output 22 kW at 1 GHz with a power gain of 15 dB. The top cylindrical structure and ring are for the anode and its cooling. The anode is normally operated at the anode voltage of $V_a = 7.5$ kV. The normal anode current is 5.5 A, and the anode dissipation is 25 kW. Therefore the anode is water cooled. It requires 15 l/min of distilled water at least. The maximum pressure at the water inlet must be 5 bar, and the water temperature at the outlet should be less than 100°C. The second ring from the top is for the screen grid. The screen grid is positively biased at 900 V. The screen grid dissipation can be as high as 120 W. The screen grid terminal ring must be water cooled. A minimum water flow of 1.5 l/min is required. The third ring from top in Figure 25 is



Figure 25. A picture of microwave power tetrode TH 582 (courtesy Thomson Tubes Electroniques).

a ring for the control grid. The control grid is biased at -200 V. This grid will have a dissipation up to 50 W. The fourth ring from the top is for the cathode. This tube uses a thoriated tungsten cathode. The maximum cathode current can be as high as 22 A. This cathode is heated by a heater which is in the bottom cylindrical structure in Figure 25. The heater current is 146 A.

The interelectrode capacitance between the cathode and the control grid is 72 pF, that between the cathode and the anode is 0.03 pF, that between the control grid and the screen grid is 93 pF, that between the control grid and the anode is 0.37 pF, and that between the screen grid and the anode is 13.2 pF. This tube produces an average amplification factor of 8 and a transconductance of 80 mA/V with the anode current $I_a = 2$ A and $V_{g2} = 300$ V.

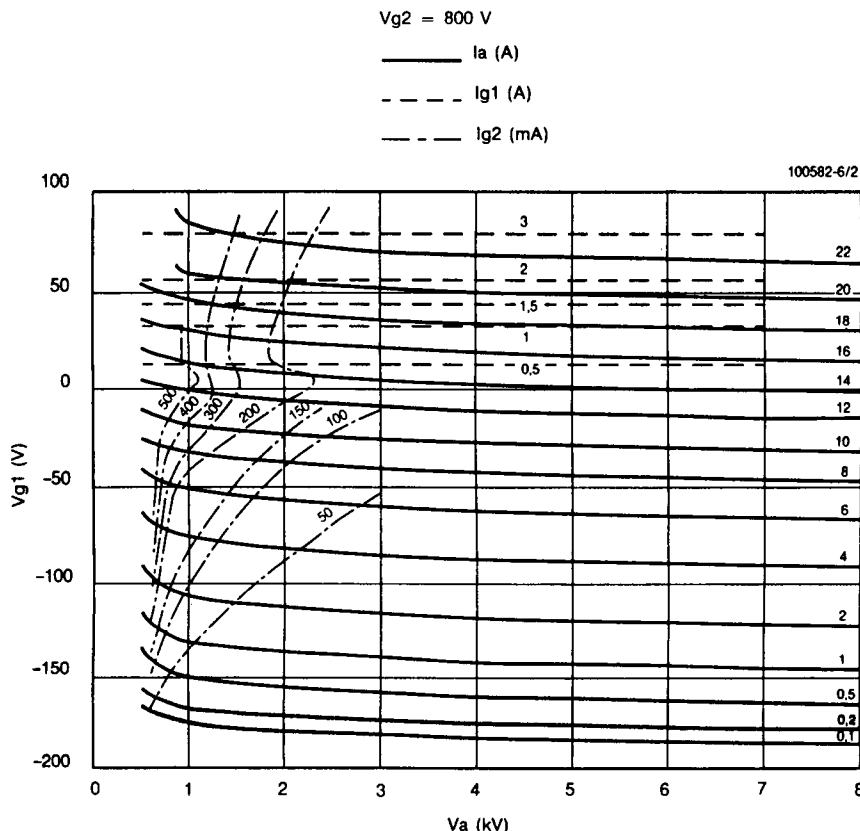


Figure 26. A performance chart of microwave power tetrode TH 582 (courtesy Thomson Tubes Electroniques).

This tube can be operated in a vertical position only with its anode up. This tube weighs 4.1 kg. The maximum diameter of this tube is 12.8 cm, and the total height of this tube is 16.6 cm. The maximum allowable tube body temperature including the electrode terminal rings and ceramic insulator is 300°C. The tube body must be cooled by forced air.

A performance chart for the TH 582 power tetrode is shown in Figure 26. The screen grid was operated at a constant voltage of $V_{g2} = 800$ V. The solid line curves show constant anode current curves with current values listed in amperes. The dashed lines are constant control grid current curves. The constant control grid current values are listed in amperes. The chain line curves are constant screen grid current curves. The constant screen grid current values are listed in milliamperes.

The electrical schematic diagram of TH 582 is the same as that in Figure 23. The mechanical outline drawing of TH 582 is the same as that in Figure 24.

5. Conclusions

Microwave vacuum power triodes and tetrodes are economical and practical power amplifiers in the frequency range of 0.3 to 1 GHz and the power range of 50 to 22,000 W. The efficiency of these power tubes ranges from 16% for a smaller power rating to 73% for pulse operated high-power tubes. In this range of high power and high frequency, solid-state devices are out of reach even by today's technology. Solid-state devices of this capability are not available with reasonable cost.

As for an emerging technology, monolithically developed microminiature solid-state vacuum triodes using cold emission cathodes have been developed and reported elsewhere [6]. The advantage of such microminiature vacuum triodes over well-developed transistors is limited. They may never hit the market except for limited specifications.

References

- [1] T. Koryu Ishii, *Microwave Engineering*. San Diego: Harcourt Brace Jovanovich, 1989.
- [2] T. Koryu Ishii, *Practical Electron Devices*. San Diego: Academic Press, 1990.
- [3] S. Y. Liao, *Microwave Electron-Tube Devices*. Englewood Cliffs, NJ: Prentice-Hall, 1988.
- [4] Thomson-CSF Electron Tube Div., "TV and FM-Radio Power-Grid Tubes and Matched RF-Circuit Assemblies," Boulogne-Billancourt, Cedex, France, 1987.
- [5] C. Loring, Jr., and M. Shrader, The Klystrode, a new high efficiency, high power electron tube for UHF industrial applications, *J. Microwave Power Electromagn. Energy*, Vol. 28, No. 3, pp. 174-182, 1993.
- [6] H. Busta and A. Adler, Session 8: Vac. Electron.—Vac. Microelectron., *IEEE Int. Electron Devices Meet.*, Washington, DC, Dec. 1991.

Microwave Impedance Matching Techniques

S. N. Prasad

I. Introduction

Impedance matching is an essential part of the design of microwave devices or systems. Impedance matching is important for (a) maximum transfer of power from a generator to a device, from a device to a load, or between devices, (b) improving the sensitivity of receivers, (c) reducing the amplitude and phase imbalances in power distribution networks, and (d) minimizing power loss in feed lines. There are a variety of matching networks that can be synthesized to match two given impedances. The important factors to be considered in the selection of a matching network are: (a) complexity, (b) bandwidth, and (c) ease of implementation.

In this chapter, impedance matching techniques for narrow-band and wide-band applications are presented in Sections 2 and 3, respectively. The techniques for synthesizing lumped as well as distributed matching networks are illustrated by means of examples. In Section 4, selected balanced to unbalanced transformers are covered. The impedance matching techniques presented here are in general applicable to systems using parallel wire lines, coaxial lines, waveguides, or planar transmission lines such as strip lines, microstrip lines, and coplanar waveguides.

The extent of published literature on impedance matching is vast. In this chapter the author has made an attempt to cover only the important and commonly used techniques. For further reading on this subject,

several references have been given. The author hopes that the material covered in this chapter is useful to microwave engineers.

2. Narrow-Band Matching

In this section, the techniques of narrow-band matching will be illustrated with examples. The matching is accomplished perfectly only at the desired frequency. A bandwidth around the design frequency can be defined if the tolerable reflection coefficient in the band is specified.

The relationship between the impedances at the two ports of a lossless, reciprocal matching network designed to transform Z_2 to Z_1 are summarized in Figure 1. If an impedance, Z_2 , is connected at port 2 of the network, the impedance measured at port 1 is Z_1 . Then if an impedance, Z_1^* , is placed at port 1, the impedance measured at port 2 will be Z_2^* . Therefore, if Z_1^* represents the internal impedance of a source, then maximum power transfer to the load impedance Z_2 is ensured.

The foregoing property of a lossless, reciprocal network implies that the same network is capable of transforming Z_2 to Z_1 as well as Z_1^* to Z_2^* and hence offers one the option to choose from two design approaches: (a) transformation of Z_2 to Z_1 or (b) transformation of Z_1^* to Z_2^* . This property of the matching network may be verified in the design examples presented in this section.

The design of lossless matching networks consisting of lumped as well as distributed elements will be presented in the following sections. The graphical design procedures making use of the Smith chart as a tool are illustrated by means of examples. The theory and applications of the Smith chart are covered in detail in References [1–4]. Analytical solutions to matching circuit design problems can be found in References [2, 3, 5]. Smith chart solutions are sufficiently accurate for most applications. However, if better accuracy is needed, one may resort to analytical solutions.

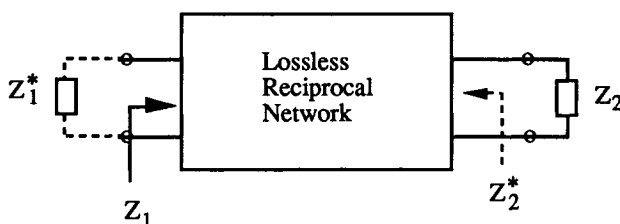


Figure 1. Impedance transformation by a lossless reciprocal network.

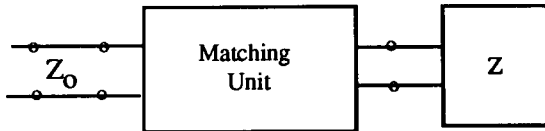


Figure 2. Matching impedance Z (complex) to impedance Z_0 (real).

Distributed Element Techniques

A lossless transmission line having characteristic impedance Z_0 and length l can be used in the transformation of $Z_1 (R_1 \pm jX_1)$ into $Z_2 (R_2 \pm jX_2)$. The values of Z_0 and l needed for the transformation can be determined analytically or graphically. However, practically realizable design usually involves tedious iterative process. Further, a realizable solution may not always exist.

The matching network design techniques which make use of lossless transmission lines as network elements will be presented here. A typical matching problem in practice involves matching a complex impedance (input or output impedance of a device) to a real impedance (source, load, or characteristic impedance of a line), as shown in Figure 2.

Single-Stub Matching

Shunt Stubs The basic single-stub matching system is shown in Figure 3. The transmission lines in the matching unit can be realized as coaxial lines, parallel wire lines, or planar transmission lines such as microstrip lines, strip lines, and coplanar waveguides.

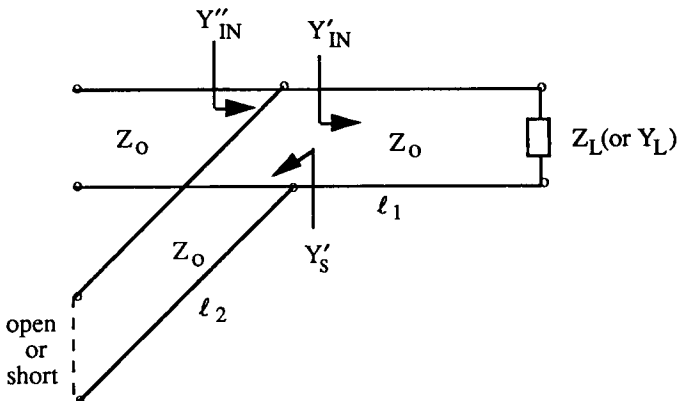


Figure 3. Single-stub matching system.

Principles of Single-Stub Matching The normalized load admittance Y'_L (normalized with respect to the characteristic admittance Y_0 of the line to which it is connected) is transformed to the unit conductance circle on the Smith chart by the transmission line of length l_1 . The normalized admittance looking toward the load is, then, $Y'_{IN} = 1 \pm jB'$. Now a length l_2 , of an open or short-circuited stub can be chosen such that the admittance Y'_S ($\mp jB'_S$) of the stub equals $\pm jB'$, thereby canceling the susceptance provided by Y'_{IN} . Then the admittance Y''_{IN} looking toward the load from just left of the stub is $1 + j0$. Thus the match is accomplished.

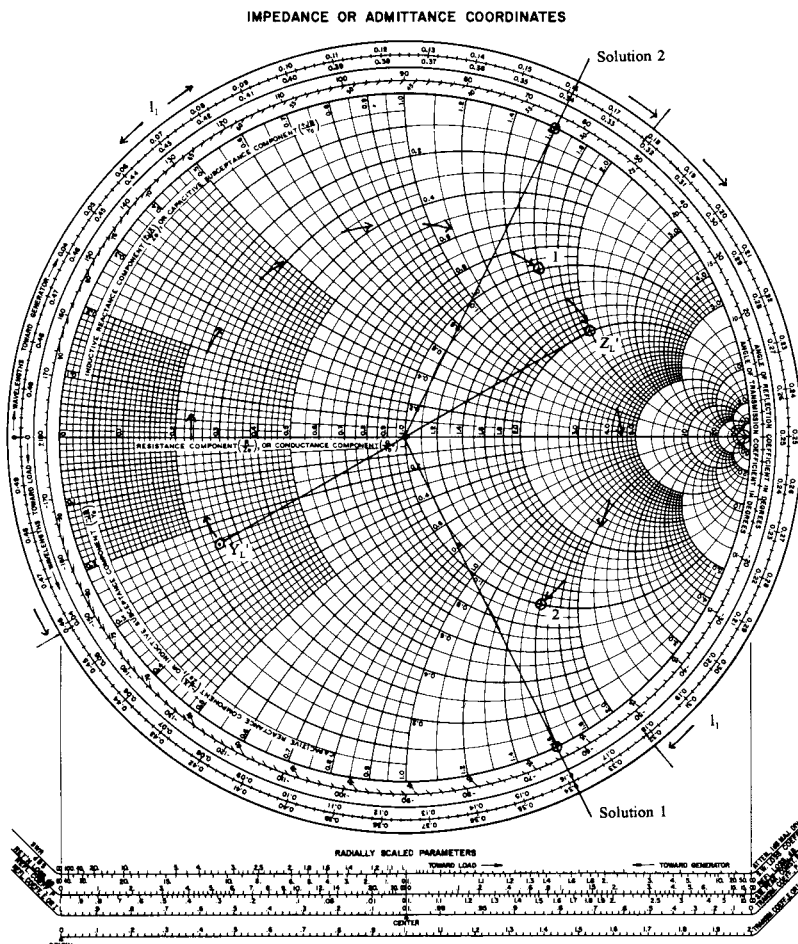


Figure 4. Solutions to the single-stub matching example problem.

Design Example Consider the problem of matching $Z_L = 100 + j100 \Omega$ to a line having a characteristic impedance $Z_0 = 50 \Omega$. The single-stub matching is illustrated on the Smith chart in Figure 4 for this example. The two solutions (using short-circuited stubs) to the design problem are shown in Figures 5a and 5b.

The matching solution in Figure 5a is preferable because it has a greater bandwidth and uses shorter lengths of transmission lines, and consequently the losses are smaller. The bandwidth of the matching unit is an important selection criterion. It should be noted that the addition of $n\lambda/2$ (where n is an integer) lengths of lines in the designs in Figure 5 will not affect the match.

In this example the line and the stub have the same characteristic impedance. If different characteristic impedances are used for the line and the stub, the impedances (or admittances) have to be appropriately normalized while using the Smith chart. The disadvantage of a single-stub system is that it requires an adjustable length of line of constant characteristic impedance in order to match to an arbitrary load. Such lines are difficult to construct in practice.

Series Stubs The schematic of a series stub matching system is shown in Figure 6. The distance d is selected so that the impedance, Z_{IN} , seen looking into the line at distance d from the load is of the form $Z_0 \pm jX$. Then the stub reactance is chosen as $\mp jX$, resulting in a match to the feed line impedance Z_0 . The line length, d , and the stub length, l , can be determined using a Smith chart. The reader is referred to the design example in Reference [2]. The series stub is difficult to fabricate in coaxial, strip-line, and microstrip-line systems, and hence this technique is not commonly used in practice. However, series stubs can be constructed easily in coplanar waveguide systems in which the center conductor as well as the ground plane is located on the same side of the circuit board.

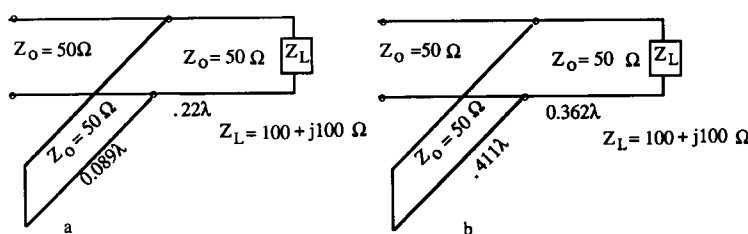


Figure 5. Solutions to the single-stub design problem.

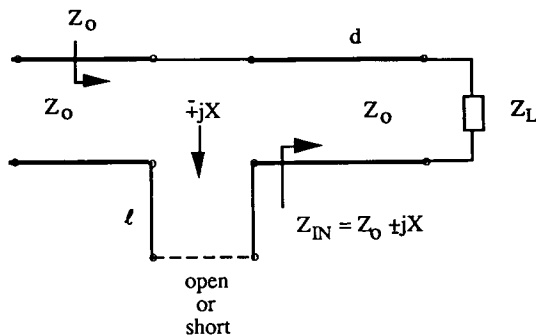


Figure 6. Series stub matching system.

Double-Stub Matching

A double-stub matching system is shown in Figure 7. The advantage of a double-stub system is that it uses only adjustable length stubs and a fixed length of line, unlike a single-stub tuner. However, a double-stub tuner cannot match an arbitrary load impedance, unlike a single-stub tuner.

Principle of Double-Stub Matching The length l_1 must be chosen such that the admittance of the load and stub (open or shorted) in parallel is transformed to the unit conductance circle on the Smith chart by the fixed length d of the line. Then the normalized admittance Y'_{IN} seen looking toward the load is $1 \pm jB'$. Then the length l_2 of the second stub (open or shorted) must be chosen such that its admittance Y'_s ($\mp jB'_s$) cancels $\pm jB'$. Then the normalized admittance Y''_{IN} looking toward the load from just

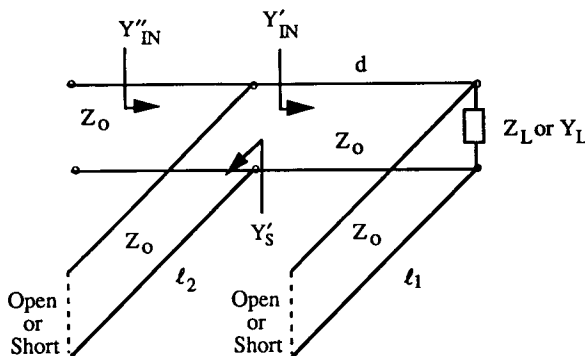


Figure 7. Double-stub matching system.

left of the second stub is $1 + j0$, and hence the match to the feed line impedance Z_0 is obtained.

In order to determine the length (l_1) of the first stub, the unity conductance circle is rotated on the Smith chart toward the load through a distance, d . Then the susceptance needed from the first stub is determined from the point of intersection of the load conductance contour and the rotated unity conductance circle. The susceptance needed from the second stub can then be determined from the corresponding point on the unity conductance circle.

Design Example Consider the problem of matching $Z_L = 100 + 100j (\Omega)$ to $Z_0 = 50 (\Omega)$; $d = \lambda/8$. The double-stub matching is illustrated on the Smith chart in Figure 8. The two solutions (using shorted stubs) are depicted in Figures 9a and 9b.

In this example problem, there is no appreciable difference between the solutions with regard to losses in the lines. But the solution in Figure 9a has a greater bandwidth. The distance d between the stubs must be chosen such that the conductance contour of the load admittance intersects the rotated unity conductance circle. Stub spacings of $\lambda/8$ and $3\lambda/8$ have been found to be reasonable choices in practice as far as matching range and critical adjustments are concerned.

If the load should happen to fall in the portion of the chart such that matching is not possible using a specified distance between the stubs, then it is necessary to add a fixed length of line between the load and the first stub in order to adjust the load to a value that can be matched. In this design example, the lines and the stubs have the same characteristic impedance. If different characteristic impedances are used for the line and the stubs, the impedances (or admittances) have to be appropriately normalized while using the Smith chart.

In practice, when stub matching is used in devices containing active components which need DC bias, the short circuits in the stubs are replaced by capacitors in order to provide DC bias through the stubs. The stub lengths in these cases must be calculated taking the capacitive reactance into account. Open stubs can be used only if designed properly to prevent radiation (e.g., open ended microstrip lines). The fringing capacitance at the open end must be accounted for in the design of the stubs.

Quarter-Wave Transformer

A load impedance (Z_L) having only a real part (R_L) can be matched to a transmission line having a characteristic impedance Z_0 by means of a quarter-wavelength ($\lambda/4$) of a transmission line as shown in Figure 10.

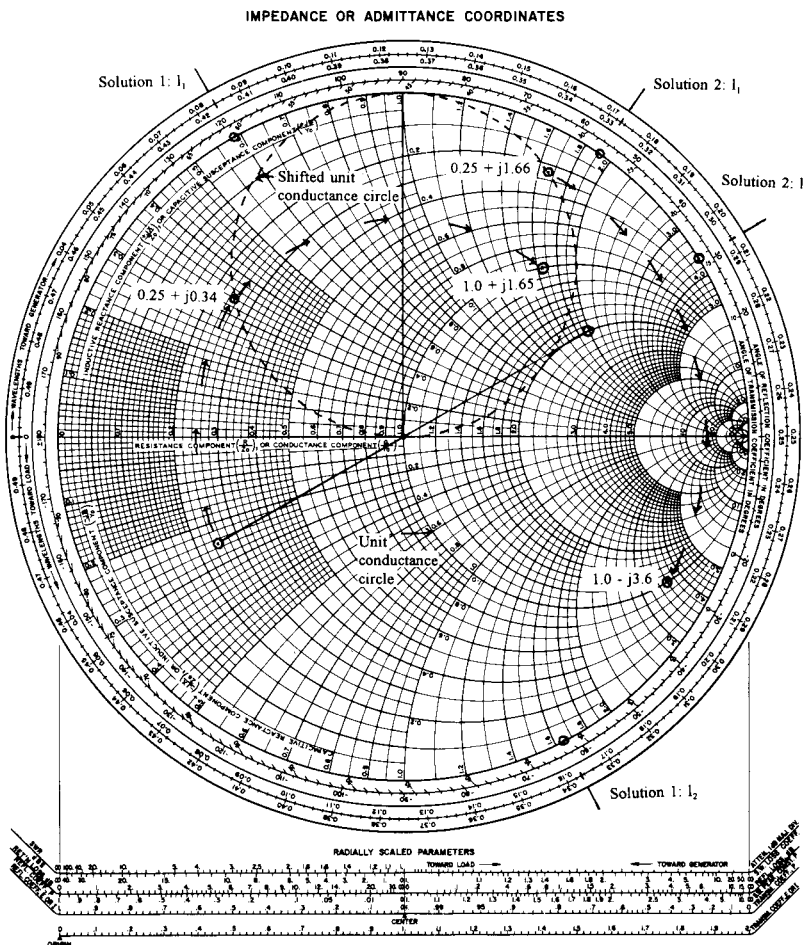


Figure 8. Solutions to the double-stub matching example problem.

λ is the wavelength in the quarter-wave section at the design frequency. The characteristic impedance of the quarter-wave section is given by

$$Z_T = \sqrt{R_L Z_0}$$

If the load impedance is complex ($R_L + jX_L$), one must convert it into a real impedance (R'_L) by means of an additional length (l) of line, as shown in Figure 11a or by tuning out the reactive part by means of a stub, as shown in Figure 11b, before designing the quarter-wave transformer.

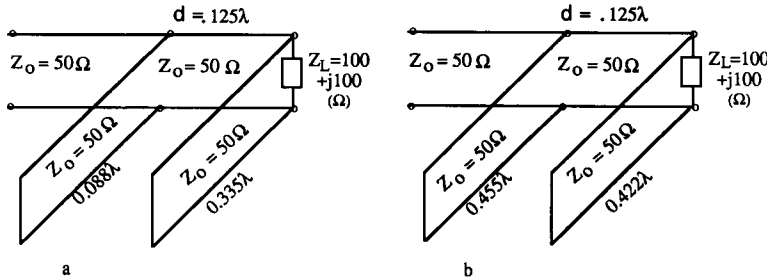


Figure 9. Solutions to the double-stub design problem.

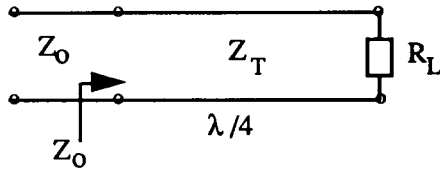


Figure 10. Quarter-wave impedance transformer.

Then,

$$Z_T = \sqrt{R'_L Z_0} .$$

The complex load impedance (Z_L) can also be converted into a real impedance (R'_L) by means of an $n\lambda/8$ (where n is an odd integer) length of line having a characteristic impedance equal to the magnitude of the load impedance ($|Z_L|$). The load impedance Z_L , however, must be normalized with respect to $|Z_L|$ before using the Smith chart. The fractional

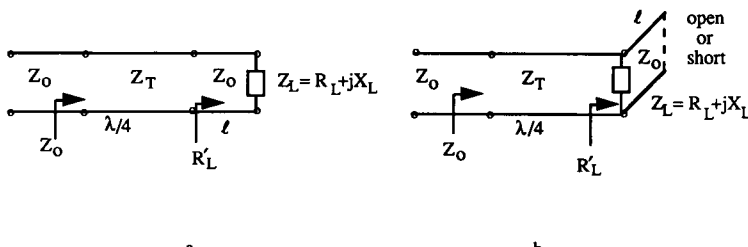


Figure 11. Matching a complex load to a real impedance by means of a quarter-wave transformer.

bandwidth of a quarter-wave transformer is given by

$$\frac{\Delta f}{f_0} = 2 - \frac{4}{\pi} \cos^{-1} \left[\frac{\rho_m}{\sqrt{1 - \rho_m^2}} \frac{2\sqrt{Z_0 R_L}}{|R_L - Z_0|} \right], \quad (1)$$

where ρ_m is the magnitude of the tolerable reflection coefficient in the band Δf , and f_0 is the band center frequency.

Formula (1) is valid for TEM lines only. In non-TEM lines the phase velocity and wave impedance are frequency dependent, and hence the analysis based on which formula has been derived is not valid unless the bandwidth of operation is small.

The discontinuities in the cross-sectional dimensions of the lines due to step change in impedance produce junction capacitance. This effect can be compensated for by making an adjustment in the length of the transformer.

Real to Complex Impedance Transformation

The real to complex impedance transformation can be performed using the techniques already discussed in this section. The need for such a transformation arises, for example, in transistor amplifiers in which the real load and source impedances have to be transformed to appropriate complex impedances at the transistor output and input terminals, respectively. The matching network designs are illustrated here with the help of three examples.

Design Example 1 Consider the design of a matching network to transform R_L (50Ω) to Z_{IN} ($25 - j25 \Omega$). The technique of impedance transformation using a quarter-wave transformer and a transmission line ($Z_0 = 50 \Omega$) is illustrated in Figure 12a.

The reference impedance in this problem is 50Ω . Therefore, $Z'_{IN} = Z_{IN}/50$. Z'_{IN} is located at point A on the Smith chart in Figure 12b. By moving toward the load on a constant SWR circle on the Smith chart, point B on the real axis is located. At point B the normalized impedance

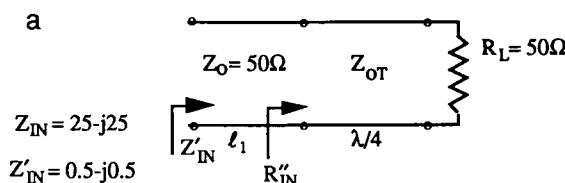


Figure 12a. Matching circuit for Example 1.

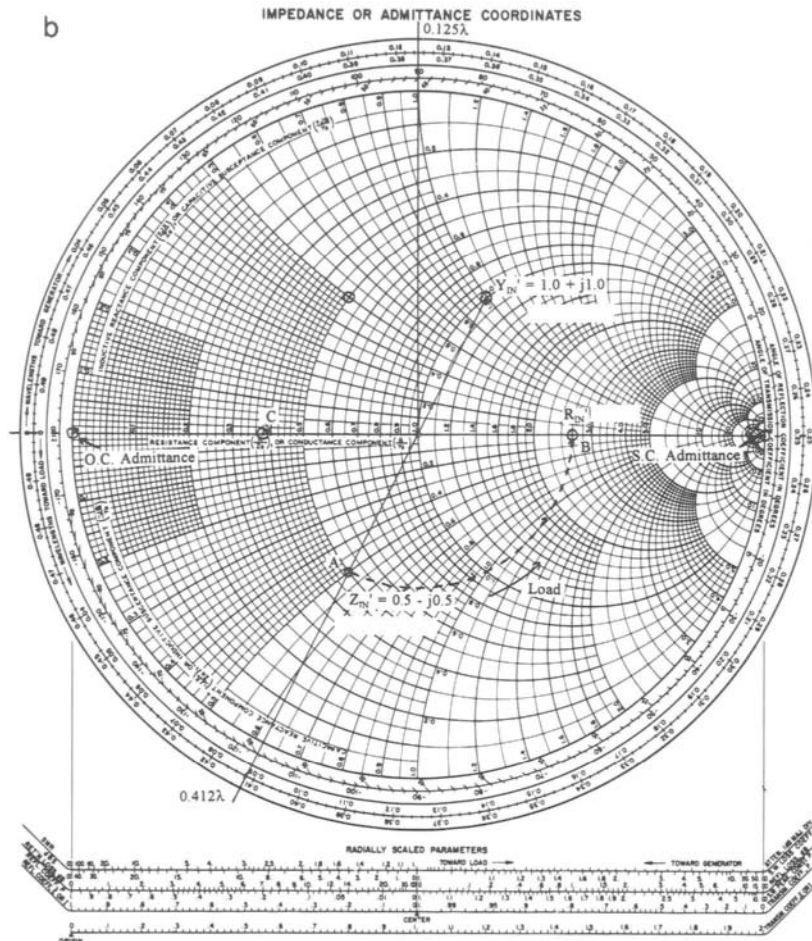


Figure 12b. Solutions to example 1. A quarter-wave transformer and a transmission line.

R''_{IN} (2.6) is purely real. The length l_1 of the 50- Ω transmission line needed to accomplish this is 0.162λ . R_{IN} ($R''_{IN} \times 50$) can be transformed to 50 Ω by means of a quarter-wave ($\lambda/4$) transformer having a characteristic impedance, Z_{OT} ($\sqrt{2.6} \times 50 \times 50 = 80.62 \Omega$).

The second solution to this matching problem is obtained by going along the constant SWR circle toward the load on the Smith chart and intersecting the real axis at point C to the left of the chart center. The length l_1 of the line needed is 0.412λ and $Z_{OT} = 30.82 \Omega$.

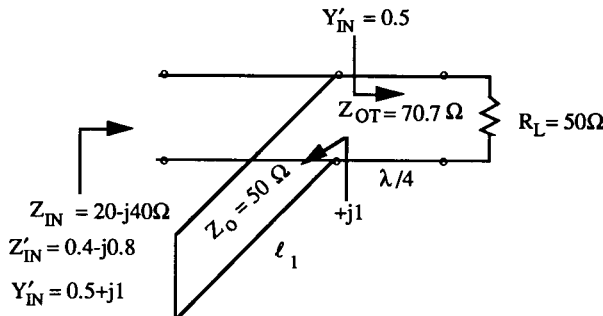


Figure 13. Matching circuit for example 2.

Design Example 2 In this example the impedance transformation from R_L (50Ω) to $20 - j40 \Omega$ is accomplished by means of a stub and a quarter-wave transformer as shown in Figure 13. The imaginary part ($+j1$) of Y'_{IN} can be produced by a short-circuited stub of length l_1 (0.375λ). The real part (0.5) of Y'_{IN} is obtained by means of a quarter-wave transformer having a characteristic impedance, Z_{OT} ($\sqrt{100 \times 50}$) of 70.7Ω .

Design Example 3 Consider the transformation of R_L (50Ω) to Z_{IN} ($12.25 + j8.25 \Omega$). The solution is illustrated in Figure 14a. The match is accomplished by means of a length of line and a stub. The matching technique is illustrated on the admittance chart in Figure 14b. Y'_{IN} is located at point B on the Smith chart. The shortest length of line and stub can be designed by using an open stub of length 0.156λ to move from the center of the chart ($G'_L = 1$) to point A, and then point B can be reached by using a transmission line of length 0.099λ .

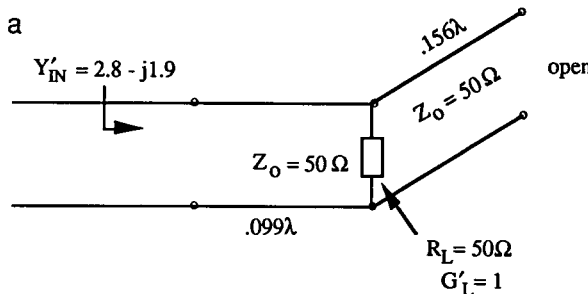


Figure 14a. Matching network for example 3.

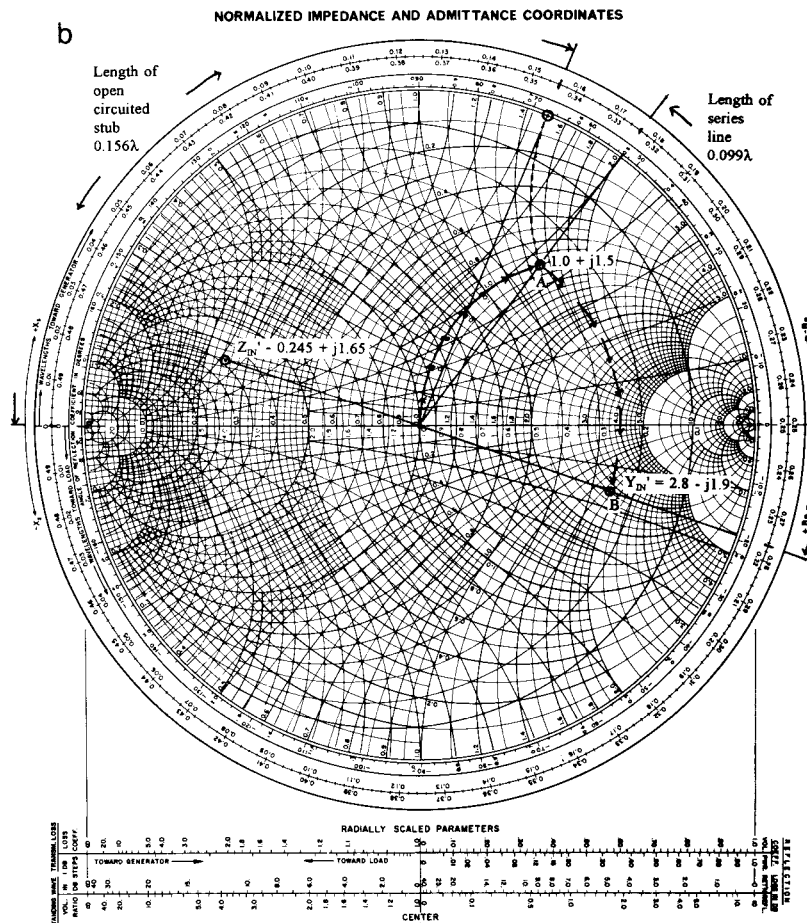


Figure 14b. Solution to example 3: a transmission line and a stub.

The matching networks in examples 1, 2, and 3 could have been designed by transforming Z_{in}^* to R_L , which is evident, for example, in Figure 12b. This is due to the property of a reciprocal lossless matching network, illustrated in Figure 1.

Lumped Element Matching

Two basic topologies (L-sections) of lumped element matching networks are shown in Figures 15a and 15b. These networks consist of purely

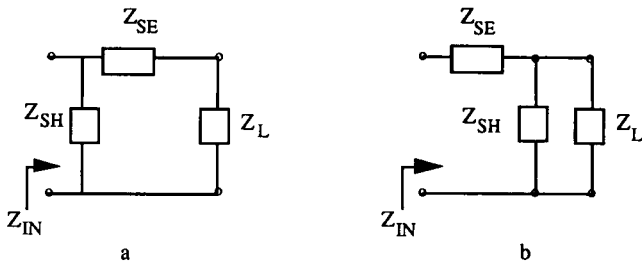


Figure 15. Basic topologies of lumped element matching networks. Z_{SE} , impedance of a series element (inductive or capacitive); Z_{SH} , impedance of a shunt element (inductive or capacitive).

reactive elements. The series and shunt lumped elements (inductor or capacitor) can be realized in microwave integrated circuits as short lengths of microstrip lines, spiral inductors, or thin-film capacitors. However, there is a wide range of frequencies and circuit sizes in which lumped elements may not be realizable. This is a limitation of the L-section matching technique. The matching networks are required to transform real to complex, complex to complex, and complex to real impedances. A matching network designed to convert Z_L to Z_{IN} also enables one to transform in effect Z_{IN}^* to Z_L^* as illustrated in Figure 1.

ZY Smith Chart

It is easier to design these networks using the *ZY* Smith chart. In this chart the normal Smith chart (*Z*-chart) is rotated by 180° and superimposed on the original chart. The rotated chart is an admittance chart (*Y*-chart); as a result the conversion from impedance to admittance coordinates is obtained easily.

On a Smith chart, the effect of adding a reactance in series constitutes a movement along a constant resistance circle, and the effect of adding a shunt susceptance results in a movement along a constant conductance circle. Each motion gives the value of the component to be added. The load impedance Z_L as well as the impedance Z_{IN} to which Z_L needs to be transformed is in general complex. A typical practical situation consisting of matching circuits is a multistage transistor amplifier, illustrated in Figure 16.

On the basis of the matching network topologies shown in Figures 15a and 15b, one can conclude that, depending on the combinations of lumped elements chosen, eight different matching networks are available, as shown in Figure 17. In a given matching network design problem, more than one of the solutions in Figure 17 are possible, and some of the

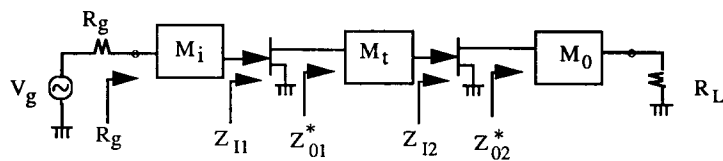


Figure 16. Impedance matching of a multistage amplifier. R_L (load resistance) and R_g (source resistance) are usually 50Ω in practice. M_i , input matching network; M_0 , output matching network; M_t , interstage matching network; Z_{I1} and Z_{I2} , impedances seen at the input terminals; Z_{01} and Z_{02} , impedances seen at the output terminals, looking into the device.

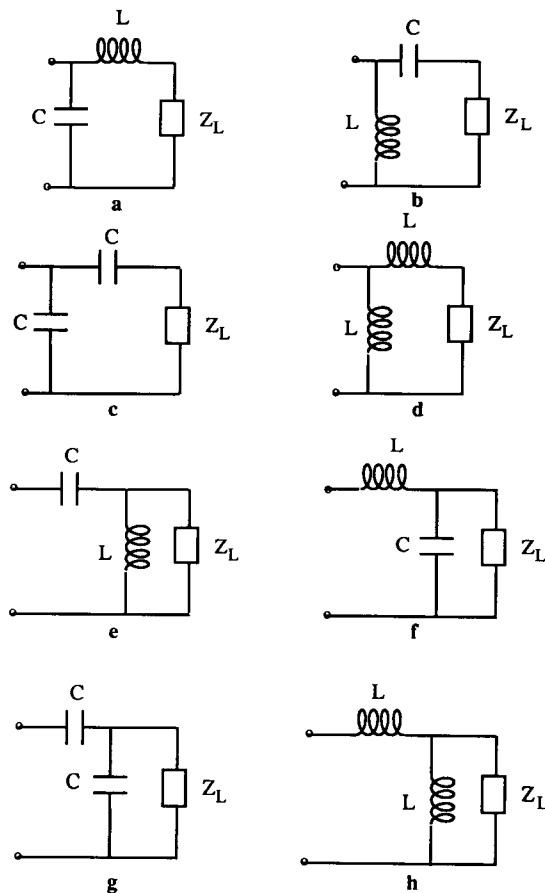


Figure 17. Matching networks.

matching networks may not yield the desired match as will be shown later in this section. In general, the networks shown in Figure 17a–17d yield the desired match if Z'_L is outside the normalized unity resistance circle on the Smith chart and the networks shown in Figures 17e–17h give the required match for Z'_L inside the normalized unity circle.

Complex to real and real to complex impedance transformations using lumped element matching networks are illustrated by means of examples to follow. The admittances and impedances are normalized to $1/50$ (U) and 50 (Ω) references, respectively, and represented by primed symbols.

Complex to Real Impedance Transformation

Design Example 1 Consider the transformation of $Y_L = (8 - j12) \times 10^{-3} \text{ U}$ to $Z_{IN} = 50 \Omega$ at 1 GHz. Here Y'_L (Y_L normalized to $1/50 \text{ U}$) = $0.4 - j0.6$; $Z'_L = 0.77 + j1.15$.

The load impedance (Z'_L) is located at point A on the ZY Smith chart in Figure 18a. The load impedance cannot be matched to 50Ω by means of the network shown in Figure 18b because the Z'_L (although outside the normalized unity resistance circle) is in the forbidden region on the Smith chart for this network! The region shown in Figure 18a is a forbidden region for this network because, adding L in series produces motion in a clockwise direction, away from the unity normalized-conductance circle that passes through the origin.

The design of the matching network shown in Figure 18c will be described below using the Smith chart in Figure 18a.

$$Y'_L = 0.4 - j0.6; \quad Z'_L = 0.77 + j1.15 \text{ at point A.}$$

We need to move to point B on the unity conductance circle, where

$$Y' = 1 + j0.52; \quad Z' = 0.77 - j0.42 \text{ at point B.}$$

Therefore, the reactance (X_C) needed to reach point B is $-j78.5 \Omega$ ($-j1.57 \times 50$).

The value of the series capacitive element is

$$C = \frac{1}{2\pi f \times 78.5}.$$

Since $f = 1 \text{ GHz}$, $C = 2.027 \text{ pF}$.

The reactance (X_L) of the shunt inductor needed to reach the center (C) of the chart is $j96.15 \Omega$ ($j1.923 \times 50$). Therefore, the value of the shunt inductor is

$$L = 96/2\pi \times 10^9 = 15.3 \text{ nH.}$$

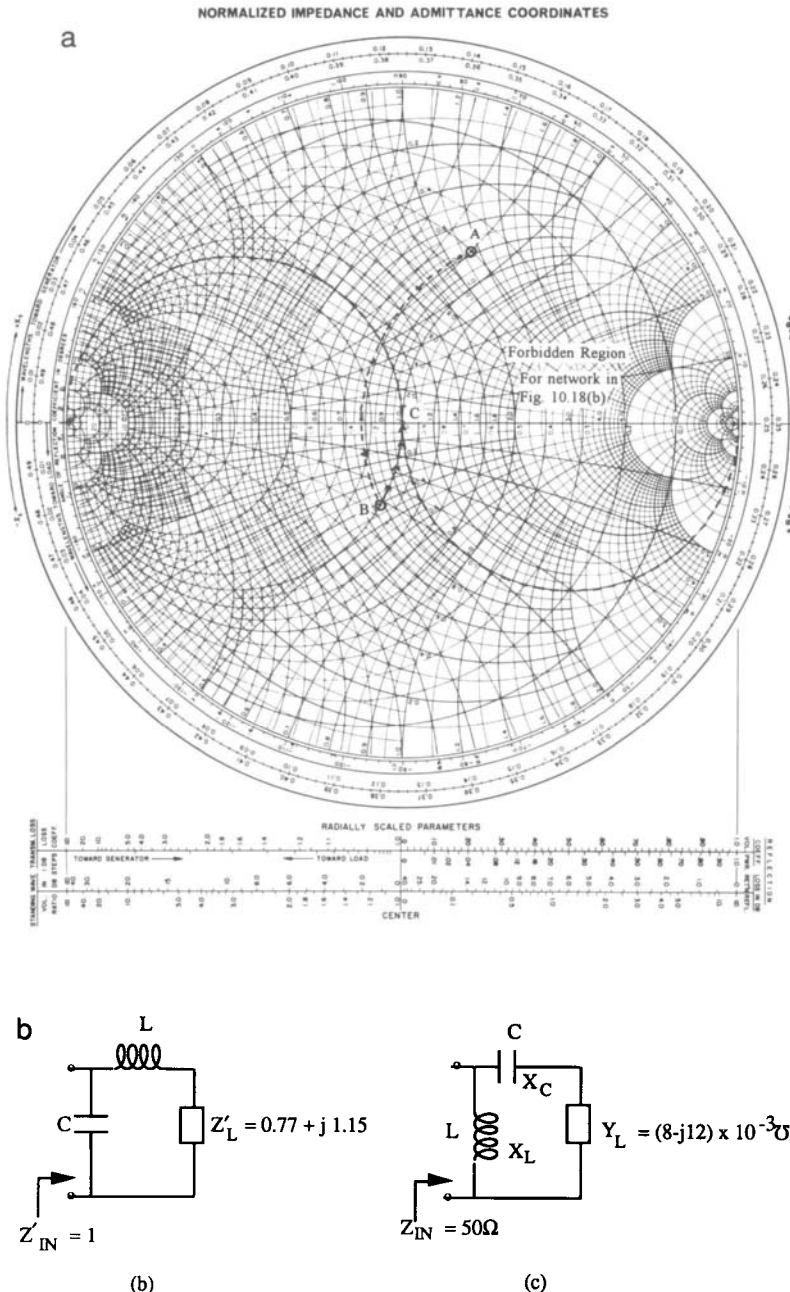


Figure 18. (a) Solution to the problem in example 1. (b) Matching networks considered in example 1.

Thus the network in Figure 18c transforms the given Y_L to the specified Z_{IN} (50Ω).

Design Example 2 Consider the design of a matching network to convert $Z_L = 10 + j40 \Omega$ to $Z_{IN} = 50 \Omega$. Z'_L is located at point A on the Smith chart in Figure 19a. The procedures are similar to those in example 1. The movements of the coordinates on the Smith chart are depicted in Figure 19a. The four possible designs in this case are shown in Figures 19b through 19e. The element values can be determined as in example 1.

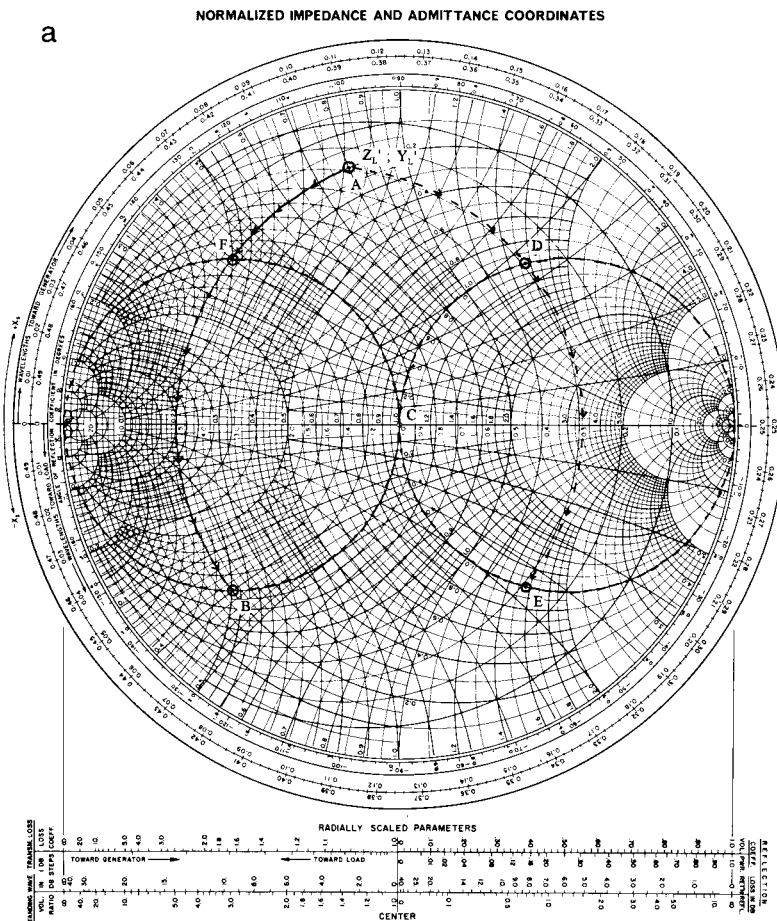


Figure 19a. Solutions to the problem in example 2.

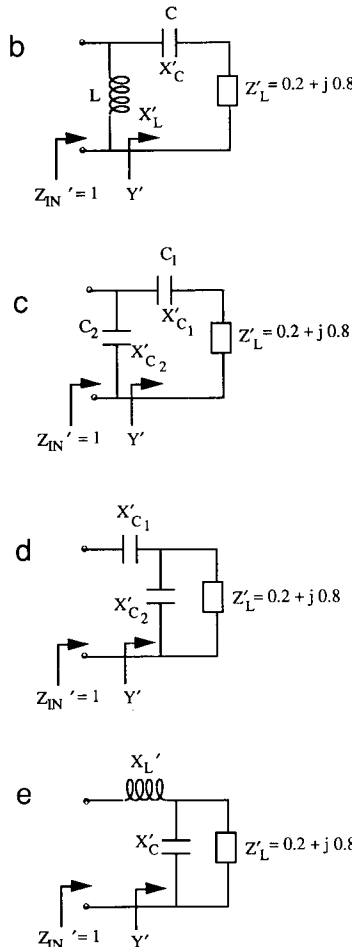


Figure 19b – 19e. (b) Moving along the constant resistance circle from A to B. At B, $Y' = 1 + j2.0$; $Z' = 0.2 - j0.4$. Therefore we need $X'_{C'} = -j1.2$; $X'_L = +j0.5$ to accomplish the match, $Z'_{IN'} (or Y'_{IN'}) = 1$. (c) Moving along the constant resistance circle from A to F. At F, $Y' = 1 - j2.0$; $Z' = 0.2 + j0.4$. Therefore we need, $X'_{C_1} = -j0.4$ and $X'_{C_2} = -j0.5$ to accomplish the match. (d) Moving along the constant conductance circle from A to D. At D, $Y' = 0.28 - j0.45$; $Z' = 1 + j1.55$. Therefore we need $X'_{C_2} = -j1.36$ and $X'_{C_1} = -j1.55$ to accomplish the match. (e) Moving along the constant conductance circle from A to E. At E, $Y' = 0.28 + j0.45$; $Z' = 1 - j1.55$. Therefore we need $X'_C = -j0.613$ and $X'_L = j = 1.55$ to accomplish the match.

One could select any one of the four matching network designs in this problem. In practice, the realizability of the circuit elements at the given frequency and physical size of the components may dictate the choice of a matching network.

Real to Complex Impedance Transformation

Design Example 3 In this example the design of a matching network, shown in Figure 20a, to transform a real impedance to a complex impedance will be illustrated. It is required to transform a 50Ω resistance to an admittance, Y_L , at 700 MHz. $Y_L = (4 - j4) \times 10^{-3}$ (S). The procedures are illustrated on the Smith chart in Figure 20b.

The normalized load resistance is located at the center (point A) on the Smith chart. A movement along the constant resistance circle to point B transforms the load resistance to a normalized impedance, Z'_{IN} at B. $Z'_{IN} = 1 - j1.98$. This requires a series reactance of $-j99.0$ (Ω). The value of C required to accomplish this is 2.297 pF. Y'_{IN} at B is $0.2 + j0.4$. We need to reach point C, where Y'_L , the normalized admittance to which the 50Ω resistance needs to be transformed, is $0.2 - j0.2$. We need to move along the 0.2 constant conductance circle to reach point C. This is accomplished by a shunt inductive reactance of $j5$ (Ω). At 700 MHz this reactance is obtained by an inductance (L) equal to 18.94 nH.

Distributed and Lumped Element Techniques

In the previous two sections, impedance matching techniques by means of exclusively distributed and lumped elements were described. In this section, techniques which make use of both distributed and lumped elements

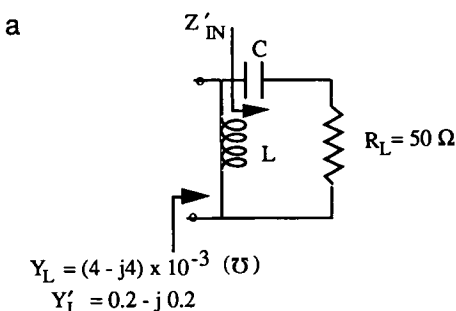


Figure 20a. Matching network to transform R_L to Y_L in example 3.

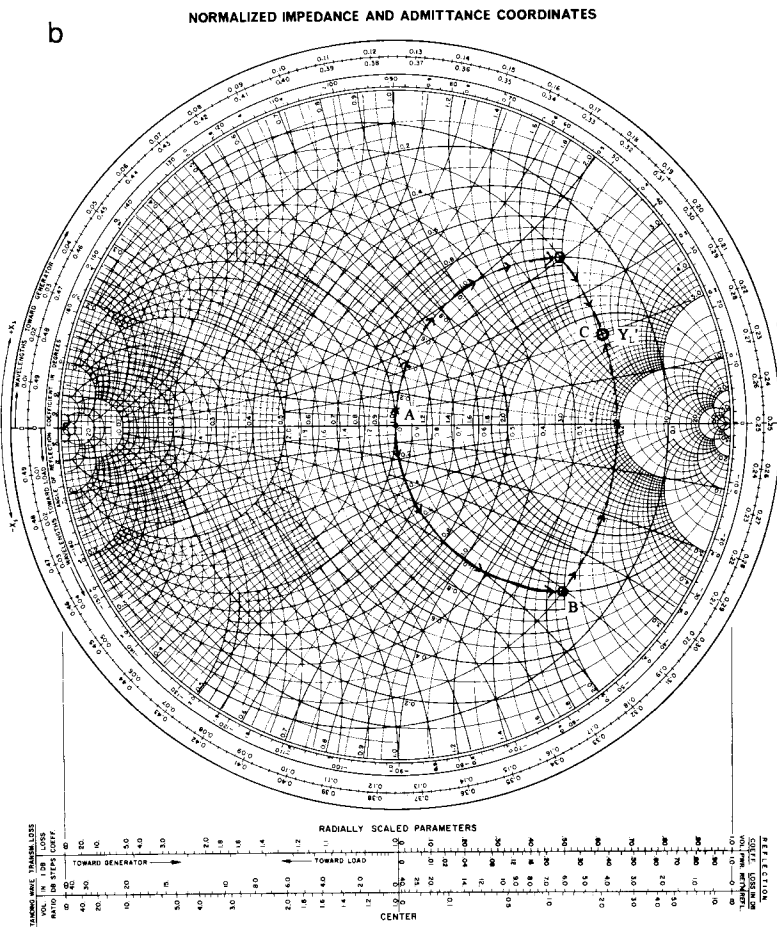


Figure 20b. Solutions to the problem in example 3.

in the design of impedance matching networks will be illustrated with the help of examples.

Complex to Real Impedance Transformation

Design Example 1 Consider the problem of matching the load impedance $Z_L = 100 + j100$ (Ω) to a $50\text{-}\Omega$ transmission line. The impedance transformation can be accomplished by the networks shown in Figures 21a and 21b and as illustrated on the Smith chart in Figure 21c.

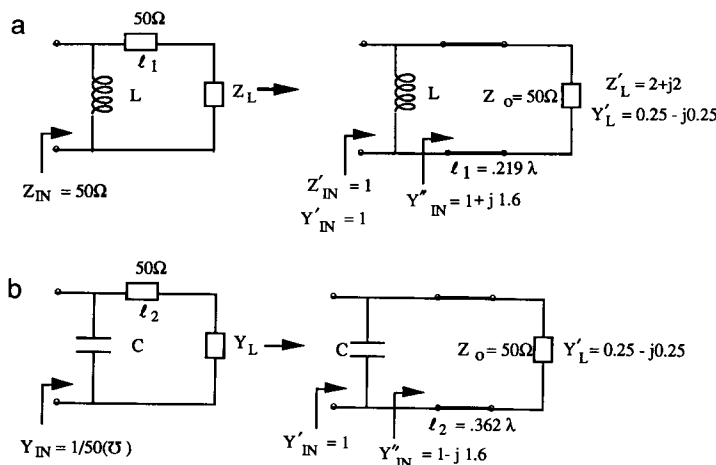


Figure 21a and b. Matching networks considered in example 1.

Y'_L is first transformed to Y''_{IN} ($1 + j1.6$) at point B on the Smith chart. Point B lies on the unit conductance circle. Point B is reached by traveling along the constant SWR circle toward the generator. This transformation is accomplished by means of a length, l_1 (0.219λ) of a transmission line ($Z_0 = 50 \Omega$). The shunt susceptance needed to cancel jB''_{IN} ($+j1.6$) is obtained by a lumped inductor having an inductance, $L = 50/2\pi f(1.6)$ (H), where f is the design frequency (in Hertz). Y'_{IN} is now unity.

If Y'_L is transformed to Y''_{IN} ($1 - j1.6$) at point C on the Smith chart, then the match can be accomplished by connecting a lumped capacitor in shunt (to produce a susceptance of $+j1.6$), as shown in Figure 21b. The capacitance C is given by $C = 1.6(50)/2\pi f$ (F). The length l_2 of the transmission line needed is 0.362λ .

Design Example 2 The load impedance of Z_L ($100 + j100 \Omega$) can be matched to 50Ω by means of the networks shown in Figures 22a and 22b. The impedance Z'_L at point D on the Smith chart in Figure 22c is transformed to Z''_{IN} ($1 + j1.6$) at point C on the unit resistance circle. This is accomplished by means of a length, l_1 (0.112λ), of the $50-\Omega$ transmission line. Then by connecting a lumped inductor, L ($1.6 \times 50/2\pi f$) in series, the match is accomplished as shown in Figure 22a.

In Figure 22b a second solution is illustrated. Here, the impedance Z'_L is converted to Z''_{IN} ($1 + j1.6$) by traveling along the constant SWR circle on the Smith chart and intersecting the unity resistance circle at point B. This is accomplished by means of a length, l_2 , (0.478λ) of the $50-\Omega$

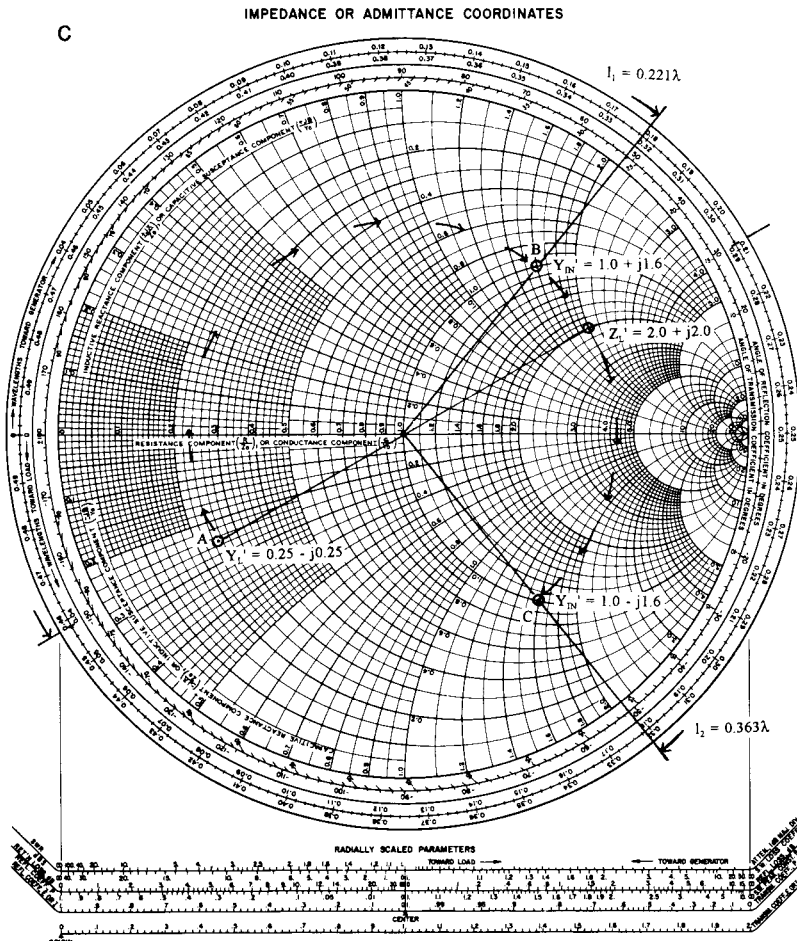


Figure 21c. Solutions to the problem in example 1.

transmission line. Z_{IN}'' is transformed to Z_L' (1) by a lumped capacitor in series. The capacitance C is given by $C = (1.6)50/2\pi f$ (F).

Real to Complex Impedance Transformation

Design Example 1 Consider the problem of transforming R_L (50Ω) to Z_{IN} ($25 - j25 \Omega$). The design of the matching network using a distributed and a lumped element is illustrated in Figure 23a. The impedance transformation is accomplished by means of a quarter-wave transformer and a lumped capacitor in series.

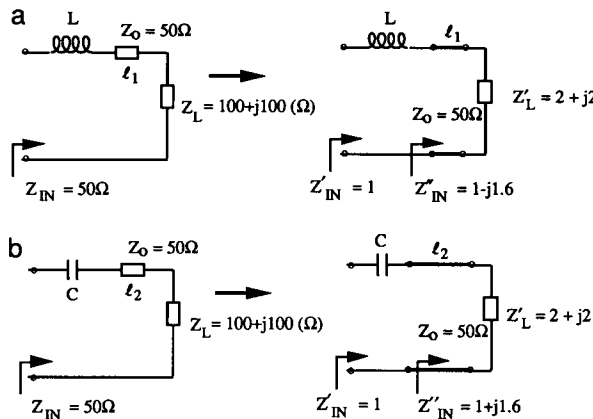


Figure 22a and 22b. Matching networks considered in example 2.

A second design solution to the impedance transformation problem is shown in Figure 23b. In this network, a 50- Ω transmission line of length l_1 and a lumped capacitor in shunt are used.

3. Wide-Band Matching

Multisection Quarter-Wave Transformers

The schematic of a multisection quarter-wave transformer is shown in Figure 24, in which the load impedance Z_L is transformed to Z_0 , the characteristic impedance of the feed line. The load Z_L is assumed to be real and may be greater or smaller than Z_0 . The transformer consists of discrete sections of lines having different characteristic impedances but the same electrical length, $\beta l = \theta$. The electrical length will be a quarter-wavelength at the matching frequency f_0 , the band center frequency. The transformer is symmetrical; therefore, the reflection coefficients at the junctions of the sections are related as $|\Gamma_0| = |\Gamma_N|$, $|\Gamma_1| = |\Gamma_{N-1}|$, etc.

The transformer can be realized in the form of a coaxial line, a waveguide, or planar transmission lines such as microstrip lines. In this section, two widely known multisection quarter-wave transformers, viz. (a) binomial and (b) Chebyshev, will be presented. The design equations and data based on approximate as well as exact theories of multisection quarter-wave transformers will be given. The design procedures will be illustrated by means of examples.

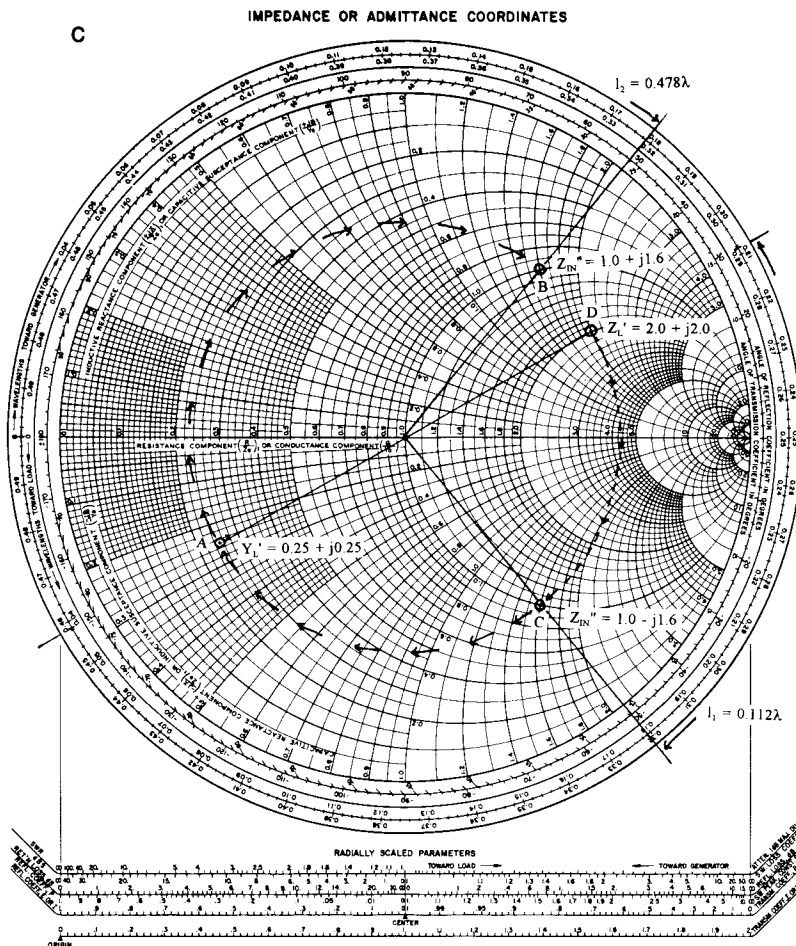


Figure 22c. Solutions to the problem in example 2.

Binomial Transformer

In a binomial transformer, the function $\Gamma(\theta)$ is chosen such that $|\Gamma| = \rho$ and the first $N - 1$ derivatives (N is the number of sections) with respect to frequency (or θ) vanish at the band center frequency f_0 , where $\theta = \pi/2$. Therefore, a maximally flat passband characteristic for the transformer is obtained. The maximally flat pass-band characteristic of a binomial transformer is shown in Figure 25. ρ_m is the maximum tolerable reflection coefficient in the pass band. The transformer sections will be a quarter-wavelength long at the band center frequency. θ_m (Figure 25) is

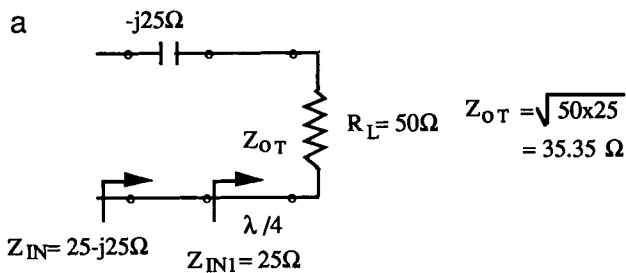


Figure 23a. Matching network design using a quarter-wavelength transmission line and a lumped capacitor in series.

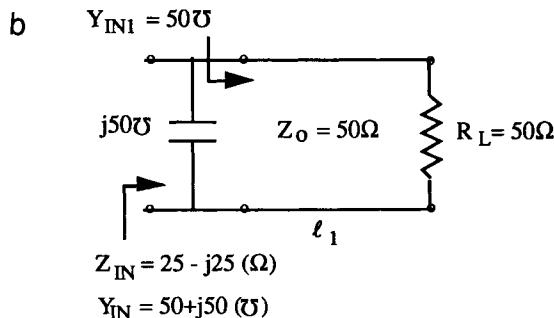


Figure 23b. Matching network design using a transmission line and a shunt capacitor.

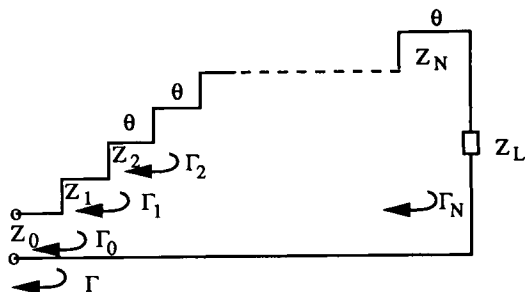


Figure 24. A multisection quarter-wave transformer. N , number of sections.

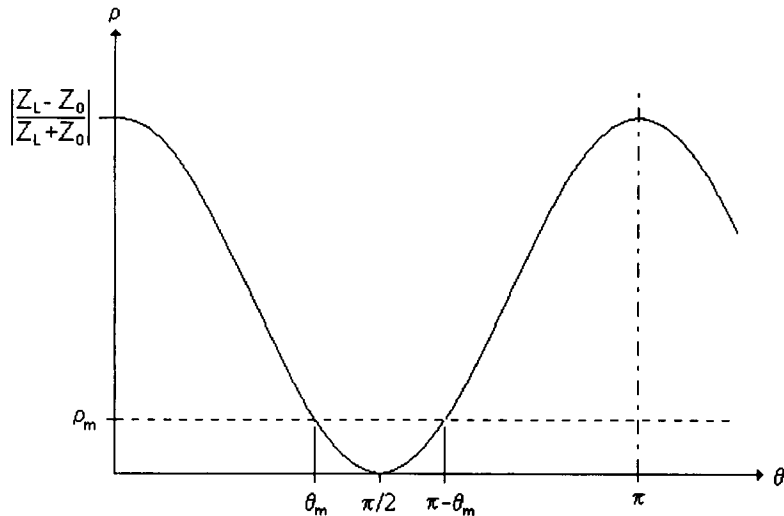


Figure 25. Characteristic of a binomial transformer.

given by

$$\theta_m = \cos^{-1} \left| \frac{2\rho_m}{\ln \left(\frac{Z_L}{Z_0} \right)} \right|^{1/N}. \quad (2)$$

In the case of transmission line sections, $\theta = \pi f / 2f_0$, and therefore the fractional bandwidth is given by

$$\frac{\Delta f}{f_0} = \frac{2(f_0 - f_m)}{f_0} = 2 - \frac{4}{\pi} \cos^{-1} \left| \frac{2\rho_m}{\ln \left(\frac{Z_L}{Z_0} \right)} \right|^{1/N} \quad (3)$$

since $\theta_m = \pi f_m / 2f_0$. Note that the solution to Equation (2) is chosen such that $\theta_m < \pi/2$. The maximum out-of-band reflection coefficient occurs for $\theta = 0$ or π and is given by

$$\rho_{\max} = \left| \frac{Z_L - Z_0}{Z_L + Z_0} \right|. \quad (4)$$

ρ_{\max} is the reflection coefficient when Z_L is directly connected to the transmission line having the characteristic impedance Z_0 .

Design Based on Approximate Theory The impedances of the sections may be calculated using the following equations.

$$\ln \frac{Z_{n+1}}{Z_n} = 2\rho_n = 2^{-N} C_n^N \ln \frac{Z_L}{Z_0} \quad (5a)$$

$$C_n^N = \frac{N!}{(N-n)!n!}, \quad (5b)$$

where Z_n and Z_{n+1} are the impedances of the n th and $(n + 1)$ th sections, respectively, ρ_n is the reflection coefficient at the junction between Z_n and Z_{n+1} , and C_n^N are the binomial coefficients. Since the theory upon which the equations are based in this section is approximate, the range of Z_L is limited to about

$$0.5Z_0 < Z_L < 2Z_0.$$

Design Example Consider the design of a two-section transformer to match $Z_L = 100 \Omega$ to $Z_0 = 50 \Omega$. The required ρ_m is 0.05. The transformer is to be realized in the form of air-filled coaxial lines. The band center frequency is 4 GHz. From Equation (5a),

$$\ln \frac{Z_1}{Z_0} = \frac{1}{4} \ln \frac{Z_L}{Z_0} \quad \text{since } C_0^2 = 1$$

and

$$\ln \frac{Z_2}{Z_1} = \frac{1}{2} \ln \frac{Z_L}{Z_0} \quad \text{since } C_1^2 = 2.$$

Therefore, we have,

$$Z_1 = Z_L^{1/4} Z_0^{3/4} = (100)^{1/4} (50)^{3/4} = 59.45 \Omega$$

and

$$Z_2 = Z_L^{3/4} Z_0^{1/4} = (100)^{3/4} (50)^{1/4} = 84.09 \Omega.$$

Since $\rho_m = 0.05$, from Equation (3), the fractional bandwidth ($\Delta f/f_0$) is 0.496 and the absolute bandwidth is 1.98 GHz. ρ_{\max} , from Equation (4), is 0.33. The length of each section of the transformer is 75 mm. A schematic diagram of the transformer is shown in Figure 26.

Design Based on Exact Theory Exact results can be obtained by solving transmission line equations for each section numerically. Table 1 lists the exact impedance data for $N = 2, 3$, and 4 sections. The table lists

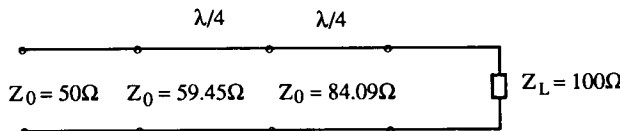


Figure 26. Two-section binomial transformer.

data for $Z_L/Z_0 > 1$. For $Z_L/Z_0 < 1$, the results for Z_0/Z_L should be used, with Z_1 beginning from the load end. This is because of the symmetry in the transformer; therefore, the transformer which matches Z_L to Z_0 can be reversed and used to match Z_0 to Z_L .

Chebyshev Transformer

In a Chebyshev transformer, ρ is allowed to vary between 0 and ρ_m in a periodic manner in the pass band. Thus the transformer has an equal-ripple characteristic as shown in Figure 27. A transformer of this type provides a considerable improvement in bandwidth over the binomial transformer.

The equal-ripple characteristic is obtained by forcing ρ to behave according to a Chebyshev polynomial, thus, the name Chebyshev transformer, ρ can be made to vanish at as many frequencies in the pass band as there are sections of transformer.

The reflection coefficient Γ is given by

$$\begin{aligned}\Gamma &= 2e^{-jN\theta} [\rho_0 \cos N\theta + \rho_1 \cos(N-2)\theta + \dots \\ &\quad + \rho_n \cos(N-2n)\theta + \dots] \\ &= Ae^{-jN\theta} T_N(\sec \theta_m \cos \theta),\end{aligned}\quad (6)$$

TABLE I
Binomial Transformer Design Data

Z_L/Z_0	$N = 2$		$N = 3$			$N = 4$			
	Z_1/Z_0	Z_2/Z_0	Z_1/Z_0	Z_2/Z_0	Z_3/Z_0	Z_1/Z_0	Z_2/Z_0	Z_3/Z_0	Z_4/Z_0
1.0	1.0000	1.0000	1.0000	1.0000	1.0000	1.0000	1.0000	1.0000	1.0000
1.5	1.1067	1.3554	1.0520	1.2247	1.4259	1.0257	1.1351	1.3215	1.4624
2.0	1.1892	1.6818	1.0907	1.4142	1.8337	1.0444	1.2421	1.6102	1.9150
3.0	1.3161	2.2795	1.1479	1.7321	2.6135	1.0718	1.4105	2.1269	2.7990
4.0	1.4142	2.8285	1.1707	2.0000	3.3594	1.0919	1.5442	2.5903	3.6633
6.0	1.5651	3.8336	1.2544	2.4495	4.7832	1.1215	1.7553	3.4182	5.3500
8.0	1.6818	4.7568	1.3022	2.8284	6.1434	1.1436	1.9232	4.1597	6.9955
10.0	1.7783	5.6233	1.3409	3.1623	7.4577	1.1613	2.0651	4.8424	8.6110

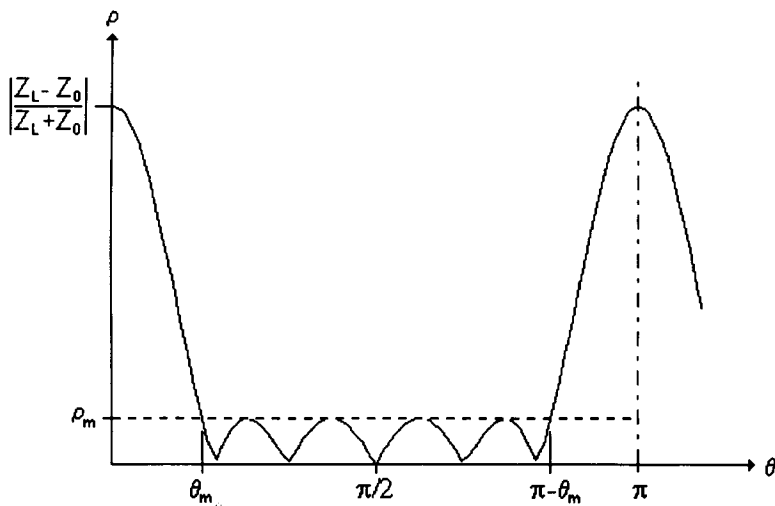


Figure 27. Characteristic of a chebyshev transformer.

where $\rho_0, \rho_1, \dots, \rho_N$ are the magnitudes of the reflection coefficients at the junctions (see Figure 24) and A is a constant to be determined. $T_N(\sec \theta_m \cos \theta)$ is a Chebyshev polynomial of the N th degree. The last term in the series in Equation (6) is $\rho_{(N-1)/2} \cos \theta$ for N odd and $\frac{1}{2} \rho_{N/2}$ for N even. The electrical length of the transformer sections is $\pi/2$ at the band center frequency f_0 .

Design Based on Approximate Theory The design equations based on approximate theoretical analysis are given below. These equations are valid if Z_L is restricted to about

$$0.5Z_0 < Z_L < 2Z_0$$

$$\Gamma = \frac{1}{2} e^{-jN\theta} \ln \frac{Z_L}{Z_0} \frac{T_N(\sec \theta_m \cos \theta)}{T_N(\sec \theta_m)} \quad (7)$$

$$\rho_m = \frac{\ln(Z_L/Z_0)}{2T_N(\sec \theta_m)} \quad (8a)$$

$$\sec \theta_m = \cos \left[\frac{1}{N} \cos^{-1} \frac{\ln(Z_L/Z_0)}{2\rho_m} \right] \quad (8b)$$

$$\ln \frac{Z_{n+1}}{Z_n} = 2\rho_n. \quad (9)$$

It is evident from Equation (8) that, if the pass band, and hence θ_m , is specified, the pass-band tolerance ρ_m is fixed and vice versa.

The fractional bandwidth of the transformer is given by

$$\frac{\Delta\theta}{\pi/2} = \frac{\Delta f}{f_0} = \frac{4}{\pi}(\pi/2 - \theta_m). \quad (10)$$

The maximum out-of-band reflection coefficient, ρ_{max} , occurs at $\theta = 0$ and $\theta = \pi$, and is given by,

$$\rho_{max} = |Z_L - Z_0/Z_L + Z_0|. \quad (11)$$

The expressions for $T_n(\sec \theta_m \cos \theta)$ useful in designing transformers up to four sections are given below.

$$T_1(\sec \theta_m \cos \theta) = \sec \theta_m \cos \theta \quad (12a)$$

$$T_2(\sec \theta_m \cos \theta) = \sec^2 \theta_m(1 + \cos 2\theta) - 1 \quad (12b)$$

$$T_3(\sec \theta_m \cos \theta) = \sec^3 \theta_m(\cos 3\theta + 3 \cos \theta) - 3 \sec \theta_m \cos \theta \quad (12c)$$

$$\begin{aligned} T_4(\sec \theta_m \cos \theta) &= \sec^4 \theta_m(\cos 4\theta + 4 \cos 2\theta + 3) \\ &\quad - 4 \sec^2 \theta_m(\cos 2\theta + 1) + 1. \end{aligned} \quad (12d)$$

Expressions for $T_n(\sec \theta_m \cos \theta)$ for degrees greater than 4 can be derived using the following equations.

$$T_n(x) = 2xT_{n-1}(x) - T_{n-2}(x) \quad (13a)$$

$$T_n(x) = \cos(n \cos^{-1} x), \quad \text{for } |x| < 1 \quad (13b)$$

$$T_n(x) = \cosh(n \cosh^{-1} x), \quad \text{for } |x| > 1 \quad (13c)$$

$$\begin{aligned} (\cos \theta)^n &= 2^{-n} e^{-jn\theta} (1 + e^{2j\theta})^n = 2^{-n} e^{-jn\theta} \sum_{m=0}^n C_m^n e^{jm\theta} \\ &= 2^{-n+1} [C_0^n \cos n\theta + C_1^n \cos(n-2)\theta + \dots \\ &\quad + C_m^n \cos(n-2m)\theta + \dots]. \end{aligned} \quad (13d)$$

The last term in Equation (13d) is $\frac{1}{2}C_{n/2}^n \cos \theta$ for n even and $C_{(n-1)/2}^n \cos \theta$ for n odd. It can be shown that the constant A in Equation (6) is equal to ρ_m . For a given ρ_m , Z_L , and Z_0 , $T_N(\sec \theta_m)$ can be found from Equation (8a). ρ_n in Equation (6) can be determined by using the expressions for $T_N(\sec \theta_m \cos \theta)$ in Equation (12) and equating similar terms of the form $\cos(N-2n)\theta$ in Equation (6). Z_n can then be found using Equation (9).

Alternatively, $T_N(\sec \theta_m)$ and θ_m can be determined using the following equations.

$$T_N(\sec \theta_m) = \frac{1}{\rho_m} \left| \frac{Z_L - Z_0}{Z_L + Z_0} \right| \quad (14a)$$

$$\sec \theta_m = \cosh \left[\frac{1}{N} \cosh^{-1} \left(\frac{1}{\rho_m} \left| \frac{Z_L - Z_0}{Z_L + Z_0} \right| \right) \right] \quad (14b)$$

Then ρ_n in Equation (6) can be determined by using expressions for $T_N(\sec \theta_m \cos \theta)$ in Equation (12) and equating similar terms of the form $\cos(N - 2n)\theta$ in Equation (6). Z_n can then be found using the following equations.

$$\rho_0 = \frac{Z_1 - Z_0}{Z_1 + Z_0} \quad (14c)$$

$$\rho_n = \frac{Z_{n+1} - Z_n}{Z_{n+1} + Z_n} \quad (14d)$$

$$\rho_N = \frac{Z_L - Z_N}{Z_L + Z_N} \quad (14e)$$

Design Example Consider the design of a two-section Chebyshev transformer to match impedance $Z_0 = 50 \Omega$ to $Z_L = 100 \Omega$. The maximum pass-band tolerance required is $\rho_m = 0.05$.

Using Equations (8) and (12b) we obtain,

$$T_2(\sec \theta_m) = 2 \sec^2 \theta_m - 1 = \frac{\ln(100/50)}{2(0.05)} = 6.93.$$

Therefore, $\sec \theta_m = 1.99$, and $\theta_m = 1.045$. From Equation (10) the fractional bandwidth is

$$\frac{\Delta f}{f_0} = 0.669.$$

From Equations (6), (7), and (12b) we obtain

$$\begin{aligned} 2\rho_0 \cos 2\theta + \rho_1 &= \rho_m T_2(\sec \theta_m \cos \theta) \\ &= \rho_m \sec^2 \theta_m \cos \theta + \rho_m (\sec^2 \theta_m - 1). \end{aligned}$$

Therefore, we have

$$\rho_0 = \frac{1}{2}\rho_m \sec^2 \theta_m = \rho_2 = 0.099$$

$$\rho_1 = \rho_m (\sec^2 \theta_m - 1) = 0.148.$$

The impedances of the sections can be calculated using Equation (9). Thus,

$$Z_1 = e^{2\rho_0} Z_0 = 60.95 \Omega$$

and

$$Z_2 = e^{2\rho_1} Z_1 = 81.95 \Omega.$$

The schematic of the transformer is shown in Figure 28.

Design Based on Exact Theory The design equations and data necessary to design Chebyshev transformers based on exact theory are given here. The design data for a three-section transformer are given. The power loss ratio P_{LR} for the transformer is given by [3]

$$P_{LR} = \frac{1}{1 - \rho^2}, \quad (15)$$

where ρ is the magnitude of the reflection coefficient. P_{LR} can be expressed in the form

$$P_{LR} = 1 + Q_{2N}(\cos \theta), \quad (16)$$

where $Q_{2N}(\cos \theta)$ is an even polynomial of degree $2N$ in $\cos \theta$ having coefficients which are functions of the impedances Z_n . For a Chebyshev transformer, P_{LR} is specified to be

$$P_{LR} = 1 + k^2 T_N^2(\sec \theta_m \cos \theta), \quad (17)$$

where k^2 is the pass-band tolerance on P_{LR} . The maximum value of P_{LR} in the pass-band is $1 + k^2$.

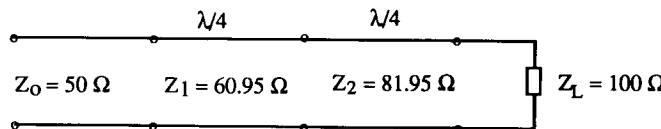


Figure 28. Two-Section chebyshev transformer.

By equating Equations (16) and (17), the equations that can be solved for the various characteristic impedances are obtained. The pass-band tolerance k^2 and maximum tolerable pass-band ripple ρ_m are related by

$$\rho_m = \left(\frac{k^2}{1 + k^2} \right)^{1/2}. \quad (18)$$

From Equation (18) for a specified k^2, ρ_m can be determined and vice versa. For a specified value of k^2 and the number of sections in the transformer, θ_m can be determined. The fractional bandwidth of the transformer is given by

$$\frac{\Delta f}{f_0} = \frac{2(\pi/2 - \theta_m)}{\pi/2}. \quad (19)$$

The Chebyshev quarter-wave transformer design data for three sections are given in Table 2. More extensive tables can be found in Reference [6]. Using Table 2, for a given Z_L/Z_0 , k^2 , and bandwidth, the impedances of the sections can be determined. The design procedures are illustrated by the following example.

Design Example Consider the design of a three-section Chebyshev transformer to match $Z_L = 100 \Omega$ to $Z_0 = 50 \Omega$ over a fractional bandwidth of 0.6 and having a maximum VSWR of 1.02 in the pass-band. From the given maximum VSWR, $\rho_m = 1.02 - 1/1.02 + 1 = 9.9 \times 10^{-3}$, and from Equation (18),

$$k^2 = \rho_m^2 / 1 - \rho_m^2 = 9.8 \times 10^{-5}.$$

TABLE 2
Chebyshev Transformer Design Data

Z_L/Z_0	$\Delta f/f_0 = 0.2$		$\Delta f/f_0 = 0.4$		$\Delta f/f_0 = 0.6$	
	Z_1/Z_0	k^2	Z_1/Z_0	k^2	Z_1/Z_0	k^2
2	1.09247	1.19×10^{-7}	1.09908	7.98×10^{-6}	1.1083	9.57×10^{-5}
4	1.19474	5.35×10^{-7}	1.20746	3.55×10^{-5}	1.23087	4.31×10^{-4}
10	1.349	1.92×10^{-7}	1.37482	1.28×10^{-4}	1.4232	1.55×10^{-3}
20	1.48359	4.29×10^{-7}	1.52371	2.85×10^{-4}	1.60023	3.45×10^{-3}
100	1.87411	2.33×10^{-6}	1.975	1.55×10^{-3}	2.17928	1.87×10^{-2}

Note. $Z_2 = \sqrt{Z_L Z_0}$; $Z_3 = Z_L Z_0 / Z_1$.

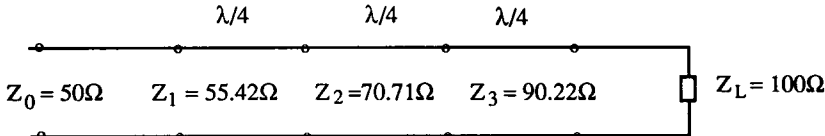


Figure 29. Schematic of the three-section chebyshev transformer.

In this design problem, $Z_L/Z_0 = 2$. From Table 2 for $Z_L/Z_0 = 2$ and $\Delta f/f_0 = 0.6$, $k^2 = 9.57 \times 10^{-5}$. This value of k^2 is less than what we need and hence can be accepted. If an acceptable value of k^2 cannot be obtained for the chosen number of sections, the number of sections must be increased.

From Table 2, we get $Z_1/Z_0 = 1.1083$. Therefore,

$$Z_1 = 1.1083 \times 50 = 55.42 \Omega$$

$$Z_2 = \sqrt{Z_L Z_0} = \sqrt{100 \times 50} = 70.71 \Omega$$

$$Z_3 = Z_L Z_0 / Z_1 = \frac{100 \times 50}{55.42} = 90.22 \Omega.$$

The schematic of the transformer is shown in Figure 29. The sections are a quarter-wavelength long at the band center frequency. The guide wavelength in the sections may be different as in microstrip transformers. In a microstrip transmission line the impedance as well as wavelength are functions of the microstrip width to substrate height ratio. The maximum out-of-band reflection coefficient for this transformer is

$$\rho_{max} = |Z_L - Z_0/Z_L + Z_0| = |100 - 50/100 + 50| = 0.33.$$

Additional Remarks

In the realization of multisection quarter-wave transformers, the designer has to contend with the discontinuities in the cross-sectional dimensions of the sections. These discontinuities have to be modeled, and the lengths of the sections should be appropriately adjusted. If the discontinuities are not compensated for in the design, the frequency response of the reflection coefficient will be modified. For example, at an abrupt change in the microstrip width, there will be additional fringing electric fields. The effect of the fringing field can be modeled as a shunt capacitance at the junction. The equivalent circuit of the step in the width of a microstrip line consists of an ideal impedance step and a shunt capacitive susceptance. The junction capacitance can be compensated for by changing the length

of each section. The junction capacitance for a step change in the width of a microstrip line can be evaluated [3].

Another important fact which modifies the performance of the transformer is the dispersion in the lines constituting the sections. The effects of dispersion must be taken into account in the design of the transformer.

Finally, it should be noted that for a given number of sections and a tolerable value of ρ (i.e., ρ_m) in the pass band, the fractional bandwidth provided by the Chebyshev transformer is greater than that of the binomial transformer. A binomial design gives a maximally flat frequency response with a zero reflection coefficient at the band center frequency irrespective of the number of sections, unlike a Chebyshev transformer. A Chebyshev transformer will have fewer sections than a binomial transformer for a given ρ_m and fractional bandwidth. Therefore, the Chebyshev design is considered to be the optimum multisection quarter-wave impedance transformer design. The bandwidths of the Chebyshev and binomial designs are compared in References [2] and [3].

Tapered Transmission Line Transformers

In multisection quarter-wave transformers, the impedance transformation is obtained by changing the impedance in discrete steps. An alternative technique is to change the impedance level by using a tapered transition in which the characteristic impedance of the line varies continuously.

The schematic of a tapered transmission line matching unit is shown in Figure 30a, in which the normalized load impedance Z'_L is matched to a feed line having a normalized impedance, $Z'_c = 1$. The impedance of the taper $Z'(z)$ varies with distance z along the impedance taper. Figure 30b illustrates that the taper can be considered to be made up of a very large number of sections, each having an infinitesimally small length, dz , and an impedance step, dZ' , from section to section.

From the approximate theory (small reflections) of multisection quarter-wave transformers, the input reflection coefficient (Γ_{in}) can be shown to be [3]

$$\Gamma_{in} = \frac{1}{2} \int_0^L e^{-j\beta z} \frac{d}{dz} (\ln Z') dz, \quad (20)$$

where L is the length of the taper.

For a given variation of Z' with z , Γ_{in} can be evaluated using Equation (20). Three types of practical tapers will be presented in the following sections.

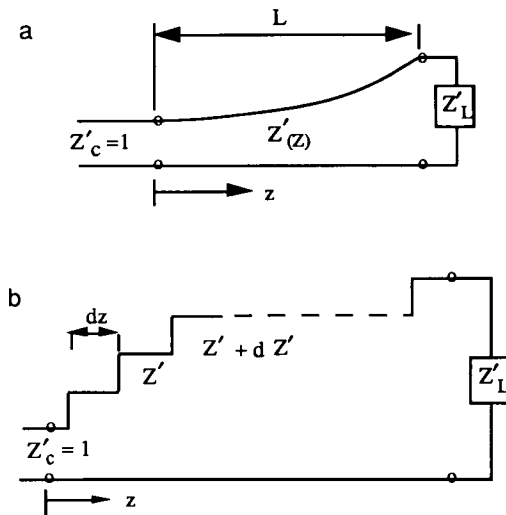


Figure 30. Tapered transmission line transformer.

Exponential Taper

In exponential tapers, \$Z'\$ varies exponentially with \$z\$ and is given by

$$Z' = e^{(z/L)\ln Z'_L}. \quad (21)$$

\$\Gamma_{in}\$ is given by

$$\Gamma_{in} = \frac{1}{2} e^{-j\beta L} \ln Z'_L \frac{\sin \beta L}{\beta L}, \quad (22)$$

where it is assumed that the transmission line is a TEM line in which \$\beta\$ is not a function of \$z\$. A plot of \$\rho_{in}\$ (\$|\Gamma_{in}|\$) as a function of \$\beta L\$ is shown in Figure 31. For a given length of taper, Figure 31 depicts the plot of \$\rho_{in}\$ vs frequency.

Triangular Distribution Taper

In a triangular distribution taper, \$d(\ln Z')/dz\$ is chosen as a triangular function of \$z\$. Therefore,

$$\frac{d(\ln Z')}{dz} = \begin{cases} \frac{4z}{L^2} \ln Z'_L & 0 \leq z \leq \frac{L}{2} \\ \frac{4}{L^2}(L-z) \ln Z' & \frac{L}{2} \leq z \leq L. \end{cases} \quad (23)$$

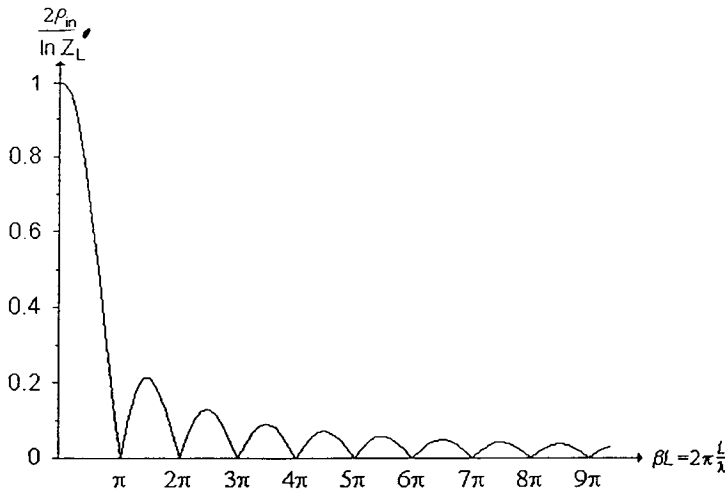


Figure 31. Reflection coefficient characteristic of an exponential taper.

Γ_{in} is given by,

$$\Gamma_{\text{in}} = \frac{1}{2} \ln Z'_L \left[\frac{\sin(\beta L/2)}{\beta L/2} \right]^2 e^{-j\beta L}. \quad (24)$$

A plot of ρ_{in} vs βL is depicted in Figure 32. It is evident, by comparison with Figure 31, that the triangular distribution taper has a first minor lobe peak value less than of the exponential taper. However, this minor lobe peak occurs for a length of nearly $3 \lambda/2$.

Chebyshev Taper

The Chebyshev taper is obtained by increasing the number of sections in a Chebyshev transformer indefinitely while keeping the length L of the transformer fixed. The input reflection coefficient is given by

$$\Gamma_{\text{in}} = \frac{1}{2} e^{-j\beta L} \ln Z'_L \frac{\cos L \sqrt{\beta^2 - \beta_0^2}}{\cosh \beta_0 L},$$

where β_0 is the value of β at the lower edge of the pass-band, as shown in Figure 33. The Chebyshev taper has an equal-ripple characteristic in the pass-band and is an optimum design because it gives the smallest ripple amplitude for a fixed taper length, and, conversely, for a specified ripple amplitude it has the shortest length.

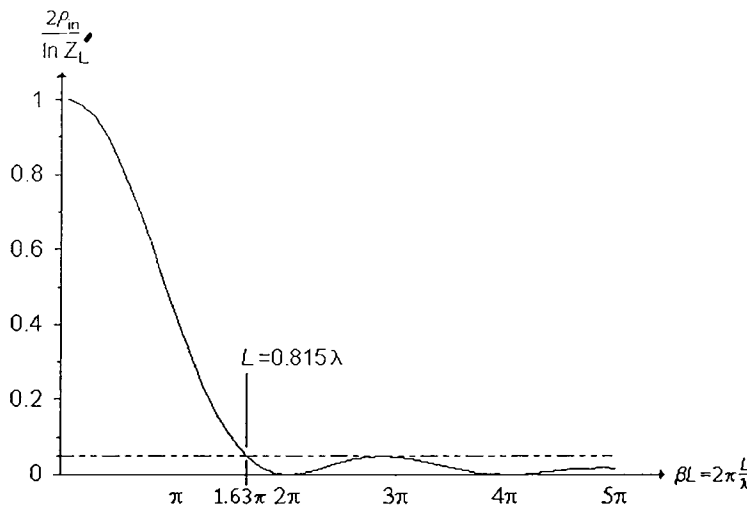


Figure 32. Reflection coefficient characteristic of a triangular taper.

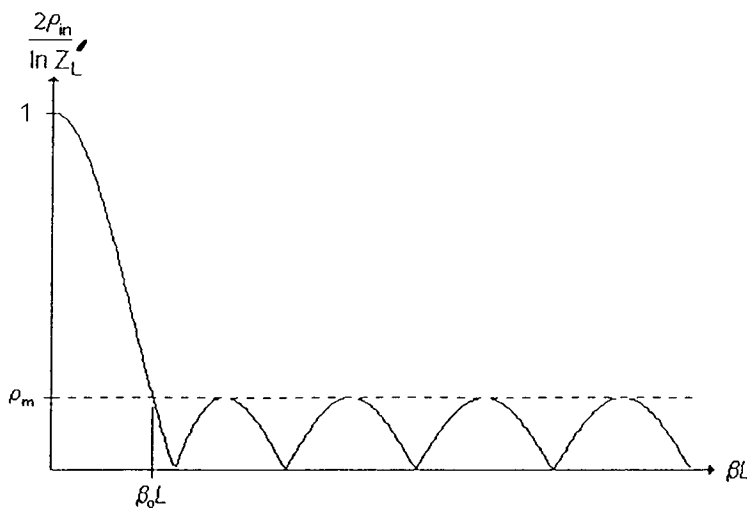


Figure 33. Reflection coefficient characteristic of a chebyshev taper transformer.

The exact theory of tapered transmission lines and their syntheses procedures can be found in Reference [3]. In Reference [2] the designs of three types of tapered transmission line transformers are illustrated by means of examples. The variation of impedance with distance along the taper as well as the frequency response of the reflection coefficients is also presented in Reference [2].

Lumped and Distributed Element Matching Networks

The synthesis of wide-band matching networks (distributed as well as lumped element) having a prescribed gain (S_{21}) slope will be presented in this section. The need for such matching networks arises in wide-band amplifier designs.

Consider a two-stage microwave FET amplifier schematic, shown in Figure 34. By a proper choice of the transistors and matching network characteristics, the amplifier may be designed for: (a) high output power, (b) low-noise figure, (c) high gain, or (d) a combination of these requirements over a specified frequency range. The output, input, and interstage matching networks may also be required to have a prescribed gain (S_{21}) slope over the given frequency range. The following requirements in the design are commonly encountered:

1. Z_L (usually 50Ω) to Z_{LP} (or Γ_{LP}) for high power; real to complex transformation.
2. Z_{I_2} (or Γ_{I_2}) to Z_{0_1} (Γ_{0_1}) for maximum power transfer; complex to complex transformation.
3. Z_{I_1} (Γ_{I_1}) to Z_S (usually 50Ω) for maximum power transfer; complex to real transformation.
4. Z_S to Z_{opt} (Γ_{opt}) for low-noise figure; real to complex transformation.

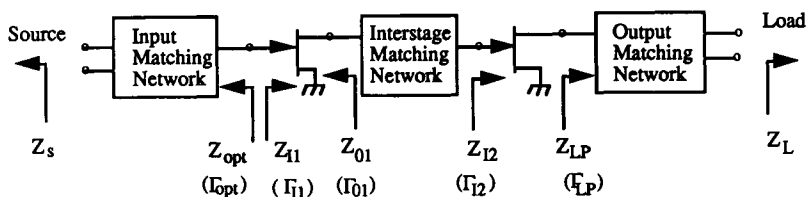


Figure 34. A two-stage microwave amplifier schematic.

The matching networks may also be required to have a prescribed $|S_{21}|$ vs frequency characteristic; either a zero slope or an appropriate positive slope (to compensate for the transistor gain roll-off). Generally a zero gain slope is used to obtain low VSWR at input and output. A positive gain slope for an interstage network is necessary to obtain a flat gain vs frequency response for the amplifier. The design of wide-band amplifiers and the criteria for selection of appropriate matching network characteristics are discussed extensively in Reference [7]. The matching networks in Figure 34 can be designed using lumped elements, distributed elements, or both.

Extensive work has been done in the area of synthesis of wide-band lumped and distributed matching networks. The method known as the real frequency technique has been developed [8]. In Reference [9] the syntheses of networks having equal-ripple characteristics have been presented. The real frequency technique of synthesis has been found to produce networks having simpler topology and superior frequency response characteristics when compared with equal-ripple designs. Further, the real frequency technique requires simple description of the load and source. Once the numerical data for the source and load are provided, the design process involves an iterative optimization procedure to arrive at the appropriate matching network.

A commercial matching network synthesis software known as MATCHNET [10] uses the real frequency technique to synthesize low-pass, high-pass, and bandpass lumped and distributed matching networks having a prescribed gain slope. Figure 35a and 35b show the schematics of wide-band (2–18 GHz) amplifiers. The matching networks were designed using MATCHNET. Figure 35a depicts lumped element matching networks, and Figure 35b shows distributed element matching networks. The distributed elements in Figure 35b are lengths of transmission lines, and open or shorted stubs. The other commercial software which aid in the design of wide-band matching networks are AMPSYN [11] and ESYN [12].

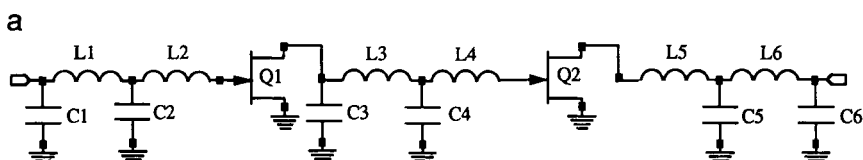


Figure 35a. Wide-band power amplifier schematic. Lumped element matching networks.

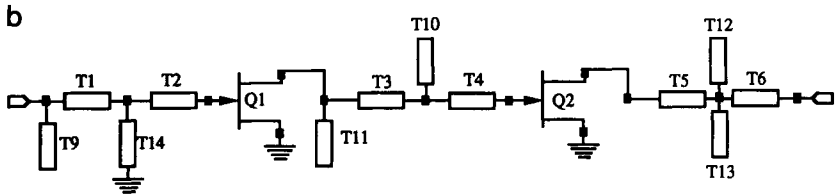


Figure 35b. Wide-band power amplifier schematic. Distributed element matching networks. T , microstrip lines.

Image Impedance Terminations

Image impedance terminations are required in networks designed on an image parameter basis, such as filter networks [13]. The image impedances of these networks are frequency dependent but real in the pass-band. Therefore, it is necessary to synthesize networks which transform frequency-independent loads to impedances which vary with frequency in a prescribed manner. The designs of image impedance terminations for low-pass and bandpass networks are illustrated in the following examples.

Low-Pass Network

In Figure 36 a wide-band low-pass distributed amplifier [14] schematic is shown. The input and output lines are low-pass filters designed on an image parameter basis. I in Figure 36 is an m -derived half-section filter [13] which transforms R_{01} and R_{02} (both real) to T -section image

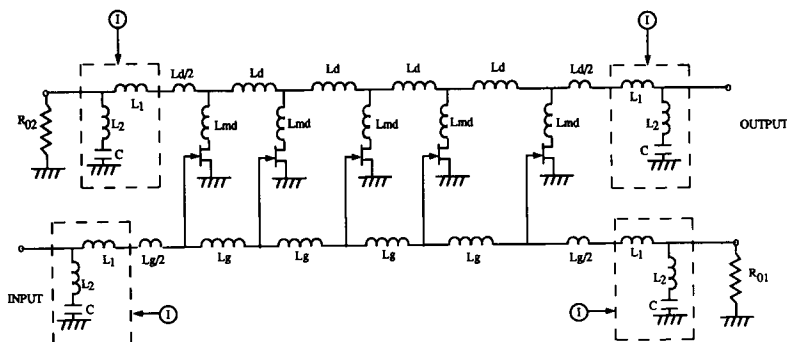


Figure 36. Low-pass distributed amplifier schematic. I , m -derived half-section filter.

impedances in the pass-band. The equations needed for the design are

$$L_1 = mL_g/2$$

$$L_2 = (1 - m^2/2m) L_g$$

$$C = mC_{gs}/2$$

$$m = 0.6,$$

where C_{gs} is the FET gate-source capacitance.

Bandpass Network

In Figure 37a a wide-band bandpass distributed amplifier [15] schematic is shown. The input and output lines are designed to be

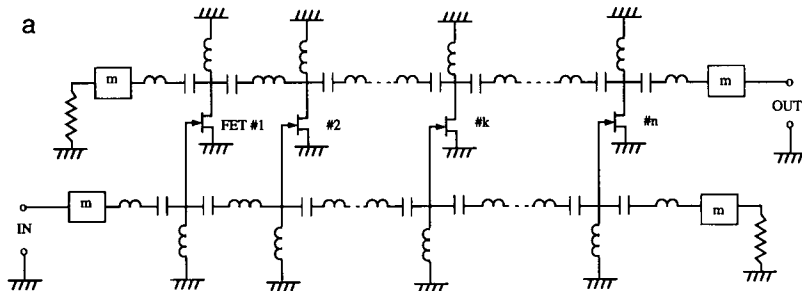


Figure 37a. Bandpass distributed amplifier schematic. m : m -derived half-section filter.

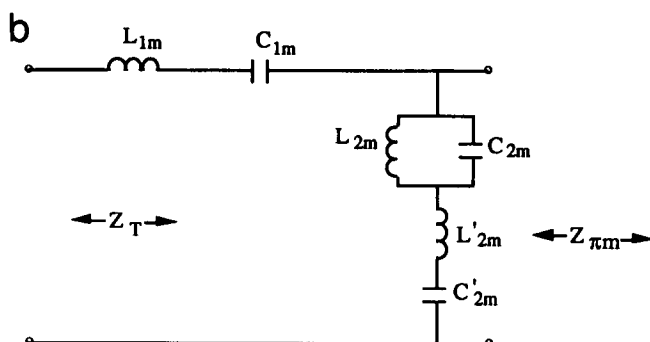


Figure 37b. Image impedance termination network. $L_{1m} = (m/2)L_{|k|}$; $C_{1m} = 2C_{|k|}/m$; $L_{2m} = (2/m)L_{|k|}$; $C_{2m} = (m/2)C_{|k|}$; $L'_{2m} = [(1 - m^2)/2m]L_{|k|}$; $C'_{2m} = [2m/(1 - m^2)]C_{|k|}$, $m \cong 0.6$.

bandpass structures. The image terminations (m in the diagram) are m -derived half-section filters [13]. In Figure 37b the image impedance termination network and the design equations are given. The topologies of other bandpass structures can be found in Reference [16].

4. Balanced to Unbalanced Transformations

Balanced to unbalanced transformers or baluns are essential in the design of devices which need balanced excitation (equal amplitude and 180° out-of-phase signals with respect to the ground). Examples of such devices are balanced antennas (such as dipoles), push-pull amplifiers, and balanced mixers. A pair of parallel wires, a slot-line, and a pair of coplanar strips are examples of balanced wave propagating systems. Commonly used transmission lines such as coaxial lines, strip lines, and microstrip lines are unbalanced. Therefore, a balun is necessary to convert the signals from these lines into balanced signals.

Passive Baluns

In Figure 38 several narrow-band passive balun configurations are shown. The design in Figure 38a provides 1:4 impedance transformation in addition to serving as a balun.

In Figure 39 a wideband tapered balun is shown. Here, the transition from coaxial line to open two-wire line is accomplished by cutting open the outer wall of the coaxial line gradually [17]. As one progresses along the balun from the coaxial end, the open sector varies from zero to almost 2π radians, yielding a transition to a two-conductor line. The balun impedance has been tapered so that the input reflection coefficient follows a Chebyshev response in the pass-band. The maximum VSWR of the test balun is 1.25 in a bandwidth of 50:1 and the dissipative loss is 0.1 dB over most of the range [17].

The foregoing idea of a tapered coaxial line balun has been adopted to design tapered printed circuit baluns in References [18, 19]. In Reference [18], a tapered printed circuit balun, from a coaxial line ($Z_0 = 50 \Omega$) feed, to a symmetrical pair of striplines has been designed as shown in Figure 40. The balun operates in the range 2.6–7.5 GHz.

In Reference [19], a tapered balun from a microstrip line to symmetrical pair of strip lines has been presented. The ground plane of the microstrip line and the microstrip line width are tapered in this balun to obtain impedance transformation and balun action, as shown in Figure 41. The balun operates at 3.5 GHz with a maximum VSWR of 1.3 in a 20% bandwidth.

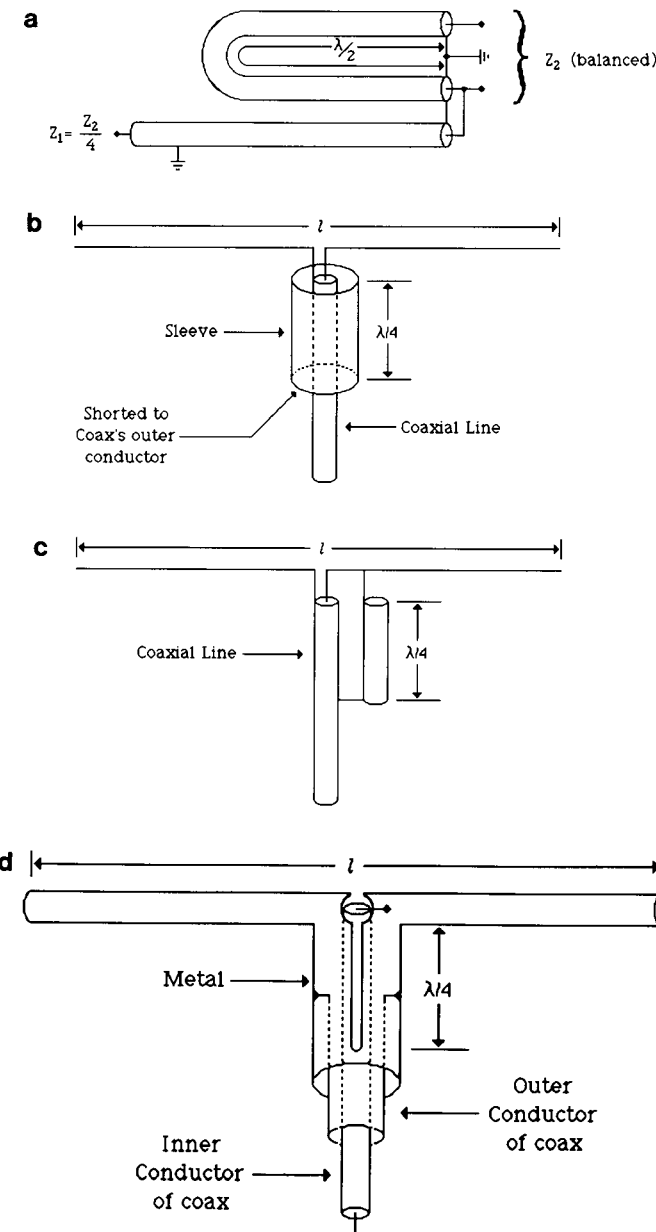


Figure 38. Configurations of baluns. (a) Half-wavelength balun (4:1 or 1:4); (b) Bazooka balun (1:1); quarter-wavelength balun (1:1); (d) coaxial balun (1:1).

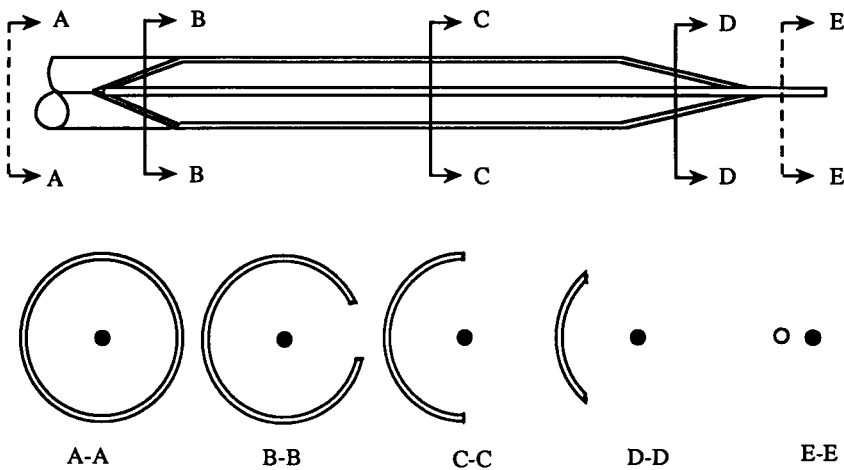


Figure 39. A wideband tapered coaxial line balun.

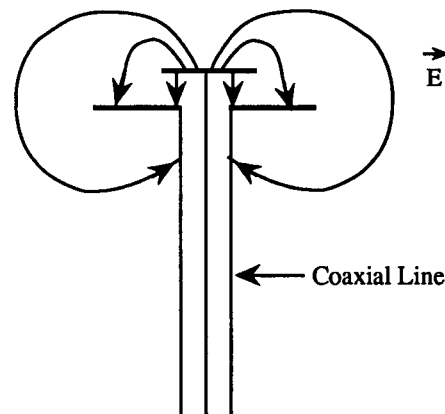
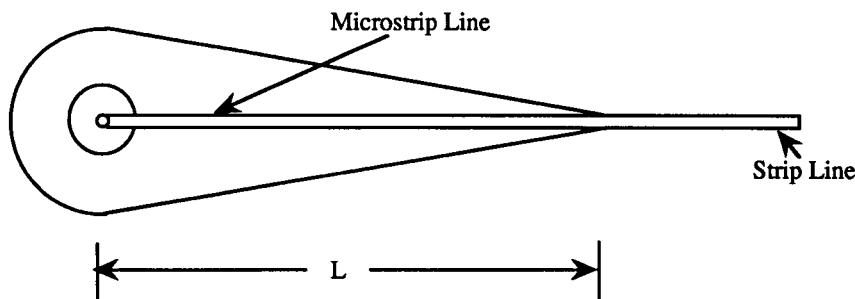


Figure 40. A wideband tapered printed circuit balun.

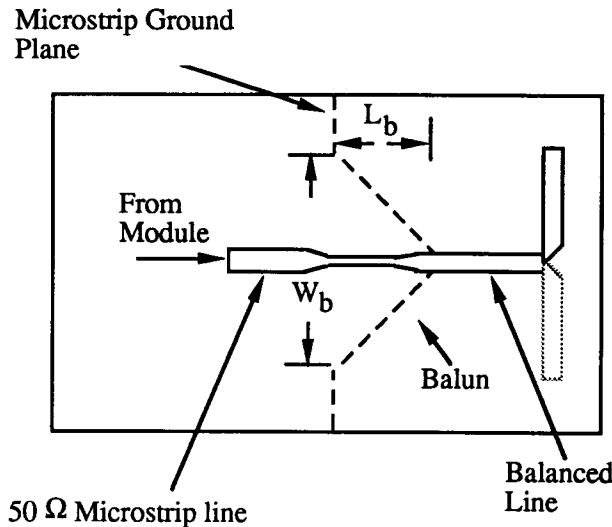


Figure 41. A wideband tapered microstrip balun.

In Figure 42a a hybrid-ring junction is shown. The signal from port 1 is split into equal amplitude and 180° out of phase signals at ports 2 and 4. The signal from port 1 is not coupled to port 3. Therefore, a hybrid-ring can be used as a narrowband balun. A modified hybrid-ring balun [20] having a wider bandwidth is shown in Figure 42b. At a given wavelength, l_3 , R , and l_{opt} have been optimized to increase the bandwidth. A bandwidth of 50% at an operating frequency of 2.5 GHz has been reported for this balun [20].

In Figure 43 is shown a schematic drawing of a coaxial line balun proposed by Roberts [21]. It has been found that at frequencies above 2 GHz, severe mechanical problems limit its use. A printed circuit version of the same balun which overcomes these problems at higher microwave frequencies, has been reported [22]. The balun was designed to feed a dual-arm spiral antenna operating over one octave band.

In references [23] and [24], other configurations of wideband passive baluns for use in amplifiers, mixers and antennas can be found. The disadvantage of a passive balun is its insertion loss. An active balun, which makes use of transistors, can be designed to provide gain.

Active Baluns

A paraphase amplifier, schematically shown in Figure 44a can be used as an active narrow-band balun. It consists of common source and common

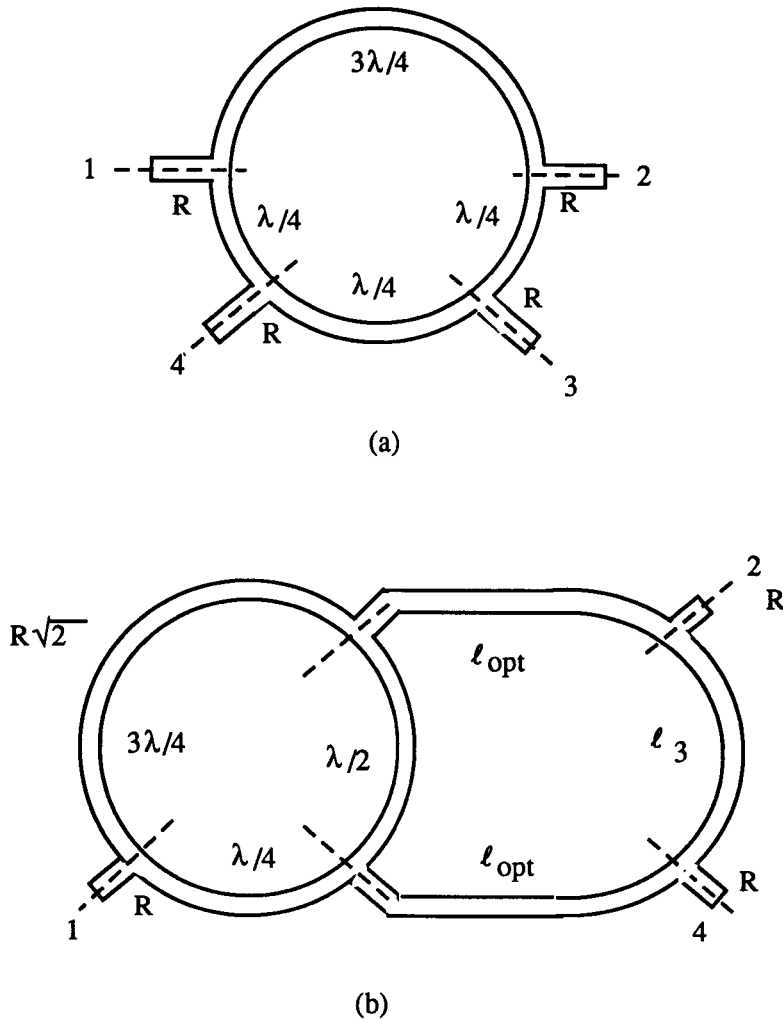


Figure 42. Hybrid-ring baluns.

gate transistors configured as shown. The paraphase amplifier cell when distributed as depicted in Figure 44b provides a wide bandwidth. The distributed paraphase amplifier splits the input signal into two equal amplitude and 180° out of phase signals at the output ports over a wide-band [25]. Therefore it can be used as an active wide-band balun.

A differential amplifier shown in Figure 45a can also be used as an active narrow-band balun. The constant current source can be realized by

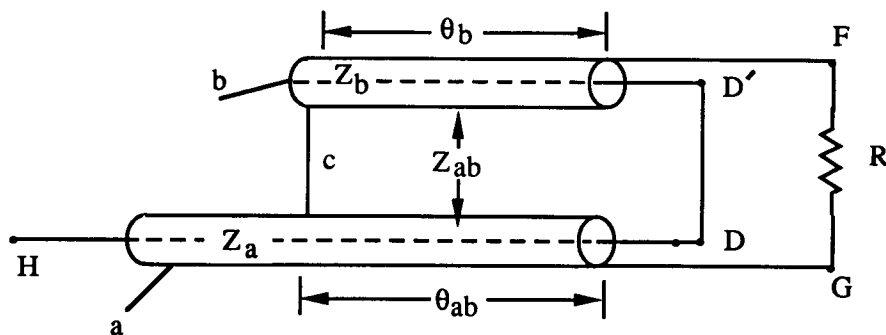


Figure 43. Roberts balun.

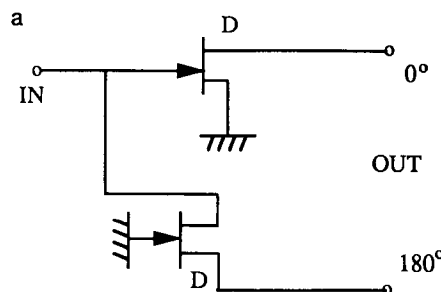


Figure 44a. A paraphase amplifier cell.

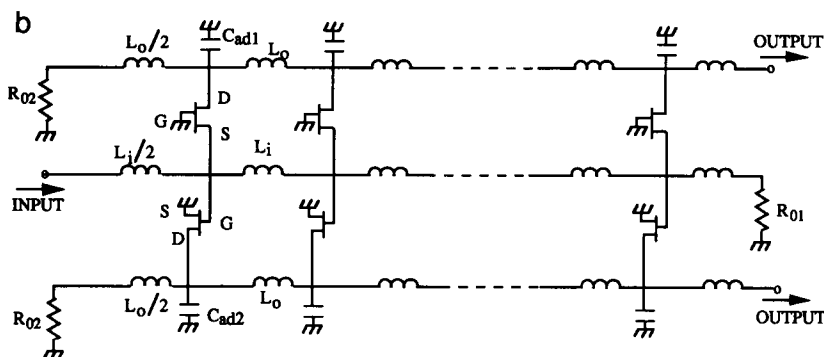


Figure 44b. Wideband paraphase amplifier schematic.

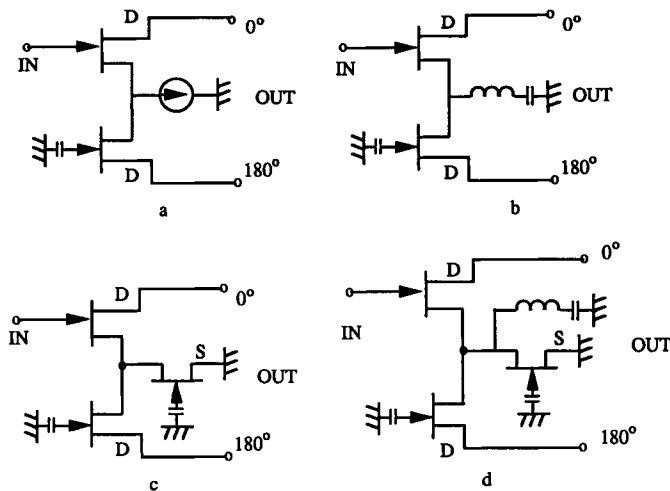


Figure 45. Differential amplifier configurations.

means of (1) a large inductor as shown in Figure 45b; (2) a grounded gate transistor as shown in Figure 45c; and (3) a combination of grounded-gate transistor and inductor [26] as shown in Figure 45d. These differential amplifier cells when distributed as illustrated in Figure 46 can provide unbalanced to balanced transformation over a wide-band.

The distributed paraphase amplifier as well as the distributed differential amplifier can also be configured to combine two balanced input signals into a single unbalanced output signal.

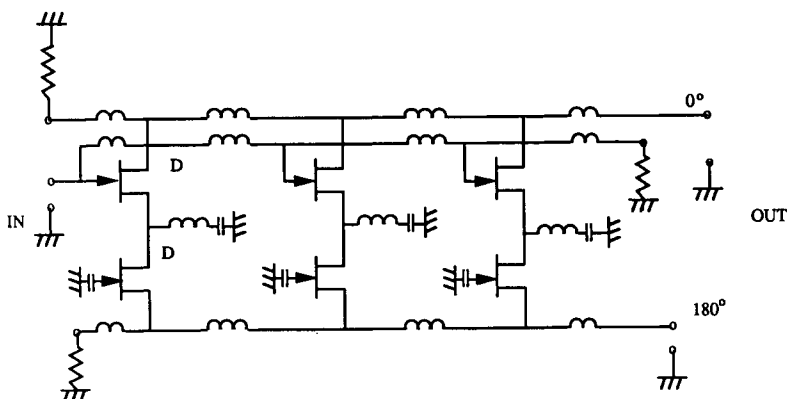


Figure 46. Schematic of a differential distributed amplifier.

Acknowledgment

I would like to acknowledge my sincere appreciation for the patience and cooperation shown by Ms. Betty Beckner in typing this manuscript. Her skill especially in computer graphics and typing complex equations are praiseworthy.

For further reading, please see References [27–49].

References

- [1] R. G. Brown, R. A. Sharpe, and W. L. Hughes, *Lines, Waves and Antennas*. New York: Ronald Press, 1961.
- [2] D. M. Pozar, *Microwave Engineering*. Reading, MA: Addison-Wesley Publishing Co., 1990.
- [3] R. E. Collin, *Foundations for Microwave Engineering*, 2nd Ed. New York: McGraw-Hill, 1992.
- [4] G. Gonzalez, *Microwave Transistor Analysis and Design*. Englewood Cliffs, NJ: 1984.
- [5] J. Smith, *Modern Communication Circuits*. New York: McGraw-Hill, 1986.
- [6] G. L. Matthei, L. Young, and E. M. T. Jones, *Microwaves Filters, Impedance Matching Networks and Coupling Structures*. Dedham, MA: Artech House, 1980.
- [7] G. Vendelin, *Design of Amplifiers and Oscillators by the S-Parameter Method*. New York: John Wiley and Sons, 1981.
- [8] H. J. Carlin and J. J. Komiak, A new method of broad-band equalization applied to microwave amplifiers, *IEEE Trans. Microwave Theory Tech.*, Vol. MTT-27, pp. 93–99, Feb. 1979.
- [9] H. J. Carlin and P. Amstutz, On optimum broad-band matching, *IEEE Trans. Circuits Syst.*, Vol. CAS-28, pp. 401–405, May 1981.
- [10] S. E. Sussman-Fort, *MATCHNET: Microwave Matching Network Synthesis Software and User's Manual*. Dedham, MA: Artech House, 1991.
- [11] "AMPSYN," Compact Software, Inc., 1131, San Antonio Road, Palo Alto, CA 94303.
- [12] Esyn, EEsof Inc., Westlake Village, CA 91362.
- [13] E. A. Guillemin, *Communication Networks*, Vol. II. New York: John Wiley & Sons, 1946.
- [14] S. N. Prasad, J. B. Beyer, and I. S. Chang, Power-band-width considerations in the design of MESFET distributed amplifiers, *IEEE Trans. Microwave Theory Tech.*, Vol. MTT-36, pp 1117–1123, July 1988.
- [15] S. N. Prasad and J. B. Beyer, Band-pass distributed amplifiers, *Microwave Opt. Technol. Lett.*, Vol. 2, pp. 349–354, Oct. 1989.
- [16] *Reference Data for Radio Engineers*. New York: Howard W. Sams & Co., 1982.
- [17] J. W. Duncan, and V. P. Minerva, 100:1 Bandwidth balun transformer, *Proc. IRE*, p 156, February 1960.
- [18] M. Gans *et. al.*, Frequency independent baluns," *Proc. IEEE*, p. 647, June 1965.
- [19] A. Gallegro, F. Esposito, and M. Pallas, Dipole antenna on a high dielectric substrate, *Proc. European Microwave Conf.*, p. 387, 1969.
- [20] H. Bex, New broadband balun, *Electron. Lett.*, Vol. 11, No. 2, p. 47, 23rd January 1975.
- [21] W. K. Roberts, A new wideband balun, *Proc. IRE*, Vol. 45, p. 1625, December 1957.
- [22] R. Bawer and J. J. Wolfe, A printed circuit balun for use with spiral antenna, *IRE Trans. Microwave Theory Tech.*, p. 319, May 1960.

- [23] R. Bassett, Three balun designs for push-pull amplifiers, *Microwaves*, pp. 47–52, July 1980.
- [24] R. Sturdavant, Balun designs for wireless, . . . mixers, amplifiers and antennas, *App. Microwave Wireless*, pp. 34–44, Summer 1993.
- [25] Y. W. Chen, J. B. Beyer, and S. N. Prasad, MESFET wideband distributed paraphase amplifier, *Int. J. Electron.*, Vol. 58, No. 4, pp. 553–569, 1985.
- [26] V. Sokolov and R. E. Williams, Development of GaAs power amplifiers in X-band, *IEEE Trans. Electron Devices*, Vol. ED-27, pp 1164–1171, June 1980.

Further Reading

Reference

- [27] J. J. Karakash, *Transmission Lines and Filter Networks*. New York: Macmillan, 1950.
- [28] R. M. Fano, Theoretical limitations on the broad-band matching of arbitrary impedances, *J. Franklin Inst.*, Vol. 249, pp. 57–83, Jan. 1950; Vol. 249, pp. 139–154, Feb. 1950.
- [29] D. C. Youla, A new theory of broadband matching, *IEEE Trans. Circuit Theory*, Vol. CT-11, pp. 30–50, Mar. 1964.
- [30] W. K. Chen, Synthesis of optimum Butterworth and Chebyshev broadband impedance matching networks, *IEEE Trans. Circuits Syst.*, Vol. CAS-24, pp. 152–169, Apr. 1977.
- [31] D. J. Mellor and J. G. Linvill, Synthesis of interstage networks of prescribed gain versus frequency slopes, *IEEE Trans. Microwave Theory Tech.*, Vol. MTT-23, pp. 1013–1020, Dec. 1975.
- [32] W. H. Ku and W. C. Peterson, Optimum gain-bandwidth limitations of transistor amplifiers as reactively constrained active two-port networks, *IEEE Trans. Circuits Syst.*, Vol. CAS-22, pp. 523–533, June 1975.
- [33] Y. Wang, New method for tapered transmission line design, *Electron. Lett.*, Vol. 27, No. 25, pp. 2396–2397, 5th December 1991.
- [34] R. E. Collin, Theory and design of wide band multisection quarter-wave transformers, *Proc. IRE*, Vol. 43, pp. 179–185, Feb. 1955.
- [35] S. B. Cohn, Optimum design of stepped transmission line transformers, *IRE Trans. Microwave Theory Tech.*, Vol. MTT-3, pp. 16–21, Apr. 1955.
- [36] H. J. Riblet, General synthesis of quarter-wave impedance transformers, *IRE Trans. Microwave Theory Tech.*, MTT-5, pp. 36–43, Jan. 1957.
- [37] L. Young, Tables for cascaded homogeneous quarter-wave transformers, *IRE Trans. Microwave Theory Tech.*, Vol. MTT-7, pp. 233–237, Apr. 1959; see also *IRE Trans. Microwave Theory Tech.*, Vol. MTT-8, pp. 243–244, 1960, for corrections.
- [38] L. Solymar, Some notes on the optimum design of stepped transmission line transformers, *IRE Trans. Microwave Theory Tech.*, Vol. MTT-6, pp. 374–378, Oct. 1958.
- [39] R. W. Klopfenstein, A transmission line taper of improved design, *Proc. IRE*, Vol. 44, pp. 31–35, Jan. 1956.
- [40] R. E. Collin, The optimum tapered transmission line matching section, *Proc. IRE*, Vol. 44, pp. 539–548, Apr. 1956.
- [41] P. L. D. Abrie, *The Design of Impedance-Matching Networks for Radio Frequency and Microwave Amplifiers*. Dedham, MA: Artech House, 1985.
- [42] P. A. Rizzi, *Microwave Engineering Passive Circuits*. Englewood Cliffs, NJ: Prentice-Hall, 1988.
- [43] V. Trifunović and B. Jakanović, Review of printed Marchand and double Y Baluns: Characteristics and applications, *IEEE Trans. Microwave Theory Tech.*, Vol. MTT-42, pp. 1454–1462, Aug. 1994.

- [44] R. Schwindt and C. Nguyen, Computer-aided analysis and design of a planar multilayer Marchand Balun, *IEEE Trans. Microwave Theory Tech.*, Vol. MTT-42, pp. 1429–1434, July 1994.
- [45] C. A. Balanis, *Antenna Theory Analysis and Design*. New York: Harper & Row, 1982.
- [46] B. G. Evans, Chebyshev quarter-wave stepped balun transformer,” *Electron. Lett.*, Vol. 9, No. 22, 1st November 1973.
- [47] W. Wiesbec, Dipol—und YAGI—Antenna fur die Mikrowellen-Streifenleitungstechnik, *Mikrowellen J.*, 3, p. 171, 1975.
- [48] P. A. R. Holden, X-band integrated circuits using slotlines and co-planar waveguides, *Radio Electron. Engineer*, Vol. 48, No. 1/2, pp. 38–42, January/February 1978.
- [49] C. L. Ruthroff, Some broad-band transformers,” *Proc. IRE*, Vol. 47, pp. 1337–1342, August 1959.

This Page Intentionally Left Blank

Index

A

Absorbing microstrip terminations, 131–135
Active baluns, 663–666
Admittance, 61–62, 620
All-pass filters, 161–162
All-pole bandpass transformations, 164, 170
Alumina (Al_2O_3), 48, 95, 112
Aluminum (Al), 19, 96, 369
AM detectors, *see* Amplitude modulation detectors
AM noise, *see* Amplitude modulation noise
Amplifiers, 391–392, 589–590
 bipolar amplifiers, 405–406
 design, 394–423
 differential amplifiers, 666
 GUNN amplifiers, 346–350
 IMPATT devices, 377–381
 impedance matching, 630, 631, 656
 isolators, 254–257, 408–410, 423
 low-noise amplifiers, 392–394, 405–428,
 487
 moderate bandwidth amplifiers, 392, 393,
 395, 426
 noise, 384–386, 407, 411, 413, 415–419
 octave band amplifiers, 392–393, 412, 416,
 428
 parametric amplifiers, 487
 paraphrase amplifiers, 663–666
 power amplifiers, 423–428
 triode amplifiers, 589–591
 ultra-low-noise amplifiers, 415, 428
 ultra-wide-band amplifiers, 394, 413, 414
 wide-band amplifiers, 405, 414, 657, 658
Amplitude modulation (AM) detectors,
 461–470
bridge detectors, 462

coaxial line detectors, 464–466
microstrip line detectors, 467, 469–470
microwave FM detection, 474–475
quadruple detectors, 462–463
ring detectors, 462
series diode detectors, 461–462
shunt diode detectors, 461–462
two-wire line detectors, 463–465
waveguide detectors, 465–468, 492
Amplitude modulation (AM) noise, 487–489
 GUNN oscillators, 350, 351, 353
AMPSSYN (software), 657
Antimony (Sb), diodes, 371
Antipodal finlines, 28–31
Applied magnetic field, 235
Approximate narrow-band filters, 168
Arbitrary loss, dielectric film capacitors,
 111–113
ARGUS (software), 528
Arithmetic symmetry, bandpass transforms,
 171–172
Arsenic (As), diodes, 371
Arsenic trichloride, vapor-phase epitaxy,
 314–315
Arsine, vapor-phase epitaxy, 314, 315
Asymmetric couplers, 214–216
Asymmetric series gap capacitors, 118–121
Attenuation
 circular waveguides, 26
 coaxial lines, 12–13
 imageguides, 39–40
 insertion loss, 569
 low-pass filter prototypes, 159–160
 microstrip lines, 51
 mismatch attenuation, 159

- Attenuation constant
 circular waveguides, 22, 27
 coaxial lines, 6, 10
 dielectric rectangular waveguides, 38
 imageguides, 39–40
 rectangular waveguides, 18
 suspended substrate technique, 143–144
 TEM lines, 3
- Attenuators, solid state, 586–588
- AUTOGRID (software), 519
- Avalanche region, 283, 363, 367
- Average power rating, waveguides, 21–22, 27–28
- B**
- Backward diodes, 261, 262
- Balanced amplifier design, 410–411
- Baluns (balanced to unbalanced
 transformers), 660–666
- Bandpass filters, 156, 164–170, 179–182
 combline bandpass filters, 181
 dissipation loss, 186
 hairpin bandpass filters, 180–181
 interdigital bandpass filters, 181–182
 loaded Q definition, 185
 parallel-coupled half-wave resonator
 bandpass filters, 179–180
 symmetric transforms, 169–170
 top-C-coupled, 166–168, 171
 top-L-coupled, 168–169, 171–172
 tubular, 170
 yttrium iron garnet, 256–257
- Bandpass loss, 186
- Bandpass networks, 659–660
- Bandpass transforms, 164–172
- Bandstop filters, 165, 185
- Bandstop filter transforms, 165–166
- Barium ferrite spheres, 341
- Barrier injection transit-time (BARITT)
 diodes, 261, 364, 365
- Barrier potential, diodes, 264
- Bazooka baluns, 661
- Beam-lead diodes, 261–264, 268–269, 273
- Beam shavers, 498
- Beryllium (Be), 372
- Bessel function zeros, 74
- Bessel prototype values, 161, 162
- Bethe-hole couplers, 202–205
- Bethe holes, 202
- Bias current, 277, 281
- Biassing
 attenuators, 586–588
 direct current, 585–587
 phase shifters, 582–586
 transistors, 396–397
- Bias-tuned GUNN oscillators, 340–341
- Bias voltage, 277, 281, 282, 340, 582
- Bilateral finlines, 28–31, 33–34
- Binomial couplers, 207, 208
- Binomial transformers, 641–645
- Bipolar amplifiers, 405–406
- Bipolar junction transistors (BJT), 284–293, 405, 419, 432
- Blinchikoff flat delay bandpass transform, 172
- Boron (B), varactor diode, 271
- Branch-guide couplers, 225–226, 228
- Branch-line couplers, 223, 225–228, 232
- Brass, 19, 344
- Bridge detectors, 462
- Brillouin field level, 539, 540
- Brillouin focusing, 548, 549
- Broadside-coupled stripline coupler, 218
- Bulk resonators, 196
- Butterworth approximation, 156–158, 160, 161
- Butterworth filters, 159
- C**
- CAD, *see* Computer-aided design
- Cadmium telluride (CdTe), 276, 309
- Capacitance, 186–187
 avalanche capacitance, 283
 capacitors, 112, 115–121
 coaxial lines, 7
 detectors, 462, 463
 diodes, 263, 266, 269–271, 273, 277, 279, 283
 domain capacitance, 279
 effective capacitance, 115
 end capacitance, 122
 equivalent capacitance, 54
 filters, 167
 ground capacitance, 99, 101
 inductors, 99, 101, 106, 109–110
 junction capacitance
 quarter-wave transformers, 651–652
 solid-state devices, 263, 266, 269, 270, 271, 273–275, 276, 571
 microstrip lines, 53–58

- open-end capacitance, 53, 121
package capacitance, 277, 571
parallel capacitance, 128
parasitic capacitance, 263, 271, 273, 413
shunt capacitance, 462
total capacitance, 263, 273
transistors, 301
two-wire lines, 4
winding capacitance, 106, 109–110
- Capacitors**, 186–188
capacitance, 112, 115–121
chip capacitors, 187
coupling capacitors, 167
dielectric-film overlay capacitors, 111–115
disk capacitors, 115–118
radio frequency choke, 464, 466, 470
series gap capacitors, 118–121
- Cathode heaters**, 516–518
- Cathodes**
computer-aided design, 517
dispenser cathodes, 514–515, 517
heaters, 516–518
loading, 513–514
oxide cathodes, 515–516
type M cathode, 515
- Cauer–Chebyshev prototypes**, 162–163
- Cavity-stabilized GUNN oscillators (CSGO)**, 342–346
- Cavity-tuned oscillators**, 433, 435–436
- Center frequency**
bandpass filter prototypes, 164
circulators, 251–252
- Ceramics**, 194–195
- Chamfered symmetric bend**, 130–131
- Characteristic conductance**, transmission lines, 62
- Characteristic impedance**
bilateral finlines, 33–34
coaxial lines, 6
dielectric waveguides, 42–43
finlines, 33–34
imageguides, 41–43
microstrip lines, 48, 49–52, 55
TEM lines, 3
unilateral finlines, 33–34
waveguides, 13
- Chebyshev approximation**, 159–161
- Chebyshev couplers**, 208–210, 226–228
- Chebyshev tapers**, 654–655
- Chebyshev transformers**, 645–651, 654
- Child–Langmuir law, 511–512
Chip capacitors, 187
Chip diodes, 273
Chip transistors, 403
Circular cylindrical waveguide cavities, 73–80
Circular disk capacitors, 115–116
Circular ring inductors, 103
Circular spiral inductors, 103–107
Circular waveguides, 14, 22–28
attenuation, 22, 26, 27
phase shifters, 244–246
- Circulators**, 249–250
ferrites, 249–254, 347
switches, 257–258
- C–L law**, 511–512
- Closed ring resonators**, 87–88
- Coarse-step frequency synthesizer**, 454
- Coaxial-cavity GUNN oscillators**, 326, 327–328, 336–338
- Coaxial lines**, 1, 5–13
AM detectors, 464–466
attenuation, 12–13
baluns, 660, 662, 663
equations, 6, 7, 12–13
microwave mixers, 479–480
modes, 8–10
Q-factor, 7
- Coaxial resonators**, 66–68, 196, 433, 436–437
oscillators, 433, 436, 437, 445, 446
- Coaxial-to-microstrip transitions**, 136–138
- Codes**, *see* Software
- Collector efficiency**, transistors, 288
- Collectors**
Faraday cage collectors, 552
multistage depressed collectors, 556, 558–559
secondary emission, 559–560
single-stage collectors, 552–555
spent beam models, 553–556
- Comline bandpass filters**, 181
- Complex to real impedance transformation**, 632–636, 637–639
- Computer-aided design (CAD)**
amplifiers, 421
cathodes, 517
electron gun design, 502–503, 505–508
IMPATT oscillators, 383
transistors, 292–293, 302
- Computer simulation**, *see* Simulation
- Computer software**, *see* Software

- Conductance, characteristic, 62
 Conductivity modulation, 275
 Conductor attenuation constant, coaxial lines, 7
 Conductor loss
 dielectric film capacitors, 114–115
 microstrip lines, 51–52
 Conductor quality factor, 7
 Conductor thickness, microstrip lines, 50
 Conductor width, microstrip lines, 55–56, 127–128
 Confined flow focusing, 549–550, 551
 Constituent cavity, 251, 254
 Continuous coupling, 211
 Continuous-wave (CW) oscillators, 383, 384
 Controlled phase prototypes, 160–162
 Conventional elliptic bandpass transforms, 170, 171
 Converters, 485–486
 noise, 487–489
 packaging, 494
 Coplanar waveguide coupler, 218
 Copper (Cu), 18, 20, 27, 369
 Cores, 195
 Corona rings, 539
 Coupled-line couplers, 200, 213–225
 Coupled lines, suspended substrate technique, 145, 149–153
 Coupled round rod couplers, 218
 Coupled slotline couplers, 218
 Coupled wave voltage, 214
 Couplers
 amplifier design, 410–411, 590
 directional, 199–201, 232
 branch-guide couplers, 225–226, 228
 branch-line couplers, 223, 225–228, 232
 coupled-line couplers, 200, 213–225
 rat-race couplers, 229–232
 waveguide aperture couplers, 201–213
 impedance, 214, 223–224, 228
 Coupling capacitors, bandpass filters, 167
 Coupling factors, 62, 64
 Coupling inductors, 168
 Critical microwave magnetic field, 237
 Crossed-guide coupler, 212–213
 Cross junction, microstrip lines, 58
 Cryogenically cooled low-noise amplifier, 419, 421
 CSGO, *see* Cavity-stabilized GUNN oscillators
 Current density, electron guns, 513–514
 Current sensitivity, diodes, 265
 Cutoff frequency
 bandpass filter prototypes, 164
 coaxial transmission lines, 67
 diodes, 263, 264, 270, 272–274
 distributed resonators, 192
 dynamic cutoff frequency, 270
 scaling prototype values, 157
 transistors, 286, 290, 299
 Cutoff wavelength
 circular waveguides, 23, 26
 coaxial lines, 7, 9, 10
 rectangular waveguides, 15, 18
 resonant cavities, 328
 CW oscillators, *see* Continuous-wave oscillators
 Cylindrical cores, 195
 Cylindrical resonators, 73–80
- D**
- Damping factor, 236
 DC biasing, *see* Direct current biasing
 Deformable triangular mesh (DTM) gun codes, 522–523, 525–526, 530
 Delay, coaxial lines, 7
 DEMEOS (software), 502, 518–525, 532–533, 535, 551, 552, 556, 558
 Depressed efficiency, 558
 Detector diodes, 261–268
 AM detectors, 461, 463, 465, 467, 471
 packaging, 491–492
 Detectors
 amplitude modulation, 461–470
 frequency modulation, 470–477
 noise, 487–489
 packaging, 491–492
 phase modulation, 477–478
 video impedance, 265
 Diamond, 369, 374
 Dielectric attenuation constant, coaxial lines, 7
 Dielectric constant
 effective dielectric constant
 finlines, 32
 microstrip lines, 48, 49–51
 software for, 224
 Dielectric coupler, scattering parameters, 217
 Dielectric film capacitors, 111–115

- Dielectric loaded TEM mode, 196
Dielectric loss
 dielectric film capacitors, 114–115
 microstrip lines, 51
 suspended substrate technique, 143
Dielectric resonators, 80–83, 196, 346,
 436–438
 oscillators, 436–438, 445, 447
Dielectric ring resonators, 83
Dielectric substrates, 48, 95
 ceramics, 194–195
Dielectric waveguides, 34–35
 characteristic impedance, 42–43
 losses, 38–42
 propagation constant, 35–38
Differential amplifiers, 666
Dimensional ratio, resonant cavities, 344
Diodes, 307
 backward diodes, 261, 262
 BARITT diodes, 261, 364, 365
 beam-lead diodes, 261–264, 268–269, 273
 capacitance, 263, 266, 269–271, 273, 277,
 279, 283
 Child–Langmuir law, 511–512
 detector diodes, 261–268, 461, 463, 465,
 467, 471
 packaging, 491–492
 DOVETT diodes, 365
 forward-biased diodes, 271, 274
 GUNN diodes, 276–280, 307
 amplifiers, 424–435
 design, 316–325
 oscillators, 332–334, 337, 342
 power combiners, 354
 IMPATT diodes, 276, 280–284, 348, 354,
 363–368
 amplifier design, 377–381
 commercial specifications, 373–377
 fabrication, 368–373
 noise, 384–386
 oscillator design, 382–386
 impedance, 283, 284
 inductance, 263, 273–274, 277, 283
 Josephson junction diodes, 261
 junction diodes, 268, 269, 271
 MITATT diodes, 365
 mixer diodes, 261–268, 478–485
 packaged, 463, 465, 467, 491–492
 PIN diodes, 272–276, 489, 491–492,
 569–582, 586–588
 point-contact diodes, 261, 262
 QWITT diodes, 365, 370
 Read diodes, 368
 rectification, 265, 266
 resistance, 263, 266, 270–271, 273, 275,
 582–583, 586
 Schottky-barrier diodes, 261–268, 463, 465,
 491–492
 SIS junction diodes, 261
 switches, solid-state, 569–582
 TRAPATT diodes, 365
 TUNNETT diodes, 364, 365
 varactor diodes, 268–272, 487, 490,
 582–586, 587
 whisker diodes, 261–264, 269
Diplexers, 579–580
Direct current biasing, 585–587
Direct frequency synthesis, 449–452
Direct grounded lumped terminations,
 132–133
Directional couplers, 199–201, 232
 branch-guide couplers, 225–226, 228
 branch-line couplers, 223, 225–228, 232
 coupled-line couplers, 200, 213–225
 microwave mixers, 481
 rat-race couplers, 229–232
 waveguide aperture couplers, 201–213
Directivity response, couplers, 200, 206–211
Direct wave voltage, 214
Discontinuities
 distributed filters, 174–175
 microstrip lines, 53–58
 impedance steps, 55–56, 127–128
 open-ended microstrip, 121–123
 right-angle bends, 56–57, 128–130
 short circuits, 122, 124–126
 quarter-wave transformers, 651
 simulations, 183–184
Discriminator mode (resonator), 474, 475
Disk capacitors, 115–118
Dispenser cathodes, electron emission,
 514–515, 517
Dispersion
 microstrip lines, 50–51
 suspended substrate technique, 143–153
 transformer design, 652
Dissipation loss, 184–186
Distortion, bandpass transforms, 171–172
Distributed amplification, 412–414, 422, 423,
 666

Distributed element matching networks, 656–658
 Distributed filters, 156, 172–182
 Distributed resonators, cutoff frequency, 192
 Distributed terminations, 131, 135
 Domain capacitance, 279
 Doping profile, diodes, 320–321, 367
 Double-drift IMPATT diodes, 280, 370, 375
 Double period permanent magnet (DPPM) focusing, 553–554
 Double stub impedance matching, 622–623
 Double-velocity transit-time (DOVETT) diodes, 365
 Down-converters, 486
 DPPM focusing, *see* Double period permanent magnet focusing
 Drain lines, 413
 Drain-source current, 301, 400
 Drift region, impedance, 283
 DTM gun codes, *see* Deformable triangular mesh (DTM) gun codes
 Dual-mode electron guns, 506, 507
 Dual-mode phase shifters, 244–245
 Dynamic cutoff frequency, 270
 Dynamic quality factor, 270

E

Edge-coupled stripline couplers, 218, 219, 224–225
 EEsorf (software), 421
 Effective capacitance, 115
 Effective dielectric constant
 finlines, 32
 microstrip lines, 48, 49–51
 Effective gyromagnetic ratio, 236
 Effective inductance, 189, 283
 Effective permeability, core, 195
 Efficiency, transistors, 290
 Efficiency gain, 558–559
 EGUN (software), 522, 528, 532, 535, 551
 Electric field, waveguides, 15–17, 23–25
 Electromagnetic waves, in ferrite medium, 237–241
 Electron beams, 497
 beam optical design, 518–530, 561
 collection, 552–560
 electron emission, 511–518
 focusing, 498, 505, 506, 539–552
 measurement, 560–561

Electron emission
 cathode heaters, 516–518
 cathode loading, 513–514
 dispenser cathodes, 514–515, 517
 microwave tubes, 511–518
 oxide cathodes, 515–516
 Electron guns, 498–510
 advanced centerpost guns, 509, 510
 beam optical design, 518–530
 cathodes
 dispenser cathodes, 514–515, 517
 heating, 516–518
 loading, 513–514
 oxide cathodes, 515–516
 design, 502–503, 505–508, 530–539
 dual-mode electron guns, 506, 507
 gridded guns, 502–505
 gun codes, 522–528
 gyrotron electron guns, 508, 509
 high-perveance hollow-beam guns, 507–508
 high-perveance intercepting gridded guns, 506
 hollow-beam guns, 507–510
 hybrid grid electron guns, 504, 505
 intercepting gridded electron guns, 503, 506
 low-noise guns, 505–506
 magnetic centerpost guns, 508–509
 magnetron injection guns, 507
 measurement, 560–561
 mod anode guns, 502
 Pierce guns, 498–504, 513–514, 530–539
 shadow-gridded electron guns, 502–504, 505, 514
 Electronically tuned oscillators, 335–342, 429–433
 Elliptic approximations, filters, 162–163
 Elliptic bandpass transforms, 170–171
 Elliptic low-pass filters, 175, 177
 EM codes, 528, 530
 EMSim (software), 184
 Enclosure, microstrip lines, 52
 End capacitance, 122
 End-coupled half-wave resonators, 178–179
 End effect length, microstrip lines, 53
 Epitaxial growth, diode fabrication, 313–316, 368, 370
 Equivalent capacitance, 54
 Equivalent dielectric constant, finlines, 32

- Equivalent end effect length, 122
ESYN (software), 657
Exponential taper, 653
- F**
- Fabry–Perot resonators, 88–89
Faraday cage collectors, 552
Faraday rotation, 237
Feedback
 lossless, 411–414
 tetrode, thermionic, 604–605
Ferrite devices
 bandpass filters, 256–257
 circulators, 249–254, 347
 Gunn oscillator, 341
 isolators, 254–256
 phase shifters, 241–248
 switches, 257–258
 waveguides, 239–240
 yttrium iron garnet devices, 256–257
- Ferrites, 195
 barium ferrite sphere, 341
 electromagnetic waves, 237–241
 ferrite/garnet, dielectric substrate, 48
 magnetized, 235–236
 microwave properties, 235–237
 partially magnetized, 236
- FET, *see* Field effect transistors
- Field displacement isolators, 255
- Field distribution
 circular waveguide, 23–25
 rectangular waveguides, 15–17, 36
- Field effect transistors (FET), 293–302, 419
 amplifiers, 413, 419, 432
- Field emission, 511, 512
- Field reversal focusing, 552
- Field simulators, 183–184
- Film capacitors, 111–115
- Filters
 all-pass filters, 161–162
 bandpass filters, 156, 164–170, 179–182
 dissipation loss, 186
 loaded Q , 185
 yttrium iron garnet, 256–257
 bandstop filters, 165
 loaded Q , 185
 capacitance, 167
 components, 186–197
 design, computer simulation, 182–184
 dissipation loss, 184–186
- distributed filters, 156, 172–182
high-pass filters, 156, 163–164
L–C filter transformation, 163–171
low-pass filters, 156, 159
 dissipation loss, 185–186
low-pass prototype, 155–163
microwave mixers, 484
radio frequency choke, 464
surface acoustic wave (SAW) devices, 197
yttrium iron garnet, 256–257
- Fine frequency synthesizers, 454
- Finlines, 29, 32–34
- Flicker noise, 488
- FLUX (software), 550
- FM detectors, *see* Frequency modulation detectors
- FM noise, *see* Frequency modulation noise
- Focusing
 electron beams
 Brillouin focusing, 548, 549
 computer codes, 550–551
 confined-flow focusing, 549–550, 551
 double period permanent magnetic focusing, 543–544
 field reversal focusing, 552
 long-period focusing, 552
 magnetic, 539–544, 561
 periodic permanent magnet focusing, 540–544, 547
 solenoidal focusing, 548–551
 solution splicing and emittance growth, 544–547
 space-charge balanced flow focusing, 549
 uniform field focusing, 544–547
 Foreshortened coaxial line resonators, 67–68
 Forward-biased diodes, 271, 274
 Fowler–Nordheim equation, 512
 Fractional bandwidth, bandpass filter prototypes, 164
- Free-running oscillators, 429, 438
- Free-space resonant frequency, 328–329
- Frequency agility, 449
- Frequency doublers, 458–459
- Frequency modulation (FM) detectors, 470–477
- Frequency modulation (FM) noise, GUNN oscillators, 342–343
- Frequency multiplier, 335, 458–460
- Frequency of oscillation, 278, 299

Frequency sweepers, GUNN voltage-controlled oscillators, 341–342
 Frequency synthesizers, 448–458
 Frequency of unity current gain, 290, 299
 FVR (software), 543

G

Gain

amplifiers, 399–400, 402, 403, 419
 IMPATT diodes, 382
 reflection gain, 347
 transistors, 290, 299
 triode amplifiers, 591
 triodes, thermionic, 591, 594, 598

Gallium arsenide (GaAs)

amplifiers, 405, 413
 capacitors, 112
 dielectric substrate, 48, 95
 diodes, 261–269, 271, 276–277, 280, 367, 373–374, 377, 432
 GUNN diodes, 307, 308, 317–321, 323–325, 332–334, 337, 342, 348
 epitaxial growth, 314–315
 metallization, 371–372
 negative differential mobility, 309–313
 properties, 368, 369
 transferred electron effect, 308
 transistors, 284, 285, 287, 288, 293–295, 297, 298, 300, 302, 405, 419

Gallium arsenide phosphide (GaAsP)

Gunn diodes, 276
 negative differential mobility, 309

Gap

microstrip line, 54–55
 series gap capacitors, 118–121

Gate lines

413

Germanium (Ge)

, 369, 371, 372

Glass, dielectric substrate

, 48

Gold (Au)

, 371, 372
 diodes, 274

GUNN devices, 319, 321, 324

inductors, 96, 99, 105

properties, 369

G points

, 523

Gridded electron guns

, 502–505
 design, 519

focusing, 539, 540

tunnel emittance, 536–537

Ground capacitance, inductors

, 99, 101

Group delay

, 161

Group velocity, waveguides

, 15, 23

Guide wavelength

microstrip lines, 48, 49

waveguides, 15, 23

Gun codes

, 522–528

GUNN amplifiers

, 346–350

GUNN devices

, 307–308
 design and fabrication, 313–325

history, 308–309

negative differential mobility, 309–313

noise characteristics, 350–354

power combiners, 354–356

GUNN diodes

, 276–280, 307

amplifiers, 424–435

design, 316–325

oscillators, 332–334, 337, 342

power combiners, 354

GUNN effect

, 276

GUNN mode

, 278–279

GUNN oscillators

, 307, 324, 325–346

bias-tuned GUNN oscillators, 340–341

cavity-stabilized, 342–346

cavity tuned, 433, 435–436

electronically tuned, 335–342

injection-locked, 348, 353, 382, 385

local oscillators, 342

magnetically tuned, 341

noise, 342–343, 350–353

phase-locked, 353–354, 438–448

voltage-controlled, 335–340, 429–431

GUNPPMC (software)

, 518–520, 530, 540

Gyromagnetic ratio, effective

, 236

Gyrotron electron guns

, 508, 509

H

Hairpin bandpass filters

, 180–181

Hairpin curves

, 537, 538

Half-wavelength baluns

, 661

Half-wave line, impedance

, 3

Harmonic generators

, 489–491, 494–495

Harmonic operation, GUNN diodes

, 332–335

HBT, *see* Heterojunction bipolar transistors

Heaters, cathodes

, 516–518

Heat sink, GUNN diodes

, 325

HEMT, *see* High electron mobility

transistors

Heterojunction bipolar transistors (HBT)

, 284–289, 292, 294, 295

- Heterostructure field effect transistors (HFET), 293
- HFET, *see* Heterostructure field effect transistors
- High electron mobility transistors (HEMT), 285, 287, 288, 293–302, 405, 419
- High-pass filters, 156, 163–164, 175, 177–178
- High-perveance hollow-beam guns, 507–508
- High-perveance intercepting gridded guns, 506
- Hollow-beam electron guns, 507–510
- Hybrid grid electron guns, 504, 505
- Hybrid high-pass filters, 175, 177–178
- Hybrid microwave integrated circuits, 95–96
- I
- Ideality factor, diodes, 263
- ILO, *see* Injection-locked oscillator
- Imageguides, 35–42
- Image impedance terminations, 658–660
- Impact-ionization avalanche transit-time (IMPATT) diodes, 276, 280–284, 348, 354, 363–368
- amplifier design, 377–381
- commercial specifications, 373–377
- double-draft IMPATT diodes, 280, 370, 375
- fabrication, 368–373
- noise, 384–386
- oscillator design, 382–386
- Impedance, *see also* Characteristic impedance
- avalanche region, 283
 - capacitors, 114
 - coaxial lines, 6
 - couplers, 214, 223–224, 228
 - detector video impedance, 265
 - diodes, 283, 284
 - drift region, 283
 - half-wave lines, 3
- IMPATT devices
- amplifiers, 378–381
 - oscillators, 382
- load impedance, 624–625, 632, 637–638, 640
- open wire lines, 3
- quarter-wave lines, 3
- quarter-wave transformers, 643–644
- resonant cavities, 329
- short circuit post, 124
- software for, 224
- suspended substrate lines, 145–147, 150–151
- TEM lines, 3, 4
- total device impedance, 284
- waveguides, 13, 15, 23
- Impedance matching, 617
- amplifiers, 630, 631, 656
 - baluns, 660–666
 - narrow-band, 618–640
 - wide-band, 640–660
- Impedance steps, microstrip line, 55–56, 127–128
- Impedance transformations
- complex to real, 632–636, 637–639
 - quarter-wave transformers, 652
 - real to complex, 626–629, 636, 639–640
 - tapered transmission line transformers, 652
- Indirect frequency synthesis, 452–458
- Indium (In), 372
- Indium antimonide (InSb), 308, 309
- Indium arsenide (InAs), negative differential mobility, 309, 310
- Indium phosphide (InP)
- epitaxial growth, 315
 - GUNN diodes, 276, 318–319, 321, 323, 335, 341, 348
 - negative differential mobility, 309, 310
 - properties, 369
 - transferred electron effect, 308
 - transistors, 287, 293–294, 296, 298
- Inductance, 188
- diodes, 263, 273–274, 277, 283
 - effective inductance, 189, 283
 - inductors
 - circular ring, 103
 - ribbon, 97–99
 - round wire, 100, 101
 - spiral, 103, 106
 - package inductance, 277
 - parasitic inductance, 263, 273
 - series inductance, 187
 - short circuit post, 124
 - static series inductance, 128
 - transistors, 301
 - transmission lines
 - coaxial, 7
 - microstrip, 55–58
 - two-wire, 4

- Inductors, 188–191
 capacitance, 99, 101, 106, 109–110
 coupling inductors, 168
 permeability loaded, 195–196
 resistance, 97, 100–103
 ribbon inductors, 96–99
 ring inductors, 101–103
 spiral inductors
 planar circular, 103–107
 planar rectangular and square, 107–111
 wire inductors, 99–101
- Injection-locked oscillators (ILO), 348, 353, 382, 385
- I**
 Input impedance
 dielectric film capacitors, 114
 TEM lines, 3
- Insertion loss, 249, 409
 solid-state devices
 phase shifters, 584
 switches, 569, 571, 573–575
- Insular guides, 44
- Insulated finlines, 28–31
- Integer frequency multiplication (division), 450
- Integral heat sink (IHS) devices, 321–323
- Intensity of magnetization, 235
- Intercepting gridded electron guns, 503, 506, 526, 529
- Interdigital bandpass filters, 181–182
- Interdigitated couplers, 218, 222
- Internal intensity of magnetization, 235
- Internal magnetic field strength, 236
- Invar, 344
- Inverted stripguides, 43, 44
- Isolation
 circulators, 249
 switches, solid-state, 570, 572–575
- Isolators (isocirculators), 254–257, 408–410, 423
- J**
 JFET, *see* Junction field effect transistors
- Josephson junction diodes, 261
- Junction capacitance
 quarter-wave transformers, 651–652
 solid-state devices, 263, 266, 269, 270, 271, 273–275, 276, 571
- Junction diodes, 268, 269, 271
- Junction field effect transistors (JFET), 293
- Junction resistance, diodes, 263, 266, 273, 571–573, 582–583, 586
- Junction-type circulators, 250–254
- K**
- Klystrons, 515–517, 549, 553
- L**
- Lange couplers, 218
- LC-tuned oscillators, 433–434
- Length, open-ended microstrips, 122
- Lighthouse tubes, 589, 591
- Limited space-charge accumulation (LSA) mode, 278–279
- Linear accelerators (linacs), 506, 528
- Linear beam tubes, 497–498
- Line resonators, two-wire, 65–66
- LINMIC + (software), 183
- Liquid-phase epitaxy (LEP), 315
- Litton codes, 519
- Loaded quality factor
 filters, 185
 resonant cavities, 327, 344, 346
 resonators, 62–64
- Load impedance, 624–625, 632, 637–638, 640
- Local oscillators, 342
- Locking bandwidth, 353, 382
- Locking frequency, 353
- Longitudinal electric field, waveguides, 17, 23
- Longitudinal magnetization
 ferrites, 237, 239–240
 waveguides, 15, 23
- Long-period focusing, 552
- Loop coupled harmonic generator, 489, 490
- Loop-gap resonators, 83–85
- Losses, 39–42
 arbitrary loss, 111–115
 bandpass loss, 186
 dielectric film capacitor, 111–115
 dielectric waveguides, 35, 38–42
 dissipation loss, 184–186
 filters, 184–186
 finlines, 34
 insertion loss, 249
 low-pass loss, 185–186
 microstrip lines, 51–52, 192
 mixer conversion loss, 264–265
 suspended substrate technique, 143–153
- Lossless feedback, amplifiers, 411–414
- Lossless matching network, 618

- Low-loss isolators, amplifiers, 408–410
Low-loss lines, 3
Low-noise amplifiers, 392–394, 405–428
 cryogenically cooled, 419, 421
 design, 405–410
 parametric amplifiers, 487
Low-noise electron guns, 505–506
Low-pass filters, 156, 159
 Butterworth approximation, 156–158, 160, 161
 Cauer–Chebyshev approximation, 162–163
 Chebyshev approximation, 159–161
 controlled-phase prototypes, 160–162
 dissipation loss, 185–186
 elliptic approximations, 162–163
 microwave mixers, 484
Low-pass loss, 185–186
Low-pass network, 658–659
Low-power devices, 321–324
LPE, *see* Liquid-phase epitaxy
LSA mode, *see* Limited space-charge accumulation mode
LSC (software), 521, 554, 555
Lumped constant circulators, 251
Lumped-distributed equivalents, distributed filters, 172–174
Lumped-element matching networks, 656–657
Lumped-element microwave integrated circuits
 absorbing microstrip terminations, 131–135
 capacitive components
 dielectric-film overlay capacitors, 111–115
 disk capacitors, 115–118
 series gap capacitors, 118–121
 coaxial-to-microstrip transitions, 136–138
 inductive components
 ribbon inductors, 96–99
 ring inductors, 101–103
 spiral inductors, 103–111
 wire inductors, 99–101
 microstrip discontinuities
 impedance steps, 127–128
 open-ended microstrips, 50, 121–123
 right-angle bends, 128–130
 short circuits, 122, 124–126
 unloaded Q definition, 184–185
Lumped parameter microwave mixers, 484–485, 493
Lumped parameter up-converters, 486
Lumped terminations, 131–135
- M**
- MAGIC (software), 528
Magic-T, 200–201
MAGLENS (software), 558
Magnetically tuned GUNN oscillators, 341
Magnetic centerpost guns, 508–509
Magnetic field
 electron beam focusing, 539–544, 561
 waveguides, 14–17, 23–25
Magnetic flux density, 235
Magnetization, ferrites, 235–241
Magnetron injection guns (MIG), 507
MAGSYN (software), 510, 519
MAGUN (software), 526
MASK (software), 528, 553–554
Matched terminations, 131
Matching networks, impedance testing, 618–666
MATCHNET (software), 657
Maximum device temperature, GUNN diodes, 319
Maximum peak power
 coaxial lines, 7
 rectangular waveguides, 18, 20
MBE, *see* Molecular beam epitaxy
Mechanically tuned oscillators, 433–438
MESFET, *see* Metal semiconductor field effect transistors
Metallization
 inductors
 ribbon inductors, 98–99
 round wire inductors, 99, 100
 spiral inductors, 105, 107, 111
 materials, 371–372
Metal–organic chemical vapor deposition (MOCVD), 316, 368, 370
Metal semiconductor field effect transistors (MESFET), 285, 287, 288, 293–295, 297–302
Micropervance, 500
Microphase phase shifters, 247–248, 252, 253
Microstrip coupled line couplers, 218, 221, 224–225, 232
Microstrip disk capacitors, 115–118

- Microstrip lines, 47–58
 AM detectors, 467, 469–470
 attenuation, 51
 capacitance, 53–58
 characteristic impedance, 48, 49–52, 55
 coaxial-to-microstrip transitions, 136–138
 components
 capacitors, 111–121
 inductors, 96–111
 suspended substrate technique, 143–153
 terminations, 131–135
 cross junction, 58
 discontinuities, 53–58
 impedance, steps, 56–57, 127–128
 open-ended microstrip, 121–123
 right-angle bends, 56–57, 128–130
 short circuits, 122, 124–126
 dispersion, 50–51
 effective dielectric constant, 48, 49–51
 gap, 54–55
 losses, 51–52, 192
 microwave mixers, 483–484, 492–493
 step changes, 55–56, 127–128
 T-junctions, 57
 up-converters, 485, 486
 Microstrip resonant cavity, 327, 330–331
 Microstrip resonators, 86–88
 Microstrip series gap capacitors, 118–121
 Microwave tubes, 497–498
 electron emission, 511–518, 561–562
 MIG, *see* Magnetron injection guns
 Minimum interelectrode spacing, 538
 Minimum noise
 amplifiers, 407, 411
 transistors, 290, 293, 299
 Mismatch attenuation, 159
 Mixed tunnel–avalanche transit-time (MITATT) devices, 365
 Mixer conversion loss, 264–265
 Mixer diodes, 261–268, 478–485
 Mixers, 478–485
 coaxial line mixers, 479–480
 down-converters, 486
 lumped parameter mixers, 484–485
 microstrip line mixers, 483–484
 noise, 487–489
 packaging, 492–494
 up-converters, 485–486
 waveguide mixers, 480–482
 MMBC, *see* Moster–Molnar B-field code
 MMIC, *see* Monolithic microwave integrated circuits
 MOCVD, *see* Metal–organic chemical vapor deposition
 Mod anode electron guns, 502
 Mode, coaxial lines, 8–10
 Mode chart, resonators, 81
 Mode lattice, resonators, 69, 75, 76, 329
 Modeling
 GUNN devices, 313
 transistor design, 292–293, 302
 Moderate bandwidth amplifiers, 392, 393, 395, 426
 Modulation-doped field effect transistors (MODFET), 293–294
 Molecular beam epitaxy (MBE), 315–316, 368, 370
 Monolithic microwave integrated circuits (MMIC), 95–96, 342
 Moreno cross-guide couplers, 212–213
 Moster–Molnar B-field code (MMBC), 550, 551
 Motion detector, 324
 Multihole waveguide couplers, 205–211
 Multilayer couplers, 232
 Multiloop frequency synthesizers, 454
 Multipliers, *see* Frequency multipliers
 Multistage amplifier design, 415–418
 Multistage depressed collectors, 556, 558–559
- N**
- Narrow-band bandpass transforms, 166–171
 Narrow-band impedance matching
 distributed element technique, 626–629, 636–640
 double-stub matching, 622–623
 quarter-wave transformer, 623–626
 single-stub matching, 619–622
 lumped element matching, 629–640
 Negative differential mobility (NDM), 308–313
 Negative resistance devices
 diodes, 276, 277, 279, 280, 282, 363
 history, 308–309
 Network theory, 251
 Nickel (Ni), 369, 372
 Noise
 amplifiers, 384–386, 407, 411, 413, 415–419
 amplitude modulation noise, 487–489

- converters, 487–489
figure circles, 407–409
flicker noise, 488
microwave mixers, 479–485
oscillators, 342–343, 350–353, 428, 439
 GUNN, 342–343, 350–353
 IMPATT, 385
 phase-locked, 439
parametric amplifiers, 487
phase modulation noise, 489
shot noise, 487, 488
tangential signal sensitivity, 463, 488–489
tap noise, 488
thermal noise, 487–488
transistors, 288, 290, 296, 401
Noise temperature ratio, diodes, 265
Nonchamfered symmetric bend, 129–130
Nontransverse electromagnetic mode (non-TEM), 1, 2, 13, 67
Normalized equivalent length, 122
- O**
- Octave band amplifiers, 392–393, 412, 416, 428
Offset-coupled stripline couplers, 218, 220
One loop-one gap resonators, 83–84
One-port reflection resonators, 61–63
Open-end capacitance, 53
Open-ended microstrips, 50, 121–123
Open ring resonators, 87–88
Open wire lines, 1, 3, 5
Optimum chamfer, 130
Oscillation, 308, 591
Oscillator frequency, resonant cavities, 327–328
Oscillators, 428–429
 cavity-stabilized oscillators, 342–346, 433, 435–436
 electronically tuned oscillators, 335–342, 429–433
 free-running oscillators, 429, 438
 frequency multipliers, 458–460
 frequency synthesizers, 448–458
 GUNN oscillators, 307, 324, 325–346
 bias-tuned, 340–341
 injection-locked, 348, 353, 382, 385
 local oscillators, 342
 magnetically tuned, 341
 IMPATT diodes, 382–384
 LC tuned oscillators, 433, 434
mechanically tuned oscillators, 433–438
noise, 342–343, 350–353, 428, 439
phase-locked oscillators, 353–354, 438–448
pulsed IMPATT oscillators, 374, 376
switched oscillators, 451
triode oscillators, 591
voltage-controlled oscillators, 335–340, 429–431
yttrium iron garnet tuned oscillators, 341, 429–430, 432–433
- Oxide cathodes, electron emission, 515–516
- P**
- Package capacitance, 277, 571
Packaged transistors, 402
Package inductance, 277
Packaging, 491–495
Palladium (Pd), 369, 372
Pancake heaters, 517
PANDIRA (software), 518–520, 528
Parallel capacitance, 128
Parallel capacitors, bandpass filters, 167–168
Parallel-coupled half-wave resonators, 179–180
Parallel resonators, bandpass filters, 166–168
Parametric amplifiers, 487
Paraphrase amplifiers, 663–666
Parasitic capacitance
 diodes, 263, 271, 273
 transistors, 413
Parasitic inductance, diodes, 263, 273
Parasitic resistance
 diodes, 271
 inductors, 101, 107, 110–111
Pass-band characteristic, transformers, 641
Pass-band ripple, 159
Passive baluns, 660–661, 663
Peak power rating, waveguides, 18, 20, 27
Peltier cooling, 419
Percentage bandwidth, bandpass filter
 prototypes, 164
Periodic permanent magnet (PPM) focusing, 540–544, 547
Permeability, core, 195
Permeability loaded inductors, 195–196
Permeability tensor, ferrites, 235–236
Permittivity, suspended substrate lines, 145, 147–149, 152–153
Perveance, 499–500, 537
Phase comparators, 472

- Phase constant, TEM lines, 3
 Phase-error ripple, 161
 Phase-locked oscillators
 cavity oscillators, 444–445
 coaxial resonator oscillators, 445, 446
 dielectric resonator oscillators, 445, 447
 GUNN oscillators, 353–354
 noise, 353–354, 438–448
 VCXOs, 443–444
 Phase lock loop integrated circuits (PLL IC),
 470, 472–473
 Phase modulation (PM) detectors, 477–478
 Phase modulation (PM) noise, 489
 Phase noise, 433, 452
 Phase shifters, 241–248, 582–586
 Phase shift keying (PSK) detectors, 477–478
 Phase velocity
 coaxial lines, 7
 waveguides, 15, 23
 Phosphorus (P), 371
 PIC codes, 528, 530, 553–555
 Pierce electron guns, 498–504, 529
 current density, 513–514
 design, 530–539
 field enhancement, 538
 synthesis codes, 519
 PIERCE (software), 519, 531
 Pinch-off voltage, 270, 271, 401
 PIN diodes, 272–276, 489
 packaging, 491–492
 solid-state devices
 attenuators, 586–588
 switches, 569–582
 Planar circular spiral inductors, 103–107
 Planar dielectric-film overlay capacitors,
 111–115
 Planar field, computer simulation, 183–184
 Planar rectangular spiral inductors, 107–111
 Planar ribbon inductors, 96–99
 Planar ring inductors, 101–103
 Planar square spiral inductors, 107–111
 Platinum (Pt), 369, 372
 PLL IC, *see* Phase lock loop integrated
 circuits
 PM detectors, *see* Phase modulation
 detectors
 PM HEMT, *see* Pseudomorphic high
 electron mobility transistors
p-n diodes, 266
p-n junction varactors, 268, 269, 271
 Point-contact diodes, 261, 262
 POISSON (software), 518–520, 528, 551
 Poisson's equation, 522–523, 526
 Polarizers, phase shifters, 245
 Polystyrene, 48
 Potted heaters, 505, 516
 Power-added efficiency, transistors, 290, 294,
 295, 299–300
 Power amplifiers, 423–428
 Power capability, rectangular waveguides,
 18–22
 Power combining, 354–356, 381
 Power-current ratio, 13
 Power density
 GUNN diodes, 319–320
 transistors, 288, 295
 Power dividers, 423, 424
 Power limiters, yttrium iron garnet, 257
 Power transmission coefficient, 64
 Power-voltage ratio, 13
 PPMFLD (software), 558
 PPM focusing, *see* Periodic permanent
 magnet focusing
 PPMG00 (software), 518, 519
 Probe coupled harmonic generators, 490
 Propagation constants
 finlines, 29, 32–33
 imageguides, 35–38
 TEM lines, 3
 waveguides
 circular, 23
 dielectric, 35–38
 rectangular, 15
 Pseudomorphic high electron mobility
 transistors (PM HEMT), 294, 296, 297,
 405
 PSK detectors, *see* Phase shift keying
 detectors
 Puck, 436
 Pulsed IMPATT oscillators, 374, 376
Q
 Quadrature hybrids, 200
 Quadruple detectors, 462–463
 Quality factor (*Q* factor)
 capacitor, dielectric film, 114, 115
 coaxial lines, 7
 conductor quality factor, 7
 diodes, 27
 dynamic quality factor, 270

- inductors
 - ribbon inductors, 98
 - round wire inductors, 100
 - spiral inductors, 107, 111
- loaded
 - filters, 185
 - resonant cavities, 327, 344, 346
 - resonators, 62–64
- resonators, 61, 63–65, 67, 88
- unloaded
 - capacitors, 187–188
 - filters, 184–185
 - inductors, 189–191
 - resonant cavities, 327, 328, 341
 - resonators, 61–63, 65, 67, 88, 191–192
 - surface acoustic wave (SAW) devices, 197
 - waveguides, 192–193
- Quantum-well injection transit-time (QWITT) diodes, 365, 370
- Quarter-wavelength baluns, 661
- Quarter-wave line, impedance, 3
- Quarter-wave plates, phase shifters, 245
- Quarter-wave transformers, impedance matching, 623–626, 640–652
- Quartz, 48, 95
- Quasi-TEM mode, 191–192
 - couplers, 216, 229
 - phase shifters, 247, 253–254
- QWITT diodes, *see* Quantum-well injection transit-time diodes
- R**
- Radio frequency choke (RFC)
 - detectors, 464, 466, 470
 - microwave mixer, 481
- Rat-race couplers, 229–232
- Rat-race hybrid, 201
- RDEMEOS (software), 525, 529
- Reactance
 - capacitors, 187
 - shunt inductors, 632
 - variable, varactor diodes, 268–272
- Reaction mode (resonators), 474, 476
- Reaction-type cavity-stabilized GUNN oscillators, 343, 346
- Read diodes, 368
- Real frequency technique, 657
- Real to complex impedance transformation, 626–629, 636, 639–650
- Reciprocal dual-mode phase shifters, 244–245
- Rectangular-cavity GUNN oscillators, 326, 328–330, 336, 337
- Rectangular disk capacitors, 116–118
- Rectangular ring inductors, 101–103
- Rectangular spiral inductors, 107–111
- Rectangular waveguides, 14–22
 - attenuation, 18
 - cavities, 68–72
 - dielectric, 35, 38–39
 - equations, 15
 - phase shifters, 241–243, 246–247
- Rectification
 - AM detectors, 461
 - diodes, 265, 266
- Reentrant coaxial cavity resonators, 67–68
- Reflection coefficient, 62
- IMPATT devices, 377, 380
- oscillators, 347
- TEM lines, 3
- transformers
 - quarter-wave, 643, 645, 647
 - tapered transmission line, 652, 654, 655
- transistors, 407
- Reflection gain, 347, 377
- Reflection resonators, one-port, 61–63
- Reflection type cavity-stabilized GUNN oscillators, 343–345
- Reggia–Spence phase shifters, 246–247
- Relative chamfer, 130
- Resistance
 - detectors, 462, 463
 - diodes, 263, 266, 270–271, 273, 275, 582–583, 586
 - inductors, 97, 100–103
 - junction resistance, 263, 266, 273, 571–572, 582–583, 586
 - parasitic resistance, 101, 107, 110–111, 271
 - series resistance, 263, 267, 270, 271, 273
 - spreading resistance, 582
 - transistors, 301
- Resistivity
 - direct grounded lumped termination, 132
 - ribbon inductors, 98
- Resistors
 - microstrip terminations, 131–135
 - sensitors, 419
 - variable, PIN diodes, 274
- Resonance, 65, 251–252

- Resonance frequency
 inductors, 110, 190
 resonators, 67–68, 72, 73, 83–85, 87–89, 196, 341, 344–345
- Resonance isolators, 255
- Resonant cavities, 326, 329
- Resonant cavity combiners, 354–355
- Resonant frequency, free-space resonant frequency, 328–329
- Resonators
 circular cylindrical waveguide cavities, 73–80
 coaxial resonators, 66–68, 196, 433, 436–437, 445, 446
 dielectric resonators, 80–83, 196, 436–438
 distributed, 191–192
 Fabry–Perot resonators, 88–89
 ferrites, 256
 filters
 bandpass filters, 166–170
 distributed filters, 178–180
 lighthouse tubes, 589–591
 loop-gap resonators, 83–85
 microstrip resonators, 85–88
 microwave FM detectors, 474–475
 one-port reflection resonators, 61–63
 open-ended microstrips, 121
 rectangular waveguide cavities, 68–72
 traveling-wave resonators, 90
 two-port transmission resonators, 63–65
 two-wire line resonators, 65–66
 yttrium iron garnet resonators (YIG), 89–90, 256
- Return loss ripple, 159
- Reverse-bias operation, diodes, 271, 272, 274, 282, 582–583
- Reversed-phase couplers, 211–212
- RFC, *see* Radio frequency choke
- Ribbon inductors, 96–99
- Riblet short-slot couplers, 211
- Richardson–Dushman equation, 511
- Right-angle bend, microstrip lines, 56–57, 128–130
- Ring detectors, 462
- Ring inductors, 101–103
- Ripple, 159–161
- Roberts balun, 665
- Round metal post, short circuiting, 124–126
- Round wire inductors, 99–101
- S**
- Sapphire
 dielectric film capacitors, 111–112
 dielectric substrate, 48, 95
- SAW devices, *see* Surface acoustical wave devices
- Scalar permeability, 236, 237
- Scaling, filter prototype values, 157–159
- Scaling factor, imageguide, 40, 41
- Scattering matrix, directional couplers, 200, 214
- Scattering parameters, dielectric couplers, 217
- Schottky-barrier diodes, 261–268, 463, 465
 packaging, 491–492
- Schottky varactors, 268–269, 271
- Schwinger reversed-phase couplers, 211–212
- Screw tuners, 327, 345, 465
- SDHT, *see* Selectively doped heterostructure field effect transistors
- Secondary emission, 511, 512–513, 559–560
- Selectively doped heterostructure field effect transistors (SDHT), 294
- Selenium (Se), 372
- Self-resonance frequency, spiral inductors, 106–107
- Semiconductor devices
 diodes
 GUNN diodes, 276–280
 IMPATT diodes, 280–284
 mixer and detector diodes, 261–268
 PIN diodes, 272–276
 varactor diodes, 268–272
 history, 308–309
 microwave mixers, 478–485
 transistors, 419, 432
 bipolar junction transistors, 284–293, 495
 field effect transistors, 293–302
 varactors, 335
- Semiconductors, negative differential mobility, 309
- Sensitors, 419
- Series diode detectors, 461–462
- Series gap capacitors, 118–121
- Series inductance, 198
- Series-operation combiners, 355–356
- Series resistance, diodes, 263, 267, 270, 271, 273

- Series resonators, bandpass filters, 169–170
Series stubs, 621
SFPMIC + (software), 184
Shadow-gridded electron guns, 502–504, 505, 514
Short circuits, microstrips, 122, 124–126
Short-slot couplers, 211
Shot noise, 487, 488
Shunt diode detectors, 461–462
Shunt stubs, 619
Silica (SiO_2), dielectric film capacitor, 111–112
Silicon (Si)
 dielectric substrate, 48
 diodes, 261, 262, 266, 268, 280–281, 373, 374, 463, 465
 IMPATT oscillators, 386
 metallization, 371
 properties, 369
 transistors, 284–286, 288, 289–293
Silver (Ag), 19, 372
Simulation
 electron beam collection, 552–553
 electron gun design, 502–503, 505–508
 filter design, 182–184
 GUNN devices, 312
 transistor design, 292–293
Single-drift IMPATT diode, 280, 370
Single-hole coupler, 205
Single-loop frequency synthesizer, 453–454, 455
Single pull double throw (SPDT) switches, 569–570, 575–577, 579, 581
Single pull multiple throw (SPMT) switches, 569–570, 577, 578, 581
Single pull single throw (SPST) switches, 569–571, 573–575, 581
Single-stage amplifiers, 407, 409
Single-stage collectors, 552–553
Single-stub impedance matching, 619–622
SIS junction diodes, *see*
 Superconductor-insulator-superconductor junction diodes
Skin depth, 65, 98
Slot-coupled stripline couplers, 218
Smith chart, 621, 623, 630
Software
 amplifier design, 421
 cathode design, 517
 electron beam focusing systems, 550–551
 electron beam optical design codes, 518–530
 electron gun design, 502
 filter design, 183, 184
 impedance and dielectric constants, 224
 matching network synthesis, 657
Solenoidal focusing, 548–551
Solenoids, 188–191
SOLENOID (software), 551
Solid-state devices
 attenuators, 586–588
 diodes
 GUNN diodes, 276–280, 307, 316–325, 332–334, 337, 342, 354, 424–435
 IMPATT diodes, 280–284, 348, 354, 363–386
 mixer and detector diodes, 261–268, 461, 463, 465, 467, 471, 491–492
 PIN diodes, 272–276, 489, 491–492
 varactor diodes, 268–272, 487, 490, 582–587
 phase shifters, 241–248, 582–586
 switches, 569–582
 SPDT, 569–570, 575–577, 579, 581
 SPMT, 569–570, 577, 578, 581
 SPST, 569–571, 573–575, 581
 transfer switches, 577–579, 581
 transistors, 419, 432
 bipolar junction transistors, 284–293, 405
 field effect transistors, 293–302
 vacuum triodes, 616
Solution splicing, 544–547
SOS (software), 528
Space-charge balanced flow focusing, 549
S-parameters, 398–404, 584
Spent beam collectors, 553–556
Spin-wave manifolds, 236
Spiral inductors, 103–111
Splicing, 544–545
Spreading resistance, 582
Spurious outputs, 452–453
Square spiral inductors, 107–111
Square waveguides
 phase shifters, 244–246
 resonators, 69
SSO (software), 518, 521
Stabilization factor, 343

- Standing-wave ratio
phase shifter, 584
resonators, 64
TEM lines, 3
- Static series inductance, 128
- STB (software), 518, 521
- Stepped impedance low-pass filters, 175–177
- Steps, microstrip lines, 55–56, 127–128
- Straight planar ribbon inductors, 96–99
- Strip conductors, 96–99
- Stripline phase shifters, 247–248, 250, 252, 253
- Stub matching, 619–623
- Substrates
ceramics, 194, 195
dielectric, 48, 95
- Super Compact (software), 421
- Superconductor–insulator–superconductor (SIS) junction diodes, 261
- Surface acoustical wave (SAW) devices, 196–197
- Surface resistivity
direct grounded lumped terminations, 132
ribbon inductors, 98
- Suspended substrate technique, 143–153, 218
- Sweepers, GUNN voltage-controlled oscillators, 341–342
- Switched oscillators, 451
- Switches
ferrite, 257–258
SPDT, 569–570, 575–577, 579, 581
SPMT, 569–570, 577, 578, 581
SPST, 569–571, 573–575, 581
transfer switches, 577–579, 581
- Switching cutoff frequency, diodes, 273–274
- Symmetric bandpass transform, 172
- Symmetric couplers, 214–216
- Symmetric series gap capacitors, 119–120
- Symmetric transform filters, 169–170
- Synthesizers, *see* Frequency synthesizers
- T**
- Tangential signal sensitivity, 463, 488–489
- Tantalum oxide (Ta_2O_5 , dielectric film) capacitors, 112
- Tapered baluns, 660, 662
- Tapered couplers, 216
- Tapered transmission line transformers, 652–656
- Tap noise, 488
- TBCATH (software), 517
- TEGFET, *see* Two-dimensional electron gas field effect transistors
- Tellurium (Te), 372
- TEM, *see* Transverse electromagnetic mode
- TE mode
circular waveguide, 23, 27
coaxial line, 8–9
dielectric resonators, 81
rectangular waveguide, 14, 15, 18–22
waveguide cavities, 70–80
- Terminations
image impedance, 658–660
microstrip, 131–135
- Tetrodes, thermionic, 606–616
- Thermal beam model, electron guns, 536
- Thermal noise, 487–488
- Thermionic emission, 511–512
- Thermionic tetrodes, 606–616
- Thermionic triodes, 589–605
- Thin-film capacitors, 111
- Three-branch couplers, 225–228
- Three-dimensional simulation, filter design, 184
- Three loop-two gap resonators, 85
- Three-port circulator, 249–250
- Threshold critical field, 237
- TIMs, 426
- Tin (Sn), 372
- Titanium (Ti), 369, 372
- T-junctions
microstrip line, 57
microwave mixer, 481
- TMLBMC (software), 518, 519, 530–531, 533–535
- TM mode
coaxial lines, 8, 9
waveguide cavities, 70–80
waveguides, 15, 18, 23, 27
- Top-C-coupled bandpass filters, 166–168, 171
- Top-C-coupled distributed resonators, 175, 178
- Top-L-coupled bandpass filters, 168–169, 171–172
- Toroidal phase shifters, 241–243
- Toroid cores, 195–196
- Total amplitude modulation noise, 488
- Total capacitance, diodes, 263, 273
- Total device impedance, 284

- Total node capacitance, bandpass filters, 167
Transconductance, 594, 597
Transferred electron devices, 307–308
 amplifiers, 346–350
 design and fabrication, 313–325
 GUNN diodes, 276–280, 301, 313–325
 GUNN oscillators, 324, 325–346
 history, 308–309
 negative differential mobility, 308–313
 noise characteristics, 350–354
 power combining techniques, 354–356
Transferred electron effect, 276, 277, 308
Transfer switches, 577–579, 581
Transformers
 balanced to unbalanced, *see* Baluns
 quarter-wave transformers, 623–626,
 640–652
 binomial, 641–645
 Chebyshev, 645–651
 tapered transmission line transformers,
 652–656
Transistors
 amplifier design, 394–402, 405, 407, 426
 biasing, 396–397
 BJT, 284–293, 405, 419, 432
 capacitance, 301
 chip transistors, 403
 collector efficiency, 288
 computer-aided design, 292–293, 302
 cutoff frequency, 286, 290, 299
 FET, 293–302, 419, 432
 gallium arsenide, 284, 285, 287, 288,
 293–295, 297, 298, 300, 302, 405, 419
 HBT, 284–289, 292, 294, 295
 HEMT, 285, 287, 288, 293–302, 405, 419
 HFET, 293
 JFET, 293
 matched, 426
 MESFET, 285, 287, 288, 293–295, 297–302
 MODFET, 293–294
 packaged, 402
 PM HEMT, 294, 296, 297, 405
 power density, 288, 295
 resistance, 301
 SDHT, 294
 TIMs, 426
 ULTRA HEMT, 405
 voltage, 401
Transitions, coaxial to microstrip, 136–138
Transit-time devices, 363–365
 BARITT, 261, 364, 365
 DOVETT, 365
 IMPATT, 276, 280–284, 348, 354, 363–386
 MITATT, 365
 QWITT, 365, 370
 TRAPATT, 365
 TUNNETT, 364, 365
Transmission lines, 1
 characteristic conductance, 62
 coaxial lines, 1, 5–13
 couplers, 213
 dielectric waveguides, 34–44
 finlines, 28–34
 lumped distributed equivalents, 172–174
 microstrip lines, 47–58, 131, 135, 143–153
 tapered, 652–656
 two-wire lines, 2, 4, 12–13
 waveguides, 13–28
Transmission resonance method, 271, 474,
 476
Transmission resonators, two-port, 63–65
Transmission-type cavity-stabilized GUNN
 oscillators, 343, 345
Transverse electric field, waveguides, 17, 23
Transverse electromagnetic mode (TEM),
 1–2, 191–192
 coaxial line mode, 8, 9
 coaxial line resonators, 67
 couplers, 216, 223
 dielectric loaded TEM mode, 196
 equations, 2, 3
Transverse magnetic field, waveguides, 15,
 23
Transverse magnetization, in ferrite medium,
 237–239
Transverse split, microstrip line, 55
Trapped imageguide, 42–43
Trapped-plasma /avalanche-triggered
 transit-time (TRAPATT) devices, 365
Triangular distribution taper, 653–654
Triodes, thermionic, 589–605
TRUE103 (software), 518, 521, 554, 556, 557
TSS, *see* Tangential signal sensitivity
Tubular bandpass filters, 170
Tuner screws, 327, 345, 465
Tuning capacitor diodes, 583
Tunnel emittance, 520–521, 536–537, 546,
 547, 556

- Tunnel injection transit-time (TUNNETT) diodes, 364, 365
- Twin-slab phase shifters, 243
- Two-branch couplers, 224–226, 228
- Two-dimensional electron gas field effect transistors (TEGFET), 293–294
- Two loop-one gap resonators, 84–85
- 2.5D simulators, 184
- Two-port transmission resonator, 63–65
- Two-wire lines, 2
- AM detectors, 463–465
 - attenuation, 12–13
 - capacitance, 4
 - equations, 2, 12–13
 - resonators, 65–66
- Type M cathode, 515
- U**
- Ultra high electron mobility (ULTRA HEMT) transistors, 405
- Ultra-low-noise amplifiers, 415, 428
- Ultra-wide-band amplifiers, 394, 413, 414
- Uniform field focusing, 544–547
- Uniform mesh (UM) gun codes, 522–523, 525, 530
- Unilateral finlines, 28–34
- Unilateral gain, transistors, 290
- Unloaded quality factor
- capacitors, 187–188
 - filters, 184–185
 - inductors, 189–191
 - resonant cavities, 327, 328, 341
 - resonators, 61–63, 65, 67, 88, 191–192
 - surface acoustic wave (SAW) devices, 197
 - waveguides, 192–193
- Up-converters, 485–486
- V**
- Vapor-phase epitaxy (VPE), 314–315
- Varactor diodes, 268–272
- commercial, 587
 - harmonic generator, 490
 - parametric amplifiers, 487
 - phase shifters, 582–586
- Varactors, 335
- Schottky varactors, 268–269, 271
- Varactor-tuned oscillators, *see* Voltage-controlled oscillators
- VARGUS (software), 528
- Variable reactance devices, varactor diodes, 268–272
- VCO, *see* Voltage-controlled oscillators
- VCXO, *see* Voltage-controlled oscillators, crystal
- Velocity-field characteristics, GaAs, 310–312
- Vertical-coupled stripline couplers, 218
- VHF fine-tune frequency, 451
- Video impedance, detectors, 265
- Virtual grounded lumped terminations, 134–135
- Voltage**
- bias voltage, 277, 281, 282, 582
 - couplers, 214
 - direct wave voltage, 214
 - direct wave, 214
 - pinch-off voltage, 270, 271, 401
 - transistors, 401
- Voltage-controlled oscillators (VCO), 335–340, 429–431
- crystal oscillators (VCXO), 442–444
 - FM detectors, 470, 472–473
- Voltage coupling coefficient, 214
- Voltage-current ratio, 13
- Voltage standoff, electron guns, 538
- VPE, *see* Vapor-phase epitaxy
- W**
- Wafer capacitors, 111
- Waveguide aperture couplers, 201–213
- Bethe-hole couplers, 202–205
 - Moreno cross-guide couplers, 212–213
 - multihole waveguide couplers, 205–211
 - Riblet short-slot couplers, 211
 - Schwinger reversed-phase coupler, 211–212
- Waveguide branch-guide couplers, 223, 225
- Waveguide cavities, 68–80
- Waveguide devices
- AM detectors, 465–468, 492
 - circulators, 249–254
 - couplers, 201–213, 223, 225
 - harmonic generator, 489–490
 - IMPATT amplifiers, 379
 - isocirculators, 254
 - microwave mixers, 480–482, 492–493
 - phase shifters, 241–248
 - resonators, 69
 - up-converters, 485, 486

Waveguides, 13–14, 192–193
 circular, 14, 22–28, 244–246
 dielectric, 34–43
 ferrites, 238–240
 impedance, 13, 15, 23
 magic T, 201
 rectangular, 14–22, 35, 38–39, 241–243,
 246–247
 square, 69, 244–246
Wavelength
 microstrip line, 48, 49, 49–50
 waveguides, 15, 23
Whisker diodes, 261–264, 269
Whispering gallery mode dielectric
 resonators, 83
Wide-band amplifiers, 405, 414, 657, 658
Wide-band impedance matching, 640–660
 image impedance terminations, 658–660
 matching networks, 656–658
 multisection quarter-wave transformers,
 640–652
 tapered transmission line transformers,
 653–656

Wide-band matching networks, 656–657
Wide-band tapered baluns, 660, 662
Wilkinson power dividers, 423, 424
Winding capacitance, spiral inductors, 106,
 109–110
Wire inductors, 99–101

Y

YIG devices, *see* Yttrium iron garnet devices
Y-junction circulators, 251–254
Yttrium iron garnet (YIG) devices
 ferrites, 256–257
 filters, 256–257
 oscillators, 341, 429–430, 432–433
 power limiters, 257
 resonators, 89–90, 256

Z

Zig-zag transformation, 170–171
Zinc (Zn), 369, 371, 372
Zinc selenide (ZnSe), 276, 309
ZY Smith chart, 630

ISBN 0-12-374696-5



90038

9 780123 746962